Lalit M. Pandey
Raghvendra Gupta
Rajkumar P. Thummer
Rajiv Kumar Kar *Editors*

Healthcare Research and Related Technologies

Proceedings of NERC 2022

Springer

Healthcare Research and Related Technologies

Lalit M. Pandey · Raghvendra Gupta ·
Rajkumar P. Thummer · Rajiv Kumar Kar
Editors

Healthcare Research and Related Technologies

Proceedings of NERC 2022

Springer

Editors
Lalit M. Pandey
Department of Biosciences
and Bioengineering
Indian Institute of Technology Guwahati
Guwahati, Assam, India

Rajkumar P. Thummer
Department of Biosciences
and Bioengineering
Indian Institute of Technology Guwahati
Guwahati, Assam, India

Raghvendra Gupta
Department of Chemical Engineering
Indian Institute of Technology Guwahati
Guwahati, Assam, India

Rajiv Kumar Kar
Jyoti and Bhupat Mehta School of Health
Sciences and Technology
Indian Institute of Technology Guwahati
Guwahati, Assam, India

Foreword

It is a matter of great satisfaction for me that Indian Institute of Technology Guwahati successfully hosted North-East Research Conclave (NERC) 2022 during May 20–22, 2022. The NERC 2022 was conducted on the theme "Sustainable Science and Technology." Concurrently, Assam Biotech Conclave (ABC) was also organized from May 21–22, 2022. Both the events attracted huge participation from policy-makers, researchers, industrialist, army, and students. Even the participation of school children was overwhelming.

NERC and ABC had many events, including panel discussions, exhibitions, keynote lectures, competitions, and paper presentations. Presentation of technical papers form the core of any research conference. NERC attracted 879 research papers on various themes, covering science, technology, and humanities. Out of these, some select papers have been published by Springer Nature in the form of 15 volumes. These papers have been peer reviewed and thoroughly edited by Indian Institute of Technology Guwahati faculty members. I am sure that these volumes will prove to be excellent resource material for research. Most of the papers presented in these

volumes highlight the special needs and aspiration of eight states of North-East India. I congratulate and thank authors, reviewers, editors, and publisher for publishing the proceedings.

Motivation for organizing NERC came from none other than the Honorable Minister of Education, Government of India, Shri Dharmendra Pradhan Ji. It helped to bring policy-makers, researchers, industrialists, academicians, students, and children in one forum. It is perhaps the rarest conclave covering almost all possible research themes. For better readability the proceedings have been divided into 15 volumes, but each volume reflects diversity in terms of topics and researchers. Only common thread is sustainable development of North-East India. Invariably, sustainable North-East India is a prerequisite for sustainable India and the whole world. In that sense, these 15 volumes will serve guiding and stimulating light for all the stakeholders of the development. I am pleased to dedicate these volumes to the nation as a part of Azadi ka Amrit Mahotsav.

<div align="right">

T. G. Sitharam
Chairman
All India Council for Technical
Education
New Delhi, Delhi, India

</div>

Preface

This book volume aims to focus on the intersection of healthcare and technology-related scientific communication and exchange of the North-East Research Conclave (NERC) 2022, held at the Indian Institute of Technology Guwahati. Overall, there were 36 oral presentations in all five sessions along with a large number (92) of posters for this track (Healthcare Research and Related Technologies). The collection of chapters highlights the latest research and development trend in this field. With the rapidly growing technological interventions, several advancements in diagnostics, intervention, therapeutics, and overall healthcare services have been witnessed. Nevertheless, these advancements are not emerging from a single branch of basic science or engineering but are an amalgamation of fundamental and applied innovations. In our recent experience of unprecedented health challenges, including the COVID-19 pandemic, we realized that the term 'related technology' became indispensable for exploring possible healthcare solutions. In line with this theme, the topics explored in this volume have become increasingly important and practically relevant.

The chapters in this volume cover a wide range of healthcare topics, focusing on broad bioengineering applications like *Biomaterials and Tissue Engineering*, *Biomedical Science and Engineering*, *Drug Delivery and Therapeutics* and *Cell and Molecular Biology*. These fields are the cutting-edge deliverables of innovative solutions that have been explored for several decades. More importantly, it will contribute to the ongoing conversation on how the technology can be harnessed and leveraged to improve community health and deliver allied technology as services. Be that as it may, looks promising; still, several developments are required to address health challenges, such as replacing damaged cell, tissues and organs, improving drug delivery systems, and using novel bio-compatible materials. The chapters relevant to these topics provide a comprehensive overview of such advancement. It also showcases cutting-edge research having the potential to transform the way we view healthcare.

In addition to the above sections, the volume also features chapters on vital health science and technology areas, including cell and molecular biology, biomaterials, biomedical devices, nanomedicine, and drug delivery. In particular, molecular

biology has been exploited for the upregulation and downregulation of key bio-macromolecules. Biomaterials have been designed for the better healthcare. Biosensors have revolutionized healthcare diagnostics by introducing point-of-care technology. Though the field is interdisciplinary, it can integrate analytical chemistry, biophysics, and material science to gain critical information concerning treatment decisions. Drug delivery is another required field that has gained significant research interest aiming to bring new methods for increased efficiency, efficacy, and safe use of drugs. Finally, nanotechnology emerged as a vantage point for integrating new therapeutics, diagnostics, and interventions for improved healthcare delivery.

Besides the experimental measurements, a few chapters in this volume explore the role of computational algorithms and simulations in bioengineering and healthcare technology. The chapters demonstrate the state-of-art classical phenomenon, quantum information, and optimization of concepts that interface between quantum-classical regimes. It provides insights into complex biological processes, progression of neurodegenerative diseases like Alzheimer, predicts biomaterials' behaviour and optimizes medical device design. The increased application of data analytics is reflected in these chapters. It showcases the latest examples of how simulations can help solve critical healthcare technology problems, and we believe it will be of great interest to researchers in this field.

Overall, we are excited to showcase the advancement in these fields brought by researchers and scholars from the North-Eastern part of India. We hope this volume will be a valuable resource for our comprehensive and sophisticated readers (including researchers, students alike, and practitioners). We believe the compiled book chapters will inspire further research and innovation in the future. We express great gratitude to all the authors who contributed to making this publication successful.

Guwahati, India

Lalit M. Pandey
Raghvendra Gupta
Rajkumar P. Thummer
Rajiv Kumar Kar

About This Book

This volume mainly covers the research related to healthcare and related technologies. It includes board bioengineering applications divided into four parts namely *Biomaterials and Tissue Engineering*, *Biomedical Science and Engineering*, *Drug Delivery and Therapeutics*, and *Cell and Molecular Biology*. The book encompasses the latest research and advancements related to healthcare and related technologies. A few studies based on computer simulations in bioengineering are also described. In addition, the fundamental and basic aspects are also discussed for the better understanding of readers.

About IIT Guwahati

Indian Institute of Technology (IIT) Guwahati established in 1994 has completed 25 years of glorious existence in 2019. At present, the Institute has 11 departments, seven inter-disciplinary academic centres and five academic schools covering all the major engineering, science, healthcare, management and humanities disciplines, offering B.Tech., B.Des., M.A., M.Des., M.Tech., M.Sc., and Ph.D. programmes. The institute presently offers a residential campus to 435 faculty members and more than 7,500 students at present. Besides its laurels in teaching and research, IIT Guwahati has been able to fulfil the aspirations of people of the North-East region to a great extent since its inception in 1994. The picturesque campus is on a sprawling 285 hectares plot on the north bank of the Brahmaputra, around 20 kms from the heart of the Guwahati city.

IIT Guwahati is the only academic institution in India that occupied a place among the top 100 world universities—under 50 years of age—ranked by the London-based Times Higher Education (THE) in the year 2014 and continues to maintain its superior position even today in various International Rankings. IIT Guwahati gained rank 37 globally in the 'Research Citations per Faculty' category and overall 384 rank in the QS World University Rankings 2023 released recently. IIT Guwahati has retained the 7th position among the best engineering institutions of the country in the 'India Rankings 2021' declared by the National Institutional Ranking Framework (NIRF) of the Union Ministry of Education. IIT Guwahati has been also ranked 2nd in the 'Swachhata Ranking' conducted by the Government of India. Recently, IIT Guwahati has been ranked as the top-ranked University in 2019 for IT developers by HackerRank in the Asia-Pacific region.

Among other frontier areas of research and innovation, IIT Guwahati is working towards augmenting critical science research initiatives in Genomics, Developmental Biology, Health Care and Bioinformatics, Flexible Electronics, Advanced Functional Materials, Sustainable Polymers, Rural Technologies, Renewable Energy, Artificial Intelligence, Disaster Resilience and Risk Reduction, and Water Resources and Management. In its silver jubilee year, IIT Guwahati is poised to scale newer heights through all-round growth and development.

Indian Institute of Technology Guwahati has dedicated itself to the cause of improving and empowering North-East India through cutting-edge research, region relevant projects, innovations, individual and multilateral collaborations, and special initiatives. Being the only IIT in the entire North-Eastern region, IIT Guwahati has an immense amount of responsibility to develop the region and empower the people of the region.

While the entire country is celebrating the 'Azadi ka Amrit Mahotsav'—75 glorious years of Independence, and the great pride with which our nation of more than a billion people has been steadily growing today, IIT Guwahati is strongly committed to support that pace of growth for the entire NE so that we can keep pace along with the rest of the country. The specific areas of focus where IIT Guwahati has been contributing immensely to the region are:

(a) Infrastructure development across multiple sectors,
(b) Providing solutions for multiple natural disasters such as recurring floods, landslides, earthquakes, cyclones, hailstorms and other natural calamities,
(c) Improving the education sector and creating opportunities for employment,
(d) Internet, telecommunication and cultural integration,
(e) Technological intervention in interdisciplinary areas,
(f) Healthcare services and education,
(g) Renewable energy generation (solar, wind, biomass, hydro, geothermal),
(h) Overall industrialization, refining fossil fuels and setting up biorefineries.

Besides bringing in the state-of-the-art technical knowhow for most of the above sectors, the institute has been partnering with the local governments and enhancing the technological and educational interactions such that the next generation youth are empowered with knowledge, skills and necessary entrepreneurial ability. These measures in Assam as well as all other North-East states will usher in a new era of growth and the opportunities it will provide for interaction with the ASEAN countries as part of the Act East Policy of the Government of India that will bring prosperity to this region.

Prof. Parameswar K. Iyer
Dean, PRBR
Indian Institute of Technology Guwahati
Guwahati, India

North East Research Conclave-2022: Toward Sustainable Science and Technology

It is extremely important and imperative to have knowledge-driven growth based on innovation in the case of academic higher education institutes of high repute. The North-Eastern region endowed with rich biodiversity comprises eight states. However, the climatic conditions, limited connectivity, lack of research infrastructure and institutes, territorial conflicts, and the mountainous terrain of these regions are major impediments to the research ecosystem in the North-East. Quality higher education focusing on industry-academia collaboration and translational research is extremely beneficial for society. It has also been rightly pointed out by the Hon'ble Prime Minister Shri Narendra Modi that, "*India cannot develop till Eastern India develops*".

With this idea and as India marks 75 years of Independence, Indian Institute of Technology Guwahati organized "The North-Eastern Research Conclave" from 20 to 22 May 2022. This grand event was jointly conducted with Science, Technology

and Climate Change Department and the Department of Education, Government of Assam at IIT Guwahati Campus.

The mission behind the conclave was to showcase the best R&D activities from educational and research institutions across North-East India and to create an environment, conducive to development of local indigenous technologies and innovations, creating the scope and laying the foundation for entrepreneurship.

In order to attract people and spread awareness about the event, a roadshow was initiated from IIT Guwahati on 7th May 2022 in order to reach all the partnering academic institutes and make them an integral part of the mega event. The Director, IITG waved the NERC-2022 flag and sent off the road show vehicle from the institute. More than 400 students, staff, and faculty participated actively in the roadshow.

A huge response was received by participants from throughout the country. The total number of participating institutions in this conclave included 7 IITs, 10 NITs, 5 IIITs and other CFTIs, 23 research labs, 17 central funded universities, 47 other universities and institutes along with about 100 schools. Eminent personalities from industries, startups, research councils, and PSUs also joined in.

The presence of dignitaries from important Ministries was observed, such as Shri Dharmendra Pradhan, Hon'ble Union Minister of Education and Minister of Skill Development and Entrepreneurship, GOI; Dr. Himanta Biswa Sarma, Hon'ble Chief Minister of Assam State; Dr. Ranoj Pegu, Hon'ble Minister of Education,

Government of Assam; Dr. Rajkumar Ranjan Singh, Hon'ble Minister of State for Education, GOI; Dr. Subhas Sarkar, Hon'ble Minister of State for Education, GOI; Shri Keshab Mahanta, Hon'ble Minister of Science Technology and Climate Change, Government of Assam and many more.

The inauguration ceremony of the conclave was followed by the signing of an MoU between IIT Guwahati and the Government of Assam to establish 'The Assam Advanced Health Innovation Institute (AAHII)'. This MoU would prove to be a unique partnership between the Government of Assam and IIT Guwahati in order to set up a Research Institution to leverage advanced technologies to transform medical science. This joint venture company will be able to invite participation from intending parties, including corporates, businesses, research institutions, and philanthropic organizations.

The third edition of Assam Biotech Conclave 2022 was also held as part of NERC 2022. It brought together the biotech entrepreneurs, industry leaders, researchers, academicians, government representatives, policymakers, innovators, and investors together on one platform to explore the possibilities of biotechnology in North-East India and to discuss the new opportunities in the transition.

Officers from the Indian Army also actively participated in the conclave. A talk on "Atmanirbhar Bharat—Indian Army Initiatives towards Self Reliance" was delivered by Lt. Gen. D. S. Rana AVSM, YSM, SM General Officer Commanding, Gajraj Corps on 21st May 2022. The talk was aligned with the vision of the apex leadership of the Government of India and initiatives undertaken by the Indian Armed Forces with a focus on the integration of civil-military establishment in the field of self-reliance. He also elucidated that institutions, such as IIT Guwahati which has many running research projects and elaborate student exchange and joint collaboration setup with a large number of countries that have the wherewithal to take up defence-related R&D and also facilitate delivery with industry partners. He also invited IIT Guwahati to participate in EAST TECH Symposium planned at Kolkata in July 2022. This led to the signing of an MoU between Indian Army Eastern Command and IIT Guwahati on 7th July 2022 during East Tech 2022. This would further impetus to Indigenisation and Raksha Atmanirbharta.

Royal Society of Chemistry, Global Battery Experiment was performed by more than 1,300 students in three sessions starting from 20th May to 22nd May at IIT Guwahati. Along with the Global Battery Experiment, Creating Skilful Educators Program (Teacher training program) was also conducted in parallel sessions. Students had arrived from various schools across Assam and other North-Eastern states.
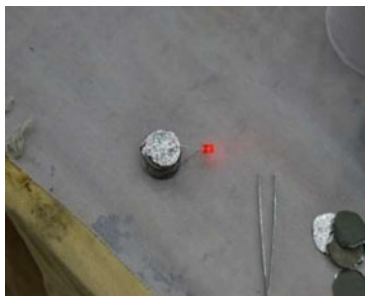
The Guwahati Declaration was launched at the valedictory ceremony of the conclave by Shri Lok Ranjan, Secretary, Ministry of Development of North-Eastern Region (DoNER), in the presence of Shri Kailash Karthik, Deputy Commissioner, Kamrup. The Declaration is intended to create a set of guidelines, through which individual as well as a collective responsibility to promote and encourage innovation at the grass-root level and strive to stimulate and execute indigenization and entrepreneurship, can be taken up.
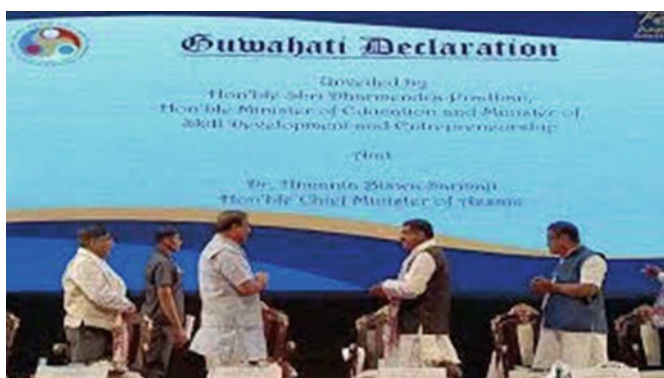
Science, education, research, and innovation are the four pillars on which the development, as well as the work culture of a nation, rests. This was well articulated by the promising number of exhibitors being seen participating from all across the NE states in the NERC 2022. All the NITs, CFTIs, and CFIs were allocated two stalls each, where the delegates showcased the working models of their inventions. Distinctive pavilions were arranged for IIT, NIT, CFIs, and CFTIs. Excellent response was obtained from the startups all across the NE states. Federation of Industry Commerce of North-Eastern Region (FINER) had partnered with NERC-2022 as an Industry Partner and they showcased 50 startups as a part of the exhibition under the FINER Pavilion. Other significant organizations that came forward to showcase their allied R&D startups were the Oil and Natural Gas (Oil and Natural Gas Pavilion), Indian Army (Defense Pavilion), and NE-Railway (NE-Railway Pavilion).

Multifarious research work on topics of societal relevance was presented by researchers from different organizations and institutes. The presentations were conducted in oral and poster presentation modes. The thematic areas for these presentations were part of some of the Sustainable Development Goals (SDGs), such as SDG-3: Good health and Wellbeing; SDG-7: Affordable and Clean Energy; SDG-9:

Industry, Innovation and Infrastructure; SDG-11: Sustainable Cities and Communities and SDG-12: Responsible Consumption and Production. Some of the papers highlighted environmental sustainability, efficiency, and management issues, which are important to be presented in the case of North-East regions. Two awards were given under each technical category for these presentations. Overall the technical sessions were a grand success due to the active cooperation from editors, chairpersons of all the sessions and student volunteers of IITG.

The government of India has taken various steps to encourage women in the field of science and technology. In this line, the IIT Guwahati Woman Researcher Award was approved to recognize the contribution of women Faculty members of IIT Guwahati fraternity. This prestigious award was conferred to Dr. Latha Rangan, Senior Professor in the Department of Biosciences and Bioengineering, Indian Institute of Technology Guwahati, India. Professor Rangan has played a key role in Plant Biotechnology and Sustainable development, especially in the areas of energy security, food security, and medicinal crops.

The conclave paved the way for creating mass awareness of research and innovation for developing a sustainable society. There was knowledge exchange and dissemination that led to the establishment of Centres of Excellence in Translational Collaborative Research and Innovation. This mega event led to the bridging of the gap between Industry-Academia and creating hand holding pathways for setting up long-term collaboration for R&D innovations towards the goal of establishing sustainable NE India. The conclave brought together over 8,000 participants, including hon'ble ministers, official bureaucrats, eminent professors, scientists, renowned industrialist, school children and teachers and others delegates. This revolutionized the R&D road map of all the NE states through various dissemination of policies which will benefit the sustainable development of all NE states in near future.

It is an honour and a moment of extreme pride for getting the NERC proceedings published in the prestigious Springer volumes. We would like to thank and acknowledge the globally active publisher Springer for helping us being able to publish the

articles on 15 broad areas. We would also like to thank all the authors for their contribution to the grand success of NERC 2022 and wish them great success in all of their future endeavours.

Prof. Vimal Katiyar
Dean, R&D
Department of Chemical Engineering
Centre for the Sustainable Polymer
Indian Institute of Technology Guwahati
Guwahati, India
e-mail: vkatiyar@iitg.ac.in

Prof. Subhendu Sekhar Bag
Associate Dean, R&D
Department of Chemistry
Centre for the Environment
Indian Institute of Technology Guwahati
Guwahati, India
e-mail: ssbag75@iitg.ac.in

From the Desk of Chairman of Technical Committee of NERC 2022

North-East Research Conclave 2022 was successfully organized during May 20−22, 2022 with the participation of thousands of delegates. A total of 879 oral and poster papers were presented in the conference on 16 different tracks. The theme of the conclave was Sustainable Science and Technology, which is very pertinent in the modern era of globalization. Science and technology has to address economic, environmental, and social problems of the world. Technology and sustainability are not incompatible. In fact, technology can achieve the goal of sustainability, which also includes preserving our rich cultural heritage. Concurrently with North-East Research Conclave (NERC), Assam Biotech Conclave 2022 was also organized on May 21–22, 2022. These mega events were organized at Indian Institute of Technology Guwahati (IITG) in physical mode after two years of pandemic period. Along with IITG, Science, Technology and Climate Change Department, and Department of Education, Government of Assam were also organizers of these events under the patronage of Shri Dharmendra Pradhan Ji, Honorable Minister of Education and Minister of Skill Development and Entrepreneurship in the Government of India, and Shri Himanta Biswa Sarma Ji, Honorable Chief Minister of Assam.

It is a matter of great pleasure that Springer Nature is publishing the select papers from the conclave in 15 volumes. These are Advanced Functional Materials, Low Cost Manufacturing Technologies, Agro and Food Processing Technologies, Artificial Intelligence and Data Science based R&D interventions, Conservation of Biodiversity in the North-Eastern States of India, Disaster Management, Healthcare Research and Related Technologies, Innovative Design for Societal Needs, Policies for Research and Innovation, Research and Innovation for Sustainable Development Goals, Sustainable Environment, Sustainable Energy Generation and Storage, Sustainable Transportation and Urban Development, Teaching and Learning Technologies, Technologies for Rural Development. These volumes are useful archival and reference materials for policy-makers, researchers, and students.

As the Chairman of Technical Committee, I am thankful to all editors of all volumes, reviewers, and student volunteers who have put tireless efforts to review, select, and edit the papers of respective divisions, overcoming the time-constraint.

Support provided by Convener, Prof. Vimal Katiyar, Dean R&D, IITG, and Co-conveners Prof. Subhendu Sekhar Bag, Associate Dean R&D, IITG and Shri Kailash Karthik N, IAS is commendable. It is difficult to express words of gratitude for the Director, IITG, Prof. T. G. Sitharam who has been motivating and guiding all the teams of NERC 2022 and ABC 2022.

Uday S. Dixit
Professor
Department of Mechanical Engineering and
Head Center for Indian Knowledge Systems

Contents

Drug Delivery and Therapeutics

Biomaterials and Tissue Engineering

About the Editors

Prof. Lalit M. Pandey is Associate Professor at the Department of Biosciences and Bioengineering, IIT Guwahati. He received his Ph.D. in Chemical Engineering from the Indian Institute of Technology, Delhi. He was awarded Erasmus Mundus India4EU fellowship to pursue research at the Laboratoire des Matériaux et du Génie Physique (LMGP), Grenoble-INP, France from 2010 to 2012. Before joining IIT Guwahati, he worked as Scientist with the Central Pollution Control Board, Ministry of Environment and Forests, Government of India from 2009 to 2014, and researched on water and air pollution in agro-based industries. He has received several awards, including the BRSI Malaviya Memorial Award (Young Faculty) 2020, Shastri COVID-19 Pandemic Response Grant (SCPRG) 2020, the DST-UKIERI Award (2018), the IEI (The Institution of Engineers [India]) Young Engineers Award (2017), Innovation in Science Pursuit for Inspired Research (INSPIRE) Faculty Award (2014), and Early Career Research Award from the Science and Engineering Research Board (SERB), Department of Science and Technology, Government of India. His main research interests include biointerfaces and biomaterials, biochemical engineering, and environmental biotechnology. He has published over one hundred three research articles in international journals, more than thirty three book chapters and serves on the editorial board of five international journals. He is serving as Associate Editor in Frontiers in Bioengineering and Biotechnology. He has co-edited three books, titled *Biointerface Engineering: Prospects in Medical Diagnostics and Drug Delivery*, *Microbial*

Enhanced Oil Recovery: Principles and Potential and *Nanoscale Engineering of Biomaterials: Properties and Applications*, published by Springer Nature. He is a life member of the International Association of Engineers (IAENG), the National Academy of Sciences (NASI), the Indian Institute of Chemical Engineers (IIChE), and Nano and Molecular Society (India), and serves as a reviewer for several peer-reviewed journals.

Dr. Raghvendra Gupta is Associate Professor in the Department of Chemical Engineering and Associate Faculty at the Jyoti and Bhupat Mehta School of Health Sciences and Technology and Centre for Sustainable Polymers at IIT Guwahati. He obtained B.Tech. in Chemical Engineering from Harcourt Butler Technological Institute (now HBTU), Kanpur, UP, India and M.Eng. in Aerospace Engineering from Indian Institute of Science, Bengaluru, Karnataka, India. After working for few years in the industry, he joined for Ph.D. in the Department of Chemical Engineering at the University of Sydney, NSW, Australia. Before joining Department of Chemical Engineering at IIT Guwahati in 2014, he worked at the University of Sydney, Institute of High Performance Computing, A-STAR, Singapore; BITS Pilani, K. K. Birla Campus, Goa. He is interested in understanding transport processes in different chemical process equipment and systems, physiological systems, and biomedical devices. He has extensively worked on the flow and heat transfer in two-phase systems in microchannels using a synergistic combination of experimental, theoretical, and computational techniques. In health sciences, he is particularly interested in understanding transport processes in cardiovascular and pulmonary system. He has more than thirty publications in international journals and serves as a reviewer for a number of international journals.

Dr. Rajkumar P. Thummer is Assistant Professor and Principal Investigator of the lab "Laboratory for Stem Cell Engineering and Regenerative Medicine" at IIT Guwahati, India. He completed his B.Pharm. from Anand Pharmacy College, Anand, Gujarat, and then obtained his master's in biotechnology from the University of Essex, UK. Later, he completed his Ph.D. in Stem Cell Biology from the University of Groningen, The Netherlands in the year 2010. Further, he gained more than three years of post-doctoral research experience at the University of Bonn, Bonn, Germany and then moved back to India at IIT Guwahati. His specialization is in stem cell biology with an experience of more than 15 years. He is the recipient of Young Scientist Award by the Science and Engineering Research Board, Department of Science and Technology, Government of India. He has published several manuscripts in national and international peer-reviewed journals and serves as editorial board member and reviewer of many journals.

Dr. Rajiv Kumar Kar is Assistant Professor at Jyoti and Bhupat Mehta School of Health Sciences and Technology, IIT Guwahati. He obtained B.Pharm. in Pharmaceutical Sciences from BPUT, Odisha and M.S. from the National Institute of Pharmaceutical Education and Research (NIPER) with a specialization in informatics. He received his Ph.D. from Bose Institute, Department of Science and Technology (DST), Government of India. While working as a doctoral scholar, he designed anti-freeze peptides, which now have proven utility in medical cryopreservation. Other areas of his thesis include antimicrobial and anti-amyloid peptides, which later won him the Jharna Rani Samal Best Ph.D. student award from the Nuclear Magnetic Resonance Society of India at IISc, Bengaluru, in 2016. He did a Post-doctoral degree in quantum mechanics at Fritz Haber Center for Molecular Dynamics, Hebrew University of Jerusalem, Israel (HUJI). His post-doctoral research was supported by Lady Davis (2017–2020) Trust as Shunbrun Post-doctoral Fellowship and Arskin Post-doctoral Fellowship. Later, he worked as Scientist at Technische Universitat Berlin, where he focused on applying advanced simulations and data science methods to biological systems. Einstein Foundation Berlin financially supported his research in Germany (2020–2021).

His current research at IIT Guwahati includes developing biomarker detection processes for point-of-care diagnostics and translating them into suitable sensors and medical devices. It consists of an application-oriented approach with experimental biotechnology, nanotechnology, and computational spectroscopy. He authored more than 35 original research and five review articles in journals of international repute.

Student Volunteers

Laipubam Gayatri Sharma a Ph.D. student of BSBE department at IIT Guwahati, a team member of Biointerface and Environmental Engineering Lab working under the supervision of Prof. Lalit Mohan Pandey.

Aman Bharadwaj a Ph.D. student of BSBE department at IIT Guwahati, a team member of Biointerface and Environmental Engineering Lab working under the supervision of Prof. Lalit Mohan Pandey.

Mudrika Singhal is a Ph.D. student in the Department of Chemical Engineering and is the receipient of the Prime Minsister's Research Fellowship. She works under the guidance of Prof. Raghvendra Gupta. Her work is based around patient-specific modelling in coronary arteries.

Chinmaya Panda is a 2nd year Ph.D. student working under the guidance of Prof. Lalit Mohan Pandey in the field of protein aggregation and amyloidosis.

Atreyee Borthakur is a 2nd year Ph.D. student working in the Laboratory for Stem Cell Engineering and Regenerative Medicine, IIT Guwahati, under the supervision of Prof. Rajkumar P. Thummer.

Vartik Shandilya is an M.Tech. graduate from the Department of Chemical Engineering, jointly guided by Prof. Raghvendra Gupta and Prof. Biman B. Mandal, respective heads of the Transport Phenomena Research Lab and Biomaterials and Tissue Engineering Lab.

Cell and Molecular Biology

Generation of Recombinant Version of a Bioactive Human MEF2C Transcription Factor from *E. coli*

Krishna Kumar Haridhasapavalan , **Pradeep Kumar Sundaravadivelu** ,
Udayashree Voorkara , **Vishwas Kaveeshwar** ,
and Rajkumar P. Thummer

1 Introduction

Myocyte enhancer factor 2C (MEF2C) is a muscle-specific factor belonging to the
MADS-box family transcription factors. It has a DNA binding domain called the
MADS-box domain, which binds to A/T-rich regulatory regions and regulates several
cardiac and skeletal muscle genes [1, 2]. It collaborates with the MyoD family of basic

---

K. K. Haridhasapavalan · P. K. Sundaravadivelu · R. P. Thummer (✉)
Laboratory for Stem Cell Engineering and Regenerative Medicine, Department of Biosciences
and Bioengineering, Indian Institute of Technology Guwahati, Guwahati 781039, Assam, India
e-mail: rthu@iitg.ac.in

K. K. Haridhasapavalan
e-mail: hk.kumar@iitg.ac.in

P. K. Sundaravadivelu
e-mail: p.sundaravadivelu@iitg.ac.in

U. Voorkara
Department of Obstetrics and Gynaecology, SDM College of Medical Sciences and Hospital, Shri
Dharmasthala Manjunatheshwara University, Dharwad 580009, Karnataka, India
e-mail: drudayashree@yahoo.com

V. Kaveeshwar (✉)
Central Research Laboratory, SDM College of Medical Sciences and Hospital, Shri Dharmasthala
Manjunatheshwara University, Dharwad 580009, Karnataka, India
e-mail: vishwas.kaveeshwar@sdmmedicalcollege.org

helix-loop-helix transcription factors to play a vital role in skeletal muscle development [1, 3], especially in sarcomere integrity [3]. Primarily, MEF2C is reported to be expressed in cardiac and skeletal muscle, spleen, and brain [4]. During early embryogenesis, MEF2C is expressed in myocardiogenic precursor cells, somites, endochondral cartilage, and early cardiac cells [1, 2, 5].

In addition, MEF2C is vital for anterior heart field development. It has been reported that ISL1 and GATA4 activate MEF2C by binding to its enhancer, aiding in the right ventricle development [6]. Also, the homozygous inactivation of *MEF2C* leads to embryonic lethality at E9.5 with severe cardiovascular developmental defects [7]. Nevertheless, conditional knockout of *MEF2C* in developing bone leads to the death of the neonate within a week. All the bones in the neonatal body fail to ossify, illustrating the importance of MEF2C in bone development [5]. Furthermore, MEF2C has a prominent role in chondrocyte hypertrophy and vascularization [5].

Apart from muscle and bone development, the expression of MEF2C is crucial for craniofacial development [8]. Conditional deletion of *MEF2C* in the neural crest results in the death of the offspring within an hour of their birth due to defective tongue positioning leading to constriction of airway and with severe defects in craniofacial structures [8]. Also, MEF2C assists in the differentiation of neural stem and progenitor cells whose conditional knockout in the latter lead to abnormal electrophysiology and behavioral defects [9]. As mentioned earlier, MEF2C plays a critical role in cardiogenesis, and hence, it is used along with other transcription factors, namely GATA4 and TBX5, to reprogram human and mouse fibroblasts into induced cardiomyocytes [10–12]. In direct cardiac reprogramming, MEF2C is one of the core reprogramming as well as indispensable factors in generating cardiomyocytes for various biomedical applications [10–12].

The role of recombinant proteins has been indispensable in the field of therapeutics and basic research since the early 1980s. The heterologous expression of these proteins has a broad range of applications in the biopharmaceutical industry [13]. A number of expression host systems are used for the heterologous expression of these recombinant proteins, but the most commonly used host system is the bacterial system, specifically *Escherichia coli (E. coli)* strains, because of their well-studied genetics, easy handling, high protein yield, and so forth [14]. But this heterologous expression has certain caveats like the presence of rare codons for the host system in our gene of interest (codon bias), presence of proteases in the host, mRNA degradation, constitutive expression of recombinant protein leading to impaired cell growth, protein aggregation due to the formation of inclusion bodies, protein misfolding post-expression and purification, and so forth [13, 15–17]. A fair number of in silico tools like Gene Optimizer by ThermoScientific (used in this study), Codon Optimization by GenSmart, Codon optimization by GeneWiz, Codon optimization by Vector Builder, etc. are available for optimizing the codons to counteract some of the above-mentioned barriers, thereby increasing the heterologous expression. Despite these barriers, recombinant proteins have been expressed in a soluble or insoluble form and then purified to homogeneity from *E. coli*. One of the most commonly used methods for purifying recombinant proteins is the usage of affinity tags [18, 19]. These affinity tags enable an efficient, cost-effective purification strategy with a

high yield of the pure recombinant protein [18, 19]. Once the recombinant proteins are purified, they can eventually be used for various biological applications. Notably, introducing recombinant proteins into mammalian cells is considered to be a safer approach as it does not integrate and alter the cellular genome, and also cell fate can be manipulated in a time and dosage-dependent manner [20–23, 53].

This study has tried to address and solve the hurdles mentioned above in expressing the recombinant human MEF2C (rhMEF2C) protein. Accordingly, we have codon-optimized our gene of interest (*MEF2C*) to overcome codon bias and mRNA degradation. Also, we used an inducible vector system to avoid constitutive expression and *E. coli* BL21(DE3) strain to avoid proteasomal degradation. Moreover, we have screened various expression conditions to obtain the soluble expression of the recombinant protein and purified this protein to homogeneity. Importantly, we analyzed its secondary structure using circular dichroism spectroscopy and demonstrated its biological activity in anti-angiogenesis as well as in the synergistic activation of the α-Myosin Heavy Chain (α-MHC) gene. Potentially, this homogeneous rhMEF2C macromolecule can replace its other forms in direct cardiac reprogramming, where any somatic cell can be directly reprogrammed to functional beating myocytes. Since recombinant proteins do not integrate and alter the genome, the resulting myocytes will be integration-free and, therefore, can be used for cell therapeutics. Moreover, this purified rhMEF2C protein can also aid in elucidating its molecular role in various diseases and cellular processes.

2   Materials and Methods

2.1   Construction of Recombinant MEF2C Expression Plasmids Based on pET28a(+)

We retrieved the nucleotide sequence that codes for the human MEF2C protein from the NCBI RefSeq database (NM_001193350.1). The retrieved codons of the human *MEF2C* gene were optimized for its high-level heterologous protein expression in *E. coli* and validated as previously described and as mentioned in Fig. 1 [24, 25]. This optimized sequence, along with a set of fusion tags, was commercially synthesized and then sub-cloned into the expression vector, as illustrated in Fig. 1. The final developed recombinant plasmids (pET-HTN-*MEF2C* and pET-*MEF2C*-NTH) were confirmed using restriction digestion analysis and further verified by DNA sequencing. The codon-optimized nucleotide sequence of the *MEF2C* gene (for expression in *E. coli*) can be accessed via GenBank using the accession code OK033158.
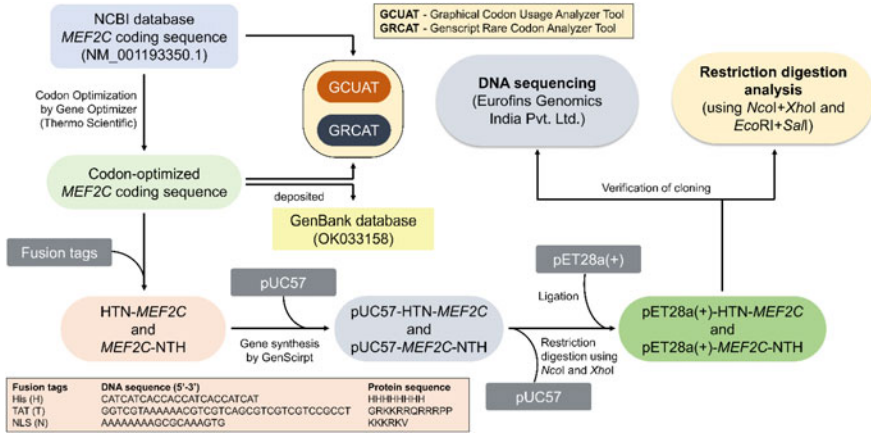
Fig. 1 Schematic overview of the workflow of codon optimization and cloning methodology

2.2 Expression Analysis of rhMEF2C Fusion Proteins

E. coli BL21(DE3) competent cells were transformed with the two constructed recombinant plasmids (pET-HTN-*MEF2C* and pET-*MEF2C*-NTH) and cultured as described previously [24, 25]. To determine the optimal induction parameters, the secondary culture was prepared in Lysogeny Broth (HiMedia) and induced at 37 °C with different inducer (Isopropyl β-D-1-thiogalactopyranoside, HiMedia) concentrations at various cell densities for 2, 4, and 8 h. The values used for screening the individual parameters are listed in Table 1. Further to analyze the solubility of the rhMEF2C fusion protein, we first induced the culture at 37 or 18 °C with the optimal induction parameters, and then the cultured cells were harvested. Subsequently, harvested cells were resuspended (in resuspension buffer containing 20 mM phosphate buffer (HiMedia), 300 mM NaCl (HiMedia), 20% glycerol (HiMedia), and 20 mM imidazole (HiMedia)), lysed, and clarified to separate soluble from insoluble protein molecules. The protein samples from total cell lysate, insoluble, and soluble fractions were analyzed using sodium dodecyl sulfate–polyacrylamide gel electrophoresis (SDS-PAGE) and immunoblotting (Western blotting). Uninduced cultures were used as a control for all the experiments.

2.3 Affinity Purification of rhMEF2C Fusion Protein

The rhMEF2C-NTH protein was induced in a large culture volume (1.2 L) with the identified optimal induction parameters. The *E. coli* BL21(DE3) cells were then harvested, resuspended (in 45 mL of resuspension buffer), lysed, and clarified to separate soluble fractions. From the clarified fraction (supernatant), the target protein

Table 1 Identification of obtained induction parameters for the high expression of the rhMEF2C fusion proteins in *E. coli* at 37 °C

Expression parameters	Values screened	Optimal value[a]
Inducer concentration (IPTG) (in mM)	0.05, 0.1, 0.25, 0.50	0.05
Pre-induction cell density (OD$_{600}$)	~0.5, ~1.0, ~1.5	~0.5
Induction time point (in hours)	2, 4, 8	2

[a]Minimum of 2–3 different cultures from different colonies were analyzed for each parameter using SDS-PAGE and Western blotting

was purified using immobilized metal ion affinity chromatography by utilizing Ni–NTA as the resin. Briefly, for the proper binding of the target protein to resin, we incubated the supernatant fraction and resin overnight at 4 °C. After incubation, they were loaded onto a protein purification column (Bio-Rad). Subsequently, the unbound fraction was unloaded, and the column was washed with three different wash buffers (50 mL each; 20 mM phosphate buffer and 300 mM NaCl) containing imidazole in incremental concentrations (50, 100, and 150 mM for the three wash buffers, respectively). The bound rhMEF2C fusion protein was eluted with 500 mM imidazole elution buffer (20 mM phosphate buffer, 300 mM NaCl, 20% glycerol). The purity of the target protein was evaluated by SDS-PAGE and immunoblotting. The pH of the purification buffers was adjusted to 7.6 at room temperature and prechilled on ice.

2.4 SDS-PAGE and Immunoblotting

The total protein concentration of the samples was measured using the Bradford method. Protein samples (normalized) were separated on 12% polyacrylamide gel and either performed Coomassie staining or immunoblotted as described previously [24, 25]. To detect target fusion proteins, anti-Histidine (BB-AB0010, BioBharati) and anti-Mef2c (MA5-25,477, Invitrogen) antibodies were used. IgG-HRP conjugated anti-mouse (31,430, Invitrogen) and anti-rabbit (31,460, Invitrogen) secondary antibodies were used to visualize primary antibody-bound target proteins.

2.5 Circular Dichroism Spectroscopy

The homogeneously purified proteins were first desalted against sodium phosphate buffer (20 mM; pH 8 at room temperature) and then analyzed using circular dichroism spectroscopy as demonstrated earlier [24, 25]. From the circular dichroism spectrum

of this desalted rhMEF2C-NTH protein, we estimated its secondary structure using the Beta Structure Selection (BeStSel) online tool.

2.6   Cell Culture

HeLa and H9C2 (cardiomyoblast) cell lines were procured from Cell Repository, National Centre for Cell Science, Pune, India. HeLa cell line was cultured as described earlier [26]. H9C2 cell line was cultured in low-glucose DMEM supplemented with 10% fetal bovine serum (FBS) and 1% penicillin–streptomycin solution at standard cell culture conditions. HiFi™ human umbilical vein endothelial cells (HUVECs) were procured from HiMedia (Mumbai, India) and grown on gelatin in HiEndoXL™ endothelial cell expansion medium (HiMedia). At 70–80% confluency, cells were dissociated with trypsin–EDTA (Invitrogen) and reseeded in a fresh culture dish at 1:4–1:6 ratio.

2.7   Protein Transduction, Immunocytochemistry, and Microscopy

HeLa cells were seeded at 1×10^5 cells/well in a 12-well culture plate in complete growth media. On the next day, the media was changed to the protein transduction media, which was prepared by mixing the rhMEF2C-NTH protein at the final concentration of 400 nM with reduced serum (2% FBS) growth medium. After 4–6 h of incubation, immunostaining was carried out as described earlier [25]. In this study, cells were probed with an anti-Mef2c antibody (MA5-25,477, Invitrogen) at a dilution of 1:100 for atleast 1 h at room temperature. Goat anti-Mouse IgG (H + L) secondary antibody Alexa Fluor®594 conjugate (A-11032, Invitrogen) was used at 1:1000 dilution for 30–45 min at room temperature for detection of MEF2C in transduced cells. Nuclei were stained with Hoechst 33,342 (Invitrogen), and then the image stacks were acquired at 2 µm intervals using an inverted fluorescence microscope (20x/0.45NA objective; IX83, Olympus, Japan) equipped with a DP80 CCD camera.

2.8   In Vitro Scratch Migration Assay

1×10^5 HUVECs/well were plated in a 12-well culture plate and grown until 95% confluence was achieved in the endothelial cell expansion medium. The confluent monolayers were scratched with a sterile pipette tip (0–20 µL) and then rinsed with sterile phosphate buffer saline. Consequently, scratched monolayers were treated

with 400 μM rhMEF2C-NTH protein or vehicle control (in endothelial cell expansion media) for 24 h. The scratched monolayers were then visualized under an inverted brightfield microscope (ZOE Fluorescent Cell Imager, Bio-Rad) at 20 × magnification, and images were captured at a particular interval of time. The migration efficiency was evaluated using ImageJ (1.48 v) software.

2.9　Chicken Chorioallantoic Membrane (CAM) Assay

The CAM assay was carried out as previously described [27, 28]. Briefly, the CAM layers of 3–4 days old embryonated chicken eggs were exposed by gently cutting open their top eggshells, and then the filter paper discs soaked in the purified rhMEF2C-NTH protein (diluted with PBS to 400 nM concentration) or vehicle control solutions were placed directly on them (one disc/egg). Subsequently, the eggs were sealed and incubated at 37 °C for 24 h with 60% humidity. Images were captured at different time intervals using an LCD Digital Stereomicroscope equipped with a 2MP camera at 2 × magnification, followed by documentation with the help of Adobe Photoshop CC 2019 software. The embryonated chicken eggs were purchased from the local egg hatching unit.

2.10　α-MHC Reporter Assay

Briefly, 1×10^5 H9C2 cells/well were plated in a gelatin-coated 12-well culture plate and grown in a complete growth medium. Once the cells attained 70–80% confluency, the cells were washed with PBS and transduced with an α-MHC-eGFP lentiviral vector in the presence of 5 μg/mL of polybrene [29]. Subsequently, on the next day (D0), cells were reseeded (1:3 ratio) in a fresh gelatin-coated culture plate, and on the following day (D1), cells were washed with PBS and treated with a protein transduction medium containing 400 nM of rhMEF2C-NTH and/or rhHTN-HAND2 [25] proteins or an equivalent volume of vehicle control. The medium was renewed every alternative day. After the treatment, the cells were visualized under an inverted fluorescent microscope (ZOE Fluorescent Cell Imager, Bio-Rad), and images were captured in the green channel at 20 × magnification.

2.11　Flow Cytometry

For GFP expression analyses, harvested cells were washed with PBS, fixed with 4% paraformaldehyde, and then analyzed using a BD FACS Calibur Flow Cytometer (B. D. Biosciences) with FlowJo software.

2.12   Statistical Analysis

T-tests were performed using GraphPad Prism 8.0 software to analyze the obtained quantitative data. P < 0.05 was considered significant, and the values are expressed as mean ± S.D.

3   Results and Discussion

3.1   Codon Optimization Eliminates Rare Codons in Human MEF2C Gene as Per in Silico Analysis to Enable Enhanced Heterologous Expression

To understand whether codon optimization is required for the heterologous expression of the human *MEF2C* gene, we first analyzed its non-optimized nucleotide sequence using different online tools. Notably, 22 codons (Fig. 2 (*top*)) were identified to be rare codons with the Graphical Codon Usage Analyzer tool because their relative adaptiveness value is ≤30% (*magenta*). Likewise, ~11% of the codons were identified to be rare codons with the Genscript Rare Codon Analysis tool, as their codon usage frequency is ≤30 (Fig. 3 (*red*)). Importantly, the presence of rare codons in the gene sequence may influence its protein expression mainly by reducing the translation rate, further decreasing protein production [30], and ribosome stalling resulting in premature termination of translation [30–32]. Collectively, these studies and our results suggest codon optimization of the full-length protein-coding sequence of the human *MEF2C* gene to remove rare codons, which might compromise its heterologous expression. Thus, we performed codon optimization and validated the optimized sequence for *E. coli* using the in silico tools.

The Graphical Codon Usage Analyzer and Genscript Rare Codon Analysis in silico tools confirmed that the optimized *MEF2C* gene sequence is free from rare codons (Figs. 2 (*bottom*) and 3 (*green*)) that has been identified earlier (before optimization), and were replaced with the most commonly used codons in *E. coli*. Additionally, the codon adaptation index was significantly improved to 0.92 from 0.60 after codon optimization. Consistent with previous studies on various cardiac reprogramming factors, ETS2, MESP1, GATA4, HAND2, and TBX5 [24–26, 33, 34], we also observed similar improvements in the target gene sequence after optimization. Thus, we confirmed the absence of rare codons in the optimized sequence, which would result in the successful heterologous expression of the human *MEF2C* gene in the bacterial expression system, *E. coli*.
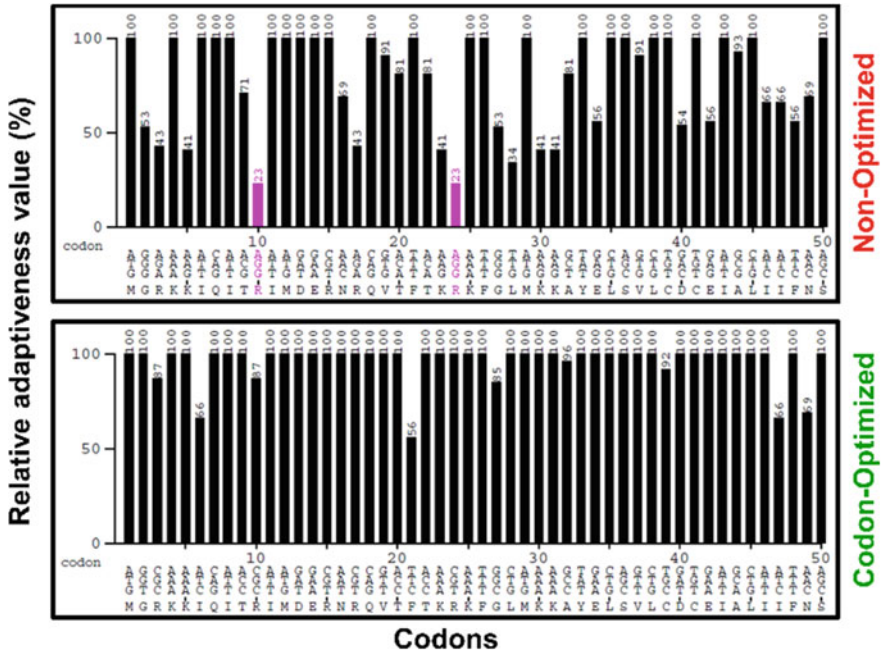
Fig. 2 GCUAT analysis of codon-optimized *MEF2C* gene sequence compared to its non-optimized one. The bar graph shows the codon's relative adaptiveness value. The magenta colored bars indicate the codons whose relative adaptiveness value is less than or equal to 30% and that are more likely to diminish the expression of *MEF2C* in *E. coli*

Fig. 3 GRCAT analysis of codon-optimized *MEF2C* gene sequence compared to its non-optimized one. Bar graph showing the percentage distribution of codons in computed quality groups (non-optimized (*red*) and codon-optimized (*green*)). The dotted line indicates the threshold and codons that lie below that are more likely to diminish the expression of *MEF2C* in *E. coli*
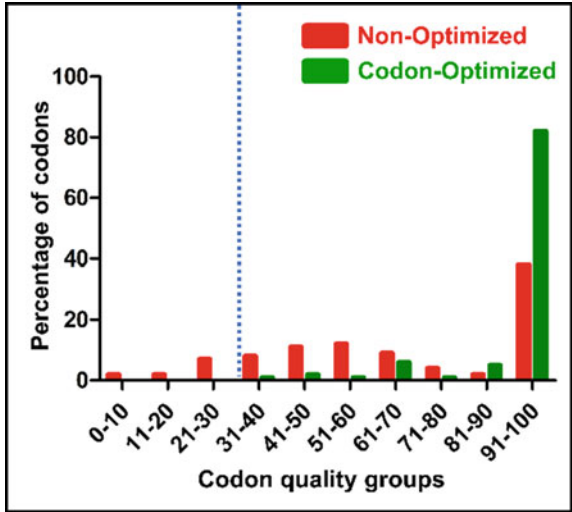
3.2 Impact of Induction Parameters on the Heterologous Expression of rhMEF2C Fusion Proteins

To generate a transducible version of the highly pure rhMEF2C protein, we first inserted the fusion tags (NLS, TAT, and His) either at the N- or C-terminus of rhMEF2C protein by inserting the cDNA sequence, which encoded these fusion tags into the matching open reading frame of the desired protein (HTN-*MEF2C* and *MEF2C*-NTH; Fig. 4a (*top*)). The main reason to have these tags on either side of this protein was to elucidate its influence on the expression level, solubility, and stability. Earlier, others and our research group have previously demonstrated the importance of the position of fusion tags in recombinant protein production [24, 25, 33, 35, 36]. The *MEF2C* fusion gene inserts were commercially synthesized and then cloned into the pET28a(+) expression vector under the control of a tightly regulated T7 promoter. The restriction digestion analysis with specific enzymes (Fig. 4b (*bottom*)) confirmed the successful cloning of these fusion gene inserts into the expression vector. To ensure the fidelity and proper orientation of the target gene, we performed DNA sequencing of the developed recombinant plasmids (data not shown). We thus developed the recombinant pET28a(+) plasmids harboring the human *MEF2C* fusion genes, which could be used for its heterologous expression in the bacterial system to obtain a cell and nuclear permeant rhMEF2C protein.

After having successfully constructed the recombinant pET28a(+) plasmids bearing *MEF2C* fusion genes, we next sought to analyze its expression in *E. coli* based on the influence of various induction parameters. The impact of optimal induction

(a)

(b)
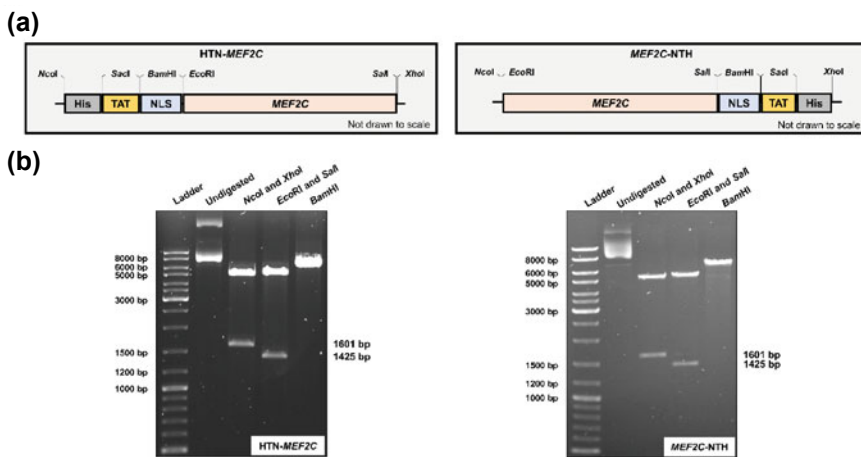
Fig. 4 Tagging pattern of the human *MEF2C* gene constructs and verification of its cloning. **a** Diagram of HTN-*MEF2C* (*left*) and *MEF2C*-NTH (*right*) gene constructs used in this study. **b** Cloning confirmation of recombinant plasmids harboring the fusion gene constructs (shown in (**a**)) using restriction digestion analysis. Polyhistidine tag (His; H); Transactivator of Transcription (TAT; T); Nuclear localization signal (NLS; N)

parameters in the production of biologically active recombinant proteins has been emphasized in a number of studies previously [37–43]. In that aspect, the most crucial induction parameters, namely pre-induction cell density, inducer concentration, and induction time, were screened and optimized (listed in Table 1) in order to obtain maximal expression of rhMEF2C fusion proteins using an inducible T7 expression system.

Recombinant proteins expressed in the bacterial system either end up in a properly folded soluble form or in an insoluble form consisting of inclusion bodies [44]. Purifying proteins from inclusion bodies involves the usage of strong detergents to solubilize them and then requires refolding, which is a complex process [44, 45]. Therefore, in the case of rhMEF2C fusion proteins, obtaining maximal soluble expression was given utmost importance. Accordingly, we first examined the influence of fusion tags at either terminus on the solubility of rhMEF2C fusion proteins induced at 37 °C using SDS-PAGE and Western blotting. Strikingly, the presence of fusion tags at the N-terminus of the rhMEF2C protein hindered its solubility, in contrast to its C-terminus-fused counterpart (Fig. 5). However, more or less, a similar overall expression profile of these fusion proteins was observed with all (rhHTN-MEF2C) or majority (rhMEF2C-NTH) of the protein molecules laying in the insoluble pellet fractions. We assume that this might be the effect of misfolding or aggregation (in the case of folded ones in inclusion bodies) of the target fusion proteins.
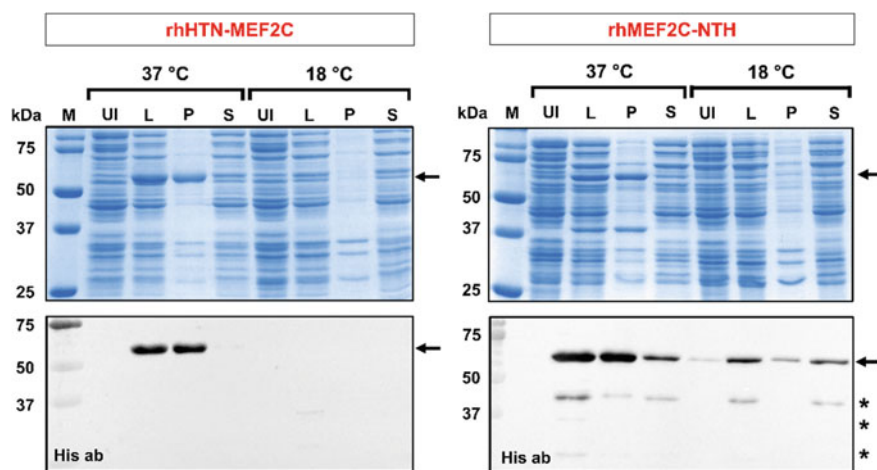
Fig. 5 Effect of induction temperature on the solubility of rhMEF2C fusion proteins. The N- and C-terminally fused recombinant proteins were induced at 37 °C for 2 h or 18 °C for 24 h with 0.05 mM IPTG. The induced cells were harvested, lysed, and clarified. The different cell fractions (normalized loading) were resolved on 12% polyacrylamide gels and then performed either Coomassie staining or immunoblotting (n = 4). Protein marker (M); lysate fraction (L); insoluble pellet fraction (P); soluble supernatant fraction (S); *truncated fragments of rhMEF2C proteins

Next, we hypothesize that reducing the induction temperature will assist in the enhanced soluble expression of rhMEF2C fusion proteins, which helped in cases of various other recombinant proteins like we and others observed [33, 37, 39, 42]. Indeed, aggregation-prone recombinant proteins expressed at lower temperatures promote their solubility and stability by preventing the formation of insoluble aggregates [33, 37]. Apart from minimizing the aggregation of proteins [39], low-temperature induction results in generating biologically functional proteins [42]. But reducing the induction temperature to 18 °C did not help in enhancing the soluble expression of rhHTN-MEF2C; contrastingly, its expression was completely hindered (Fig. 5). Interestingly, enhanced soluble expression was observed in the case of the rhMEF2C-NTH fusion protein on reduction of induction temperature to 18 °C. However, the overall expression of rhMEF2C-NTH fusion protein declined at 18 °C in contrast to 37 °C. Taken together, these results conclude that the position of fusion tags and induction temperature significantly impact the overall and soluble expression of rhMEF2C fusion proteins. Inferring from the above results, rhMEF2C-NTH protein-induced either at 37 or 18 °C were used for further experiments.

3.3   rhMEF2C-NTH Protein Purified to Homogeneity Under Native Conditions

To retain the native folding conformation of the rhMEF2C fusion protein, we first induced its soluble expression and then performed one-step affinity chromatography-based purification under native conditions. Several studies demonstrated that recombinant proteins purified under native conditions retain their folding conformation, often retaining their functional activity [26, 36, 46–54]. Therefore, we employed a widely used immobilized metal ion affinity chromatography (IMAC) technique under native conditions to purify this poly-his tag-fused rhMEF2C fusion protein in its native form. We selected a C-terminally fused genetic construct from the soluble expression analysis and induced its expression in large culture volumes with the above-identified parameters (listed in Table 1) at 37 or 18 °C for 2 or 24 h, respectively. The obtained crude lysate was clarified to isolate soluble cell fractions and then purified with Ni–NTA-based affinity chromatography. The SDS-PAGE analysis clearly showed a single high-intensity band at ~58 kDa corresponding to the full-length rhMEF2C-NTH protein, signifying the homogeneously purified proteins in the elution fractions irrespective of induction temperature (Fig. 6a (for 37 °C) and data not shown (for 18 °C)). This purification data thus implies that the purified fusion protein is free of other proteins from the host expression system, which is critical in producing therapeutic or reprogramming proteins as these bacterial contaminant proteins might be cytotoxic to the target mammalian cells [55]. Immunoblotting with Histidine and protein-specific antibodies revealed the loss of rhMEF2C-NTH protein in the flow-through fractions (Fig. 6a (middle and bottom)), which might be probably due to overloading of protein molecules or low resin volume in the affinity column.
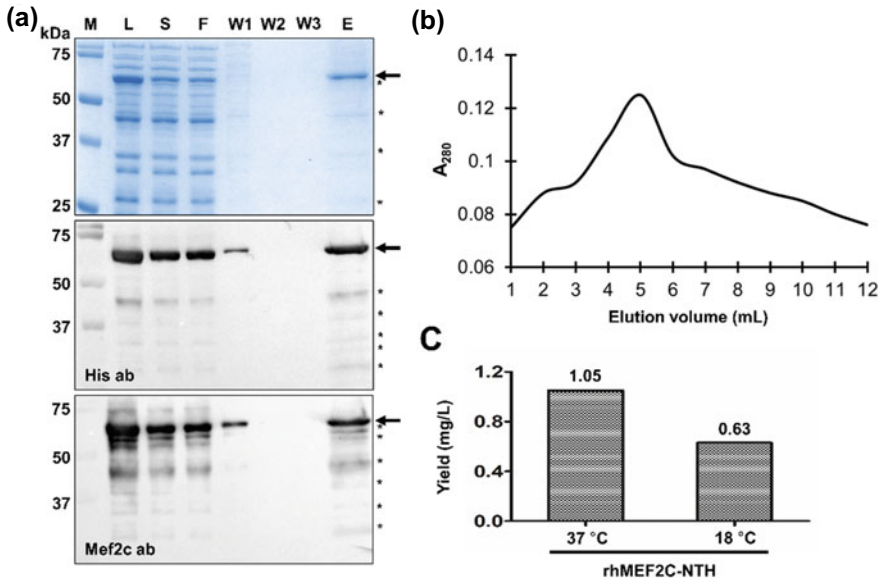
Fig. 6 Purification of the rhMEF2C-NTH protein-induced at 37 °C under native conditions. **a** The collected purification samples during various steps were analyzed (normalized loading) using SDS-PAGE (*top*) or immunoblotting using an α-his/α-HAND2 (*middle/bottom*) antibody. **b** Elution profile of one-step purification of rhMEF2C-NTH protein-induced at 37 °C. **c** The bar graph shows the final yield of purified rhMEF2C-NTH protein-induced at 37 and 18 °C. Protein marker (M); lysate fraction (L); insoluble pellet fraction (P); soluble supernatant fraction (S); flow-through fraction (F); wash fraction (W); eluted fraction (E); *truncated fragments of rhMEF2C-NTH protein

This rhMEF2C-fusion protein (induced at 37 °C) purification profile (only elution) is shown in Fig. 6b.

Moreover, immunoblotting with a protein-specific antibody confirmed the identity of this purified rhMEF2C fusion protein (Fig. 6a (bottom)). Notably, the final yield of around 1.05 (induced at 37 °C) and 0.63 (induced at 18 °C) mg/L of purified rhMEF2C-NTH proteins was obtained (Fig. 6c). The main reason behind this low yield is the difference between the overall expression of rhMEF2C-NTH protein-induced at 37 and 18 °C. Several other reprogramming transcription factors, namely, OCT4, SOX2, ETS2, PDX1, MESP1, GATA4, GLIS1, NGN3, and TBX5, were generated using similar strategies from *E. coli* in the form of recombinant proteins [24–26, 33, 36, 52, 54, 56]. In addition, these studies have also used a similar fusion strategy to facilitate the sub-cellular and sub-nuclear delivery of the recombinant reprogramming proteins into the target mammalian cells. Thus, we demonstrated the one-step homogeneous purification of rhMEF2C-NTH protein under native conditions. The purified protein can further be delivered to the target site of any mammalian cells with TAT and NLS fusion strategy and without the requirement of any transduction reagents.

3.4 Homogeneously Purified Protein Maintains Secondary Structure Folding Conformation

The rhMEF2C protein has been purified under native conditions because the functionality of a protein majorly relies on the native conformation. Once the protein is purified, its secondary structure composition can be studied using different methods, one of which is circular dichroism spectroscopy [57, 58]. In circular dichroism spectroscopy, the incident light consists of superimposed right and left circularly polarized light. The different secondary structures present in the protein absorb these right and left circularly polarized light differently, resulting in a spectrum. The shape and magnitude of the spectra are dependent on the different amounts of secondary structures present in the protein, which can be quantified [57, 59]. The wavelength corresponding to the absorption maxima and minima of various secondary structure components, namely α-helices, β-sheets, turns, and random coils, are listed in Fig. 7a (*top*). Since the secondary structure and crystal structure of MEF2C protein is not reported to date, we tried to deduce the secondary structure of the purified rhMEF2C fusion protein (induced at two different temperatures) using circular dichroism spectroscopy. The secondary structure was quantified from the obtained spectra using an online tool named BeStSel [60, 61]. A similar analysis of the secondary structure of purified recombinant proteins was performed in our recent studies [24, 25, 33]. Analysis of the spectra showed that the purified rhMEF2C fusion protein retained its secondary structure irrespective of induction temperature (Fig. 7a (*bottom*)). In contrast, a previous study reported that induction temperature alters the secondary structure of the desired recombinant protein purified from *E. coli* [34]. Additionally, quantification of the spectra revealed that this purified rhMEF2C fusion protein (induced at 37 or 18 °C) majorly consists of α-helices, β-sheets, and random coils, along with a small amount of turns (Fig. 7b). From these results, we can infer that the purified rhMEF2C fusion protein retains its secondary structure at both induction temperatures.

3.5 Purified rhMEF2C-NTH Protein Penetrates Mammalian Cells and Translocates to the Nucleus

We next sought to analyze the cell penetration and nuclear translocation ability of this purified rhMEF2C-NTH protein in human cells. To validate our fusion strategy on the transduction ability, we first exposed HeLa cells for 4–6 h with 200 and 400 nM of rhMEF2C fusion protein or glycerol buffer (vehicle control) as a control, and then we performed immunocytochemistry followed by fluorescence microscopy. We selected HeLa cells as it is a widely reported cell line for the protein transduction analysis [26, 54] and also lacks endogenous expression of the MEF2C transcription factor. The fluorescence microscopy analysis revealed that the TAT and NLS fused purified rhMEF2C protein transduces the cell, then translocates to its nucleus (Fig. 8).

(a)

Standard circular dichroism spectra (nm)		
Content	Positive Peak	Negative Peak(s)
α-helices	193	222 and 208
β-sheets	195	218
Random coils	210	195

(b)

Secondary structure	rhMEF2C-NTH	
	37 °C	18 °C
α-helices	22%	22%
β-sheets	26%	22%
Turns	16%	14%
Random coils	36%	42%
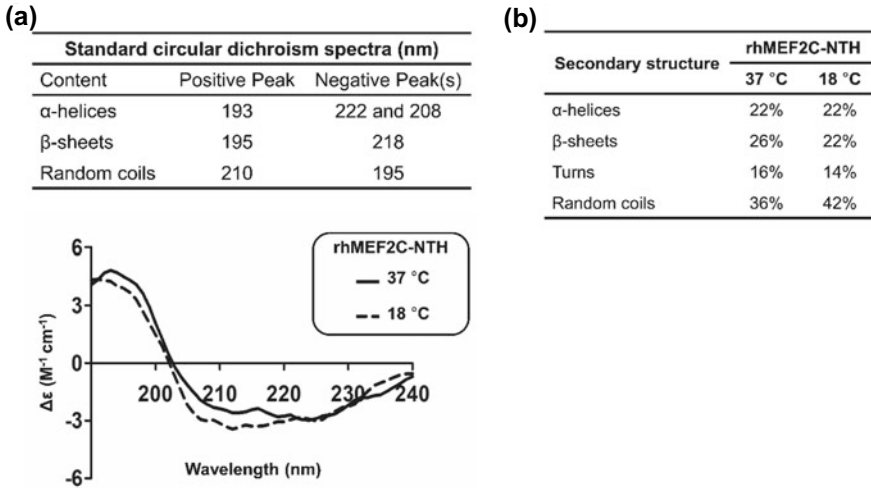
Fig. 7 Secondary structure determination of purified rhMEF2C fusion protein. **a** Using circular dichroism spectroscopy, the purified and desalted rhMEF2C-NTH protein spectra were obtained and then analyzed with the BeStSel online tool. Summary of positive and negative peaks of the standard secondary structures of the protein (*top*) corresponding to the wavelength [59]. The final analyzed spectra were plotted with wavelength against delta epsilon (*bottom*). **b** Summary of the determined secondary structure content of this MEF2C fusion protein

As shown in the vehicle control panel, our results confirmed that the HeLa cells do not express the MEF2C factor and further rule out the possibility of glycerol buffer mediated endogenous expression of MEF2C or false positive signal during analysis (Fig. 8). Thus, our fusion strategy successfully mediates the purified rhMEF2C-NTH protein to cross the sub-cellular and sub-nuclear regions of the mammalian cells without any additional protein transduction reagent.

Previously, several studies, including ours, have employed similar strategies to generate transducible versions of different recombinant reprogramming transcription factors from *E. coli* [25, 26, 36, 46–48, 50–52, 54, 56]. Indeed, in the majority of these studies, the fusion tags do not affect the functionality of the desired proteins to which they were fused [26, 36, 46–48, 50–52, 54, 62]. Notably, the biological activity of these transducible recombinant reprogramming proteins was comparable to their genetic counterparts [47, 48, 51]. Henceforth, this transducible version of rhMEF2C fusion protein can replace its genetic form to derive integration-free cells and also for other biomedical applications. Thus, eliminating the problems associated with the plasmid or viral-based approaches [53, 63, 64].
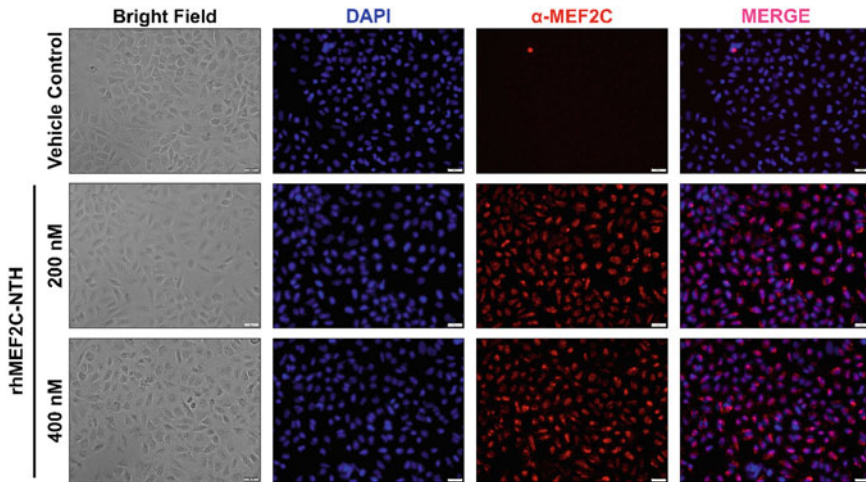
Fig. 8 Sub-cellular and sub-nuclear delivery of purified rhMEF2C-NTH protein into mammalian target cells. HeLa cells were treated with 200 or 400 nM of purified rhMEF2C fusion protein or vehicle control for 4–6 h and then fixed, permeabilized, and blocked. Subsequently, cells were probed with an anti-Mef2c antibody and detected with an Alexa Fluor® 594 conjugated anti-rabbit secondary antibody. Nuclei were stained with Hoechst, and images were taken at 20 × magnification. All images were taken with identical camera settings. The scale bar indicates 50 μm (n = 3)

3.6   rhMEF2C-NTH Protein Inhibits the Migration of Endothelial Cells

To examine whether the purified rhMEF2C-NTH fusion protein is biologically active, we first analyzed its effect on the migration ability of endothelial cells. For this analysis, we performed an in vitro scratch wound healing assay, a widely used assay to study the migration-inducing/inhibiting potential of any specific biological molecules, including recombinant proteins [27, 28]. Interestingly, studies have shown that the MEF2C transcription factor negatively regulates sprouting angiogenesis by inhibiting migration and tube formation of endothelial cells [65, 66]. In line with this, we also observed significantly reduced migration potential of rhMEF2C-NTH protein transduced HUVECs compared with the non-transduced control cells after 12 and 24 h of incubation (Fig. 9a, b). However, HUVEC migration was significantly increased in the presence of VEGF (Fig. 9a, b) after 12 h of incubation, which was used as a control. Notably, a previous study reported that MEF2C influence only the migration and does not affect the proliferation of endothelial cells [65]. On the other hand, studies have reported the enhanced migration of endothelial cells by *E. coli*-derived recombinant human dermatopontin [28] and *Brugia malayi* asparaginyl-tRNA synthetase [27] proteins. These data thus confirm that our purified human MEF2C fusion protein decreases the migration potential of endothelial cells.
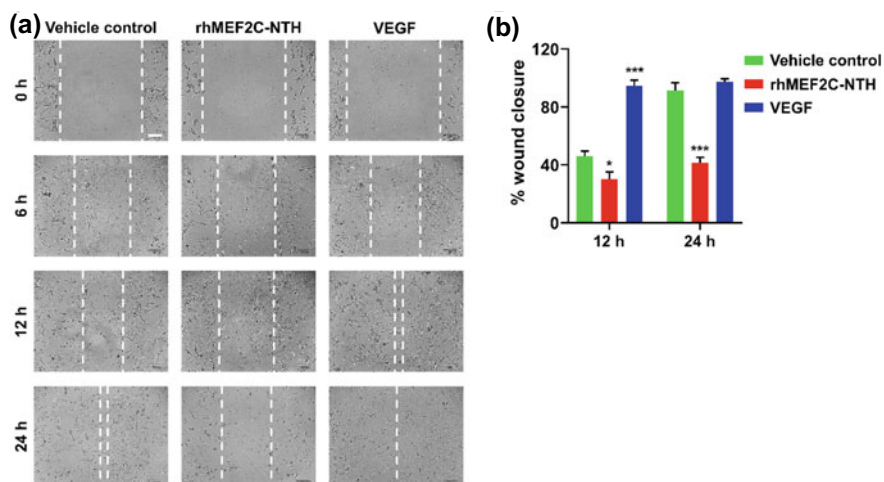
Fig. 9 Effect of purified rhMEF2C-NTH protein on the migration potential of endothelial cells. **a** Microscopy analysis of the migration potential of HUVECs upon treatment with MEF2C fusion protein or VEGF. The scale bar indicates 100 μm. **b** The quantitative representation of (**a**) and data shown are mean $\pm$ S.D. (n $=$ 3). *P $<$ 0.05; ***P $<$ 0.0001

3.7 rhMEF2C-NTH Protein Negatively Regulates Angiogenesis

Although this purified fusion protein inhibits the migration potential of endothelial cells, further examination is required to corroborate its effect on angiogenesis. Therefore, to elucidate the anti-angiogenic potential of this MEF2C protein, we performed a CAM assay on the chicken embryo model. This assay is the most commonly used assay for examining the angiogenic/anti-angiogenic potential of numerous biocompatible molecules, including macromolecules such as recombinant proteins [27, 28]. To analyze the anti-angiogenic potential of the rhMEF2C-NTH protein, we first soaked the filter paper discs in the protein or control solutions for the slow diffusion of proteins and then placed them directly on the CAMs. Surprisingly, we did not observe any sprouting blood vessels (small capillaries) from the pre-existing ones in the rhMEF2C-NTH protein diffused CAM compared to its control CAM after 12 h of incubation (Fig. 10). Contrastingly, enhanced sprouting blood vessels were observed in the VEGF treated CAM at the end of 12 h (Fig. 10). This inhibition of sprouting angiogenesis might be due to decreased migration and tube formation potential of endothelial cells mediated by the MEF2C transcription factor [65]. Consistent with this, we also observed the migration inhibition potential of purified rhMEF2C fusion protein on endothelial cells (Fig. 9a, b).

Although studies suggest that MEF2C binds to the Notch intracellular domain in cardiomyocytes [67, 68], it does not regulate angiogenesis through the Notch
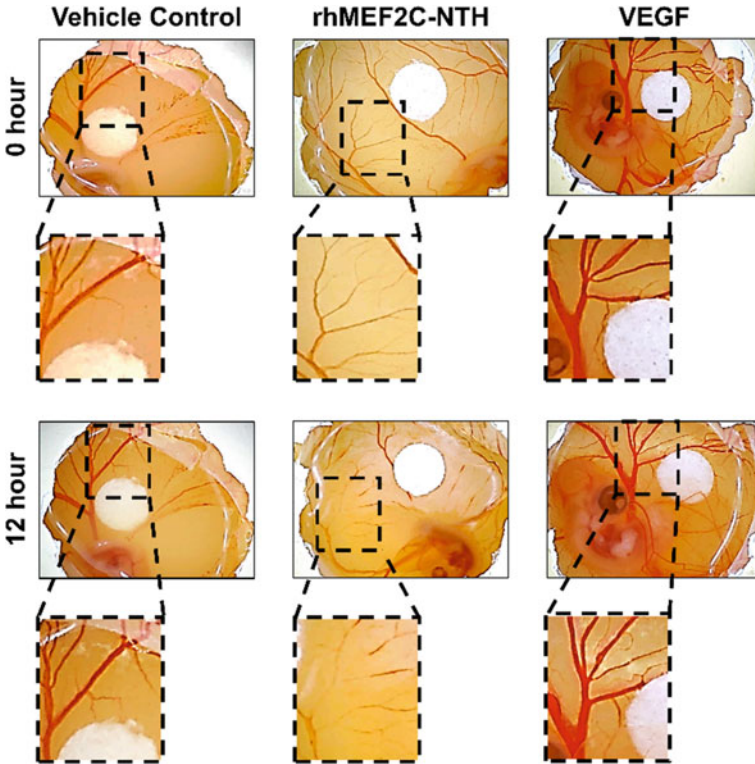
Fig. 10 Effect of purified rhMEF2C-NTH protein on angiogenesis in ex vivo chicken CAM model. The CAM of 3–4 days old embryonated chicken eggs were exposed and treated with purified rhMEF2C fusion protein or VEGF or respective control at 37 °C for 12 h. Macroscopic images of CAM were captured with identical camera settings before and after the treatment (n = 3)

signaling pathway [65], unlike HAND2 [69]. Notably, MEF2C induces the expression of alpha-2-macroglobulin in endothelial cells, which then negatively regulates angiogenesis [65]. These results imply that the purified rhMEF2C-NTH protein inhibits the sprouting angiogenesis, which might be mediated through the induction of alpha-2-macroglobulin, which in turn inhibits the endothelial cells migration and tube formation potential.

3.8 rhMEF2C-NTH Protein Synergistically Activates the α-MHC Gene

We further focused on investigating the transcriptional activity of this purified fusion protein. For validating its transcriptional activity, we have chosen an α-MHC gene, one of its cardiomyocyte-specific downstream targets [70], and performed a reporter

assay using the α-MHC promoter-driven eGFP reporter system in cardiomyoblast cells. We first infected the H9C2 cells with the lentivirus α-MHC-eGFP reporter and then treated them with the purified rhMEF2C-NTH protein (Fig. 11a). Even after 3–4 rounds of protein transduction, we did not observe any GFP expression in H9C2 cells when treated only with the rhMEF2C-NTH protein (Fig. 11b). Interestingly, induction of GFP expression was observed when the H9C2 cells were treated with the rhMEF2C-NTH protein along with purified rhHTN-HAND2 protein [34]. Further analyses with the flow cytometry revealed that around 22% of the H9C2 cells were GFP$^+$ when treated with either fusion proteins, while <1% GFP$^+$ cells were observed when treated with only MEF2C or HAND2 fusion protein. (Fig. 11c). These results were in line with the previous report that demonstrated the synergistic activation of an α-MHC gene (~fivefold) by the MEF2C and HAND2 transcription factor in H9C2 cells using a luciferase-based reporter system [70]. However, in contrast to our results the authors also observed a significant difference in the α-MHC expression when they overexpressed only MEF2C or HAND2 transcription factor in H9C2 cells [70]. These contrasting results might be similar to why the efficiency of recombinant protein-based reprogramming is less than that of viral vector-based reprogramming [54].
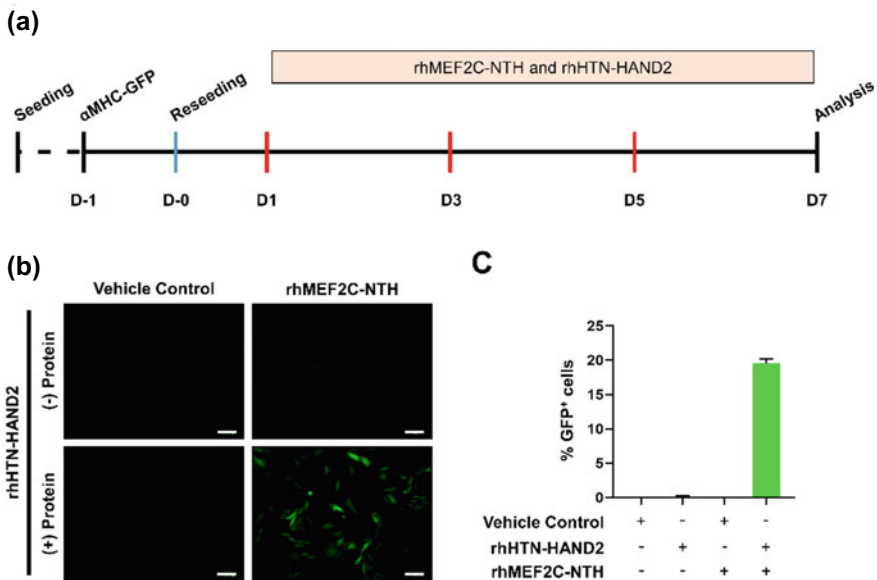
Fig. 11 A synergy of purified rhMEF2C-NTH protein with HAND2 fusion protein in the activation of the α-MHC. **a** Experimental scheme of the α-MHC-eGFP reporter. **b** α-MHC-eGFP transduced H9C2 cells were treated with MEF2C and/or HAND2 fusion protein(s) or respective controls for 7–8 days. Images were captured after treatment with identical camera settings and analyzed. **c** Flow cytometry quantitative analysis of the GFP$^+$ cells. The quantitative data shown are mean ± S.D. (n = 4)

Moreover, cardiac restricted transcription factors interact with each other to regulate various target genes. For example, GATA4 recruits MEF2C to regulate the ANP transcriptional activity [71]. Similarly, MEF2C recruits HAND2 to the α-MHC and ANP promoters and regulates transcription through protein–protein interaction [70]. Studies demonstrated that the MEF2C protein physically interacts with HAND2 protein both in vitro and in vivo [70, 72]. Thus, this purified rhMEF2C-NTH protein physically interacts with the HAND2 fusion protein and forms a protein complex to regulate the transcription of an α-MHC gene. Taken together, our results thus signify transcriptional synergy of the MEF2C fusion protein with HAND2 protein in the activation of the α-MHC promoter.

4 Conclusion

In conclusion, we demonstrated the heterologous production of rhMEF2C-NTH protein induced at two different temperatures with high purity and secondary structure stability (post-purification). We employed a codon-optimized gene sequence to attain the enhanced production of this rhMEF2C-NTH protein. However, gene optimization alone is insufficient to obtain the maximum soluble expression of this fusion protein, as shown from the result of this study. Hence, we have identified the optimal expression conditions and appropriate genetic construct for maximal soluble expression. Notably, we have established the one-step homogeneous purification of the recombinant human MEF2C fusion protein under native conditions. Additionally, we have showed that this purified fusion protein has retained its secondary structure post-purification and has the ability for cell penetration and nuclear translocation. Further, we have demonstrated that the purified protein has anti-angiogenic properties and synergistically activated α-MHC gene in the presence of recombinant human HAND2 protein. However, further refinements might assist in enhancing the yield of the purified fusion protein. Eventually, this purified MEF2C fusion protein can be used to study its functional role in various biological processes and also can be employed as a replacement for its genetic counterpart in the direct reprogramming of cardiomyocytes. The resulting cardiomyocytes will be integration free and of clinical-grade that will have prospective biomedical applications.

Author Contribution KKH was responsible for conception and design, collection and/or assembly of data, data analysis and interpretation, manuscript writing, and final approval of the

manuscript; **PKS, UV** and **VK** were responsible for collection and/or assembly of data, data analysis and interpretation, and final approval of the manuscript; **RPT** was responsible for conception and design, collection and/or assembly of data, data analysis and interpretation, manuscript writing, final editing and approval of the manuscript and financial support. All the authors gave consent for publication.

Compliance with Ethical Standards

Conflict of Interest The authors declare that they have no known competing financial interests or personal relationships that could have appeared to influence the work reported in this paper.

Ethical Approval This article does not contain any studies with human participants or animals performed by any of the authors.

References

1. Edmondson DG, Lyons GE, Martin JF, Olson EN (1994) Mef2 gene expression marks the cardiac and skeletal muscle lineages during mouse embryogenesis. Development 120(5):1251–1263
2. Subramanian SV, Nadal-Ginard B (1996) Early expression of the different isoforms of the myocyte enhancer factor-2 (MEF2) protein in myogenic as well as non-myogenic cell lineages during mouse embryogenesis. Mech Dev. https://doi.org/10.1016/0925-4773(96)00542-4
3. Potthoff MJ, Arnold MA, McAnally J, Richardson JA, Bassel-Duby R, Olson EN (2007) Regulation of Skeletal muscle sarcomere integrity and postnatal muscle function by Mef2c. Mol Cell Biol 27(23):8143–8151. https://doi.org/10.1128/mcb.01187-07
4. Martin JF, Schwarz JJ, Olson EN (1993) Myocyte enhancer factor (MEF) 2C: a tissue-restricted member of the MEF-2 family of transcription factors. Proc Natl Acad Sci USA 90(11):5282–5286. https://doi.org/10.1073/pnas.90.11.5282
5. Arnold MA, Kim Y, Czubryt MP, Phan D, McAnally J, Qi X et al (2007) MEF2C transcription factor controls chondrocyte hypertrophy and bone development. Dev Cell 12(3):377–389. https://doi.org/10.1016/j.devcel.2007.02.004
6. Dodou E, Verzi MP, Anderson JP, Xu SM, Black BL (2004) Mef2c is a direct transcriptional target of ISL1 and GATA factors in the anterior heart field during mouse embryonic development. Development 131(16):3931–3942. https://doi.org/10.1242/dev.01256
7. Lin Q, Lu J, Yanagisawa H, Webb R, Lyons GE, Richardson JA, Olson EN (1998) Requirement of the MADS-box transcription factor MEF2C for vascular development. Development 125(22):4565–4574
8. Verzi MP, Agarwal P, Brown C, McCulley DJ, Schwarz JJ, Black BL (2007) The transcription factor MEF2C Is required for craniofacial development. Dev Cell 12(4):645–652. https://doi.org/10.1016/j.devcel.2007.03.007
9. Li H, Radford JC, Ragusa MJ, Shea KL, McKercher SR, Zaremba JD et al (2008) Transcription factor MEF2C influences neural stem/progenitor cell differentiation and maturation in vivo. Proc Natl Acad Sci U S A 105(27):9397–9402. https://doi.org/10.1073/pnas.0802876105
10. Ieda M, Fu JD, Delgado-Olguin P, Vedantham V, Hayashi Y, Bruneau BG, Srivastava D (2010) Direct reprogramming of fibroblasts into functional cardiomyocytes by defined factors. Cell 142(3):375–386. https://doi.org/10.1016/j.cell.2010.07.002
11. Fu JD, Stone NR, Liu L, Spencer CI, Qian L, Hayashi Y et al (2013) Direct reprogramming of human fibroblasts toward a cardiomyocyte-like state. Stem Cell Rep 1(3):235–247. https://doi.org/10.1016/j.stemcr.2013.07.005
12. Wada R, Muraoka N, Inagawa K, Yamakawa H, Miyamoto K, Sadahiro T et al (2013) Induction of human cardiomyocyte-like cells from fibroblasts by defined factors. Proc Natl Acad Sci U S A 110(31):12667–12672. https://doi.org/10.1073/pnas.1304053110

13. Demain AL, Vaishnav P (2009) Production of recombinant proteins by microbes and higher organisms. Biotechnol Adv 27(3):297–306. https://doi.org/10.1016/j.biotechadv.2009.01.008
14. Huang CJ, Lin H, Yang X (2012) Industrial production of recombinant therapeutics in *Escherichia coli* and its recent advancements. J Ind Microbiol Biotechnol 39(3):383–399. https://doi.org/10.1007/s10295-011-1082-9
15. Makrides SC (1996) Strategies for achieving high-level expression of genes in *Escherichia coli*. Microbiol Rev 60(3):512–538. https://doi.org/10.1128/mmbr.60.3.512-538.1996
16. Jonasson P, Liljeqvist S, Nygren P-Å, Ståhl S (2002) Genetic design for facilitated production and recovery of recombinant proteins in *Escherichia coli*. Biotechnol Appl Biochem 35(2):91. https://doi.org/10.1042/ba20010099
17. Chen R (2012) Bacterial expression systems for recombinant protein production: *E. coli* and beyond. Biotechnol Adv 30(5):1102–1107. https://doi.org/10.1016/j.biotechadv.2011.09.013
18. Young CL, Britton ZT, Robinson AS (2012) Recombinant protein expression and purification: a comprehensive review of affinity tags and microbial applications. Biotechnol J 7(5):620–634. https://doi.org/10.1002/biot.201100155
19. Wood DW (2014) New trends and affinity tag designs for recombinant protein purification. Curr Opin Struct Biol 26(1):61. https://doi.org/10.1016/j.sbi.2014.04.006
20. O'Malley J, Woltjen K, Kaji K (2009) New strategies to generate induced pluripotent stem cells. Curr Opin Biotechnol 20(5):516–521. https://doi.org/10.1016/j.copbio.2009.09.005
21. Sommer CA, Mostoslavsky G (2013) The evolving field of induced pluripotency: recent progress and future challenges. J Cell Physiol 228(2):267–275. https://doi.org/10.1002/jcp.24155
22. Dey C, Narayan G, Krishna Kumar H, Borgohain M, Lenka N (2017) Cell-penetrating peptides as a tool to deliver biologically active recombinant proteins to generate transgene-free induced pluripotent stem cells. Stud Stem Cells Res Ther 3(1):006–015. https://doi.org/10.17352/sscrt.000011
23. Borgohain MP, Haridhasapavalan KK, Dey C, Adhikari P, Thummer RP (2019) An Insight into DNA-free reprogramming approaches to generate integration-free induced pluripotent stem cells for prospective biomedical applications. Stem Cell Rev Rep 15(2):286–313. https://doi.org/10.1007/s12015-018-9861-6
24. Haridhasapavalan KK, Sundaravadivelu PK, Thummer RP (2020) Codon optimization, cloning, expression, purification, and secondary structure determination of human ETS2 transcription factor. Mol Biotechnol 62(10):485–494. https://doi.org/10.1007/s12033-020-00266-8
25. Haridhasapavalan KK, Sundaravadivelu PK, Bhattacharyya S, Ranjan SH, Raina K, Thummer RP (2021) Generation of cell-permeant recombinant human transcription factor GATA4 from *E. coli*. Bioprocess Biosyst Eng. https://doi.org/10.1007/s00449-021-02516-8
26. Haridhasapavalan KK, Das NJ, Thummer RP (2022) Generation of a transducible version of a bioactive recombinant human TBX5 transcription factor from *E. coli*. Curr Res Biotechnol 4:66–77. https://doi.org/10.1016/j.crbiot.2022.01.004
27. D JJ, Dhanraj M, Solaiappan S, Sivanesan S, Kron M, Dhanasekaran A (2016) Brugia malayi Asparaginyl - tRNA synthetase stimulates endothelial cell proliferation, vasodilation and angiogenesis. PLOS ONE 11(1):e0146132. https://doi.org/10.1371/journal.pone.0146132
28. Seetaraman Amritha TM, Mahajan S, Subramaniam K, Chandramohan Y, Dhanasekaran A (2020) Cloning, expression and purification of recombinant dermatopontin in *Escherichia coli*. PLOS ONE, 15(11):e0242798. https://doi.org/10.1371/journal.pone.0242798
29. Addis RC, Ifkovits JL, Pinto F, Kellam LD, Esteso P, Rentschler S et al (2013) Optimization of direct fibroblast reprogramming to cardiomyocytes using calcium activity as a functional measure of success. J Mol Cell Cardiol 60:97–106. https://doi.org/10.1016/j.yjmcc.2013.04.004
30. Yang Q, Yu C-H, Zhao F, Dang Y, Wu C, Xie P, et al (2019) eRF1 mediates codon usage effects on mRNA translation efficiency through premature termination at rare codons. Nucleic Acids Res 47(17):9243–9258. https://doi.org/10.1093/nar/gkz710
31. Tanner DR, Cariello DA, Woolstenhulme CJ, Broadbent MA, Buskirk AR (2009) Genetic identification of nascent peptides that induce ribosome stalling. J Biol Chem 284(50):34809–34818. https://doi.org/10.1074/jbc.M109.039040

32. Sabi R, Tuller T (2015) A comparative genomics study on the effect of individual amino acids on ribosome stalling. BMC Genomics 16(S10):S5. https://doi.org/10.1186/1471-2164-16-S10-S5

33. Haridhasapavalan KK, Ranjan SH, Bhattacharyya S, Thummer RP (2021) Soluble expression, purification, and secondary structure determination of human MESP1 transcription factor. Appl Microbiol Biotechnol 105(6):2363–2376. https://doi.org/10.1007/s00253-021-11194-1

34. Haridhasapavalan KK, Sundaravadivelu PK, Joshi N, Das NJ, Mohapatra A, Voorkara U et al (2022) Generation of a recombinant version of a biologically active cell-permeant human HAND2 transcription factor from E. coli. Sci Rep 12(1):16129. https://doi.org/10.1038/s41598-022-19745-w

35. Braun P, Hu Y, Shen B, Halleck A, Koundinya M, Harlow E, LaBaer J (2002) Proteome-scale purification of human proteins from bacteria. Proc Natl Acad Sci USA 99(5):2654–2659. https://doi.org/10.1073/pnas.042684199

36. Bosnali M, Edenhofer F (2008) Generation of transducible versions of transcription factors Oct4 and Sox2. Biol Chem 389(7):851–861. https://doi.org/10.1515/BC.2008.106

37. Vasina JA, Baneyx F (1997) Expression of aggregation-prone recombinant proteins at low temperatures: a comparative study of the *Escherichia coli* cspA and tac promoter systems. Protein Expr Purif 9(2):211–218. https://doi.org/10.1006/prep.1996.0678

38. Galloway CA, Sowden MP, Smith HC (2003) Increasing the yield of soluble recombinant protein expressed in *E. coli* by Induction during late log phase. BioTechniques 34(3):524–530. https://doi.org/10.2144/03343st04

39. Sørensen HP, Mortensen KK (2005) Advanced genetic strategies for recombinant protein expression in *Escherichia coli*. J Biotechnol 115(2):113–128. https://doi.org/10.1016/j.jbiotec.2004.08.004

40. Rabhi-Essafi I, Sadok A, Khalaf N, Fathallah DM (2007) A strategy for high-level expression of soluble and functional human interferon α as a GST-fusion protein in *E.coli*. Protein Eng Des Sel 20(5):201–209. https://doi.org/10.1093/protein/gzm012

41. Azaman SNA, Ramakrishnan NR, Tan JS, Rahim RA, Abdullah MP, Ariff AB (2010) Optimization of an induction strategy for improving interferon-α2b production in the periplasm of *Escherichia coli* using response surface methodology. Biotechnol Appl Biochem 56(4):141–150

42. San-Miguel T, Pérez-Bermúdez P, Gavidia I (2013) Production of soluble eukaryotic recombinant proteins in *E. coli* is favoured in early log-phase cultures induced at low temperature. SpringerPlus *2*(1):1–4. https://doi.org/10.1186/2193-1801-2-

43. Liu B, Kong Q, Zhang D, Yan L (2018) Codon optimization significantly enhanced the expression of human 37-kDa iLRP in *Escherichia coli*. 3 Biotech 8(4):1–7. https://doi.org/10.1007/s13205-018-1234-y

44. Borgohain MP, Narayan G, Krishna Kumar H, Dey C, Thummer RP (2018) Maximizing Expression and yield of human recombinant proteins from bacterial cell factories for biomedical applications. In: Kumar P, Patra JK, Chandra P (eds) Advances in microbial biotechnology, 1st edn. Apple Academic Press, New York, pp 447–486. https://doi.org/10.1201/9781351248914

45. Baneyx F, Mujacic M (2004) Recombinant protein folding and misfolding in *Escherichia coli*. Nat Biotechnol 22(11):1399–1407. https://doi.org/10.1038/nbt1029

46. Peitz M, Münst B, Thummer RP, Helfen M, Edenhofer F (2014) Cell-permeant recombinant Nanog protein promotes pluripotency by inhibiting endodermal specification. Stem Cell Res 12(3):680–689. https://doi.org/10.1016/j.scr.2014.02.006

47. Thier M, Münst B, Edenhofer F (2011) Exploring refined conditions for reprogramming cells by recombinant Oct4 protein. Int J Dev Biol 54(11–12):1713–1721. https://doi.org/10.1387/ijdb.103193mt

48. Thier M, Münst B, Mielke S, Edenhofer F (2012) Cellular reprogramming employing recombinant Sox2 protein. Stem Cells Int. https://doi.org/10.1155/2012/549846

49. Wingfield PT (2015) Overview of the purification of recombinant proteins. Curr Protoc Protein Sci 80(1):1–6

50. Münst B, Thier MC, Winnemöller D, Helfen M, Thummer RP, Edenhofer F (2016) Nanog induces suppression of senescence through downregulation of p27KIP1 expression. J Cell Sci 129(5):912–920. https://doi.org/10.1242/jcs.167932

51. Stock K, Nolden L, Edenhofer F, Quandel T, Brüstle O (2010) Transcription factor-based modulation of neural stem cell differentiation using direct protein transduction. Cell Mol Life Sci 67(14):2439–2449. https://doi.org/10.1007/s00018-010-0347-1

52. Narayan G, Agrawal A, Joshi N, Gogoi R, Nagotu S, Thummer RP (2021) Protein production and purification of a codon-optimized human NGN3 transcription factor from *E. coli*. Protein J 40(6):891–906. https://doi.org/10.1007/s10930-021-10020-x

53. Dey C, Raina K, Haridhasapavalan KK, Thool M, Sundaravadivelu PK, Adhikari P et al (2021) An overview of reprogramming approaches to derive integration-free induced pluripotent stem cells for prospective biomedical applications. Recent Adv iPSC Technol 231–287. https://doi.org/10.1016/B978-0-12-822231-7.00011-4

54. Dey C, Venkatesan V, Thummer RP (2022) Identification of optimal expression parameters and purification of a codon-optimized human GLIS1 transcription factor from *Escherichia coli*. Mol Biotechnol 64(1):42–56. https://doi.org/10.1007/s12033-021-00390-z

55. Araki Y, Hamafuji T, Noguchi C, Shimizu N (2012) Efficient recombinant production in mammalian cells using a novel IR/MAR gene amplification method. PLoS ONE 7(7):1–10. https://doi.org/10.1371/journal.pone.0041787

56. Narayan G, Sundaravadivelu PK, Agrawal A, Gogoi R, Nagotu S, Thummer RP (2021) Soluble expression, purification, and secondary structure determination of human PDX1 transcription factor. Protein Expr Purif 180:105807. https://doi.org/10.1016/j.pep.2020.105807

57. Kelly SM, Jess TJ, Price NC (2005) How to study proteins by circular dichroism. Biochimica et Biophysica Acta—Proteins Proteomics 1751(2):119–139. https://doi.org/10.1016/j.bbapap.2005.06.005

58. Kessenbrock M, Groth G (2017) Circular dichroism and fluorescence spectroscopy to study protein structure and protein–protein interactions in ethylene signaling. Methods Mol Biol 1573:141–159. https://doi.org/10.1007/978-1-4939-6854-1_12

59. Greenfield NJ (2007) Using circular dichroism spectra to estimate protein secondary structure. Nat Protoc 1(6):2876–2890. https://doi.org/10.1038/nprot.2006.202

60. Micsonai A, Wien F, Kernya L, Lee YH, Goto Y, Réfrégiers M, Kardos J (2015) Accurate secondary structure prediction and fold recognition for circular dichroism spectroscopy. Proc Natl Acad Sci USA 112(24):E3095–E3103. https://doi.org/10.1073/pnas.1500851112

61. Micsonai A, Wien F, Bulyáki É, Kun J, Moussong É, Lee YH et al (2018) BeStSel: a web server for accurate protein secondary structure prediction and fold recognition from the circular dichroism spectra. NuclC Acids Res 46(W1):W315–W322. https://doi.org/10.1093/nar/gky497

62. Dey C, Thool M, Bhattacharyya S, Sudhagar S, Thummer RP (2021) Generation of biologically active recombinant human OCT4 protein from *E. coli*. 3 Biotech 11(5):1–16. https://doi.org/10.1007/S13205-021-02758-Z

63. Islas JF, Liu Y, Weng KC, Robertson MJ, Zhang S, Prejusa A et al (2012) Transcription factors ETS2 and MESP1 transdifferentiate human dermal fibroblasts into cardiac progenitors. Proc Natl Acad Sci U S A 109(32):13016–13021. https://doi.org/10.1073/pnas.1120299109

64. Haridhasapavalan KK, Borgohain MP, Dey C, Saha B, Narayan G, Kumar S, Thummer RP (2019) An insight into non-integrative gene delivery approaches to generate transgene-free induced pluripotent stem cells. Gene 686. https://doi.org/10.1016/j.gene.2018.11.069

65. Sturtzel C, Testori J, Schweighofer B, Bilban M, Hofer E (2014) The transcription factor MEF2C negatively controls angiogenic sprouting of endothelial cells depending on oxygen. PLoS ONE 9(7):e101521. https://doi.org/10.1371/journal.pone.0101521

66. Xu Z, Gong J, Maiti D, Vong L, Wu L, Schwarz JJ, Duh EJ (2012) MEF2C ablation in endothelial cells reduces retinal vessel loss and suppresses pathologic retinal neovascularization in oxygen-induced retinopathy. Am J Pathol 180(6):2548–2560. https://doi.org/10.1016/j.ajpath.2012.02.021

67. Wilson-Rawls J, Molkentin JD, Black BL, Olson EN (1999).Activated notch inhibits myogenic activity of the MADS-box transcription factor myocyte enhancer factor 2C. Mol Cell Biol 19(4):2853–2862. https://doi.org/10.1128/MCB.19.4.2853
68. Pallavi SK, Ho DM, Hicks C, Miele L, Artavanis-Tsakonas S (2012) Notch and Mef2 synergize to promote proliferation and metastasis through JNK signal activation in Drosophila. EMBO J 31(13):2895–2907. https://doi.org/10.1038/emboj.2012.129
69. VanDusen NJ, Casanovas J, Vincentz JW, Firulli BA, Osterwalder M, Lopez-Rios J et al (2014) Hand2 Is an essential regulator for two notch-dependent functions within the embryonic endocardium. Cell Rep 9(6):2071–2083. https://doi.org/10.1016/j.celrep.2014.11.021
70. Zang M-X, Li Y, Wang H, Wang J-B, Jia H-T (2004) Cooperative Interaction between the Basic Helix-loop-helix transcription Factor dHAND and myocyte enhancer factor 2C regulates myocardial gene expression. J Biol Chem 279(52):54258–54263. https://doi.org/10.1074/jbc.M408502200
71. Morin S, Charron F, Robitaille L, Nemer M (2000) GATA-dependent recruitment of MEF2 proteins to target promoters. EMBO J 19(9):2046–2055. https://doi.org/10.1093/emboj/19.9.2046
72. Zang M-X, Li Y, Xue L-X, Jia H-T, Jing H (2004) Cooperative activation of atrial naturetic peptide promoter by dHAND and MEF2C. J Cell Biochem 93(6):1255–1266. https://doi.org/10.1002/jcb.20225

Identification of Candidate RNA Binding Proteins Associated with RNPS1 3'UTR

Bhagyashree Deka and Kusum Kumari Singh

Keywords RNPS1 · Serine-rich domain · Alternative splicing · 3'UTR · Aptamers · MS2 coat protein · RBPs

1 Introduction

The coordinated, multi-layered process of gene expression involves a large number of trans-acting factors. While most genomic studies have focused on transcriptional regulation, post-transcriptional regulation has only lately been studied. RNA-binding proteins (RBPs) and non-coding RNAs are two critical factors in post-transcriptional regulation that act in a combinatorial or cooperative manner to control the spatio-temporal expression of target proteins. Computational, genetic, and biochemical strategies have been employed to identify and confirm RBP-binding sites on mRNAs and their corresponding RBPs. However, traditional approaches identify only a limited number of RNA–protein interactions. Therefore, exploring the binding characteristics of RBPs at a systems level is essential to comprehensively understand the regulatory mechanisms mediated by RBPs and determine the "RNP code" of an mRNA.

RNP immunoprecipitation (RIP-chip) was the first developed high-throughput method to detect targets of a specific RBP using cDNA arrays [1]. RIP is performed under endogenous conditions that preserve RNA–protein interactions. RIP studies have unraveled several putative regulatory factors in response to different stimuli. Further, this method provided evidence for the operon model, in which RBPs synchronize the expression of functionally connected proteins [2, 3].

B. Deka · K. K. Singh (✉)
RNA Binding Proteins Laboratory, Department of Biosciences and Bioengineering, Indian Institute of Technology Guwahati, Guwahati 781039, Assam, India
e-mail: kusumsingh@iitg.ac.in

Subsequent high-throughput methods employed cross-linking followed by immunoprecipitation to accurately determine the position of the binding sites of RBPs within mRNA. One of these methods is PAR-CLIP (photoactivatable ribonucleoside cross-linking and immunoprecipitation). PAR-CLIP employs a long UV wave (365 nm) to cross-link photoactive thiouridine integrated into RNA [4]. This cross-linking does not induce extensive photo damage to RNA and protein in contrast to a short UV wave (254 nm). These techniques have been developed to isolate RNAs from particular RBPs in vivo. On the other hand, developing appropriate strategies to identify and explore proteins that associate to a particular RNA is challenging.

In previous studies, RNA is chemically modified during in vitro transcription to study the interactome of a specific RNA. One of the widely used labels in in vitro studies is the incorporation of biotin within the desired RNA. The tagged RNA is then incubated with cell lysates to let RBPs bind RNA, followed by RNA pulldown using streptavidin-coated beads and detection of bound proteins [5]. In order to study RNA–protein interactions within cells or under endogenous conditions, chemically labeled RNAs are expressed in cells. Subsequently, the labeled RNA is isolated from the RNA pool using specific antibodies or affinity compounds. However, the challenges of these approaches are ensuring proper localization of chemically altered transcripts and avoiding nonspecific association with proteins. To this end, alternate strategies have been developed that contain tagging and pulldown of exogenously expressed transcripts. Various small RNA tags, also known as aptamers, are tagged to the RNA of interest and pulldown using compounds that have affinity for the aptamer. For instance, RNA aptamers D8 and S1 have an affinity for streptavidin and Sephadex, respectively [6–8]. The S1 aptamer was employed to analyze the bound proteins of RNase P by tagging RPR1 RNA, the large subunit of RNase P. The aptamer tag showed that RNaseP occurs as a monomer and is loosely associated with RNase MRP [6].

Although RNPS1 plays an important role in splicing activity, there are no reports on regulatory proteins controlling the expression of RNPS1. To study the RBP-mediated regulation of RNPS1 expression, we devised a strategy to analyze the association between *RNPS1* 3'UTR and proteins. The technique utilizes the RNA aptamer, MS2 tag, a widely used tag. It is a virus derived RNA sequence of 19 nt length that folds into a hairpin loop structure. This structure is identified by the MS2 bacteriophage coat protein with very high affinity and specificity. The MS2 is added to *RNPS1* 3'UTR, followed by co-expression of the MS2-tagged *RNPS1* RNA along with the MS2 coat protein fused to a Flag tag. The MS2 RNP complex is purified using an antibody against Flag, and finally, the proteins bound to *RNPS1* 3'UTR were analyzed via mass spectrometry. Intriguingly, *RNPS1* 3'UTR was found to interact with several RBPs, including heterogeneous nuclear ribonucleoprotein C (HNRNPC), interleukin enhancer-binding factor 2 (ILF2) and ILF3.

2   Materials and Methods

2.1   Construction of Plasmids

The plasmid vector pcDNA5-FRT-TO was a kind gift from Prof. Niels Gehring, University of Cologne, Germany. First, dtTomato was cloned in pcDNA5-FRT-TO using NheI and XhoI restriction sites. Second, 6X MS2 aptamer sequences were cloned in pcDNA5-FRT-TO-dtTomato using XhoI and SalI restriction sites. Finally, *RNPS1* 3'UTR was cloned downstream of MS2 aptamer in pcDNA5-FRT-TO-dtTomato-MS2 using SalI and NotI restriction sites. Cloned gene sequences were further validated by Sanger sequencing.

The plasmid vector PB-Cuo-Flag-MS2-IRES-GFP-EF1α-CymR-Puro was a kind gift from Prof. Niels Gehring, University of Cologne, Germany.

2.2   Transformation of Recombinant Vector

The ligation mixture or the plasmid was added to the competent cells. The tubes were incubated in ice for 30 min. Heat shock was given at 42 °C for 45 s and immediately transferred to the ice for 2 min. The cells were plated on Luria–Bertani agar with ampicillin and incubated at 37 °C for 16 h. Positive colonies were verified by colony PCR, followed by restriction enzyme digestion and sequencing.

2.3   Cell Culture

Flp-In T-REx-293 cells were maintained as per the earlier protocol explained in [9]. Briefly, Dulbecco's Modified Eagle's Medium with high glucose (Himedia) was used. The media was supplemented with 10% fetal bovine serum (Himedia) and 1% penicillin/streptomycin (Himedia). The cells were kept at 37 °C in a humidified atmosphere containing 5% CO_2.

2.4   Generation of Stable Cells

Flp-In T-REx-293 cells were seeded in 6-well plates. 24 h after seeding, the cells were transfected with pcDNA5-FRT-TO-dtTomato-MS2-RNPS1 3'UTR and pOG44 (FLP recombinase). 48 h after transfection, the cells were subcultured and fresh medium containing 150 µg/ml hygromycin B was added. After 3 weeks, single colonies were picked and expanded. These single stable cells were again seeded in 6-well plates.

24 h after seeding, the cells were transfected with PB-Cuo-FLAG-MS2-IRES-GFP-EF1 α-CymR-Puro and Piggybac transposase vector. 72 h after transfection, the cells were subcultured and fresh medium containing 2 μg/ml puromycin was added. The cells were maintained in puromycin-supplemented medium for 2 weeks until resistant colonies were obtained. Single colonies were picked and expanded to get double stable cell lines.

2.5 RNA Isolation and cDNA Synthesis

Total cellular RNA was isolated as per the earlier protocol using TRIzol reagent (Invitrogen) and the chloroform separation method [9]. In order to abolish genomic DNA from isolated RNA, total RNA was incubated with DNase I (Promega). cDNA was prepared by reverse transcribing DNase treated total RNA using the high capacity cDNA reverse transcription kit (Applied Biosystems) [9].

2.6 Quantitative Real-Time PCR

The qRT-PCR was accomplished as per the protocol explained in [9]. cDNA was utilized as a template for the qPCR. 5 μl of 2X Sybr green master mix was mixed with 0.25 μM of each primer, 1 μl of diluted cDNA (1:3 dilution of the cDNA) and the rest were filled with nuclease-free water [9]. Specific primers were used for quantifying gene expression and normalized with β-actin expression. Relative gene expression was calculated using the $\Delta\Delta C_T$ method.

The fold enrichment of each RIP reaction was calculated from qPCR data.

ΔCt [Normalized RIP] = Ct [IP] − Ct [Input].

$\Delta\Delta$Ct [RIP/Control] = ΔCt [Normalized RIP] − ΔCt [Normalized control].

Fold enrichment = $2^{(-\Delta\Delta\text{Ct [RIP/Control]})}$.

2.7 Preparation of Cell Lysates

Double stable Flp-In T-REx-293 cells were at first induced with tetracycline (final conc. 1ug/ul) and next day, the cells were induced with cumate (final conc. 300 ug/ml) and tetracycline. After 48 h, the cells were washed twice with DPBS (Dulbecco's phosphate-buffered saline) and scraped from the cell culture dish in EJC buffer (20 mM HEPES–KOH (pH 7.9), 200 mM NaCl, 2 mM MgCl2, 0.2% Triton X-100, 0.1% Nonidet P40, 0.05% Na-deoxycholic acid). Lysed cells were transferred to 1.5 ml eppendorf tubes on ice followed by sonication (15 cycles at 25% amplitude;

1 s ON, 4 s OFF). The lysate was centrifuged at 13,000 rpm for 10 min at 4 °C and the supernatant was transferred to a new tube.

2.8 RNP Immunoprecipitation

The RNP immunoprecipitation was performed by incubating the cell lysate with anti-FLAG-M2 magnetic beads (Sigma-Aldrich) and incubated for 5 h in a shaker at 4 °C. After incubation, beads were washed four times with EJC buffer. After the last washing step, FLAG peptides were used to elute the bound protein. The total bound proteins were then used for mass-spectrometry analysis.

2.9 Silver Staining

The SDS-PAGE gel was prepared using the BIO-RAD mini gel cast system. The input and RNP IP samples were resolved on 10% SDS-PAGE gel in a vertical electrophoresis tank. After SDS-PAGE, the gel was shortly rinsed in water. Fixation solution (30% ethanol, 10% acetic acid, H_2O) was added on the gel and incubated for 2 h with gentle shaking. The gel was then washed with gentle shaking with 30% ethanol 3 × 10 min followed by washing gel with water 2 × 10 min. The gel was incubated with a sensitizer solution (Sodium dithionite 25 mg/100 ml) for 1 min followed by washing gel with dist. water 2 × 1 min. The staining solution (0.2% AgNO3, 3 µl/40 ml formaldehyde solution (36–38%)) was added on the gel and incubated for 25 min. The gel was washed with water for 1 min and the developer solution (6% sodium carbonate, 4 µg/ml sodium thiosulfate, formaldehyde) was added and incubated for 2–3 min with gentle mixing. Finally stop solution (4% (w/v) Tris and 2% (v/v) acetic acid) was added before the protein bands get dark stained.

2.10 Mass Spectrometry

Specific pull downs were performed to enrich 3'UTR regions and its associated RNA binding proteins. The total immunoprecipitated samples were outsourced for mass spectrometry analysis to V proteomics, New Delhi, India. The sample was used for in-gel trypsin digestion and analyzed by Nano ESI LC–MS/MS using the Orbitrap platform. The MS RAW files were analyzed with MaxQuant suite. The peptides were identified by using the human UniProt database and Andromeda search engine.

2.11   RBP Binding Site Prediction

The binding sites of putative RBPs within RNPS1 3'UTR were predicted using the RBPmap online tool. The input for RBPmap is the RNPS1 3'UTR nucleotide sequence in fasta format and then the tool was executed on standard settings.

2.12   Statistical Analysis

All the quantitative data are represented as mean $\pm$ SD. In all the statistical tests, p < 0.05 was considered as significant. Statistical significances were calculated with the Student's t-test using the GraphPad PRISM.

3   Results

3.1   Construction of Double Stable Cells for Interactome Capture of RNPS1 3'UTR

Besides miRNAs, RBPs are other essential regulators of post-transcriptional gene regulation. Therefore, to isolate RBPs associated with *RNPS1* 3'UTR double stable cell lines were generated. The stable cell expresses both MS2-RNPS1 3'UTR and FLAG-tagged MS2 coat protein. Double stable cells were generated using two types of systems: Flp-In T-REx system and PiggyBac transposon system. The Flp-In TREx system is designed to generate cell lines that stably express the gene of interest in an isogenic and inducible manner. As a result, this eliminates any variation in expression levels caused by the integration of the gene of interest into various sites of the chromosome. It also allows cells to be cultured without expressing the gene of interest, thereby averting probable harmful effects on cell growth. Furthermore, the expression level can be regulated to ensure expression of the desired gene at the near-physiological level, thus avoiding false RNA–protein associations resulting from over-expression. The PiggyBac transposon system is an efficient non-viral vector system for stable expression of the gene of interest. This system utilizes the transposon-mediated integration mechanism to "cut and paste" the desired gene into the genome of mammalian cells. It takes advantage of cabbage looper moth-derived PiggyBac transposon and is one of the most efficient transposons for modifying the mammalian genome. Moreover, the expression of proteins can be switched on or induced by adding small molecule cumate to the cells.

A schematic outline of the generation of the double stable cell method used in this study is shown in Fig. 1. In order to construct MS2-RNPS1 3'UTR expression plasmid, we have used the vector pcDNA5/FRT/TO. It is an expression plasmid of size 5.1 kb specifically developed for use in conjunction with the Flp-In T-REx

system. It comprises FRT (Flp Recombination Target) site linked to the hygromycin resistance gene for Flp recombinase-mediated integration into the mammalian cells. Flp-In T-REx-293 cells were cotransfected with a vector expressing tdTomato-MS2-RNPS1 3'UTR and pOG44 plasmid (Fig. 1). Upon cotransfection, the Flp recombinase enzyme produced by pOG44 initiates a homologous recombination phenomenon between the FRT sites present in the genome and pcDNA5/FRT/TO such that the gene of interest and hygromycin resistance gene are inserted at the FRT site. The stable cells were selected using hygromycin and the expression of chimeric RNA, tdTomato-MS2-RNPS1 3'UTR, was validated via RT-PCR (Fig. 2). These stable cells were further cotransfected with the PiggyBac transposon vector containing FLAG-tagged MS2 coat protein and PiggyBac transposase (Fig. 1). Upon transfection, transposase identifies the inverted terminal repeat sequences (ITRs) on the transposon vector and successfully transfers the gene of interest from the vector into the TTAA chromosomal locations. The stable cells were selected via puromycin resistance and finally, the double stable cells express both tdTomato-RNPS1 3'UTR MS2 and FLAG-tagged MS2 coat protein. The negative control stable cells express tdTomato-MS2 and FLAG-tagged MS2 coat protein.

3.2   MS2 Tagged RNA Affinity Capture of RBPs

Double stable cells were induced with doxycycline and cumate to express tdTomato-RNPS1 3'UTR-MS2 and FLAG-tagged MS2 coat protein, respectively. A schematic outline of the affinity pull down–mass spectrometry method used in this study is shown in Fig. 3. Next, lysates were prepared from the double stable cells for RNP-IP and the RBPs that associate with *RNPS1* 3'UTR in vivo were then captured by affinity purification using magnetic beads coated anti-FLAG antibody. A part of the IP complexes was used to isolate the total RNA pulled down, followed by qRT-PCR to verify the quantity of *RNPS1* 3'UTR enriched in the RNP-IP assay. The other part of the IP was analyzed on an SDS-PAGE gel and proceeded for mass spectrometry analysis. A negative control RNP-IP was performed on stable cells expressing chimeric RNA tdTomato-MS2 without *RNPS1* 3'UTR. The qRT-PCR result revealed that *RNPS1* 3'UTR was dramatically enriched in the pulldown of stable cells expressing tdTomato-MS2bs-RNPS1 3'UTR- compared to negative control stable cells (Fig. 4b). Silver staining of the gel loaded with *RNPS1* 3'UTR-IP identified several bands (Fig. 4a). These data demonstrate that chimeric *RNPS1* 3'UTR can be specifically immunoprecipitated from the cell lysate.

3.3   Analysis of Candidate RNPS1 3'UTR Binding Proteins

Mass spectrometry analysis identified 148 unique proteins with a protein False Discovery Rate lower than 1% and log2 fold change ≥ 0.5 (Table 1 in Chap. 5). To
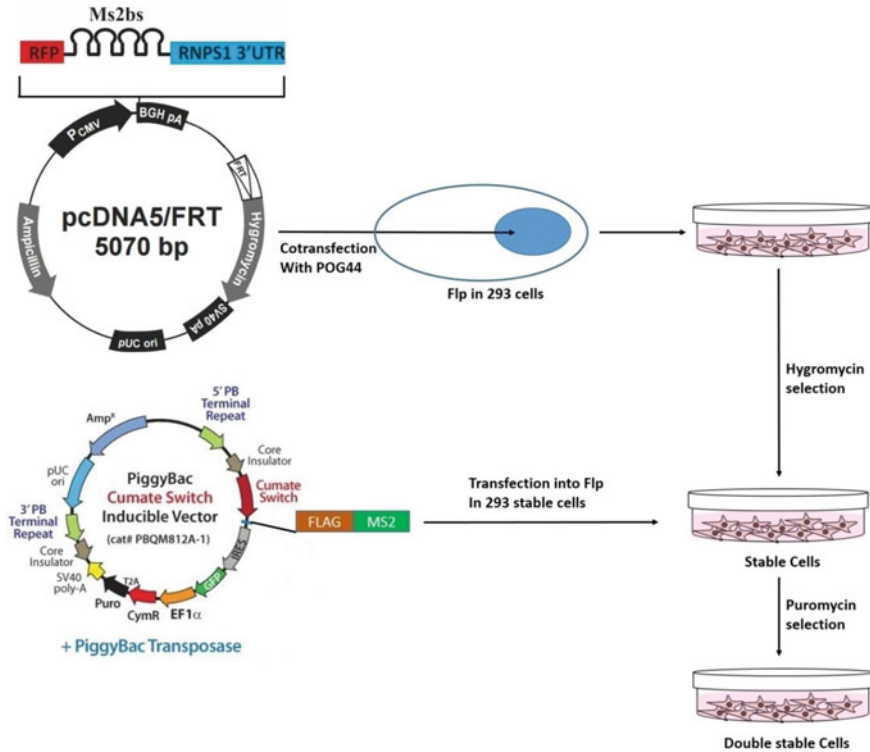
Fig. 1 Schematic representation of generation of double stable cells. Flp-In T-REx-293 cells expressing simultaneously tdTomato-MS2bs-RNPS1 3'UTR and FLAG-MS2cp. MS2bs stands for MS2 binding site. Flp-In T-REx-293 cells were cotransfected with a plasmid expressing tdTomato-MS2-RNPS1 3'UTR and pOG44 plasmid. The stable cells were selected using hygromycin. These stable cells were further cotransfected with PiggyBac transposon vector containing FLAG-tagged MS2 coat protein and PiggyBac transposase. The stable cells were selected via puromycin resistance

determine the potential biological pathways associated with *RNPS1* 3'UTR interacting proteins, we performed enrichment analysis in the Gene Ontology (GO) domain "Biological Pathway" using FunRich tool. The study unraveled that *RNPS1* 3'UTR binding proteins were most significantly enriched in the "Gene expression" processes (Fig. 5). Further, "3' UTR-mediated translational regulation" is also one of the predominant processes in the GO analysis. These findings suggest that RNPS1 expression is probably regulated by many key regulators via its 3'UTR. Interestingly, proteins associated with *RNPS1* 3'UTR are also involved in "Influenza viral RNA transcription and elongation" processes (Fig. 5). Along the same line, a previous meta-analysis of genome-wide research has identified RNPS1 as one of the host cell factors essential for influenza virus infection [10].

Additionally, we performed enrichment analysis in the Gene Ontology (GO) domain "Cellular component". RNPS1 mRNA binding proteins were found to be
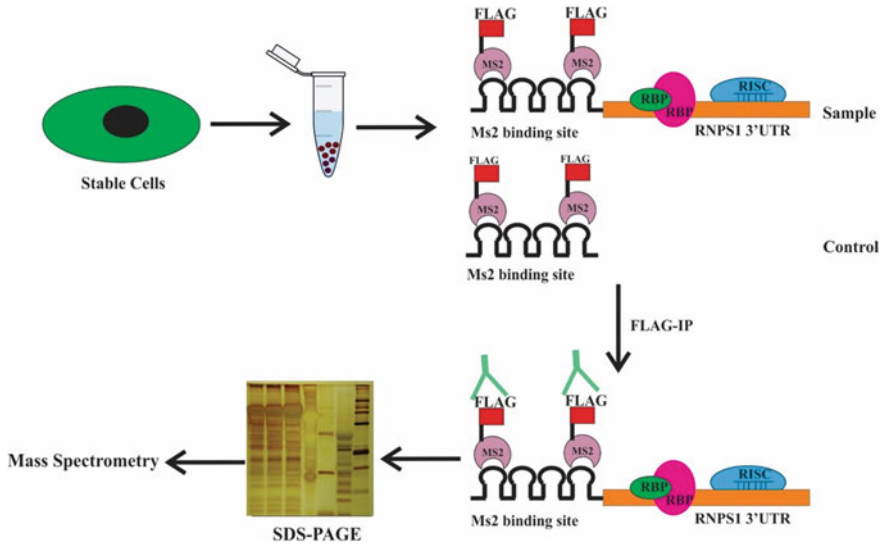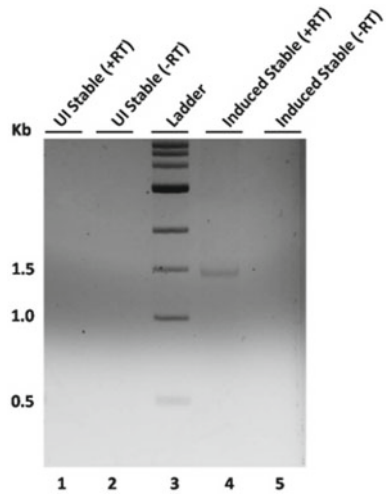
Fig. 3 Schematic representation of MS2 tagged RNA affinity capture of proteins bound to *RNPS1* 3'UTR. *RNPS1* 3'UTR stable cells express tdTomato-MS2-RNPS1 3'UTR and FLAG-MS2cp, whereas control cells express tdTomato-MS2 and FLAG-MS2cp. Lysates were prepared from the double stable cells for RNP-IP and the RBPs that associate with RNPS1 3'UTR in vivo were then captured by affinity purification using magnetic beads coated anti-FLAG antibody. The IP was analyzed on an SDS-PAGE gel and sent for mass spectrometry analysis
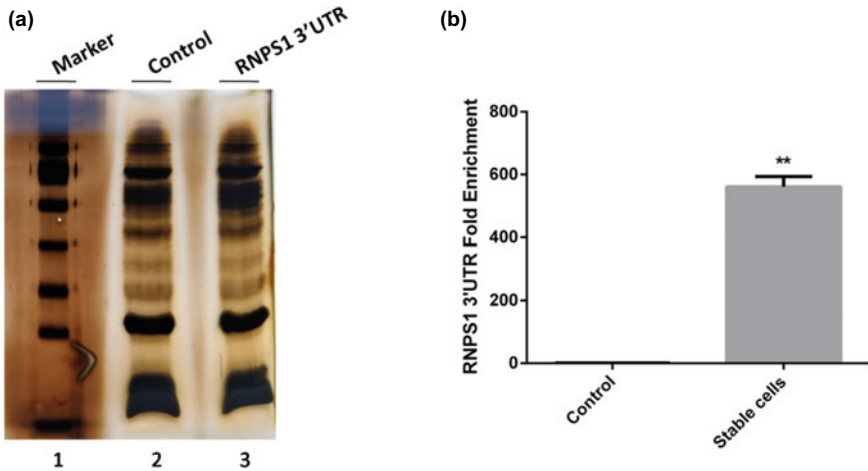
Fig. 4 Identification of *RNPS1* 3'UTR binding proteins by MS2-tagged RNA affinity purification. **a** Immunoprecipitation complexes from control and *RNPS1* 3'UTR stable cells were separated on 10% SDS-PAGE and the gel was subsequently stained using silver staining. Control cells express tdTomato-MS2 and FLAG-MS2cp, whereas *RNPS1* 3'UTR stable cells express tdTomato-MS2-RNPS1 3'UTR and FLAG-MS2cp **b** The enrichment of *RNPS1* 3'UTR in samples obtained after FLAG RNP IP was measured by qRT-PCR. The values represent mean $\pm$ SEM (n = 3). **P < 0.01
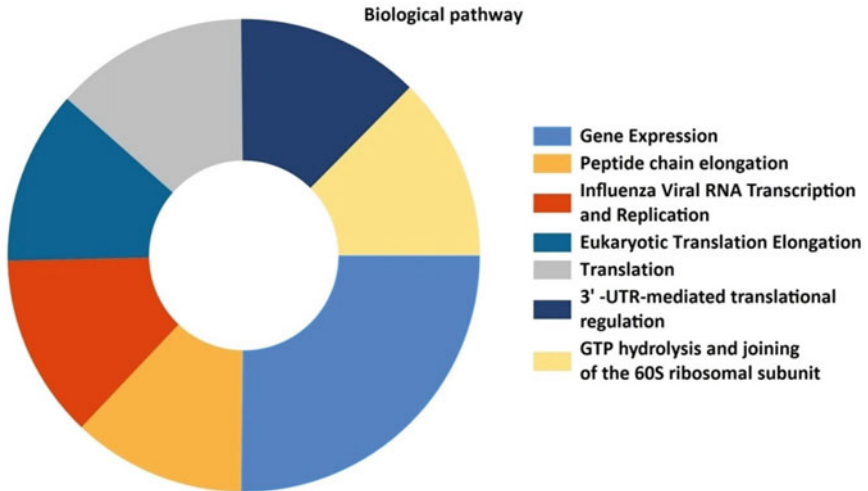
Fig. 5 The biological pathways associated with RNPS1 binding proteins in Gene Ontology analysis by FunRich. The RNPS1 binding proteins were most highly enriched in gene expression (35.6%) followed by translation (18.8%) and 3'UTR-mediated translational regulation (17.8%). A significant number of proteins were also enriched in Influenza Viral RNA Transcription and Replication (17.8%)
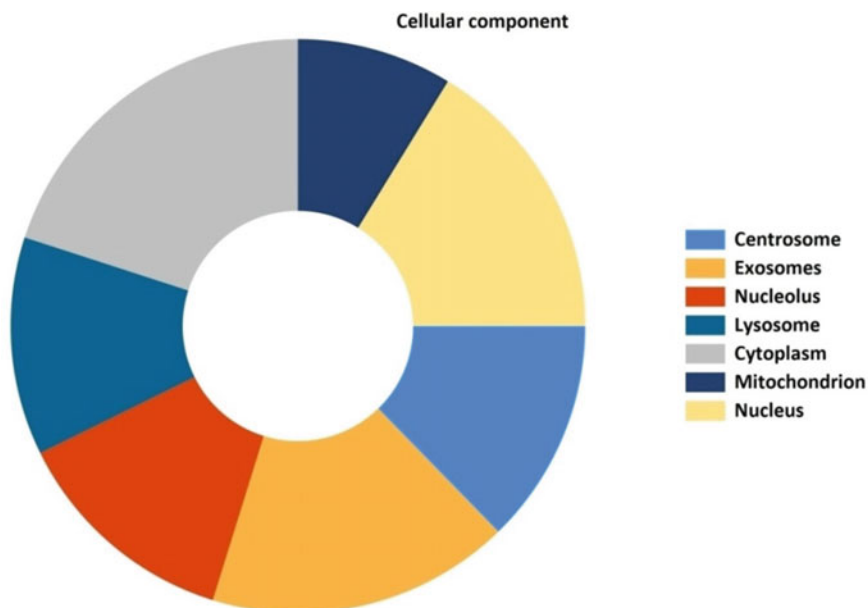
Fig. 6 Cellular component category of RNPS1 binding proteins in Gene Ontology analysis by FunRich. The RNPS1 binding proteins were most highly enriched in the cytoplasm (72.2%), followed by exosome (62.1%) and nucleus (59%). A significant number of proteins were also enriched in the centrosome (46.2%) and nucleolus (46.9%)

predominantly localized in the cytoplasm, exosome and nucleus (Fig. 6). Moreover, GO analysis unraveled a significant enrichment of candidate RNPS1 binding proteins in cellular compartments such as the centrosome, lysosome, and mitochondrion. These analyses suggest that RNPS1 transcript binding proteins comprise key transport regulators and indicate possible cellular compartments in which the RNPS1 transcript localizes.

3.4 HNRNPC Interacts with RNPS1 mRNA

Among all candidate binding proteins, a few proteins were selected based on their functions in RNA metabolism. One of the candidate proteins is HNRNPC, albeit the log2 fold change of HNRNPC was below 0.5. HNRNPC is a well-known RBP with functions in RNA splicing, RNA export, RNA stability, 3'end processing and translation. To confirm whether HNRNPC is indeed an RNPS1 binding factor, we immunoprecipitated FLAG-tagged HNRNPC from HEK 293 cell lysates and analyzed its interaction with *RNPS1* mRNA. Flag-HNRNPC was overexpressed in HEK293 cells and RNA-IP was performed from whole-cell lysates using anti-FLAG
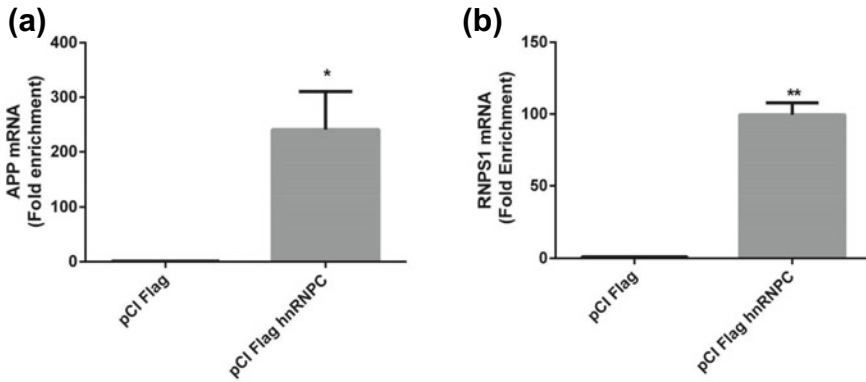
Fig. 7 Verification of candidate *RNPS1* 3'UTR binding protein. RNA immunoprecipitation was performed with HEK293 cell lysates transfected with pCI-FLAG or pCI-FLAG-HNRNPC using FLAG antibody to enrich RNA bound to HNRNPC. The presence of APP and RNPS1 was detected by qPCR. APP mRNA served as positive control. *P < 0.05, **P < 0.01

magnetic beads. qRT-PCR result shows that endogenous *RNPS1* mRNA was significantly enriched in FLAG-HNRNPC IP, thereby implying that HNRNPC associates with *RNPS1* mRNA (Fig. 7). It was previously demonstrated through RNA-IP that HNRNPC associates with *APP* mRNA (Amyloid precursor protein). As expected, the APP mRNA was also detected in HNRNPC RNA IP in the current study (Fig. 7). We also found many putative HNRNPC binding sites in the RNPS1 3'UTR by 'RBPmap', this suggests a possible direct interaction between *RNPS1* mRNA and HNRNPC (Fig. 8). It is intriguing to speculate that the binding of HNRNPC to *RNPS1* mRNA probably modulates the stability, splicing or translation of *RNPS1* mRNA. Taken together, these data show the reliability of the IP-MS strategy and confirm association of HNRNPC with *RNPS1* mRNA. The study presents proof of concept that MS2-mediated pulldown of *RNPS1* 3'UTR is a valuable approach for screening proteins that interact with the *RNPS1* transcript in a physiological setting (Table 1).

4   Discussion

RNA-binding proteins play a crucial role in the complex regulation of genes and therefore, there is a growing interest in determining these proteins and how they affect gene expression. Several studies were conducted to identify RBPs by utilizing affinity purification. For instance, the Schroeder laboratory has used the streptomycin aptamer tag to validate many predicted sRNA-protein interactions, including 6S RNA/RNAP [11]. Likewise, the aptamer tag approach was employed to identify RBPs associated with the U1 small nuclear ribonucleoprotein particles (snRNP) [12, 13].

Position	Motif	Occurrence
49	huuuuuk	cuguaacuuauaccccacccagcucaguuuugucacuuuucuagccaaaggaagacc
50	huuuuuk	uguaacuuauaccccacccagcucaguuuugucacuuuucuagccaaaggaagacca
51	huuuuuk	guaacuuauaccccacccagcucaguuuugucacuuuucuagccaaaggaagaccag
52	uuuuu	uaacuuauaccccacccagcucaguuuugucacuuuucuagccaaaggaagacca
58	huuuuuk	auaccccacccagcucaguuuugucacuuuucuagccaaaggaagaccaguaggaaa
59	huuuuuk	uaccccacccagcucaguuuugucacuuuucuagccaaaggaagaccaguaggaaag
60	uuuuu	accccacccagcucaguuuugucacuuuucuagccaaaggaagaccaguaggaaa
61	uuuuu	ccccacccagcucaguuuugucacuuuucuagccaaaggaagaccaguaggaaag
685	huuuuuk	gguuaucuuggcaacauguacauugcuuuuauuuuuuuucuuuuuugcuuucauugu
686	huuuuuk	guuaucuuggcaacauguacauugcuuuuauuuuuuuucuuuuuugcuuucauugua
687	huuuuuk	uuaucuuggcaacauguacauugcuuuuauuuuuuuucuuuuuugcuuucauuguac
688	huuuuuk	uaucuuggcaacauguacauugcuuuuauuuuuuuucuuuuuugcuuucauuguaca
689	huuuuuk	aucuuggcaacauguacauugcuuuuauuuuuuuucuuuuuugcuuucauuguacag
690	huuuuuk	ucuuggcaacauguacauugcuuuuauuuuuuuucuuuuuugcuuucauuguacagu
691	huuuuuk	cuuggcaacauguacauugcuuuuauuuuuuuucuuuuuugcuuucauuguacaguc
692	huuuuuk	uuggcaacauguacauugcuuuuauuuuuuuucuuuuuugcuuucauuguacaguca
693	huuuuuk	uggcaacauguacauugcuuuuauuuuuuuucuuuuuugcuuucauuguacagucag
694	uuuuu	ggcaacauguacauugcuuuuauuuuuuuucuuuuuugcuuucauuguacaguca
695	huuuuuk	gcaacauguacauugcuuuuauuuuuuuucuuuuuugcuuucauuguacagucagua
696	huuuuuk	caacauguacauugcuuuuauuuuuuuucuuuuuugcuuucauuguacagucaguac
697	huuuuuk	aacauguacauugcuuuuauuuuuuuucuuuuuugcuuucauuguacagucaguacu
698	huuuuuk	acauguacauugcuuuuauuuuuuuucuuuuuugcuuucauuguacagucaguacua
699	huuuuuk	cauguacauugcuuuuauuuuuuuucuuuuuugcuuucauuguacagucaguacuau
700	huuuuuk	auguacauugcuuuuauuuuuuuucuuuuuugcuuucauuguacagucaguacuaua
701	uuuuu	uguacauugcuuuuauuuuuuuucuuuuuugcuuucauuguacagucaguacuau
702	uuuuu	guacauugcuuuuauuuuuuuucuuuuuugcuuucauuguacagucaguacuaua
734	huuuuuk	uucauuguacagucaguacuauaaauuucucuuuugaguuuuauaccuuuuguuagca
735	uuuuu	ucauuguacagucaguacuauaaauuucucuuuugaguuuuauaccuuuuguagc
738	huuuuuk	uuguacagucaguacuauaaaauuucucuuuugaguuuuauaccuuuuguagcauuuu
739	huuuuuk	uguacagucaguacuauaaaauuucucuuuugaguuuuauaccuuuuguagcauuuua
740	uuuuu	guacagucaguacuauaaaauuucucuuuugaguuuuauaccuuuuguagcauuuu
741	uuuuu	uacagucaguacuauaaaauuucucuuuugaguuuuauaccuuuuguagcauuuua
746	huuuuuk	ucaguacuauaaaauuucucuuuugaguuuuauaccuuuuguagcauuuuagaugaca
747	huuuuuk	caguacuauaaaauuucucuuuugaguuuuauaccuuuuguagcauuuuagaugacau
748	uuuuu	aguacuauaaaauuucucuuuugaguuuuauaccuuuuguagcauuuuagaugaca
749	uuuuu	guacuauaaaauuucucuuuugaguuuuauaccuuuuguagcauuuuagaugacau
756	huuuuuk	aaaauuucucuuuugaguuuuauaccuuuguagcauuuuagaugacauuguguuuugu
757	uuuuu	aaauuucucuuuugaguuuuauaccuuuguagcauuuuagaugacauuguguuug
764	huuuuuk	ucuuuugaguuuuauaccuuuguagcauuuuagaugacauuguguuuuguacuuuguu
765	huuuuuk	cuuuugaguuuuauaccuuuguagcauuuuagaugacauuguguuuuguacuuuguug
766	uuuuu	uuuugaguuuuauaccuuuguagcauuuuagaugacauuguguuuuguacuuuguu
780	huuuuuk	ccuuuguagcauuuuagaugacauugugaguuuguacuuuguuuguguagaguggaagaa
781	uuuuu	cuuuguagcauuuuagaugacauugugaguuuguacuuuguuuguguagaguggaaga
783	uuuuu	uuguagcauuuuagaugacauugugaguuuguacuuuguuuguguagaguggaagaau
789	huuuuuk	cauuuuagaugacauugugaguuuguacuuuguuugguguagaguggaagaauuguguuga
790	huuuuuk	auuuuagaugacauugugaguuuguacuuuguuuguguagaguggaagaauuguguugaa
791	uuuuu	uuuuagaugacauugugaguuuguacuuuguuuguguagaguggaagaauuguguuga

Fig. 8 Putative binding sites of HNRNPC within RNPS1 3'UTR predicted via RBPmap online tool. RNPS1 3'UTR was used as an input sequence for RBPmap tool. Position refers to the starting position of the HNRNPC binding site in the input sequence (RNPS1 3'UTR). The motif refers to the motif that is mapped to the query sequence (RNPS1 3'UTR). Occurrence displays the presence of the motif in the query sequence

In this study, we have used the interaction between MS2 RNA aptamer tagged *RNPS1* 3'UTR and MS2 coat protein to screen proteins associated with *RNPS1* mRNA in the cell. The MS2 aptamer interacts with high affinity with MS2cp with K values of 1–3 nM. This technique has the advantage of identifying protein-RNA interactions in cells. In comparison to in-vitro-based techniques, the expression of aptamer-tagged RNA inside the cell may have advantages. For example, transcription of RNA in the cell might be a prerequisite for the assembly of those RBPs that get deposited co-transcriptionally. Second, reversible formaldehyde cross-linking may

Table 1 List of candidate *RNPS1* 3'UTR interacting proteins identified through MS analysis

Gene name	Description	Score	Log2 FC	Queries matched
GPI	Glucose-6-phosphate isomerase	207.36	3.2192	15
KLHL41	Kelch-like protein 41	70.799	3.0059	11
CSTA	Cystatin-A	27.527	2.7133	2
PGK1	Phosphoglycerate kinase 1	106.21	2.6164	12
RPL13A	60S ribosomal protein L13a	46.911	1.8461	5
CKB	Creatine kinase B-type	323.31	1.8057	16
RPL4	60S ribosomal protein L4	33.437	1.7826	8
FKBP4	Peptidyl-prolyl cis–trans isomerase	92.897	1.7727	17
PGAM1	Phosphoglycerate mutase 1	162.54	1.6863	9
RPL22	60S ribosomal protein L22	6.4384	1.6826	2
BAG5	BAG family molecular chaperone regulator 5	17.259	1.6508	5
GDI2	Rab GDP dissociation inhibitor beta	73.143	1.635	14
ALDH9A1	4-trimethylaminobutyraldehyde dehydrogenase	6.6876	1.5634	4
RPL27	60S ribosomal protein L27	8.4243	1.5345	4
CALR	Calreticulin	264.02	1.5323	13
ENO1	Alpha-enolase	211.21	1.5011	14
U2AF1	Splicing factor U2AF 35 kDa subunit	32.904	1.4892	3
ILF2	Interleukin enhancer-binding factor 2	55.794	1.4484	8
PGD	6-phosphogluconate dehydrogenase	136.11	1.4297	12
PDIA4	Protein disulfide-isomerase A4	111.48	1.4063	14
ADSS	Adenylosuccinate synthetase isozyme 2	12.991	1.3858	4
GAPDH	Glyceraldehyde-3-phosphate dehydrogenase	312.96	1.3849	14
LDHA	L-lactate dehydrogenase A chain	59.569	1.3834	10
MTHFD1	C-1-tetrahydrofolate synthase	105.12	1.3396	24
TARS	Threonine–tRNA ligase	60.083	1.3336	15
EIF4A3	Eukaryotic initiation factor 4A-III	24.186	1.3172	11
AGPAT1	1-acyl-sn-glycerol-3-phosphate acyltransferase alpha	28.586	1.2838	1
TKT	Transketolase	124.95	1.2805	16
PPP1CC	Serine/threonine-protein phosphatase	52.844	1.28	7
LDHB	L-lactate dehydrogenase B chain	129.09	1.2766	9
EIF4A1	Eukaryotic initiation factor 4A-I	57.255	1.2588	15
GANAB	Neutral alpha-glucosidase AB	102.1	1.2567	18
ST13	Hsc70-interacting protein	27.435	1.2559	5
ETFA	Electron transfer flavoprotein subunit alpha	22.525	1.1714	5

(continued)

Table 1 (continued)

Gene name	Description	Score	Log2 FC	Queries matched
RPL5	60S ribosomal protein L5	42.995	1.1521	5
LCP1	Plastin-2	28.172	1.1463	11
DLD	Dihydrolipoyl dehydrogenase	13.544	1.1433	5
VDAC1	Voltage-dependent anion-selective channel protein 1	116.19	1.1354	6
API5	Apoptosis inhibitor 5	14.26	1.1313	5
S100A9	Protein S100-A9	47.29	1.1223	3
TPI1	Triosephosphate isomerase	149.9	1.1057	12
RPL23A	60S ribosomal protein L23a	21.525	1.0753	3
HSP90B1	Endoplasmin	238.74	1.0687	23
PKM	Pyruvate kinase PKM	323.31	1.0601	24
IGF2BP1	Insulin-like growth factor 2 mRNA-binding protein 1	26.15	1.0554	9
ALDOA	Fructose-bisphosphate aldolase	110.38	1.0439	11
NCL	Nucleolin	123.84	1.0381	16
SND1	Staphylococcal nuclease domain-containing protein 1	41.573	1.0336	11
ACTN4	Alpha-actinin-4	168.56	1.02	26
NSUN2	tRNA (cytosine(34)-C(5))-methyltransferase	44.164	1.0196	10
JUP	Junction plakoglobin	24.405	1.0052	9
DDX39B	Spliceosome RNA helicase DDX39B	75.249	0.9998	10
CACYBP	Calcyclin-binding protein	111.81	0.9959	9
PFKP	ATP-dependent 6-phosphofructokinase	114.28	0.9941	13
RPLP0	60S acidic ribosomal protein P0	34.394	0.9924	7
RPL26	60S ribosomal protein L26	8.4212	0.9839	4
ANXA6	Annexin A6	64.566	0.9746	10
TRAP1	Heat shock protein 75 kDa	73.977	0.9735	15
APEX1	DNA-(apurinic or apyrimidinic site) lyase	80.274	0.9715	7
HNRNPL	Heterogeneous nuclear ribonucleoprotein L	136.33	0.9623	11
YWHAZ	14–3-3 protein zeta/delta	197.64	0.9549	11
RPL27A	60S ribosomal protein L27a	17.498	0.9431	3
TUFM	Elongation factor Tu	52.299	0.9407	10
HNRNPA3	Heterogeneous nuclear ribonucleoprotein A3	34.951	0.9402	9
FSCN1	Fascin	41.679	0.9394	8
RPL15	60S ribosomal protein L15;Ribosomal protein L15	26.188	0.9363	9

Table 1 (continued)

Gene name	Description	Score	Log2 FC	Queries matched
HSP90AB2P	Putative heat shock protein HSP 90-beta 2	50.684	0.9149	8
YWHAB	14–3-3 protein beta/alpha	242.06	0.9081	9
RPL11	60S ribosomal protein L11	16.493	0.893	3
RAB1A	Ras-related protein Rab-1A	8.2647	0.8849	5
CCDC97	Coiled-coil domain-containing protein 97	14.59	0.8801	4
U2AF2	Splicing factor U2AF 65 kDa subunit	42.127	0.8624	6
BSG	Basigin	6.3922	0.8565	2
YWHAH	14–3-3 protein eta	30.372	0.8555	5
ACACA	Acetyl-CoA carboxylase 1	23.434	0.8544	5
MDH2	Malate dehydrogenase	58.18	0.8508	10
HNRNPA1	Heterogeneous nuclear ribonucleoprotein A1	145.23	0.8335	12
PSAT1	Phosphoserine aminotransferase	28.531	0.8327	9
BAT3;BAG6	Large proline-rich protein BAG6	18.689	0.8292	5
PTBP1	Polypyrimidine tract-binding protein 1	77.442	0.8234	6
MAGED2	Melanoma-associated antigen D2	22.616	0.8204	2
HNRNPH1	Heterogeneous nuclear ribonucleoprotein H	230.37	0.811	14
KIAA1033	WASH complex subunit 7	6.1897	0.8087	3
RPL3	60S ribosomal protein L3	61.735	0.808	11
EIF2S3	Eukaryotic translation initiation factor 2 subunit 3	77.706	0.8073	8
PRKCSH	Glucosidase 2 subunit beta	168.56	0.8037	10
DHX9	ATP-dependent RNA helicase A	180.95	0.8032	24
DDX6	Probable ATP-dependent RNA helicase DDX6	20.613	0.7988	5
AHSA1	Activator of 90 kDa heat shock protein ATPase homolog 1	32.245	0.7958	6
G3BP1	Ras GTPase-activating protein-binding protein 1	56.906	0.7668	8
DLAT	Dihydrolipoyllysine-residue acetyltransferase	14.174	0.7421	7
AHCY	Adenosylhomocysteinase	85.067	0.7397	13
RPL35A	60S ribosomal protein L35a	4.768	0.7314	4
RUVBL1	RuvB-like 1	230.86	0.7299	14
CSE1L	Exportin-2	154.71	0.7283	19
HSP90AA1	Heat shock protein HSP 90-alpha	323.31	0.7162	31
RAB11A	Ras-related protein Rab-11A	15.335	0.7158	4

(continued)

Table 1 (continued)

Gene name	Description	Score	Log2 FC	Queries matched
ANP32A	Acidic leucine-rich nuclear phosphoprotein 32 A	79.613	0.7103	8
CTPS1	CTP synthase 1	92.619	0.7015	9
ARHGEF10	Rho guanine nucleotide exchange factor 10	107.87	0.6874	17
HNRNPR	Heterogeneous nuclear ribonucleoprotein R	91.483	0.682	14
POLR2A	DNA-directed RNA polymerase II subunit RPB1	21.389	0.6716	7
MYBBP1A	Myb-binding protein 1A	34.009	0.666	12
RPL23	60S ribosomal protein L23	28.332	0.664	6
STIP1	Stress-induced-phosphoprotein 1	63.365	0.6618	16
ATP2A2	Sarcoplasmic/endoplasmic reticulum calcium ATPase 2	85.469	0.6572	16
SET	Protein SET	323.31	0.6479	7
DSP	Desmoplakin	78.121	0.646	27
PLS3	Plastin-3	51.822	0.6427	15
TMPO	Lamina-associated polypeptide 2	69.45	0.636	6
ATP6V1B2	V-type proton ATPase subunit B, brain isoform	40.983	0.6311	6
SRSF7	Serine/arginine-rich splicing factor 7	20.995	0.6287	4
RPL18	60S ribosomal protein L18	47.041	0.6283	6
YWHAE	14–3-3 protein epsilon	158.28	0.626	16
RPL13	60S ribosomal protein L13	39.28	0.6137	5
BLMH	Bleomycin hydrolase	10.12	0.6073	4
PDHB	Pyruvate dehydrogenase E1 component subunit beta	22.666	0.6037	5
DDOST	Dolichyl-diphosphooligosaccharide–protein glycosyltransferase	21.779	0.6007	7
RPS17	40S ribosomal protein S17	9.9434	0.58	4
EEF2	Elongation factor 2	323.31	0.5741	29
DDX17	Probable ATP-dependent RNA helicase DDX17	91.108	0.5733	16
RPS23	40S ribosomal protein S23	10.907	0.5687	4
CAND1	Cullin-associated NEDD8-dissociated protein 1	71.342	0.5685	13
HNRNPF	Heterogeneous nuclear ribonucleoprotein F	124.62	0.5672	8
SAE1	SUMO-activating enzyme subunit 1	75.896	0.5663	5
UBA1	Ubiquitin-like modifier-activating enzyme 1	135.09	0.5629	17

Table 1 (continued)

Gene name	Description	Score	Log2 FC	Queries matched
POLR3C	DNA-directed RNA polymerase III subunit RPC3	23.367	0.5621	4
PAICS	Multifunctional protein ADE2	68.055	0.5611	9
HNRNPA2B1	Heterogeneous nuclear ribonucleoproteins A2/B1	211.19	0.561	16
ANXA2	Annexin	26.244	0.555	8
RDX	Radixin	30.389	0.5541	12
SSB	Lupus La protein	74.392	0.5489	12
EIF5A	Eukaryotic translation initiation factor 5A-1	42.535	0.5461	6
ILF3	Interleukin enhancer-binding factor 3	116.77	0.5411	14
SFPQ	Splicing factor, proline- and glutamine-rich	127.02	0.5405	16
DSG1	Desmoglein-1	32.702	0.5366	8
XPO1	Exportin-1	67.824	0.5357	14
SUPT5H	Transcription elongation factor SPT5	17.567	0.5326	5
HNRNPM	Heterogeneous nuclear ribonucleoprotein M	67.433	0.5323	22
PA2G4	Proliferation-associated protein 2G4	183.71	0.5313	11
PRMT1	Protein arginine N-methyltransferase 1	39.372	0.5277	9
RPS7	40S ribosomal protein S7	156.5	0.5251	8
EIF2S1	Eukaryotic translation initiation factor 2 subunit 1	16.709	0.5245	6
DCD	Dermcidin	4.2344	0.5082	2
SRSF1	Serine/arginine-rich splicing factor 1	26.9	0.5057	7
WDR61	WD repeat-containing protein 61	45.46	0.5006	5
EEF1A2	Elongation factor 1-alpha 2	34.964	0.5001	12

be performed to trap transient RBPs that associate weakly or temporally with the tagged RNA. Additionally, the expression of aptamer-tagged RNAs can be used to visualize the spatial expression pattern of the RNA.

The MS2 RNA aptamer was used successfully as an RNA affinity tag to isolate RBPs associated with *RNPS1* 3'UTR. A total of 148 candidate interacting proteins were pulled down by affinity purification from HEK 293 cells. Our mass spectrometry results show that *RNPS1* 3'UTR can bind to a variety of proteins, including ILF2, ILF3, HNRNPC, and PTBP1. ILF2, also known as nuclear factor 45 (NF45), forms a stable heterodimer with ILF3 (also called NF90) and acts as a crucial regulatory factor in cellular processes, including transcription, splicing, mRNA stability, translation, cell proliferation, and apoptosis [14–17]. Intriguingly, recent studies report ILF2 as a key host protein that is required in the replication of viruses, including human immunodeficiency virus type 1 (HIV-1) and hepatitis virus [18–20]. In the same line, our gene ontology analysis showed that RBPs bound to *RNPS1* 3'UTR play a role

in influenza virus infection. Previous studies determined that RNPS1 interacts with nucleoprotein of Influenza A Virus (H7N9) and RNPS1 is plausibly involved in the replication process of influenza virus [21, 22].

Conclusively, this approach captured the protein interactome profile of *RNPS1* mRNA. Gene ontology analysis demonstrated that the identified proteins have diverse functions inside the cell. The association of *RNPS1* 3'UTR with regulatory proteins identified in this study provides a new direction for future studies on the regulation of RNPS1.

References

1. Scott AT et al (2000) Identifying mRNA subsets in messenger ribonucleoprotein complexes by using cDNA arrays. Proc Natl Acad Sci 97(26):14085–14090
2. Keene JD, Tenenbaum SA (2002) Eukaryotic mRNPs may represent posttranscriptional operons. Mol Cell 9(6):1161–1167
3. Hogan DJ et al (2008) Diverse RNA-binding proteins interact with functionally related sets of RNAs, suggesting an extensive regulatory system. PLoS Biol 6(10):e255
4. Hafner M et al (2010) Transcriptome-wide Identification of RNA-binding protein and MicroRNA target sites by PAR-CLIP. Cell 141(1):129–141
5. Durie D et al (2011) RNA-binding protein HuR mediates cytoprotection through stimulation of XIAP translation. Oncogene 30(12):1460–1469
6. Srisawat C, Engelke DR (2001) Streptavidin aptamers: affinity tags for the study of RNAs and ribonucleoproteins. RNA 7(4):632–641
7. Srisawat C, Goldstein IJ, Engelke DR (2001) Sephadex-binding RNA ligands: rapid affinity purification of RNA from complex RNA mixtures. Nucleic Acids Res 29(2):e4–e4
8. Leppek K, Stoecklin G (2014) An optimized streptavidin-binding RNA aptamer for purification of ribonucleoprotein complexes identifies novel ARE-binding proteins. Nucleic Acids Res 42(2):e13–e13
9. Deka B et al (2022) RNPS1 functions as an oncogenic splicing factor in cervical cancer cells. IUBMB Life
10. Capitanio JS, Wozniak RW (2012) Host cell factors necessary for influenza a infection: meta-analysis of genome wide studies. Cell Behavior
11. Windbichler N et al (2008) Isolation of small RNA-binding proteins from E. coli: evidence for frequent interaction of RNAs with RNA polymerase. RNA Biol 5(1):30–40
12. Bardwell VJ, Wickens M (1990) Purification of RNA and RNA-protein complexes by an R17 coat protein affinity method. Nucleic Acids Res 18(22):6587–6594
13. Bachler M, Schroeder R, von Ahsen U (1999) StreptoTag: a novel method for the isolation of RNA-binding proteins. RNA 5(11):1509–1516
14. Guan D et al (2008) Nuclear factor 45 (NF45) is a regulatory subunit of complexes with NF90/110 involved in mitotic control. Mol Cell Biol 28(14):4629–4641. https://doi.org/10.1128/MCB.00120-08. Epub 2008 May 5., 2008
15. Shamanna RA et al (2011) The NF90/NF45 complex participates in DNA break repair via nonhomologous end joining. Mol Cell Biol 31(23):4832–4843. https://doi.org/10.1128/MCB.05849-11. Epub 2011 Oct 3., 2011

16. Rigo F et al (2012) Synthetic oligonucleotides recruit ILF2/3 to RNA transcripts to modulate splicing. Nat Chem Biol 8(6):555–561. https://doi.org/10.1038/nchembio.939
17. Higuchi T et al (2016) Suppression of microRNA-7 (miR-7) biogenesis by nuclear factor 90-nuclear factor 45 complex (NF90-NF45) controls cell proliferation in hepatocellular carcinoma. J Biol Chem 291(40):21074–21084. https://doi.org/10.1074/jbc.M116.748210. Epub 2016 Aug 12., 2016
18. Shin HJ et al (2002) Host cell proteins binding to the encapsidation signal ε in hepatitis B virus RNA. Adv Virol 147(3):471–491
19. Li Y, Belshan M (2016) NF45 and NF90 Bind HIV-1 RNA and modulate HIV gene expression. Viruses 8(2):47
20. Isken O et al (2007) Nuclear factors are involved in hepatitis C virus RNA replication. RNA 13(10):1675–1692
21. Rogan PK, Mucaki EJ, Shirley BC (2021) A proposed molecular mechanism for pathogenesis of severe RNA-viral pulmonary infections. F1000Research 9(943)
22. Sun N et al (2015) Proteomics analysis of cellular proteins co-immunoprecipitated with nucleoprotein of influenza virus (H7N9). Int J Mol Sci 16(11):25982–25998

Roles of Metastasis Suppressor Gene, OGR1 and Casein Kinase 2α Intronless Gene, CSNK2A3 in Megakaryocytic Differentiation

Naorem Tarundas Singh, Puyam Milan Meitei, and Lisam Shanjukumar Singh

1 Introduction

The increase of immature/undifferentiated blood cell precursors in the bone marrow and peripheral circulation is a feature of myeloid leukemia. Protein kinase CK2's high level of activity is essential for multiple myeloma cell survival [16, 23]. More than 300 proteins, largely regulatory proteins of crucial physiological signaling pathways, can be phosphorylated by the pleiotropic and widely distributed serine/threonine kinase CK2 [17]. To play crucial roles in cell survival, differentiation, and proliferation through modulation of apoptotic pathways, CK2 expression is strictly controlled in normal cells [2, 5, 9, 19]. CK2 expression is found to be particularly upregulated and the upregulated state of CK2α expression showed a correlation with the sustenance of undifferentiated malignant phenotype and promotion of metastasis [8, 23]. In Chronic Myelogenous Leukemia cells (K562), inhibition of CK2 function has been shown to induce cell death [18]. Most of the currently available anticancer drugs that target the upregulated CK2α are basically to downregulate CK2 expression or inhibit CK2 function to result in loss of cell viability via induction of apoptosis [1, 27]. Interestingly, we have discovered an intronless gene (CSNK2A3) encoding for CK2α from megakaryocyte cells [25]. Now, there are two genes encoding CK2α in humans; the normal gene (CSNK2A1), located on chromosome 20 with a size

N. T. Singh · P. M. Meitei · L. S. Singh (✉)
Department of Biotechnology, Manipur University, Canchipur, Imphal, India
e-mail: shanju.lisam@manipuruniv.ac.in

of 20 kb, and an intronless gene (CSNK2A3) on chromosome 11. The intronless gene has the same size as the cDNA of CSNK2A1 (1.2 kb). There are no introns in CSNK2A3. CSNK2A1 has a housekeeping promoter: absence of TATA box, high GC content, and presence of many GC boxes [29]. However, CSNK2A3 has a strong promoter: a CAAT box and two TATA boxes upstream of the start codon. CNSK2A3's DNA sequence is 99.9% identical to that of CSNK2A1 [4]. Therefore, it is probable that the intronless gene having a strong promoter is responsible for most of the increased expression of CK2α in cancer cells rather than the normal gene which has a housekeeping promoter. Some studies have claimed CK2α intronless or CSNK2A3 to be an oncogene and activation of CSNK2A3 expression during cancer has also been reported [10]. Although the role of CK2 has been well investigated in cell proliferation, its role in cell differentiation is not yet investigated. Despite the good demonstrations of the multitask role of CK2; its regulation is not clear till now. GPR68 or OGR1 (Ovarian cancer G-protein coupled receptor 1), is a member of the G-protein coupled receptors. It has been also shown as a proton sensing receptor and plays role in pH homeostasis [15]. It has also been shown to be a metastasis suppressor gene [26]. Till now the functional role and molecular mechanism action of CK2α intronless in cell differentiation and how the gene is regulated have not been investigated. Recently, we discovered that OGR1 abrogated the migration of A549 cells (human lung cancer cells) by upregulating the expression of CSNK2A3 and NEP (neutral endopeptidase) genes via the activation of Rac/Cdc and mitogen-activated protein kinase (MAPK) pathways [24]. This study aims to investigate the roles of OGR1 in the megakaryocytic differentiation of K562 and the regulation of CSNK2A1 and CSNK2A3 expressions.

2   Materials and Methods

2.1   *Reagents*

Dimethyl sulfoxide (DMSO) and phorbol 12-myristate 13-acetate (PMA) were procured from Sigma-Aldrich, USA. Anti-p38 and anti-phospho-p38 antibodies were procured from Cell Signaling Technology, USA while anti-β-actin and anti-CK2 antibodies were obtained from Santa Cruz Biotechnology, USA. The specific inhibitors for p38 (SB203580) and JNK (SP600125) and anti-OGR1 antibody were purchased from Abcam, UK, and inhibitors for ERK (FR180204), pertussis toxin (PTX) were purchased from the Sigma-Aldrich, USA. Neon Transfection System was obtained from Thermo Fisher Scientific, USA. Dominant-negative mutants: pcDNA3.1-cdcT17N and pcDNA3.1-RacT17N plasmids were purchased from Addgene, USA.

2.2 Cell Culture

K562 cells (Chronic Myelogenous Leukemia) were obtained from the National Center for Cell Science, Pune, India. The cells were incubated at 37 °C, 5% CO_2 in RPMI-1640 medium (Gibco, USA) containing 10% FBS (Gibco, USA) and 1% pen Strep (Thermo Fisher Scientific, USA).

2.3 PMA Treatment

K562 cells (~1×10^6) seeded in a 60 mm culture plate in RPMI-1640 medium were used for the treatments. For cell differentiation analysis, K562 cells were treated with 0.1% DMSO as the control or PMA with a final concentration of 100 nM. After 48 h of the treatment cell, morphological features were analyzed and photographed using a phase-contrast microscope (Leica, USA).

2.4 Semi-quantitative and Real Time-PCR Analysis

Following the manufacturer's protocol, total RNA from the cells was isolated using the RNeasy Mini kit (Qiagen, Germany). On-column DNase1 (Thermo Fisher Scientific, USA) digestion eliminated the genomic DNA contamination. RNA concentrations were assessed by a spectrometer (Invitrogen, USA). 1 μg each of the total RNAs was reverse transcribed using the M-MuLV Reverse Transcriptase kit (NEW ENGLAND BioLabs, USA) to first-strand cDNA. RT-PCR was performed using the SuperScript Platinum Taq kit (Invitrogen, USA) following the manufacturer's protocol in a thermocycler (Applied Biosystems, USA). Expressions of PF4, CSNK2A1, CSNK2A3, and OGR1 were analyzed with the primers; PF4: (Forward) 5′-TTGCTGCTCCTGCCACTTG-3′ and (Reverse) 5′-GCTTGCAGGTCCAAGCAAAT-3′ which amplify 209 bp fragment; CSNK2A1: (Forward) 5′-CCAAACATCAAGTCCAGCTTTGTC-3′ and (Reverse) 5′-ACCTCGGCCTAATTTTCGAACCA-3′ which amplify 184 bp fragment; CSNK2A3: (Forward) 5′-ATTGCTCCCCACTCCATCG-3′ and (Reverse) 5′- AAGCAGCTTGGGGGTAAGAC-3′ which amplify 128 bp and OGR1: (Forward) 5′-CTGTCCTGCCAGGTGTGC-3′ and (Reverse) 5′-GAACTGGTGGAAGCGGAAGG-3′ to amplify 123 bp and β-actin: Forward 5′-CTCACCATGGATGATGATATCGC-3′ and Reverse 5′-CACATAGGAATCCTTCTGACCC-3′ to amplify 168 bp fragment. Real-time PCR was performed using SYBR Green (Applied Biosystems, USA) in a Step One Plus PCR (Applied Biosystems, USA). β-actin was used as an endogenous control.

2.5 Western Blotting

Cells were washed with phosphate-buffered saline (PBS) and then lysed in RIPA buffer (1X PBS, 0.5% sodium deoxycholate, 0.1% SDS, 5 mM EDTA, 1% NP40, and 1 mM sodium orthovanadate) on ice. Standard BCA assay (Thermo Fisher Scientific, USA), was used to quantify the protein concentrations. Equal amounts of protein samples were loaded and resolved on 12% SDS-PAGE gels. The membranes were incubated with primary antibodies with the dilution of 1:3000 after transferring onto the PVDF membrane and then with a secondary antibody with the dilution of 1:6000. The fluorescence signals were captured using ChemiDoc (BioRad, USA).

2.6 Plasmids Transfection

OGR1 was cloned into a mammalian expression vector pcDNA3.1. On the day of transfection cells were maintained at 90% confluent. 20 µg each of the control vector (pcDNA3.1) and pcDNA3.1-OGR1, were transfected into approximately 1×10^7 of K562 cells in an antibiotic-free medium using Neon Transfection System (Thermo Fisher Scientific, USA). The conditions of transfection were: voltage 1450, pulse 10 milli-seconds, and pulse number 3.

After 48 h of transfection, cell morphological features were analyzed and photographed using a phase-contrast microscope. The expression of PF4 which is the marker for megakaryocytic differentiation was analyzed through semi-quantitative and validated with real-time PCR. Further expressions of both casein kinase 2 genes, CSNK2A3 and CSNK2A1 were also analyzed through semi-quantitative PCR and validated with real-time PCR, and then confirmed by immunoblotting.

To check the involvement of G α i in the regulation of CK2α by OGR1, a specific inhibitor for G α i activity; pertussis toxin (PTX), was used. 100 µg/ml of PTX was treated toOGR1 transfected cells. Expressions of OGR1, CSNK2A3, and CSNK2A1 were analyzed after 48 h.

2.7 Analysis of the Involvement of Ras Family Small G-proteins and MAPK Pathway in the Regulation of CSNK2A3 by OGR1

To check the involvement of Ras family small G-proteins, Rac1 and cdc42 in the downregulation of CSNK2A3 by OGR1, 10 µg of the dominant-negative mutants of cdc42 (pcDNA3.1-cdcT17N) or Rac1 (pcDNA3.1-RacT17N) plasmids were co-transfected with 10 µg each of vector (pcDNA3.1) and pcDNA3.1-OGR1. Expressions of OGR1 and CSNK2A3 were analyzed after 48 h by semi-quantitative PCR. The involvement of MAPK pathway proteins was investigated using specific MAPK

inhibitors. 20 µM of SP600125 (inhibitor for JNK) or SB203580 (inhibitor for p38) or FR180204 (inhibitor for ERK) were treated to control cells and OGR1 transfected cells. After 48 h of treatment, CSNK2A3 and CSNK2A1 expressions were investigated by semi-qPCR. Immunoblotting using specific antibodies further confirmed the result.
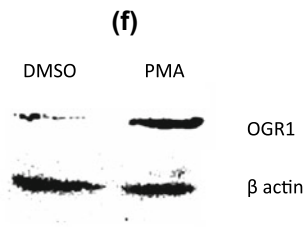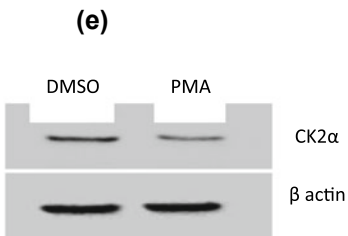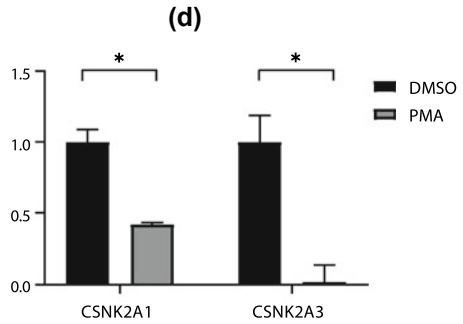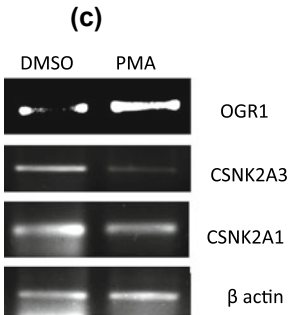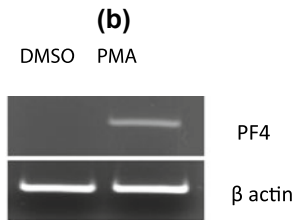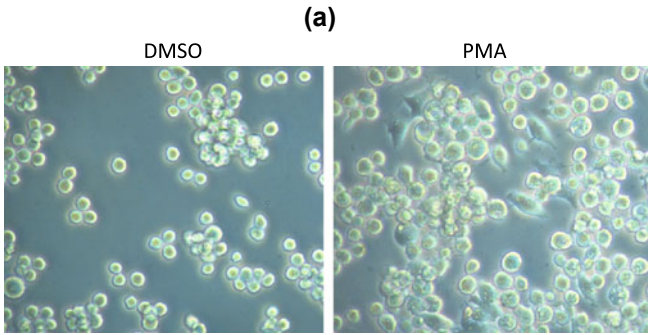
2.8 Statistical Analysis

All the statistical analysis was performed using GraphPrismversion 9.4.0 or Microsoft Excel. Data obtained were expressed as (Mean ± SD) and all experiments were performed in triplicates. The statistical association between the control and treated groups was analyzed using an appropriate T-test. The probability value, P< 0.05 was deemed significant.

3 Results

3.1 CSNK2A1 and CSNK2A3 Expressions are Downregulated But OGR1 Expression is Upregulated During Megakaryocytic Differentiation of K562 Cells

Phorbol 12-myristate 13-acetate (PMA) is a widely used tumor-promoting agent which induces differentiation into myelocytic cells. To investigate the expressions of CK2α genes during K562 differentiation, PMA was used to induce the differentiation of K562 cells into megakaryocyte cells. After the treatment, morphological features commonly associated with megakaryocytes like cellular adhering to the dishes, formation of pseudopod-like protrusions from the adherent cells, irregularly shaped cells, and increased cell sizes were prominently observed but the control cells (treated with 0.1% DMSO) showed no differentiation (Fig. 1a). An increase in the transcript of a megakaryocytic differentiation marker gene PF4 upon PMA treatment was observed (Fig. 1b).

Expressions of both CSNK2A1 and CSNK2A3 were downregulated (Fig. 1c, d) but OGR1 expression was upregulated markedly during PMA treatment (Fig. 1c, f). Similarly, CK2α protein expression markedly decreased and OGR1 protein expression increased (Fig. 1e, f). There was a ~85% decrease in the expression of CSNK2A3 and ~60% in the expression of CSNK2A1in the PMA-treated cells compared to the control.

(a)

DMSO   PMA

(b)

DMSO   PMA

PF4

β actin

(c)

DMSO   PMA

OGR1

CSNK2A3

CSNK2A1

β actin

(d)

(e)

DMSO   PMA

CK2α

β actin

(f)

DMSO   PMA

OGR1

β actin

◄**Fig. 1 PMA induces megakaryocytic differentiation of K562 cells**. **a** Formation of pseudopod-like structures, elongation, and irregular shape of the cell membrane was observed. **b** Increased expression of megakaryocytic differentiation marker, PF4 in PMA-treated K562 cells was observed. **c** Upregulated expression of OGR1 and downregulation of both CSNK2A1 and CSNK2A3 in differentiated K562 cells upon PMA treatment were observed. **d** Real-time PCR data showing downregulation of CK2α genes. About 85% decrease in the expression of CSNK2A3 and 60% for CSNK2A1 were observed in the PMA-treated cells **e** Western blotting confirmed the downregulation of CK2α. **f** Upregulated state of OGR1 protein in differentiated K562 cells. Bars indicate standard deviation and * indicates the $p < 0.05$

3.2 OGR1 Induces Megakaryocytic Differentiation of K562 Cells

As the expression of OGR1 was upregulated during megakaryocytic differentiation of K562, we were interested to know if OGR1 had any role in K562 differentiation. Therefore, OGR1 was overexpressed into K562 cells. Changes in cellular morphology induced by PMA were observed (Fig. 2a). Increased expression of megakaryocytic differential marker PF4 was also observed (Fig. 2b, c). There was about ~10 times increase in the expression of PF4 in the OGR1 transfected cells. Therefore, OGR1 alone can induce megakaryocytic differentiation of K562 cells like PMA.

3.3 OGR1 Downregulates CSNK2A3 but Upregulates CSNK2A1

As we expected, the expression of CSNK2A3 was downregulated upon OGR1 over-expression (Figs. 3a, b). But CSNK2A1 expression was upregulated (Figs. 3a, b). There was about a ~60% decrease in the expression of CSNK2A3 but a ~40% increase in CSNK2A1 expression. Even though we found differences in the expressions of the CK2α genes, not much difference was found in the CK2α protein expressions (Fig. 3c). This may be because the anti-CK2α antibody recognizes both the CK2α proteins produced by CSNK2A3 and CSNK2A1 as there are only four amino acids difference between the two proteins. The result of OGR1 differentially regulating the two genes is anticipated as the two genes have different promoter regions.

3.4 OGR1 Downregulates CSNK2A3 Through Gαi Activation

Previously we have reported that CSNK2A3 expression is upregulated by OGR1 via Gαi activation in A549 cells [24]. Therefore, to find out if the downregulation of CSNK2A3 by OGR1 in K562 is dependent on Gαi activation, the expression of

(a)

(b)

(c)
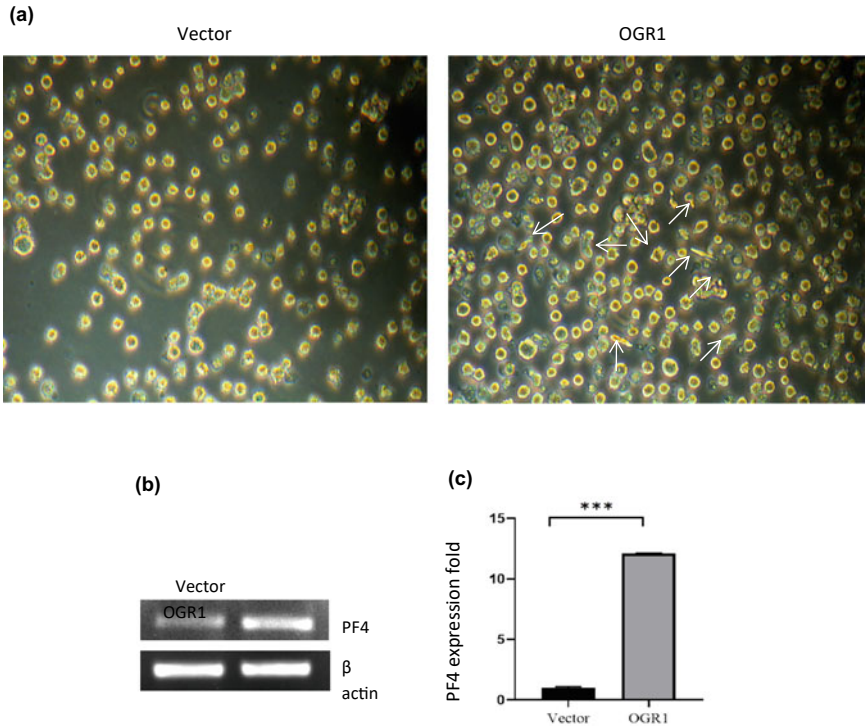
Fig. 2 OGR1 induces differentiation of K562 cells. **a** The formation of pseudopod-like structures in the cell membranes was observed. **b** Increased expression of megakaryocytic differentiation marker PF4 was observed, confirming K562 differentiation into megakaryocytic cells. **c** Real-time PCR showing ~10 times increase in the expression of PF4. Bars indicate standard deviation (SD) and *** indicates the $p < 0.001$

CSNK2A3 was analyzed with or without pertussis toxin (PTX). The result showed that PTX abrogated the downregulation of CSNK2A3 (Fig. 4). This shows that OGR1 downregulates CSNK2A3 through G α i activation. No effect of PTX was observed in the expression of CSNK2A1.

3.5 Involvement of Ras Family Small G-proteins and P38 Pathway in the Downregulation of CSNK2A3 by OGR1

Cdc42 and Rac1 which are Ras superfamily small G-proteins regulate many cellular events, like activation of protein kinases, cell growth control, and cytoskeletal reorganization. When the activities of Cdc42 and Rac1 were inhibited by the overexpression of the genetic inhibitors or dominant-negative mutant plasmids of Rac1 (pcDNA3.1-RacT17N) or cdc42 (pcDNA3.1-cdcT17N), the downregulation

(a)

(b)

(c)
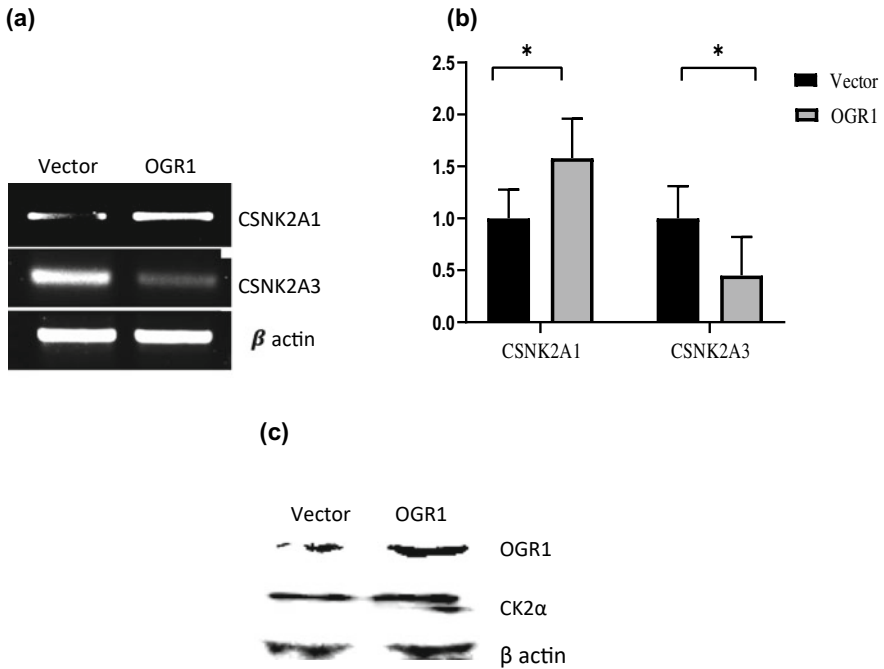
Fig. 3 OGR1 differentially regulates CSNK2A1 and CSNK2A3. **a** Downregulation of CSNK2A3 and upregulation of CSNK2A1 in OGR1 overexpressed K562 cells. **b** Real-time PCR confirming differential regulation of CK2α genes by OGR1. **c** Western blotting data showing regulation of CK2α proteins by OGR1. (Anti-CK2α antibody recognized both the CK2 proteins encoded by CSNK2A1 and CSNK2A3 and could not differentiate as they differ by only 4 amino acids) Bars indicate standard deviation (SD) and * indicates $p < 0.05$

Fig. 4 PTX abrogates OGR1 downregulation of CSNK2A3. The expressions of CK2α genes were investigated in the K562 cells upon OGR1 overexpression with or without PTX. There was no downregulation of CSNK2A3 in PTX treated OGR1 overexpressed K562 cells
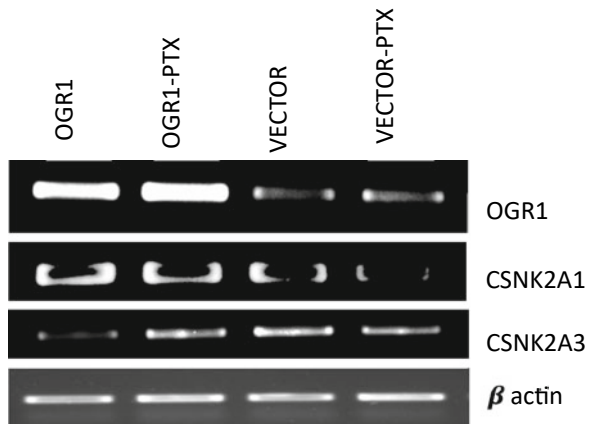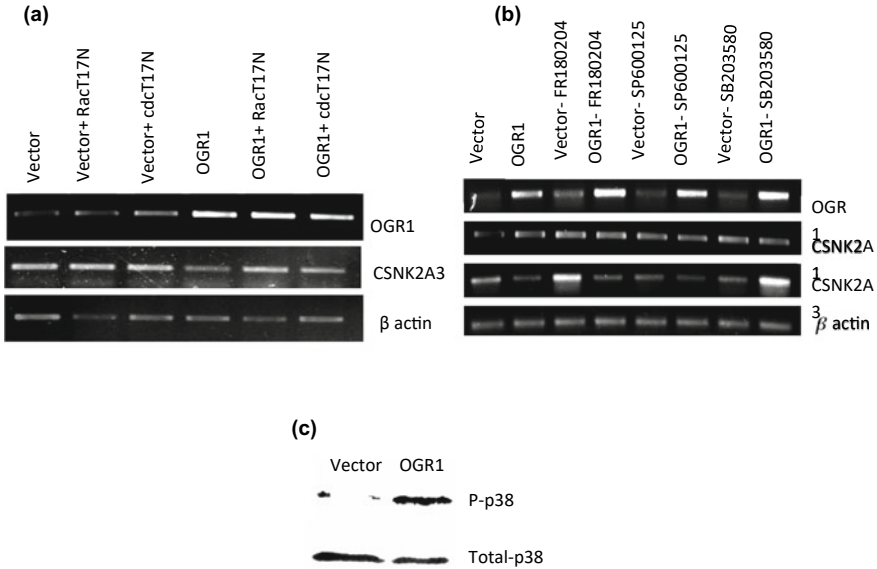
Fig. 5 Involvement of Cdc42 and Rac1 in the downregulation of CSNK2A3 by OGR1. **a** Dominant-negative mutant plasmids of Rac1 (pcDNA3.1-RacT17N) or cdc42 (pcDNA3.1-cdcT17N) abrogate CSNK2A3 downregulation by OGR1. **b** OGR1 downregulates CSNK2A3 via the P38 pathway (inhibitors of JNK; SP600125, p38; SB203580 and ERK; FR180204). **c** Western blotting confirms the role of the p38 pathway in the CSNK2A3 downregulation by OGR1

of CSNK2A3 (Fig. 5a) was prevented. The results showed that Cdc42 and Rac1 play role in the OGR1 induced CSNK2A3 downregulation.

Since mitogen-activated protein kinase (MAPK) cascades have essential roles in cell differentiation, proliferation, migration, and death, their involvement in the OGR1 pathway was investigated. Treatment with a specific inhibitor of p38 (SB203580) abrogated the downregulation of CSNK2A3 in the OGR1 overexpressed cells (Fig. 5b). The involvement of p38 in the action of OGR1 is further supported

by the finding that OGR1 increases the phosphorylation (activation) of p38 protein (Fig. 5c). This shows that OGR1 downregulates CSNK2A3 through activation of the p38 pathway.

4 Discussion

CK2α is now a key therapeutic target for cancer treatment [3, 7, 13, 27]. Many studies have focused on targeting the downregulation or inhibition of the upregulated expression of CK2α in cancers [12, 20, 28]. Induction of cell death by inhibiting CK2 function in Chronic Myelogenous Leukemia cells (K562) has been reported [18]. The differentiation therapy approach to treat acute myeloid leukemia (AML) has been demonstrated where the accumulation of the malignantly transformed immature myeloid precursors could be relieved by inducing chemical agents to undergo terminal differentiation [6]. Our findings show that both the CSNK2A3 and CSNK2A1 genes are downregulated during PMA induced differentiation of K562 into megakaryocytic cells. In another study, CK2 downregulation in human glioblastoma cells M059K and T98G has shown autophagic cell death [20]. Our overall results show the correlation between the downregulation of CK2α and the differentiation of K562 cells.

We have previously reported that OGR1 plays role in inhibiting cell metastasis in prostate cancer (PC3) and lung cancer cells (A549) through the regulation of both the CK2α genes expression [24, 26]. Therefore, the current study investigates the expression of OGR1 during K562 differentiation. Interestingly, OGR1 expression is found to be increased during K562 differentiation. Also, OGR1 alone can induce K562 morphological changes and increase the expression of the megakaryocytic differentiation marker, PF4 similar to the case of PMA treatment. In the same way, OGR1 overexpression in K562 downregulates the expression of CSNK2A3. However, unlike PMA, OGR1 upregulates the expression of CSNK2A1.

Some studies have claimed CK2α intronless or CSNK2A3 to be an oncogene and activation of CSNK2A3 expression during cancer has also been reported [10]. Taking together the results of both the PMA and OGR1 induced megakaryocytic differentiation of K562, it can be concluded that downregulation of CK2α intronless gene (CSNK2A3) is necessary or required for K562 differentiation. This also suggests that the sustenance of the undifferentiated phenotype of K562 cells may be due to the upregulated expression of particularly the CK2α intronless gene (CSNK2A3), not the CSNK2A1 gene. Our findings also support the indication that CSNK2A3 is an oncogene. The upregulation of CSNK2A1 induced by OGR1 may have other functions rather than cell differentiation. Our finding is the first report to suggest that the OGR1 induces megakaryocytic differentiation in K562. However, more investigation is warranted.

CSNK2A3 expression is upregulated by OGR1 via Gαi activation and involvement of Ras family small G-proteins in A549 cells [24]. Our results also show the activation of Gαi, cdc42, and Rac1 in the OGR1 regulation pathway in K562. Further, the result

shows that the p38 pathway is also involved. The MAPK p38 pathway is crucial for controlling a variety of cellular functions, including growth, inflammation, cell differentiation, and cell death [22]. Activation of p38 has been found to result in cancer cell apoptosis [14, 21]. Therefore, from the above findings, it can be suggested that OGR1 plays role in K562 differentiation by regulating the expression of the CSNK2A3 (intronless gene) and OGR1 downregulates CSNK2A3 expression via activation of the Gαi, small G-proteins, and p38 pathway in K562.

5   Conclusion

OGR1 or GPR68 has been reported to play roles in pH homeostasis and inflammation and to act as a metastasis suppressor gene. Findings from the current study show a new role of OGR1 in cell differentiation. The study can have potential applications in differentiation therapeutic approaches that target upregulated CK2α for the treatment of myeloid leukemia.

References

1. Ahmad KA, Wang G, Slaton J, Unger G, Ahmed K (2005) Targeting CK2 for cancer therapy. Anticancer Drugs 16(10):1037–1043
2. Ahmed K, Gerber DA, Cochet C (2002) Joining the cell survival squad: an emerging role for protein kinase CK2. Trends Cell Biol 12(5):226–230
3. Chua MM, Ortega CE, Sheikh A, Lee M, Abdul-Rassoul H, Hartshorn KL, Dominguez I (2017) CK2 in cancer: cellular and biochemical mechanisms and potential therapeutic target. Pharmaceuticals 10(1):18
4. Devilat I, Carvallo P (1993) Structure and sequence of an intronless gene for human casein kinase II-α subunit. FEBS Lett 316(2):114–118
5. Dominguez I, Sonenshein GE, Seldin DC (2009) Protein kinase CK2 in health and disease. Cell Mol Life Sci 66(11):1850–1857
6. Gocek E, Marcinkowska E (2011) Differentiation therapy of acute myeloid leukemia. Cancers 3(2):2402–2420
7. Gowda C, Sachdev M, Muthusami S, Kapadia M, Petrovic-Dovat L, Hartman M et al (2017) Casein kinase II (CK2) as a therapeutic target for hematological malignancies. Curr Pharm Des 23(1):95–107
8. Guerra B, Issinger OG (2008) Protein kinase CK2 in human diseases. Curr Med Chem 15(19):1870–1886
9. Guerra B, Issinger OG (1999) Protein kinase CK2 and its role in cellular proliferation, development, and pathology. ELECTROPHORESIS: Int J 20(2):391–408
10. Hung MS, Lin YC, Mao JH, Kim IJ, Xu Z, Yang CT et al (2010) Functional polymorphism of the CK2a intronless gene plays oncogenic roles in lung cancer
11. Kang H, Jung JW, Kim MK, Chung JH (2009) CK2 is the regulator of SIRT1 substrate-binding affinity, deacetylase activity, and cellular response to DNA-damage. PLoS ONE 4(8):e6611
12. Lee SW, Song YS, Lee SY, Yoon YG, Lee SH, Park BS et al (2011) Downregulation of protein kinase CK2 activity facilitates tumor necrosis factor-α-mediated chondrocyte death through apoptosis and autophagy. PloS one 6(4):e19163

13. Lian H, Su M, Zhu Y, Zhou Y, Soomro SH, Fu H (2019) Protein kinase CK2, a potential therapeutic target in carcinoma management. Asian Pac J Cancer Prev: APJCP 20(1):23
14. Losa JH, Cobo CP, Viniegra JG, Lobo VJSA, Sanchez-Prieto R (2003) Role of the p38 MAPK pathway in cisplatin-based therapy. Oncogene 22(26):3998-4006
15. Ludwig MG, Vanek M, Guerini D, Gasser JA, Jones CE, Junker U et al (2003) Proton-sensing G-protein-coupled receptors. Nature, 425(6953):93–98
16. Manni S, Brancalion A, Tubi LQ, Colpo A, Pavan L, Cabrelle A et al (2012) Protein kinase CK2 protects multiple myeloma cells from ER stress–induced apoptosis and from the cytotoxic effect of hsp90 inhibition through regulation of the unfolded protein response. Clin Cancer Res 18(7):1888–1900
17. Meggio F, Pinna LA (2003) One-thousand-and-one substrates of protein kinase CK2? FASEB J 17(3):349–368
18. Mitrovský O, Myslivcová D, Macháčková-Lopotová T, Obr A, Čermáková K, Ransdorfová Š et al (2021). Inhibition of casein kinase 2 induces cell death in chronic myelogenous leukemia cells with different mechanisms of resistance to tyrosine kinase inhibitors. bioRxiv
19. Montenarh M (2010) Cellular regulators of protein kinase CK2. Cell Tissue Res 342(2):139–146
20. Olsen BB, Svenstrup TH, Guerra B (2012) Downregulation of protein kinase CK2 induces autophagic cell death through modulation of the mTOR and MAPK signaling pathways in human glioblastoma cells. Int J Oncol 41(6):1967–1976
21. Olson JM, Hallahan AR (2004) p38 MAP kinase: a convergence point in cancer therapy. Trends Mol Med 10(3):125–129
22. Ono K, Han J (2000) The p38 signal transduction pathway activation and function. Cell Signal 12(1):1–13
23. Piazza FA, Ruzzene M, Gurrieri C, Montini B, Bonanni L, Chioetto G et al (2006) Multiple myeloma cell survival relies on high activity of protein kinase CK2. Blood 108(5):1698–1707
24. Sharma AL, Meitei PM, Machathoibi TC, Singh NT, Singh TR, Singh LS (2022) Ovarian cancer G protein-coupled receptor 1 inhibits A549 cells migration through casein kinase 2α intronless gene and neutral endopeptidase. BMC Cancer 22(1):1–12
25. Singh LS, Kalafatis M (2002) Sequencing of full-length cDNA encoding the α and β subunits of human casein kinase II from human platelets and megakaryocytic cells. Expression of the casein kinase IIα intronless gene in a megakaryocytic cell line. Biochemistry 41(28):8935–8940
26. Singh LS, Berk M, Oates R, Zhao Z, Tan H, Jiang Y et al (2007) Ovarian cancer G protein-coupled receptor 1, a new metastasis suppressor gene in prostate cancer. J Natl Cancer Inst 99(17):1313–1327
27. Trembley JH, Chen Z, Unger G, Slaton J, Kren BT, Van Waes C, Ahmed K (2010) The emergence of protein kinase CK2 as a key target in cancer therapy. BioFactors 36(3):187–195
28. Wang G, Unger G, Ahmad KA, Slaton JW, Ahmed K (2005) Downregulation of CK2 induces apoptosis in cancer cells–a potential approach to cancer therapy. Mol Cell Biochem 274(1):77–84
29. Wirkner U, Pyerin W (1999) CK2α loci in the human genome: structure and transcriptional activity. In: A molecular and cellular view of protein kinase CK2, pp 59–64

Production of a Bioactive Recombinant Human UTF1 Protein from *E. coli*

Chandrima Dey, Khyati Raina, and Rajkumar P. Thummer

1 Introduction

UTF1 expression is specific to undifferentiated cells and to placental mammals [1–5]. The protein shows homology with two highly conserved regions named the conserved domains 1 and 2 [1, 3, 4]. The conserved domain 1 is responsible for localizing the protein into the nucleus, whereas the conserved domain 2 domain (containing a leucine zipper motif) is responsible for the proteins' tight DNA binding, much like the histones [1–4, 6, 7].

UTF1 expression starts at the blastocyst phase in its inner cell mass and eventually gets restricted to primordial germ cells of the mouse embryo [2, 5, 8–11]. The maximum level of UTF1 expression was seen in the primordial germ cells and the epiblast [9]. Deletion of *Utf1* from mice embryos showed developmental defects such as developmental arrest or death within two days after birth, suggesting its importance in proper murine development [5, 10, 11]. Given the expression of UTF1 in epiblast and its importance in embryonic development, it was speculated that this protein can

C. Dey · K. Raina · R. P. Thummer (✉)
Laboratory for Stem Cell Engineering and Regenerative Medicine, Department of Biosciences and Bioengineering, Indian Institute of Technology Guwahati, Guwahati 781039, Assam, India
e-mail: rthu@iitg.ac.in

C. Dey
e-mail: dey.chandrima@iitg.ac.in

K. Raina
e-mail: raina176106110@iitg.ac.in

be a promising factor to reprogram differentiated cells to induced Pluripotent Stem Cells (iPSCs). To establish this, a study showed that UTF1 in the presence of Oct3/ 4, Sox2, Klf4, and c-Myc (Yamanaka factors) and a small interfering RNA against p53 resulted in >200-fold increase in reprogramming efficiency when compared to the Yamanaka cocktail alone, and the iPSCs generated were of superior quality [12]. Additionally, some studies have confirmed pluripotency by using UTF1 as one of the biomarkers [13–17]. Additionally, although UTF1 expression has been observed in various cancer tissues, the expression is tissue-specific, either as a tumor suppressor or an oncogene [18, 19]. Over the last four decades, recombinant proteins in the field of therapeutics have been indispensable. Recombinant protein production in various host organisms; bacteria, algae, insect, yeast, and so forth has been a complex yet effective process [20–22]. Wide range of purified recombinant proteins have been utilized for multiple biotechnological purposes [23].

Thus, the safest approach to utilize UTF1 in a clinical setup for pluripotency or anti-cancer-related applications is to use a transducible version of UTF1 protein. The molecular nature of the protein itself eliminates the risk of integration and alteration of the genome, unlike DNA-based and many viral-based approaches [24–26]. Additionally, proteins provide the benefit of control over dosage, various possible protein combinations, and treatment time points [24, 26–29]. In our study, we have used the simplest host system: *Escherichia coli* (*E. coli*), for generating recombinant human UTF1 protein due to its well-established molecular machinery and high protein yield [30–32]. However, the generation of heterologous proteins, i.e., expressing and producing a human protein in a bacterial system, involves several roadblocks such as codon bias, purity of the eluted proteins, proteolytic cleavage by the host system, misfolding of proteins, etc. [24, 29, 33]. In this study, we sought to overcome these roadblocks and have successfully and reproducibly generated a cell and nuclear permeant bioactive human UTF1 protein for the first time, which further can be assessed for multiple biological applications and in the reprogramming cocktail for generating integration-free iPSCs.

2 Materials and Methods

2.1 Generation of Plasmid Constructs and Optimization of Parameters for Maximum Expression of Human UTF1 Protein in Soluble Form

Codon-optimized plasmid constructs (pUC-HTN-*GOI* and pUC-*GOI*-NTH) were obtained from GenScript. The gene of interest with fusion tags at either end was excised out from pUC57 vector using restriction enzymes (*Nco*I and *Xho*I) and were cloned into pET28a(+) expression vector (Fig. 1). These genetic constructs [pET28a(+)-HTN-*hUTF1* and pET28a(+)-*hUTF1*-NTH] were transformed into chemical competent *E. coli* strain BL21(DE3) using calcium chloride method.
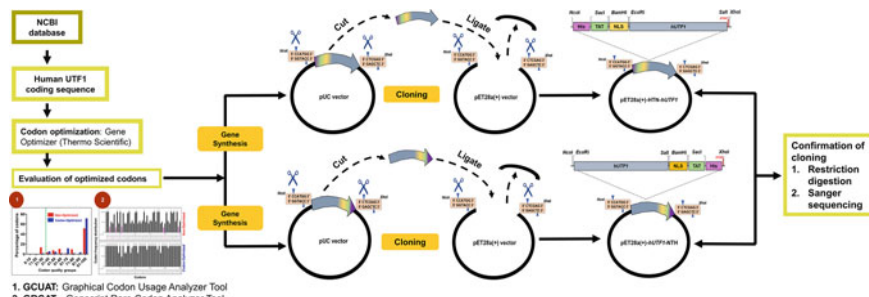
Fig. 1 Diagrammatic representation of codon optimization procedure and gene cloning

Table 1 Screening of parameters for obtaining the optimal expression conditions of the human UTF1 fusion protein in *E. coli*

Transcription factors	Screened parameters	Optimized parameters
IPTG (mM)	0, 0.05, 0.1, 0.25, 0.5	0.25
OD_{600} (nm)	~0.5, 1, 1.5	~0.5–0.6
Time (hours)	24, 2	2
Temperature (°C)	18, 37	37

IPTG, Isopropyl ß-D-1-thiogalactopyranoside; OD, Optical density

Expression parameters (Temperature, IPTG and OD_{600}) were screened as listed in Table 1. Reagents such as bacterial growth media [Luria–Bertani (M1245-500G)] and Terrific broth (MV1250-500G) (TB)), antibiotics (kanamycin and ampicillin), sodium phosphate mono (SRL-1949144) and dibasic (GRM257) salts, sodium chloride salt (MB023) and imidazole (GRM1864) were procured from HiMedia for conducting the experiments. The concentration of total protein was measured for the cell lysates using Bradford Assay. Samples were analyzed for the respective parameters. 40 µg/well of protein was loaded and visualized using Coomassie brilliant blue G-250 stain.

2.2 Purification and PD10 Size Exclusion Chromatography of Recombinant Human UTF1 Protein

pET28a(+)-*hUTF1*-NTH was inoculated and induced in 600 ml TB culture media. The induced bacterial suspension was incubated at two different temperatures (37 and 18 °C) in a shaker incubator (180 rpm) for 2 and 24 h, respectively. Cell pellets were homogenized in 20 ml lysis buffer (Table 2) followed by sonication (ON: 5 s; OFF: 25 s) until clear. The purification was carried out as shown in Fig. 2. Eluted purified

Table 2 Buffer components and their respective strengths for resuspending/lysis of harvested bacterial pellets

Buffer components	Values
PB (mM)	20
NaCl (mM)	0
Imidazole (mM)	20
Glycerol (%)	20
pH (at RT)	~7.8

PB, sodium phosphate buffer; RT, room temperature
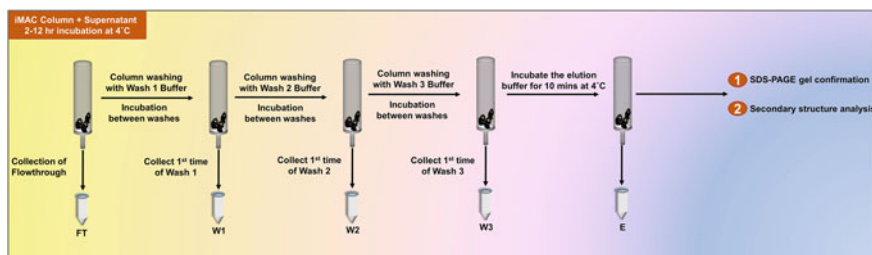
Fig. 2 Schematic representation of the steps involved in purification of human UTF1 fusion protein

protein was dialyzed using PD10 chromatography column (10 ml; GE healthcare) [34–36]. Further, the eluted protein was flash-freeze and kept at −80 °C for later use.

2.3 SDS-PAGE, Coomassie Staining and Western Blotting (Immunoblotting) Analysis

SDS-PAGE, Coomassie staining, and Western blotting (immunoblotting) were performed as previously described [35]. The supernatant of the centrifuged samples was taken and analyzed by Western blotting analysis using protein-specific primary antibodies [anti-UTF1 antibody (1:500, R&D systems-AF3958) and anti-His (BioBharati, BB-AB0010; 1:5000)] and secondary antibodies [anti-Goat IgG-HRP (1:5000, Invitrogen)].

2.4 Characterization of Secondary Structure Using Circular Dichroism Spectroscopy

The full-length human UTF1-NTH protein secondary structure was carried out with far-UV circular dichroism (CD) spectroscopy [J-1500 spectropolarimeter (Jasco, MD, USA)]. The parameters for the analysis were similar to our previously published

articles [37, 38]. The raw data analysis was performed using online tool [BeStSel: Beta Structure Selection] [39].

2.5 Translocation of Purified Recombinant Human UTF1 Protein in Hela Cells

Cervical cancer cell line HeLa was plated (0.7×10^5 cells/well in a 24-well plate) and placed for incubation at 37 °C with 5% CO_2 under humidified conditions in the incubator till the confluence of 80% was reached. The cells were treated with protein transduction media (400 nM UTF1-NTH protein, 5% fetal bovine serum (FBS), 1% penicillin–streptomycin (P/S) solution in Dulbecco's Modified Eagle Medium (DMEM) for Hela; 400 nM protein and 20 mM phosphate buffer, 5% FBS, 1% P/S, 1% NEAA in DMEM media for vehicle control) for 12 h. Immunocytochemistry was performed following the protocol as per our recently published studies [34, 38, 40–42]. Antibodies used in this study were α-UTF1 (1:200, AF-3958, R&D systems) and secondary antibody (A11029, 1:2000, Invitrogen) for immunocytochemistry.

2.6 Cell Migration and Cell Proliferation Assay

HeLa cells were plated (0.6×10^5 cells) per well of a 24-well plate for migration assay. The cells were later incubated at standard cell culture conditions. Upon achieving 80–90% confluency, clean scratches were drawn using a sterile tip (10 µL) and then the media was aspirated out and washed with PBS. After PBS wash, media was replaced with 400 nM UTF1-NTH protein media and vehicle control media. Protein media was replaced every 24 h and imaging was performed at 0, 24 and 48 h, using an inverted microscope (Make: Bio-Rad; Model: ZOE Fluorescent Cell Imager); 20X magnification). The rate of migration was evaluated and calculated at 48 h using ImageJ software. The migration percentage formula used:

$$\text{Migration}(\%) = \frac{(\text{initial area} - \text{final area})}{\text{initial area}} \times 100$$

Cell proliferation assay was performed by plating HeLa cells (0.4×10^5 cells per 96 well plate). The assay was performed as per our previously published article [34].

2.7 Colony Formation Assay

HeLa cells were counted and diluted in complete growth media. 400 cells/well of a 6-well plate were plated and incubated at standard cell culture conditions. After 24 h,

Table 3 Primer sets for the detection of p27^{Kip1} gene using RT-qPCR

Genes	Primer sequences (5'–3')	Annealing temp. (°C)	Product size (bp)
p27^{Kip1}	F—CTGCCCTCCCCAGTCTCTCT R—CAAGCACCTCGGATTTT	52.6	101
GAPDH	F—GTCTCCTCTGACTTCAACAGCG R—ACCACCCTGTTGCTGTAGCCAA	57	131

the cell culture media was replaced with 400 nM UTF1-NTH protein transduction media and its respective vehicle control. The spent protein media was replaced with fresh media after every 48 h. The treatment cycle was followed for 10–12 days until distinct colonies were visible. The obtained colonies were visualized and counted using ImageJ software upon fixing with methanol/acetic acid solution (3:1) for 20 min and stained with 5% crystal violet solution.

2.8 RT-qPCR Analysis

HeLa cells (0.4×10^6) were plated in a 6-well plate and treated for 24 h. After 24 h the culture media was substituted with protein transduction media (UTF1-NTH at a concentration of 400 nM) and vehicle control (media without the protein). Protein transduction media was changed every 24 h until the stipulated treatment time duration. RNA was extracted using TRIzol method (Invitrogen), then cDNA synthesis was carried out using iScript cDNA synthesis kit (Bio-Rad) as reported earlier [41]. RT-qPCR was performed using gene-specific primers (Table 3) and analyzed as previously described [41].

2.9 Statistical Analysis

Statistical analysis was performed employing student unpaired t-test or multiple t-test (GraphPad Prism 8 software). Data are shown as mean ± SEM. $P < 0.05$ was considered significant.

3 Results

3.1 Construction, Cloning and Analysis of the Sequence of Recombinant Human UTF1 Gene in Expression Plasmid pET28a(+)

In general, protein being a macromolecule lacks inherent cell penetration capacity when exogenously administered. Therefore, we devised a fusion strategy to facilitate cellular membrane penetration and translocation into the nucleus of the recombinant fusion protein. Others and our previously published reports have emphasized on the importance of the position of fusion tags on the overall expression, solubility and stability of recombinant proteins [34–38, 40–44] and hence the codon-optimized gene human *UTF1* (*hUTF1*) was cloned along with fusion tags (NLS, TAT and 8X His) into pET28a(+) vector at both 5' and 3' end of this gene (Fig. 3a, c). The generated constructs; pET28a(+)-HTN-*UTF1* and pET28a(+)-*UTF1*-NTH were analyzed using restriction digestion analysis. *Eco*RI/*Sal*I and *Nco*I/*Xho*I were used to confirm the cloning (Fig. 3b, d). The integrity of these cloned constructs was further assessed using Sanger sequencing analysis.

## 3.2 Identification of Parameters Enhancing the Production of UTF1 Protein in E. coli

To determine the parameters for the maximal heterologous expression of human UTF1 protein in expression host (*E. coli*), temperature, IPTG and OD_{600} were screened. Temperature is a critical parameter to be optimized for any protein expression system. To obtain biologically active protein, soluble expression of the protein is essential. Hence, upon screening two temperatures 37 and 18 °C, as well as to understand the effect of the position of fusion tags. We observed that at both temperatures the UTF1-NTH protein was expressed in the soluble fraction of the lysate upon induction (Fig. 4b, *top and bottom*), however in HTN-UTF1 no expression was seen at any temperature (Fig. 4a, *top and bottom*). Therefore, HTN-UTF1 was excluded from further analysis in this study. The range of IPTG concentration was screened and the results showed that the maximum expression of human UTF1-NTH fusion protein was observed at 0.25 mM (Fig. 4c, *top and bottom*). The next parameter to be optimized was optical density which corresponds to the bacterial growth phases. The results obtained show that UTF1-NTH protein was maximally expressed at ~0.5 OD_{600} (Fig. 4d, *top and bottom*). This proved that position of fusion tags has a prominent effect on the overall expression and stability of the protein, and hence, UTF1-NTH was used for further purification and functional analysis.
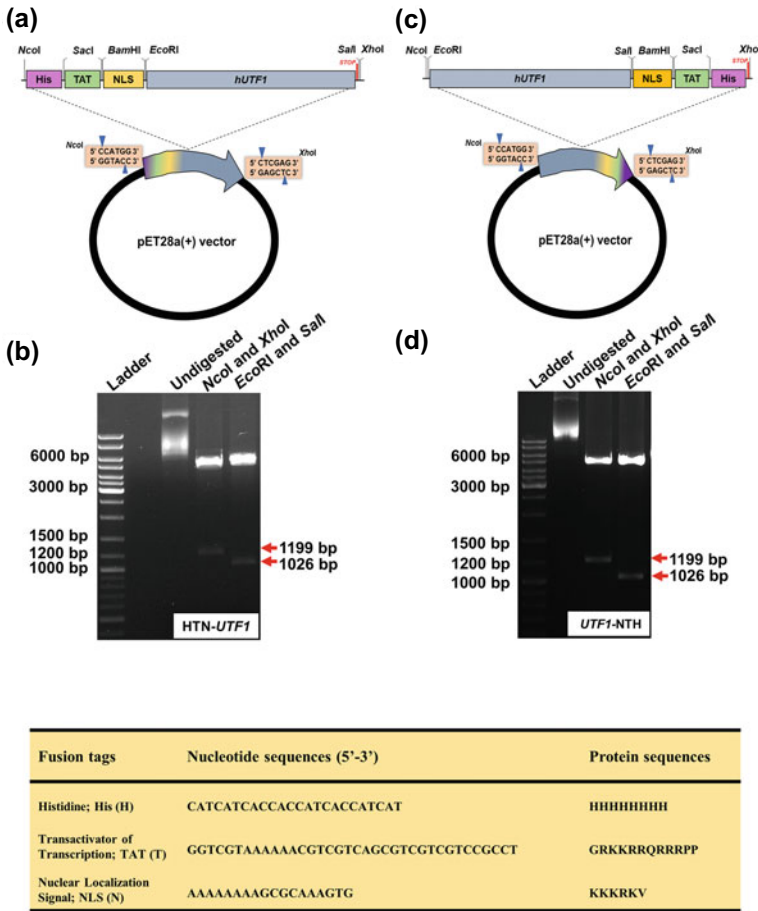
Fig. 3 Cloning and restriction analysis of human UTF1 protein. **a** and **c** Cloning strategy used for generating pET28a(+)-HTN-*UTF1* and pET28a(+)-*UTF1*-NTH gene construct. **b** and **d** Confirmation of cloning using restriction digestion analysis gene construct and confirmation using restriction digestion analysis. Experiments were carried out n = 3 times

3.3 Purification of Soluble Human UTF1 Protein from Bacterial Host E. coli

Heterologous protein expression and purification from *E. coli* is a challenging process as it requires the separation of the protein of interest from unwanted contaminating components with purity, yield, reasonable efficiency, and bioactivity [45]. Therefore, it is essential to screen for the basic fundamental conditions such as salt, glycerol, imidazole, pH, and buffer strength to purify proteins using affinity purification method [45, 46].
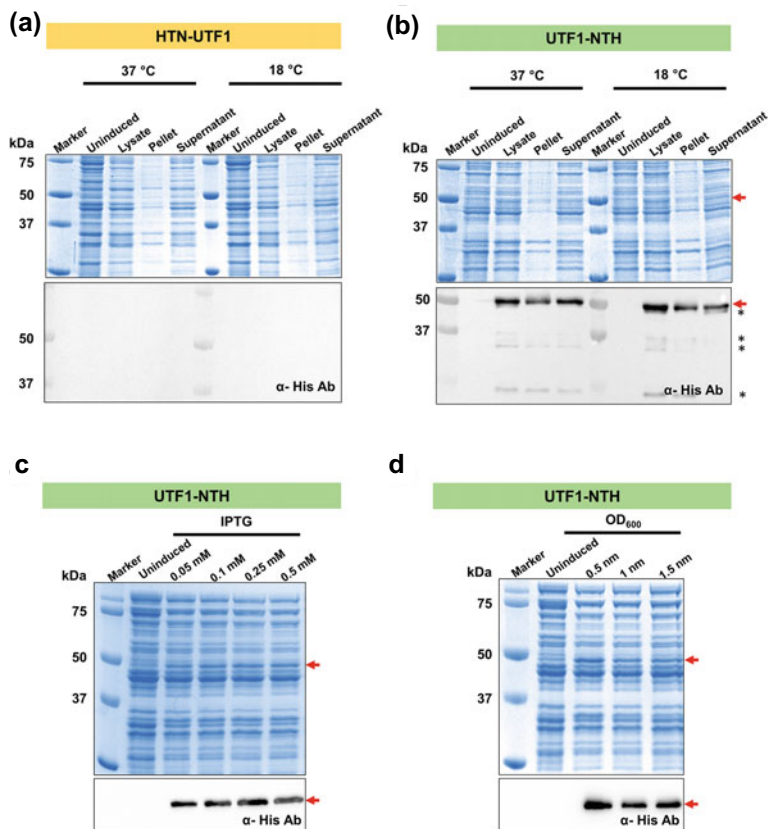
Ab, Antibody; IPTG, Isopropyl ß-D-1-thiogalactopyranoside; OD, Optical density

Fig. 4 Screening for suitable fusion tags and optimization of induction parameters for the maximal soluble expression of human UTF1-NTH protein in *E. coli*. **a** and **b** Screening for optimal temperature and identifying the position of fusion tag for the maximum soluble expression. **c** and **d** Optimization of induction parameters for obtaining maximum expression of UTF1-NTH fusion protein

The recombinant protein UTF1-NTH present in the soluble fraction of the total lysate was purified using native Ni^{+2}-NTA affinity purification. The production of protein in the soluble fraction was screened based on different salt concentrations. The induced bacterial pellets were subjected to lysis buffers containing a gradient of salt concentrations (0, 150, 300, 600, 900, and 1200 mM). The SDS-PAGE results revealed that different salt concentrations did not affect the production of protein in the soluble fraction of the lysate. The results showed full-length protein purification of human UTF1-NTH protein in 0 mM salt condition. Truncations were observed when purified with 150 and 600 mM salt buffer (data not shown). This shows unfavorable interaction between protein and salt leading to salt-dependent aggregation

Fig. 5 Purification of human UTF1 fusion protein. **a** and **b** Purification of human UTF1-NTH protein under native condition at 37 °C and 18 °C. The purified protein bands were resolved using SDS-PAGE and analyzed using Coomassie Brilliant Blue (*top*) and immunoblotting using α-His antibody (*bottom*). α, Antibody; *, truncations. Experiments were carried out n ≥ 4 times
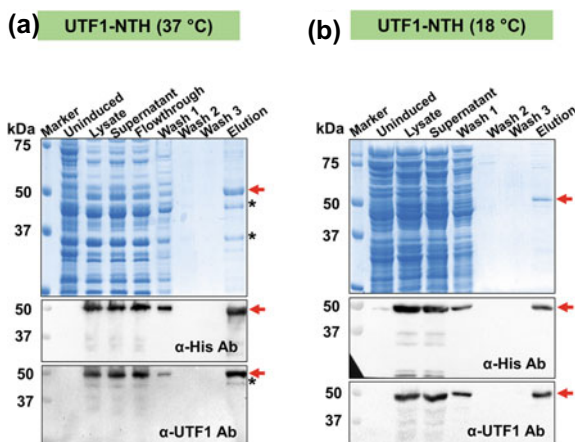

of the protein [47]. In an earlier study, ferritin and MESP1 proteins expressed in *E. coli* also showed similar results [40, 48]. Thus, purification was performed in the absence of salt, suggesting UTF1 protein to be an ion-sensitive protein, like ferritin and MESP1. Therefore, purification was performed using no salt condition and the soluble fractions of UTF1-NTH protein expressed at both 37 and 18 °C were successfully purified (Fig. 5a, b; *top, middle and bottom*). The total protein yield for UTF1 fusion protein expressed at 37 and 18 °C was 0.81 mg/L and 0.54 mg/L, respectively. The total protein yield was less because of the low expression of the protein and loss in flow-through and wash buffer 1. Although yield is less, but the SDS-PAGE and Western blotting confirmed the successful purification of UTF1-NTH fusion proteins. In this study, we are the first to establish a method for purifying full-length human recombinant UTF1 fusion protein under native conditions and this purified fusion protein was used for further analysis.

3.4 Secondary Structure Analysis of Human UTF1 Protein from E. coli

The secondary structure determination and characterization using far-UV CD spectroscopy is a crucial step after purification as it is one of the determinants of the potentiality of the bioactivity of the purified protein. The criteria of analysis are based on the protein conformation and the peak and trough depict the presence of different types of secondary structures, namely β-sheet, α-helix, turn and random coil [49, 50].

To date, no reports of the secondary structure of UTF1 protein are available. The CD spectral analysis of UTF1-NTH purified from the soluble fraction induced at 37 °C displayed a positive peak at ~194 nm and two negative peaks at ~211 and ~218 nm. Similarly, UTF1-NTH purified from the soluble fraction induced at 18 °C
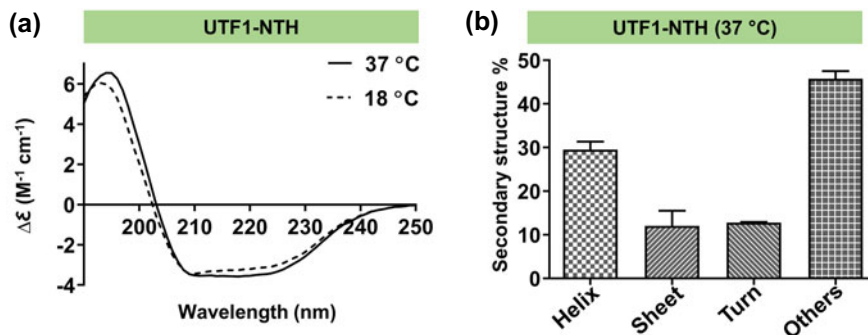
Fig. 6 Secondary structure determination and quantification of human UTF1-NTH protein using far UV CD spectroscopy and BeStSel online tool. **a** Far UV CD spectral analysis of UTF1 fusion protein at 37 and 18 °C using far UV CD spectroscopy. Spectral measurements were analyzed using BeStSel online server. The spectra were plotted delta epsilon (M-1 cm-1) on X-axis and wavelength (nm) on Y-axis. **b** The secondary structure quantification of the purified UTF1-NTH protein at 37 °C was analyzed using BeStSel online server. The secondary structures (α-helices, β-sheets, turns and others) were represented using the bar graphs (n ≥ 3)

exhibited positive peak at ~193 nm and two negative peaks at ~208 and ~214 nm (Fig. 6a). These spectral patterns of both were almost similar and were suggestive of a mixed secondary structure conformation. Upon analysis using BeStSel online tool, the secondary structure for 37 °C UTF1-NTH were α-helices (~29%), β-sheets (~12%), turns (~13%), and random coils (~46%) (Fig. 6b). This data confirms that UTF1 fusion proteins had upheld their secondary structure. However, as the yield of UTF1-NTH expressed at 37 °C is higher compared to UTF1-NTH expressed at 18 °C, thus we proceeded with UTF1-NTH expressed at 37 °C for further functional assays.

3.5 Cell Membrane and Nuclear Translocation of Recombinant Human UTF1 Protein

Purified proteins and their functions are location specific and hence, their translocation into respective cellular compartments is crucial. Our protein UTF1 is a transcription factor and its function lies in the nucleus. To determine the stability of the protein at cell culture conditions and its translocation ability into the cell and nuclear membrane, we performed stability assay, followed by immunofluorescence assay. We assessed the stability and solubility of UTF1-NTH protein in protein media comprising of DMEM, 5% FBS and 1% P/S. The protein stocks were diluted in the protein media and incubated at normal cell culture conditions for 0, 24 and 48 h. The samples were centrifuged and the supernatant was loaded and analyzed on SDS-PAGE gel. The results showed that protein purified from 37 °C was stable for 48 h (Fig. 7a, *top and bottom*). Thus, UTF1-NTH protein purified from 37 °C fulfilled the
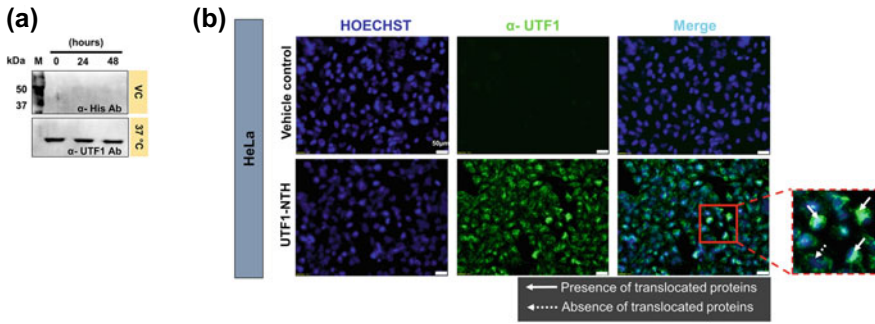
Fig. 7 Assessment of stability of human UTF1-NTH protein. Stability assessment was done using immunoblotting with α-UTF1 antibody (**a**) and cellular translocation ability using an inverted fluorescent microscopy (**b**) in HeLa cells at standard cell culture conditions**.** Inset image showing solid white arrows indicate nuclear uptake and white dotted arrows indicate non-transduced cells

foremost criteria of protein stability in protein transduction media and can be used for further reprogramming as well as for other cell-based assays.

To determine the ability to translocate the purified UTF1-NTH protein, HeLa cells were transduced with protein media for 12 h. The fluorescent microscopy result showed successful cellular and nuclear entry in protein treated cells and no signal in vehicle control treated cells (Fig. 7b, *top and bottom*). Thus, this proved that our construct containing TAT successfully assisted in facilitating cellular entry of the protein and NLS assisted the entry into the nucleus. The result shows successful entry of the protein and is potentially bioactive.

3.6 Analysis of the Biological Activity of Purified Recombinant Human UTF1 Protein

To validate that the protein is biologically active, we first analyzed the clonogenic potential and rate of migration in HeLa cells. Previous study has deemed UTF1 as a tumor suppressor protein [51]. Upon expressing UTF1 in HeLa and overexpressing UTF1 in SiHa cells (Cervical cancer cell lines), they demonstrated a significant reduction in cell proliferation compared to control cells [51]. Also, the clonogenic potential of UTF1 transduced cells was observed to have dramatically reduced upon treatment [51]. Thus, the previous report established that ectopic expression of UTF1 suppressed cancer cell growth in vitro [51]. The question was whether purified UTF1-NTH protein when transduced in HeLa cells will also lead to the reduction in cell proliferation and clonogenic potential of the cells. To understand the proliferation rate, MTT assay was performed [52] and the results showed a significant decrease in cell proliferation in HeLa cells upon 6 days of treatment in the UTF1-NTH treated cells as compared to the vehicle control treated cells (Fig. 8a). No abrogation in the proliferation of cells was observed in vehicle control.
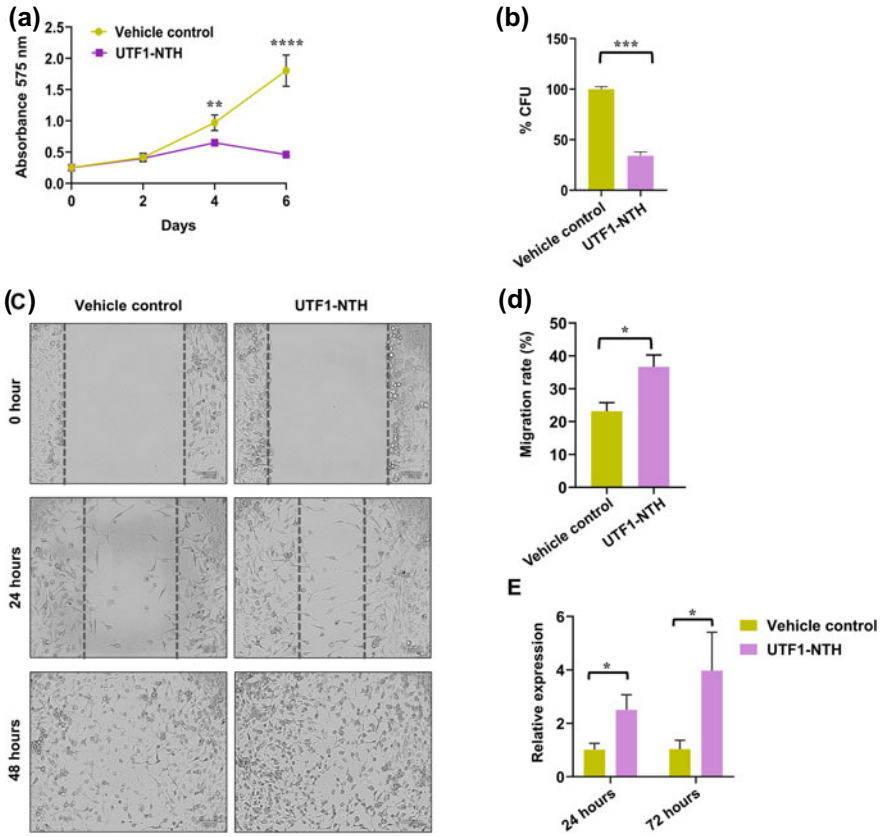
Fig. 8 Effect of purified UTF1-NTH fusion protein on HeLa cells. **a** The MTT data showed significant reduction in cell proliferation with UTF1-NTH protein treated wells compared to vehicle control from Day 4 (**P = 0.0083), Day 6 (****P = 0.0001) (n = 3). **b** Quantitative analysis of the clonogenic potential of UTF1-NTH and vehicle control treated HeLa cells (***P = 0.0002). **c** Scratch assay performed on HeLacells for 48 h. **d** Graph showing change in the migration rate upon treatment with UTF1-NTH and vehicle control. The data shows significant reduction in migration rate with UTF1-NTH protein treated wells compared to vehicle control (*P = 0.0380). **e** The relative gene expression analysis of p27^{Kip1} on control and UTF1-NTH transduced HeLa cells, analyzed using RT-qPCR method [24 h (*P = 0.0144); 72 h (*P = 0.0257)]. The quantitative data shown are mean ± SEM (n = 3). *P < 0.05; **P < 0.01; ***P < 0.001; ****P < 0.0001

We sought to understand whether UTF1-NTH protein abrogated the clonogenic potential of HeLa cells. Upon treatment of cells for 10 days, the results showed a drastic decline in the number of foci formed in UTF1-NTH treated cells compared to the vehicle control (Fig. 8b). Both these observations corroborated the previous results, demonstrating ectopically expressing UTF1 retarded cell proliferation and inhibited colony forming potential in HeLa cells [51]. Although, earlier study showed G1/S transition arrest in UTF1 overexpressed HeLa cells [51], however, we did not observe any significant difference in the G1/S-phase in UTF1-NTH treated cells after

72 h compared to vehicle control (data not shown). The reason might be due to the duration of treatment, which might not be sufficient to significantly affect the cell cycle in HeLa cells.

We were curious to assess the migration potential of HeLa cells upon UTF1-NTH treatment for 48 h and understand whether it also reduced the migration potential of the cells. Earlier reports have demonstrated that although cell proliferation and cell migration follow two different cell signaling pathways, but are interconnected in the process of wound healing [53]. Interestingly, UTF1-NTH treated cells showed an increase in the migration rate percentage compared to vehicle control transduced cells (Fig. 8c, d). Further, a detailed understanding of the migratory genes and the impact of short and long-term expression of UTF1-NTH on the invasiveness of HeLa can be assessed.

We next analyzed the effect of UTF1-NTH protein on expression of $p27^{Kip1}$ on HeLa cells. Wu and colleagues screened the potential genes responsible in arresting cell cycle at G1/S transition phase, consequently leading to a decrease in cell proliferation and clonogenic potential of HeLa cells. They identified that among many genes, mRNA levels of $p27^{Kip1}$ were elevated in UTF1 overexpressing HeLa cells. They proposed that UTF1 functions as a tumor suppressor protein in cervical cancer cells through the activation of $p27^{Kip1}$ [51]. Thus, to further examine the role of UTF1-NTH protein in regulating the expression of *p27^{Kip1}* gene, we transduced the cells for 24 and 72 h with purified UTF1-NTH protein. The relative gene expression analysis showed a significant increase in the mRNA levels with an increase in time of treatment in comparison to vehicle control treated cells (Fig. 8e), similar to the previously published report where ~1.5-fold increase in the relative expression of the UTF1 gene was observed. However, further understanding of the detailed mechanism involved in tumor suppressor activity of UTF1 in cancer paradigm, especially in cervical cancer cells is important.

4 Discussion

UTF1 protein is well known for being primarily associated with embryonic stem cells and extra-embryonic cells [2], generation of *bona fide* iPSCs [54], germ cell development [10, 11], and various cancer tissues such as embryonic carcinoma cells [3, 4], testicular germ cell neoplasms [55, 56], endometrial, prostate, breast, oral and multiple other cancers [18, 57]. With this study, we expressed and purified a transducible and biologically active form of the recombinant human UTF1-NTH protein from bacteria (*E. coli).*

We have found that UTF1 gene being a highly GC-rich DNA sequence can be toxic to the bacterial growth upon expression, thus codon optimization was performed. It was then cloned in pET28a(+) vector and expressed in *E. coli* (bacterial system). Codon optimization helps in enhancing the heterologous recombinant protein expression in different host systems. Heterologous expression of the recombinant fusion

proteins in bacterial system brings forth the various technical and economic challenges that the research and development pipelines must face to express and generate proteins in large amounts. *E. coli* as an expression system has various advantages such as unparalleled fast growth kinetics compared to other expression systems, easily achievable high densities and inexpensive culture conditions [58]. Previous reports have emphasized on the essential prerequisites such as identification of optimal IPTG, cell density and temperature as critical players in enhancing the expression of recombinant proteins using heterologous expression system [59–65]. We have also observed that maximum soluble expression for UTF1-NTH protein was obtained at optimized induction parameters. Influence of fusion tags and their respective position at either terminal of the protein was reported to affect protein stability, solubility and overall conformation, thereby affecting the functionality of the protein [43, 66]. Recently, our published reports have attested the importance of the position of fusion tags on protein expression, solubility, stability and functionality [34, 36, 67]. In this study, we identified the optimal induction conditions for the maximum soluble expression of UTF1 fusion protein and presumably the first to generate a fusion strategy containing NLS, TAT and His, facilitating the successful purification of the protein using native affinity purification method and seamless cellular and nuclear entry. Importantly, the addition of fusion tags did not affect with the protein folding of UTF1-NTH, maintaining a secondary structure conformation. Upon purification of UTF1 fusion protein under native condition, we observed that the protein retained its secondary structure. Similar fusion strategy has been applied for numerous recombinant transcription factors like OCT4, SOX2, GLIS1, ETS2, PDX1, MESP1, TBX5, HAND2, and NGN3 [34–38, 40–42, 44, 67]. In our study, immunofluorescence imaging of UTF1-NTH protein transduced HeLa cells confirmed the successful entry of the protein into the cell and its nucleus, thus confirming that the fusion strategy is extremely potent in delivering the proteins into cells to carry out its biological functions.

Previously, this fusion strategy has been used to generate transducible and biologically active forms of recombinant transcription factors NGN3, OCT4, TBX5, and HAND2 from *E. coli* [34, 41, 42, 44]. These previous studies have shown that the proteins purified from *E. coli* were functional, for example upon transducing pluripotent-specific recombinant OCT4-NTH protein onto human foreskin fibroblast cells reduced cell migration rate and cell proliferation rate, proving that OCT4 is functionally active [34]. Similarly, another study reported that cardiac-specific proteins TBX5-NTH when transduced onto colon cancer cells (SW620) showed a reduction in clonogenic potential, ablation of S-phase indicating cell-cycle arrest, induction of apoptosis, and regulating anti-metastatic and pro-metastatic genes [41]. Thereby, confirming TBX5-NTH to be tumor suppressor, whereas recombinant HTN-HAND2 protein when transduced on mouse embryonic fibroblast cells showed increased migration rate and increased angiogenic potential on chicken allantoic membrane window model, thus showing tumor enhancing property [42]. This study highlights the functionality of UTF1 fusion protein from *E. coli* using similar fusion strategy through its role in cervical cancer cells.

UTF1 has been reported as a tumor suppressor in HeLa cells [51]. Expressing UTF1 protein ectopically in HeLa cells showed a reduction in cell proliferation,

reduced clonogenic potential, G1/S-phase arrest, and an increase in the mRNA levels of p27^{Kip1}. In our study, administering purified UTF1-NTH protein in HeLa cells reduced the cell proliferation and clonogenic potential of the cells which were treated for 6–10 days, suggesting that UTF1-NTH acts as a tumor suppressor. These results were in line with the previously published reports, however, the rate of migration increased upon protein transduction. The result does not correlate with the decrease in cell proliferation upon UTF1-NTH treatment, however, we speculated that UTF1 increased the rate of migration in the first 48 h but longer exposure of the protein on HeLa cells eventually might attenuate the migratory potential similar to cell proliferation. The previous study by Wu and colleagues reported that expressing UTF1 protein on HeLa cells inhibited cell proliferation via G1 phase arrest and attenuated the formation of tumor in nude mice [51]. Canonical cell cycle progression or attenuation or absence of apoptosis generally contributes in abrogation of cell growth [68, 69]. At gene level, earlier reports showed transactivation of *p27^{Kip1}*, correlated with cell cycle arrest, thus corresponding to a reduction in cell proliferation [51] as normally in cervical cancer cells, cell cycle inhibitor *p27^{Kip1}* is lost [70, 71]. Although, we did not observe a significant change in cell cycle, however, the mRNA levels of p27^{Kip1} showed significant increase, thus, confirming that indeed UTF1 repressed the growth and expansion of HeLa cells by reducing the proliferation rate and clonogenic potential by regulating cell cycle inhibitor p27^{Kip1}. Our results confirm that we have successfully generated a transducible version of UTF1-NTH protein that is biologically active and can be used to further elucidate the detailed interactions and outcomes of various cell signaling genes, cell cycle checkpoint genes, effect on migration potential of the cells when expressed on cancer cells and other reprogramming genes associated with the ectopic expression of UTF1 protein on somatic cells.

UTF1 being an important factor in the reprogramming paradigm for the generation of *bona fide* iPSCs, this study provides a platform for the generation of full-length recombinant human UTF1 fusion protein which will open up a plethora of ways to map the stage-specific functions of UTF1 in reprogramming and potentiates its use in the generation of integration-free iPSCs. It will also help in investigating the detailed functional implications of the protein in a myriad of complex cellular pathways associated with cancers.

5   Conclusion

In our study, we have performed cloning of the codon-optimized human UTF1 coding sequence and expressed it in bacteria (*E. coli*). We optimized the parameters for maximizing the protein in soluble form and purified using one-step purification method to procure pure as well as functionally active recombinant protein. The methodology established to purify human UTF1 fusion protein is inexpensive and the protocol is highly replicable. Using soluble cell fraction for purification facilitated the retention of native-like protein conformation comprising majorly of α-helix and non-canonical

structures. We reported that purified human UTF1 fusion protein at both 37 and 18 °C retained their secondary structure. Our fusion strategy also showed successful cytoplasmic and nuclear translocation in HeLa cells and upon transduction showed reduced clonogenic potential, reduction in cell proliferation and increase in p27^{Kip1} expression. Thus, we have successfully developed a transducible form of human UTF1 fusion protein which holds great potential to reprogram somatic cells and substitute oncogenic reprogramming factors like c-Myc, thereby aiding in generating integration-free iPSCs, as well as understanding various molecular functions concerning various cancers.

Author Contribution Chandrima Dey designed and performed the experiments, assembled, analyzed and interpreted the data, wrote the manuscript; Khyati Raina analyzed and interpreted the data, and wrote the manuscript; and Rajkumar P Thummer conceptualized and designed the study, analyzed and interpreted the data, supervised the experiments, wrote the manuscript, and provided financial support. The final draft of the manuscript was approved by all the authors for publication.

Conflict of Interest None.

References

1. Fukushima A, Okuda A, Nishimoto M, Seki N, Hori T-A, Muramatsu M (1998) Characterization of functional domains of an embryonic stem cell coactivator UTF1 which are conserved and essential for potentiation of ATF-2 activity. J Biol Chem 273(40):25840–25849. https://doi.org/10.1074/jbc.273.40.25840
2. Okuda A, Fukushima A, Nishimoto M, Orimo A, Yamagishi T, Nabeshima Y et al (1998) UTF1, a novel transcriptional coactivator expressed in pluripotent embryonic stem cells and extra-embryonic cells. EMBO J 17(7):2019–2032. https://doi.org/10.1093/emboj/17.7.2019
3. van den Boom V, Kooistra SM, Boesjes M, Geverts B, Houtsmuller AB, Monzen K et al (2007) UTF1 is a chromatin-associated protein involved in ES cell differentiation. J Cell Biol 178(6):913–924. https://doi.org/10.1083/jcb.200702058
4. Kooistra SM, Thummer RP, Eggen BJ (2009) Characterization of human UTF1, a chromatin-associated protein with repressor activity expressed in pluripotent cells. Stem Cell Res 2(3):211–218. https://doi.org/10.1016/j.scr.2009.02.001
5. Nishimoto M, Katano M, Yamagishi T, Hishida T, Kamon M, Suzuki A et al (2013) In vivo function and evolution of the eutherian-specific pluripotency marker UTF1. PLoS ONE 8(7):e68119. https://doi.org/10.1089/dna.2009.0981
6. Thummer RP, Drenth-Diephuis LJ, Carney KE, Eggen BJ (2010) Functional characterization of single-nucleotide polymorphisms in the human undifferentiated embryonic-cell transcription factor 1 gene. DNA Cell Biol 29(5):241–248. https://doi.org/10.1089/dna.2009.0981
7. Thummer RP, Drenth-Diephuis L, Eggen B, (2012) Constitutive GFP-UTF1 expression interferes with ES and EC cell differentiation. J Stem Cell Res Ther 2(127):1–7. https://doi.org/10.4172/2157-7633.1000127

8. de Sousa Lopes SMC, van den Driesche S, Carvalho RL, Larsson J, Eggen B, Surani MA, Mummery CL (2005) Altered primordial germ cell migration in the absence of transforming growth factor β signaling via ALK5. Dev Biol 284(1):194–203. https://doi.org/10.1016/j.ydbio.2005.05.019

9. Galonska C, Smith ZD, Meissner A (2014) In Vivo and in vitro dynamics of undifferentiated embryonic cell transcription factor 1. J Stem Cell Rep 2(3):245–252. https://doi.org/10.1016/j.stemcr.2014.01.007

10. Bao Q, Morshedi A, Wang F, Bhargy S, Pervushin K, Yu W-P, Dröge P (2017) Utf1 contributes to intergenerational epigenetic inheritance of pluripotency. Sci Rep 7(1):14612. https://doi.org/10.1038/s41598-017-14426-5

11. Kasowitz SD, Luo M, Ma J, Leu NA, Wang PJ (2017) Embryonic lethality and defective male germ cell development in mice lacking UTF1. Sci Rep 7(1):1–10. https://doi.org/10.1038/s41598-017-17482-z

12. Zhao Y, Yin X, Qin H, Zhu F, Liu H, Yang W et al (2008) Two supporting factors greatly improve the efficiency of human iPSC generation. Cell Stem Cell 3(5):475–479. https://doi.org/10.1016/j.stem.2008.10.002

13. Graumann J, Hubner NC, Kim JB, Ko K, Moser M, Kumar C et al (2008) Stable isotope labeling by amino acids in cell culture (SILAC) and proteome quantitation of mouse embryonic stem cells to a depth of 5,111 proteins. Mol Cell Proteomics 7(4):672–683. https://doi.org/10.1074/mcp.M700460-MCP200

14. Williamson AJ, Smith DL, Blinco D, Unwin RD, Pearson S, Wilson C et al (2008) Quantitative proteomics analysis demonstrates post-transcriptional regulation of embryonic stem cell differentiation to hematopoiesis. J Mol Cell Proteomics 7(3):459–472. https://doi.org/10.1074/mcp.M700370-MCP200

15. Lin C-H, Yang C-H, Chen Y-R (2012) UTF1 deficiency promotes retinoic acid-induced neuronal differentiation in P19 embryonal carcinoma cells. Int J Biochem Cell Biol 44(2):350–357. https://doi.org/10.1016/j.biocel.2011.11.008

16. Wong JC, Jack MM, Li Y, O'Neill C (2014) The epigenetic bivalency of core pancreatic β-cell transcription factor genes within mouse pluripotent embryonic stem cells is not affected by knockdown of the polycomb repressive complex 2, SUZ12. PLoS ONE 9(5):e97820. https://doi.org/10.1371/journal.pone.0097820

17. Yang C-S, Chang K-Y, Rana TM (2014) Genome-wide functional analysis reveals factors needed at the transition steps of induced reprogramming. Cell Rep 8(2):327–337. https://doi.org/10.1016/j.celrep.2014.07.002

18. Mouallif M, Albert A, Zeddou M, Ennaji MM, Delvenne P, Guenin S (2014) Expression profile of undifferentiated cell transcription factor 1 in normal and cancerous human epithelia. Int J Exp Pathol 95(4):251–259. https://doi.org/10.1111/iep.12077

19. Raina K, Dey C, Thool M, Sudhagar S, Thummer RP (2021) An insight into the role of UTF1 in development, stem cells, and cancer. Stem Cell Rev Rep 17:1280–1293. https://doi.org/10.1007/s12015-021-10127-9

20. Specht E, Miyake-Stoner S, Mayfield S (2010) Micro-algae come of age as a platform for recombinant protein production. Biotechnol Lett 32:1373–1383. https://doi.org/10.1007/s10529-010-0326-5

21. Mattanovich D, Branduardi P, Dato L, Gasser B, Sauer M, Porro D (2012) Recombinant protein production in yeasts. Recomb Gene Expr 329–358. https://doi.org/10.1007/978-1-61779-433-9_17

22. Overton TW (2014) Recombinant protein production in bacterial hosts. Drug Discov Today 19(5):590–601. https://doi.org/10.1016/j.drudis.2013.11.008

23. Carter PJ (2011) Introduction to current and future protein therapeutics: a protein engineering perspective. Exp Cell Res 317(9):1261–1269. https://doi.org/10.1016/j.yexcr.2011.02.013

24. Dey C, Narayan G, Krishna Kumar H, Borgohain M, Lenka N, Thummer R (2017) Cell-penetrating peptides as a tool to deliver biologically active recombinant proteins to generate transgene-free induced pluripotent stem cells. Stud Stem Cells Res Ther 3(1):006–015. https://doi.org/10.17352/sscrt.000011

25. Borgohain MP, Haridhasapavalan KK, Dey C, Adhikari P, Thummer RP (2018) An insight into DNA-free reprogramming approaches to generate integration-free induced pluripotent stem cells for prospective biomedical applications. Stem Cell Rev Rep 15:286–313. https://doi.org/10.1007/s12015-018-9861-6

26. Dey C, Raina K, Haridhasapavalan KK, Thool M, Sundaravadivelu PK, Adhikari P et al (2021) An overview of reprogramming approaches to derive integration-free induced pluripotent stem cells for prospective biomedical applications. Recent Adv iPSC Technol 231–287. https://doi.org/10.1016/B978-0-12-822231-7.00011-4

27. O'Malley J, Woltjen K, Kaji K (2009) New strategies to generate induced pluripotent stem cells. Curr Opin Biotechnol 20(5):516–521. https://doi.org/10.1016/j.copbio.2009.09.005

28. Sommer CA, Mostoslavsky G (2013) The evolving field of induced pluripotency: recent progress and future challenges. J Cell Physiol 228(2):267–275. https://doi.org/10.1002/jcp.24155

29. Borgohain MP, Narayan G, Kumar HK, Dey C, Thummer RP (2018) Maximizing expression and yield of human recombinant proteins from bacterial cell factories for biomedical applications. Adv Microb Biotechnol 431–468

30. Huang C-J, Lin H, Yang X (2012) Industrial production of recombinant therapeutics in *Escherichia coli* and its recent advancements. J Ind Microbiol Biotechnol 39(3):383–399. https://doi.org/10.1007/s10295-011-1082-9

31. Baeshen MN, Al-Hejin AM, Bora RS, Ahmed MM, Ramadan HA, Saini KS et al (2015) Production of biopharmaceuticals in *E. coli*: current scenario and future perspectives. J Microbiol Biotechnol 25(7):953–962. https://doi.org/10.4014/jmb.1412.12079

32. Al-Hejin AM, Bora RS, Ahmed MMM (2019) Plasmids for optimizing expression of recombinant proteins in *E. coli*. Plasmid 13:40–60. https://doi.org/10.5772/intechopen.82205

33. Kaur J, Kumar A, Kaur J (2018) Strategies for optimization of heterologous protein expression in *E. coli*: Roadblocks and reinforcements. Int J Biol Macromol 106:803–822. https://doi.org/10.1016/j.ijbiomac.2017.08.080

34. Dey C, Thool M, Bhattacharyya S, Sudhagar S, Thummer RP (2021) Generation of biologically active recombinant human OCT4 protein from *E. coli*. 3 Biotech 11:1–16. https://doi.org/10.1007/s13205-021-02758-z

35. Haridhasapavalan KK, Sundaravadivelu PK, Bhattacharyya S, Ranjan SH, Raina K, Thummer RP (2021) Generation of cell-permeant recombinant human transcription factor GATA4 from *E. coli*. Bioprocess Biosyst Eng 44:1131–1146. https://doi.org/10.1007/s00449-021-02516-8

36. Thool M, Dey C, Bhattacharyya S, Sudhagar S, Thummer RP (2021) Generation of a recombinant stem cell-specific human SOX2 protein from *Escherichia coli* under native conditions. Mol Biotechnol 63:327–338. https://doi.org/10.1007/s12033-021-00305-y

37. Haridhasapavalan KK, Sundaravadivelu PK, Thummer RP (2020) Codon optimization, cloning, expression, purification, and secondary structure determination of human ETS2 transcription factor. Mol Biotechnol 62:485–494. https://doi.org/10.1007/s12033-020-00266-8

38. Narayan G, Sundaravadivelu PK, Agrawal A, Gogoi R, Nagotu S, Thummer RP (2021) Soluble expression, purification, and secondary structure determination of human PDX1 transcription factor. Protein Expr Purif 180:105807. https://doi.org/10.1016/j.pep.2020.105807

39. Micsonai A, Wien F, Bulyáki É, Kun J, Moussong É, Lee Y-H et al (2018) BeStSel: a web server for accurate protein secondary structure prediction and fold recognition from the circular dichroism spectra. NuclC Acids Res 46(W1):W315–W322. https://doi.org/10.1093/nar/gky497

40. Haridhasapavalan KK, Ranjan SH, Bhattacharyya S, Thummer RP (2021) Soluble expression, purification, and secondary structure determination of human MESP1 transcription factor. Appl Microbiol Biotechnol 105:2363–2376. https://doi.org/10.1007/s00253-021-11194-1

41. Haridhasapavalan KK, Das NJ, Thummer RP (2022) Generation of a transducible version of a bioactive recombinant human TBX5 transcription factor from *E. coli*. Curr Res Biotechnol 4:66–77. https://doi.org/10.1016/j.crbiot.2022.01.004

42. Haridhasapavalan KK, Sundaravadivelu PK, Joshi N, Das NJ, Mohapatra A, Voorkara U et al (2022) Generation of a recombinant version of a biologically active cell-permeant human

HAND2 transcription factor from *E. coli*. Sci Rep 12(1):16129. https://doi.org/10.1038/s41598-022-19745-w

43. Bosnali M, Edenhofer F (2008) Generation of transducible versions of transcription factors Oct4 and Sox2. Biol Chem. https://doi.org/10.1515/BC.2008.106

44. Narayan G, Agrawal A, Joshi N, Gogoi R, Nagotu S, Thummer RP (2021) Protein production and purification of a codon-optimized human NGN3 transcription factor from *E. coli*. Protein J 40:891–906. https://doi.org/10.1007/s10930-021-10020-x

45. Burgess-Brown NA, Sharma S, Sobott F, Loenarz C, Oppermann U, Gileadi O (2008) Codon optimization can improve expression of human genes in *Escherichia coli*: a multi-gene study. Protein Expr Purif 59(1):94–102. https://doi.org/10.1016/j.pep.2008.01.008

46. Remans K, Lebendiker M, Abreu C, Maffei M, Sellathurai S, May MM et al (2022) Protein purification strategies must consider downstream applications and individual biological characteristics. Microb Cell Fact 21(1):1–16. https://doi.org/10.1186/s12934-022-01778-5

47. Tsumoto K, Ejima D, Senczuk AM, Kita Y, Arakawa T (2007) Effects of salts on protein–surface interactions: applications for column chromatography. J Pharm Sci 96(7):1677–1690. https://doi.org/10.1002/jps.20821

48. Sun W, Jiao C, Xiao Y, Wang L, Yu C, Liu J et al (2016) Salt-dependent aggregation and assembly of *E. coli*-expressed ferritin. Dose-Response. 14(1):1559325816632102. https://doi.org/10.1177/1559325816632102

49. Kelly SM, Jess TJ, Price NC (2005) How to study proteins by circular dichroism. Biochimica et Biophysica Acta—Proteins Proteomics. 1751(2):119–139. https://doi.org/10.1016/j.bbapap.2005.06.005

50. Greenfield NJ (2006) Using circular dichroism spectra to estimate protein secondary structure. Nat Protoc 1(6):2876–2890. https://doi.org/10.1038/nprot.2006.202

51. Wu X-L, Zheng P-S (2013) Undifferentiated embryonic cell transcription factor-1 (UTF1) inhibits the growth of cervical cancer cells by transactivating p27 Kip1. Carcinogenesis 34(7):1660–1668. https://doi.org/10.1093/carcin/bgt102

52. Santos L, Ferraz MP, Shirosaki Y, Lopes MA, Fernandes MH, Osaka A, Santos JD (2011) Degradation studies and biological behavior on an artificial cornea material. Investig Ophthalmol Vis Sci 52(7):4274–4281. https://doi.org/10.1167/iovs.10-6861

53. De Donatis A, Ranaldi F, Cirri P (2010) Reciprocal control of cell proliferation and migration. Cell Commun Signal 8(1):1–4. https://doi.org/10.1186/1478-811X-8-20

54. Pfannkuche K, Fatima A, Gupta MK, Dieterich R, Hescheler J (2010) Initial colony morphology-based selection for iPS cells derived from adult fibroblasts is substantially improved by temporary UTF1-based selection. PLoS ONE 5(3):e9580. https://doi.org/10.1371/journal.pone.0009580

55. Kristensen DM, Nielsen JE, Skakkebaek NE, Graem N, Jacobsen GK, Meyts ER-D, Leffers H (2008) Presumed pluripotency markers UTF-1 and REX-1 are expressed in human adult testes and germ cell neoplasms. Hum Reprod 23(4):775–782. https://doi.org/10.1093/humrep/den010

56. Wang P, Li J, Allan RW, Guo CC, Peng Y, Cao D (2010) Expression of UTF1 in primary and metastatic testicular germ cell tumors. Am J Clin Pathol 134(4):604–612. https://doi.org/10.1309/AJCPB44HBKINJNYU

57. Xu C, Zhou Y, Chen W (2014) Expression of undifferentiated embryonic cell transcription factor-1 (UTF1) in breast cancers and their matched normal tissues. Cancer Cell Int 14:1–4. https://doi.org/10.1186/s12935-014-0116-6

58. Rosano GL, Ceccarelli EA (2014) Recombinant protein expression in *Escherichia coli*: advances and challenges. Front Microbiol 5:172. https://doi.org/10.3389/fmicb.2014.00172

59. Vasina JA, Baneyx F (1997) Expression of aggregation-prone recombinant proteins at low temperatures: a comparative study of the *Escherichia coli* cspa and tac promoter systems. Protein Expr Purif 9(2):211–218. https://doi.org/10.1006/prep.1996.0678

60. Galloway CA, Sowden MP, Smith HC (2003) Increasing the yield of soluble recombinant protein expressed in *E. coli* by induction during late log phase. Biotechniques 34(3):524–530. https://doi.org/10.2144/03343st04

61. Sørensen HP, Mortensen KK (2005) Soluble expression of recombinant proteins in the cytoplasm of *Escherichia coli*. Microb Cell Fact 4:1–8. https://doi.org/10.1186/1475-2859-4-1
62. Rabhi-Essafi I, Sadok A, Khalaf N, Fathallah DM (2007) A strategy for high-level expression of soluble and functional human interferon α as a GST-fusion protein in *E. coli*. Protein Eng, Des Sel 20(5):201–209. https://doi.org/10.1093/protein/gzm012
63. Azaman SNA, Ramanan RN, Tan JS, Rahim RA, Abdullah MP, Ariff AB (2010) Screening for the optimal induction parameters for periplasmic producing interferon-α 2b in *Escherichia coli*. Afr J Biotech 9(38):6345–6354. https://doi.org/10.5897/AJB10.556
64. Ryan BJ, Henehan GT (2013) Overview of approaches to preventing and avoiding proteolysis during expression and purification of proteins. Curr Protoc Protein Sci 71(1):5.25.1–5.25.7. https://doi.org/10.1002/0471140864.ps0525s71
65. San-Miguel T, Pérez-Bermúdez P, Gavidia I (2013) Production of soluble eukaryotic recombinant proteins in *E. coli* is favoured in early log-phase cultures induced at low temperature. Springerplus 2:1–4. https://doi.org/10.1186/2193-1801-2-89
66. Köppl C, Lingg N, Fischer A, Kröß C, Loibl J, Buchinger W et al (2022) Fusion tag design influences soluble recombinant protein production in *Escherichia coli*. Int J Mol Sci 23(14):7678. https://doi.org/10.3390/ijms23147678
67. Dey C, Venkatesan V, Thummer RP (2022) Identification of optimal expression parameters and purification of a codon-optimized human GLIS1 transcription factor from *Escherichia coli*. Mol Biotechnol 1–15. https://doi.org/10.1007/s12033-021-00390-z
68. Lowe S, Lin A (2000) Apoptosis in cancer. Carcinogenesis 21(3):485–495. https://doi.org/10.1093/carcin/21.3.485
69. Sherr CJ (2000) The Pezcoller lecture: cancer cell cycles revisited. Can Res 60(14):3689–3695
70. Spallek J, Arnold M, Razum O, Juel K, Rey G, Deboosere P et al (2012) Cancer mortality patterns among Turkish immigrants in four European countries and in Turkey. Eur J Epidemiol 27:915–921. https://doi.org/10.1007/s10654-012-9746-y
71. Lukas J, Drabek J, Lukas D, Dusek L, Gatek J (2013) The epidemiology of thyroid cancer in the Czech Republic in comparison with other countries. Biomed Papers 157(3):266–275. https://doi.org/10.5507/bp.2012.086

Immunohistochemical Profiling and Clinico-Pathological Correlation of Breast Cancer: A Study from Regional Cancer Center in Northeast India

Monalisa Hawaibam, Deepak Singh Lourembam, and Sushma Khuraijam

Keywords Breast cancer · Molecular subtype · Immunohistochemistry · Hormone receptor

1 Introduction

Breast carcinoma is the most frequently diagnosed cancer in Indian females with the highest ASR of 25.8 per 100,000 women [1]. As per GLOBOCAN 2020, it is the leading site of cancer in terms of both incidences as well as mortality in India [2]. Within India, the incidence rate of breast cancer shows a marked difference in rural and urban population [1]. According to the latest National Cancer Registry Program, breast cancer incidence has been maximally reported in the major metropolitan cities and north-eastern states of India. The highest age-adjusted incidence rate among the north-eastern states was observed in the Aizawl district of Mizoram [3].

Breast cancer is a complex heterogeneous disease with the tumor expressing varied diversity of histopathological characteristics, molecular subtypes, and clinical behavior. Tumors having similar clinical and histological features show differential behavior with regard to response and outcome to treatment. The classical well-established predictive and prognostic markers of breast carcinoma include histological subtype, tumor grade, tumor size, nodal involvement, and stage of the tumor. However, the morphological and clinicopathological classification alone does not reveal the diverse nature of this cancer and hence becomes inadequate to predict tumor behavior as well as therapeutic outcome [4]. Therefore, a further need to classify these tumors into subtypes led to the innovative work done by Perou, Sorlie, and

M. Hawaibam (✉) · D. S. Lourembam · S. Khuraijam
Department of Pathology, Regional Institute of Medical Sciences, Imphal, India
e-mail: monalisahawaibam@yahoo.in

colleagues, which categorized breast cancer on the similarity basis of the gene expression patterns using cDNA microarray [5, 6]. The intrinsic molecular subtypes were Luminal A, Luminal B, Her2-enriched, and Triple-negative breast cancer. Identification of these respective subtypes has led to a fundamental change in breast cancer treatment modalities. Each molecular subtype is associated with varying degrees of prevalence, clinical prognosis, therapeutic response, recurrence, and disease-free survival outcomes and requires specific treatment as well as different monitoring strategies [4, 6]. Unfortunately, molecular and genetic analyses are high-end techniques and are not readily accessible to everyone in a middle-income country like India. Therefore, clinicians generally recommend immunohistochemical tests, which are cost-effective and more widely available.

Immunohistochemistry contributes a major part in the precise identification of breast cancer subtype by providing a surrogate for gene analysis [7]. Identification of hormone receptors Estrogen receptor (ER), progesterone receptor (PR), and human epidermal growth factor receptor 2 (Her2) in the tumor section is a well-established methodology used in immunohistochemistry. ER and PR belong to the nuclear steroid receptor superfamily present in the mammary epithelium. ER exhibits a critical function during proliferation and differentiation of normal breast epithelial cells as well as in mammary gland tumorigenesis. PR also plays a crucial role in progression of breast cancer by modulating the transcription of key target genes. The expression of these two receptors serves as a driving force behind cancer cell progression and proliferation [8–10]. Hormonal receptor positivity helps dictate the response and outcome to endocrine therapy such as anti-estrogen (tamoxifen) [11]. Her2 is a transmembrane glycoprotein that acts as an oncogene when overexpressed and promotes the uncontrolled growth of cancer cells [8]. Her2 status serves as a critical marker for the evaluation of the heterogeneous behavior of the tumor and the benefit of targeted therapy [11]. Tumors overexpressing the Her2 gene act as a potential target for anti-Her2 monoclonal antibodies such as Trastuzumab therapy (Herceptin) [12]. Triple Negative Breast Cancer (TNBC) represents a different molecular subtype characterized by the lack of expression of hormonal receptors (ER, PR), as well as Her2 receptors. TNBC is generally presented as a highly aggressive form of tumor and is more prevalent in younger patients. TNBC subtypes are unresponsive to hormonal therapies and hence combined chemotherapy remains the standard treatment regimen for this subtype [4, 13]. With regard to the molecular subtype, Luminal A comparatively has a favorable prognosis than the TNBC subtype as it lacks any specific targeted therapy [4].

Similar studies regarding molecular subtyping of breast cancer patients have been reported from different regions of India [6, 14–16]. However, there are very limited studies on breast cancer molecular subtyping in the north-eastern region of India except for studies with special reference to triple-negative subtype [17, 18]. Therefore, our present study aimed to gain a better understanding between the association of hormonal receptors and distinct molecular subtypes with sociodemographic and clinical parameters of breast cancer patients in the north-eastern region of India.

2 Materials and Methods

This study was conducted in the Department of Pathology, RIMS, Manipur between November 2019 and November 2021. This study was approved by the Institutional Research Ethics Board, Regional Institute of Medical Sciences. A total of 115 biopsy-proven invasive breast cancer patients were analyzed for our study. All the relevant patient's clinical data, demographic and clinicopathological information were retrieved from the hospital's medical history and recorded for this study. The surgical samples were also received from the Department of Surgery. For this study, the samples diagnosed using fine-needle aspiration cytology and recurrent cases were excluded. Core biopsy samples and patients undergoing surgical procedures such as breast conservation surgery (lumpectomy) and mastectomy were considered in this study. Cases already having complete immunohistochemistry data on ER, PR, and Her2 expression were also included in our analysis.

All the sections were processed and stained using routine hematoxylin and eosin (H&E) stain and examined for the presence of invasive cancer. Histopathological features were determined and graded according to Elston and Ellis modified Bloom Richardson system [19]. Further, the sections containing tumor cells and adjoining normal breast tissue (internal control) were subjected to immunohistochemical staining using an automated IHC platform (Ventana GX). The histopathological classification and IHC results were interpreted following the guidelines of the American Society of Clinical Oncology/College of American Pathologists (ASCO/CAP) guidelines. All cases of ER/PR positive cells showing distinct nuclear staining in at least 1% of positive cells were considered and scored accordingly by the Allred scoring system [20, 21]. For Her2 overexpression, interpretation was done based on the membrane staining intensity and scored from 0 to 3+ [22].

3 Statistical Analysis

All the statistical analysis was carried out using GraphPad Prism 9 and Microsoft Excel package. Association of socio-demographic and clinical parameters with hormonal receptors and molecular subtypes were analyzed.

Comparisons between different groups were calculated using the Chi-square test or Fisher's exact test as appropriate. A probability value of less than 0.05 was considered significant for all analyses.

4 Results

4.1 General Characteristics

A total number of 115 breast cancer patients were enrolled in our study. Table 1 displays the baseline characteristics of the patients. According to our study, breast cancer incidence was higher in the rural population when compared with urban population (72% vs. 28%). Patient characteristics showed Invasive Ductal Carcinoma Not Otherwise Specified (IDC, NOS) (83.4%) as the most frequently diagnosed histological type. According to the Tumor, Lymph Node, Metastasis (TNM) staging system, 58 (50.44%) patients were diagnosed in stage II, 36 (31.30%) in stage III, 13 (11.30%) in stage I, 6 (5.22%) in stage IV and only 2 (1.74%) in stage 0. According to Modified Bloom Richardson histological grading, poorly (Grade III) and moderately differentiated (Grade II) tumors have a higher proportion when compared to well-differentiated (Grade I) tumors (86.95% vs. 13.04%).

To evaluate the correlation of hormonal receptors and molecular subtypes with age at presentation, histological type, grade, and stage in patients, the studied parameters were stratified according to age groups (<48 and ≥48 years). Subsequently, an IHC study (ER, PR, and Her2) was done in all the cases as mentioned [21].

Invasive Ductal Carcinoma, Not Otherwise Specified (IDC, NOS); Invasive Lobular Carcinoma (ILC); Others include Invasive Papillary Carcinoma, Metaplastic Carcinoma.

4.2 Overall Expression of ER, PR, and Her2

Table 2 presents the proportion of ER, PR, and Her2 receptor expression in our study. Figure 1 shows the representative images of positive immunohistochemical staining of ER, PR, and Her2. The IHC evaluation showed an overall incidence of hormonal receptor-positive cases to be 63 (54.78%). The number of patients with ER-positive was 61 (53.04%), PR positive was 53 (46.09%) and Her2 positive was 35 (30.43%). Her2 was negative in 71 (61.74%) and equivocal in 9 (7.83%) patients. The most frequently expressed hormone receptor pattern was ER^+/PR^+, which was observed in 63 (54.78%) patients and the least observed hormone receptor pattern was ER^-/PR^+ observed in 2 (1.74%) patients.

Estrogen receptor (ER); progesterone receptor (PR); human epidermal growth factor receptor 2 (Her2).

Table 1 Socio-demographic and clinical characteristics of patients (n = 115)

Variables	N (%)
Age group (years)	
<48	54 (46.95)
≥48	61 (53.04)
Marital status	
Married	110 (95.65)
Single	4 (3.48)
Divorce	1 (0.87)
Level of education	
Illiterate	38 (33.04)
Primary	13 (11.30)
Secondary	44 (38.26)
Higher	20 (17.39)
Place of residence	
Urban	33 (28.7)
Rural	82 (71.3)
Tumor subtype	
IDC, NOS	96 (83.47)
ILC	14 (12.17)
Others	5 (4.34)
Stage	
0	2 (1.74)
I	13 (11.30)
II	58 (50.44)
III	36 (31.30)
IV	6 (5.22)
Histological grade	
I	15 (13.4)
II	46 (40.00)
III	54 (46.96)

4.3 Age-Wise Receptor Expression Pattern

In our study, we found an increasing trend of ER and PR expression with age but this was not statistically significant. Further, a higher PR positivity was observed in older patients (≥48 years) compared to younger ones (<48 years) (47.5% vs. 12.42% respectively). However, we observed a higher proportion of HER2 receptor positivity in the lower age group (<48 years) when compared with the older age

Table 2 ER, PR, and Her2 receptor status (n = 115)

Hormonal receptor	Status	N (%)
ER	Positive	61 (53.04)
	Negative	54 (46.96)
PR	Positive	53 (46.09)
	Negative	62 (53.91)
Her2	Positive (3+)	35 (30.43)
	Negative (0, 1+)	71 (61.74)
	Equivocal (2+)	9 (7.83)
Hormonal (+) tumors	ER^+/PR^+	63 (54.78)
Hormonal (−) tumors	ER^-/PR^-	52 (45.22)
	ER^+/PR^-	10 (8.70)
	ER^-/PR^+	2 (1.74)
Molecular subtype	Luminal A	35 (30.43)
	Luminal B	12 (10.43)
	Her 2-enriched	19 (16.52)
	Triple-negative	30 (26.09)
	Others	19 (16.52)
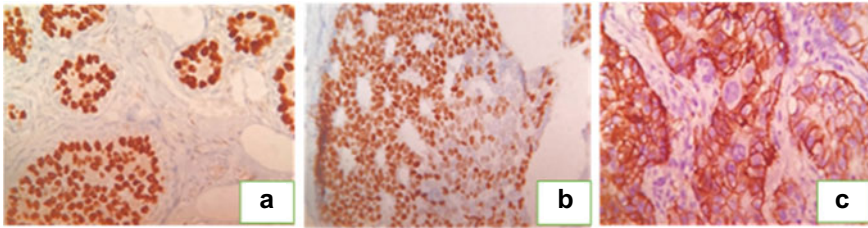
Fig. 1 **a** Strong positive nuclear staining for ER, 40X, **b** Strong to moderate positive staining for PR, 40X, **c** Complete and continuous membrane staining for Her2, 40X

group (≥48 years) (35.1% vs. 26.2%, respectively). Similarly, the incidence of triple-negative cancer was slightly higher in younger patients (Table 3).

Table 3 Receptor expression patterns in different age groups of the study population

Age	<48 (n = %)	≥48 (n = %)	p-value
Her2+	35.19	26.23	
Triple-Negative	29.63	22.95	
Hormone receptor			0.6755
ER+	50	55.74	
PR+	12.42	47.54	

**Table 4** Combined ER/PR status with relation to age, grade, and stage of the disease (n = 115)

|		ER⁺/PR⁺	ER⁺/PR⁻	ER⁻/PR⁺	ER⁻/PR⁻	*p*-value
Age	<48	22 (40.74)	5 (9.26)	1 (1.85)	26 (48.15)	
	≥48	29 (47.54)	5 (8.20)	1 (1.64)	26 (42.62)	0.91
Grade	I	8 (57.14)	3 (21.4)	0	3 (21.43)	
	II	24 (51.06)	5 (10.6)	0	18 (38.30)	0.04
	III	19 (35.19)	2 (3.7)	2 (3.7)	31 (57.41)	
Stage	0	1 (50)	1 (50)	0	0	
	I	5 (38.46)	0	0	8 (61.54)	
	II	28 (48.28)	5 (8.62)	2(3.45)	23 (39.66)	0.59
	III	15 (41.67)	3 (8.33)	0	23 (39.66)	
	IV	2 (33)	1 (16.67)	0	3 (50)	

4.4　Combined Hormonal Receptor Status

On comparing the overall ER/PR status with regard to age, grade, and staging, statistical significance was found only in histological grade ($p = 0.04$) (Table 4). Both ER⁺/PR⁺ tumors were 29 (47.54%) in ≥48 years age group whereas both ER⁻/PR⁻ tumors were more in <48 years age group 26 (48.15%). The majority of Grade II (51.06%) and stage II (48.28%) tumors were both ER⁺/PR⁺, on the other hand, grade III (57.41%) and stage III (50%) tumors were more ER⁻/PR⁻ (Table 4).

4.5　Correlation of Molecular Subtype with Age, Grade, and Stage

In the present study, Luminal A (30.43%) and TNBC subtype (26.09%) were the two common molecular subtypes found followed by Her2 overexpressed and Luminal B types with 16.52% and 10.43%, respectively. We also had patients with unclassified subtypes categorized as others (16.52%) (Fig. 2). TNBC molecular subtype was diagnosed in the majority of the patients of age below 48 years (n = 16; 29.62%), while Luminal A was largely predominant in older patients (n = 23; 37.7%). In our study, Her2 enriched subtype was the least common subtype observed in younger age groups (<48 years) (n = 8; 14.8%) while older age groups (≥48 years) showed Luminal B tumors to be the least diagnosed subtype (n = 3; 4.91%) (Fig. 3). Among grade I and II tumors, the maximum numbers were found in the Luminal A subtype (46.67 and 36.96%), respectively. However, the TNBC subtype (31.48%) was found more associated with grade III tumors. Most of the stage II tumors were Luminal A (37.29%). In stage III, the Her2-enriched (27.78%) type was of higher incidence when
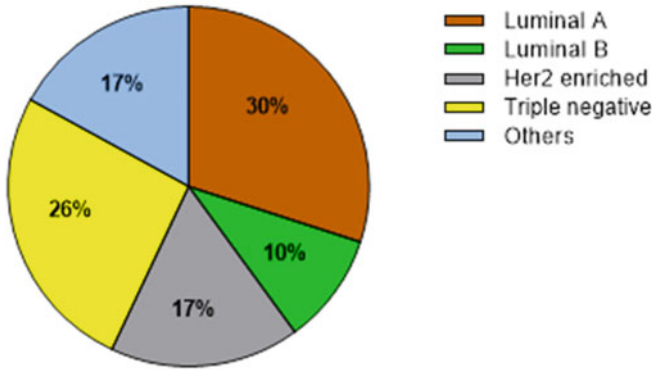
Fig. 2 Percentage distribution of various molecular subtypes classified based on the immunohistochemical expression pattern of tumor; others (N = 115)
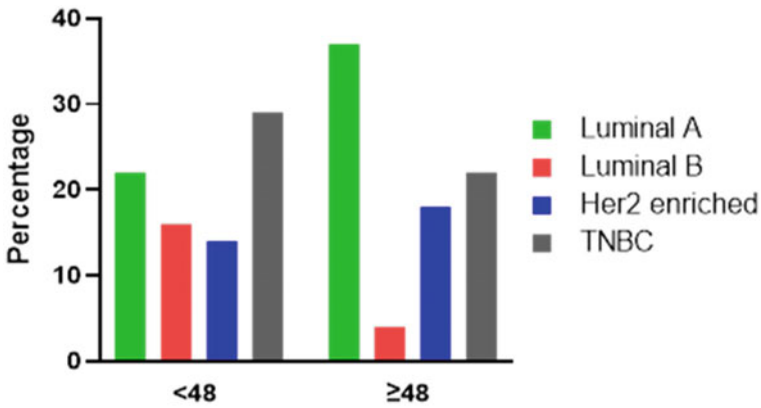
Fig. 3 Age-wise percentage incidence of molecular subtypes (<48 and ≥48). Luminal A type is common in ≥48 years age group while TNBC predominates in <48 years group (N = 115)

compared to other subtypes. However, there was no statistical significance found in the combined molecular subtype analysis concerning age, grade, and staging (Table 5).

5 Discussion

Breast cancer constitutes the maximum number of cancer cases in women globally with an increasing trend of incidence in Asian countries, specifically among perimenopausal women. Despite being the most commonly diagnosed disease in women, breast cancer is characterized by its biological and phenotypic heterogeneity

Table 5 Combined Molecular Subtype analysis with Age, Grade, and Stage (n = 115)

		Luminal A n (%)	Luminal B n (%)	Her2 enriched n (%)	TNBC n (%)	Others n (%)	p-value
Age	<48	12 (22.22)	9 (16.66)	8 (14.81)	16 (29.62)	9 (16.66)	0.15
	≥48	23 (37.70)	3 (4.91)	11 (18.03)	14 (22.95)	10 (16.39)	
Grade	I	7 (46.67)	1 (6.67)	2 (13.33)	2 (13.33)	3 (20.00)	
	II	17 (36.96)	4 (8.70)	6 (13.04)	11 (23.91)	8 (17.39)	0.51
	III	11 (20.37)	7 (12.96)	11 (20.37)	17 (31.48)	8 (14.81)	
Staging	0	0.00	1 (50.00)	0.00	0.00	1 (50.00)	
	I	3 (23.08)	2 (15.38)	2 (15.38)	6 (46.15)	0.00	
	II	22 (37.29)	5 (8.62)	6 (10.34)	16 (27.59)	9 (15.52)	0.26
	III	9 (25.00)	3 (8.33)	10 (27.78)	6 (16.67)	8 (22.22)	
	IV	1 (16.66)	1 (16.66)	1 (16.66)	2 (33.33)	1 (16.67)	

with the tumor manifesting clinically diverse behavior and treatment responses [23]. Hence, the identification of vital prognostic markers is of utmost importance in successfully managing breast cancer patients. The immunohistochemical staining is a well-established technique for identifying different gene products in the tumor cell providing a surrogate tool for gene analysis. ER, PR, and Her2 expressions are considered prognostic markers associated with breast cancer [24]. Our study aimed at classifying breast cancer into molecular subtypes on the basis of the IHC expression pattern of the respective markers as mentioned earlier, and further analyzed the correlation of different subtypes with various clinicopathological parameters.

Our study reported a median age of 48 years (29–74), which is consistent with previous Indian studies where the median age ranged from 48 to 53 years [6, 15]. This reinforces the fact that in Indian women, the median age of diagnosis occurs at a comparatively younger age when compared with Western countries [25].

In our study, among 115 patients ER$^+$ cases accounted for 53.04% and PR$^+$ cases were 46.08%. However, a lower positivity rate for both receptors has been documented by other Indian studies. Contrary to our results, Desai et al. have reported 32.6% ER$^+$ cases and 46.1% PR$^+$ cases of breast cancers [26]. Furthermore, the study by Shet, T. et al. also indicated that the percentage expression of hormone receptor among Indian patient is lower in comparison to Western countries [27]. Similarly, Rashmi Patnayak, et al. have reported 47.6% ER$^+$ and 48.8% PR$^+$ cases [28].

Combined analysis of hormonal receptor study by Fatma Senel reported 62.3% ER$^+$/PR$^+$ cases, 15.3% ER$^-$/PR$^-$, 21.2% ER$^+$/PR$^-$, and 1.2% ER$^-$/PR$^+$ [29]. However, our study reported higher percentage of ER$^-$/PR$^-$ cases (45.22%), which is in contrast to the above study. ER$^+$/PR$^-$ (8.7%) cases were also much lesser in our analysis whereas ER$^-$/PR$^+$ cases were almost equally distributed between the two studies. According to a study reported by Yunhai Li et al., double hormonal receptor-positive tumors were most common in patients aged ≥60 years, however, among patients aged 30 to 49 years, ER$^-$/ PR$^+$ tumors were most prevalent [30].

In our study, the majority of double hormone receptor-positive tumors (56.86%) were in the advanced age (≥48) group whereas ER$^-$/PR$^-$ tumor (50%) was more common in the younger age group (<48). ER and PR expression correlates with the tumor grade ($p = 0.04$). Our findings are similar to earlier studies reported elsewhere [29–32] while other studies have reported no correlation [33]. However, our results showed no statistical correlation between ER/PR status with respect to age and disease staging.

On the basis of cDNA microarray profiling, breast cancer is categorized into the following intrinsic molecular subtypes: Luminal A, Luminal B, Her2 enriched, and TNBC [34]. The hormone receptor positivity rate determines the suitability of patients for endocrine therapy which can be safely administered orally [35]. Our findings on the distribution of molecular subtypes are consistent with previous findings [6, 27, 36, 37] as shown in Table 6. A similar pattern of results was obtained by Pandit et al., in which the distribution of subtypes was as follows Luminal A subtype (37%), TNBC (26%), Her2 enriched (11.1%), and Luminal B (7.6%) [6]. Further, a large number of TNBC subtypes in our analysis were observed in younger women (>48), which were consistent with findings reported in other studies [38]. Some studies with special reference to TNBC have also reported that the triple-negative phenotype is prevalent in a large population of the north-eastern region of India [17, 39]. Another study also reported 31.9% TNBC cases in the north-eastern India with a median age of 40 years indicating the association of this particular subtype with younger age [39]. Previous studies have reported that the occurrence of TNBC shows significant variation with ethnicity. A higher rate of TNBC has been observed in African and African-American women [13]. We speculate that the higher proportion of TNBC subtypes observed in the northeast region could be multifactorial. Unlike the rest of India, the north-eastern region represents a different spectrum of ethnicity having typical food habits and lifestyles. Furthermore, genetic susceptibility and biological and non-biological factors could be the underlying determinants for such racial disparities exhibited by this subtype [17, 18, 39, 40].

Table 6 Molecular subtypes distribution with reference to other studies

Study	Luminal A (%)	Luminal B (%)	Her2 enriched (%)	TNBC (%)	Others
Pandit et al. [6]	37	7.6	11.1	26	18.3%
Gogoi et al. [17]	19.51	21.13	17.88	38.21	3.27%
Nikhilesh Kumar et al. [31]	34	18	18	25	5%
Soni et al. [36]	38.20	11.80	14.80	17	18.20%
Ansari M et al. [37]	41.7	15	12.5	30.8	NA
Shanmugam et al. [41]	26.7	18.3	35	20	NA
Our study	30.43	10.43	16.52	26.09	16.52%

6 Conclusion

In summary, our results found a higher breast cancer incidence in rural population. Luminal A (n = 35; 30.4%) and IDC NOS (n = 96; 83.4%) represent the most common molecular and histopathological subtype in this study. Our findings showed 47% poorly differentiated tumors and 31% at clinical stage III disease representing the maximum proportion of cases. Tumors with negative hormonal receptors (ER$^-$/PR$^-$) were associated with poorly differentiated tumor and IDC-NOS. Moreover, we did not find any significant difference in the correlation of molecular subtypes with age, histological grades, and staging details. PR expression was higher in elderly females (47.54%) as compared to younger females (12.42%) while ER and HER2 neu expression showed no significant differences. A higher percentage of patients (29.63%) expressing triple-negative profiles in the younger age group denotes the aggressive behavior and dismal prognosis of IDC-NOS. The results of our study mandate the need for increased screening and sensitization programs especially in rural areas to encourage people to seek health care facilities at the earliest to avoid any late-stage presentation of the disease.

Conflict of Interest　All the authors declare that they have no conflict of interest.

References

1. Malvia S, Bagadi SA, Dubey US, Saxena S (2017) Epidemiology of breast cancer in Indian women. Asia Pac J Clin Oncol 13(4):289–295. https://doi.org/10.1111/ajco.12661
2. Sung H, Ferlay J, Siegel RL, Laversanne M, Soerjomataram I, Jemal A et al (2021) Global cancer statistics 2020: GLOBOCAN estimates of incidence and mortality worldwide for 36 cancers in 185 countries. CA Cancer J Clin 71(3):209–249. https://doi.org/10.3322/caac.21660
3. Research ICoM (2020) National Centre for Disease Informatics and Research. Report of National Cancer Registry Programme (2012–2016)
4. do Nascimento RG, Otoni KM (2020) Histological and molecular classification of breast cancer: what do we know. Mastology 30:e20200024
5. Sørlie T, Perou CM, Tibshirani R, Aas T, Geisler S, Johnsen H et al (2001) Gene expression patterns of breast carcinomas distinguish tumor subclasses with clinical implications. Proc Natl Acad Sci 98(19):10869–10874
6. Pandit P, Patil R, Palwe V, Gandhe S, Patil R, Nagarkar R (2020) Prevalence of molecular subtypes of breast cancer: a single institutional experience of 2062 patients. Eur J Breast Health 16(1):39
7. Schlatter RP, Matte U, Polanczyk CA, Koehler-Santos P, Ashton-Prolla P (2015) Costs of genetic testing: Supporting Brazilian public policies for the incorporating of molecular diagnostic technologies. Genet Mol Biol 38:332–337
8. Mohanty SS, Sahoo CR, Padhy RN (2020) Role of hormone receptors and HER2 as prospective molecular markers for breast cancer: an update. Genes Dis

9. Althuis MD, Fergenbaum JH, Garcia-Closas M, Brinton LA, Madigan MP, Sherman ME (2004) Etiology of hormone receptor–defined breast cancer: a systematic review of the literature. Cancer Epidemiol Biomark Prev 13(10):1558–1568

10. Folkerd EJ, Dowsett M (2010) Influence of sex hormones on cancer progression. J Clin Oncol 28(26):4038–4044

11. Chen Z, Yang J, Li S, Lv M, Shen Y, Wang B et al (2017) Invasive lobular carcinoma of the breast: a special histological type compared with invasive ductal carcinoma. PLoS ONE 12(9):e0182397. https://doi.org/10.1371/journal.pone.0182397

12. Huang HJ, Neven P, Drijkoningen M, Paridaens R, Wildiers H, Van Limbergen E et al (2005) Association between tumour characteristics and HER-2/neu by immunohistochemistry in 1362 women with primary operable breast cancer. J Clin Pathol 58(6):611–616

13. Jha PK, Ansari MA, Srivastava V, Verma AK, Mangla M (2020) Triple negative breast cancer: alarming burden and future challenges in Indian perspective. J Sci Res 64(2)

14. Doval DC, Sharma A, Sinha R, Kumar K, Dewan AK, Chaturvedi H et al (2015) Immuno-histochemical profile of breast cancer patients at a tertiary care hospital in New Delhi, India. Asian Pac J Cancer Prev 16(12):4959–4964

15. Kumar RV, Panwar D, Amirtham U, Premalata CS, Gopal C, Narayana SM et al (2018) Estrogen receptor, progesterone receptor, and human epidermal growth factor receptor-2 status in breast cancer: a retrospective study of 5436 women from a regional cancer center in South India. South Asian J Cancer 7(01):07–10

16. Tiwari S, Malik R, Trichal VK, Nigam RK, Rai A, Balani S et al (2015) Breast cancer: correlation of molecular classification with clinicohistopathology. Sch J App Med Sci. 3(2G):1018–1026

17. Gogoi G, Borgohain M, Saikia P, Fazal SA (2016) Profile of molecular subtypes of breast cancer with special reference to triple negative: a study from Northeast India. Clin Cancer Investig J. 5(5):374–383

18. Sharma JD, Khanna S, Ramchandani S, Kakoti LM, Baruah A, Mamidala V (2021) Prevalence of molecular subtypes of breast carcinoma and its comparison between two different age groups: a retrospective study from a tertiary care center of Northeast India. South Asian J Cancer 10(04):220–224

19. Bloom HJG, Richardson WW (1957) Histological grading and prognosis in breast cancer: a study of 1409 cases of which 359 have been followed for 15 years. Br J Cancer 11(3):359

20. Hammond MEH, Hayes DF, Dowsett M, Allred DC, Hagerty KL, Badve S et al (2010) American society of clinical oncology/college of american pathologists guideline recommendations for immunohistochemical testing of estrogen and progesterone receptors in breast cancer (unabridged version). Arch Pathol Lab Med 134(7):e48–e72

21. Allred DC, Bustamante MA, Daniel CO, Gaskill HV, Cruz AB (1990) Immunocytochemical analysis of estrogen receptors in human breast carcinomas: evaluation of 130 cases and review of the literature regarding concordance with biochemical assay and clinical relevance. Arch Surg 125(1):107–113

22. Wolff AC, Hammond MEH, Allison KH, Harvey BE, Mangu PB, Bartlett JMS et al (2018) Human epidermal growth factor receptor 2 testing in breast cancer: American society of clinical oncology/college of American pathologists clinical practice guideline focused update. Arch Pathol Lab Med 142(11):1364–1382

23. Feng Y, Spezia M, Huang S, Yuan C, Zeng Z, Zhang L et al (2018) Breast cancer development and progression: risk factors, cancer stem cells, signaling pathways, genomics, and molecular pathogenesis. Genes Dis 5(2):77–106

24. Donegan WL (1997) Tumor-related prognostic factors for breast cancer. CA: Cancer J Clin 47(1):28–51

25. Bustreo S, Osella-Abate S, Cassoni P, Donadio M, Airoldi M, Pedani F et al (2016) Optimal Ki67 cut-off for luminal breast cancer prognostic evaluation: a large case series study with a long-term follow-up. Breast Cancer Res Treat 157(2):363–371

26. Desai SB, Moonim MT, Gill AK, Punia RS, Naresh KN, Chinoy RF (2000) Hormone receptor status of breast cancer in India: a study of 798 tumours. Breast 9(5):267–270

27. Shet T, Agrawal A, Nadkarni M, Palkar M, Havaldar R, Parmar V et al (2009) Hormone receptors over the last 8 years in a cancer referral center in India: what was and what is? Indian J Pathol Microbiol 52(2):171
28. Patnayak R, Jena A, Rukmangadha N, Chowhan AK, Sambasivaiah K, Phaneendra BV et al (2015) Hormone receptor status (estrogen receptor, progesterone receptor), human epidermal growth factor-2 and p53 in South Indian breast cancer patients: a tertiary care center experience. Indian J Med Paediatr Oncol 36(02):117–122
29. Senel F (2021) The hormone receptor status in breast cancer and the relationship of subtypes with clinicopathological features. Indian J Pathol Microbiol 64(4):671
30. Li Y, Yang D, Yin X, Zhang X, Huang J, Wu Y et al (2020) Clinicopathological characteristics and breast cancer–specific survival of patients with single hormone receptor–positive breast cancer. JAMA Netw Open 3(1):e1918160-e
31. Kumar N, Patni P, Agarwal A, Khan MA, Parashar N (2015) Prevalence of molecular subtypes of invasive breast cancer: a retrospective study. Med J Armed Forces India 71(3):254–258
32. Ghosh S, Sarkar S, Simhareddy S, Kotne S, Rao PBA, Turlapati SPV (2014) Clinico-morphological profile and receptor status in breast cancer patients in a South Indian institution. Asian Pac J Cancer Prev 15(18):7839–7842
33. Gnanamuttupulle M, Henke O, Ntundu SH, Serventi F, Mwakipunda LE, Amsi P et al (2021) Clinicopathological characteristics of breast cancer patients from Northern Tanzania: common aspects of late stage presentation and triple negative breast cancer. Ecancermedicalscience 15
34. Goldhirsch A, Winer EP, Coates AS, Gelber RD, Piccart-Gebhart M, Thürlimann B et al (2013) Personalizing the treatment of women with early breast cancer: highlights of the St Gallen international expert consensus on the primary therapy of early breast cancer. Ann Oncol 24(9):2206–2223
35. Perou CM, Sørlie T, Eisen MB, Van De Rijn M, Jeffrey SS, Rees CA et al (2000) Molecular portraits of human breast tumours. Nature 406(6797):747–752
36. Savita Soni NS, Gupta A, Srivastava AS (2020) Breast carcinoma histopathological correlation with molecular classification: a comparative study. Indian J Pathol Oncol 7(4):613–9. https://doi.org/10.18231/j.ijpo.2020.121
37. Ansari M, Mittal A, Mehta J, Jain N (2019) Molecular Subtypes of breast cancer according to immunohistochemical expression of hormone receptors in a region of North West India: a comparative study with other regions in India and Around the Globe
38. Al-Nuaimy WMT, Ahmed AH, Al-Nuaimy HAA (2015) Immunohistochemical evaluation of triple markers (ER, PR and HER-2/neu) in carcinoma of the breast in the North of Iraq. Donnish J Med Lab Diagn 1(1):001–009
39. Sharma M, Sharma JD, Sarma A, Ahmed S, Kataki AC, Saxena R et al (2014) Triple negative breast cancer in people of North East India: Critical insights gained at a regional cancer centre. Asian Pac J Cancer Prev 15(11):4507–4511
40. Sultana R, Chisty SJS (2021) Elevated mRNA expression levels of inflammation-related genes in triple-negative breast cancer: a pilot study from North East India. Ann Oncol Res Ther 1(2):105
41. Subbiah S, Gopu G, Senthilkumar P, Muniasamy P (2017) Molecular subtypes as a predictor of response to neoadjuvant chemotherapy in breast cancer patients. Indian J Cancer 54(4):652

Soluble Expression and Purification of Biologically Active Human NANOG from *Escherichia coli*

Madhuri Thool, S. Sudhagar, and Rajkumar P. Thummer

1 Introduction

Homeobox (homeodomain) protein NANOG is a transcription factor of the ANTP (Antennapedia) class and is conserved in vertebrates [1, 2]. NANOG expression is observed during the initial stages of mouse embryonic development and in primordial germ cells [3–8]. During mouse embryonic development, lack of NANOG expression in the inner cell mass failed to produce epiblast, and instead, formed parietal endoderm-like cells [4]. Thus, the expression of NANOG is crucial for the epiblast formation [4, 9, 10]. Furthermore, the mRNA level of NANOG is downregulated after implantation [3]. High expression of NANOG holds epiblast essence, whereas low expression promotes differentiation into primitive endoderm. In embryonic stem cells (ESCs), NANOG is a vital player in the transcriptional pluripotency regulatory network along with OCT4 and SOX2 [11–13]. Moreover, the role of NANOG in ESCs is to maintain self-renewal and pluripotency in a cytokine-independent fashion [3, 4]. Intriguingly, the deletion of NANOG did not disrupt the chimera formation potential of ESCs [3].

M. Thool · R. P. Thummer (✉)
Laboratory for Stem Cell Engineering and Regenerative Medicine, Department of Biosciences and Bioengineering, Indian Institute of Technology Guwahati, Guwahati 781039, Assam, India
e-mail: rthu@iitg.ac.in

M. Thool · S. Sudhagar
Department of Biotechnology, National Institute of Pharmaceutical Education and Research Guwahati, Changsari, Guwahati 781101, Assam, India
e-mail: sudhagar.s@niperguwahati.ac.in

Furthermore, ESCs are identical to induced pluripotent stem cells (iPSCs), and NANOG holds the potential for reprogramming due to the presence of the homeodomain, which is functionally preserved among all vertebrates [2]. The dose of NANOG is critical in cell-fusion-mediated reprogramming, and its overexpression improved the efficiency of reprogramming by 200-fold [14]. Several studies have reported that NANOG overexpression can enhance and hasten iPSC generation [9, 15]. Additionally, the role of NANOG in reprogramming is critical for reaching the pluripotent ground state by enabling the conversion of pre-induced pluripotent stem cells to bonafide iPSCs [9, 16]. Moreover, NANOG not only induces pluripotency but can also overcome reprogramming obstacles [17]. Inconsistent with these studies, a few studies have reported that including NANOG in the reprogramming cocktail does not improve reprogramming efficiency and is thus not critical for iPSC generation [18, 19]. Despite the deletion of the NANOG gene from somatic cells, these cells can be reprogrammed to form iPSCs and form teratomas and chimeras [19], indicating their dispensability in the reprogramming process. Another study reported that, although the elimination of NANOG decreased reprogramming efficiency, it was not required for iPSC generation [20]. Thus, these studies indicate that other members of the transcriptional network of pluripotency can substitute for NANOG loss. However, the same studies have suggested that NANOG is essential during the final stage of the reprogramming process and that its depletion affects reprogramming efficiency [19, 20]. Numerous reports have demonstrated the generation of human iPSCs using NANOG via lentiviral transduction [21–24]. In addition, the derivation of mouse and human iPSCs has also been reported using retroviral vectors, which include NANOG in the reprogramming cocktail [25, 26]. It is noteworthy that the use of viral-based approaches showed high reprogramming efficiency but induces genomic alteration. To circumvent these limitations of including viral components, several other approaches, such as recombinant proteins, mRNA, Sendai virus and miRNAs, are favored [27, 28]. Among all the approaches for iPSC generation, the recombinant protein-based method is the safest [29].

Recombinant proteins are of great importance for industrial applications and clinical research. The benefits of using bacterial systems, such as *Escherichia coli* (*E. coli*), for the production of recombinant proteins are easy genetic manipulation and low production costs. However, this system also has several unavoidable blockages, such as codon usage bias, weak expression, insoluble expression, complicated purification protocols, protein misfolding and so forth. Thus, the expression of recombinant proteins opens an avenue for the generation of iPSCs. These cells can serve as patient-specific cells for cell therapies. Herein, the generation of a recombinant human NANOG fusion protein along with its secondary structure determination is reported, which possesses cytoplasmic and nuclear translocation ability, and is demonstrated to be biologically active. This recombinant version of human NANOG can potentially be used in the cocktail of transcription factors for iPSC generation.

In addition to the role of NANOG in iPSCs generation, anomalous NANOG expression has been shown in different types of human malignancies. Furthermore, ectopic expression of NANOG caused augmented proliferation and downregulation of tumor suppressors, however, it did not result in tumor formation. Therefore, unlike

other reprogramming factors, NANOG cannot be considered an oncogene [30]. In stark contrast to earlier finding, several studies have reported NANOG expression in different tissues, including the breast, cervix and kidney [31–33]. Several such studies will provide a deeper understanding of molecular networks in cancer and help in prognosis and treatment. Thus, the recombinant version of human NANOG generated in this study can further be helpful to understand the biological role of NANOG in cancer.

2 Materials and Methods

2.1 Plasmids, Strains, Reagents and Cell Lines

The personalized plasmids (pUC-HTN-*GOI* and pUC-*GOI*-NTH) were procured from GenScript. *E. coli* BL21 (DE3) cells were utilized as host for recombinant protein expression. Isopropyl β-D-1-thiogalactopyranoside (IPTG), Luria–Bertani broth, terrific broth, kanamycin, sodium phosphate mono/dibasic, sodium chloride and imidazole was purchased from HiMedia. Bradford reagent was purchased from Bio-Rad. Dulbecco's Modified Eagle medium (DMEM), fetal bovine serum (FBS) and penicillin–streptomycin solution (P/S) were purchased from Invitrogen.

Apart from this, two human cell lines, HeLa (NCCS, India) and human dermal fibroblasts [HDFs; HiMedia CL011-2XT25)], were cultured in a complete growth medium [DMEM, FBS (5%) and P/S (1%)].

2.2 Construction of Expression Vector and Optimization for Soluble NANOG Expression

A schematic figure detailing the stepwise process from retrieval of gene sequence [codon-optimized coding sequence of *NANOG* along with a set of fusion tags (Table 1) (gene inserts)] to cloning to confirmation of cloning of *NANOG* in desired vector is shown in Fig. 1. Furthermore, pET28a(+)-HTN-*NANOG* and pET28a(+)-*NANOG*-NTH were transformed into BL21(DE3) cells using CaCl$_2$ method. To identify the optimal expression, the same approach was used as designated earlier [34, 35]. The cells were lysed using the lysis buffer mentioned in Table 2.

Table 1 Fusion tags used in the study

Fusion tags	DNA sequence (5'-3')	Protein sequence
His (H)	CATCATCACCACCATCACCATCAT	HHHHHHHH
TAT (T)	GGTCGTAAAAAACGTCGTCAGCGTCGTCGTCCGCCT	GRKKRRQRRRPP
NLS (N)	AAAAAAAAGCGCAAAGTG	KKKRKV
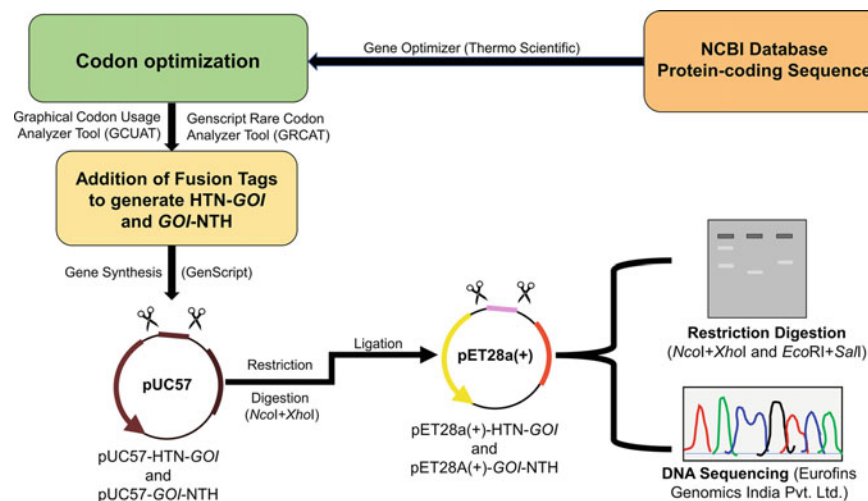
Fig. 1 Diagram representation of the codon optimization and cloning strategy used in this study. H, Histidine; T, TAT, Trans-activator of transcription; N, NLS, Nuclear localization sequence/signal

Table 2 List of buffers and their composition used for the purification

Ingredients	Lysis buffer	Wash buffer 1	Wash buffer 2	Wash buffer 3	Elution buffer
Phosphate buffer (mM)	20	20	20	20	20
Sodium chloride (mM)	150	150	150	150	150
Imidazole (mM)	20	50	100	200	500
pH (room temperature)	7.8	7.8	7.8	7.8	7.8

2.3 One-Step Purification of NANOG Via Metal Affinity Chromatography

To purify HTN-NANOG fusion protein, 1.2 L of lysate of the recombinant *E. coli* BL21(DE3) cells harboring pET28a(+)-HTN-NANOG were established as

mentioned above. The resulting lysate was loaded onto the pre-equilibrated nickel-NTA column, followed by complete washing with buffers and then eluted with elution buffer. The composition of all buffers for purification purpose is mentioned in Table 2.

After purification, size-exclusion chromatography of the eluted fractions was performed as previously described [34]. The collected protein fractions were quantified using the Bradford assay [36].

2.4 SDS-PAGE, Coomassie Staining and Western Blotting (Immunoblotting) Analysis

SDS-PAGE, Coomassie staining and Western blotting (immunoblotting) was performed as previously described [35]. The primary antibodies [anti-His (BioBharati, BB-AB0010; 1:5000), anti-NANOG (Merck Millipore, AB9220; 1:5000)], anti-GAPDH (BioBharati, BB-AB0060; 1:5000), anti-H3 (BioBharati, BB-AB0055; 1:5000), anti-p27 (Cell Signaling Technology, D69C12; 1:4000), β-actin (BioBharati, BB-AB0024); 1:5000], and secondary antibodies [anti-rabbit IgG antibody (Invitrogen, 31,460; 1:5000)] were used in the immunoblot analysis.

2.5 Circular Dichroism (CD) Spectroscopy

The full-length HTN-NANOG protein secondary structure was determined by CD spectroscopy [J-1500 spectropolarimeter (Jasco, MD, USA)] and further scrutinized by online tool BeStSel (Beta Structure Selection) [37, 38] as previously described [34, 35].

2.6 Stability of HTN-NANOG Protein

Stability was performed as described previously [39] and clarified samples were then evaluated by immunoblotting using the NANOG antibody.

2.7 Subcellular Fractionation

HDFs cells (1×10^5) were seeded in a T-25 flask and incubated overnight with vehicle control or HTN-NANOG protein (400 nM). Subcellular fractionation was carried

out as previously described [40] and analyzed by immunoblotting with specific antibodies.

2.8 Cell Proliferation Assay

HDFs (1×10^4 cells/well) were seeded in 24-well plates and were treated with HTN-NANOG (200 nM) or vehicle control. After reaching approximately 70–80% confluency, the cells were trypsinized. Cell counting was performed using a hemocytometer [41]. A cell suspension was intermixed with exclusion dye solution (Bio-Rad) and loaded into the cell counting chamber. Later, the live cells within a specific area were counted and recorded. Because the chamber volume is well-defined (commonly 0.1 mm^3), the number of cells calculated per area multiplied by the dilution factor determines the number of live cells per mL. The data are presented with a graph of the cumulative cell number against days.

2.9 Cell Migration (Scratch) Assay

HeLa cells (0.6×10^5) were seeded in a 24-well plate in a growth medium. Scratch assay was performed as earlier [42]. The rate of cell migration was calculated as previously described [43].

2.10 RT-qPCR Analysis

HeLa cells (1×10^5 cells per well) were seeded in a six-well plate and treated with vehicle control or HTN-NANOG protein (200 nM) for 3 consecutive days. RNA isolation, synthesis of complementary DNA and RT-qPCR were performed and analyzed as described previously [44]. The primers used in this study are mentioned in Table 3.

2.11 Statistical Analysis

Data analysis (unpaired student's t-test) were analyzed using GraphPad Prism 8 software and presented as mean $\pm$ standard deviation (SD) of three independent experiments. Values of $p < 0.05$ (*$p < 0.05$; ***$p < 0.001$) were with statistical significance.

Table 3 Primers used in this study

Gene	Primer sequence (5'–3')	Annealing temperature (°C)	Product size (bp)
GAPDH	Reverse: ACCACCCTGTTGCTGTAGCCAA	58	131
	Forward: GTCTCCTCTGACTTCAACAGCCAA		
P^{27}	Reverse: CAAGCACCTCGGATTTT	52.6	101
	Forward: CTGCCCTCCCCAGTCTCTCT		

3 Results

3.1 Cloning and Expression Parameter Optimization

The coding (codon-optimized) sequence of human *NANOG* was fused with three fusion tags as shown in Table 1, Fig. 1. The fused gene insert was cloned in pET28a(+) to generate two constructs as shown in Fig. 1. These genetic constructs were verified using restriction analysis using enzymes (Fig. 2) and DNA sequencing. These genetic constructs were transformed in *E. coli* strain BL21(DE3) for expression. Next, expression parameters were identified by screening different values (Table 4) for maximal soluble expression.

Based on these observations, maximal soluble expression of NANOG fusion proteins was observed with the gene constructs (HTN-NANOG and NANOG-NTH) induced at 18 °C (Fig. 3). However, no soluble expression of HTN-NANOG was
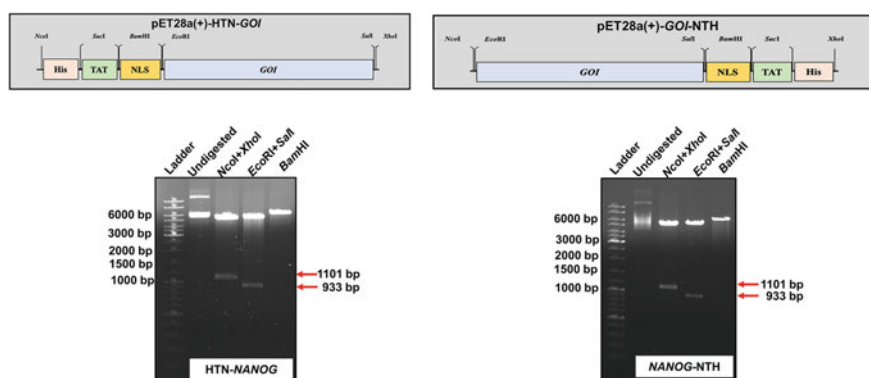
Fig. 2 Cloning of gene inserts, HTN-*NANOG* and *NANOG*-NTH, in pET28a(+) expression vector. The *GOI* was fused as per the schematic diagram (*top*) with human *NANOG* cDNA sequence to generate pET28a(+)-HTN-*NANOG* and pET28a(+)-*NANOG*-NTH. The resulting plasmids were then confirmed by restriction digestion using various restriction enzymes. *GOI*, *Gene of interest*; H, His; T, TAT and N, NLS

Table 4 Summary of the optimal expression conditions to obtain maximal expression of the human HTN-NANOG fusion protein in *E. coli*

| Expression parameters	Values screened	Optimal value
Inducer concentration (IPTG) (in mM)	0.05, 0.1, 0.25, 0.50	0.1
Induction cell density (OD_{600})	~0.5, ~1.0, ~1.5	~0.5
Post-induction incubation time (in hours)	2, 4, 8, 12	12
Induction temperature (in °C)	18, 37	18

induced at 37 °C, and many truncations were observed for NANOG-NTH (37 °C) (Fig. 3). Hence, these constructs were excluded from further analyses. Notably, in the case of NANOG, only N-terminally tagged NANOG (HTN-NANOG) induced at 18 °C showed the maximal soluble expression with no truncations. Hence, this gene construct (HTN-NANOG), induced at 18 °C with a post-induction incubation time of 12 h, was selected for further experiments (Fig. 3). These results demonstrate that the solubility of the protein was improved by reducing the temperature of the induced culture. Several studies have demonstrated the expression and purification of full-length and truncated recombinant NANOG proteins from several mammalian species [12, 45–51]. However, these studies only showed the interaction of NANOG with its consensus DNA binding sequence [12, 45, 49–51], however, the comprehensive demonstration of bioactivity of full-length human NANOG is still obscure. Thus, this study mainly focuses on the exploration of the bioactivity of full-length recombinant NANOG protein.

3.2 Purification and Secondary Structure Estimation of HTN-NANOG Protein

After screening the parameters for soluble expression analysis, HTN-NANOG was expressed in soluble form when induced at 18 °C. Hence, we aimed to purify this protein using a simple and straightforward affinity chromatography-based purification procedure. The HTN-NANOG protein band (~55 kDa) was observed in the elution fractions (Fig. 4). The purified HTN-NANOG protein was identified using SDS-PAGE (Fig. 4; top) and immunoblotting using a histidine antibody (Fig. 4; middle) and NANOG antibody (Fig. 4; bottom). Both antibodies detected all protein fragments, proving that there was no bacterial protein. Thus, we have demonstrated simple and straightforward native purification of the NANOG fusion protein.

The far-ultraviolet CD spectroscopic method is widely used to unveil the folding features of certain proteins where the secondary structure is obscure [52, 53]. Thus,
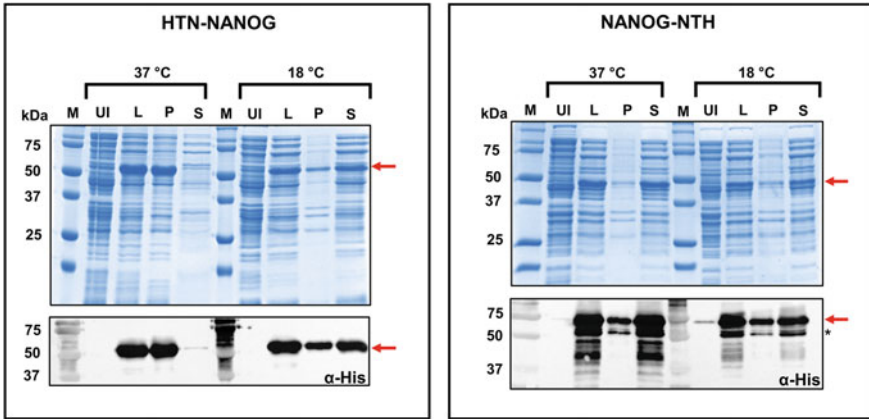
Fig. 3 Identification of the optimal induction temperature to achieve maximal soluble expression of recombinant human NANOG fusion protein. *E. coli* BL21(DE3) strain was transformed with pET28a(+) vectors harboring the fusion gene inserts and the expression of both N-terminally tagged and C-terminally tagged recombinant NANOG protein was at two different temperatures: 37 °C (post-incubation time of 2 h) and 18 °C (post-incubation time of 12 h). Then, the harvested cells were lysed to obtain the total cell lysate (L) fraction and further centrifuged to obtain a soluble/supernatant (S) cell fraction and an insoluble/pellet (P). Protein samples (20 µg) were loaded on 12% SDS-PAGE gel and further verified by immunoblotting (bottom). M, Marker; UI, uninduced (total cell lysate); L, cell lysate; P, pellet portion; S, supernatant portion; kDa, kilodaltons; α, antibody. (n = 4) * Truncation of fusion proteins

Fig. 4 SDS-PAGE and immunoblot analysis of NANOG fusion protein purification by metal affinity chromatography. HTN-NANOG protein. M, Marker; L, Lysate; S, Supernatant portion; FT, Flow-through portion; W (1–3), Wash buffer (1–3); E, Elution portion; kDa, Kilodalton; α, Antibody
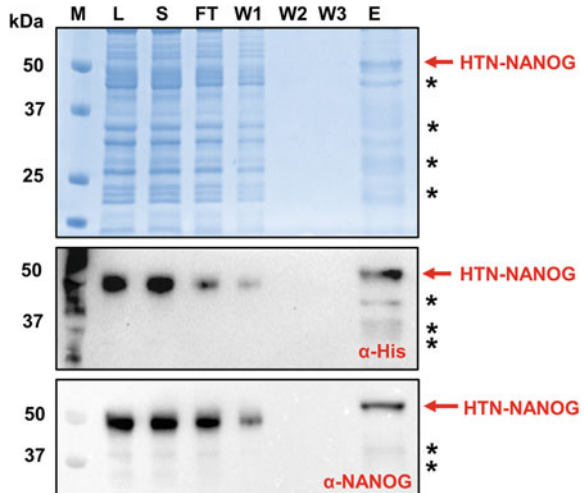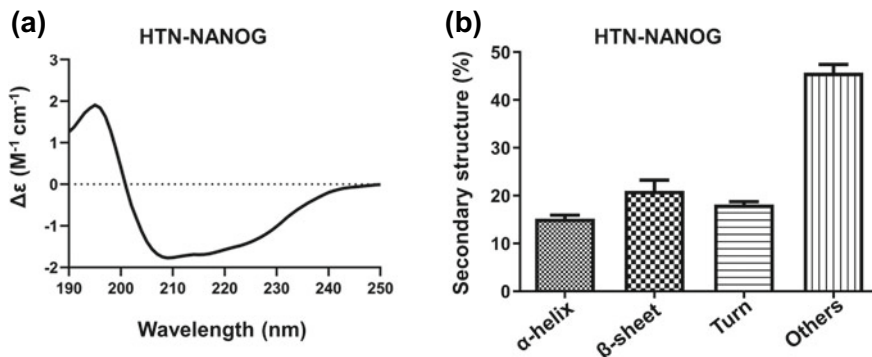
Fig. 5 Determination of the secondary structure of the NANOG protein using far-UV CD spectroscopy. The purified NANOG protein was analyzed for its secondary structures using far-UV CD spectroscopy. **a** The CD spectra were represented as delta epsilon (M − 1 cm − 1; Y-axis) vs wavelength (nm; X-axis). **b** CD spectra were evaluated with the BeStSel online tool, and the resulting structural configuration (α-helix, β-sheets, turn and others) is represented using bar graphs (n = 3)

the secondary structural conformation of purified recombinant HTN-NANOG was evaluated using CD (Fig. 5a). CD spectrum analysis using the BeStSel tool suggested that this fusion protein consisted primarily of random coils (~46%), followed by β-sheets (~21%), turns (~18%) and α-helices (~15%) (Fig. 5b). The results account that purified recombinant HTN-NANOG protein has a secondary structure retained post-purification.

3.3 Stability and Transduction Ability of HTN-NANOG Fusion Protein

Further, the protein stability of the purified NANOG protein was studied. This fusion protein was found to be stable for at least 24 h, which was identified using immunoblotting with the NANOG antibody (Fig. 6a, b).

Next, we demonstrated the transduction ability of HTN-NANOG fusion protein in HDFs using subcellular fractionation. HDFs have no endogenous expression of NANOG; therefore, these cells were used in this study. Similar to immunofluorescence staining, subcellular fractionation can also be used to know the protein localization in a cell [40, 54]. Moreover, subcellular localization is vital for proper protein function. The fractions (nuclear and cytoplasmic) of the human cell lines were separated by centrifugation. These fractions were further analyzed by immunoblotting. In this study, GAPDH (Glyceraldehyde-3-Phosphate Dehydrogenase) and Histone H3 were used as internal loading controls for the cytoplasmic (GAPDH) and nuclear (H3) fractions (Fig. 6c), respectively. Immunoblotting analysis exhibited that the majority of the HTN-NANOG fusion proteins were present in the nuclear fraction
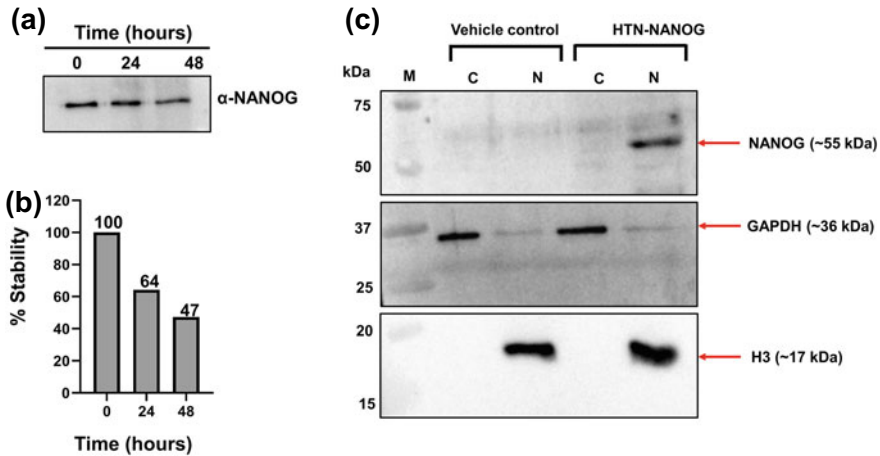
Fig. 6 Stability and localization of HTN-NANOG protein determined with a subcellular fractionation assay. **a** Stability of purified recombinant proteins under standard cell culture conditions was analyzed by immunoblotting. **b** Densitometric analysis of data from (**a**) and (**c**) representative immunoblot showing cytoplasmic (C) and nuclear (N) fractions of NANOG fusion protein-treated or untreated (vehicle control) HDFs cells using NANOG, GAPDH and Histone H3 antibodies. M, Marker; C, Cytosolic portion; N, Nuclear portion

of cells treated with NANOG. This implied that the fusion tag nuclear localization signal (NLS) is responsible for the efficient nuclear translocation of the recombinant fusion protein. The homeodomain in human NANOG tends to be localized in the nucleus, implying that it has a NLS [55]. The presence of a stretch of six amino acids [YKQVKT (136–141 aa)] in the homeobox is responsible for nuclear localization [56]. Adding an extra NLS to NANOG sequence has further enabled efficient nuclear delivery of the purified recombinant NANOG protein.

3.4 Effect of the Recombinant HTN-NANOG Protein on Cell Proliferation of HDFs

Several studies have reported that exogenous expression of NANOG in ESCs and fibroblasts resulted in increased cell proliferation [57, 58]. In view of this, we also explored the effect of NANOG on human fibroblast (HDF) cells. To investigate cell proliferation, we counted the cells using a hemocytometer at different time intervals and observed augmented cell proliferation of HDFs. The data was analyzed and are shown in Fig. 7. The results of our study are in concordant with prior studies [57, 58]. Hence, our study provides evidence that NANOG plays a proliferative role in HDFs and is bioactive.

Fig. 7 Effect of purified HTN-NANOG protein on cell proliferation. Cell proliferation was assessed via cell counting. Y-axis signifies the cumulative cell number, and the X-axis signifies days of treatment (n = 3)
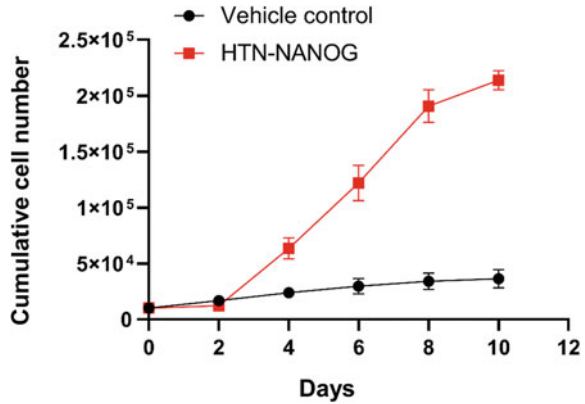

3.5 Effect of the Recombinant HTN-NANOG Protein on the Migration of HeLa Cells

The oncogenic potential of NANOG is well established and its presence has been detected in cervical cancer [33, 59, 60]. Forced NANOG expression has been reported to result in increased migration, invasion and tumorigenesis in HeLa cells [61]. Thus, to confirm that the purified HTN-NANOG fusion protein was biologically active, the migration rate of HeLa cells was evaluated using an in vitro scratch assay. Based on the observation of the effect of HTN-NANOG protein transduction in HeLa cells, NANOG protein-treated wells showed faster cell migration compared to the wells treated with the vehicle control (Fig. 8a, b; ***p < 0.001). These results were consistent with previously published results [61]. An earlier study used NANOG mRNA, but we used NANOG as a recombinant protein in our study for functional investigation. Thus, this study demonstrated that the HTN-NANOG fusion protein facilitated the migration of HeLa cells and was bioactive.

3.6 Effect of the Recombinant HTN-NANOG Protein on the Cell Cycle Inhibitor P27 Gene

To further explore the functional characteristics of NANOG, we investigated the effect of NANOG on cell cycle factor p27 (CDKN1B). Furthermore, p27^{Kip1} is a tumor suppressor and inhibitor of Cyclin/Cyclin-Dependent Kinase (CDK) complexes. Thus, p27 plays a vital role in the regulation of the cell cycle. Transient activation of NANOG in fibroblasts is linked to the downregulation of p27 [62]. Hence, we also attempted to examine the effect of HTN-NANOG on p27 mRNA and protein levels in HeLa cells. Cells were harvested for RNA isolation and complementary DNA (cDNA) synthesis was carried out from total RNA. Quantitative real-time
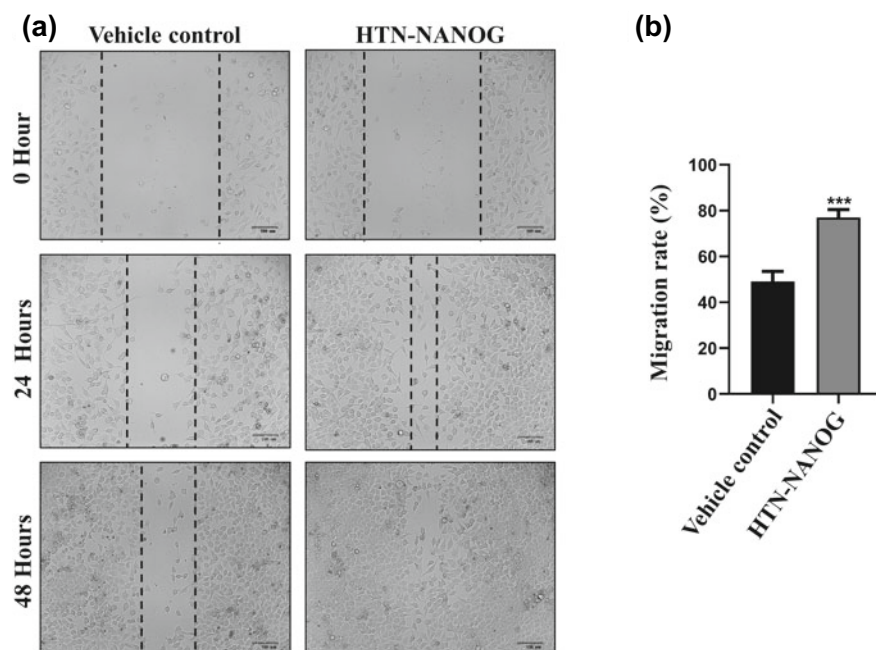
Fig. 8 Effect of purified HTN-NANOG protein on the migration of HeLa cells. **a** Scratch assay of HeLa cells. Cell migration was induced in the presence of HTN-NANOG. Scale bar: 100 μm. **b** Graphical representation of the changes in migration rate following treatment with vehicle control or NANOG protein. Quantitative data are expressed as the mean ± SD (n = 3). ***p < 0.0001

PCR (RT-qPCR) was performed using GAPDH as a reference. The data indicated a significant decrease in the p27 at RNA level (Fig. 9a; *p < 0.05). To further validate this at the protein level, we performed immunoblotting using β-actin as a loading control for normalization (Fig. 9b). Immunoblotting analysis showed that the expression of p27 was downregulated at the protein level in the presence of HTN-NANOG. These data demonstrate that the downregulation of the p27 (at RNA and protein level) in the presence of protein is in line with an earlier reported study [62]. Hence, this confirms that the purified recombinant HTN-NANOG protein is bioactive.

4   Discussion

Human NANOG (915 bp) contains four exons and three introns. The human NANOG protein is a long chain of 305 amino acids and has N-terminal, homeobox domain and C-terminal region. The N-terminal region (94 aa) is abundant in serine, proline and threonine and is responsible for governing the transcription of NANOG. The homeobox domain (60 aa) binds to the DNA core region. The C-terminal region (151 aa)

Fig. 9 Effect of the purified HTN-NANOG fusion protein on p27 levels in HeLa cells. **a** Relative expression of the p27 mRNA in vehicle control and HTN-NANOG analyzed by RT-qPCR. Quantitative statistics are shown as the mean $\pm$ SD ($n = 3$). *$p < 0.05$. **b** Immunoblot analysis of p27 protein expression in the presence of the vehicle control and NANOG protein ($n = 3$)
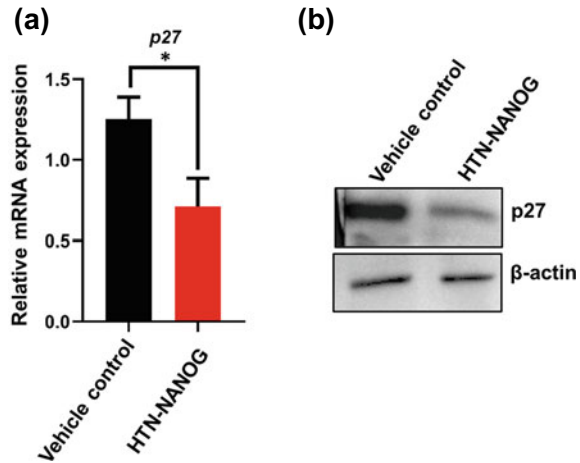
is tryptophan-rich, and investigations have shown that this region is responsible for homodimerization. Thus, NANOG acts as a transcription factor by controlling transcription through interactions with the promoters of myriad genes via these domains [55, 56, 63]. NANOG is a transcriptional activator that binds to the 5'–TAAT–3' essential regions of the DNA sequence [64, 65]. A triad of transcription factors, including OCT4, SOX2 and NANOG, appear to be at the heart of pluripotency [11]. Unlike OCT4 and SOX2, solitary NANOG cells conserve pluripotency in the absence of pluripotency maintenance signals. Knockdown studies have revealed the crucial role of NANOG in embryogenesis staging. NANOG is important for the maintenance of self-renewal and pluripotency. These properties prevent the ESCs and iPSCs from differentiation [11].

Additionally, NANOG facilitates pre-iPS cells to attain ground-state pluripotency (iPSCs), which is crucial in the process of molecular reprogramming [9]. During the reprogramming of somatic cells, NANOG plays a critical role in inducing pluripotency [9]. NANOG boosts the activation of STAT3; hence, the synergistic action between them promotes the establishment of naive pluripotency in ESCs and during the initial stages of reprogramming [66]. iPSCs that are deficient in NANOG are identical to wild-type iPSCs in transcriptional status; and upon further exploration, teratomas and chimeric formation are underpinned. Hence, this study demonstrates that NANOG is dispensable for iPSC formation [19]. A recent study has demonstrated the distinctive ability of human NANOG to initiate prion-like clusters. These assemblies could act as a means for delivering DNA elements for their interactions with others, which is essential for the re-organization of chromatin structures and activation of ground-state pluripotency in a dose-dependent manner [67].

We successfully purified HTN-NANOG from a soluble fraction of *E. coli* cultures using affinity chromatography. Based on these observations, the soluble protein expression was relatively low (purity >90%) and might be due to its aggregation property when induced at larger volumes. Additionally, another study reported the

purification of human NANOG, in which, among all the domains, the C-terminal domain has limited solubility. In contrast, the homeodomain and N-terminal domains are favorably soluble [51]. Strikingly, another study also showed the expression of full-length human NANOG protein along with 17 kDa protein (Skp) chaperone [51]. The role of Skp is to aid the folding of outer membrane proteins and their entry into membranes. Furthermore, Skp is well established to enhance the folding of recombinant proteins and further, directs the cargo to the periplasm of *E. coli* [68]. In agreement with the preceding evidence, the wild-type NANOG-GB1 fusion protein was also expressed and found to be soluble when co-expressed with the Skp chaperone. This study reasoned that the Skp chaperone is equipped with a hydrophobic cage that encases wild-type NANOG and further co-operates with tryptophan residues upon exposure [67]. In addition, human NANOG, by virtue of its C-terminal domain, is apt for aggregation, which accounts for the limited biophysical characterization of the protein and its individual domains [67]. Therefore, we aimed to determine the secondary structure of the full-length NANOG fusion protein.

The crystal structure of homeodomain NANOG has been documented as a structural scaffold formed by three helices in both mice and humans [45, 69]. A recent study showed that the CD spectra of each domain individually, the N-terminal domain of human NANOG, comprises intrinsically disordered regions responsible for displaying a random-coil signature in NMR spectra and are further found in line with the computational prediction [67]. In contrast, the far-UV CD spectra of the C-terminal domain revealed β-sheets and resulted in a reduced number of β-sheets in the mutated version of human NANOG [67]. According to available data, our study showed that the secondary structure of the full-length HTN-NANOG protein is retained and is likely to be bioactive.

A multitude of studies has been reported on the generation of reprogramming factors, namely, OCT4, SOX2, NANOG, PDX1, NGN3, GLIS1, GATA4, TBX5, HAND2, ETS2, MEF2C and MESP1, in *E. coli* using similar approaches [35, 40, 42, 44, 58, 62, 70–78]. These investigations also revealed the utility of NLS in proteins that facilitate the delivery of recombinant proteins to the nucleus in human cells. Several reports have observed that the fusion tags [post protein delivery into cells (via TAT) and their nucleus (via NLS)] do not hamper the bioactivity of recombinant proteins [35, 39, 40, 44, 58, 62, 70–73, 78]. Thus, cytoplasmic and nuclear transport of reprogramming factors can be attained via TAT and NLS fusion without requiring additional transduction reagents. For this, we demonstrated that the protein is stable under standard cell culture conditions and has the ability to enter the nucleus using a subnuclear fractionation assay.

Additionally, our study highlights the proliferative effect of recombinant NANOG on human dermal fibroblasts, emphasizing its role in malignancy. Next, we analyzed the impact of exogenously delivered NANOG fusion proteins on HeLa cell migration. Thus, we revealed that the stem cell-linked factor NANOG possesses tumorigenic properties in cervical cancer. Furthermore, we observed the downregulation of p27 in HeLa cells in the presence of NANOG at the mRNA and protein levels. This study provides evidence that tagging the protein at either terminal does not hinder its bioactivity. The generation of biologically active NANOG might trigger the endogenous

expression of NANOG and may also participate in the auto- and inter-regulatory loops of pluripotency during the induction of iPSCs. The proliferative effect of NANOG on cells may offer an excellent platform for the expansion of mature cells in vitro. From a cancer perspective, it may act as a molecular marker for prognosis and cure.

Author Contribution MT designed and performed the experiments, assembled and analyzed the data, wrote the manuscript; SS analyzed and interpreted the data; and RPT conceptualized and designed the study, analyzed the data, supervised the experiments, wrote the manuscript, and provided financial support. The final draft of the manuscript was approved by all the authors for publication.

Declarations None.

Conclusion The purification of HTN-NANOG fusion protein from *E. coli* with a retained secondary structure and its bioactivity in human cells is demonstrated in this study. This study reported that human NANOG fusion protein enhanced proliferation, migration and downregulated p27 gene expression in HeLa cells, demonstrating its bioactivity. This biologically active human NANOG protein can be utilized to elucidate the biological function of NANOG in various cellular processes associated with cancer and induced pluripotent stem cells.

References

1. Booth HAF, Holland PWH (2004) Eleven daughters of NANOG. Genomics 84(2):229–238. https://doi.org/10.1016/j.ygeno.2004.02.014
2. Theunissen TW, Costa Y, Radzisheuskaya A, van Oosten AL, Lavial F, Pain B et al (2011) Reprogramming capacity of Nanog is functionally conserved in vertebrates and resides in a unique homeodomain. Development 138(22):4853–4865. https://doi.org/10.1242/dev.068775
3. Chambers I, Colby D, Robertson M, Nichols J, Lee S, Tweedie S, Smith A (2003) Functional expression cloning of Nanog, a pluripotency sustaining factor in embryonic stem cells. Cell 113(5):643–655. https://doi.org/10.1016/s0092-8674(03)00392-1
4. Mitsui K, Tokuzawa Y, Itoh H, Segawa K, Murakami M, Takahashi K et al (2003) The homeoprotein nanog is required for maintenance of pluripotency in mouse epiblast and ES cells. Cell 113(5):631–642. https://doi.org/10.1016/S0092-8674(03)00393-3
5. Komatsu K, Fujimori T (2015) Multiple phases in regulation of Nanog expression during pre-implantation development. Dev Growth Differ 57(9):648–656. https://doi.org/10.1111/dgd.12244
6. Chambers I, Silva J, Colby D, Nichol J, Nijmeijer B, Robertson M et al (2007) Nanog safeguards pluripotency and mediates germline development. Nature 450(7173):1230–1234. https://doi.org/10.1038/nature06403
7. Yamaguchi S, Kimura H, Tada M, Nakatsuji N, Tada T (2005) Nanog expression in mouse germ cell development. Gene Expr Patterns 5(5):639–646. https://doi.org/10.1016/j.modgep.2005.03.001
8. Lavial F, Acloque H, Bertocchini F, MacLeod DJ, Boast S, Bachelard E et al (2007) The Oct4 homologue PouV and Nanog regulate pluripotency in chicken embryonic stem cells. Development 134(19):3549–3563. https://doi.org/10.1242/dev.006569
9. Silva J, Nichols J, Theunissen TW, Guo G, van Oosten AL, Barrandon O et al (2009) Nanog is the gateway to the pluripotent ground state. Cell 138(4):722–737. https://doi.org/10.1016/j.cell.2009.07.039

10. Messerschmidt DM, Kemler R (2010) Nanog is required for primitive endoderm formation through a non-cell autonomous mechanism. Dev Biol 344(1):129–137. https://doi.org/10.1016/j.ydbio.2010.04.020

11. Boyer LA, Lee TI, Cole MF, Johnstone SE, Levine SS, Zucker JP et al (2005) Core transcriptional regulatory circuitry in human embryonic stem cells. Cell 122(6):947–956. https://doi.org/10.1016/j.cell.2005.08.020

12. Loh YH, Wu Q, Chew JL, Vega VB, Zhang W, Chen X et al (2006) The Oct4 and Nanog transcription network regulates pluripotency in mouse embryonic stem cells. Nat Genet 38(4):431–440. https://doi.org/10.1038/ng1760

13. Wang J, Rao S, Chu J, Shen X, Levasseur DN, Theunissen TW, Orkin SH (2006) A protein interaction network for pluripotency of embryonic stem cells. Nature 444(7117):364–368. https://doi.org/10.1038/nature05284

14. Silva J, Chambers I, Pollard S, Smith A (2006) Nanog promotes transfer of pluripotency after cell fusion. Nature 441(7096):997–1001. https://doi.org/10.1038/nature04914

15. Hanna J, Saha K, Pando B, Van Zon J, Lengner CJ, Creyghton MP et al (2009) Direct cell reprogramming is a stochastic process amenable to acceleration. Nature 462(7273):595–601. https://doi.org/10.1038/nature08592

16. Gingold JA, Fidalgo M, Guallar D, Lau Z, Sun Z, Zhou H et al (2014) A genome-wide RNAi screen identifies opposing functions of snai1 and snai2 on the nanog dependency in reprogramming. Mol Cell 56(1):140–152. https://doi.org/10.1016/j.molcel.2014.08.014

17. Theunissen TW, Van Oosten AL, Castelo-Branco G, Hall J, Smith A, Silva JCR (2011) Nanog overcomes reprogramming barriers and induces pluripotency in minimal conditions. Curr Biol 21(1):65–71. https://doi.org/10.1016/j.cub.2010.11.074

18. Zhao Y, Yin X, Qin H, Zhu F, Liu H, Yang W et al (2008) Two supporting factors greatly improve the efficiency of human iPSC generation. Cell Stem Cell 3(5):475–479. https://doi.org/10.1016/j.stem.2008.10.002

19. Schwarz BA, Bar-Nur O, Silva JCR, Hochedlinger K (2014) Nanog is dispensable for the generation of induced pluripotent stem cells. Curr Biol 24(3):347–350. https://doi.org/10.1016/j.cub.2013.12.050

20. Carter AC, Davis-Dusenbery BN, Koszka K, Ichida JK, Eggan K (2014) Nanog-independent reprogramming to iPSCs with canonical factors. Stem Cell Rep 2(2):119–126. https://doi.org/10.1016/j.stemcr.2013.12.010

21. Yu J, Vodyanik MA, Smuga-Otto K, Antosiewicz-Bourget J, Frane JL, Tian S et al (2007) Induced pluripotent stem cell lines derived from human somatic cells. Science 318(5858):1917–1920. https://doi.org/10.1126/science.1151526

22. Maherali N, Ahfeldt T, Rigamonti A, Utikal J, Cowan C, Hochedlinger K (2008) A high-efficiency system for the generation and study of human induced pluripotent stem cells. Cell Stem Cell 3(3):340–345. https://doi.org/10.1016/j.stem.2008.08.003

23. Haase A, Olmer R, Schwanke K, Wunderlich S, Merkert S, Hess C et al (2009) Generation of induced pluripotent stem cells from human cord blood. Cell Stem Cell 5(4):434–441. https://doi.org/10.1016/j.stem.2009.08.021

24. Li Y, Zhao H, Lan F, Lee A, Chen L, Lin C et al (2010) Generation of human-induced pluripotent stem cells from gut mesentery-derived cells by ectopic expression of OCT4/SOX2/NANOG. Cell Reprogramming (Formerly" Cloning and Stem Cells"), 12(3):237–247. https://doi.org/10.1089/cell.2009.0103

25. Lowry WE, Richter L, Yachechko R, Pyle AD, Tchieu J, Sridharan R et al (2008) Generation of human induced pluripotent stem cells from dermal fibroblasts. Proc Natl Acad Sci 105(8):2883–2888. https://doi.org/10.1073/pnas.0711983105

26. Moon J-H, Yun W, Kim J, Hyeon S, Kang PJ, Park G et al (2013) Reprogramming of mouse fibroblasts into induced pluripotent stem cells with Nanog. Biochem Biophys Res Commun 431(3):444–449. https://doi.org/10.1016/j.bbrc.2012.12.149

27. Borgohain MP, Haridhasapavalan KK, Dey C, Adhikari P, Thummer RP (2019) An insight into DNA-free reprogramming approaches to generate integration-free induced pluripotent stem cells for prospective biomedical applications. Stem Cell Rev Rep 15(2):286–313. https://doi.org/10.1007/s12015-018-9861-6

28. Haridhasapavalan KK, Borgohain MP, Dey C, Saha B, Narayan G, Kumar S, Thummer RP (2019) An insight into non-integrative gene delivery approaches to generate transgene-free induced pluripotent stem cells. Gene 686:146–159. https://doi.org/10.1016/j.gene.2018.11.069

29. Dey C, Raina K, Haridhasapavalan KK, Thool M, Sundaravadivelu PK, Adhikari P et al (2021) An overview of reprogramming approaches to derive integration-free induced pluripotent stem cells for prospective biomedical applications. Recent Adv iPSC Technol 231–287. https://doi.org/10.1016/B978-0-12-822231-7.00011-4

30. Fischedick G, Wu G, Adachi K, Araúzo-Bravo MJ, Greber B, Radstaak M et al (2014) Nanog induces hyperplasia without initiating tumors. Stem Cell Res 13(2):300–315. https://doi.org/10.1016/j.scr.2014.08.001

31. Ezeh UI, Turek PJ, Reijo RA, Clark AT (2005) Human embryonic stem cell genes OCT4, NANOG, STELLAR, and GDF3 are expressed in both seminoma and breast carcinoma. Cancer: Interdiscip Int J Am Cancer Soc 104(10):2255–2265. https://doi.org/10.1002/cncr.21432

32. Bussolati B, Bruno S, Grange C, Ferrando U, Camussi G (2008) Identification of a tumor-initiating stem cell population in human renal carcinomas. FASEB J 22(10):3696–3705. https://doi.org/10.1096/fj.08-102590

33. Ye F, Zhou C, Cheng Q, Shen J, Chen H (2008) Stem-cell-abundant proteins Nanog, Nucleostemin and Musashi1 are highly expressed in malignant cervical epithelial cells. BMC Cancer 8(1):1–5. https://doi.org/10.1186/1471-2407-8-108

34. Thool M, Dey C, Bhattacharyya S, Sudhagar S, Thummer RP (2021) Generation of a recombinant stem cell-specific human SOX2 protein from Escherichia coli under native conditions. Mol Biotechnol 63(4):327–338. https://doi.org/10.1007/s12033-021-00305-y

35. Haridhasapavalan KK, Sundaravadivelu PK, Bhattacharyya S, Ranjan SH, Raina K, Thummer RP (2021) Generation of cell-permeant recombinant human transcription factor GATA4 from E. coli. Bioprocess Biosyst Eng 44(6):1131–1146. https://doi.org/10.1007/s00449-021-02516-8

36. Bradford MM (1976) A rapid and sensitive method for the quantitation of microgram quantities of protein utilizing the principle of protein-dye binding. Anal Biochem 72(1–2):248–254. https://doi.org/10.1006/abio.1976.9999

37. Micsonai A, Wien F, Bulyáki É, Kun J, Moussong É, Lee Y-H et al (2018) BeStSel: a web server for accurate protein secondary structure prediction and fold recognition from the circular dichroism spectra. Nucleic Acids Res 46(W1):W315–W322. https://doi.org/10.1093/nar/gky497

38. Micsonai A, Bulyáki É, Kardos J (2021) BeStSel: from secondary structure analysis to protein fold prediction by circular dichroism spectroscopy. In: Structural genomics. Springer, Berlin, pp 175–189. https://doi.org/10.1007/978-1-0716-0892-0_11

39. Dey C, Thool M, Bhattacharyya S, Sudhagar S, Thummer RP (2021) Generation of biologically active recombinant human OCT4 protein from E. coli. 3 Biotech 11(5):1–16. https://doi.org/10.1007/s13205-021-02758-z

40. Narayan G, Agrawal A, Joshi N, Gogoi R, Nagotu S, Thummer RP (2021) Protein production and purification of a codon-optimized human NGN3 transcription factor from E. coli. Protein J 40(6):891–906. https://doi.org/10.1007/s10930-021-10020-x

41. Patel TB, Bertics PJ (2006) Epidermal growth factor: methods and protocols, vol 327. Springer Science & Business Media

42. Dey C, Venkatesan V, Thummer RP (2022) Identification of optimal expression parameters and purification of a codon-optimized human GLIS1 transcription factor from Escherichia coli. Mol Biotechnol 64(1):42–56. https://doi.org/10.1007/s12033-021-00390-z

43. Grada A, Otero-Vinas M, Prieto-Castrillo F, Obagi Z, Falanga V (2017) Research techniques made simple: analysis of collective cell migration using the wound healing assay. J Investig Dermatology 137(2):e11–e16. https://doi.org/10.1016/j.jid.2016.11.020

44. Haridhasapavalan KK, Das NJ, Thummer RP (2022) Generation of a transducible version of a bioactive recombinant human TBX5 transcription factor from E. Coli. Curr Res Biotechnol 4:66–77

45. Jauch R, Ng CKL, Saikatendu KS, Stevens RC, Kolatkar PR (2008) Crystal structure and DNA binding of the homeodomain of the stem cell transcription factor Nanog. J Mol Biol 376(3):758–770. https://doi.org/10.1016/j.jmb.2007.11.091

46. Hu PF, Guan WJ, Li XC, Ma YH (2012) Construction of recombinant proteins for reprogramming of endangered Luxi cattle fibroblast cells. Mol Biol Rep 39(6):7175–7182. https://doi.org/10.1007/s11033-012-1549-4

47. Yu M, Lian S, Han H, Yu K, Li G, Lian Z, Li N (2013) Four recombinant pluripotency transcriptional factors containing a protein transduction domain maintained the in vitro pluripotency of chicken embryonic stem cells. Sci China Life Sci 56(1):40–50. https://doi.org/10.1007/s11427-012-4426-4

48. Zhang H, Ma Y, Gu J, Liao B, Li J, Wong J, Jin Y (2012) Reprogramming of somatic cells via TAT-mediated protein transduction of recombinant factors. Biomaterials 33(20):5047–5055. https://doi.org/10.1016/j.biomaterials.2012.03.061

49. Yang WC, Patel KG, Lee J, Ghebremariam YT, Wong HE, Cooke JP, Swartz JR (2009) Cell-free production of transducible transcription factors for nuclear reprogramming. Biotechnol Bioeng 104(6):1047–1058. https://doi.org/10.1002/bit.22517

50. Yang WC, Welsh JP, Lee J, Cooke JP, Swartz JR (2011) Solubility partner IF2 Domain I enables high yield synthesis of transducible transcription factors in Escherichia coli. Protein Expr Purif 80(1):145–151. https://doi.org/10.1016/j.pep.2011.06.017

51. Ha SC, Pereira JH, Jeong JH, Huh JH, Kim SH (2009) Purification of human transcription factors Nanog and Sox2, each in complex with Skp, an Escherichia coli periplasmic chaperone. Protein Expr Purif 67(2):164–168. https://doi.org/10.1016/j.pep.2009.05.003

52. Kelly SM, Jess TJ, Price NC (2005) How to study proteins by circular dichroism. Biochimica et Biophysica Acta (BBA)-Proteins and Proteomics, 1751(2):119–139. https://doi.org/10.1016/j.bbapap.2005.06.005

53. Micsonai A, Wien F, Kernya L, Lee Y-H, Goto Y, Réfrégiers M, Kardos J (2015) Accurate secondary structure prediction and fold recognition for circular dichroism spectroscopy. Proc Natl Acad Sci 112(24):E3095–E3103. https://doi.org/10.1073/pnas.1500851112

54. Yu Z, Huang Z, Lung ML (2013) Subcellular fractionation of cultured human cell lines. Bio-Protoc 3(9):e754–e754

55. Do HJ, Lim HY, Kim JH, Song H, Chung HM, Kim JH (2007) An intact homeobox domain is required for complete nuclear localization of human Nanog. Biochem Biophys Res Commun 353(3):770–775. https://doi.org/10.1016/j.bbrc.2006.12.100

56. Chang DF, Tsai SC, Wang XC, Xia P, Senadheera D, Lutzko C (2009) Molecular characterization of the human NANOG protein. Stem Cells 27(4):812–821. https://doi.org/10.1634/stemcells.2008-0657

57. Zhang J, Wang X, Chen B, Suo G, Zhao Y, Duan Z, Dai J (2005) Expression of Nanog gene promotes NIH3T3 cell proliferation. Biochem Biophys Res Commun 338(2):1098–1102. https://doi.org/10.1016/j.bbrc.2005.10.071

58. Peitz M, Münst B, Thummer RP, Helfen M, Edenhofer F (2014) Cell-permeant recombinant Nanog protein promotes pluripotency by inhibiting endodermal specification. Stem cell Res 12(3):680–689. https://doi.org/10.1016/j.scr.2014.02.006

59. Gu TT, Liu SY, Zheng PS (2012) Cytoplasmic NANOG-positive stromal cells promote human cervical cancer progression. Am J Pathol 181(2):652–661. https://doi.org/10.1016/j.ajpath.2012.04.008

60. Ding Y, Yu AQ, Li CL, Fang J, Zeng Y, Li DS (2014) TALEN-mediated Nanog disruption results in less invasiveness, more chemosensitivity and reversal of EMT in Hela cells. Oncotarget 5(18):8393–8401. https://doi.org/10.18632/oncotarget.2298

61. Ding Y, Yu AQ, Wang XL, Guo XR, Yuan YH, Li DS (2016) Forced expression of Nanog with mRNA synthesized in vitro to evaluate the malignancy of HeLa cells through acquiring cancer stem cell phenotypes. Oncol Rep 35(5):2643–2650. https://doi.org/10.3892/or.2016.4639

62. Münst B, Thier MC, Winnemöller D, Helfen M, Thummer RP, Edenhofer F (2016) Nanog induces suppression of senescence through downregulation of p27KIP1 expression. J Cell Sci 129(5):912–920. https://doi.org/10.1242/jcs.167932

63. Oh JH, Do HJ, Yang HM, Moon SY, Cha KY, Chung HM, Kim JH (2005) Identification of a putative transactivation domain in human Nanog. Exp Mol Med 37(3):250–254. https://doi.org/10.1038/emm.2005.33

64. Jeter CR, Yang T, Wang J, Chao HP, Tang DG (2015) Concise review: NANOG in cancer stem cells and tumor development: an update and outstanding questions. Stem Cells 33(8):2381–2390. https://doi.org/10.1002/stem.2007

65. Patra SK, Vemulawada C, Soren MM, Sundaray JK, Panda MK, Barman HK (2018) Molecular characterization and expression patterns of Nanog gene validating its involvement in the embryonic development and maintenance of spermatogonial stem cells of farmed carp, Labeo rohita. J Anim Sci Biotechnol 9(1):1–17. https://doi.org/10.1186/s40104-018-0260-2

66. Stuart HT, Van Oosten AL, Radzisheuskaya A, Martello G, Miller A, Dietmann S et al (2014) NANOG amplifies STAT3 activation and they synergistically induce the naive pluripotent program. Curr Biol 24(3):340–346. https://doi.org/10.1016/j.cub.2013.12.040

67. Choi KJ, Quan MD, Qi C, Lee JH, Tsoi PS, Zahabiyon M et al (2022) NANOG prion-like assembly mediates DNA bridging to facilitate chromatin reorganization and activation of pluripotency. Nature Cell Biol 24(5):737–747. https://doi.org/10.1038/s41556-022-00896-x

68. Bothmann H, Plückthun A (1998) Selection for a periplasmic factor improving phage display and functional periplasmic expression. Nat Biotechnol 16(4):376–380. https://doi.org/10.1038/nbt0498-376

69. Hayashi Y, Caboni L, Das D, Yumoto F, Clayton T, Deller MC et al (2015) Structure-based discovery of NANOG variant with enhanced properties to promote self-renewal and reprogramming of pluripotent stem cells. Proc Natl Acad Sci U S A 112(15):4666–4671. https://doi.org/10.1073/pnas.1502855112

70. Bosnali M, Edenhofer F (2008) Generation of transducible versions of transcription factors Oct4 and Sox2. Biol Chem 389(7):851–861. https://doi.org/10.1515/BC.2008.106

71. Stock K, Nolden L, Edenhofer F, Quandel T, Brüstle O (2010) Transcription factor-based modulation of neural stem cell differentiation using direct protein transduction. Cell Mol Life Sci 67(14):2439–2449. https://doi.org/10.1007/s00018-010-0347-1

72. Thier M, Münst B, Edenhofer F (2011) Exploring refined conditions for reprogramming cells by recombinant Oct4 protein. Int J Dev Biol 54(11–12):1713–1721. https://doi.org/10.1387/ijdb.103193mt

73. Thier M, Münst B, Mielke S, Edenhofer F (2012) Cellular reprogramming employing recombinant Sox2 protein. Stem Cells Int. https://doi.org/10.1155/2012/549846

74. Narayan G, Sundaravadivelu PK, Agrawal A, Gogoi R, Nagotu S, Thummer RP (2021) Soluble expression, purification, and secondary structure determination of human PDX1 transcription factor. Protein Expr Purif 180:105807. https://doi.org/10.1016/j.pep.2020.105807

75. Haridhasapavalan KK, Sundaravadivelu PK, Voorkara U, Kaveeshwar V, Thummer RP (2022) Generation of the recombinant version of a bioactive human MEF2C transcription factor from E. coli. In: Healthcare research and related technologies-proceedings of NERC. Springer Nature

76. Haridhasapavalan KK, Sundaravadivelu PK, Thummer RP (2020) Codon optimization, cloning, expression, purification, and secondary structure determination of human ETS2 transcription factor. Mol Biotechnol 62(10):485–494. https://doi.org/10.1007/s12033-020-00266-8

77. Haridhasapavalan KK, Ranjan SH, Bhattacharyya S, Thummer RP (2021) Soluble expression, purification, and secondary structure determination of human MESP1 transcription factor. Appl Microbiol Biotechnol 105(6):2363–2376. https://doi.org/10.1007/s00253-021-11194-1

78. Haridhasapavalan KK, Sundaravadivelu PK, Joshi N, Das NJ, Mohapatra A, Voorkara U et al (2022) Generation of a recombinant version of a biologically active cell-permeant human HAND2 transcription factor from E. coli. Sci Rep 12(1):16129. https://doi.org/10.1038/s41598-022-19745-w

Studying the Role of ERK Inhibition in Glioblastoma Multiforme

Rumela Mitra ⬤ **, M. Aswanth Harish** ⬤ **, and Bithiah Grace Jaganathan** ⬤

1 Introduction

Glioblastoma or glioblastoma multiforme (GBM), originating in the glial cells of the brain, is classified by WHO as a grade IV astrocytoma and has an extremely poor prognosis with a 5-year survival rate of 5% after diagnosis [1]. Conventional therapy using temozolomide [2–4] along with radiotherapy or surgery fails to prevent disease relapse, primarily due to the presence of residual cancer stem cells (CSCs) [5]. Constitutive activation of several signaling cascades in CSCs, such as the mitogen-activated protein kinase or MAPK pathway [6, 7], promotes chemoresistance [8], tumor heterogeneity and disease progression [9].

Upregulation of growth factor receptors that belongs to the receptor tyrosine kinase (RTK) family in GBM leads to the downstream activation of the MAPK/ERK pathway [10]. In addition, high phosphorylated ERK levels correlate with higher proliferation and invasion capacity of GBM cells. Inhibition of the MEK/ERK1/2 pathway increases ECM adhesion and reduces the migration ability of the cells [11]. The FDA-approved pan-RTK inhibitor sorafenib is a drug that is orally administered [12] to patients in the advanced stages of hepatocellular carcinoma (HCC) and

R. Mitra · M. Aswanth Harish · B. G. Jaganathan (✉)
Stem Cell and Cancer Biology Research Group, Department of Biosciences and Bioengineering, Indian Institute of Technology Guwahati, Guwahati, Assam, India
e-mail: bithiahgj@iitg.ac.in

B. G. Jaganathan
Jyoti and Bhupat Mehta School of Health Sciences and Technology, Indian Institute of Technology Guwahati, Guwahati, Assam, India

119

renal cell cancer [13]. It inhibits proliferation and angiogenesis in HCC, often used in combination with other therapeutic agents [14–16] and also inhibits the migratory and invasive abilities of breast cancer cells in vitro [17]. Sorafenib targets the cell-surface RTKs (including VEGFR, PDGFR-β, c-KIT and Flt-3) as well as intracellular serine/threonine kinases (like Raf-1 and wild-type or mutated B-RAF) [18, 19]. Ulixertinib (BVD523), a reversible, small molecule inhibitor, has a high selectivity for ERK1/2. BVD523 inhibits the proliferation of cancer cells, upregulates apoptosis-related genes, and attenuates ABCB1 and ABCG2-mediated chemoresistance [20, 21], making it a suitable candidate for treating drug-resistant cancers. Preclinical trials with BVD523, in combination with or without other chemotherapeutic agents, have shown promising outcomes [22–24]. Another ERK inhibitor, BIX02188, targets ERK5 by inhibiting the kinase activity of MEK5 [25]. Although not very well characterized, BIX02188 induces apoptosis in FLT3-mutated cancers such as AML [26].

In the current study, the GBM cell line U87MG was treated with sorafenib, BVD523 and BIX02188 their effect on proliferation, survival, migration and self-renewal was determined. We found that pan-RTK inhibition significantly downregulated the proliferation and migration of glioblastoma cells compared to the selective inhibition of ERK1/2, whereas ERK5 inhibition alone did not produce any significant effect.

2   Materials and Methods

2.1   Differential Gene Expression and Pathway Analysis

The clinical data of glioblastoma patients and their respective mRNA expression profiles were obtained from The Cancer Genome Atlas (TCGA) database (https://cancergenome.nih.gov/). TCGA-Glioblastoma multiforme (GBM) dataset contains 169 GBM samples and five normal samples. R statistical software (version 4.1.3; https://www.r-project.org/) and Bioconductor packages (http://www.bioconductor.org/) were used to process and normalize the raw data. The Limma package was utilized to identify the differential gene expression between the normal and tumor tissues. Pathway enrichment analysis for differentially expressed genes was determined using gProfiler.

2.2   Reagents and Cell Lines

High glucose DMEM, propidium iodide and protease inhibitor cocktail were obtained from Sigma-Aldrich. Fetal bovine serum, trypsin, phosphatase inhibitor cocktail, primary antibodies (anti-human) against phosphoERK1/2, beta-catenin, BCL2,

GAPDH and HRP conjugated secondary antibodies (anti-mouse and anti-rabbit) were procured from ThermoFisher Scientific. Fluorescent dye conjugated antibody against CD24 was purchased from ThermoFisher Scientific. BVD523 and BIX02188 were purchased from Selleck Chemicals LLC. Sorafenib was purchased from Natco Pharma Ltd. Glioblastoma cell line U87MG was purchased from NCCS, Pune, and plastic wares for cell culture were purchased from Eppendorf.

2.3   Colony Assay

Colony assay was carried out as previously described [27]. 100 cells/well were seeded in a 6-well plate and treated with the inhibitors. During pre-treatment, inhibitors were added for the initial 48 h, after which fresh media was added to induce the formation of the colonies. In some cases, treatment was extended until the completion of the experiment. The resulting colonies were counted microscopically after staining them with 0.1% crystal violet solution.

2.4   Protein Isolation and Immunoblotting

Cells were seeded, allowed to attach for 24 h, and treated with sorafenib or BVD523 for 48 h. As described previously, cells were lysed using RIPA buffer at the end of treatment period to collect the total protein [17, 27]. ~25 µg protein was loaded per well in a 10% polyacrylamide gel and transferred to a nitrocellulose membrane through semi-dry blotting. The membrane was incubated with the desired antibodies to detect the protein expression level.

2.5   Wound Healing Migration Assay

A previously published protocol was followed for the wound healing migration assay [17, 27]. 10,000 cells/cm^2 were added to each well of a 12-well plate and incubated until they formed a monolayer, following which they were serum-starved for 12 h. A scratch was made using a micro tip, and media containing the respective inhibitors was added to each well. Microscopic images were taken at regular intervals and analyzed further to determine the migration speed.

2.6   Spheroid Assay

Glioblastoma cells were seeded at a density of $0.5–2 \times 10^4$ cells/mL in a low-attachment 96-well plate for the formation of spheroids. The spheroids were imaged periodically, and their area was determined using ImageJ software.

2.7   Proliferation Assay

5000 cells/cm^2 were seeded in each well of a 24-well plate and allowed to attach. Cells were then treated with different concentrations of BVD523 for 48 h. The cells were trypsinized, counted, stained with propidium iodide (PI) and analyzed using a flow cytometer.

2.8   Surface Marker Analysis

Cell surface expression of CD24 was determined using a flow cytometer. Cells were trypsinized and stained with fluorescence conjugated antibody against CD24 for 30 min in the dark at 4°C and analyzed by flow cytometry.

2.9   Cell Cycle Analysis

A previously published protocol was followed to perform cell cycle analysis [28]. Following treatment with the respective inhibitors, the cells were fixed and permeabilized with 70% ice-cold ethanol, followed by RNase A treatment. DNA was stained using PI and analyzed with a flow cytometer.

2.10   Data Analysis

Images from colony and spheroid formation assays were analyzed using the ImageJ software. The migration of cells in the wound healing assay was analyzed using the TScratch software, and flow cytometric data were analyzed with FCS Express5. Quantification of protein bands in the Western blots was done using the ImageLab software (Bio-Rad) and normalized to GAPDH expression levels.
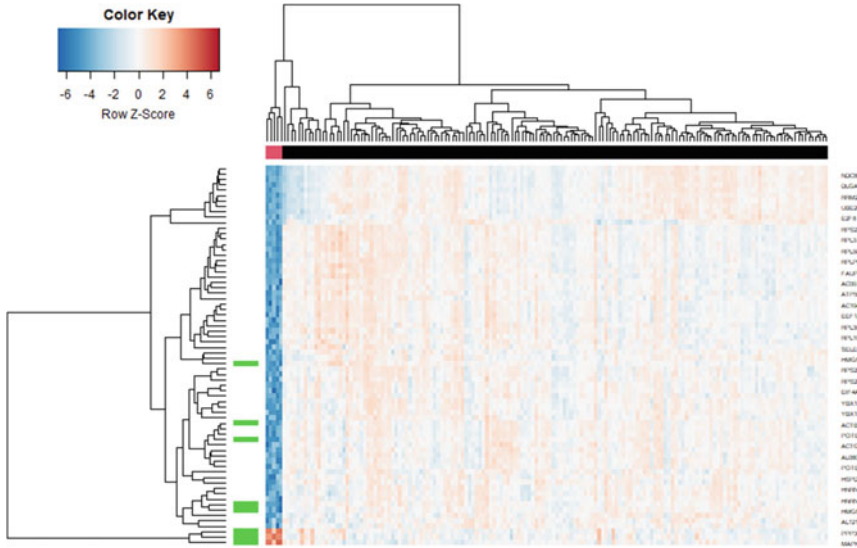
Fig. 1 Heatmap representing differentially expressed genes between normal and glioblastoma patients

3 Results

3.1 Identification of Differentially Expressed Genes and Pathways

The genes that are significantly differentially expressed between normal and glioblastoma tumor samples are shown in the heatmap (Fig. 1). The pathways linked to the differentially expressed genes are shown in the table (Table 1). MAPK signaling pathway was found to be dysregulated in the TCGA-GBM cohorts, along with the Wnt/β-catenin pathway. So, we studied the role of the MAPK pathway in vitro in glioblastoma cells using MAPK pathway inhibitors.

3.2 RTK Inhibition Decreases the Self-renewal, Proliferation and Migration of Glioblastoma Cells

Sorafenib was reported to inhibit the growth of glioblastoma cells and selectively inhibit the tumor-initiating population in primary cells [29, 30]. We previously reported that sorafenib (10 μM) significantly inhibits the proliferative, migratory and invasive abilities of breast cancer cells and modifies their intracellular signaling pathways [17]. Sorafenib treatment inhibited the tumor-initiating ability in GBM, where

Table 1 Pathways associated with differentially expressed genes in glioblastoma indicate dysregulation of the MAPK pathway

Significant	p value	Overlap. size	Term id	Term name
TRUE	0.0179	3	GO:0,002,764	Immune response-regulating signaling pathway
TRUE	0.00689	3	GO:0,002,768	Immune response-regulating cell surface receptor signaling pathway
TRUE	0.00439	2	KEGG:04,659	Th17 cell differentiation
TRUE	0.00851	2	KEGG:04,310	Wnt signaling pathway
TRUE	0.0351	2	KEGG:04,010	MAPK signaling pathway
TRUE	0.00695	2	KEGG:04,728	Dopaminergic synapse
TRUE	0.0138	2	KEGG:05,167	Kaposi sarcoma-associated herpesvirus infection
TRUE	0.0122	2	KEGG:05,152	Tuberculosis
TRUE	0.0178	2	KEGG:05,170	Human immunodeficiency virus 1 infection
TRUE	0.00406	2	KEGG:04,660	T cell receptor signaling pathway
TRUE	0.00623	2	KEGG:04,380	Osteoclast differentiation
TRUE	0.00322	2	KEGG:04,658	Th1 and Th2 cell differentiation
TRUE	0.00431	2	KEGG:04,625	C-type lectin receptor signaling pathway
TRUE	0.0229	2	MIRNA:hsa-miR-1178-3p	hsa-miR-1178-3p

the sorafenib-treated U87MG cells failed to form colonies (Fig. 2a). Furthermore, upon treatment with sorafenib, the GBM cells formed smaller spheroids, indicating that sorafenib inhibits cell proliferation and self-renewal ability (Figs. 2b, 4b). CD24 is a marker of stem cells in several cancers, including glioma [31–34] and we found a significant decrease in the CD24 + population after sorafenib treatment (Fig. 2c–d), suggesting that sorafenib treatment reduces the CSC population in GBM.

Protein expression analysis showed that sorafenib induces the accumulation of phosphoERK1/2 and downregulates the expression of β-CATENIN, implying that cell growth and proliferation were hindered. Further, a reduction in BCL2 expression was observed, which suggests that sorafenib redirected the cells towards apoptosis (Fig. 2e). Thus, we conclude that sorafenib decreases the self-renewal of glioblastoma cells and alters the MAPK/ERK signaling cascade, which is essential for proper cellular functioning.
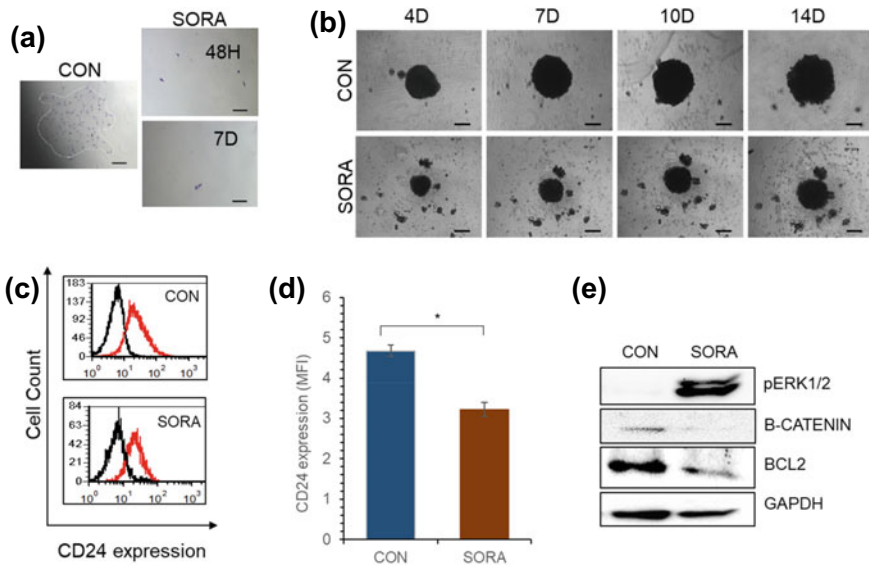
Fig. 2 a Colony formation assay was performed with control untreated U87MG cells (CON) or cells treated with sorafenib (SORA, 10 μM) for 48 h (48H) or 7 days (7D) **b** Spheroid formation assay was done without (CON) or with sorafenib treatment, and the spheroids were imaged at the intervals of 4, 7, 10 and 14 days (4, 7, 10, 14D). The black line indicates the scale bar (200 μm) in all the microscopic images **c** Flow cytometry analysis was done to determine the expression levels of CD24 on the surface of U87MG cells in untreated (CON), and sorafenib (SORA) treated cells **d** Represents the normalized Mean Fluorescence Intensity (MFI) of CD24 in U87MG cells. Values are mean ± SE, n = 3, *p < 0.05 **e** Western blotting was performed to determine the expression of phosphorylated ERK1/2 (pERK1/2), BCL2 and β-catenin after 48 h of SORA treatment, CON represents the untreated control cells

3.3 ERK1/2 Inhibition Decreased the Viability of Glioblastoma Cells in a Concentration-Dependent Manner

To further understand the effect of MAPK inhibition in GBM, we treated U87MG with the ERK1/2 selective inhibitor BVD523 (BVD) and determined its effect on proliferation and migration. The viability of U87MG glioblastoma cells decreased with increasing BVD concentration, with an IC_{50} of 10 μM (Fig. 3a, b). This reduction in cell survival was accompanied by a dramatic increase in the accumulation of phosphoERK1/2 and downregulation of β-CATENIN protein levels (Fig. 3c). Based on these results, 10 μM of BVD was used for further experiments.
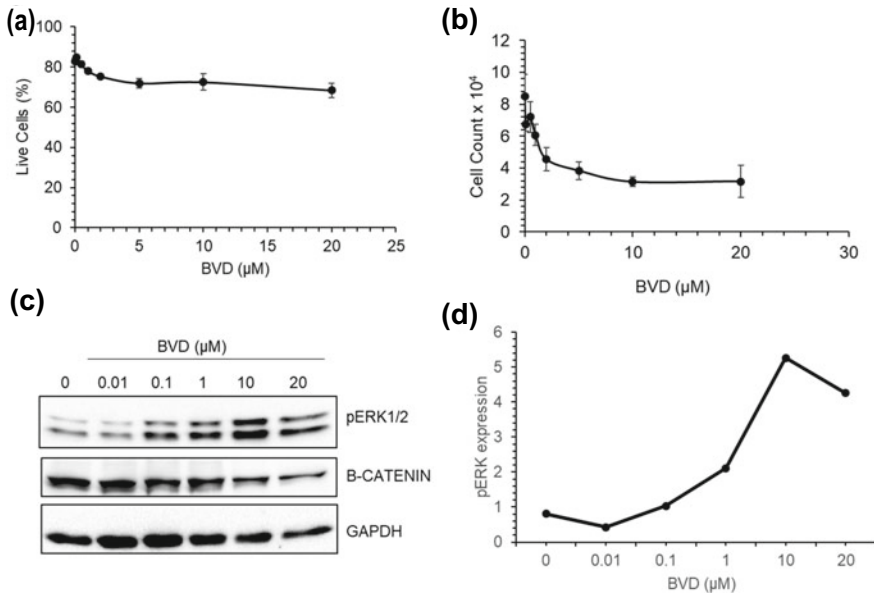
Fig. 3 **a** Live cell percentage post-treatment with the indicated concentrations of BVD523 (BVD) for 48 h was determined by staining with propidium iodide (PI) and analyzed using flow cytometer. **b** The cell count was determined after treatment with BVD for 48 h **c** Immunoblotting analysis was performed to determine the phosphoERK1/2 (pERK1/2) and β-CATENIN expression level after treatment with the indicated concentrations of BVD for 48 h. **d** The pERK1/2 levels shown in **c** were quantified and normalized against their respective GAPDH levels

3.4 ERK1/2 Inhibition Affects the Proliferative, Migratory and Self-renewal Ability of Glioblastoma Cells

Spheroid formation assay was performed to find the effect of BVD on the survival and proliferation of U87MG cells. BVD treatment significantly inhibited spheroid growth, and the inhibitory effect was sustained until 14 days (Fig. 4a, b). Cell cycle analysis showed that BVD treatment induces G0/G1 arrest in U87MG cells (Fig. 4c) in agreement with the reduced proliferation. However, we noticed a significant increase in the expression levels of CD24 after BVD treatment (Fig. 4d, e). BVD treatment, however, lowered the migration ability (Fig. 5a, b) and significantly decreased the colony formation ability (Fig. 5c, d). The colony formation ability was completely abrogated when treatment with BVD was extended beyond 72 h, suggesting that prolonged BVD treatment inhibits the self-renewability of U87MG cells. The effect of BVD on self-renewal was found to be irreversible, where the cells did not regain their colony formation ability when BVD was removed after 72 h of treatment.
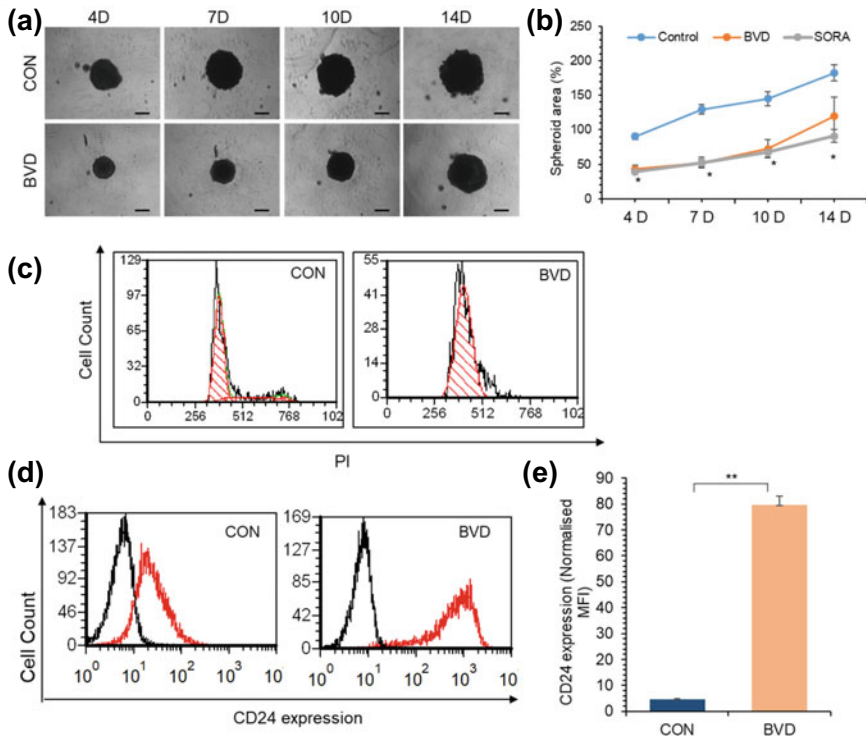
Fig. 4 **a** U87MG cells were allowed to form 3D spheroids in the absence (CON) or presence of BVD523 (10 µM, BVD). The black line shows the scale bar of 200 µm **b** The graph represents the spheroid size of U87MG cells upon treatment with sorafenib (SORA) or BVD523 (BVD) for the indicated time. **c** The cell cycle profile of untreated (CON) and BVD-treated U87MG cells was determined by PI staining through flow cytometric analysis. The histogram shows the cell cycle profile. **d** The cell surface expression of CD24 in control (CON) or BVD (10 µM, 48 h) treated U87MG cells was determined by flow cytometry analysis. The black and red lines indicate the isotype control and CD24 stained sample respectively. **e** Graph represents the CD24 expression levels in control (CON) and BVD-treated U87MG cells. Values are mean $\pm$ SE, n = 2–3, *$p < 0.05$, **$p < 0.005$

3.5 Effect of ERK5 Inhibition on Glioblastoma Migration and Self-renewal Ability

Next, we studied the effect of MEK5 inhibition on the self-renewal and migration of U87MG cells. MEK5, an upstream activator of ERK5, was inhibited by treatment with BIX02188. MEK5 inhibition did not affect the migration ability of U87MG cells, where the migration speed after treatment with BIX02188 (BIX) was similar to that observed with the control cells (Fig. 5a, b). The migration ability was significantly
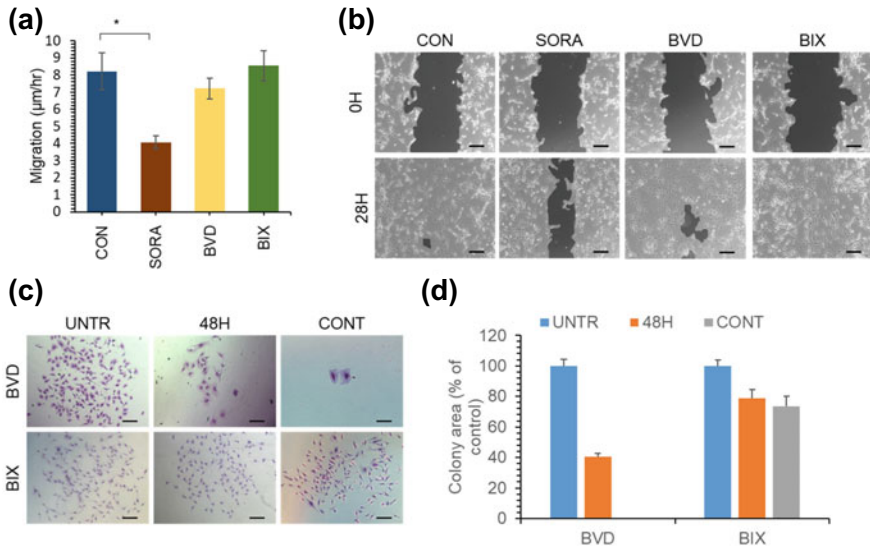
Fig. 5 **a**, **b** Migration of U87MG cells was checked by wound healing assay after treatment with sorafenib (SORA, 10 μM), BVD523 (BVD, 10 μM) and BIX02188 (BIX, 2 μM). **c** The ability of U87MG cells to self-renew was determined by colony formation assay after treatment with BVD or BIX for 48 h (48H) or continuously (CONT) throughout the duration of the assay. UNTR represents the untreated control **d** The graph represents the colony area represented in **c**. Values are mean ± SE, n = 2–3, *$p < 0.05$. The scale bar (200 μm) was indicated by black lines in all the microscopic images

inhibited, however, after sorafenib treatment. Nevertheless, we observed a moderate reduction in the colony formation ability with BIX treatment, and the prolonged treatment with BIX did not further inhibit the ability of U87MG cells to form colonies (Fig. 5c, d).

4   Discussion

Survival of a stem cell-like population in glioblastoma tumors after conventional treatment with temozolomide poses a significant challenge in preventing disease relapse [5]. This highlights the need for alternative therapeutic strategies to target self-renewing and chemoresistant cells in cancer. In this study, we found that MAPK pathway genes were differentially expressed in TCGA-GBM cohorts. So, we initially examined the effects of the broad-spectrum RTK inhibitor sorafenib on the proliferation, migration and self-renewal of glioblastoma cells. As reported by previous studies in glioblastoma [29], breast cancer [17] and hepatocellular carcinoma [35], sorafenib treatment inhibited colony formation in vitro, indicating that sorafenib abrogates the self-renewal ability. This was accompanied by a reduction in the cell

surface expression of CD24, a CSC marker [31–34]. Decreased migration in 2D culture and smaller spheroid size in 3D culture indicate that sorafenib treatment inhibits the metastatic and proliferation ability of glioblastoma cells.

Furthermore, the decreased survival and proliferation ability of GBM cells after sorafenib treatment was indicated by reduced BCL2 and beta-catenin levels, respectively. Interestingly, pERK1/2 levels were upregulated, in contrast to reduced pERK1/2 levels reported in hepatocellular and breast carcinomas [17, 36]. The mechanism of this upregulation in glioblastoma is not well understood but may be caused by the multikinase inhibitory activity of sorafenib on ERK1/2 rather than on its upstream activators, leading to altered feedback loops within the RAS/RAF/ERK pathway.

It is reported that elevated expression of pERK1/2 is associated with glioblastoma progression. In order to understand the mechanism, ERK1/2 inhibitor BVD523 was utilized in this study. BVD effectively reduced cell viability and proliferation in 2D and 3D cultures [37–39] and induced cell cycle arrest. BVD also inhibited the colony formation and migration ability of U87MG cells. BVD treatment altered two intrinsic signaling pathways, the RAS/RAF/ERK pathway and the Wnt/β-catenin pathway. β-catenin downregulation leads to reduced proliferation [40, 41]. However, a concentration-dependent increase of pERK1/2 levels after BVD treatment indicates its aberrant kinase activity rather than its phosphorylation status, thereby preventing activation of downstream targets [20]. Although sorafenib and BVD523 showed a similar effect in terms of abrogating tumor initiation, proliferation and migration, the effects observed were more pronounced with the former, implying that the activity of sorafenib is mediated by ERK1/2 inhibition in conjunction with inhibition of other tyrosine kinase receptors. Selective inhibition of MEK5 kinase activity, thereby ERK5 inhibition with BIX02188, moderately decreased the self-renewal ability of U87MG but did not alter the cell migration. Nevertheless, it cannot be concluded that ERK5 inhibition does not affect tumor proliferation or metastasis since the effect might become pronounced when used in combination with one or more inhibitors.

Thus, sorafenib and BVD523 effectively reduced tumor initiation, proliferation, survival and metastasis by altering the ERK signaling cascade, whereas BIX02188, when used alone, was not effective against the glioblastoma cells. However, combinatorial therapy with drugs and inhibitors that target alternate cellular mechanisms is therapeutically more beneficial than single pathway inhibition.

References

1. Tamimi AF, Juweid M (2017) Epidemiology and outcome of glioblastoma. In: De Vleeschouwer S (ed) Glioblastoma. Codon Publications Copyright, The Authors, Brisbane (AU)
2. Friedman HS, Kerby T, Calvert H (2000) Temozolomide and treatment of malignant glioma. Clin Cancer Res 6(7):2585–2597
3. Strobel H et al (2019) Temozolomide and other alkylating agents in glioblastoma therapy. Biomedicines 7(3)
4. Zhang J, Stevens MF, Bradshaw TD (2012) Temozolomide: mechanisms of action, repair and resistance. Curr Mol Pharmacol 5(1):102–114
5. Chen J et al (2012) A restricted cell population propagates glioblastoma growth after chemotherapy. Nature 488(7412):522–526
6. Colella B et al (2019) Autophagy induction impairs Wnt/β-catenin signalling through β-catenin relocalisation in glioblastoma cells. Cell Signal 53:357–364
7. Pearson JRD, Regad T (2017) Targeting cellular pathways in glioblastoma multiforme. Signal Transduct Target Ther 2:17040
8. Auffinger B et al (2015) The role of glioma stem cells in chemotherapy resistance and glioblastoma multiforme recurrence. Expert Rev Neurother 15(7):741–752
9. Friedmann-Morvinski D (2014) Glioblastoma heterogeneity and cancer cell plasticity. Crit Rev Oncog 19(5):327–336
10. Guo YJ et al (2020) ERK/MAPK signalling pathway and tumorigenesis. Exp Ther Med 19(3):1997–2007
11. Ramaswamy P, Nanjaiah ND, Borkotokey M (2019) Role of MEK-ERK signaling mediated adhesion of glioma cells to extra-cellular matrix: possible implication on migration and proliferation. Ann Neurosci 26(2):52–56
12. Wilhelm SM et al (2004) BAY 43–9006 exhibits broad spectrum oral antitumor activity and targets the RAF/MEK/ERK pathway and receptor tyrosine kinases involved in tumor progression and angiogenesis. Cancer Res 64(19):7099–7109
13. Bæk Møller N et al (2019) Drug-induced hypertension caused by multikinase inhibitors (Sorafenib, Sunitinib, Lenvatinib and Axitinib) in renal cell carcinoma treatment. Int J Mol Sci 20(19)
14. Decaens T et al (2021) Phase 1b/2 trial of tepotinib in sorafenib pretreated advanced hepatocellular carcinoma with MET overexpression. Br J Cancer 125(2):190–199
15. Hainsworth JD et al (2010) Concurrent radiotherapy and temozolomide followed by temozolomide and sorafenib in the first-line treatment of patients with glioblastoma multiforme. Cancer 116(15):3663–3669
16. Hosseinzadeh F et al (2018) Combinational immune-cell therapy of natural killer cells and sorafenib for advanced hepatocellular carcinoma: a review. Cancer Cell Int 18:133
17. Dattachoudhury S et al (2020) Sorafenib inhibits proliferation, migration and invasion of breast cancer cells. Oncology 98(7):478–486
18. Iyer R et al (2010) Sorafenib: a clinical and pharmacologic review. Expert Opin Pharmacother 11(11):1943–1955
19. Keating GM (2017) Sorafenib: a review in hepatocellular carcinoma. Target Oncol 12(2):243–253
20. Germann UA et al (2017) Targeting the MAPK signaling pathway in cancer: promising preclinical activity with the novel selective ERK1/2 inhibitor BVD-523 (Ulixertinib). Mol Cancer Ther 16(11):2351–2363
21. Ji N et al (2018) Ulixertinib (BVD-523) antagonizes ABCB1- and ABCG2-mediated chemotherapeutic drug resistance. Biochem Pharmacol 158:274–285
22. Buchbinder EI et al (2020) A phase II study of ERK inhibition by ulixertinib (BVD-523) in metastatic uveal melanoma. American Society of Clinical Oncology

23. Jiang H et al (2018) Concurrent HER or PI3K inhibition potentiates the antitumor effect of the ERK inhibitor ulixertinib in preclinical pancreatic cancer models ERK inhibition in pancreatic cancer. 17(10):2144–2155
24. Sullivan RJ et al (2018) First-in-Class ERK1/2 inhibitor ulixertinib (BVD-523) in ;atients with MAPK mutant advanced solid tumors: results of a phase I dose-escalation and expansion study. Cancer Discov 8(2):184–195
25. Tatake RJ et al (2008) Identification of pharmacological inhibitors of the MEK5/ERK5 pathway. Biochem Biophys Res Commun 377(1):120–125
26. Razumovskaya E, Sun J, Rönnstrand L (2011) Inhibition of MEK5 by BIX02188 induces apoptosis in cells expressing the oncogenic mutant FLT3-ITD. Biochem Biophys Res Commun 412(2):307–312
27. Sharma R et al (2022) BMP4 enhances anoikis resistance and chemoresistance of breast cancer cells through canonical BMP signaling. J Cell Commun Signal 16(2):191–205
28. Somaiah C et al (2015) Collagen promotes higher adhesion, survival and proliferation of mesenchymal stem cells. PLoS ONE 10(12):e0145068
29. Carra E et al (2013) Sorafenib selectively depletes human glioblastoma tumor-initiating cells from primary cultures. Cell Cycle 12(3):491–500
30. Yang F et al (2010) Sorafenib induces growth arrest and apoptosis of human glioblastoma cells through the dephosphorylation of signal transducers and activators of transcription 3. Mol Cancer Ther 9(4):953–962
31. Altevogt P et al (2021) Novel insights into the function of CD24: a driving force in cancer. Int J Cancer 148(3):546–559
32. Barash U et al (2019) Heparanase promotes glioma progression via enhancing CD24 expression. Int J Cancer 145(6):1596–1608
33. Ni YH, Zhao X, Wang W (2020) CD24, A review of its role in tumor diagnosis, progression and therapy. Curr Gene Ther 20(2):109–126
34. Wu H et al (2021) Prospects of antibodies targeting CD47 or CD24 in the treatment of glioblastoma. CNS Neurosci Ther 27(10):1105–1117
35. Liu L et al (2006) Sorafenib blocks the RAF/MEK/ERK pathway, inhibits tumor angiogenesis, and induces tumor cell apoptosis in hepatocellular carcinoma model PLC/PRF/5. Cancer Res 66(24):11851–11858
36. Caraglia M et al (2011) Oxidative stress and ERK1/2 phosphorylation as predictors of outcome in hepatocellular carcinoma patients treated with sorafenib plus octreotide LAR. Cell Death Dis 2(4):e150
37. Hsu FT et al (2019) Amentoflavone effectively blocked the tumor progression of glioblastoma via suppression of ERK/NF- κ B signaling pathway. Am J Chin Med 47(4):913–931
38. Hsu FT, Chiang IT, Wang WS (2020) Induction of apoptosis through extrinsic/intrinsic pathways and suppression of ERK/NF-κB signalling participate in anti-glioblastoma of imipramine. J Cell Mol Med 24(7):3982–4000
39. Lopez-Gines C et al (2008) The activation of ERK1/2 MAP kinases in glioblastoma pathobiology and its relationship with EGFR amplification. Neuropathology 28(5):507–515
40. Yu F et al (2021) Wnt/β-catenin signaling in cancers and targeted therapies. Signal Transduct Target Ther 6(1):307
41. Zhang Y, Wang X (2020) Targeting the Wnt/β-catenin signaling pathway in cancer. J Hematol Oncol 13(1):165

Ovarian Cancer G-Protein-Coupled Receptor 1 Inhibits Prostate Cancer Cell Migration Through the Downregulation of Casein Kinase 2 Alpha Gene

Puyam Milan Meitei, Naorem Tarundas Singh, Adhikarimayum Lakhikumar Sharma, and Lisam Shanjukumar Singh

1 Introduction

Ovarian cancer G-protein-coupled receptor (OGR1) is a member of proton-sensing GPCR [1]. OGR1 has been shown to be a metastasis suppressor gene in prostate [2], ovary and breast cancer [4, 5]. It has lower level of expression in metastatic tissues as compared to primary tumor tissues [3]. However, there had been reports of OGR1 functioning antagonistic roles in tumor and host cells. For example, when prostate cancer cells are injected into OGR1-knockout mice, there was inhibition of prostate cancer tumorigenesis [6]. Similarly, there was also significant inhibition of tumorigenesis in OGR1 knockout mice [7]. These reports suggest that although OGR1 has tumor metastasis-suppressing role, OGR1 of the host cell might play a role (involved or/and obligatory) for tumor development. The molecular mechanism employed by OGR1 for the suppression of metastasis is yet to be deciphered completely. There have been reports of activation of Rho by OGR1 but Rac1 downregulation in breast cancer cell lines [5]. We have recently reported that OGR1 inhibits A549 cells' migration through the upregulation of CSNK2A3 (CKα intronless) and NEP (neutral

P. M. Meitei · N. T. Singh · L. S. Singh (✉)
Department of Biotechnology, Manipur University, Canchipur 795003, Manipur, India
e-mail: shanju.lisam@manipuruniv.ac.in

A. L. Sharma
Center for Translational Medicine, Thomas Jefferson University, 1020 Locust Street, Philadelphia 19107, PA, USA

133

endopeptidase) genes via the activation of Rac/Cdc and MAPK pathways [8]. So, the other downstream signaling proteins of OGR1 entailed in the suppression of cancer cell metastasis need to be investigated.

Casein kinase 2 (CK2) consists of two catalytic and two regulatory subunits. There are two types of catalytic subunits—α (CK2α) and α′ (CK2α′) [9]. However, a new catalytic subunit, αP has been identified recently [10]. α is encoded by CSK2A1 and α′ is encoded by CSNK2A2 [9], and αP (CK2αP) is encoded by CSNK2A3 (also known as CK2α intronless gene or CSNK2A1P). CK2 has been implicated in many important cellular processes of vertebrates such as cell survival [11, 12], cell growth [13], cell proliferation [14], enhances cellular transformation [15, 16] and angiogenesis [17] and changes cell morphology [18]. Many studies have shown that its expression is often up-regulated in tumor cells both at transcript and protein level [19]. Its role in promoting tumorigenesis depends upon its differing modulations in important signaling pathways in various cancers. CK2α regulates numerous signaling pathways such as Hedgehog [20], JAK/STAT [21], NF-κB [22], Wnt [23, 24] and PTEN/ PI3K/ Akt-PKB [25–28] signaling pathways. However, there is no consensus in the notion that up-regulated expression of CK2 leads to tumorigenesis with poor prognosis such as its expression had been shown to be down-regulated in some tumors—(down-regulated expression of CK2α′ in ovarian, breast and pancreatic cancers) and its up-regulated expression in lung adenocarcinoma leads to higher survival time [29, 30]. Nonetheless, up-regulated expression of CK2 at both transcript and protein levels is associated with poor prognosis. Although CK2 expression in changes in gene dosage, epigenetic and post-translational regulation have been proposed, the mechanism of dysregulated expression of CK2 at both transcript and protein level in many cancers is yet to be revealed. Although CK2 expression is mainly regulated at the gene level, epigenetic and post-translational regulation of its expression has also been proposed, and the mechanisms of dysregulated expression of CK2 at both transcript and protein level in many cancers are yet to be revealed.

In this study, we investigate the cellular molecules involved and mechanism of OGR1-induced inhibition of prostate cancer metastasis.

2   Materials and Methods

Cell culture: PC3 and HEK293T cell lines were cultured according to the standard cell culture methods.

Chemicals: SP600125 (JNK inhibitor), SB203580 (p38 inhibitor) were procured from Abcam (Cambridge, UK). Pertussis toxin (PTX), FR180204 (ERK inhibitor) were procured from Sigma-Aldrich (Burlington, MA, USA).

Genes Transfer: PC3 cells were transiently transfected either with pcDNA3.1 or pcDNA3.1-OGR1; or co-transfected with pcDNA3.1-cdcT17N or pcDNA3.1-RacT17N using Lipofectamine 2000. SP600125, SB203580, FR180204 were treated to cells at working concentrations of 20 μM and PTX was used at 2.5 μM.

qPCR: Total RNAs from 8×10^5 cultured cells were extracted using RNA isolation kit (Qiagen, Hilden, Germany). cDNA was synthesized using 1 µg of isolated RNAs as template by M-MuLV Reverse Transcriptase (NEB, MA, USA). qPCR for β-actin, OGR1, CSNK2A1 and CSNK2A3 were performed using 1 µg cDNA as template in a reaction volume containing 5U Taq DNA polymerase (NEB).

The primers used for qPCR were:

Gene	Forward primer (5'–3')	Reverse primer (5'–3')
β-actin	GAGCCTCGCCTTTGCCGATG	CGATGCCGTGCTCGATGGGG
OGR1	CTGTCCTGCCAGGTGTGCGG	CACGCGGTGCTGGTTCTCGT
CSNK2A1	CCAAACATCAAGTCCAGCTTTGTC	ACCTCGGCCTAATTTTCGAACCA
CSNK2A3	ATTGCTCCCCACTCCATCGC	ACCTCGGCCTAATTTTCGAACCA

All the primers were procured from Xcerlis Genomics Laboratory (Ahmedabad, India).

Generation of CSNK2A1 lentiviral particles: To analyze the functional role of CK2α (CSNK2A1) in the suppression of PC3 cells' migration by OGR1, lentivirus construct of pLVX-CSNK2A1 along with the packaging and envelope plasmids were transfected into HEK293T cells. The medium with the viral particles was harvested after 48 h. The medium was filtered using sterile 0.2 µm syringe filter and was used to transduce control or OGR1 transfected PC3 cells for scratch assay.

In-vitro Scratch Assay: To determine the role of CK2α (CSNK2A1) on OGR1-induced suppression of metastasis, PC3 cells were seeded to 70–80% confluency in six-well plates. The cells were transfected with pcDNA3.1 or pcDNA3.1-OGR1. After 5 h, viral particles of pLVX-CSNK2A1 were used to transduce the transfected PC3 cells. Scratches were created in the monolayer cell by a 200 µl pipette tip. Images of the scratch areas were taken at 0, 12, 24 and 48 h.

Statistical analysis: All the above experiments were performed in triplicates. The results of these observations were presented as the mean $\pm$ SD using Microsoft Excel or GraphPad Prism 8.0. p values less than 0.05 were considered significant.

3 Results

3.1 OGR1 Downregulates the Expression of CSNK2A1 but Does not Change that of CSNK2A3

We have recently reported the suppression of A549 cells' migration by OGR1 through the upregulation of CSNK2A3 [8]. To investigate whether OGR1 regulates expression of CK2α in PC3 cells, pcDNA3.1 or pcDNA3.1-OGR1 was transiently transfected to PC3 cells. Transcript expressions of CK2α genes (CSNK2A1 and CSNK2A3) were determined by semi-qPCR. The results indicated that OGR1
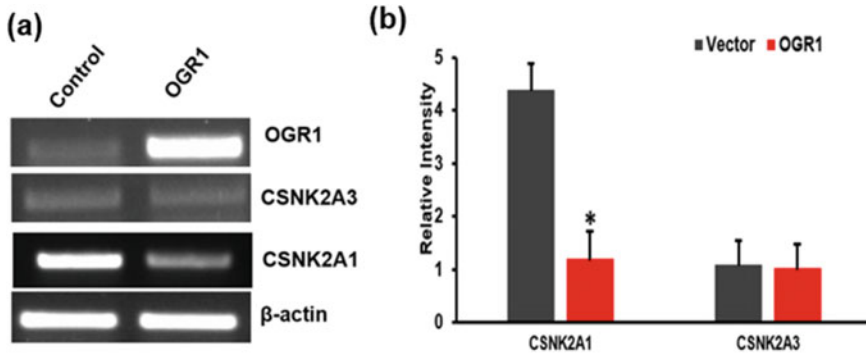
Fig. 1 OGR1 downregulates the expression of CSNK2A1 (CK2α), but do not change the expression of CSNK2A3 (CK2αP). pcDNA3.1 and pcDNA3.1-OGR1 were transfected into PC3 cells. **a** CSNK2A1 and CSNK2A3 transcript expression determined by semi-qPCR; **b** Graphical representation of relative intensities of CSNK2A1 and CSNK2A3 DNAs as interpreted by ImageJ after standardization to β-actin. Data are represented as mean $\pm$ SEM of 3 independent experiments. *$p < 0.05$
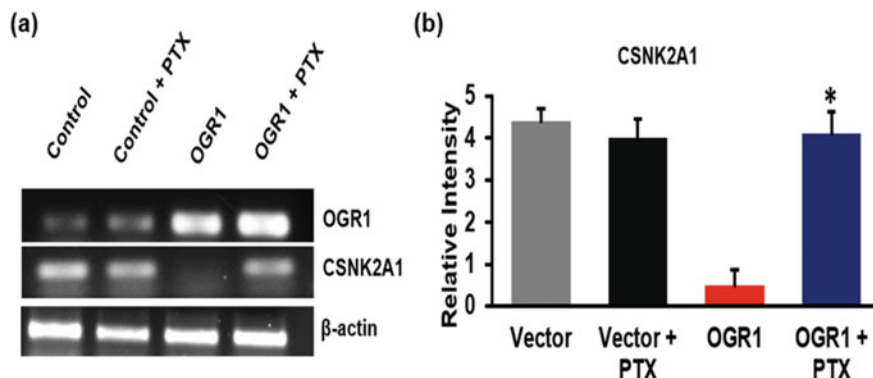
downregulated CSNK2A1 expression; however, the expression of CSNK2A3 did not alter (Fig. 1a, b). Our findings showed that the expression of CSNK2A1 is regulated despite having a housekeeping promoter.

3.2 Activation of Gαi Protein

Previously, we reported the activation of Gαi protein by OGR1 in inhibition of PC3 cell migration [2]. So, we investigated the involvement of Gαi for the downregulated expression of CSNK2A1 by OGR1 in PC3 cells by subjecting empty vector or OGR1 transfected PC3 cells with or without pertussis toxin (PTX) treatment. The result showed that the OGR1-induced down-regulated expression of CSNK2A1 was abrogated in the presence of PTX (Fig. 2a, b).

3.3 Downregulation of CSNK2A1 is Required for the Inhibition of PC3 Cells' Migration by OGR1

To determine the roles of CSNK2A1 in the suppression of PC3 cell migration by OGR1, we performed an in vitro wound-healing assay by co-expressing CSNK2A1 and OGR1 into PC3 cells. Control cells were prepared such that one set was transfected with empty vector and another set was transfected with empty vector and transduced with viral particles for CSNK2A1. The test cells were also prepared such that one set was transfected with OGR1 and another set was transfected with OGR1 and

Fig. 2 OGR1 downregulates CSNK2A1 expression in PC3 cells through the activation of Gαi protein: **a** PC3 cells were transfected with pcDNA3.1 or pcDNA3.1-OGR1 and treated with or without PTX drug (Gαi inhibitor). Transcript expression of CSNK2A1 was analyzed using semi-qPCR; **b** Graphical representation of relative intensities of CSNK2A1 and CSNK2A3 DNAs as interpreted by ImageJ after standardization to β-actin. Data are represented as mean ± SEM of three independent experiments. *p < 0.05

transduced with viral particles for CSNK2A1. OGR1-transfected PC3 cells showed suppression of migration as expected. However, there was a complete reversal of OGR1-induced suppression of cell migration in OGR1-overexpressed PC3 cells transduced with CSNK2A1 (Fig. 3a, b), suggesting that OGR1 downregulated CSNK2A1 to inhibit migration.

3.4 Down-Regulated Expression of CSNK2A1 by OGR1 Involved the Activation of Small G Proteins
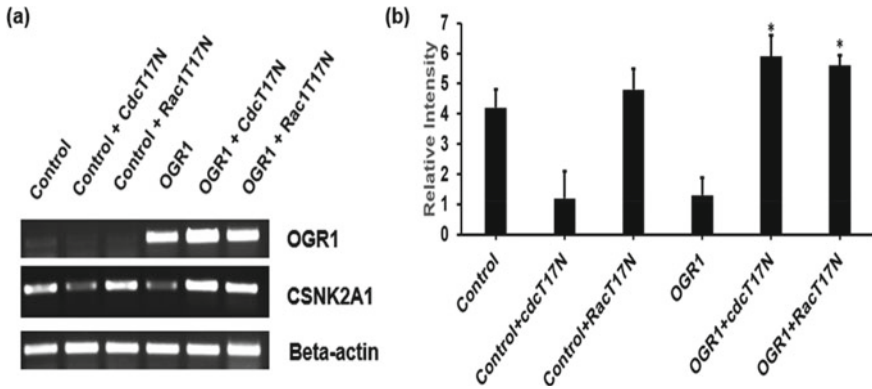
To investigate the involvement of Rac1 and cdc42 for the down-regulated expression of CSNK2A1 by OGR1, PC3 cells were transfected with pcDNA3.1 (Control) or pcDNA3.1-OGR1 (Test) alone. The control and test PC3 cells were also co-transfected with dominant negative mutant plasmids of cdc42 (cdcT17N) or Rac1 (RacT17N). The results showed that in the inhibition of cdc42 and Rac1, the down-regulated expression of CSNK2A1 by OGR1 in PC3 cells was completely abolished. The findings suggested that for the down-regulation of CSNK2A1 by OGR1 in PC3 cells involved the activities of both small G proteins, cdc42 and Rac1 (Fig. 4a, b).
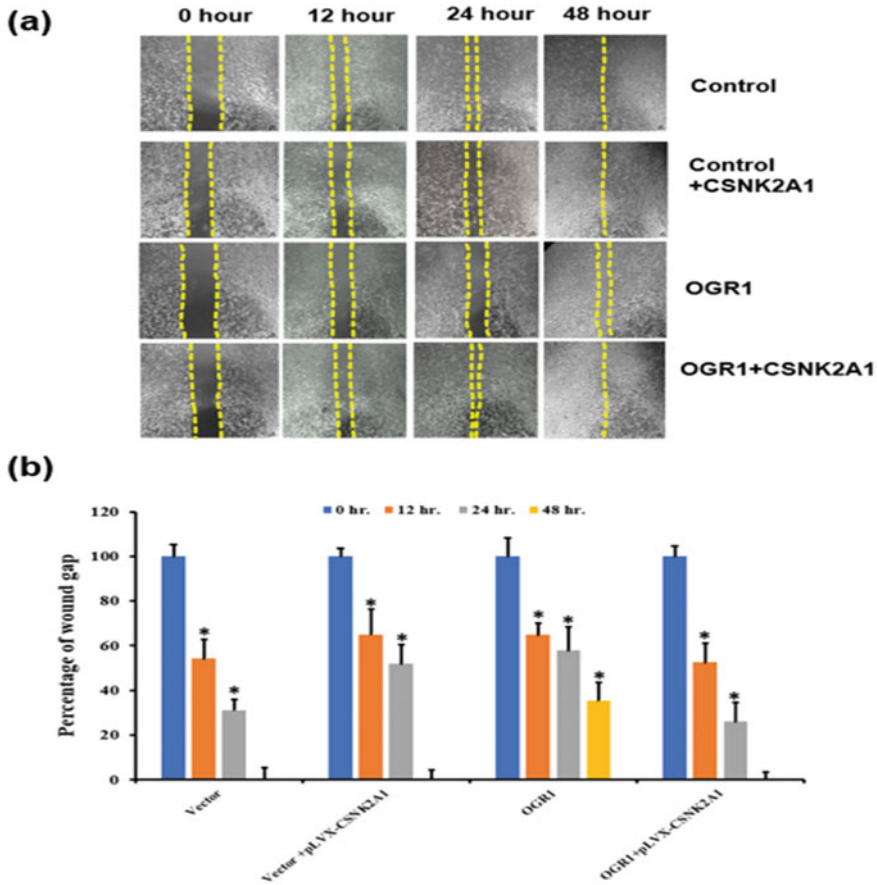
Fig. 3 **OGR1 inhibits PC3 cells' migration through the downregulation of CSNK2A1 in PC3**:
a PC3 cell migration was inhibited by OGR1, but in the overexpression of CSNK2A1, OGR1-
induced cell migration inhibition was completely abrogated. PC3 cells were transfected with
pcDNA3.1 or pcDNA3.1-OGR1 and transduced with viral particles of CSNK2A1. Cell migra-
tion was observed and images were captured at 0, 12, 24 and 48 h. after transfection; **b** The wound's
widths were measured using ImageJ software and plotted on the graph. For conversion of the
wound's widths into percentage, the wound's width of control transfected with empty vector at 0 h.
was calculated as 100%. The images are in 200 μm scale bar. Differences in the experimental data
of three independent experiments were used to calculate Mean $\pm$ SD and represented as error bars
on the graph. *$p < 0.05$

3.5 Down-Regulated Expression of CSNK2A1 by OGR1
Involved the Activation of MAPK Pathway

The MAPK pathways are involved in the relay of various cellular signals to cellular
responses [35–37] and oncogenesis [38] via the activation of G-proteins, we postu-
lated that MAPK pathway might play a major role for the downregulated expression

Fig. 4 GTPases: Rac/Cdc42 are requisite for OGR1-induced down-regulated expression of CSNK2A1 in PC3 cells: **a** OGR1-induced downregulation of CSNK2A1 was abrogated by the dominant negative mutants of Cdc42 and Rac1. PC3 cells were transfected with empty vector or OGR1 or co-transfected with dominant negative mutant plasmids of Cdc42 and Rac1 and CSNK2A1 was analyzed by qPCR. **b** Graphical representation of relative intensity of CSNK2A1 DNAs as interpreted by ImageJ after standardization to β-actin

of CSNK2A1 by OGR1, which leads to the inhibition of migration of PC3 cell. To investigate the involvement of MAPK pathways in the down-regulated expression of CSNK2A1 by OGR1, PC3 cells were transiently transfected with empty vector or OGR1, and the cells were treated with selective inhibitors for MAPK pathways. After 48 h. of transfection, CSNK2A1 expression was analyzed by qPCR. The inhibitors for MAPK pathways completely abolished the downregulated expression of CSNK2A1 by OGR1 (Fig. 5a, b). Thus, the results showed that PC3 cell migration is inhibited by OGR1 by down-regulating the expression of CSNK2A1 through the activation of the MAPK pathways.

4 Discussion

Cancer metastasis is the major cause of cancer deaths [30]. Thus, unriddling the various biological mechanisms involved in the complex process of metastasis is necessary for the combating cancer. OGR1 has been shown to be metastasis suppressor gene; however, the mechanism it employs to inhibit metastasis is yet to be unraveled. Our current study showed that OGR1 plays an important role in prostate cancer. The study presented here proved that OGR1 regulated the expression of CK2α, which is the key regulator of many aspects of cancers [11–18].

It has been well reported that the CK2α expression is elevated in most cancers examined at both transcript and protein level. The mechanisms for the overexpression and how the expression of CK2α is regulated are not clearly known. Our results showed that OGR1 downregulated CK2α expression, and this may provide an insight
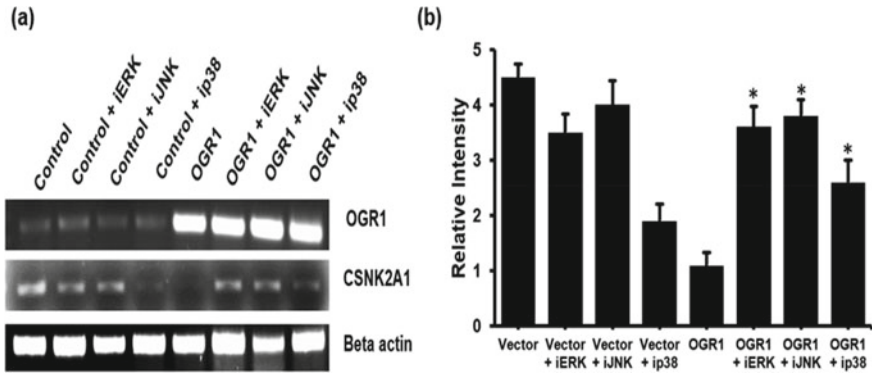
Fig. 5 MAPK pathways are requisite for OGR1-induced down-regulated expression of CSNK2A1 in PC3 cells: **a** OGR1-induced downregulated expression of CSNK2A1 was abolished by the inhibitors for MAPK pathways. PC3 cells were transfected with empty vector or OGR1 and treated with the selective inhibitors for MAPK proteins. **b** Graphical representation of relative intensity of CSNK2A1 DNAs as interpreted by ImageJ after standardization to β-actin. Data are represented as mean ± SEM of three independent experiments. *p < 0.05

of how the constitutively active enzyme is regulated and how its downregulated expression aids in the inhibition of metastasis by OGR1.

Recently, we have provided the first evidence that CK2α (CSNK2A3) is regulated by OGR1 in lung cancer cell line, A549 [8]. Further, our unpublished findings showed that OGR1 overexpression can induce K562 differentiation similar to phorbol 12-myristate 13-acetate (PMA) and downregulation of CSNK2A3 expression, but it upregulates CSNK2A1.

Rho GTPases, Rac1 and cdc42 played major roles in cancer tumorigenicity [31, 32]. Their activities are catalyzed by guanine nucleotide exchange factors (GEFs), which are activated by signaling from oncogenic cell surface receptors from various receptors including the GPCRs (G-protein-coupled receptors) [33, 34]. Our findings that inhibition of Rac1 and cdc42 abolished the downregulation of CK2α by OGR1 showed that these GTPases played an important role in inhibiting cancer cell migration through CK2α downregulation.

MAPK pathways play important roles such as cellular signaling [35–37] and oncogenesis [38]. G-proteins have been reported to activate the MAPK signaling pathways, thereby implicating the involvement of GPCRs as G-proteins are the secondary signaling molecules of GPCRs [39]. Our findings that the inhibition of MAPK pathways led to the abolishment of down-regulated expression of CSNK2A1 by OGR1 suggest the involvement of MAPK pathway in the regulation of CSNK2A1 expression by OGR1.

Our findings overall suggest that the expression of CK2α (CSNK2A1) is regulated by OGR1 in PC3 cells through the involvement of small GTPases (Rac1 and cdc42)

and MAPK pathways, thereby leading to suppression of cell migration. These mechanisms of CK2α regulation by OGR1 in prostate cancer are depicted in a graphical model (Fig. 6).

Finally, our results showed that OGR1, a G-protein-coupled receptor, is the regulator for CK2α (CSNK2A1) expression in PC3 cells and inhibits PC3 cell migration by down-regulating the expression of CK2α.

Fig. 6 Illustration diagram of OGR1 signaling pathway leading to suppression of metastasis in PC3 cells: OGR1 activates Gαi protein, which further activates Rho GTPases: Rac1 and Cdc42, ultimately activating the MAPK signaling pathways, which regulate the expression (decreases) of CK2α (CSNK2A1) gene in PC3 cells, and finally culminating into the suppression of metastasis (cell migration)
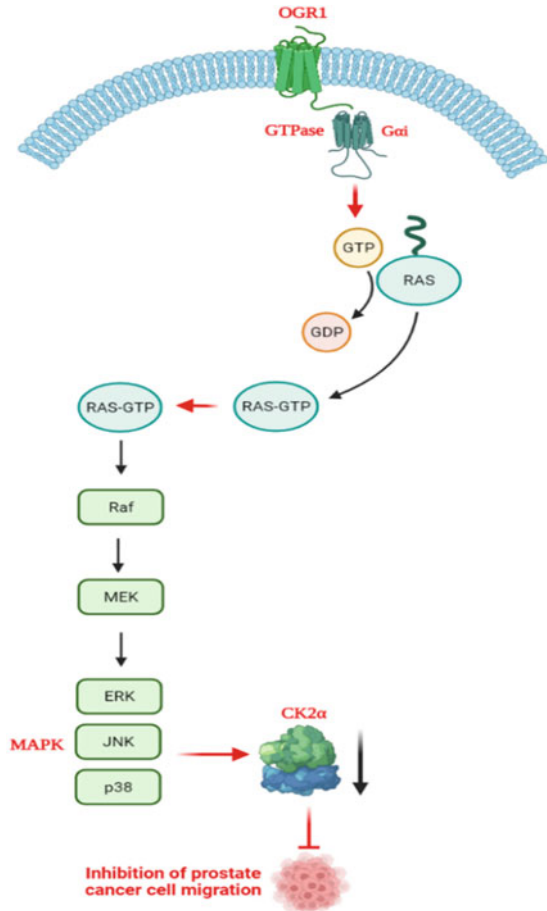
5 Conclusion

We showed that OGR1, by regulating CK2α expression in PC3 cells via the activation of G-proteins, GTPases: Rac1 and Cdc42 and MAPK pathways, inhibits migration of PC3 cells. Moreover, the present results also support our previous finding that OGR1 is the regulator of CK2α genes and consequently regulates cancer cell migration.

Author Contributions Puyam Milan Meitei, Naorem Tarundas Singh and Adhikarimayum Lakhikumar Sharma performed the experiments described in the manuscript. The experimental data were analyzed by Lisam Shanjukumar Singh and drafted the manuscript. Lisam Shanjukumar Singh audited and revised the manuscript. The whole project was supervised by Lisam Shanjukumar Singh. All authors scrutinized and accepted the final version of the manuscript.

Disclaimers The authors are solely responsible for the content and do not represent any influence or views of the funding agencies mentioned.

Disclosures No conflict of interest is declared by the authors.

References

1. Ludwig MG, Vanek M, Guerini D, Gasser JA, Jones CE, Junker U, Hofstetter H, Wolf RM, Seuwen K (2003) Proton-sensing G-protein-coupled receptors. Nature 425(6953):93–98
2. Singh LS, Berk M, Oates R, Zhao Z, Tan H, Jiang Y, Zhou A, Kirmani K, Steinmetz R, Lindner D et al (2007) Ovarian cancer G protein-coupled receptor 1, a new metastasis suppressor gene in prostate cancer. J Natl Cancer Inst 99(17):1313–1327
3. LaTulippe E, Satagopan J, Smith A, Scher H, Scardino P, Reuter V, Gerald WL (2002) Comprehensive gene expression analysis of prostate cancer reveals distinct transcriptional programs associated with metastatic disease. Cancer Res 62(15):4499–4506
4. Ren J, Zhang L (2011) Effects of ovarian cancer G protein coupled receptor 1 on the proliferation, migration, and adhesion of human ovarian cancer cells. Chin Med J (Engl) 124(9):1327–1332
5. Li J, Guo B, Wang J, Cheng X, Xu Y, Sang J (2013) Ovarian cancer G protein coupled receptor 1 suppresses cell migration of MCF7 breast cancer cells via a Galpha12/13-Rho-Rac1 pathway. J Mol Signal 8(1):6
6. Yan L, Singh LS, Zhang L, Xu Y (2014) Role of OGR1 in myeloid-derived cells in prostate cancer. Oncogene 33(2):157–164
7. Li H, Wang D, Singh LS, Berk M, Tan H, Zhao Z, Steinmetz R, Kirmani K, Wei G, Xu Y (2009) Abnormalities in osteoclastogenesis and decreased tumorigenesis in mice deficient for ovarian cancer G protein-coupled receptor 1. PLoS ONE 4(5):e5705

8. Sharma AL, Meitei PM, Machathoibi TC, Singh NT, Singh TR, Singh LS (2022) Ovarian cancer G protein-coupled receptor 1 inhibits A549 cells migration through casein kinase 2α intronless gene and neutral endopeptidase. BMC Cancer 22(1):143

9. Xu X, Toselli PA, Russell LD, Seldin DC (1999) Globozoospermia in mice lacking the casein kinase II alpha' catalytic subunit. Nat Genet 23(1):118–121

10. Singh LS, Kalafatis M (2002) Sequencing of full-length cDNA encoding the alpha and beta subunits of human casein kinase II from human platelets and megakaryocytic cells. Expression of the casein kinase IIalpha intronless gene in a megakaryocytic cell line. Biochemistry 41(28):8935–8940

11. Ahmed K, Davis AT, Wang H, Faust RA, Yu S, Tawfic S (2000) Significance of protein kinase CK2 nuclear signaling in neoplasia. J Cell Biochem Suppl Suppl 35:130–135

12. Ahmad KA, Wang G, Unger G, Slaton J, Ahmed K (2008) Protein kinase CK2–a key suppressor of apoptosis. Adv Enzyme Regul 48:179–187

13. Litchfield DW (2003) Protein kinase CK2: structure, regulation and role in cellular decisions of life and death. Biochem J 369:1–15

14. Pinna LA, Meggio F (1997) Protein kinase CK2 ("casein kinase-2") and its implication in cell division and proliferation. Prog Cell Cycle Res 3:77–97

15. Seldin DC, Landesman-Bollag E, Farago M, Currier N, Lou D, Dominguez I (2005) CK2 as a positive regulator of Wnt signalling and tumourigenesis. Mol Cell Biochem 274(1–2):63–67

16. Dominguez I, Sonenshein GE, Seldin DC (2009) Protein kinase CK2 in health and disease: CK2 and its role in Wnt and NF-kappaB signaling: linking development and cancer. Cell Mol Life Sci 66:1850–1857

17. Kramerov AA, Saghizadeh M, Caballero S, Shaw LC, Li Calzi S, Bretner M, Montenarh M, Pinna LA, Grant MB, Ljubimov AV (2008) Inhibition of protein kinase CK2 suppresses angiogenesis and hematopoietic stem cell recruitment to retinal neovascularization sites. Mol Cell Biochem 316(1–2):177–186

18. Canton DA, Litchfield DW (2006) The shape of things to come: an emerging role for protein kinase CK2 in the regulation of cell morphology and the cytoskeleton. Cell Signal 18(3):267–275

19. Tawfic S, Yu S, Wang H, Faust R, Davis A, Ahmed K (2001) Protein kinase CK2 signal in neoplasia. Histol Histopathol 16(2):573–582

20. Jia H, Liu Y, Xia R, Tong C, Yue T, Jiang J, Jia J (2010) Casein kinase 2 promotes Hedgehog signaling by regulating both smoothened and Cubitus interruptus. J Biol Chem 285(48):37218–37226

21. Zheng Y, Qin H, Frank SJ, Deng L, Litchfield DW, Tefferi A, Pardanani A, Lin FT, Li J, Sha B, Benveniste EN (2011) A CK2-dependent mechanism for activation of the JAK-STAT signaling pathway. Blood 118(1):156–166

22. Dominguez I, Sonenshein GE, Seldin DC (2009) Protein kinase CK2 in health and disease: CK2 and its role in Wnt and NF-kappaB signaling: linking development and cancer. Cell Mol Life Sci 66(11–12):1850–1857

23. Dominguez I, Mizuno J, Wu H et al (2004) Protein kinase CK2 is required for dorsal axis formation in Xenopus embryos. Dev Biol 274(1):110–124

24. Dominguez I, Mizuno J, Wu H, Imbrie GA, Symes K, Seldin DC (2005) A role for CK2alpha/beta in Xenopus early embryonic development. Mol Cell Biochem 274(1–2):125–131

25. Torres J, Pulido R (2001) The tumor suppressor PTEN is phosphorylated by the protein kinase CK2 at its C terminus. Implications for PTEN stability to proteasome-mediated degradation. J Biol Chem 276(2):993–998

26. Miller SJ, Lou DY, Seldin DC, Lane WS, Neel BG (2002) Direct identification of PTEN phosphorylation sites. FEBS Lett 528(1–3):145–153

27. Di Maira G, Salvi M, Arrigoni G, Marin O, Sarno S, Brustolon F, Pinna LA, Ruzzene M (2005) Protein kinase CK2 phosphorylates and upregulates Akt/PKB. Cell Death Differ 12(6):668–677

28. Park JH, Kim JJ, Bae YS (2013) Involvement of PI3K-AKT-mTOR pathway in protein kinase CKII inhibition-mediated senescence in human colon cancer cells. Biochem Biophys Res Commun 433(4):420–425

29. Wirkner U, Voss H, Lichter P, Weitz S, Ansorge W, Pyerin W (1992) Human casein kinase II subunit alpha: sequence of a processed (pseudo)gene and its localization on chromosome 11. Biochim Biophys Acta 1131(2):220–222
30. Eccles SA, Welch DR (2007) Metastasis: recent discoveries and novel treatment strategies. Lancet 369:1742–1757
31. Kazanietz MG, Caloca MJ (2017) The Rac GTPase in cancer: from old concepts to new paradigms. Cancer Res 77:5445–5451
32. Stengel K, Zheng Y (2011) Cdc42 in oncogenic transformation, invasion, and tumorigenesis. Cell Signal 23:1415–1423
33. Cook DR, Rossman KL, Der CJ (2014) Rho guanine nucleotide exchange factors: regulators of Rho GTPase activity in development and disease. Oncogene 33:4021–4035
34. Wertheimer E, Gutierrez-Uzquiza A, Rosemblit C, Lopez-Haber C, Sosa MS, Kazanietz MG (2012) Rac signaling in breast cancer: a tale of GEFs and GAPs. Cell Signal 24:353–362
35. Plotnikov A, Flores K, Maik-Rachline G, Zehorai E, Kapri-Pardes E, Berti DA, Hanoch T, Besser MJ, Seger R (2015) The nuclear translocation of ERK1/2 as an anticancer target. Nat Commun 6:6685
36. Koul HK, Pal M, Koul S (2013) Role of p38 MAP Kinase signal transduction in solid tumors. Genes Cancer 4(9–10):342–359
37. Burotto M, Chiou VL, Lee JM, Kohn EC (2014) The MAPK pathway across different malignancies: a new perspective. Cancer 120(22):3446–3456
38. Braicu C, Buse M, Busuioc C, Drula R, Gulei D, Raduly L, Rusu A, Irimie A, Atanasov AG, Slaby O, Ionescu C, Berindan-Neagoe I (2019) A Comprehensive review on MAPK: a promising therapeutic target in cancer. Cancers (Basel) 11(10):1618
39. Goldsmith ZG, Dhanasekaran DN (2007) G protein regulation of MAPK networks. Oncogene 26(22):3122–3142

Heterologous Expression, Purification, and Biological Activity Determination of Codon-Optimized Human MAFA Transcription Factor from *E. coli*

Gloria Narayan, Shirisha Nagotu, and Rajkumar P. Thummer

Keywords MAFA · *E. coli* · Recombinant protein · Secondary structure · PANC-1 cells · Bioactivity · Insulin gene

1 Introduction

Insulin is a hormone that controls the blood glucose levels by facilitating glucose uptake and is produced only by β-cells in the endocrine pancreas. Its secretion is significantly insufficient in diabetic patients due to depletion in number of functional β-cells, which causes prolonged high blood glucose level. In longer run, diabetes is reported to cause multiple health complications like neuropathy, nephropathy, retinopathy, and cardiovascular diseases [1–5]. Therefore, multiple studies have been performed over the years to comprehend the transcriptional cascade involved in diabetes [6–8].

Musculoaponeurotic fibrosarcoma oncogene family A or MAFA is one of the factors that has been investigated by different groups to understand pancreatic development in both human and mouse models and its contribution in diabetes. In mice, MafA expression is observed first at E13.5, while in human, MafA is not detected

G. Narayan · R. P. Thummer (✉)
Laboratory for Stem Cell Engineering and Regenerative Medicine, Department of Biosciences and Bioengineering, Indian Institute of Technology Guwahati, Guwahati 781039, Assam, India
e-mail: rthu@iitg.ac.in

G. Narayan
e-mail: gloria@iitg.ac.in

S. Nagotu
Organelle Biology and Cellular Ageing Lab, Department of Biosciences and Bioengineering, Indian Institute of Technology Guwahati, Guwahati 781039, Assam, India
e-mail: snagotu@iitg.ac.in

145

until 21st week, and its expression gradually increases postnatally [6]. MafA belongs to large basic leucine zipper family of the transcription factors [7]. Its expression is exclusively detected in β-cell lines [8, 9]. It binds to RIPE3b, which is an enhancer element that regulates insulin gene expression [8]. MafA was known first as β-cell-specific transcription factor, which was shown to bind to the C1 element of insulin gene [10]. Later, MafA was also reported to interact with NeuroD1 and Pdx1 and binds to Maf-responsive/recognition elements via a consensus DNA-binding sequence [TGCTGAC(G)TCAGCA] and activated insulin gene expression in rat islets [8, 11, 12]. It interacts with NeuroD1 and Pdx1 to activate insulin gene expression in β-cells by binding to Maf responsive element [8, 12, 13]. This finding was further demonstrated by Zhang and co-workers using a MafA-deficient mouse [14]. This group demonstrated that MafA double-negative mutant mice developed diabetes and showed impaired glucose-stimulated insulin secretion [14]. Moreover, pancreatic islet abnormalities and decreased expression of many key β-cell-specific transcription factors like insulin1, insulin2, Pdx1, Beta2 and Glut2 were also observed in *MafA* mutant mice [14]. Studies conducted in type 2 diabetic patients observed that these patients have compromised MafA expression, which leads to poor glucose-stimulated insulin secretion [15]. In case of type 1 diabetic patients and nonobese diabetic mouse, deletion of MafA showed decreased *Ins2* expression and activated antibodies targeting endogenous pancreatic islets [16, 17]. MafA has also been reported to contribute hugely to the field of cellular reprogramming and has been associated with generating insulin[+] β-cells from pluripotent, multipotent and terminally differentiated cells, which mimicked the endogenous β-cells in terms of glucose responsiveness [18, 19].

Recombinant protein as therapeutic agents or protein-based cellular reprogramming is the safest and a promising substitute in comparison to its viral counterparts [20, 21]. These purified proteins can then be directly delivered into target cells to activate a signaling cascade or regulate the target genes. Remarkably, this method does not manipulate the genome of the target cells, which makes it apt for the formation of clinical-grade human cells [20, 21]. Additionally, there is complete control over time and amount of proteins for application. Many studies have successfully purified recombinant protein from heterologous system and has proved these proteins to be biologically active in mammalian cells [22–30]

Here, we report fusion of a nuclear localization signal/sequence (NLS), cell-penetrating peptide (Transactivator of transcription; TAT), and a Histidine patch (8xHis) to both ends of codon-optimized human MAFA cDNA sequence prior to expressing in the bacterial expression vector. Further, native purification, determination of secondary structure, and demonstration of biological activity of the tagged protein were performed.

2 Materials and Methods

2.1 Strains, Plasmids, Reagents, and Cell Lines

The plasmids containing our gene of interest in pUC cloning vector along with fusion tags (pUC-HTN-*GOI* and pUC-*GOI*-NTH) were obtained from GenScript. BL21(DE3) strain of *E. coli* was used as expression host to produce recombinant MAFA fusion protein. Culture media like Lysogeny broth (LB), Tart-off Hobbs HiVeg broth (TB) and chemicals likesodium chloride, sodium phosphate, isopropyl β-D-1-thiogalactopyranoside (IPTG), kanamycin and imidazole were procured from HiMedia. Bradford reagent was obtained from Bio-Rad. Cell culture consumables were purchased from Invitrogen.

PANC-1 cells were purchased from NCCS, Pune (India) and was cultured in cancer growth culture media [Dulbecco's Modified Eagle medium, fetal bovine serum (10%) and penicillin–streptomycin solution (1%)].

2.2 Cloning and Soluble Expression of Heterologous MAFA Fusion Proteins

The sequence (codon-optimized) of human MAFA gene (NM_201589.3) was cloned along with a NLS, TAT, a Histidine patch (8xHis) at either end in a pET28a(+) protein expression vector to generate pET28a(+)-HTN-*MAFA* (HTN-*MAFA*) and pET28a(+)-*MAFA*-NTH (*MAFA*-NTH) constructs. Cloning was further corroborated using restriction digestion and Sanger sequencing. The detailed procedure is depicted in Fig. 1. Competent *E. coli* BL21(DE3), prepared using the traditional CaCl$_2$ method, were transformed with either HTN-*MAFA* or *MAFA*-NTH. For carrying out soluble expression studies, the same approach was used as described earlier [22, 24, 25]. The cells were lysed using the lysis buffer mentioned in Table 1.

2.3 Purification Under Native Conditions and Desalting of Purified Recombinant Protein

Purification of MAFA-NTH was carried out from 1.2 L of lysate. Lysate was centrifuged and bacterial pellet was resuspended and subjected to ultrasonication until the solution was clear. This total lysate was further centrifuged for the next 30 min at 8000 rpm (4 °C) to yield a supernatant fraction containing our protein of interest. Next, native purification was carried out as described previously [22, 31]. The detailed buffer composition is provided in Table 1. Collected samples were analyzed
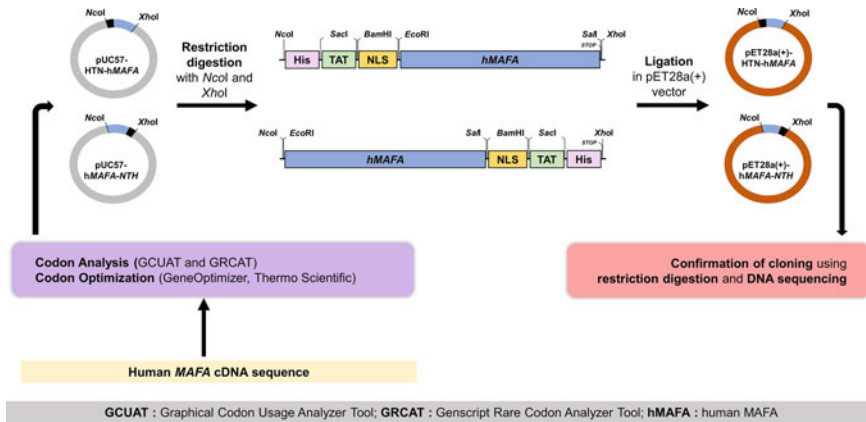
Fig. 1 **Pictorial representation of the codon optimization and cloning strategy**. H, Histidine; T, TAT, Trans-Activator of Transcription; N, NLS, Nuclear Localization Sequence/Signal

Table 1 Composition of buffers used for the MAFA-NTH native purification (at pH 7.5)

Composition	Lysis buffer	Wash buffer 1	Wash buffer 2	Elution buffer
Phosphate buffer (mM)	20	20	20	20
Sodium chloride (mM)	300	300	300	300
Imidazole (mM)	20	200	400	1500

using techniques, namely, SDS-PAGE and immunoblotting. Next, the eluted purified protein is desalted in PD10 columns (GE Healthcare), buffer exchanged against glycerol buffer and stored at freezing conditions ($-80\ °C$).

2.4 SDS-PAGE, Coomassie Staining, and Immunoblotting Analysis

SDS-PAGE, Coomassie staining, and immunoblotting were performed as previously described [24]. The antibodies used for different techniques and their respective concentrations are mentioned in Table 2.

2.5 Circular Dichroism on the Purified MAFA-NTH Protein

The far UV circular dichroism spectroscopy (CD) was used in this work to study the purified recombinant MAFA protein secondary structure. The spectra were analyzed

Table 2 Summary of primary and secondary antibodies used for different techniques

Antibodies	Dilution			Company	Cat. No
	Western blotting	Immunostaining	Subcellular fractionation		
Anti-His	1:5000	N/A	N/A	BioBharati	BB-AB0010
Anti-MAFA	1:1000	1:100	1:500	Cell signaling technology	D2Z6N
Anti-H3	N/A	N/A	1:5000	BioBharati	BB-AB0055
Anti-GAPDH	N/A	N/A	1:5000	BioBharati	BB-AB0060
Anti-Rabbit IgG, Alexa Fluor	N/A	1:1000	N/A	Invitrogen	410,407
Anti-Rabbit IgG, HRP-conjugated	1:5000	N/A	1:5000	Invitrogen	32,460

using the same parameters previously described [22, 31]. The spectra were further scrutinized by online tool BeStSel (Beta Structure Selection) [32].

2.6 Stability of MAFA Fusion Protein at Cell Culture Conditions

Stability of MAFA fusion protein at cell culture conditions was carried out as described previously [26]. Samples were collected and centrifuged to remove aggregated protein molecules and supernatants were stored (-20 °C). Samples were next thawed and mixed with sample solubilizing buffer and analyzed using anti-His antibody in immunoblotting.

2.7 Immunostaining, Microscopy, and Subcellular Fractionation

Subcellular fractionation, immunostaining, and microscopy were performed as reported earlier [22, 23, 26]. The fractions in subnuclear fractionation were analyzed by immunoblotting. The antibodies used for different techniques and their respective concentrations are mentioned in Table 2.

Table 3 Primer sequences used in this study for RT-qPCR analysis

Gene name	Primer sequence (5'–3')
Insulin	Forward: 5′-TCACACCTGGTGGAAGCTC-3′ Reverse: 5′-ACAATGCCACGCTTCTGC-3′
GAPDH	Forward: 5′-GTCTCCTCTGACTTC AACAGCG-3′ Reverse: 5′-ACCACCCTGTTGCTG TAGCCAA-3′

2.8   RT-QPCR Analysis

RNA isolation, cDNA synthesis, and RT-qPCR were performed as described earlier [23, 27]. The primer sequences of human insulin and GAPDH genes are listed in Table 3.

2.9   Statistical Analysis

Data analysis (unpaired student's t-test) was performed using the GraphPad Prism 8 software. Data are expressed as Mean $\pm$ SEM. * p < 0.05 is considered statistically significant.

3   Results and Discussion

3.1   Cloning and Expression Parameter Optimization

The human MAFA sequence (codon-optimized) along with the fusion tags (Figs. 1 and 2 (top)) was cloned into pET28a(+), and the genetic constructs were verified using restriction digestion (Fig. 2 (bottom)) and DNA sequencing. These generated genetic constructs were transformed for expression study. Multiple expression parameters like inducer concentration (IPTG in mM), cell density (OD_{600}) and time of induction (in h) were identified for maximal soluble expression (Table 4).

Expression analysis revealed that maximal soluble expression was observed for MAFA-NTH at 37 °C. In the case of HTN-MAFA, only a small amount of protein was observed in the supernatant fraction and was thus excluded from further analysis (Fig. 3). However, multiple truncations were also observed in the expression of MAFA-NTH recombinant protein (Fig. 3), most likely due to the proteolysis of few MAFA protein molecules during expression and solubilization [33]. Moreover, this analysis also demonstrated no leaky MAFA expression as uninduced cultures showed
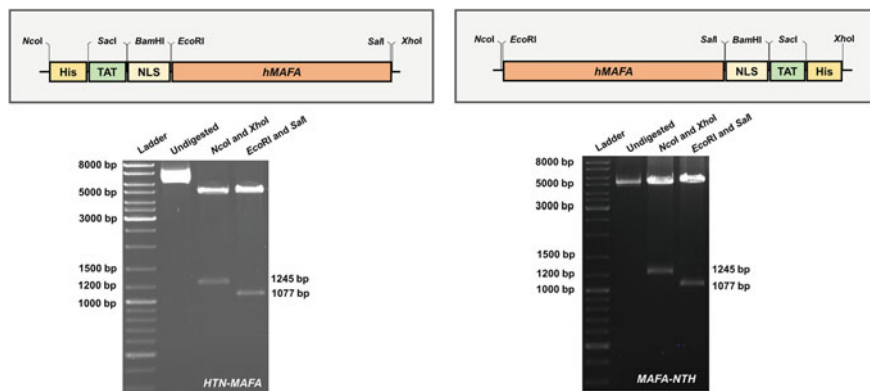
Fig. 2　Cloning of HTN-*MAFA* and *MAFA*-NTH in expression vector (pET28a(+)). The *MAFA* cDNA sequence along with the fusion tags was fused to vector backbone to generate pET28a(+)-HTN-*MAFA* and pET28a(+)-*MAFA*-NTH. The resulting genetic constructs were then analyzed by restriction digestion using a set of restriction enzymes. *GOI*, *Gene of interest*; H, His; T, TAT and N, NLS

Table 4　Summary of the expression parameters screened to attain maximal expression

| Expression parameters	Values screened	Optimal value
Inducer concentration (IPTG) (in mM)	0.05, 0.1, 0.25, 0.50	0.25
Induction cell density (OD$_{600}$)	~0.5, ~1.0, ~1.5	~0.5
Post-induction incubation time (in hours)	2, 4	2

no MAFA expression (Fig. 3). Based on these findings, MAFA-NTH recombinant protein was used for subsequent affinity-based native purification.

3.2　Purification and Secondary Structure Estimation of MAFA-NTH

We next purified MAFA-NTH using affinity chromatography from the soluble fraction. For this, MAFA-NTH was induced in 1.2 L of TB culture media, supplemented with 50% glycerol, for 2 h at 37 °C with 0.25 mM of IPTG at shaking condition. Post induction, the culture was clarified using centrifugation, and then native purification was carried out using IMAC (Fig. 4; top). Samples were collected at every purification step for further analysis. The purified MAFA-NTH protein was detected

Fig. 3 Determination of the optimal genetic construct to achieve maximal soluble MAFA fusion protein. *E. coli* BL21(DE3) strain was transformed with pET28a(+)-HTN-*MAFA* or pET28a(+)-*MAFA*-NTH at 37 °C (post-incubation time of 2 h). The harvested cells were lysed to get cell lysate fraction and centrifuged to obtain a supernatant cell fraction and pellet fraction. Collected samples (20 µg) were loaded on SDS-PAGE gel and also verified by immunoblotting. kDa, kilodaltons; α-His, anti-His Antibody. (n = 4) * Truncation of fusion proteins
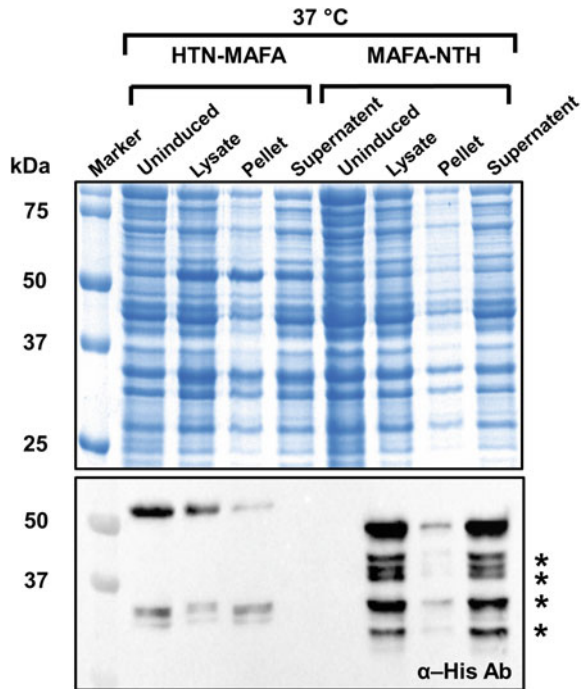
using Histidine antibody (Fig. 4; bottom). The calculated molecular weight of the protein along with the tags is 44.5 kDa and we observed our protein of interest at ~48 kDa. Interestingly, we also observed multiple truncated protein bands along with the full-length protein. Moreover, the protein loss was also observed in the flow-through fraction, which could be due to overloading of supernatant fraction to the purification column (Fig. 4; top) (for ~6 g of bacterial wet pellet, resin used is ~3 ml (2:1)).

Post-purification MAFA-NTH, we planned to determine whether the purified protein upheld its secondary structure. To understand this, we desalted and buffer exchanged the purified protein and performed far UV CD spectroscopy. This spectroscopic method is widely used method to understand the folding features of proteins where the secondary structure is not determined [32, 34]. The spectra analysis revealed that the secondary structure of the purified MAFA fusion protein was upheld (Fig. 5a). The secondary structure was then estimated using the BeStSel tool (Fig. 5b). The results showed that the secondary content of purified MAFA-NTH contained predominantly random coils (~48%) and α-helices and β-sheets contents was ~20% and ~18%, respectively, and the amount of turns was ~14% (Fig. 5b). The result confirmed that the purified recombinant MAFA-NTH upheld the secondary structure post native purification and desalting. However, the complete crystal structure of human MAFA protein is not available and thus further analysis is still required.
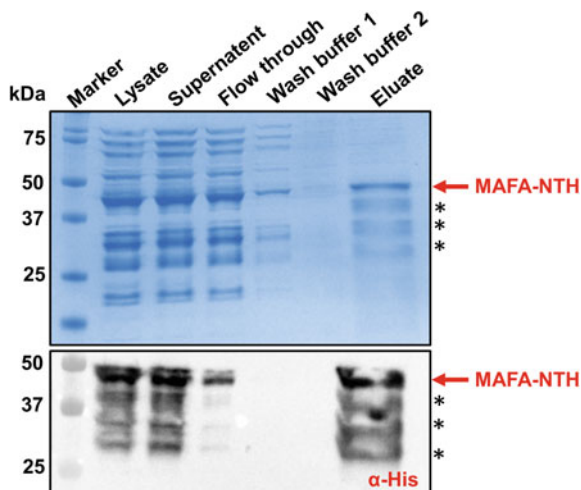
Fig. 4 Purification of recombinant MAFA-NTH under native conditions. MAFA-NTH native purification. kDa, kilodalton; α-His, anti-His Antibody
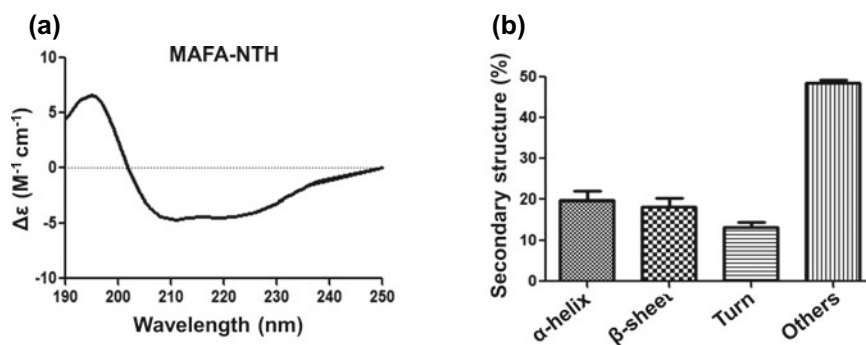
Fig. 5 Secondary structure determination of MAFA fusion protein using far-UV CD spectroscopy. The purified protein was analyzed for its secondary structures and its CD spectra are shown in (**a**). **b** Quantified secondary content is denoted using bar graphs (n = 4)

3.3 Stability and Internalization of MAFA-NTH Protein

Protein stability assay was carried out to understand the stability of the recombinant MAFA-NTH in protein transduction media containing 200 nM of purified protein. The media was incubated under standard cell culture condition and the figure clearly depicts that the fusion protein is stable for 72 h, which was identified using histidine antibody (Fig. 6a).

Next, we confirmed the transduction ability of MAFA-NTH into mammalian cells using immunofluorescence and subcellular fractionation. Pancreatic ductal cancer
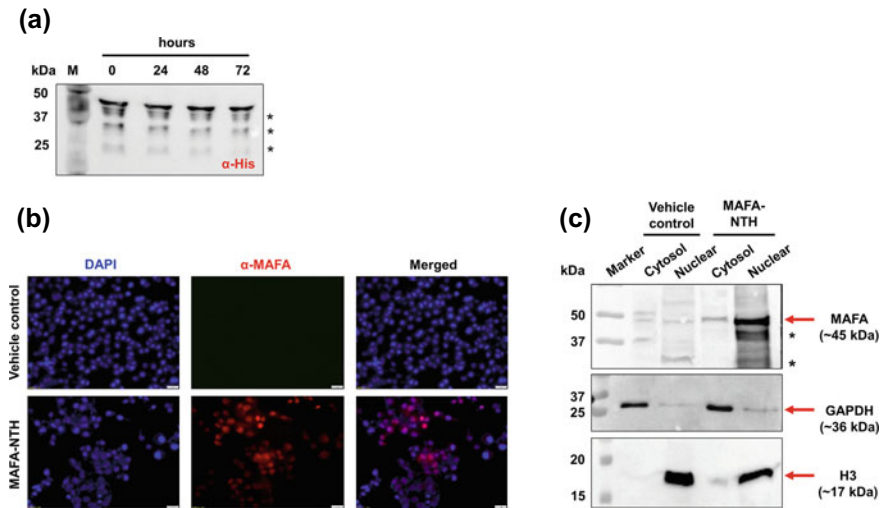
**Fig. 6 Stability and transduction ability of MAFA fusion protein**. **a** Stability of MAFA-NTH recombinant protein under cell culture conditions, analyzed using immunoblotting. **b** Image showing nuclear translocation of MAFA-NTH in PANC-1 cells **c** Representative Western blots showing cytosol and nuclear fractions of MAFA-NTH protein treated or untreated in PANC-1 cells using MAFA, GAPDH, and H3 antibodies

cells, PANC-1 do not have endogenous MAFA expression and thus, were used for these studies. The overnight treated cells were subjected to immunostaining and imaged using fluorescence microscopy. The images confirmed the effective uptake of recombinant MAFA-NTH in PANC-1 cells (Fig. 6b). Moreover, subcellular fractionation was also performed to further validate our findings. For this, Histone H3 and GAPDH antibodies were used as internal controls to confirm nuclear and cytosolic fractions, respectively. We observed that majority of the fusion protein was in the nuclear fraction and small amount of protein molecules were also present in the cytosolic fraction (Fig. 6c). This suggested that the fusion of NLS has increased the internalization capacity of the recombinant MAFA-NTH fusion protein inside the mammalian cells. Previously, Lu and group have also purified MAFA protein, however, the study had protein internalization issues due to the absence of NLS in the construct [35].

3.4 Effect of the Recombinant MAFA-NTH Protein on Insulin Gene Expression

Next, we carried out experiments to validate the biological activity of MAFA-NTH recombinant protein on mammalian cells. To achieve this, MAFA-NTH fusion protein was transduced into PANC-1 cells. It was previously reported that PANC-1

Fig. 7 Effect of the purified MAFA-NTH fusion protein on insulin gene expression in PANC-1 cells. Induction of insulin gene is observed upon MAFA-NTH treatment. Quantitative statistics are shown as the mean ± SEM (n = 3). *P < 0.05
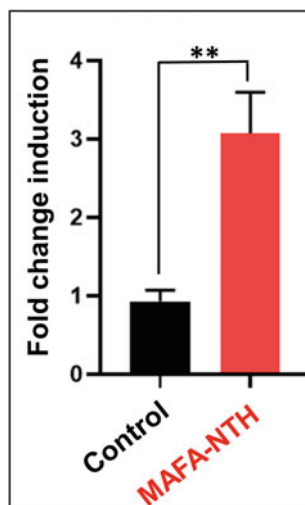
do not have endogenous insulin expression [36] and MAFA directly affects insulin gene expression by binding to the MARE element present on the insulin gene [11, 16]. As a result, treatment of cells with MAFA-NTH recombinant protein should upregulate insulin expression. To corroborate this, PANC-1 cells were treated with 200 nM of purified recombinant MAFA-NTH for 5 days and the fold change in insulin mRNA was analyzed by RT-qPCR. We observed approximately three-fold change in the insulin mRNA level in the treated cells compared to their counterparts (Fig. 7). Similar experiment was carried out by Kataoka and group where they demonstrated that MAFA alone can strongly activate insulin gene expression in NIH3T3 cells and our findings are in line with the previous findings [8]. Study conducted by Lu and co-workers reported the purification of recombinant mouse MAFA from BL21(DE3) strain. However, the protein failed to efficiently translocate to the nucleus and as a result the activation of downstream target genes were significantly impaired [35]. This could be due to the lack of addition of NLS along with the full-length coding sequence. Thus, we have successfully purified recombinant MAFA from *E. coli* from soluble fraction under native condition. Moreover, the protein also upheld secondary structure and is biologically active.

4   Conclusion

In the present study, we performed heterologous expression, native purification, and determination of biological activity of human MAFA fusion protein using bacterial system (*E. coli*). Multiple parameters like inducer concentration, bacterial density, etc. were screened for maximal protein expression in soluble form. The strategy

employed for purification is simple, economical, and highly reproducible. Additionally, MAFA-NTH fusion protein has upheld its y structure post-desalting. Secondary structure determination using BestSel revealed that the protein contains predominantly random coils with approximate equal amount of α-helices and β-sheets. The purified protein was also capable of permeabilizing cell membrane and internalizing into the nucleus of mammalian cells. Moreover, the protein upregulated insulin gene expression as validated using RT-qPCR. Thus, we conclude that the recombinant version of human MAFA has huge clinical applicability for the treatment of diabetes.

Author Contribution Gloria Narayan conceptualized, performed the experiments, collected and interpreted data, and wrote the manuscript. Shirisha Nagotu and Rajkumar P Thummer funded the project, analyzed the data, supervised the experiments, and edited the manuscript. The final draft of the manuscript was approved by all the authors for publication.

Declarations None.

Conflict of Interest None.

References

1. Tarr JM, Kaul K, Wolanska K, Kohner EM, Chibber R (2013) Retinopathy in diabetes. Adv Exp Med Biol 771(suppl 1):88–106. https://doi.org/10.1007/978-1-4614-5441-0_10
2. Holman RR, Sourij H, Califf RM (2014) Cardiovascular outcome trials of glucose-lowering drugs or strategies in type 2 diabetes. The Lancet 383(9933):2008–2017
3. Pop-Busui R, Boulton AJM, Feldman EL, Bril V, Freeman R, Malik RA et al (2017) Diabetic neuropathy: a position statement by the American Diabetes Association. Diabetes Care 40(1)136–154
4. Lyttle BM, Li J, Krishnamurthy M, Fellows F, Wheeler MB, Goodyer CG, Wang R (2008) Transcription factor expression in the developing human fetal endocrine pancreas. Diabetologia 51(7):1169–1180. https://doi.org/10.1007/s00125-008-1006-z
5. Conrad E, Stein R, Hunter CS (2014) Revealing transcription factors during human pancreatic β cell development. Trends Endocrinol Metab 25(8):407–414. https://doi.org/10.1016/j.tem.2014.03.013
6. Zhu Y, Liu Q, Zhou Z, Ikeda Y (2017) PDX1 , Neurogenin-3 , and MAFA : critical transcription regulators for beta cell development and regeneration 1–7. https://doi.org/10.1186/s13287-017-0694-z
7. Nishizawa M, Kataoka K, Goto N, Fujiwara KT, Kawai S (1989) V-Maf, a Viral Oncogene That Encodes a "Leucine Zipper" Motif. Proc Natl Acad Sci USA 86(20):7711–7715. https://doi.org/10.1073/pnas.86.20.7711
8. Kataoka K, Han SI, Shioda S, Hirai M, Nishizawa M, Handa H (2002) MafA is a glucose-regulated and pancreatic β-cell-specific transcriptional activator for the insulin gene. J Biol Chem 277(51):49903–49910. https://doi.org/10.1074/jbc.M206796200
9. Matsuoka TA, Artner I, Henderson E, Means A, Sander M, Stein R (2004) The MafA transcription factor appears to be responsible for tissue-specific expression of insulin. Proc Natl Acad Sci USA 101(9):2930–2933. https://doi.org/10.1073/pnas.0306233101

10. Olbrot M, Rud J, Moss LG, Sharma A (2002) Identification of β-cell-specific insulin gene transcription factor RIPE3b1 as mammalian MafA. Proc Natl Acad Sci USA 99(10):6737–6742. https://doi.org/10.1073/pnas.102168499

11. Zhao L, Guo M, Matsuoka TA, Hagman DK, Parazzoli SD, Poitout V, Stein R (2005) The islet β cell-enriched MafA activator is a key regulator of insulin gene transcription. J Biol Chem 280(12):11887–11894. https://doi.org/10.1074/jbc.M409475200

12. El Khattabi I, Sharma A (2015) Proper activation of MafA is required for optimal differentiation and maturation of pancreatic β-cells. Best Pract Res Clin Endocrinol Metab 29(6):821–831. https://doi.org/10.1016/j.beem.2015.09.006

13. Nishimura W, Takahashi S, Yasuda K (2015) MafA is critical for maintenance of the mature beta cell phenotype in mice. Diabetologia 58(3):566–574. https://doi.org/10.1007/s00125-014-3464-9

14. Zhang C, Moriguchi T, Kajihara M, Esaki R, Harada A, Shimohata H et al (2005) MafA Is a key regulator of glucose-stimulated insulin secretion. Mol Cell Biol 25(12):4969–4976. https://doi.org/10.1128/mcb.25.12.4969-4976.2005

15. Butler AE, Robertson RP, Hernandez R, Matveyenko AV, Gurlo T, Butler PC (2012) Beta cell nuclear musculoaponeurotic fibrosarcoma oncogene family A (MafA) is deficient in type 2 diabetes. Diabetologia 55(11):2985–2988. https://doi.org/10.1007/s00125-012-2666-2

16. Noso S, Kataoka K, Kawabata Y, Babaya N, Hiromine Y, Yamaji K et al (2010) Insulin trans-activator MafA regulates intrathymic expression of insulin and affects susceptibility to type 1 diabetes. Diabetes 59(10):2579–2587. https://doi.org/10.2337/db10-0476

17. Noso S, Kawabata Y, Babaya N, Hiromine Y, Kawasaki E et al (2013) Association study of MAFA and MAFB genes related to organ-specific autoimmunity, with susceptibility to Type-1 diabetes in Japanese and Caucasian populations. J Genet Syndr Gene Ther 4(204):2

18. Guo QS, Zhu MY, Wang L, Fan XJ, Lu YH, Wang ZW et al (2012) Combined transfection of the three transcriptional factors, PDX-1, neuroD1, and MafA, causes differentiation of bone marrow mesenchymal stem cells into insulin-producing cells. Exp Diabetes Res. https://doi.org/10.1155/2012/672013

19. Saxena P, Heng BC, Bai P, Folcher M, Zulewski H, Fussenegger M (2016) A programmable synthetic lineage-control network that differentiates human IPSCs into glucose-sensitive insulin-secreting beta-like cells. Nat Commun 7:1–14. https://doi.org/10.1038/ncomms11247

20. Dey C, Raina K, Haridhasapavalan KK, Thool M, Sundaravadivelu PK, Adhikari P et al (2021) An overview of reprogramming approaches to derive integration-free induced pluripotent stem cells for prospective biomedical applications. Recent Adv iPSC Technol 231–287

21. Sanchez-Garcia L, Martín L, Mangues R, Ferrer-Miralles N, Vázquez E, Villaverde A (2016) Recombinant pharmaceuticals from microbial cells: a 2015 update. Microbial Cell Factories 15(1):1–7. https://doi.org/10.1186/s12934-016-0437-3

22. Narayan G, Sundaravadivelu PK, Agrawal A, Gogoi R, Nagotu S, Thummer RP (2021) Soluble expression, purification, and secondary structure determination of human PDX1 transcription factor. Protein Expr Purif 180: 105807. https://doi.org/10.1016/j.pep.2020.105807

23. Narayan G, Agrawal A, Joshi N, Gogoi R, Nagotu S, Thummer RP (2021) Protein production and purification of a codon-optimized human NGN3 transcription factor from E. coli. Protein J 40(6):891–906. https://doi.org/10.1007/s10930-021-10020-x

24. Haridhasapavalan KK, Sundaravadivelu PK, Bhattacharyya S, Ranjan SH, Raina K, Thummer RP (2021) Generation of cell-permeant recombinant human transcription factor GATA4 from E. coli. Bioprocess Biosyst Eng 44(6):1131–1146. https://doi.org/10.1007/s00449-021-02516-8

25. Thool M, Dey C, Bhattacharyya S, Rajkumar SS (2021) Generation of a recombinant stem cell—specific human SOX2 protein from Escherichia coli under native conditions. Mol Biotechnol. https://doi.org/10.1007/s12033-021-00305-y

26. Dey C, Thool M, Bhattacharyya S, Sudhagar S, Thummer RP (2021) Generation of biologically active recombinant human OCT4 protein from E. coli. 3 Biotech 11(5):1–16. https://doi.org/10.1007/s13205-021-02758-z

27. Haridhasapavalan KK, Das NJ, Thummer RP (2022) Generation of a transducible version of a bioactive recombinant human TBX5 transcription factor from E. Coli. Curr Res Biotechnol 4:66–77. https://doi.org/10.1016/j.crbiot.2022.01.004

28. Haridhasapavalan KK, Sundaravadivelu PK, Joshi N, Das NJ, Mohapatra A, Voorkara U et al (2022) Generation of a recombinant version of a biologically active cell-permeant human HAND2 transcription factor from E. coli. Sci Rep 12(1):1–16. https://doi.org/10.1038/s41598-022-19745-w

29. Dey C, Venkatesan V, Thummer RP (2022) Identification of optimal expression parameters and purification of a codon-optimized human GLIS1 transcription factor from Escherichia coli. Mol Biotechnol 64(1):42–56. https://doi.org/10.1007/s12033-021-00390-z

30. Haridhasapavalan KK, Ranjan SH, Bhattacharyya S, Thummer RP (2021) Soluble expression, purification, and secondary structure determination of human MESP1 transcription factor. Appl Microbiol Biotechnol 105(6):2363–2376. https://doi.org/10.1007/s00253-021-11194-1

31. Haridhasapavalan KK, Sundaravadivelu PK, Thummer RP (2020) Codon optimization, cloning, expression, purification, and secondary structure determination of human ETS2 transcription Factor. Mol Biotechnol 62(10):485–494. https://doi.org/10.1007/s12033-020-00266-8

32. Micsonai A, Wien F, Kernya L, Lee YH, Goto Y, Réfrégiers M, Kardos J (2015) Accurate secondary structure prediction and fold recognition for circular dichroism spectroscopy. Proc Natl Acad Sci USA 112(24):E3095–E3103. https://doi.org/10.1073/pnas.1500851112

33. Ryan BJ, Henehan GT (2013) Overview of approaches to preventing and avoiding proteolysis during expression and purification of proteins. Curr Protoc Protein Sci 71(1):5–25

34. Kelly SM, Jess TJ, Price NC (2005) How to study proteins by circular dichroism. Biochimica et Biophysica Acta—Proteins and Proteomics 1751(2):119–139. https://doi.org/10.1016/j.bbapap.2005.06.005

35. Lu J, Luo H, Wu H, Lan MS, Tan J, Lu D (2011) Recombinant MafA protein containing its own protein transduction domain stimulates insulin gene expression in IEC-6 cells. Life Sci 89(3–4):72–77. https://doi.org/10.1016/j.lfs.2011.04.012

36. Noguchi H, Xu G, Matsumoto S, Kaneto H, Kobayashi N, Bonner-Weir S, Hayashi S (2006) Induction of pancreatic stem/progenitor cells into insulin-producing cells by adenoviral-mediated gene transfer technology. Cell Transplant 15(10):929–938. https://doi.org/10.3727/000000006783981843

Drug Delivery and Therapeutics

Targeting Macrophages Through Gold Nanoparticle-Induced Immunomodulation: A Therapeutic Approach in Inflammation and Cancer

Nabanita Maity and Mahuya Sengupta

Keywords Gold nanoparticles · Cancer immunotherapy · Macrophage · Inflammatory disease · Biomedical applications

1 Introduction

.According to World Health Organisation (WHO) report, nearly 19.3 million people died worldwide due to cancer alone in 2020 [1]. Scientists are looking forward to a potential cure for the disease with better prognosis, lesser collateral damage to healthy cells and tissues, ease of release and more accessibility than conventional approaches like chemotherapy, radiotherapy and/or surgery. In the year 1959, Nobel Prize laureate and American physicist Richard Feynman introduced the concept of nanotechnology in a lecture titled as "There's Plenty of Room at the Bottom" at the California Institute of Technology (Caltech) [2]. Nanoparticles (NPs) are the particles of matter with a size of about 100 nm in diameter (Greek, nano meaning dwarf). Nanotechnology has revolutionized the field of disease diagnosis and therapeutics largely due to their quantum effects like surface-plasmon resonance and opto-electronic properties [3].

NPs allow scientists to design and merge the three functions of diagnosis, targeting and therapeutics into one nanomedicine. The term "theranostic" is a portmanteau word of "therapeutics" and "diagnostics". The discovery of gold nanoparticle-based detection and diagnosis have proved to have a potential to fulfil such requirements with a more efficient and targeted drug delivery and fewer side effects than most of the conventional therapies. Gold nanoparticles (GNPs) can be easily synthesized

N. Maity · M. Sengupta (✉)
Department of Biotechnology, Assam University, Silchar, Assam, India
e-mail: mahuya.sengupta@aus.ac.in

and engineered to encapsulate with a variety of anticancer drugs, such as Paclitaxel, Doxorubicin, 5-Fluorouracil, Dexamethasone, and Polylactic-glycolic Acid (PLGA) etc. [4].

Mammalian immune system comprises of two types of immunity, innate and adaptive immunity, to maintain the body's integrity. As our immune system creates defense against any foreign particles in order to protect us, interaction of GNPs with immune cells is undoubtedly of major interest. After internalization it makes interaction with different immune cells, especially with phagocytic cells like macrophages, dendritic cells, natural killer cells (NK) and mast cells [5]. It is the surface charge and electric field of metallic nanoparticles that affect the primary interaction with immune cells and modulate their response [6]. According to different studies, it shows that GNPs work as immunomodulators that can normalize or modulate the immune system. The nature of GNPs is responsible either for stimulation or suppression of immune cells. Engineered and functionalized GNPs show immunostimulatory effects which can be used widely for cancer immunotherapy [7]. GNPs of different shapes, sizes and surface functionalization are used for immunostimulation. Due to suitable properties such as excellent biocompatibility, biodegradability, chemical stability and water solubility, GNPs are vastly used as immunostimulatory nanoparticles. Studies have shown rise in vivo, in antibody production after the exposure of antigen conjugated GNPs [8].

Macrophages are of great interest to the immunologist, because of their ability to alter their own function as per the environmental stimuli. Broadly, macrophages are divided into pro-tumorigenic (M2) and anti-tumorigenic (M1) macrophages [9]. Distortion in M1/M2 homeostasis causes impairment of the immune system and inflammation. In solid tumors, more than 50% of the population comprises of tumor associated macrophages (TAMs), a subtype of macrophage that promotes tumor growth, angiogenesis and invasion of cancer cells in a new location via epithelial to mesenchymal transition [10]. By changing the tumor microenvironment, a decline in TAMs' number or repolarization of TAMs to anti-tumorigenic M1 macrophage is reported, eventually that leads to a shrink in tumor volume through activating apoptosis in tumor cells. In vitro it is possible to control several factors of the tumor microenvironment accordingly but in vivo complexities are much higher and manipulation of the tumor environment is difficult. It encourages the scientific community to search for particular molecule or a complex of molecules which can upregulate or downregulate the expression of certain genes and thus modulate the function in support of anti-inflammatory and anti-tumor reaction. Due to the phagocytic nature of the macrophage, it engulfs GNPs efficiently [11]. Due to its size, GNPs circulate for a longer duration in blood and maximize their interaction with other biological molecules. Before its excretion through bile and feces, GNPs induce change in gene interaction through modulating different metabolic and non-metabolic pathways. Recent research reported their anti-tumor effects by inducing apoptosis in cancer cells [12]. In this chapter, first, we elucidate the origin and differentiation of various tissue residing macrophages, understanding of metabolic programming of different subtypes and their role in inflammation and cancer progression. Later, we discuss

GNPs' role in repolarization of the macrophage from its pro-tumorigenic subtype (TAMs/M2) to anti-tumorigenic subtype (M1).

2 Factors Responsible for Different Responses of Immune Cells to Gold Nanoparticles

The response of immune cells to gold nanoparticles, particularly to gold nanorods (GNRs) depends on the nanoparticles' size, shape and functionalization. We discuss these factors as follows.

2.1 Effects of Shape and Size of GNRs on Internalization by Immune Cells

The innate immune system constitutes the first line of defense to any foreign particle in animal cells and tissues. Antigen presenting cells i.e. macrophages and dendritic cells, natural killer cells, mast cells, neutrophils, eosinophils, and basophils are the cells of the innate immune system [13]. Interaction of GNPs with innate immune cells, their uptake and distribution and the study of alteration in immune cell responses are of great interest. Internalizations of nanoparticles by immune cells are mainly dependent on two critical factors, shape and size [14]. Particles with long axis parallel to the cell membrane show slower uptake than particles having short axis, like spherical shaped particles. For endocytosis, it takes a greater surface area of the cell membrane to wrap a rod-shaped particle than that of a sphere [15]. Therefore, at similar concentrations, spheres show enhanced uptake as compared to rods. Shapes of particles also influence their blood circulation time. Rods encounter lateral drift in blood and these forces are responsible for their marginalization in blood vessels. Nanorods with an aspect ratio (AR) = 2 have shown seven fold higher marginalization than gold spherical particles [16]. Discoidal and hemispheric gold particles possess higher drift than spheres that allow them to marginate towards vessel wall and escape through the gaps between the endothelium cells. Many studies in their experiments found more efficient uptake of GNRs than gold spheres by dendritic cells. GNPs are stimulatory to both macrophages and dendritic cells [17]. Their internalization increased the expression of CD86, a marker of dendritic cells.

The size of the GNPs influences their cellular uptake to a greater extent. Kumari et al. reported rapid uptake of GNPs of 50 nm diameter [18]. Size ranging between 50 and 200 nm shows preferential uptake via clathrin coated endocytosis [19]. GNPs of less than 25 nm size penetrate macrophages through pinocytosis. In macrophages, GNPs are mostly found in perinuclear spaces and lysosomes. Cell types also influence the rate of uptake. Many studies demonstrated that GNPs were found to be accumulated upto 90% in Kupffer cells and only 10% in splenic macrophages [20]. Cells in

which the predominant uptake pathway is macro-pinocytosis show higher uptake of nanoparticles than clathrin or caveolae-mediated endocytosis. Smaller GNPs of 2–12 nm have shown greater antibody production. Rods internalize themselves either by top-down or lying-up manner. Rods with different aspect ratios, a proportion between height and width of nanoparticles, play a more significant role in determining different internalization pathways of cellular uptake viz., clathrin-mediated, caveolae-mediated endocytosis or microtubule transport [21]. CTAB coated GNRs of 15×50 nm size have greater entrapment efficiency than 15 nm and 50 nm gold spheres.

2.2 Effect of Surface Functionalization on Cellular Uptake of Gold Nanoparticles

Functionalization affects interaction of nanoparticles with negatively charged cell membranes. Due to the presence of phospholipids and carbohydrate moieties like sialic acid, cell membrane possesses anionic charge on its surface. It imparts various charges on particles. Charge influences both particle uptake and interactions with other proteins present inside a cell. Cationic GNPs penetrate cells of the reticular endothelial system more effectively. Anionic NPs penetrate cell via caveolae-mediated endocytosis through their interaction with cholesterol-based cationic lipids. Adsorption of opsonins and immunoglobulins on anionic NPs change its endocytic pathway. Protein adsorbed anionic particles are taken up by caveolae-mediated endocytosis. On the other hand, cationic GNPs penetrate the cell membrane through clathrin-mediated endocytosis [22]. Particles having neutral charge have limited cellular uptake. Cationic surfactants CTAB (cetyltrimethylammonium bromide) conjugated GNPs exhibit greater cellular uptake. But, due to their higher cytotoxicity CTAB is often replaced by other ligands.

For targeted delivery and to enhance internalization of neutral and anionic surface charged GNPs, these nanoparticles are usually conjugated with different ligands. Prostate cancer cells show higher expression of transferrin receptors on their surface. GNPs conjugated with paclitaxel and transferrin exhibited greater inhibition of tumor growth than that of the non-conjugated ones. A study, reported greater pro-inflammatory cytokine response between 15 and 30 nm sized GNPs conjugated with CpG (cytosine-phosphate-guanosine; an oligonucleotide) than that of CpG alone [23]. Internalization of 15 nm CpG-GNRs was higher in RAW264.7 macrophages as compared to the 30 nm GNRs. Uptake of both gold nanorods and rods conjugated with SiO_2 in macrophages triggers pro-inflammatory cytokine secretion. Uptake of GNPs followed by a release of interferon is directly linked to the concentration of polyvalent oligonucleotides present on the surface of GNPs. In RAW264.7 cell line, it is reported that PEGylated GNPs with a diameter of 4 nm inhibited the activation of TLR-9 followed by a decrease in TNF-α and IL-6 expression levels [24]. A

study reported GNPs conjugated with tumor associated antigens can stimulate cyto-toxic T cells which lead to stronger Th1, Th2, Th17 expression and also activate B cells, hence an enhanced antibody production. Murine B-lymphocyte cell line treated with citrate stabilized GNPs displayed expression of Nf-κβ. A recent study on murine fibrosarcoma reported that GNPs coated with serum albumin can induce macrophage polarization and inhibit the tumor growth. Murine serum albumin conjugated GNPs stimulate TNF-α, IL-6, IL-12 expression and are capable to mitigate the expression of HIF-1α in a fibrosarcoma model [25].
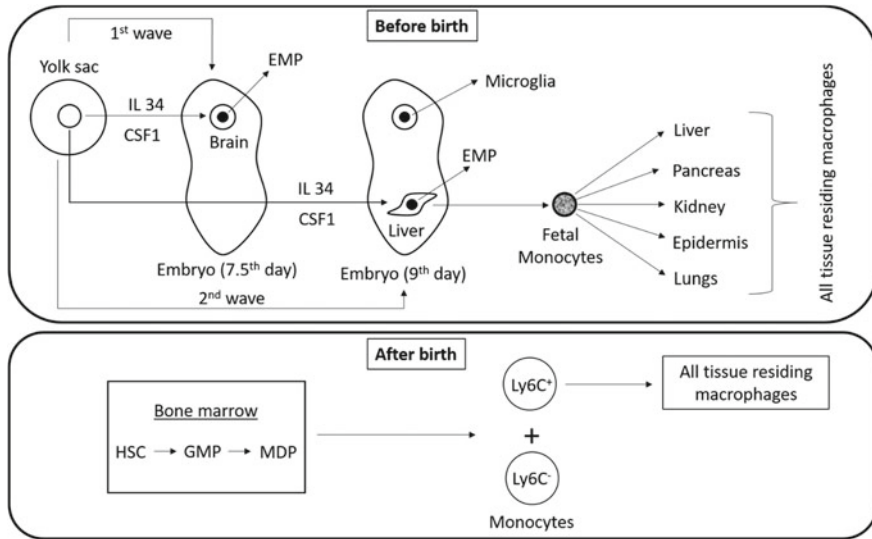
3 Macrophage

Macrophages are frontline cells of innate immunity. They are also one of the main constituents of antigen presenting cells (APC) and can activate the adaptive immune response through antibody-dependent cell-mediated cytotoxicity (ADCC). They are phagocytic mononuclear cells, present in blood as monocytes and differentiate into mature macrophages under different environmental conditions of various residing tissues.

3.1 Macrophages in Inflammation and Cancer

Most of the tissue-residing macrophages maintain their pool (except few) through embryonic macrophages. Among various hypotheses regarding the development and origin of embryonic macrophages, the commonly accepted hypothesis suggests that embryonic macrophages are derived from yolk-sac derived erythromyeloid precursor cells. Initial erythromyeloid precursor cells (EMPs) originate around 7.5 day of embryonic development. This first batch of EMPs colonize in brain and give rise to microglial cells. On the 9th embryonic day, the second batch of EMPs are gener-ated which colonize in fetal liver and later through hematopoiesis give rise to fetal monocytes [26]. Later, fetal monocytes replace liver macrophages and give rise to all tissue-residing macrophages. At the end of fetal development, liver haematopoiesis declines and bone marrow takes over (see Fig. 1).

Macrophage population is maintained by various growth factors. Macrophage colony stimulating factor 1 receptor (CSF1R) is a class III transmembrane tyrosine-kinase receptor considered to be a major factor that influences macrophage pools in various tissues. Deletion of CSF1R leads to severe loss of bone, ovary, brain, skin and testis tissue-residing macrophages. The presence of vascular endothelium growth factor-A (VEGF-A) can compensate the loss in such tissues [27]. Despite the loss of CSF1R, no change in population was observed in spleen and alveolar macrophages. This leads to the identification of other involved factors like granulocyte–macrophage colony stimulating factor (GM-CSF) and IL-34, TGF-β. GM-CSF newly known as CSF2, expression is restricted to specific tissues. IL-34 shares structural homology

Fig. 1 Hypothesis supporting the formation of all tissue-residing macrophages in two waves. Schematic representation of tissue-residing macrophage formation (top) before birth and (bottom) after birth. (Top) The macrophage formation originates from yolk sac derived erythromyeloid precursor cells (EMPs) which are produced on the 7.5th day in the first wave. In the presence of IL 34 and CSF1, first formed EMPs colonizen the brain and later differentiate into microglial cells of brain. Around the 9th day, a second wave of EMPs originates and colonizes the fetal liver. Through the process of hematopoiesis in fetal liver, EMPs differentiate into fetal monocytes which eventually result in all tissue-residing macrophages of liver, pancreas, kidney, epidermis and lungs. (Bottom) After birth, the bone marrow develops. Fetal hematopoiesis gradually declines and is overtaken by bone marrow hematopoiesis. In the bone marrow, the macrophage dendritic cell progenitor (MDP) development occurs from the hematopoietic stem cells (HSCs) via a granulocyte macrophage progenitor (GMP). In the presence of CSF1, MDP produces Ly6C$^+$ and Ly6C$^-$ monocytes. It seems that the precursors of all tissue-residing macrophages in an adult are Ly6C$^+$ monocytes. Further developmental fate of Ly6C$^-$ is unclear so far. CSF1: colony stimulating factor 1; IL-34: interleukin 34

with CSF1R and can compensate the loss of CSF1R. But, it is only expressed in brain and epidermis and influences the function of microglia and Langerhans cells. Although with the same origin and specification, tissue-residing macrophages show a narrow overlap between their transcriptional profiles. This difference develops functional heterogeneity, morphological and anatomical diversity among tissue-residing macrophages. Transcriptional factors and tissue specific signals remodel chromatin structure. Hence, it is evident that tissue specific signals are major contributing factors in shaping macrophage functions. PU.1 is one such common transcriptional factor which binds to the promoter as well as enhancer regions and promotes cell differentiation. Along with PU.1, other factors such as CEBPβ, MAF transcriptional factors play a role in terminal differentiation of macrophages. In alveolar macrophages, expression of peroxisome proliferator activated receptor γ, in peritoneal macrophages GATA6 protein [28], SPIC in spleen macrophages is high, which indicates their

tissue specific role in macrophage differentiation. SPIC is also expressed in liver and bone marrow macrophages [29]. On the other hand, metabolites along with transcriptional factors help in inducing certain signaling cascades resulting in functional heterogeneity. In spleen, heme from liver and bone marrow macrophages turn on SPIC expression required for macrophage maintenance. Sterols, retinoic acid, microbial products play a significant role in the regulation of macrophage function. Retinoic acid induces the expression of peritoneal macrophage specific GATA6 protein. Sterols with CSF1 regulate the function of marginal zone macrophage of spleen, metallophilic macrophages present in the white pulp region of spleen and bone marrow macrophages (see Fig. 2). Gut microbiome and their metabolites induce certain gene expression specific to the small and large intestinal macrophages.

Besides tissue specific functions, macrophages from all different types of tissue share some wide range of common functions. Secretion of chemokines, cytokines from immune cells, hypoxia, inflammation in the internal environment, etc. modulate the function of macrophages. Based on environment they may sometimes behave as inflammatory or anti-inflammatory cells, take part in tissue destruction or in tissue repair. This is commonly referred to as "plasticity of macrophage". According to the stimuli, macrophages polarize themselves into broadly two functional subtypes, a pro-inflammatory, classical (M1) and an anti-inflammatory, alternative (M2) type (as described in Fig. 3).

Tissue injury or pathogen invasion leads to the secretion of IFNγ, TNF-α, GM-CSF, LPS. These factors induce particular transcriptional profile that changes the phenotype and the function of macrophage to M1 phenotype. Pattern recognition receptors (PRRs) on the surface of M1 macrophages help recognize pathogen associated molecular patterns (PAMPs) present on foreign invaders and stimulate the release of pro-inflammatory cytokines IL-1β, IL-6, IL-12, IL-23, TNF-α, and CXCL4 [7, 30]. Pro-inflammatory cytokine secretion leads to high levels of reactive oxygen species (ROS), reactive nitrogen species (RNS) generation which leads to inflammation and killing of pathogens. ROS are generally known as cytotoxic by-products of various metabolic pathways. The role of ROS in gene expression through chromatin remodeling, protein interaction and cell cycle has also been reported. Generation of ROS in case of M1 phenotype is mainly because of NADPH oxidase (NOX) a non-mitochondrial source of ROS production. Macrophages when stimulated by TLR ligands, generate ROS through mitochondrial electron transport chain (ETC). ROS activates ERK, JNK, and p38 pathways, major signaling pathways of macrophage differentiation and polarization. NF-κB is another inflammatory signaling pathway found to be activated in M1 phenotypes. This pathway is considered to activate many pro-inflammatory genes. M1 macrophages display a different metabolism in comparison to the M2 phenotype. In M1 phenotype metabolism of arginine is shifted towards nitric oxide (NO) and citrulline. Nitric oxide (NO) is the result of upregulation of inducible nitric oxide synthase (iNOS) or Nox_2 genes. High level of NO inhibits pyruvate dehydrogenase (PDH) in an HIF-1α independent manner which results in disruption of the TCA cycle. Eventually it disrupts the mitochondrial electron transport chain. Macrophages via mitochondrial ETC disruption show cytotoxic behavior on tumor cells. IL-12 and IL-23 activate the polarization of CD4 T cells
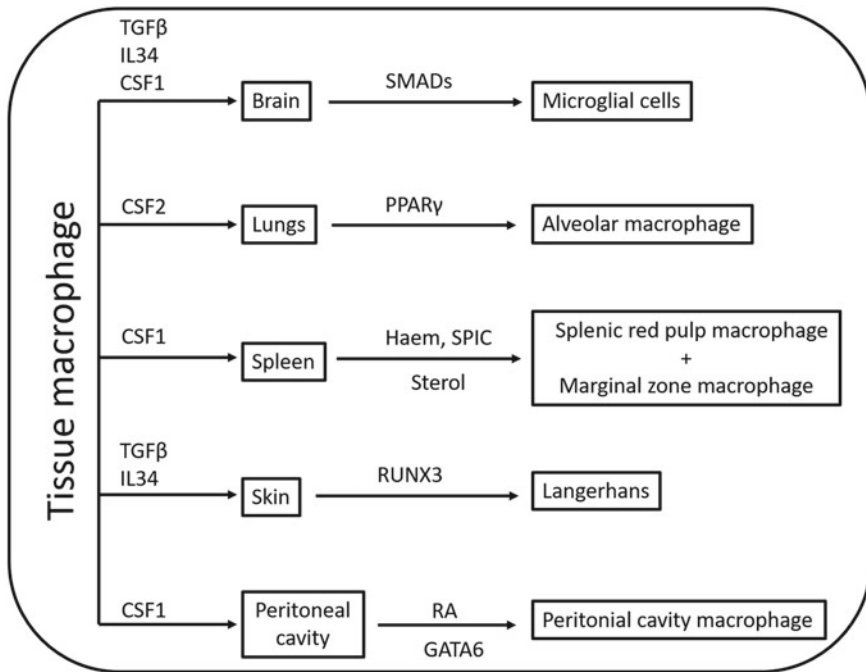
Fig. 2 Several types of tissue macrophages' differentiation depend on the key factors of a tissue environment. Differentiation of macrophages residing in the brain, lungs, spleen, skin and peritoneal cavity, are schematically represented. Different cytokines and cell metabolites induce certain gene expression and change both the phenotype and function of yolk sac derived erythromyeloid precursor cells (EMPs. (i) In brain, TGFβ, IL34 and CSF1 are locally expressed. It drives phosphorylation of SMADs, and controls unique gene expressions specific to the microglial cell differentiation. (ii) In lungs, CSF2 expression drives fetal monocytes to express PPARγ, that eventually differentiates fetal monocytes into alveolar macrophages. (iii) In spleen, together with the expression of CSF1 heme, SPIC is activated. SPIC regulates the differentiation of the splenic red pulp macrophages. Sterols, especially oxysterols control the differentiation of marginal zone macrophages. (iv) In skin, the expression of TGFβ and IL34 controls the expression of RUNX3 to drive the differentiation of langerhans macrophages. (v) In peritoneal cavity, the CSF1 expression drives the differentiation of peritoneal cavity macrophages via induced expression of RA and GATA6. CSF1: Colony Stimulating Factor 1; CSF2: Colony Stimulating Factor 2; TGFβ: Transforming Growth Factor beta; IL34: Interleukin-34; SMAD: transcription factor from TGFβ family; PPARγ: Peroxisome Proliferator Activated Receptor gamma; RUNX3: runt related transcription factor 3; RA: Retinoic Acid; GATA6: GATA binding protein 6

into Th1 and Th17 cells respectively. By promoting Th1 response, M1 also activates anti-tumor immunity. Impairment of glycolytic pathways inhibits phenotypic change of macrophage towards M1. Instead, in M1 phenotype, disruption of the tricarboxylic acid (TCA) cycle and oxidative phosphorylation (OXPHOS) is seen. Increased uptake of glucose is one of the key characteristics of M1 macrophages. Phenotypically they are characterized by the presence of CD64 and CD80 markers (see Fig. 4) [31].
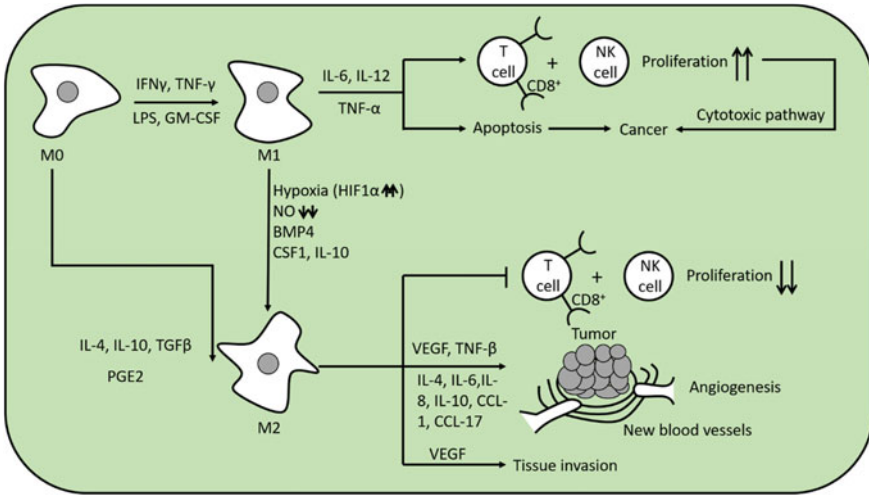
Fig. 3 Schematic representation of polarization of macrophages into two main sub-types of macrophages. One of them is pro-inflammatory and anti-tumorigenic i.e., the so-called M1 type and another one is anti-inflammatory and pro-tumorigenic i.e., the so-called M2 type. The formation of M1 and M2 types depends on the biological factors. In the presence of IFNγ, TNF-γ, LPS and GM-CSF, macrophages (M0) transform into M1 macrophage and in the presence of IL-4, IL-10, TGFβ, and PGE2, M0 macrophage transforms into M2 macrophage. In certain environmental conditions such as in the presence of HIF1-α which induces hypoxia in the tissue, NO reduction, upregulated BMP4, CSF2, IL-10, M1 macrophage can re-polarize into M_2 macrophage. M1 macrophages are characterized by the presence of highly secreted pro-inflammatory cytokines like IL-6, IL-12, and TNF-α. Pro-inflammatory cytokines increase the proliferation of T-cell and NK-cell. In cancer cells, pro-inflammatory cytokines and other secreted metabolites of M1 like ROS and NO induce certain gene expression that leads to DNA damage of the cell. DNA damage results into apoptosis of the cancer cells. Cancer cells can also be destroyed via cytotoxic pathway of T cells and NK cells. M2 is characterized by the presence of anti-inflammatory cytokines and chemokines like VEGF, TNF-β, IL-4, IL-6, IL-10, CCL-1, and CCL-17. M2 macrophage results in the reduction of T cell and NK cell proliferation, causing impairment in cytotoxicity. M2 macrophage promotes tumor progression in the presence of VEGF, TNF-β, IL-4, IL-6, IL-10, CCL-1, and CCL-17. VEGF stimulates new blood vessel formation in and around the tumor, known as angiogenesis. In addition, M2 macrophage is associated with the development of metastasis by promoting EMT. IFNγ: Interferon-γ; TNF-α: Tumor necrosis factor-γ; LPS: Lipopolysaccharides, an outer membrane component of Gram-negative bacteria; GM-CSF: Granulocyte–macrophage colony stimulating factor; IL-4: Interleukin 4; IL-6: Interleukin 6; IL-10: Interleukin 10; IL-12: Interleukin 12; CCL-1: Chemokine (C–C) motif ligand 1; CCL-17: Chemokine (C–C) motif ligand 17; TGFβ: Transforming growth factor-β; PGE2- Prostaglandin E2; HIF-1α: Hypoxia inducing factor 1α; NO: Nitric oxide; BMP4: Bone morphogenetic protein 4; CSF1: Colony stimulating factor 1; CD8+: co-receptor present on the membrane of cytotoxic T lymphocytes (T cells)

M2 phenotype is antineoplastic and mainly activated by mediators like IL-4, IL-10, tumor growth factor (TGF-β), macrophage colony stimulating factor (MSCF), and apoptotic cells. They are involved in a wide array of functions. Primarily they are involved in reducing inflammation, promoting tumor growth and proliferation. M2 macrophages show high phagocytic function and clear apoptotic cell debris. They
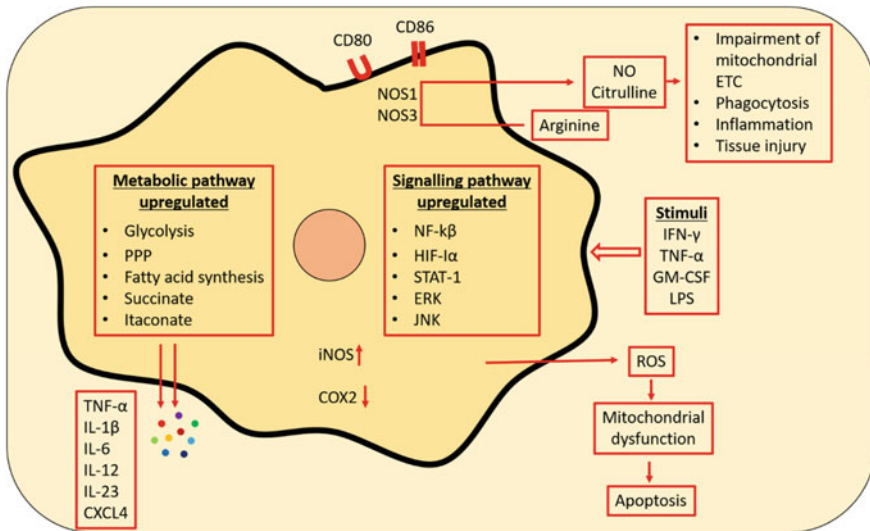
Fig. 4 Schematic representation of a pro-inflammatory, anti-tumorigenic, classically activated macrophage i.e., M1 phenotype. Several processes including metabolic and non-metabolic cascades in M1 macrophage are schematically represented with arrows and boxes. (i) The stimuli such as IFN-γ, TNF-α, GM-CSF and LPS induce the polarization of M1 macrophage from M0. (ii) The activated pattern recognition receptors (PRRs) on M1 macrophages stimulate the secretion of several pro-inflammatory cytokines and chemokines such as TNF-α, IL-1β, IL-6, IL-12, IL-23, and CXCL4. (iii) The release of such cytokines triggers the generation of reactive oxygen species (ROS) which are usually very cytotoxic. Due to cytotoxicity, ROS induce the apoptosis via mitochondrial dysfunction. (iv) In addition, ROS also induce the signaling pathway of NF-kβ, HIF-Iα, STAT-1, ERK and JNK which polarizes M1 macrophage and regulates metabolism of M1. (v) M1 macrophage shows upregulation of different metabolic pathways such as glycolysis, pentose phosphate pathway, fatty acid synthesis and generation of succinate and itaconate. (vi) Enhanced secretion of NO is due to the upregulation of iNOS. COX2 expressions get downregulated in M1. (vii) In the presence of NOS1 and NOS3, arginine metabolized into nitric oxide (NO) and citrulline results in the impairment of mitochondrial ETC, leading to apoptosis. M1 shows enhanced phagocytosis, and causes inflammation and tissue injury. (viii) M1 is characterized by the presence of surface markers CD80 and CD86. IFN-γ: Interferon γ; TNF-α:Tumor Necrosis Factor alpha; GM-CSF: Granulocyte- macrophage colony stimulating factor; LPS: Lipopolysaccharides; IL-6: Interleukin-6; IL-12: Interleukin-12; CXCL: Chemokine (C-X-C) motif ligand; NF-kβ: Nuclear factor kappa β; HIF-Iα: Hypoxia inducing factor 1α; STAT-1: Signal transducer and activator of transcription 1; ERK: Extracellular signal-regulated kinase; JNK: c-Jun N terminal kinase; PPP: Pentose phosphate pathway; iNOS: inducible nitric oxide synthase; COX2: Cyclooxygenase 2; NO: Nitric Oxide; ROS: Reactive Oxygen Species

are found to be involved in endocrine signaling. They also participate in complex organ morphogenesis. Among the myeloid-derived immune cells, tumor associated macrophages (TAM) and regulatory T cells are the major immune cells playing a significant role in promoting inflammation and tumor growth in tumor microenvironment. TAMs are classically similar to M2 phenotype macrophages [32]. In normal conditions as well as during the early developmental phases of tumor, M1 phenotype

macrophages have been found to be present in the tumor microenvironment with high expression of pro-inflammatory cytokines like TNF-α, IL-1β, IL-6 and IL-12 but low levels of anti-inflammatory cytokines. But during the later stage of tumor progression, M2 phenotype of macrophages, characterized by the low expression of TNF-α, IL-12 and high expression of IL-10, IL-4, IL-6, IL-11, IL-13, TGF-β, CCL-1, CCL-17, CCL-18, VEGF, and CXCL-13 have been observed in the tumor microenvironment. Unlike M1, M2 macrophages have a different arginase metabolism. M2 macrophages metabolize arginine into ornithine and urea. Further, ornithine participates in polyamine, proline and collagen synthesis that eventually helps in tissue repair and in mitigating inflammation. Expression of arginase-1 gene is activated in M2. Arginase-1 is an enzyme of urea cycle involved in arginine metabolism. Wang et al. [33] reported in an experiment that impairment in glycolysis showed no effect on M2 polarization. It shows that M2 macrophage has wider metabolic flexibility than M1 macrophage. M2 metabolism is mainly regulated by fatty acid oxidation and oxidative pentose phosphate pathway (OXPHOS). Inhibition of these two pathways drastically reduced M2 polarization and its anti-inflammatory effects. In M2, IL-4 stimulation activates JAK-STAT-6, a key signaling pathway, for differentiation. Stimulation leads to autophosphorylation of JAK, an ATP-dependent kinase. Phosphorylated JAK further transfer γ-phosphate of ATP on STAT-6. Phosphorylated STAT-6 further activates its downstream peroxisome proliferator activated receptor gamma (PPARγ). PPARγ, a nuclear receptor, facilitates lipid uptake. High lipid uptake and fatty acid oxidation is a key metabolic signature of the M2 macrophages. CD206, CD209, CD301, A2R, Ym1/2, and Fizz-1 are the markers for the M2 macrophages (Fig. 5).

TAMs are infiltrating cells specific to the tumor environment. They are known to intensify tumor progression by cellular invasion and metastasis thereby stimulating angiogenesis through inhibition of T cell-mediated anti-tumor immune response [34]. They are also characterized by the release of certain anti-inflammatory cytokines like Interleukin-4 (IL-4) and pro-inflammatory cytokines like Interleukin-6 (IL-6), Interleukin-10 (IL-10) and tumor necrosis factor alpha (TNF-α). TAMs secrete vascular endothelial growth factors (VEGF) and placenta growth factor (PGF) that support angiogenesis [35]. Newly developed blood vessels deliver nutrients to the cancer cells and promote tumor growth. TAMs facilitate tumor invasion to the adjacent tissue by the degradation of extracellular matrix proteins. Matrix metalloproteinase-9 (MMP-9) secretion by TAMs promotes metastasis [36, 37]. TAMs have been associated with the poor prognosis of identifying cancer cells. Treatments targeting M2 like macrophages within tumor microenvironment increased the prevalence of M1 phenotypes that initiate T cell-dependent immune response and inhibit tumor growth.

To maintain tissue homeostasis among various factors, M1/M2 balance is crucial. In case of prolonged inflammation such as cancer, this balance is highly disrupted which creates severe complications. As early as in the 1800s, after it was first identified by Virchow that there is a connection between cancer and inflammation, it has been known that inflammation in the tumor microenvironment contributes to tumor progression. Prolonged expression of pro-inflammatory cytokines like IL-6, IL-12,
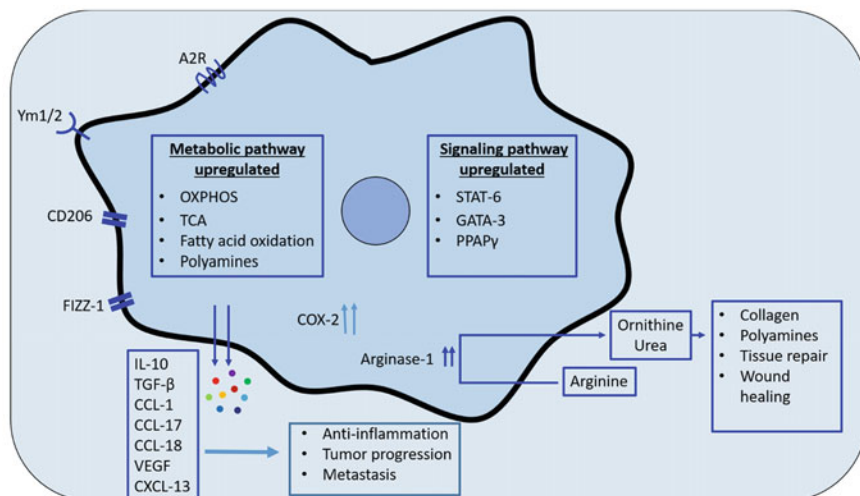
Fig. 5 Several metabolic and non-metabolic processes of M2 macrophage, are represented schematically. (i) M2 phenotype is stimulated by mediators such as IL-4, IL-10, TGF-β, and MSCF. (ii) M2 macrophages release high amount of anti-inflammatory cytokines and chemokines: IL-10, TGF-β, CCL-1, CCL-17, CCL-18, VEGF and CXCL-13. (iii) STAT-6, GATA-3, and PPAPγ signaling cascades are crucial for M2 polarization. (iv) M2 macrophage metabolism is mainly dependent on OXPHOS, TCA, fatty acid oxidation and synthesis of polyamines. (v) In the presence of arginase-1 enzyme, arginine metabolize into ornithine and urea. Ornithine results in collagen biosynthesis, proline and polyamines synthesis which helps in tissue repair and reduces inflammations. (vi) M2 is characterized by the presence of the surface marker FIZZ-1, CD206, Ym1/2, and A2R. IL-4: Interleukin-4; IL-10: Interleukin-10; TGF-β:Tumor Growth Factor beta; MSCF: Macrophage Colony Stimulating Factor; CCL: Chemokine (C–C) motif ligand; VEGF: Vascular Endothelial Growth Factor; CXGL.; STAT.; GATA.; PPAPγ: Peroxisome Proliferator Activated Receptor gamma; OXPHOS: Oxidative Pentose Phosphate; TCA: Tri-Carboxylic Acid

IL-23, and TNF-α cause tissue damage and other pathological consequences. Hence, sufficient anti-inflammatory mediators are required to supress inflammation and to retain homeostasis. By modulation of environmental stimuli, a balance between M1/M2 can be restored in cases of severe inflammation. Dextran coated GNPs were taken up by macrophages through their scavenger receptors promoting anti-inflammatory response. Polyethylenimine functionalized GNps were also found to induce release of anti-inflammatory mediators, once taken up by macrophages [38].

3.2 *Gold Nanoparticles in Re-programming of Macrophages*

Tumor microenvironment (TME) plays a critical role in cancer progression. TAMs are one of the major tumor infiltrating innate immune cells that are highly plastic in nature. Re-programming TAMs towards a tumoricidal phenotype is considered to

be a promising therapeutic strategy for cancer treatment. Previous studies demonstrated that TAMs are predominantly like M2 macrophages. Studies suggested re-programming of protumorogenic TAMs into anti-tumorogenic M1 phenotype causes killing of cancer cells. Either re-programming or depletion of M2 phenotype from tumor environment improves immunosuppression.

In a study, Conde et al. treated lung cancer cells with EGFR-siRNA conjugated GNPs to silence the expression of M2 phenotype inhibited tumor progression [39]. Bastus et al. demonstrated change in cytokine expression in macrophages when treated with sweet arrow peptide conjugated with GNPs. GNPs designed with peptides of prostate cancer associated antigen have shown a promising immunomodulatory response. Pal et al. [25] observed albumin coated GNP response on TAMs and splenic macrophages from tumor-bearing mice as compared to macrophages from healthy mice. The study concluded a concomitant decrease in IL-10 and TNF-α expression level and increase of IL-12 upon GNP treatment. In pancreatic ductal adenocarcinoma, Saha et al. found that 20 nm GNPs alter the tumor microenvironment more towards tumoricidal type. GNRs functionalized with polyvalent oligonucleotides were internalized by macrophages with its scavenger receptors and did not induce pro-inflammatory cytokines [41]. GM-CSF and IL-8 are crucial immunomodulators of cancer immune therapy. GNPs are found to decrease both of its expression. Thiolated C_pG conjugated GNPs induced pro-inflammatory cytokines, TNF-α, IL-6, and IL-12, markers of M1 phenotype. A recent study by Singh et al. [42] reported that curcumin conjugated gold nanoparticles could ameliorate the antioxidant defense in TAMs with the significant release of glutathione (GSH) and catalase enzymes and this indicates a shift of TAMs from pro-tumorigenic (M2) to anti-tumorigenic (M1) phenotype.

Solid tumors are invariably less well-oxygenated than normal tissues and this tumor hypoxia predisposes the tumor towards augmented growth and proliferation. Tumor hypoxia and the selective induction of the hypoxia-inducible factor (HIF)-1 under hypoxic conditions is a likely mechanism through which GNPs exert their effect. Hypoxia driven tumor promotion or cellular functions of any tumor microenvironment are mainly executed by pro-inflammatory cytokines, serum levels of protumorigenic cytokines like TNF-α and IL-6, all of which are estimated high in the presence of albumin coated GNPs.

4   Conclusion

As stated above, GNPs modulate the behavior of macrophages. Current understanding on immunity and functions of immune cells indicate macrophages as crucial immune cells with a critical role in inflammation and cancer. Biophysical properties of GNPs, in particular, shape, size and surface functionalization, evoke various significant immune responses. In conclusion, it can be said that GNPs are potential immunomodulators. Several studies demonstrated modes of GNP internalization. However, it is not fully understood yet and more studies are required to enhance

uptake and alleviate cytotoxic effects. Targeting macrophages through GNPs introduces a new paradigm into the world of cancer theranostics. While GNPs have shown potential therapeutic application in cancer prognosis still many challenges are needed to be addressed to ensure their clinical applications.

References

1. Sung H et al (2021) Global Cancer Statistics 2020: GLOBOCAN Estimates of Incidence and Mortality Worldwide for 36 Cancers in 185 Countries. CA CANCER J CLI 71:209–249
2. 'Plenty of room' revisited (2009) Nat Nanotechnol 4:781 https://www.nature.com/articles/nnano.2009.356.pdf
3. Paluszkiewicz P et al (2022) The Application of Nanoparticles in Diagnosis and Treatment of Kidney Diseases. Int J Mol Sci 23:131
4. Yahyaei B et al (2019) One step conjugation of some chemotherapeutic drugs to the biologically produced gold nanoparticles and assessment of their anticancer effects. Sci Rep 9:10242
5. Yafout M et al (2021) Gold nanoparticles as a drug delivery system for standard chemotherapeutics: A new lead for targeted pharmacological cancer treatments. Sci. Afr. 11:e00685
6. Liu Y et al (2017) Effects of engineered nanoparticles on the innate immune system. Semin Immunol 34:25–32
7. Liu J et al (2022) The interaction between nanoparticles and immune system: application in the treatment of inflammatory diseases. J. Nanobiotechnology. 20:127
8. Kumar S et al (2020) Emerging theranostic gold nanostructures to combat cancer: Novel probes for Combinatorial Immunotherapy and Photothermal Therapy. CTARC. 25:100258
9. Dykman LA (2020) Gold nanoparticles for preparation of antibodies and vaccines against infectious diseases. Expert Rev Vaccines 1–13
10. Williams JW et al (2018) Macrophage Biology, Classification, and Phenotype in Cardiovascular Disease: JACC Macrophage in CVD Series (Part 1). JACC. 72:2166–2180
11. Xiang X et al (2021) Targeting tumor-associated macrophages to synergize tumor immunotherapy. Signal Transduct Target Ther 6:75
12. Li Z et al (2016) Shape Effect of Glyco-Nanoparticles on Macrophage Cellular Uptake and Immune Response. ACS Macro Lett 5:1059–1064
13. Choi BBR et al (2021) Gold nanoparticles conjugated with programmed death-ligand 1 antibodies induce apoptosis of SCC-25 oral squamous cell carcinoma cells via programmed death-ligand 1/signal transducer and transcription 3 pathway. Arch Oral Biol 125:105085
14. Marshall JS et al (2018) An introduction to immunology and immunopathology. Allergy Asthma Clin Immunol 14:49
15. Behzadi S et al (2017) Cellular Uptake of Nanoparticles: Journey Inside the Cell. Chem Soc Rev 46:4218–4244
16. Oh N et al (2014) Endocytosis and exocytosis of nanoparticles in mammalian cells. Int J Nanomedicine 9:51–63
17. Park J, Butler JE (2010) Analysis of the migration of rigid polymers and nanorods in a rotating viscometric flow. Macromolecules 43:2535–2543
18. Ahmad S et al (2017) Targeting dendritic cells through gold nanoparticles: A review on the cellular uptake and subsequent immunological properties. Mol Immunol 91:123–133
19. Kumari M et al (2016) Physio-chemical condition optimization during biosynthesis lead to development of improved and catalytically efficient gold nano particles. Sci Rep 6:27575
20. Doherty GJ et al (2009) Mechanism of endocytosis. Annu Rev Biochem 78:857–902
21. Sadauskas H et al (2007) Kupffer cells are central in the removal of nanoparticles from the organism. Part Fibre Toxicol 4:1–7
22. Qiu Y et al (2010) Surface chemistry and aspect ratio mediated cellular uptake of Au nanorods. Biomaterials 31:7606–7619

23. Bannunah AM et al (2014) Mechanisms of nanoparticle internalization and transport across an intestinal epithelial cell model: effect of size and surface charge. Mol Pharm 11:4363–4373
24. Yue J et al (2018) Smaller CpG-conjugated Gold Nanoconstructs Achieve Higher Targeting Specificity of Immune Activation. ACS Appl Mater Interfaces 10:21920–21926
25. Dykman LA et al (2017) Immunological properties of gold nanoparticles. Chem Sci 8:1719–1735
26. Pal R et al (2016) Noble metal nanoparticle-induced oxidative stress modulates tumor associated macrophages (TAMs) from an M2 to M1 phenotype: An in vitro approach. Int Immunopharmacol 38:332–341
27. Perdiguero EG et al (2016) Development and maintenance of resident macrophages. Nat Immunol 17:2–8
28. Hoeffel G et al (2015) Ontogeny of tissue-resident macrophages. Front Immunol 6:486
29. Walsh JC et al (2002) Cooperative and antagonistic interplay between PU.1 and GATA-2 in the specification of myeloid cell fates. Immunity 5:665–676
30. Haldar M et al (2015) Heme-mediated SPI-C induction promotes monocyte differentiation into iron-recycling macrophages. Cell 156:1223–1234
31. Janeway CA et al (2002) Innate immune recognition. Annu Rev Immunol 20:197–216
32. Tarique AA et al (2015) Phenotypic, functional, and plasticity features of classical and alternatively activated human macrophages. Am J Respir Cell Mol Biol 53:676–688
33. Oshi M et al (2020) M1 Macrophage and M1/M2 ratio defined by transcriptomic signatures resemble only part of their conventional clinical characteristics in breast cancer. Sci Rep 10:1–12
34. Wang N et al (2014) Molecular mechanisms that influence the macrophage M1–M2 polarization balance. Front Immunol 5:614
35. Georgoudaki AM et al (2016) Reprogramming tumor associated macrophages by antibody targeting inhibits cancer progression and metastasis. Cell Rep 15:2000–2011
36. Lin L et al (2015) CCL18 from tumor associated macrophages promotes angiogenesis in breast cancer. Oncotarget 6:34758–34773
37. Chanmee T et al (2014) Tumor-associated macrophages as major players in the tumor microenvironment. Cancers 6:1670
38. Afik R et al (2016) Tumor macrophages are pivotal constructors of tumor collagenous matrix. J Exp Med 213:2315–2331
39. Alvarado, P.A. et. al.: Macrophage specific nanotechnology driven CD163 overexpression in human macrophages results in M2 phenotype under inflammatory conditions. Immunobiology 222, 900–12 (2017).
40. Conde J et al (2015) Dual targeted immunotherapy via in vivo delivery of biohybrid RNAi-peptide nanoparticles to tumor associated macrophages and cancer cells. Adv Func Mater 25:4183–4194
41. Bastus NG et al (2009) Peptides conjugated to gold nanoparticles induce macrophage activation. Mol Immunol 46:743–748
42. Saha S et al (2016) Gold nanoparticle reprograms pancreatic tumor microenvironment and inhibits tumor growth. ACS Nano 10:10636–10651
43. Singh LM et al (2017) A comparative study on the antioxidant and immunomodulatory properties of curcumin conjugated gold nanospheres and free curcumin. J Appl Pharm Sci 7:056–063

Assessment of the Anti-Anxiety Potential of the Plant *Dysphania Ambrosioides* in Mice

Rupshikha Malakar, Arundhati Medhi, Rajashri Bezbaruah, Raja Chakraborty, and Ghanshyam Panigrihi

1 Introduction

The global prevalence of mental health disorders is escalating, it has been estimated that mental health disorders affect around 970 million people worldwide [1]. Amongst which, anxiety, a mental health condition accounts for 4% of the global population [1]. In India, 197.3 million are estimated to suffer from mental health disorders with 44·9 million having anxiety disorders [2]. The treatment regime for anxiety includes a combination of psychotherapy and pharmacotherapy. Standard medications used for anxiety are escitalopram, diazepam, and lorazepam. Although

R. Malakar (✉)
Girijananda Chowdhury Institute of Pharmaceutical Science, Tezpur, India
e-mail: rupshikha63@gmail.com

A. Medhi
Girijananda Chowdhury Institute of Pharmaceutical Science, Guwahati, India

R. Bezbaruah
Department of Pharmaceutical Science, Faculty of Science and Engineering, Dibrugarh University, Dibrugarh, India
e-mail: rajashribezbaruah@dibru.ac.in

R. Chakraborty
Institute of Pharmacy, Assam Don Bosco University, Tapesia, Assam, India

G. Panigrihi
Royal College of Pharmacy and Health Sciences, Brahmapur, Odisha, India

177

these medications are quite effective in the early stages, they eventually lose their efficacy and cause side effects such as drowsiness, nausea, constipation, sexual dysfunction as well as memory loss, and impairment in the longer run. Therefore, the treatment spectrum has inclined towards plant-derived natural compounds. Their effective phytochemical constituents have been reported to exert maximum beneficial effects with lower side effects in the treatment of neuropsychiatric disorders [3].

Traditional herbal medicine has been used to treat disorders from time immemorial throughout continents. *Dysphania ambrosioides* (L), Mosyakin and Clemants (Chenopodiaceae), is an essential part of traditional herbal medicine primarily found in the sub-tropical and sub-temperate regions of America, Mexico, India, and Africa [4]. In India, Dysphania ambrosioides have been widely found in various parts of Maharashtra, Kerala, Tamil Nadu, Karnataka, and throughout Assam, and also has been a crucial part of Indian ethnomedicine [4]. Dysphania ambrosioides is used to treat a wide range of disorders, popularly used as an anthelmintic, antifungal, antiparasitic, and anti-leishmania, as well as it has been reported to have been used for the treatment of inflammatory conditions such as rheumatism, cholecystitis, and gastritis also in respiratory diseases and cardiovascular diseases [5, 6]. Dysphania ambrosioides have also been reported to be used in the treatment of neuropsychiatric disorders such as anxiety, dementia, insomnia, and epilepsy [2, 7, 8]. The bioactive phytochemicals found in the leaf and seed extracts of *Dysphania ambrosioides* are ascaridole (55.3%), p-cymene (16.2%), alpha-terpinene (9.7%), isoascaridole (4.3%), limonene (3.8%), and terpene (trans pinocarveol, aritasone, β-pinene, myrcene, phellandrene, and terpineol) [5, 9, 10]. Ascaridole is the major bioactive compound found in the essential oils of *Dysphania ambrosioides* have been reported to show sedative effects in case of insomnia via activation of the GABAergic system [11]. Different extraction methods were reported to have been employed to harness the bioactive compounds effectively and have been assessed for their potential to treat many neurological disorders. The aqueous extract of *Dysphania ambrosioides* has been found to exert anxiolytic activity through the modulation of GABAergic neurotransmitters [12].

In the northeastern parts of India, namely Assam, *Dysphania ambrosioides* have been found abundantly and are extensively been used as a part of regional ethnomedicinal remediation. This study has been conducted to investigate the hydroethanolic leaf extract of *Dysphania ambrosioides* to evaluate the anxiolytic effect through the Elevated plus-maze test (EPM), and Open field test (OFT), Light and dark test (LDT), and Hole board test (HBT), in mice. We also investigated the *Dysphania ambrosioides'* chemical composition using qualitative biochemical tests to ascertain with existing literature to identify *Dysphania ambrosioides'* bioactive compounds. Furthermore, the results from this study could pave a path to a promising lead for the management of depression using *Dysphania ambrosioides* (leaf extract), although further mechanistic studies are needed to ascertain the same.

2 Methods and Materials

2.1 Animals

Healthy male mice weighing from 20 to 25 g were obtained from the Department of Pharmacology and Toxicology, College of Veterinary Science, Assam Agricultural University, Khanapara, Assam. The experimental protocol was approved (770/ac/CPCSFA/FVSc, AAU/IAEC/367) Institutional Animal Ethical Committee (IAEC) of the College of Veterinary Science, Assam Agricultural University, Khanapara, Assam. The animals were kept under standardized housing conditions in cages (6 mice per cage). The mice were housed in a temperature controlled environment (22 $\pm$ 1 °C) with a 12:12 hours light/dark cycle.

2.2 Plant Material and Extraction

Dysphania ambrosioides plants were collected from the medicinal garden of Assam, Agricultural University, Jorhat. The plant was authenticated by the Department of Agronomy, Assam Agricultural University, and a voucher specimen is kept in the herbarium (5109, dated 25.09.14).

Preparation of *Dysphania ambrosioides* hydroethanolic extract (DAHE): The collected plant materials were washed properly and dried in shade for 15 days. The dried materials were segregated and ground in an electric grinder. The crude powder was then put through a cold maceration process, which involved soaking 500 g of dried powder for 72 h in 70% ethanol while stirring continuously every 18 h with a sterile glass rod. The resulting filtrate was concentrated under decreased pressure in a rotary evaporator (BUCHI, R-210, Labortechnik AG, Meierseggstrasse, Switzerland) to yield a dark brown residue. Until usage, this residue was kept at 4 °C in an airtight container. 18.7% w/w was discovered to be the recovery percentage for the dried hydroethanolic extract of *Dysphania ambrosioides* powder.

2.3 Preliminary Screening of Phytochemical

Preliminary qualitative phytochemical screening of the DAHE extract was performed and the leaf extract of *Dysphania ambrosioides* was examined for the presence of alkaloids, glycosides, tannins, flavonoids, triterpenoids, anthraquinones, saponins, and phenols.

2.4   Drugs and Reagents

For the anti-anxiety study, diazepam (2 mg/kg) was used as a positive control. The drug is injected via the intraperitoneal (i.p) route. For the experiment, the animals were divided into 4 groups (n = 6), and those were kept in isolation to induce anxiety-like behavior. Animals were brought to the testing room in their respective housing cages from the colony rooms and were introduced to the new environment for at least 2 h prior to testing. Each mouse was used only once. The experiments were performed between 10:00 AM and 5:00 PM.

Four experimental protocols were designed. Each experimental protocol comprises 4 groups: Group I—Control, received vehicle (0.25 ml, p.o.); Group II—Standard, received diazepam (2 mg/ kg, i.p.); Groups III—Test, received 100 mg/kg doses of DAHE; Groups IV—Test, received 200 mg/kg doses of DAHE.

Diazepam was administered via the i.p route and the extracts were administered orally. After administering the appropriate dose of compounds, mice were kept in the housing cage for an hour before evaluating the respective behavioral test.

2.5   Evaluation of the Anti-Anxiety Properties via Behavioral Tests

Elevated Plus-Maze Test (EPM): A plus-maze with two closed arms (50 × 10 × 40 cm) and two open arms (50 × 10 × 40 cm) is used to assess anxiety using EPM test. The device was raised above the ground (50 cm). DAHE (100 and 200 mg/kg; test groups), diazepam (2 mg/kg; positive control group), and vehicle (0.25 mL/kg; normal group) were each given orally to four groups of six mice. Each animal was separately put in the raised plus-center maze after an hour, and 5 min of behavior observations were made [13]. Each mouse's number of admissions into open or closed arms as well as how long they stayed in either open or closed arms were counted and noted. Additionally, the number of grooming and head dipping as well as the weight of faecal boli were noted.

Open Field Test (OFT): The OFT utilized in the experiment is designed for anti-anxiety investigations and is made up of a wooden square box (72 × 72 × 36 cm) whose floor was divided into 16 identically sized squares (18 × 18 cm). Each of the four experimental groups of six mice received a different dosage of oral *Dysphania ambrosioides* extracts. Animals were put one at a time in the center of the open field apparatus after an hour of DAHE extract administration, and they were given 2 days to explore their experimental setting for 5 min each. The number of grooming, rearing, crossing (no. of square floor units entered), the weight of faecal boli, and raising (no. of times the animal stood on its hind legs) were all recorded for each group [13].

Light and dark test (LDT): LDT enables the assessment of the influence of medications on anxiety-like behavior by examining the preference of the animal for

the light and dark areas of the box. Minor adjustments were made to the test before running it [14]. The test box contains two chambers, each measuring 1/3 (16×50 cm) and 2/3 (34×50 cm) of the testing surface in bright and dark plastic, respectively. An 80 W light bulb was used to illuminate the light section. Only a little portion of the room's illumination reached the dark one. The animals were permitted to explore the light–dark arena 60 min after receiving dosages. The two halves are connected by a central opening (7×7 cm) at the floor level. Individual mouse behavior was tracked for 5 min, and the time spent by the mice in the light compartment of the apparatus was recorded.

Hole Board Test (HBT): HBT is performed to evaluate anxiety-like activity in mice according to the experiment [15]. The board consists of a wooden chamber ($40 \times 40 \times 25$ cm) with 16 holes (each measuring 3 cm in diameter) on the floor, raised from the ground to allow mice to peek through the holes. The two closest walls, as well as the surrounding corners, were 10 cm from the center of each hole. To reduce the transfer effect, mice were moved from the housing room to the testing room inside their home cages. Animals were given 30 min to adapt away from the observational apparatus in order to avoid any potential visual and/or olfactory impacts. The ambient temperature was kept constant at the same level as the housing room's temperature. Each animal was initially placed in the center of the arena and given 5 min to explore on its own.

2.6 Statistical Analysis

For each animal, the data are presented as Mean $\pm$ Standard Error of the Mean (S.E.M.). Statistical analysis of significance was evaluated by one-way analysis of variance (ANOVA). P-values less than 0.05 was considered statistically significant.

3 Results

3.1 Preliminary Phytochemical Screening of Hydroethanolic Extracts of Dysphania Ambrosioides (DAHE)

The DAHE has been screened for the presence or absence of carbohydrates, alkaloids, and flavonoids. The fraction of DAHE was investigated for their phytoconstituents, which led to the characterization of the extracts. The DAHE fraction was found to contain flavonoids, as confirmed by the Shinoda test as well as the lead acetate test. The absence of phytosterols was confirmed using Salkowski's test and Libermann Burchard's test. The gelatin test was used as a confirmatory measure for the presence of tannins. However, detection of carbohydrates, alkaloids, glycosides, proteins,

Table 1 Biochemical composition of DAHE

Biochemical chemical test	*Dysphania ambrosioides* Hydro ethanolic Extract (DAHE)
(A) Carbohydrates	
(1) Molisch's Test	−ve
(2) Benedict Test	−ve
(B) Alkaloids	
(1) Mayer's Test	−ve
(2) Wagner's Test	−ve
(C) Glycosides	
(1) Modified Borntrager's Test	−ve
(2) Legal's Test:	−ve
(D) Proteins and amino acids	
(1) Xanthoproteic Test	−ve
(2) Ninhydrin Test	−ve
(E) Flavonoids	
(1) Shinoda Test	+ve
(2) Lead acetate Test	+ve
(F) Phytosterols	
(1) Salkowski's Test	−ve
(2) Libermann-Burchard's Test	−ve
(G) Tannin	
(1) Gelatin Test	+ve

and amino acids in the hydroethanolic fractions could not be achieved by standard biochemical methods (Table 1).

3.2 Anxiolytic Effects of Dysphania Ambrosioides Hydroethanolic Extract (DAHE) on Different Behavioral and Locomotor Mice Models

Different dose concentrations of DAHE i.e., DAHE (100 mg/kg) and DAHE (200 mg/kg) were administered to the mice orally. Their effects were recorded at various intervals to study the behavioral and locomotor activities with the standard dose of the drug, i.e., diazepam (2 mg/kg) taken as a positive control. In the elevated plus-maze (EPM) model, with an increase in the dosage concentration of DAHE, there is an increment in the number of entries and the time spent in open arms in the test samples as compared to the control. In the case of the behavioral model of OFT, DAHE (200 mg/kg) shows a substantive elevation in the number of crossings. In

the case of the light and dark (LDT) model, there is an increase in the time spent by mice in the light space amongst the control group, standard drug group, and the DAHE group, but there are no significant changes found between the standard drug group and the DAHE groups suggesting both the drug and the DAHE might exert similar anxiolytic effects to the mice. Furthermore, in the case of HBM, the number of head dipping was found to be the same in both standard drug diazepam and DAHE (200 mg/kg) concentrations suggesting mild anxiolytic activity of the *Dysphania ambrosioides* leaf extract. In all the test groups, ANOVA indicated that the test samples resulted in a significant response ($p < 0.05$) in comparison to the control groups (Fig. 1).

4   Discussion

In the present study, it has been found that hydroethanolic extracts of *Dysphania ambrosioides* leaf exert anxiolytic effects in a dosage-dependent manner. DAHE extracts of *Dysphania ambrosioides* show potent anxiolytic activity at a dose of 200 mg/kg as demonstrated by a prominent increase in the number of crossings in the OFT model and an increment in the frequency of entries and time spent in the open arm of the EPM test suggesting mild anxiolytic activity. Moreover, flavonoids, and tannins are present in different extracts of *Dysphania. ambrosioides* also suggestively correlate to their anxiolytic activity.

The crude extracts of *Dysphania ambrosioides* leaves were prepared using hydroethanolic solvents, and their respective bioactive phytochemical constituents were identified using qualitative biochemical tests. It has been found that the fractions of DAHE contain flavonoids, as confirmed by the Shinoda test and lead acetate test. The absence of phytosterols was confirmed using Salkowski's test and Libermann Burchard's test in the extracts. Furthermore, the gelatin test confirms the presence of tannins in the extracts. The presence of flavonoid compounds derived from plant sources has been reported to show anxiolytic effects [10]. Thus, these active phytoconstituents in the fractions of DAHE correlate to their anxiolytic activity.

Previously, behavioral studies done in experimental mice using aqueous extracts of *Dysphania ambrosioides* have shown an increase in the percentage of entries into and percentage of time in open arms, and reduced rearing, head dipping, and percentage of time in closed arms, in the EPM test as well as a reduction in rearing and excretion, and an increased crossing in the OFT [12, 13], thus corresponding to its anxiolytic activity. The present study demonstrated that the hydroethanolic extract of *Dysphania ambrosioides* (DAHE) exerts anxiolytic effects in different behavioral and locomotive mice test models. DAHE at different dose concentrations has shown an escalation in the activity of mice in the open arms, a decrease in head dipping, an elevation in the number of crossing, and the percent of time spent in closed arms suggesting an anxiety reduction. This indicates that *Dysphania ambrosioides* hydroethanolic extract has the same anxiolytic properties as the aqueous extract.
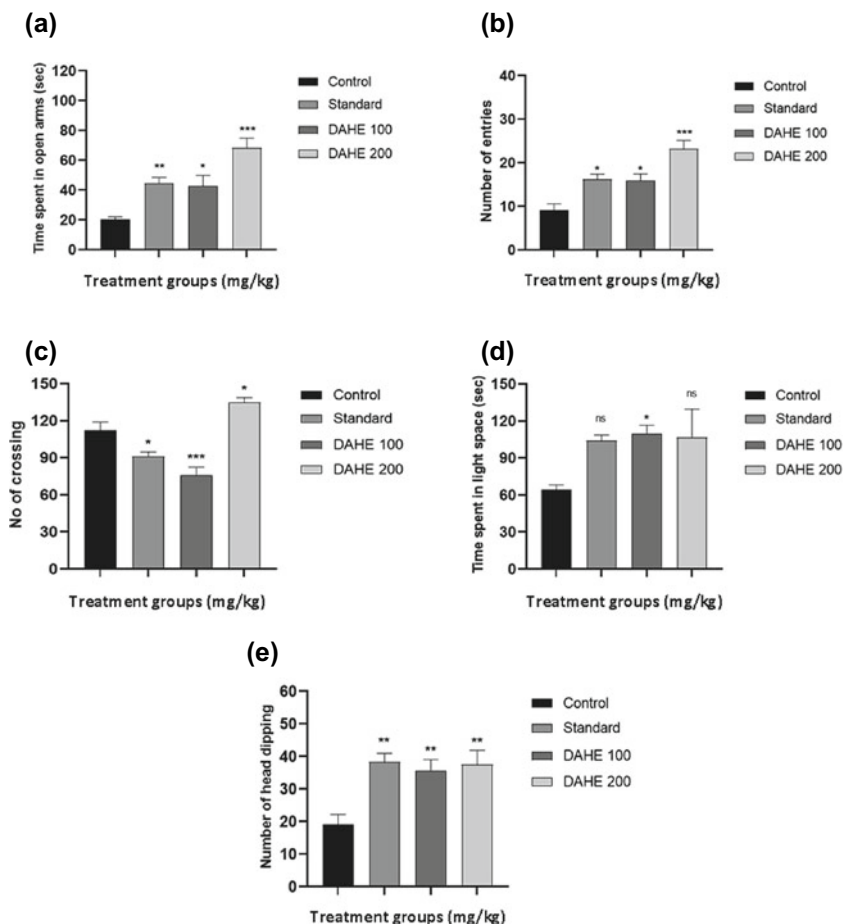
Fig. 1 Effects of *Dysphania ambrosioides* hydroethanolic extract (DAHE) were assessed on different behavioral and locomotive mice models: **a** in elevated plus maze test with time spent in open arm, **b** in elevated plus maze test with the number of entries, **c** in open field test with the number of crossing, **d** in light and dark test with time spent in the light space, **e** in hole board test with the number of head dipping (*p < 0.05; **p < 0.01; ***p < 0.001 as compared to the control groups; ns = non-significant)

5 Conclusion

In this study, *Dysphania ambrosioides*, a short-lived perennial plant, isolated from the north-eastern state of Assam, India, have been evaluated for their anti-anxiety activity in the mice model. From the results, it can be inferred that the *Dysphania ambrosioides* hydroethanolic extract showed mild anxiolytic-like activity. Thus, the study suggests that *Dysphania ambrosioides* leaf extract at a certain dosage could potentially be used for the treatment of anxiety.

References

1. Dougnon G, Ito M (2020) Role of ascaridole and p-Cymene in the sleep-promoting effects of dysphania ambrosioides essential oil via the GABAergic system in a ddY mouse inhalation model. J Nat Prod 84(1):91–100
2. Arbonnier M (2004) Trees, Shrubs, and Lianas of West African Dry Zones. MARGRAF PUBLISHERS GMBH, CIRAD
3. Kalin N (2020) The critical relationship between anxiety and depression. Am J Psychiatry 177(5):365–367
4. Renu G, Thilakar SJ, Narasimhan D, Chenopodium ambrosioides L. Synonym of Dysphania ambrosioides(L.) Mosyakin Clemants. Accessed 15 May. https://indiabiodiversity.org/biodiv/species/show/266344
5. World Checklist of Vascular Plants [Internet]. Wcvp.science.kew.org. 2021 [cited 10 November 2021]. Available from: http://wcvp.science.kew.org
6. Dattani S, Ritchie H, Roser M (2021) Mental Health [Internet]. Our World in Data. 2021 [cited 10 November 2021]. Available from: https://ourworldindata.org/mental-health
7. Belovicova K, Bogi E, Csatlosova K, Dubovicky M (2017) Animal tests for anxiety-like and depression-like behavior in rats. Interdiscip Toxicol 10(1):40–43
8. O'Connor J, Lawson M, André C, Moreau M, Lestage J, Castanon N et al (2008) Lipopolysaccharide-induced depressive-like behavior is mediated by indoleamine 2,3-dioxygenase activation in mice. Mol Psychiatry 14(5):511–522
9. Frances A, Manning D, Marin D, Kocsis J, McKinney K, Hall W et al (1992) Relationship of anxiety and depression. Psychopharmacology 106(S1)
10. Ko Y, Kim S, Lee S, Jang C (2020) Flavonoids as therapeutic candidates for emotional disorders such as anxiety and depression. Arch Pharmacal Res 43(11):1128–1143
11. de Lacerda Neto L, Ramos A, da Silva R, Pereira-de-Morais L, Silva F, da Costa R et al (2021) Myorelaxant effect of the dysphania ambrosioides essential oil on sus scrofa domesticus coronary artery and its toxicity in the drosophila melanogaster model. Molecules 26(7):2041
12. Bum E, Soudi S, Ayissi E, Dong C, Lakoulo N, Maidawa F et al (2011) anxiolytic activity evaluation of four medicinal plants from cameroon. Afr J Tradit, Complement Altern Med 8(5S)

13. Bigued GST, Jacqueline Njapdounke SK, Ngaibi J, Yvette N, Neteydji S et al (2021) Behavioural and neurochemical characterization of the anxiolytic properties of an aqueous extract of Dysphania ambrosioides (L.) Mosyakin and Clemants (Chenopodiaceae) in experimental mice. GSC Biol Pharm Sci 14(03):265–276
14. Bourin M, Hascoët M (2003) The mouse light/dark box test. Eur J Pharmacol 463(1–3):55–65. https://doi.org/10.1016/s0014-2999(03)01274-3
15. Himanshu D, Sarkar D, Nutan (2020) A review of behavioral tests to evaluate different types of anxiety and anti-anxiety effects. Clin Psychopharmacol Neurosci: Off Sci J Korean CollE Neuropsychopharmacol 18(3):341–351. https://doi.org/10.9758/cpn.2020.18.3.341

Cardio-Metabolic Risk Analysis in Youths from North East India (Tripura)

Nabamita Nath and **Dipayan Choudhuri**

1 Introduction

Persistence of cardio metabolic syndrome is associated with many factors. People suffering from MetS are at increased risk of developing heart disease, stroke and diabetes [1].

Cardio-metabolic risk in different population changes according to region, life style pattern, socioeconomic and cultural factors [2, 3]. Reports reveal that ethnicity plays an important role in prevalence pattern of metabolic syndrome [4, 5]. Lifestyle changes and many other factors elevate the CVD burden and mortality. [6, 7].

Researches have shown that young adults are increasingly becoming prone to many diseases including cardio metabolic disorders [8]. However there is worldwide paucity in data on the risk profile of cardio-metabolic disorders in young adults owing to the fact that the disease is usually thought to affect people in later part of their life. However, early identification of risk factors and adoption of appropriate corrective measures help in reducing the burden of onset of disease in latter part of the individual's life. There is a serious lack in nationwide representative data on cardiovascular risk profile of adolescents from India, especially from North–Eastern states. Considering the fact, it is pertinent to undertake a study on the cardio metabolic risk profile in local young adult subjects.

N. Nath
Department of Human Physiology, Netaji Subhash Mahavidyalaya, Udaipur, Tripura, India

D. Choudhuri (✉)
Department of Human Physiology, Tripura University, Tripura, India
e-mail: dipayanchoudhuri@gmail.com

The patho-physiology of the metabolic syndrome has only been partially elucidated. Usually, it is observed that people who are obese, advanced in age, sedentary and have a measure of insulin resistance are prone to the syndrome. Central obesity is the most important risk factor of MetS [9]. In view of the above fact, in the present study we have evaluated the cardio-metabolic risk factors in a population consisting of young adults (18–25 years age) from Tripura, a North Eastern state of India.

2 Methodology

Metabolic risk factors of the subject were evaluated following NCEP ATP III guidelines for MetS. The study was designed to obtain a cross sectional population-based data on anthropometric and cardio metabolic parameters of young adult (18–25 years) subjects from Agartala, Tripura, India. Only healthy Indian tribal and non-tribal youths were selected irrespective of their sex and ethnicity. Subjects having known cardiovascular disorders, endocrine disorders (thyroid, adrenal), any type of chronic diseases (COPD, cancer, psychiatric problems) were not selected. The calculated sample size following World Health Organization (WHO) guideline on population-based study was 323. However, the total no of subjects evaluated was 463, out of which 347 subjects [Male 183 (Tribal, Non-tribal), Female 164 (Tribal, Non-tribal)] completed all the procedures and had not come under any of the exclusion criteria. The individual's personal information, general health status, history of past illness, family history of the subject were taken in a formulated form following WHO suggested protocol [10, 11]. The following parameters were recorded in the study subjects.

2.1 Recording of Anthropometric Parameters

Standard recommendation was followed [12] during the recording of anthropometric parameters. Weighing machine (Libra R) was used for weight (kg) measurement. Subjects were asked to stand erect on the machine without shoes, exerting equal pressure on both feet and in normal clothing. Stadiometer (Bio Plus R, S. NO—51,392) was used for standing height (cm) measurement. The subjects were standing erect without any footwear. During measurement, scapula, buttock and head were positioned in contact with backboard whereas arms were hung openly by the sides of the trunk. Waist circumference (WC) and hip circumference (CM) in cm were recorded by the anthropometric measuring tape. Body mass index (BMI), waist to hip ratio (WHR), waist to height ratio (WHtR) were calculated by using formula [13].

2.2   Estimation of Blood Glucose Level

Blood glucose was estimated by using a commercial kit by the glucose oxidase peroxidase (GOD-PAP) method [14].

2.3   Estimation of Serum Lipid Profile of Subject

Serum lipid profile parameters were analysed.

(a)   Estimation of serum total cholesterol

Serum cholesterol was measured by the cholesterol oxidase- peroxidase (CHOD-PAP) enzymatic method [15].

(b)   Estimation of serum triglyceride

Serum triglyceride was estimated by the glycerol phosphate- oxidase (GPO-PAP) method [16].

(c)   Estimation of serum HDL

Serum HDL cholesterol was measured by the Enzymatic method (Direct method) [17].

(d)   Estimation of serum LDL

It is calculated by using the formula. Total cholesterol minus HDL cholesterol minus triglycerides divided by five.

3   Result and Interpretation

Baseline characteristics of young subjects with and without MetS. In Table 1, all characteristics were significantly higher in MetS subjects from all groups.

In Table 2, both tribal and non-tribal young male subjects having metabolic syndrome showed significantly higher values for systolic and diastolic blood pressure and triglyceride. However, females having metabolic syndrome in both categories showed significantly higher values in maximum parameters except systolic and diastolic blood pressure and total cholesterol. High density lipoprotein cholesterol was lower in all subjects with metabolic syndrome irrespective of sex and ethnicity.

Analysis of prevalence of different risk factors in subjects revealed that among a total of 347 adolescents, 79 subjects had three or more cardio metabolic risk factors whereas 135 subjects had no risk factor at all. The percentage distribution of the categories revealed 22.75% of total subjects had profound cardio metabolic risk

Table 1 Anthropometric characteristics of study subjects

Parameters	Male (78)		Male (105)		Female (75)		Female (89)	
	Tribal		Non-tribal		Tribal		Non-tribal	
	Non-MetS (62)	MetS (16)	Non-MetS (80)	MetS (25)	Non-MetS (59)	MetS (16)	Non-MetS (67)	MetS (22)
Height (cm)	162.53 ± 5.61	$163.51 \pm 4.44^{\#}$	169.72 ± 6.17	171.71 ± 5.32	155.75 ± 4.29	156.27 ± 2.96	159.54 ± 3.62	160.85 ± 4.23
Weight (kg)	57.86 ± 5.40	$66.34 \pm 3.20^{***}$	60.41 ± 7.23	$69.12 \pm 5.61^{***}$	54.94 ± 4.57	$58.96 \pm 3.09^{***}$	56.12 ± 5.09	$60.71 \pm 4.14^{***}$
BMI (kg/m^2)	21.94 ± 2.13	$24.87 \pm 1.84^{***}$	21.49 ± 2.40	$23.47 \pm 1.90^{***}$	23.57 ± 2.05	24.16 ± 1.39	22.07 ± 2.17	$23.50 \pm 1.93^{**}$
WC (cm)	80.34 ± 19.09	$106.58 \pm 3.30^{***}$	84.82 ± 19.29	$106.39 \pm 4.62^{***}$	83.64 ± 8.05	$90.91 \pm 3.06^{***}$	82.74 ± 7.22	$90.73 \pm 1.56^{***}$
HC (cm)	90.60 ± 19.71	$111.91 \pm 8.32^{***}$	95.30 ± 18.64	$113.62 \pm 5.34^{***}$	93.00 ± 7.41	$98.86 \pm 3.09^{**}$	92.28 ± 7.32	$98.30 \pm 1.88^{***}$
WHR	0.88 ± 0.04	$0.96 \pm 0.06^{***}$	0.89 ± 0.06	$0.94 \pm 0.03^{***}$	0.90 ± 0.06	$0.92 \pm 0.02^{\#}$	0.90 ± 0.04	$0.92 \pm 0.02^{*}$
WHtR	0.50 ± 0.12	$0.65 \pm 0.03^{***}$	0.51 ± 0.12	$0.62 \pm 0.03^{***}$	0.55 ± 0.06	$0.58 \pm 0.02^{*}$	0.52 ± 0.05	$0.56 \pm 0.02^{***}$

*$p - < 0.05$; **$p - < 0.01$; ***$p - < 0.001$; #$-$ not significant

Table 2 Comparison of cardio metabolic parameters in study subjects

Parameters	Male (78)		Male (105)		Female (75)		Female (89)	
	Tribal		Non-tribal		Tribal		Non-tribal	
	Non-MetS (62)	MetS (16)	Non-MetS (80)	MetS (25)	Non-MetS (59)	MetS (16)	Non-MetS (67)	MetS (22)
SBP (mmHg)	120.63 ± 8.27	129.94 ± 8.77***	122.25 ± 9.18	131.56 ± 8.23***	122.83 ± 7.40	122.25 ± 10.07#	123.36 ± 6.60	123.64 ± 7.92#
DBP (mmHg)	77.58 ± 5.41	82.38 ± 6.28**	78.19 ± 7.53*	83.80 ± 6.06**	80.51 ± 4.53	80.13 ± 5.68#	79.75 ± 3.43	80.82 ± 5.32#
TG (mg/dl)	131.59 ± 20.48	168.29 ± 21.74***	131.80 ± 27.54	164.38 ± 9.83***	137.93 ± 14.67	166.06 ± 16.47***	134.75 ± 16.87	163.27 ± 16.60***
TC (mg/dl)	175.69 ± 24.06	180.63 ± 25.11#	176.84 ± 26.34	177.69 ± 24.06#	191.14 ± 18.62	200.00 ± 24.73#	186.82 ± 21.57	189.96 ± 22.93#
HDL-C (mg/dl)	38.18 ± 6.87	34.63 ± 5.06*	39.60 ± 6.11	36.18 ± 3.10**	49.76 ± 7.61	40.93 ± 6.40***	48.19 ± 9.38	36.84 ± 8.03***
LDL-C (mg/dl)	111.19 ± 22.66	112.34 ± 20.34#	110.88 ± 24.86	108.64 ± 23.86#	113.79 ± 13.56	125.86 ± 18.60**	111.68 ± 16.97	120.47 ± 16.74*
FBS (mg/dl)	84.69 ± 11.73	90.15 ± 14.74#	87.30 ± 12.22	90.44 ± 14.52#	84.31 ± 11.04	94.02 ± 16.69**	82.39 ± 12.21	92.80 ± 16.39**

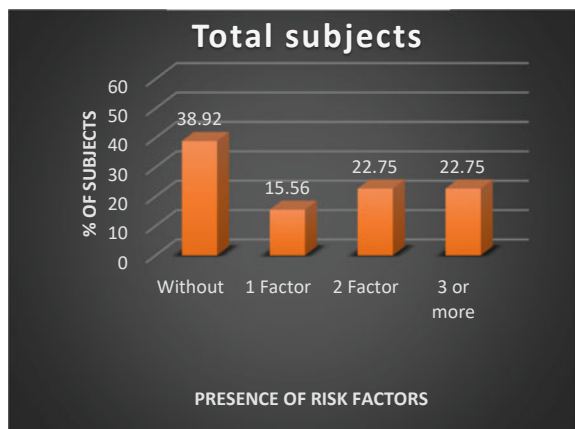*$p - < 0.05$; **$p - < 0.01$; ***$p - < 0.001$; # – not significant

whereas 38.92% of subjects had no risk. Out of 347 subjects, 183 were male. Among the male subjects, we found that 24.04% of males had three or more risk factors, 12.02% had two risk factors, 23.49% had one of the risk factor and 40.44% had no risk factor. The numbers of total female subjects were 164. Among them, 23.78% had three or more risk factors,16.46% having two risk factors, 21.95% of female have one of the risk factors, and 37.80% of female subjects had no risk factor (Figs. 1a, b and 2a, b).
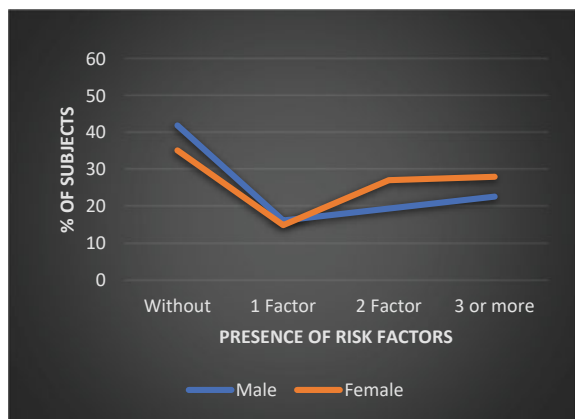
Age group wise distribution showed, among subjects belonging to 18–21 years of age, the percentage of subjects with metabolic syndrome were 20.75 and 17.24% respectively for male and female subjects. For subjects belonging to 22–25 years of age, the percentage was 23.08% for male and 25.47% for female subjects (Table 3).

Fig. 1 Distribution of subjects in different categories of cardio metabolic risk. **a** Total subjects (male and female). **b** Male and female subjects separately
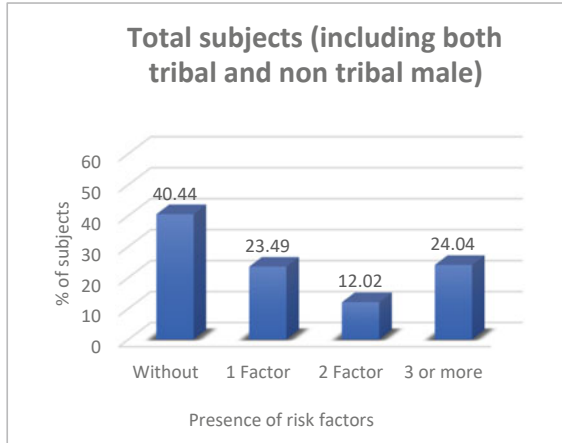
(a) Total subjects (male and female)

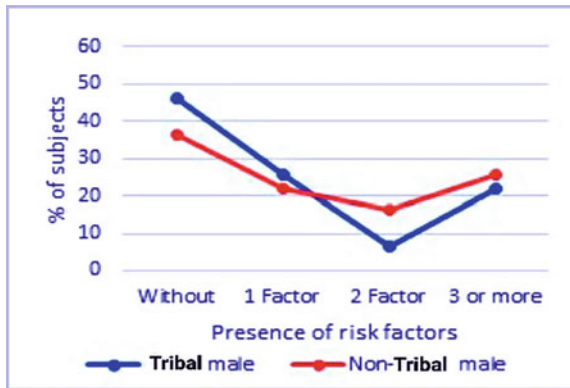**(b) Male and female subjects separately**

(a)

Total subjects (Male):

Tribal and non-tribal males separately:

Prevalence of individual risk factors among study subjects revealed, in both male and female as well as tribal and non-tribal groups, most prevalent risk factors were central obesity marked by increased waist circumference and altered lipid profile marked by elevation of triglyceride level and reduced HDL-C level. Hypertension marked by increased SBP and DBP; and hyperglycaemia marked by increased FBS were least prevalent risk factors among all the groups of the study subjects (Fig. 3a, b).

Analysis of the metabolic syndrome components for tribal and non-tribal subjects, by binary method revealed that the higher risk shown by the factor serum TG (Wald test score $= 90.38$, p $= <0.001$ and 105.07, p $= <0.001$). The second most affecting factor was WC for both tribal and non-tribal subjects followed by HDL-C, FBS and BP (Tables 4 and 5).

Fig. 2 (continued)

(b)

Total subjects (Female):
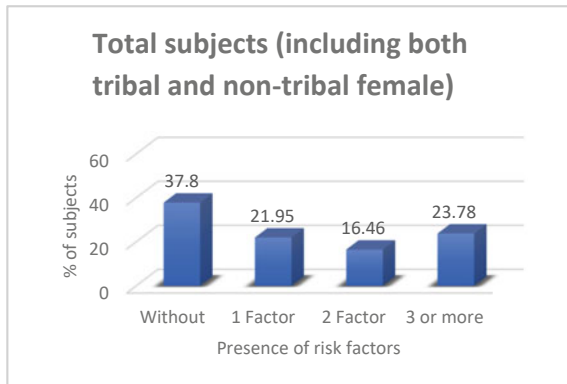
Tribal and non-tribal females separately
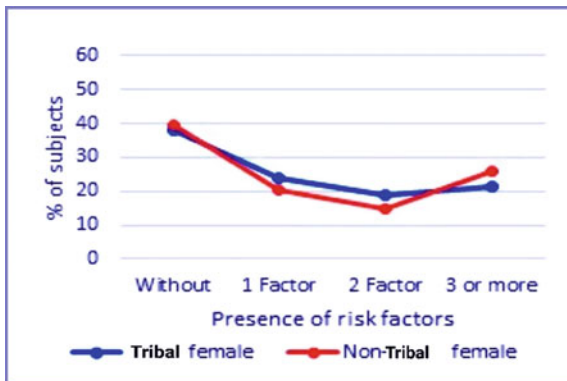
Table 3 Number of subjects with MetS according to age group

Age intervals (in yrs)	Total study subjects			Metabolic syndrome subjects (N, %)	
	Male	Female	Total	Male	Female
18–21	53	58	111	11 (20.75)	10 (17.24)
22–25	130	106	236	30 (23.08)	27 (25.47)
18–25	183	164	347	41 (22.40)	37 (22.56)

The present study revealed that 22.75% of adolescent (18–25 yrs) subjects from Tripura had profound cardio-metabolic risk. Subjects belonging to higher age group (22–25 yrs) had more prevalence MetS than the subjects in the younger age group (18–21 yrs) age group. The most prevalent risk factors among the subjects were

Fig. 3 Prevalence of individual risk factors in study subjects. **a** Total subjects. **b** Tribal and non-tribal subjects

(a) Total subjects:
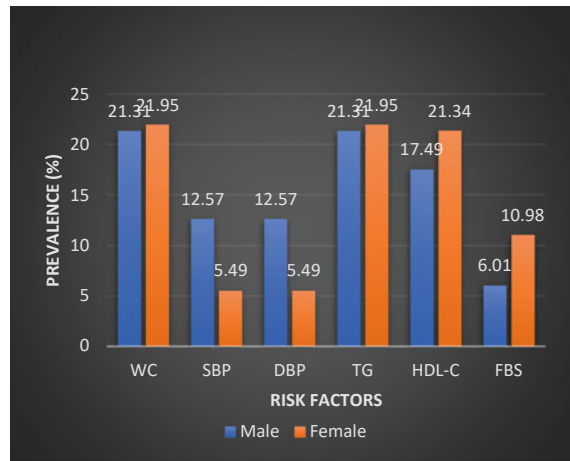
(b) Tribal and non-tribal subjects:

central obesity and altered lipid profile. According to binary logistic regression analysis, the individual risk component for MetS in all categories of the subject was serum TG followed by other components.

4   Discussion

The overall prevalence of MetS was found to be almost similar in male (22.40%) and in female (22.56%) subjects in our study. A secular trend between 1986 and 2001 in young Finns study suggested an increased occurrence of MetS in youths

Table 4 Binary logistic regression analysis on components of metabolic syndrome in tribal subjects

Tribal (153) variables	Metabolic syndrome		Wald test statistics value	P-value
	Present (N, %)	Absent (N, %)		
Waist Circumference, WC (cm)				
Female < 88, Male < 102	1 (0.65)	104 (67.97)	80.635	<0.001***
Female ≥ 88, Male ≥ 102	31 (20.26)	17 (11.11)		
SBP (mm Hg)				
<130	20 (13.07)	110 (71.90)	15.9908	0.001***
≥130	12 (7.84)	11 (7.19)		
DBP (mm Hg)				
<85	20 (13.07)	110 (71.90)	15.9908	0.001***
≥85	12 (7.84)	11 (7.19)		
TG [mmol/L]				
<1.7	3 (1.96)	111 (72.55)	90.3849	<0.001***
≥1.7	29 (18.95)	10 (6.54)		
HDLC (mmol/L)				
Female > 1.29, Male > 1.03	5 (3.27)	95 (62.09)	44.2057	<0.001***
Female < 1.29, Male < 1.03	27 (17.65)	26 (16.99)		
FBS (mmol/L)				
<5.6	19 (12.42)	111 (73.55)	20.7485	<0.001***
≥5.6	13 (8.50)	10 (6.54)		

*$p – < 0.05$; **$p – < 0.01$; ***$p – < 0.001$; # – not significant

which was higher in male than the female subjects [18]. In a study among young adults (18–30 years) from Ellisars, South Africa, the overall prevalence was found to be 23.1%, however, it was very much high in females (36.8%) compared to males (8.6%) [19]. In Tehran Lipid and Glucose study (TGGS), a cumulative incidence of MetS among young adults (age 11–18 years) was elevated in young men (25.5%) comparing women (20.0%) [20]. In a study on correlates of MetS among young Brazilian adolescent population (age 12–18 years), an overall prevalence of 4.7% was observed [21].

Kaushal et al. in a study among urban young population of Agra, observed a overall MetS prevalence of (37.0%) with female subjects suffering more (65.96%) than the male subjects (34.04%) [22]. Mangat et al. also reported similar prevalence (38.5%) in Chandigarh [23]. Ramchandran et al. reported a slightly higher prevalence (41.1%) from Chennai [24]. A study conducted among the medical students of age 17 and above in Wardha showed a prevalence of 11.2% with females having higher (13.5%) prevalence than males (9.7%) [25]. Another study among medical students

Table 5 Analysis on components of metabolic syndrome in non-tribal subjects

Non-tribal (194) variables	Metabolic syndrome		Wald test statistics value	P-value
	Present (N, %)	Absent (N, %)		
Waist circumference, WC (cm)				
F < 88, M < 102	3 (1.55)	121 (62.37)	89.0273	<0.001***
F ≥ 88, M ≥ 102	44 (22.68)	26 (13.40)		
Systolic blood pressure (mm Hg)				
<130	27 (13.92)	127 (65.46)	18.2333	0.001***
≥130	20 (10.31)	20 (10.31)		
Diastolic blood pressure (mm Hg)				
<85	27 (13.92)	128 (65.98)	19.4637	0.001***
≥85	20 (10.31)	19 (9.79)		
TG (mmol/L)				
<1.7	1 (0.52)	124 (63.92)	105.0696	<0.001***
≥1.7	46 (23.71)	23 (11.46)		
HDLC (mmol/L)				
F > 1.29, M > 1.03	6 (3.09)	117 (60.31)	67.128	< 0.001***
F < 1.29, M < 1.03	40 (20.62)	30 (15.46)		
Fasting blood sugar (mmol/L)				
<5.6	31 (15.98)	132 (68.04)	15.0739	0.001***
≥5.6	16 (8.25)	15 (7.73)		

*$p - < 0.05$; **$p - < 0.01$; ***$p - < 0.001$; # – not significant

(age 17–22 years) from Bangalore showed 11.1% prevalence of MetS [26]. Similar to our findings, a North Indian study conducted among subjects of 16–45 years revealed 22.4% prevalence of MetS and the prevalence was comparable in both the genders [27]. The difference in prevalence is observed due to the age group difference of subjects and the criteria used to identify the risk factors. Overall, the study revealed a substantial portion of young adults having prevalence of MetS. Such people need to be stratified according to the CVD or DM risk and these high-risk population should undergo regular screening.

Our study revealed, among different factors; increased TG emerged as the prime factor in both genders; while low HDLC did not play any significant role in male subjects, it emerged as the second most prominent risk factor among female subjects. Deepa et al. from their study revealed increased triglycerides in 25.2% and lower HDLC in 63.5% of the subjects with MetS [28]. Accordingly comparison of various atherogenic markers in our study, showed a significantly higher TG: HDL-C ratio in subjects with MetS. Correlation between various traditional cardio metabolic risk factors with obesity and atherogenic marker revealed that most of the risk factors are correlated with markers like BMI, WC and WHR. It was reported that both WC and

HC were low in Asian population than the Caucasian population and both WC and BMI can predict cardio metabolic risk in Asian Indians [29].

5 Conclusion of the Study

Relatively higher proportion of Indian young adults from North Eastern state of Tripura is having cardio metabolic risk factors which may ultimately lead to the development of CVD or T2DM in future.

The proportion of subjects with MetS is comparable with young adults from different countries of the world and from different states and regions of India. The trend is similar across gender and ethnicity of the subject.

As emergence of MetS in young adults is associated with various factors like demographic shift, nutritional and life style transition, urbanization and mechanization and as MetS present a serious threat to current and future health of the subject, early screening for MetS in adolescents as well as young adults will increase the utility of intervention strategies and help in reversing associated co-morbidities.

6 Significance of the Study

- The study for the first time, has generated a comprehensive database on the risk of metabolic syndrome among young adults consisting of both tribal and non-tribal subjects from Tripura, India.
- Data generated from the study can be utilized by policymakers to take initiative for providing appropriate healthcare facilities for young adults belonging to the study population and to the nation as a whole.
- Early identification of cardio metabolic health status will help in taking proper preventive measures against future development of cardiovascular and metabolic disorders in such population from the state.
- The findings will help to identify the targeted groups and also help to minimize CVDs and metabolic disorders in them.

7 Limitations of Study

- The study included subjects from only the major tribal community of Tripura- the Tripuris and the major non-tribal community residing in and around Agartala, the capital city of Tripura. Subjects from other tribal and non-tribal communities of Tripura and subjects from other parts of state would have given an overall picture of all the adolescence residing in Tripura.

- It is a cross-sectional study which did not follow up with the subjects to find out whether risk factors for MetS lead ultimately to the development of heart diseases or type II DM. Longitudinal studies are required to investigate future progression of the metabolic syndrome to CVD or DM in subjects.

8 Future Prospects of the Study

- In future, longitudinal studies can be planned to further evaluate progression of the risk factors to the development of cardiovascular and metabolic disorders.
- Studies can be taken up involving subjects from other communities covering the entire state to have an overall picture of the status metabolic syndrome among the adolescents of the state.
- Studies on genetic predisposition behind variation in prevalence of different risk factors in subjects from different communities and sexes can be planned.

References

1. Amiri P, Hosseinpanah F, Farahani SJ et al (2014) Is persistence of metabolic syndrome associated with poor health-related quality of life in non-diabetic Iranian adults: Tehran Lipid and Glucose Study. J Diabetes Invest 5:687–693. https://doi.org/10.1111/jdi.12222
2. Pandit K, Goswami S, Ghosh et al (2012) The metabolic syndrome in south Asians. Indian J Endocrnol. Metab 16(1):44–55
3. Lin SX, Carnethon M, Szklo M, Bertoni A (2011) Racial/Ethnic difference in association of triglyceride with other metabolic syndrome components: the multi-ethnic study of Atherosclerosis. Metab SynRelatDisord 9(1):35–40
4. Lee YJ, Woo SY, Ahn JH, Cho S, Kim SR (2012) Health-related quality of life in adults with metabolic syndrome: the Korea national health and nutrition examination survey, 2007–2008. Ann NutrMetab 61:275–280. https://doi.org/10.1159/000341494
5. Pisa PT, Behanan R, Vorster HH, kruger A (2012) Social drift of cardiovascular diseases risk factors in Africans from the North West Provinces of South Africa: the PURE study. Cardio-Vascular J Africa 23(7):371–388
6. Sanal MG, Sarin K (2011) Association of non-alcoholic fatty liver disease with metabolic syndrome in Indian population. Diabetes MetabSyndr 5(2):76–80
7. Gupta R, Sharma KK, Gupta A et al (2012) Persistent high prevalence of cardio metabolic risk factors in urban middle class in India: Jaipur Heart watch 5. J Assoc Physician India 60:11–16
8. Abbs ES, Viñoles J, Alarcón JO et al (2017) High prevalence of cardiovascular risk factors in Peruvian adolescents living in a peri-urban shantytown: a cross-sectional study. J Health Popul Nutr 36:19. https://doi.org/10.1186/s41043-017-0093-1
9. Mustaq MU, Gall S, Abdullah HM (2011) Waist circumference, waist hip ratio and waist-height ratio percentile and central obesity among Pakistani children aged five to twelve years. BMC Pedatr 11:105–112
10. World Health Organization. Physical status: The use and interpretation of Anthropometry. Technical Report Series No. 854: WHO, Geneva. 1995
11. Pelegrino R, Viegi G, Brusasco V et al (2005) Interpretative strategies for lung function tests. Euro Respir J 26:948–968

12. Miiler MR, Hankinson J, Brusasco V et al (2005) Standardization of spirometry. Eur Respir J 26:319–338

13. Chen Y, Rennie D, Cormier YF, Dosman J (2007) Waist circumference is associated with pulmonary function in normal-weight, overweight, and obese subjects. Am J Clin Nutr 85:35–39

14. Trinder P (1969) Quantitative determination of glucose using GOP-PAP method. Clinical Biochem 6:24–27

15. Allain CC, Poo LS, Chan CSG et al (1974) Enzymatic determination of total serum cholesterol. Clin Chem 20:470–475

16. Bucolo G, David H (1973) Quantitative determination of serum triglyceride by the use of enzymes. Clin Chem 19(5):476–482

17. Castelli GT, Hjortland MC, Kannel WB, Dawber TR (1977) High density lipoprotein as a protective factor against coronary heart disease. The Framingham study. Am J Med 62(5):707–714

18. Mattsson N, Ro¨nnemaa T, Juonala M, Viikari JSA, Raitakari OT (2007) The prevalence of the metabolic syndrome in young adults. The Cardiovascular Risk Young Finns Study. J Intern Med 261:159–169

19. Sekgala MD, Monyeki KD, Mogale A et al (2018) The risk of metabolic syndrome as a result of lifestyle among Ellisras rural young adults. J Hum Hypertens 32:572–584

20. Barzin M, Asghari G, Hosseinpanah F, Mirmiran P, Azizi F (2012) The association of anthropometric indices in adolescence with the occurrence of the metabolic syndrome in early adulthood: Tehran Lipid and Glucose study (TLGS). Pediatr Obes 8:170–177

21. dos Santos MC, de Castro Coutinho APC, de Souza Dantas M et al (2018) Correlates of metabolic syndrome among young Brazilian adolescents' population. Nutr J 17:66. https://doi.org/10.1186/s12937-018-0371-9

22. Kaushal SK, Gupta V, Prakash G, Misra SK (2016) Correlates of metabolic syndrome and prevalence among urban population of Agra, Uttar Pradesh, India. Int J Community Med Public Health 3(12):3570–3575

23. Mangat C, Goel NK, Walia DK et al (2010) Metabolic syndrome a challenging health issue in highly urbanized Union Territory of North India. Diabetol Metab Syndr 23:2–19

24. Ramachandran A, Snehalatha C, Satyavani K, Sivasankari S, Vijay V (2003) Metabolic s syndrome in urban Asian Indian adults–a population study using modified ATP III criteria. Diabetes Res Cli Pract 60(3):199–204

25. Jain J, Rao T, Deshmukh P, Banait S (2015) Prevalence and correlates of metabolic syndrome in young population: a cross sectional study. J Diabetes MetabIsm 6:3–8

26. Usha SM, Chandrika N, Shetty HV, Reena R (2014) A study of the components of metabolic syndrome in young adults. Biomed Res 25(1):45–50

27. Chandey M, Kaur S, Kaur H (2017) Prevalence of metabolic syndrome in young adults: a study from North India. Int J Adv Med 4(2):463–466. https://doi.org/10.18203/2349-3933.ijam20171042

28. Deepa M, Farooq S, Datta M, Deepa R, Mohon V (2007) Prevalence of metabolic syndrome using WHO, ATP iii and IDF definitions in Asian Indians: The Chennai urban rural epidemiology study. Diabetes Metab Res Rev 23:127–134

29. Kanjilal S, Shanker J, Rao VS (2008) Prevalence and component analysis of metabolic syndrome: an Indian atherosclerosis research study perspective. Vasc Health Risk Manag 4:189–197

An Overview on the Therapeutic Strategies for Covid-19

Nayanmoni Baruah ⓘ**, Hemanta Kumar Sharma** ⓘ**, Pallab Kalita** ⓘ**,
Aditya Bora** ⓘ**, Kamallochan Barman** ⓘ**, Bhanita Das** ⓘ**, Jayita Das,
Quri Kiron Hazarika** ⓘ**, and Sudarshana Borah** ⓘ

1   Introduction

The virus is known as SARS-CoV-2 by the International Committee on Taxonomy of Viruses because it resembles the SARS Coronavirus in some ways. SARS-origin CoV-2 is still a mystery, and it is being discussed from extraordinary perspectives by amazing people. The World Health Organization refers to the condition as the Coronavirus disorder-2019 (COVID-19).

This virus is a β-Coronavirus and both SARS and SARS-CoV2 belong to this species of virus. The S protein of SARS-CoV2 is a glycoprotein and arbitrates the access of the virus into the host cells. The S protein of the virus takes a homotrimeric (a) protein which is composed of three identical units of polypeptide) shape to engage with the host cell. The S1 location is capable because of the receptor-binding domain (RBD) and stabilizes the perfusion conformation, while the S2 location is capable as a fusion protein. The homotrimer region of S1 appears to subsist in partially opened conditions in perceptibly infectious human SARS-CoV2.

Comparative analysis of the sequences of SARS-CoV-2 and SARS-CoV revealed similarities in S protein, RBD, and receptor binding motif (RBM) of 76.04, 73.33 and 50.00% respectively. An analysis of the full-period genomic collection has confirmed

N. Baruah · H. K. Sharma
Department of Pharmaceutical Sciences, Faculty of Science and Engineering, Dibrugarh
University, Dibrugarh 786004, Assam, India

P. Kalita · A. Bora · K. Barman · B. Das · J. Das · Q. K. Hazarika · S. Borah (✉)
School of Pharmaceutical Sciences, University of Science and Technology Meghalaya,
Baridua 793101, Meghalaya, India
e-mail: shonapharma@gmail.com

that SARS-CoV and SARS-CoV-2 distribute 79.6% proportion of the same genetic makeup, showing that Pangolin-CoV has greater resemblance with SARS-CoV-2 than RaTG13 bat Coronavirus located between the S1 subunit and S2 subunit of the S protein of SARS-CoV-2, which has a functional furin cleavage site.

In different SARS associated β-coronaviruses and viruses, this specific division web page has now no longer been experiential. SARS-CoV and its associated different viruses have a monobasic distribution web page among S1 and S2 locations of the S protein. In the present day situation, it's far important to increase a powerful healing intervention to save you and manipulate the disease [1, 2]

2 Overview of the Therapeutic Strategies

A review of the therapeutic strategies on COVID-19 gives us a design on the Immunomodulators, Corticosteroids, Nutritional intervention, Vaccine development strategies and Stem cell therapy. Tocilizumab, an immunosuppressive medication with FDA approval, is employed to treat a variety of diseases, including systemic juvenile idiopathic arthritis and rheumatoid arthritis. It is an interleukin-6 receptor-specific monoclonal antibody that has been humanized (IL-6R). Gp130 that is membrane-bound and the IL-6 receptor complex interact to help with intracellular signaling. A variety of physiological processes, including gene activation, are regulated by this intracellular signaling [3]. Tocilizumab was suggested as a treatment option in the 7th edition of China's official medical manuals for severe SARS-CoV-2 contagions with high IL-6 concentration [4]. Rheumatoid arthritis is treated using a biopharmaceutical drug called Anakinra. This is a slightly altered recombinant human interleukin-1 (IL-1) receptor antagonist [5]. Efficiency of Anakinra in easing respiratory discomfort and hyper inflammation in patients suffering from SARS-CoV-2 is being investigated in a Phase 3 randomized, multicenter trial (NCT04324021). Anakinra doses were 100 mg QID for 15 days by IV infusion, per the experimental protocol [6]. C5a inhibitors were proven to be an effective management for rigorous SARS-CoV-2, without interfering with the MAC pathway. The goal of using corticosteroids in COVID-19 was to lessen the host's inflammatory responses in the lungs that could lead to ARDS. Corticosteroid use did not augment the survival rate in patients with SARS-CoV or MERS-CoV infection, according to observational studies, but it did show a connection to the patients' blood and respiratory tract's slower viral clearance. Hyperglycemia, psychosis, and vascular necrosis all had higher incidence of complications than other conditions [6]. Also the deferred viral consent with an augmented menace of succeeding contagion, corticosteroids were discovered to be eclipsed by unfavorable effects. Ten trials comprising 6548 patients with influenza and pneumonia were examined by a comprehensive review. Vitamin A is also recognized as anti-infective vitamin, since it is critical to the body's defense against infection [7]. The elements of the body's innate immune response are improved by vitamin A [8]. Vitamin D acts both as a vitamin as well as a hormone. Numerous cells, including immune cells, are stimulated to mature as a result. People

over the age of 65 and those who get little sun exposure are at risk for vitamin D insufficiency [8], and elderly people were found to be more vulnerable to SARS-CoV-2 [8]. Mesenchymal stem cells (MSCs) are derived from adipose tissue, bone marrow and other tissue sources [9]. They are adult multidimensional stem cells that can develop into numerous mesodermal lineages, including osteocytes, adipocytes, chondrocytes, neurocytes, and hepatocytes. They don't exhibit CD14, CD34, CD45, or HLA-DR expression, but they do have particular cell markers, such as CD90, CD29, CD44, CD73 and CD105 [9]. Four clinical trials were being carried out to evaluate MSCs from the umbilical cord and tooth pulp for the management of patients with SARS-CoV-2 [10]. To assist in the creation of SARS-CoV-2 vaccinations, the Coalition for Epidemic Preparedness Innovations (CEPI) team up with international health organizations and vaccine producers. Following the publication of the SARS-CoV-2 genetic sequence on January 11th, 2020, extensive research and development effort was undertaken to create a vaccine to prevent SARS-CoV-2 [11]. The S protein of SARS-CoV-2 is encoded by an adenovirus type 5 vector known as Ad5-nCoV. A phase 1 clinical trial with healthy participants was launched to evaluate the immunogenicity, safety, and reactogenicity of the Recombinant Novel Coronavirus Vaccine (Adenovirus Type 5 Vector). The study's main goal was to determine the safety indices for adverse responses. INO-4800, which is a DNA plasmid encoding S protein was supplied using the Inovio Pharmaceuticals-developed electroporation method. An investigation was being carried out to appraise the efficiency and security of antigen-specific cytotoxic T cell and LV-SMENP DC vaccinations in COVID-19 patients and healthy volunteers. When combined with antigen-specific cytotoxic T lymphocytes, LV-SMENP DC dendritic cells are changed with a lentiviral vector that expresses a synthetic micro gene based on viral protein domains of interest (CTLs). The participants or patients received approximately 5×10^6 LV-DC vaccine and 1×10^8 CTLs via subcutaneous injections and IV infusions, respectively. An artificial antigen-presenting cell was used in a Phase 1 clinical trial conducted by the Shenzhen GenoImmune Medical Institute. Cells were altered using a lentiviral vector that produced a synthetic mini-gene based on certain viral protein domains. Candidate vaccine molecules included DNA, RNA, virus-like peptide-based components, particles, recombinant proteins, live, attenuated, and inactivated viruses. The process of developing vaccines is laborious and difficult, and it often takes 10–15 years. There had been three corona virus epidemics in the past 17 years (Fig. 1).
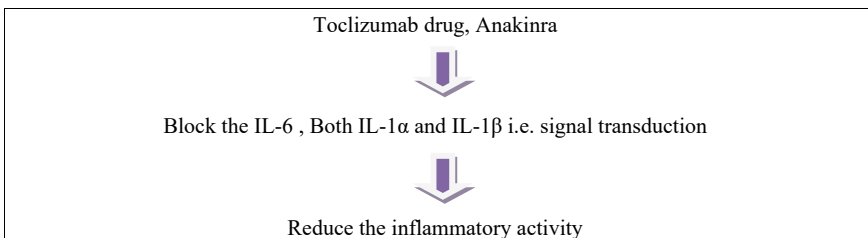

Fig. 1 Mechanism of Toclizumab and Anakinra

The anti-inflammatory medications such as colchicines, corticosteroids, interleukin-1 inhibitors, and interleukin-6 inhibitors are a few of those being investigated for use as immunomodulators in the treatment of COVID-19. In addition to being utilized as immunomodulators to treat cure disorders, SSRIs like Fluvoxamine have been studied in the control of COVID-19. Additionally being considered for use as immunomodulators in the management of COVID-19 are kinase inhibitors such JAK inhibitors and BTK inhibitors, non-SARS-CoV-2 specific intravenous immunoglobulins, and GM-CSF inhibitors.

For hospitalized patients who need supplementary oxygen or are mechanically ventilated, corticosteroids like dexamethasone are given. Systemic corticosteroids, notably those who have signs of a systemic inflammatory disease or an early severe illness, have shown clinical benefit when combined with other medications, such as other immunomodulators like Tocilizumab, certain subsets of hospitalized COVID-19 patients. Glucocorticoids including prednisone, Methylprednisolone, and Hydrocortisone are among the systemic corticosteroids other than Dexamethasone used to manage COVID-19.

In COVID-19 management, the medical nutrition therapy is supported on factors like caloric intake, macronutrients, feeding pathways, and a healthy gut. Oral administration is preferred, but in relentless cases it is substituted by enteral nourishment. Doctors that treated this ailment elaborated on calorie intake and macronutrients and suggested that power intake should be in the range of 25–30 kcal/kg body weight/ day. The macro nutrients proportion viz., proteins, with an ingestion of 1–1.2 g/kg body weight/day, with carbohydrates remaining at the customary 45–50%. This will be applied for moderate cases. Serious cases will need enteral administration route. In both illness prevention and the fight against the viral enemy, a healthy microbiome may play a critical role.

The SARS-CoV-2, based S- Protein, that is present on the external stratum of the virus and is a vital molecule for viral entrance into the host cells, is highlighted by vaccine development strategies for the management of COVID-19 syndrome, repurposing other vaccines like BCG, MMR etc., non-replicating viral vector (NRVV), protein subunits, RNA-based vaccines, replicating viral vector (RVV), inactivated vaccines (IAcV), and live attenuated vaccines (LAVs).

Mesenchymal stem cells have been heavily researched in the stem cell therapy strategy for treating COVID-19 disease. One class of research materials is mesenchymal stem cells that have been investigated for their potential immunomodulatory effects and for a variety of clinical uses in regenerative medicine. Mesenchymal stem cells may lessen severe lung damage that prevent the inflammatory cell-mediated reaction brought on by SARS-CoV-2, according to a theory [12–16].

The speed of SARS-CoV-2 vaccine development has been greatly accelerated by the available data and computational techniques. However, the main obstacles to the vaccine's rapid development were its efficacy and safety.

3 Summary

The pandemic stroke of the SARS-COVID-19 has been nerve-racking us all across the globe. A thorough investigation of the various therapeutic strategies have been carried out for the supervision over this viral disease. A methodical literature review has been carried out using a research catalog to comprehend the fundamental mechanism and appraise the drugs for anticipation of this virus.

References

1. McIntosh K, Perlman S (2015) Coronaviruses, including severe acute respiratory syndrome (SARS) and Middle East respiratory syndrome (MERS). In: Mandell, douglas, and bennett's principles and practice of infectious diseases, p 1928
2. Shanmugaraj B, Khorattanakulchai N, Phoolcharoen W (2022) SARS-CoV-2 vaccines: current trends and prospects of developing plant-derived vaccines. In: Biomedical Innovations to Combat COVID-19. Academic Press, pp 213–229
3. Venkiteshwaran A (2009) Tocilizumab. MAbs 1(5). Taylor & Francis
4. National Health Commission and National Administration of Traditional Chinese Medicine (2020) Diagnosis and treatment protocol for novel coronavirus pneumonia (Trial Version 7). Chinese Med J 133(09):1087–1095
5. Pazyar N, Feily A, Yaghoobi R (2012) An overview of interleukin-1 receptor antagonist, anakinra, in the treatment of cutaneous diseases. Curr Clin Pharmacol 7(4):271–275
6. ClinicalTrials.gov.COVID-19. https://clinicaltrials.gov. Last accessed 05 May 2020
7. Guillin OM et al (2019) Selenium, selenoproteins and viral infection. Nutrients 11(9):2101
8. Trottier C et al (2009) Retinoids inhibit measles virus through a type I IFN-dependent bystander effect. FASEB J 23(9):3203–3212
9. Horwitz EM, Keating A (2000) The nonhematopoietic mesenchymal stem cell committee workshop. Nonhematopoietic mesenchymal stem cells: what are they? Cytotherapy 2(5):387–388
10. ClinicalTrials.gov (2020) Therapy for Pneumonia Patients iInfected by 2019 Novel Coronavirus. https://clinicaltrials.gov/ct2/show/NCT04293692. Last accessed 19 May 2020
11. Le TT et al (2020) The COVID-19 vaccine development landscape. Nat Rev Drug Discov 19(5):305–306
12. ClinicalTrials.gov (2020) Phase I Clinical Trial of a COVID-19 Vaccine in 18–60 Healthy Adults (CTCOVID-19), https://clinicaltrials.gov/ct2/show/NCT04313127. Last accessed 17 Mar 2020
13. Ojha PK et al (2021) Therapeutics for COVID-19: from computation to practices—where we are, where we are heading to. Mol Divers 25(1):625–659
14. Park H-J et al (2016) The Characteristics of RNA vaccine; its strengths and weaknesses. J Bacteriol Virol 46(3):115–127
15. Peng H et al (2020) A synergistic role of convalescent plasma and mesenchymal stem cells in the treatment of severely ill COVID-19 patients: a clinical case report. Stem Cell Res Therapy 11(1):1–6
16. Li J et al (2020) Feasibility of mesenchymal stem cell therapy for COVID-19: a mini review. Curr Gene Therapy 20(4):285–288

Albumin, Globulin, and Albumin-Globulin Ratio with EBV DNA as Potential Markers for Nasopharyngeal Carcinoma: Experience from a Regional Cancer Centre in North-Eastern India

Deepak Singh Lourembam, T. Dhaneshor Sharma, and Lisam Shanjukumar Singh

Keywords Albumin-globulin ratio · Epstein barr virus · Nasopharyngeal carcinoma · Biomarker

1 Introduction

Nasopharyngeal Carcinoma (NPC) is a highly prevalent head and neck cancer in Southeast Asia, Southern China, and North Africa where the average incidence reaches 30 per 100,000 people [1, 2]. NPC is rare in most regions of India although higher incidences were observed in north-eastern states, particularly Nagaland, Manipur, and Mizoram [3, 4]. The region represents the diversity of different ethnic groups and mongoloid features in these populations have shown higher NPC incidence. NPC has a remarkable racial/ethnic and geographic variation influenced by a complex interplay of the dietary, environmental, viral infection (Epstein–Barr virus), and genetic risk factors [1, 5, 6]. Epstein- Barr virus (EBV) infection in NPC has been

D. S. Lourembam (✉)
Department of Pathology, Regional Institute of Medical Sciences, Imphal, India
e-mail: deelourembam@gmail.com

T. D. Sharma
Department of Radiation Oncology, Regional Institute of Medical Sciences, Imphal, India

L. S. Singh
Department of Biotechnology, Manipur University, Canchipur, Imphal, India
e-mail: shanju.lisam@manipuruniv.ac.in

well established in different populations and targeting EBV might provide an effective strategy in NPC management [7]. As such EBV infection presents an important role in NPC development. Many studies have investigated the potential biomarkers to predict NPC progression. Quantification of EBV DNA levels have proved to be promising clinical tools in screening, monitoring, and diagnostic evaluation of NPC patients [8–11].

Cancer progression and survival/occurrence are not determined solely based on tumor-related factors, like TNM staging, but also involve inflammatory indices and nutritional status of patients [12, 13]. Malnutrition and inflammation in cancer patients are significant problems as it aids in tumor progression, host response to the tumor, and anticancer therapies [14]. With the close association with inflammation and nutritional status, some of the serum biochemical markers, including albumin to globulin ratio (AGR) have shown remarkable value in the prognosis of many cancers [15–17]. As major components of human serum proteins, albumin (ALB) reflects the patients' nutritional status while globulin (GLB) assess the degree of chronic inflammation [18]. Interestingly, numerous studies have demonstrated albumin and globulin levels as critical markers in the diagnosis of various cancer types [19–21].

Many studies have reported albumin and globulin levels as indicators of better cancer survival [22–24]. However, measurement of serum albumin and globulin levels alone limits its application in the disease prognosis. Thus, a combined assessment of these serum proteins altogether might provide improved prognostic significance. Recently, AGR value emerged as a novel prognosticator in common cancer types. Prior studies have shown AGR values as a useful indicator for prognostic assessment in many cancers, including NPC [15, 25–28].

Nevertheless, the prognostic significance of these markers in NPC has not been sufficiently evaluated. Therefore, we evaluated the association of albumin, globulin, and AGR in patients with Nasopharyngeal cancer. Moreover, we also addressed the clinical significance of serum protein markers and EBV DNA for their potential ability to be used as non-invasive biomarkers in the clinical management of NPC.

2 Materials and Methods

2.1 Study Population and Ethical Statement

Our study was approved by the Human Ethics Committee of the RIMS Hospital, Manipur and Manipur University and performed under the guidelines of the Helsinki Declaration [29]. We included pathologically confirmed 105 NPC patients and 115 healthy controls recruited from the RIMS Hospital, Manipur between Nov 2011, and October 2015. Further, the TNM staging of all patients was performed following AJCC cancer staging guidelines for NPC [30]. Our exclusion criteria were defined as (1) patients who received chemotherapy or radiotherapy prior to enrolment in our study and (2) patients with any other type of malignancy except NPC. Our controls

included cancer-free healthy donors that were followed up for a year to exclude cancer and other known diseases. Written informed consent was obtained from all participants and detailed information on demographic and clinical characteristics was recorded and analyzed. Patient information was anonymized and de-identified prior to analysis.

2.2 Collection of Blood Samples and DNA Extraction

Blood samples (2–4 ml) were obtained from study participants and samples were divided into two parts. For the first part, genomic DNA was extracted using QIAamp Blood Mini Kit (QIAGEN, Hilden, Germany) from blood samples using the manufacturer's protocol. Simultaneously the second part of the samples was processed for serum separation following centrifugation at 3,000 rpm for 5 min and then collected in sterile tubes. The isolated DNA and serum samples were further aliquoted and stored at −80 ºC until used.

2.3 EBV Detection by Conventional PCR

Blood DNA samples from study participants and Raji cell DNA as positive control were screened for EBV detection as reported earlier [31] (Table 1). Raji is a Burkitt lymphoma cell line that contains 50 copies of EBV per cell [32].

Table 1 Oligonucleotides used in EBV PCR & beta globulin detection

Target	Primer name	Oligonucleotide Sequence 5'–3'	Amplicon size	GenBank accession	Ref.
EBNA-1 qPCR EBNA-1 PCR	EBNAF1 (F) EBNAR1 (R) EBNAF2 (F) EBNAR2 (R)	CGAGGAACTGCCCTTGCTAT CCAAAGGGGAGACGACTCAA TGAATACCACCAAGAAGGTG AGTTCCTTCGTCGGTAGTC	61 bp 262 bp	Accession number V01555	[31]
β-globulin qPCR	β-globulin (F) β-globulin (R)	ACACAACTGTGTTCACTAGC CAACTTCATCCACGTTCACC	119 bp		

2.4   EBV Load Determination by EBNA-1 qPCR

Quantitative real-time PCR (qPCR) was performed using EBNA1 primers (Accession number V01555) as described in Table 1 for the measurement of EBV viral load. qPCR reaction and cycling conditions were performed as described following standard curve experiments [33]. EBV DNA copy numbers were calculated using the standard curve method based on the CT value of the standards used. The results of the assay were expressed as log EBV DNA copies per ml of blood.

2.5   Serological Analysis

Serum samples from study participants were further analyzed by capillary electrophoresis (CE) to identify abnormalities in the various separated protein bands viz: albumin, alpha 1 and 2 globulins, beta 1 and 2 globulins, and gamma globulins. Sebia Capillarys (Evry Cedex, France) was used for the identification and quantification of separated protein fractions [34]. Serum protein electrophoresis was carried out using a commercially available kit, Hydra Gel Protein (E) K20 (Sebia Inc, Norcross, Ga, USA) designed for the separation of serum proteins. The albumin, globulin, and total proteins were measured as per standard operating protocols. Consequently, the albumin-globulin Ratio (AGR) was calculated using the equation [AGR = Albumin/ (total serum protein—Albumin)] as described [25]. Also, to detect the presence of hyper and normal gamma populations in study subjects, serum proteins were analyzed to identify various gammopathies.

3   Statistical Analyses

Data analysis was carried out using GraphPad Prism or MedCalc (v.9.3.9.0) software. The comparison of serum albumin, globulin, AGR, and EBV DNA levels between NPC patients and healthy controls was calculated by the Mann–Whitney test. For categorical data analysis, the Chi-square test or Fisher's exact test was used. Receiver-operating characteristic (ROC) curve analyses were used for interpreting the potential values of EBV DNA, albumin, globulin, and AGR for NPC diagnosis, with maximum Youden index for determining cut-off values. A probability value of less than 0.05 was considered significant for all analyses.

Table 2 Clinicopathological characteristics of NPC patients and healthy controls

| Variables		NPC (n = 105)	Controls (n = 115)	p-value
Gender	Male	72 (68.57%)	71 (61.74%)	0.29
	Female	33 (31.43%)	44 (38.26%)	
Age	Mean	48.9	44	0.54
	SD	15	10.1	
	Range	18–80	22–73	
Age	≤45	38 (36.19%)	45 (39.13%)	0.65
	>45	67 (63.81%)	70 (60.87%)	
Stage	I – II	38 (36.19%)		
	III-IV	67 (63.81%)		
WHO pathological classification	Type 1	6 (5.71%)		
	Type 2	16 (15.24%)		
	Type 3	83 (79.05%)		

4 Results

4.1 General Characteristics

The baseline characteristics of the study population are presented in Table 2. Of 105 NPC samples, the percentage of males and females population was 68.57 and 31.43% respectively. The patients' mean age was 48.9 years, ranging from 18 to 80 and that of controls was 44 years, ranging from 22 to 73. According to WHO pathological classification, 79.05% of the study subjects were of non-keratinizing undifferentiated carcinoma representing the majority of cases. Stage-wise analysis shows 36.19% of cases in early-stage disease and 63.81% of cases in the advanced stage of cancer. No significant differences were observed in gender and age distribution between the study population ($P > 0.05$). Among the patients, we found a higher NPC incidence in males when compared with the female population (68.5 vs. 31.4%).

4.2 Molecular Detection of EBV in Study Participants

EBV DNA was detected by conventional PCR targeting the conserved EBNA1 gene. EBV positivity was observed in 100% (105/105) of patient samples whereas only 20.8% (24/115) of controls were positive for EBV. Hence, EBV DNA positivity was found to be significantly higher in NPC patients when compared to healthy controls (Fig. 1).
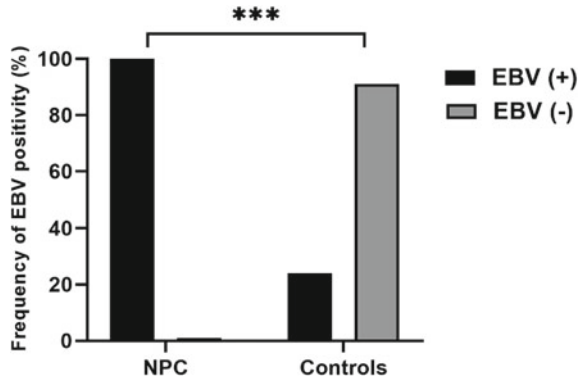
## 4.3 EBV DNA Levels in NPC Patients and Healthy Controls

EBV DNA levels in 105 NPC patients and 115 healthy controls were detected by quantitative real-time PCR (qPCR). The median EBV DNA levels in NPC patients were significantly higher than that of healthy controls ($p < 0.001$). EBV viral load in 70.43% (80/115) of the control groups have less than 100 copies/ml. EBV DNA levels were found significantly higher in advanced-stage patients than in early-stage NPC patients ($p < 0.05$) (Fig. 2).

4.4 Diagnostic Evaluation of the EBV DNA

ROC curve determines the accuracy of a laboratory test by calculating its sensitivity and specificity [35]. ROC curve analysis revealed EBV DNA levels as a useful marker for distinguishing NPC patients from controls. The area under the curve (AUC) value for EBV-DNA was found to be 0.927 (95% CI, 0.86–0.96). The optimal cut-off value determined by this analysis was 3237 copies/ml with sensitivity and specificity of 81.48 and 91.43% respectively (Fig. 3).

4.5 Comparison of Serum Proteins Between NPC and Healthy Controls

Table 3 represents the comparison of the mean value of serum total protein, albumin, globulin, and AGR value between the study subjects. Serum protein comprising albumin, globulin, total protein, and AGR value were evaluated between the study subjects using univariate analysis.
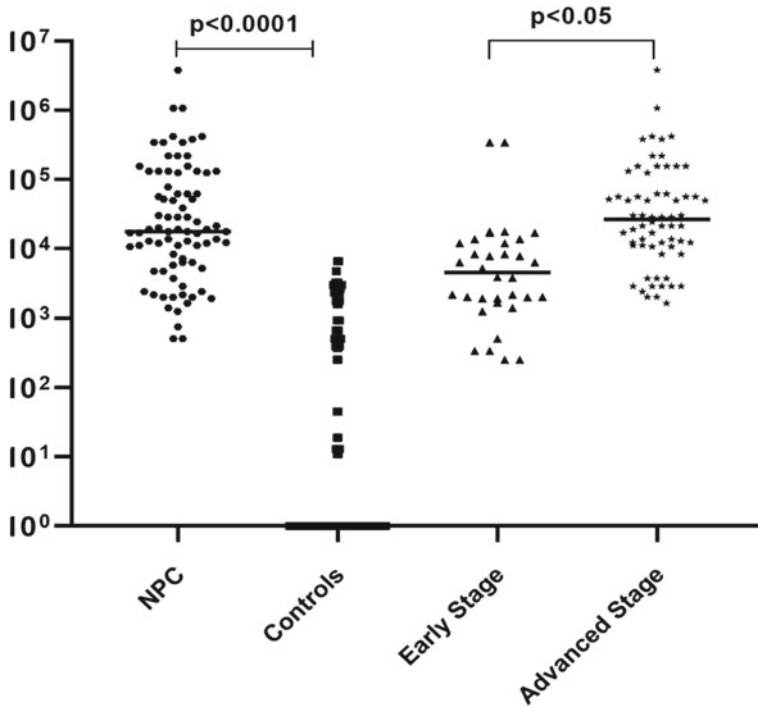
Fig. 2 Comparison of EBV load (copies/ml) in healthy controls and different stages (Early and Advanced) of NPC patients. The horizontal lines represent median values. Higher EBV load was observed in patients when compared to controls ($p < 0.0001$). EBV load between different stages of the disease was also statistically significant ($p < 0.05$)

Higher levels of globulin and low albumin levels with low AGR value were significantly associated with NPC development. Albumin level was found to be lower in patients' samples (3.48 ± 0.7 g/dL) when compared with controls (4.25 ± 0.6 g/dL; $p < 0.0001$) (Fig. 4a). On the other hand, mean globulin levels were significantly higher in NPC patients (4.07 ± 0.78 g/dL) when compared to controls (3.55 ± 0.56 g/dL) (Fig. 4b). Our analysis also shows that mean AGR value was significantly lower in NPC patients (0.8 ± 0.2 g/dL) than in controls (1.23 ± 0.26 g/dL; $p < 0.0001$) which suggested that low AGR is associated with an increased risk of NPC (Fig. 4c). However, no significant differences were found in total serum protein levels ($P > 0.05$) (Fig. 4d).

4.6 Age-Wise Analysis of Biochemical Markers

To evaluate the correlation of biochemical markers with age, patient samples were compared between two different groups (≤ 45 and >45 years)]. Our results show an
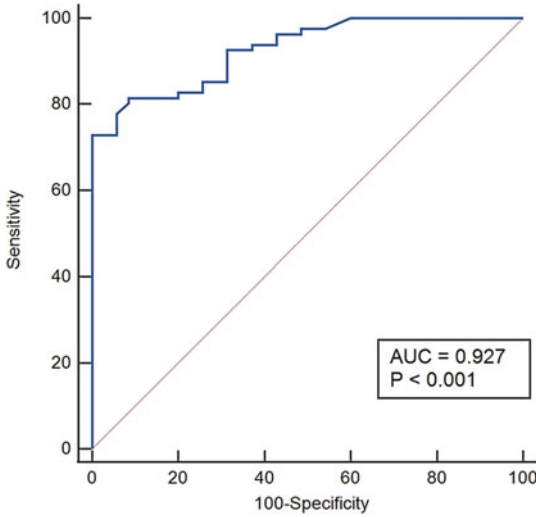
| EBV - DNA	Sensitivity	Specificity	Sensitivity + Specificity	Accuracy
3237 copies/ml	0.81(0.71-0.89)	0.91 (0.76 – 0.98)	1.72	0.72

Fig. 3 ROC curve analysis of EBV DNA levels. The optimal cut-off value was 3493 copies/mL (sensitivity 81%, specificity 91%)

Table 3 Serum protein levels in the study group (NPC patients) and healthy controls. Data represent (Mean ± SD)

Variables	NPC (n = 105)	Controls (n = 115)	p-value
Total protein (g/dL)	7.55 ± 1.11	7.79 ± 0.88	0.222
Serum Albumin (g/dL)	3.48 ± 0.7	4.25 ± 0.6	<0.0001
Serum Globulin (g/dL)	4.07 ± 0.78	3.55 ± 0.56	<0.0001
AGR	0.8 ± 0.2		<0.0001

association of AGR value with respect to age. We observed a significant decrease in AGR value in the higher age group (>45 years) when compared to the lower age group (≤45 years) (p = 0.027). However, there was no statistical correlation found between any of the other biochemical markers (albumin, globulin, and total protein) with respect to age (Table 4).
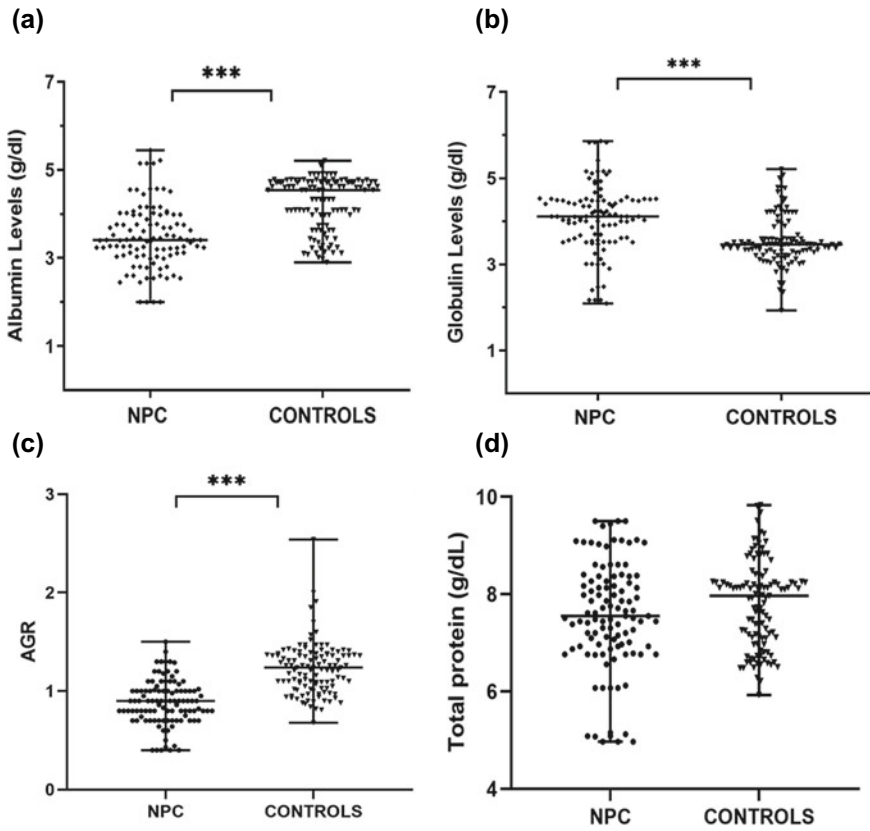
Fig. 4 Comparative analysis of serum proteins between NPC patients and healthy controls. P values were calculated by comparing patient and control groups and statistical significance was represented by the asterisks symbol

Table 4 Effect of age groups on biochemical markers

Variable	Age $\leq$ 45 (n = 38)	Age > 45 (n = 67)	p-value
Total protein (g/dL)	7.5 ± 1.1	7.6 ± 1.2	0.665
Albumin (g/dL)	3.5 ± 0.6	3.4 ± 0.7	0.88
Globulin (g/dL)	4.08 ± 0.7	4.07 ± 0.6	0.941
AGR	0.9 ± 0.2	0.8 ± 0.2	0.027 *

* indicate [p< 0.05]

Table 5 Diagnostic performance of serum proteins for detection of NPC

Variables	Total protein	Albumin	Globulin	AGR
(AUC)	0.548	0.797	0.739	0.851
p-value	0.222	<0.0001	<0.0001	<0.0001
Cut-off value	8.06	4.06	3.59	1.01
Percentage sensitivity	67.62	84.76	75.24	78.1
Percentage specificity	47.83	70.43	74.78	78.26
Youden index	0.155	0.552	0.5	0.563

4.7 Diagnostic Evaluation of Serum Proteins in Detecting NPC

ROC curve analysis was performed to identify the cut-off values of serum proteins that could distinguish NPC patients from healthy controls. Table 5 represents the performance of total protein, albumin, globulin, and AGR value in the diagnosis of NPC. The AUC of AGR was 0.851 (95% CI: 0.797–0.895; $p < 0.0001$) with a cut-off value of 1.01 at a maximum Youden index of 0.563. We also found AUC of serum albumin (0.797, $p < 0.0001$) to be higher than that of globulin (0.739, $p < 0.0001$) and total protein (0.548, $P = 0.222$). Similarly, the cut-off value of albumin was 4.06 g/dL with a sensitivity of 84.76% and specificity of 70.43%. Also, globulin has an optimal cut-off of 3.59 g/dL (sensitivity 75.24%, specificity 74.78%). Our analysis considered the diagnostic performance of albumin, globulin, and AGR value to be reasonable in comparison with the total protein. According to our optimal cut-off value (1.01) of AGR, the patient's group was further divided into two groups as AGR <1.01 and AGR $\geq$ 1.01. We found that 83 of 105 NPC patients (79%) had a low AGR (<1.01) when compared to 21% (22–105) of patients which are presented with high AGR ($\geq$1.01). Overall, our results suggests that AGR value represented the highest diagnostic performance for NPC.

5 Discussion

This study evaluated the diagnostic utility and correlation of serum proteins and EBV DNA among NPC patients and healthy controls. Our results demonstrate that low serum albumin with low AGR and high globulin levels are associated with the incidence of NPC. Our findings also indicate detection of EBV and EBV DNA load as important predictors for NPC monitoring and disease progression. EBV virus was detected in about 21% of the control population which supported the literature about its ubiquitous nature of infection with ~95% of the healthy population as asymptomatic carriers of the virus [36]. Our results also showed higher EBV load in NPC patients when compared to the controls following qPCR of the EBNA1

gene. Quantification of EBV has been demonstrated and suggested as a sensitive non-invasive marker for early diagnosis, disease monitoring, and treatment response of NPC [37–40].

Many studies have also reported the role of inflammation and nutrition in cancer occurrence and development in various cancers including NPC [41–43]. AGR is considered an inflammatory index that plays an important role in cancer progression [28, 44]. Albumins and globulins are the main components of serum proteins that are associated with immunity and inflammatory function [18]. It is thus reasonable to suggest that AGR score based on albumin and globulin is a critical marker as reported in many cancer types [45]. Our findings are consistent with an earlier study that reported decreased albumin levels and significantly lower AGR values in cancer patients in comparison with controls [46]. Also, numerous studies have shown the correlation between AGR values and globulin levels in many types of cancer indicating their role in the host immune system [21, 28, 47].

In our study, we found that albumin levels and AGR values were lower and globulin levels were significantly higher in NPC patients when compared with the controls. These results are similar to findings in other studies on nasopharyngeal cancer [48, 49]. However, we found significantly higher globulin levels in patients' samples than in controls. ROC analysis determined 3.59 g/dL as an optimal cut-off value for globulin levels for differentiating NPC patients from controls. Higher levels of globulin may arise due to an increased accumulation of other serum proteins which reflects both inflammatory and humoral immune responses of virus-associated pathogenesis of NPC. Our results are consistent with reports [15, 50, 51] which found globulin levels as an independent prognostic factor of NPC. This study also reported the median AGR value in the patient samples to be 0.9 (0.4–1.5). Based on the cut-off value of 1.1, 79% of NPC patients had a low AGR (<1.1) when compared to 21% with high AGR ($\geq$1.1) thus suggesting that low AGR is associated with NPC disease progression. Our results are consistent with other studies which reported low AGR values as an independent factor for poor survival in other cancers, including NPC [15, 25, 52]. We observed an inverse relationship between albumin and globulin levels, which dramatically decreased the AGR value, suggesting the inflammatory status of the body [47]. Therefore, albumin, globulin, and AGR values in this study might be used as potential prognostic predictors in NPC patients.

The present study is the first instance from Northeast India to assess the correlation of albumin and globulin with AGR in NPC patients. However, few limitations were seen in the current study. Firstly, our study is a single retrospective study with relatively small sample size and larger multicentric study designs are required to validate our findings. Secondly, our study did not include some of the possible confounding factors e.g., systemic inflammation, and cardiovascular and metabolic diseases which may alter serum protein levels. Despite the above limitations, our results have shown a significant association between albumin, globulin, and AGR with NPC. EBV DNA levels were elevated in NPC patients and higher EBV DNA levels also correlate with the severity of the disease.

6   Conclusion

In summary, our results suggest that albumin, globulin, and AGR values are associated with NPC development. EBV DNA levels were significantly higher in NPC patients and also correlate with disease staging. Further albumin and globulin levels along with AGR could serve as potential biomarkers in the clinical management of NPC. Overall, our results will provide important insights into NPC diagnosis and will be helpful for preventive measures and screening.

Ethics Statement   The study was approved [No: AC/112/EC/RIMS/2005/1481 dated 10th October 2011] by the Institutional Review Board (IRB), Regional Institute of Medical Sciences.

Conflict of Interest   All the authors declared no conflict of interest.

References

1. Chang ET, Adami HO (2006) The enigmatic epidemiology of nasopharyngeal carcinoma. Cancer Epidemiol Biomarkers Prev 15(10):1765–1777. https://doi.org/10.1158/1055-9965. Epi-06-0353
2. Forman D (2014) Cancer incidence in five continents: volume X. International Agency for Research on Cancer
3. Kataki AC, Simons MJ, Das AK, Sharma K, Mehra NK (2011) Nasopharyngeal carcinoma in the Northeastern states of India. Chin J Cancer 30(2):106–113. https://doi.org/10.5732/cjc. 010.10607
4. Sharma TD, Singh TT, Laishram RS, Sharma LD, Sunita AK, Imchen LT (2011) Nasopharyngeal carcinoma–a clinico-pathological study in a regional cancer centre of northeastern India. Asian Pac J Cancer Prev: APJCP 12(6):1583–1587
5. Lung ML, Cheung AK, Ko JM, Lung HL, Cheng Y, Dai W (2014) The interplay of host genetic factors and Epstein-Barr virus in the development of nasopharyngeal carcinoma. Chin J Cancer 33(11):556–568. https://doi.org/10.5732/cjc.014.10170
6. Lakhanpal M, Singh LC, Rahman T, Sharma J, Singh MM, Kataki AC et al (2015) Contribution of susceptibility locus at HLA class I region and environmental factors to occurrence of nasopharyngeal cancer in Northeast India. Tumour Biol 36(4):3061–3073. https://doi.org/10. 1007/s13277-014-2942-5
7. Hau PM, Lung HL, Wu M, Tsang CM, Wong KL, Mak NK et al (2020) Targeting Epstein-Barr virus in nasopharyngeal carcinoma. Front Oncol 10:600. https://doi.org/10.3389/fonc.2020. 00600
8. Ng WT, Yuen KT, Au KH, Chan OS, Lee AW (2014) Staging of nasopharyngeal carcinoma–the past, the present and the future. Oral Oncol 50(6):549–554. https://doi.org/10.1016/j.oraloncol ogy.2013.06.003
9. Li HP, Hsu CL, Chang YS (2018) Screening of nasopharyngeal carcinoma using plasma Epstein-Barr virus DNA for at-risk population. 2:3
10. Kimura H, Kwong YL (2019) EBV viral loads in diagnosis, monitoring, and response assessment. Front Oncol 9:62. https://doi.org/10.3389/fonc.2019.00062

11. Tan R, Phua SKA, Soong YL, Oon LLE, Chan KS, Lucky SS et al (2020) Clinical utility of Epstein-Barr virus DNA and other liquid biopsy markers in nasopharyngeal carcinoma. Cancer Commun (London, England) 40(11):564–585. https://doi.org/10.1002/cac2.12100

12. McMillan DC (2009) Systemic inflammation, nutritional status and survival in patients with cancer. Curr Opin Clin Nutr Metab Care 12(3):223–226. https://doi.org/10.1097/MCO.0b013e32832a7902

13. Laviano A, Koverech A, Mari A (2015) Cachexia: clinical features when inflammation drives malnutrition. Proc Nutr Soc 74(4):348–354. https://doi.org/10.1017/s0029665115000117

14. Lu H, Ouyang W, Huang C (2006) Inflammation, a key event in cancer development. Mol Cancer Res: MCR 4(4):221–233. https://doi.org/10.1158/1541-7786.Mcr-05-0261

15. Du XJ, Tang LL, Mao YP, Sun Y, Zeng MS, Kang TB et al (2014) The pretreatment albumin to globulin ratio has predictive value for long-term mortality in nasopharyngeal carcinoma. PLoS ONE 9(4):e94473. https://doi.org/10.1371/journal.pone.0094473

16. Willegger M, Posch F, Schieder S, Funovics PT, Scharrer A, Brodowicz T et al (2017) Serum creatinine and albumin predict sarcoma-specific survival in patients with myofibroblastic and fibroblastic sarcomas. J Orthop Res 35(12):2815–2824. https://doi.org/10.1002/jor.23598

17. Ichikawa K, Mizuno S, Hayasaki A, Kishiwada M, Fujii T, Iizawa Y et al (2019) Prognostic nutritional index after chemoradiotherapy was the strongest prognostic predictor among biological and conditional factors in localized pancreatic ductal adenocarcinoma patients. Cancers (Basel) 11(4). https://doi.org/10.3390/cancers11040514

18. Meyer EJ, Nenke MA, Rankin W, Lewis JG, Torpy DJ (2016) Corticosteroid-binding globulin: a review of basic and clinical advances. Horm Metab Res 48(6):359–371. https://doi.org/10.1055/s-0042-108071

19. Gupta D, Lis CG (2010) Pretreatment serum albumin as a predictor of cancer survival: a systematic review of the epidemiological literature. Nutr J 9:69. https://doi.org/10.1186/1475-2891-9-69

20. Jin Y, Zhao L, Peng F (2013) Prognostic impact of serum albumin levels on the recurrence of stage I non-small cell lung cancer. Clinics (Sao Paulo, Brazil) 68(5):686–693. https://doi.org/10.6061/clinics/2013(05)17

21. Li G, Gao J, Liu ZG, Tao YL, Xu BQ, Tu ZW et al (2014) Influence of pretreatment ideal body weight percentile and albumin on prognosis of nasopharyngeal carcinoma: long-term outcomes of 512 patients from a single institution. Head Neck 36(5):660–666. https://doi.org/10.1002/hed.23357

22. Adly L, Hill D, Sherman ME, Sturgeon SR, Fears T, Mies C et al (2006) Serum concentrations of estrogens, sex hormone-binding globulin, and androgens and risk of breast cancer in postmenopausal women. Int J Cancer 119(10):2402–2407. https://doi.org/10.1002/ijc.22203

23. Asher V, Lee J, Bali A (2012) Preoperative serum albumin is an independent prognostic predictor of survival in ovarian cancer. Med Oncol 29(3):2005–2009. https://doi.org/10.1007/s12032-011-0019-5

24. Guthrie GJ, Roxburgh CS, Farhan-Alanie OM, Horgan PG, McMillan DC (2013) Comparison of the prognostic value of longitudinal measurements of systemic inflammation in patients undergoing curative resection of colorectal cancer. Br J Cancer 109(1):24–28. https://doi.org/10.1038/bjc.2013.330

25. Azab BN, Bhatt VR, Vonfrolio S, Bachir R, Rubinshteyn V, Alkaied H et al (2013) Value of the pretreatment albumin to globulin ratio in predicting long-term mortality in breast cancer patients. Am J Surg 206(5):764–770. https://doi.org/10.1016/j.amjsurg.2013.03.007

26. Yao Y, Zhao M, Yuan D, Gu X, Liu H, Song Y (2014) Elevated pretreatment serum globulin albumin ratio predicts poor prognosis for advanced non-small cell lung cancer patients. J Thorac Dis 6(9):1261–1270. https://doi.org/10.3978/j.issn.2072-1439.2014.07.13

27. Shibutani M, Maeda K, Nagahara H, Ohtani H, Iseki Y, Ikeya T et al (2015) The pretreatment albumin to globulin ratio predicts chemotherapeutic outcomes in patients with unresectable metastatic colorectal cancer. BMC Cancer 15:347. https://doi.org/10.1186/s12885-015-1375-x

28. Lv GY, An L, Sun XD, Hu YL, Sun DW (2018) Pretreatment albumin to globulin ratio can serve as a prognostic marker in human cancers: a meta-analysis. Clin Chim Acta 476:81–91. https://doi.org/10.1016/j.cca.2017.11.019

29. Puri KS, Suresh KR, Gogtay NJ, Thatte UM (2009) Declaration of Helsinki, 2008: implications for stakeholders in research. J Postgrad Med 55(2):131–134. https://doi.org/10.4103/0022-3859.52846

30. Edge SB, Compton CC (2010) The American joint committee on cancer: the 7th edition of the AJCC cancer staging manual and the future of TNM. Ann Surg Oncol 17(6):1471–1474. https://doi.org/10.1245/s10434-010-0985-4

31. Tune CE, Liavaag PG, Freeman JL, van den Brekel MW, Shpitzer T, Kerrebijn JD et al (1999) Nasopharyngeal brush biopsies and detection of nasopharyngeal cancer in a high-risk population. J Natl Cancer Inst 91(9):796–800. https://doi.org/10.1093/jnci/91.9.796

32. Nonoyama M, Pagano JS (1973) Homology between Epstein-Barr virus DNA and viral DNA from Burkitt's lymphoma and nasopharyngeal carcinoma determined by DNA-DNA reassociation kinetics. Nature 242(5392):44–47. https://doi.org/10.1038/242044a0

33. Lourembam DS, Singh AR, Sharma TD, Singh TS, Singh TR, Singh LS (2015) Evaluation of risk factors for nasopharyngeal carcinoma in a high-risk area of India, the Northeastern Region. Asian Pac J Cancer Prev: APJCP 16(12):4927–4935. https://doi.org/10.7314/apjcp.2015.16.12.4927

34. Petersen JR, Okorodudu AO, Mohammad A, Payne DA (2003) Capillary electrophoresis and its application in the clinical laboratory. Clin Chim Acta 330(1–2):1–30. https://doi.org/10.1016/s0009-8981(03)00006-8

35. Hoo ZH, Candlish J, Teare D (2017) What is an ROC curve? Emerg Med J: EMJ 34(6):357–359. https://doi.org/10.1136/emermed-2017-206735

36. Mentzer AJ, Brenner N, Allen N, Littlejohns TJ, Chong AY, Cortes A et al (2022) Identification of host-pathogen-disease relationships using a scalable multiplex serology platform in UK Biobank. Nat Commun 13(1):1818. https://doi.org/10.1038/s41467-022-29307-3

37. Adham M, Greijer AE, Verkuijlen SA, Juwana H, Fleig S, Rachmadi L et al (2013) Epstein-Barr virus DNA load in nasopharyngeal brushings and whole blood in nasopharyngeal carcinoma patients before and after treatment. Clin Cancer Res 19(8):2175–2186. https://doi.org/10.1158/1078-0432.Ccr-12-2897

38. Yip TT, Ngan RK, Fong AH, Law SC (2014) Application of circulating plasma/serum EBV DNA in the clinical management of nasopharyngeal carcinoma. Oral Oncol 50(6):527–538. https://doi.org/10.1016/j.oraloncology.2013.12.011

39. He SS, Wang Y, Bao Y, Cai XY, Yang XL, Chen DM et al (2018) Dynamic changes in plasma Epstein-Barr virus DNA load during treatment have prognostic value in nasopharyngeal carcinoma: a retrospective study. Cancer Med 7(4):1110–1117. https://doi.org/10.1002/cam4.1381

40. Alfieri S, Iacovelli NA, Marceglia S, Lasorsa I, Resteghini C, Taverna F et al (2017) Circulating pre-treatment Epstein-Barr virus DNA as prognostic factor in locally-advanced nasopharyngeal cancer in a non-endemic area. Oncotarget 8(29):47780–47789. https://doi.org/10.18632/oncotarget.17822

41. Mayne ST, Playdon MC, Rock CL (2016) Diet, nutrition, and cancer: past, present and future. Nat Rev Clin Oncol 13(8):504–515. https://doi.org/10.1038/nrclinonc.2016.24

42. Ritter B, Greten FR (2019) Modulating inflammation for cancer therapy. J Exp Med 216(6):1234–1243. https://doi.org/10.1084/jem.20181739

43. Luan CW, Tsai YT, Yang HY, Chen KY, Chen PH, Chou HH (2021) Pretreatment prognostic nutritional index as a prognostic marker in head and neck cancer: a systematic review and meta-analysis. Sci Rep 11(1):17117. https://doi.org/10.1038/s41598-021-96598-9

44. Chi J, Xie Q, Jia J, Liu X, Sun J, Chen J et al (2018) Prognostic value of albumin/globulin ratio in survival and lymph node metastasis in patients with cancer: a systematic review and meta-analysis. J Cancer 9(13):2341–2348. https://doi.org/10.7150/jca.24889

45. He J, Pan H, Liang W, Xiao D, Chen X, Guo M et al (2017) Prognostic effect of albumin-to-globulin ratio in patients with solid tumors: a systematic review and meta-analysis. J Cancer 8(19):4002–4010. https://doi.org/10.7150/jca.21141

46. Rasouli M, Okhovatian A, Enderami A (2005) Serum proteins profile as an indicator of malignancy: multivariate logistic regression and ROC analyses. Clin Chem Lab Med 43(9):913–918. https://doi.org/10.1515/cclm.2005.156

47. Yoshino Y, Taguchi A, Shimizuguchi T, Nakajima Y, Takao M, Kashiyama T et al (2019) A low albumin to globulin ratio with a high serum globulin level is a prognostic marker for poor survival in cervical cancer patients treated with radiation based therapy. Int J Gynecol Cancer 29(1):17–22. https://doi.org/10.1136/ijgc-2018-000025

48. Selvyana D, Hutajulu SH, Kurnianda J (2017) The pretreatment albumin has a predictive value for overall survival in nasopharyngeal carcinoma. Ann Oncol 28:x108. https://doi.org/10.1093/annonc/mdx665.029

49. Chen X, Long X, Liang Z, Lei H, Li L, Qu S et al (2017) Higher N stage and serum ferritin, but lower serum albumin levels are associated with distant metastasis and poor survival in patients with nasopharyngeal carcinoma following intensity-modulated radiotherapy. Oncotarget 8(42):73177–73186. https://doi.org/10.18632/oncotarget.17418

50. Zhong LT, Wang H, Liang HQ, Su MR, Liu CD, Wu DH (2016) An elevated pretreatment serum globulin level predicts a poor prognosis of nasopharyngeal carcinoma. Nan Fang Yi Ke Da Xue Xue Bao 36(2):151–156

51. Du XJ, Tang LL, Mao YP, Guo R, Sun Y, Lin AH et al (2016) Circulating EBV DNA, globulin and nodal size predict distant metastasis after intensity-modulated radiotherapy in stage II Nasopharyngeal Carcinoma. J Cancer 7(6):664–670. https://doi.org/10.7150/jca.14183

52. Azab B, Kedia S, Shah N, Vonfrolio S, Lu W, Naboush A et al (2013) The value of the pretreatment albumin/globulin ratio in predicting the long-term survival in colorectal cancer. Int J Colorectal Dis 28(12):1629–1636. https://doi.org/10.1007/s00384-013-1748-z

Biomaterials and Tissue Engineering

3D Printing in Cardiovascular Science and Engineering

Mudrika Singhal [iD]**, Udit Nayan Saha** [iD]**, and Raghvendra Gupta** [iD]

Keywords Coronary circulation · 3D printing · Cardiovascular medicine stereolithography

1 Introduction

Circulation of blood in human body is a vital process for sustenance of life and can be broadly categorized into systemic and pulmonary circulation, as can be seen in Fig. 1. The systemic circulation comprises of supplying blood from heart to the whole body, whereas pulmonary circulation comprises of the blood circulation between the heart and the lungs.

Coronary circulation is a part of the systemic circulation and is responsible for supplying blood to the heart. The arteries facilitating this circulation are termed as "coronary arteries." The blood flow in the coronary arteries is dominant during diastole, as can be seen from Fig. 2 and it is contrary to the nature of blood flow in the other parts of the body. This contrary nature can be attributed to the fact that coronary arteries wrap around the heart and during systole as the pressure increases, the vessels compress and the blood flow to the left ventricle is hampered [30]. On the other hand, the blood flow in other arteries is dominant during ventricular systole, when there is increased pressure in the aorta and its distal branches.

M. Singhal (✉) · U. N. Saha · R. Gupta
Department of Chemical Engineering, Indian Institute of Technology Guwahati, Assam, India
e-mail: mudrikasinghal@iitg.ac.in

U. N. Saha
e-mail: sahaudit790@rnd.iitg.ac.in

R. Gupta
e-mail: guptar@iitg.ac.in

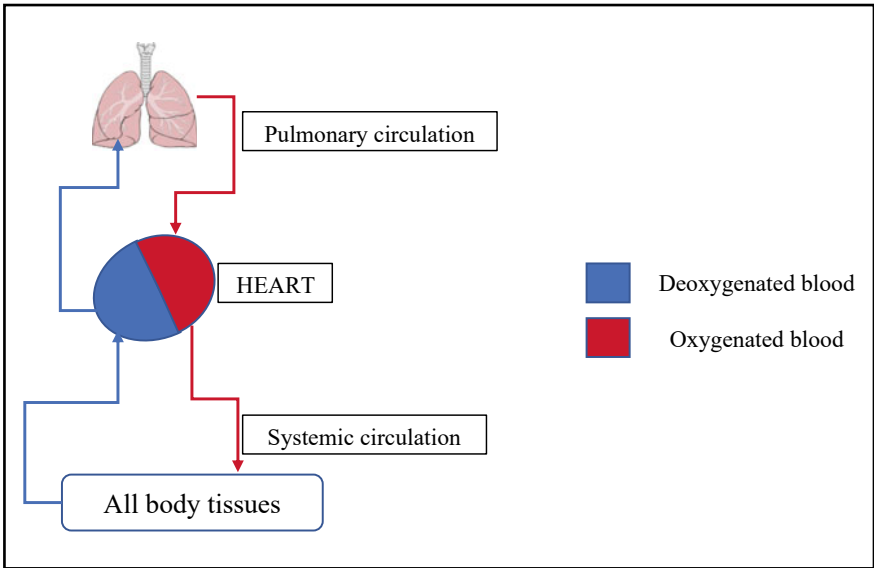**Fig. 1** Schematic of systemic and pulmonary circulation in the human body

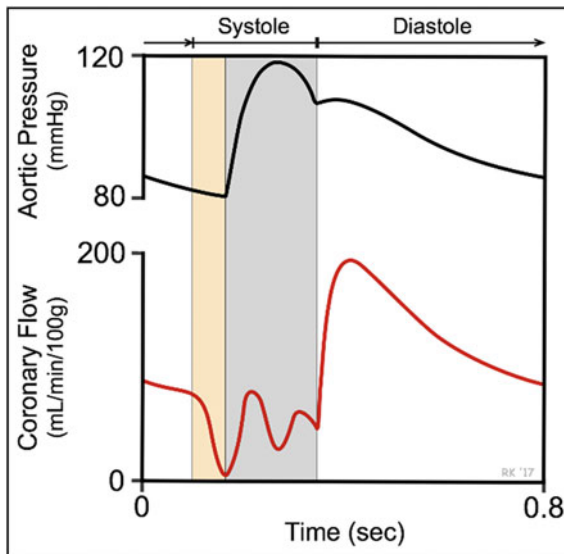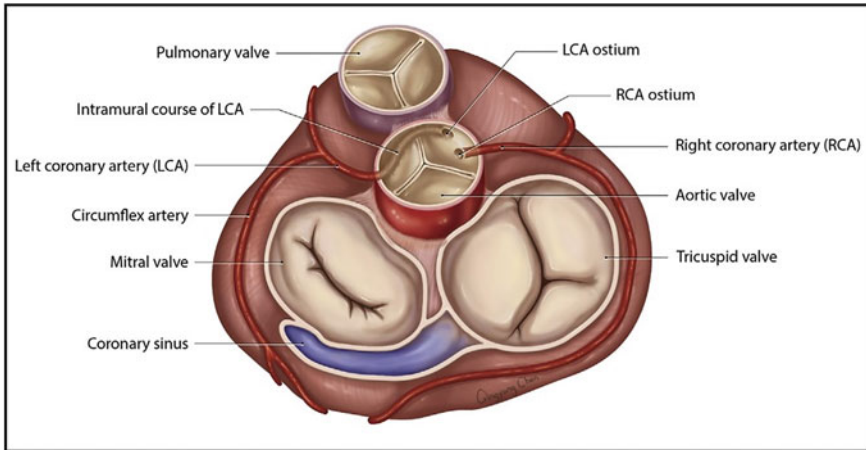**Fig. 2** Coronary flow in a cardiac cycle (Klabunde, https://cvphysiology.com/Blood%20Flow/BF001, Accessed on June, 2022)

Fig. 3 Major branches of coronary arteries [18]. Reproduced with permission

1.1 Major Branches of Coronary Arteries

The coronary arteries majorly bifurcate into the right and the left main coronary arteries originating from coronary ostia as seen in Fig. 3. These branches further subdivide into smaller sub-branches and penetrate the heart muscle, supplying blood. Each main coronary artery is 2–4 mm wide [40].

Left Main Coronary Artery

The left main coronary artery originates from the left coronary cusp and supplies blood to the left part of the heart muscle comprising the left ventricle and the left atrium. It is responsible for supplying blood to approximately 70% of the total cardiac mass [36]. It further subdivides into circumflex and left anterior descending artery.

Right Coronary Artery

The right coronary artery originating from the anterior sinus is responsible for supplying blood to the right atrium and the right ventricle. It further divides into acute marginal branch and posterior descending artery.

1.2 Cardiovascular Diseases

Cardiovascular diseases are a leading cause of death globally and have claimed 17.8 million lives worldwide in 2017 [21]. Coronary artery disease being one of them is caused because of *Atherosclerosis,* characterized by the deposition of fatty acids and other molecules on the inner lining of the arteries [8]. It can be seen from Fig. 4 that
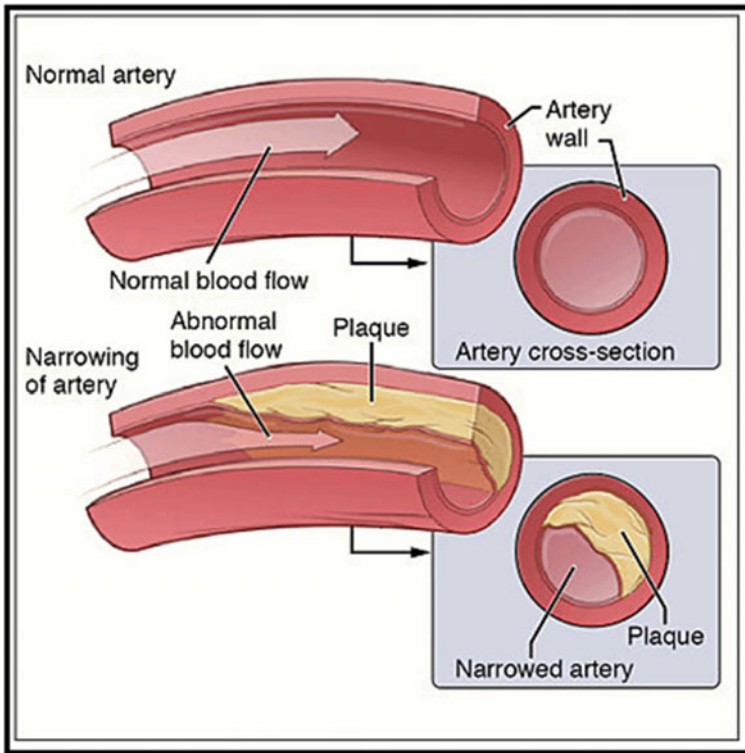
Fig. 4 Plaque build up in the arteries (https://commons.wikimedia.org/wiki/File:2113ab_Athero sclerosis.jpg, Accessed on August, 2022. Under creative commons license)

deposition leads to narrowing down of arteries and hampers the blood supply to the heart.

Apart from the invasive diagnostic methods, non-invasive methods such as the use of 3D printed models for surgical pre-planning are emerging [42]. 3D printed models provide a comprehensive understanding regarding the structure of the vessels or the heart and hence its use has been initiated in the field of cardiovascular medicine for surgical planning. In this book chapter, we describe the techniques of 3D printing and how 3D printing has been used in the cardiovascular field in recent years.

2   Fundamentals of 3D Printing

3D printing is the process of manufacturing physical models from digital signals and was first introduced by Charles Hulls in 1986 [42]. Fabrication of anatomical structures from medical image datasets is termed as *Medical 3D printing* [11]. The working chain for obtaining a 3D model from a medical image can be seen in Fig. 5.

The first step of the processing chain is to obtain the medical images and it plays a crucial role as the quality of image governs the quality of the 3D model generated. Some commonly used imaging modalities are multidetector computed tomography (MDCT), magnetic resonance imaging (MRI), ultrasonography, and positron emission tomography. Irrespective of the imaging modality, the medical images are stored in the DICOM format (Digital Imaging and Communications in Medicine). The acquisition of the medical images is followed by the post-processing of these images. The post-processing steps comprise segmentation, and some visualization tools such as volume/surface rendering and planar reformations [32]. The acquisition step is followed by the identification of anatomical regions of interest. Then, segmentation of the region of interest is carried out which is facilitated by numerous software programs, such as SimVascular (https://simvascular.github.io/), Materialise Mimics (https://www.materialise.com), and Synopsys Simpleware (https://www.synopsys.com/simpleware.html). The 3D model is created from these segmented regions by lofting. By using an appropriate printing technique, these 3D models can be printed.

There are various technologies of 3D printing that can be chosen according to the requirements of the user. Some of the most commonly used 3D printing techniques are stereolithography, fused deposition modeling, and PolyJet printing.
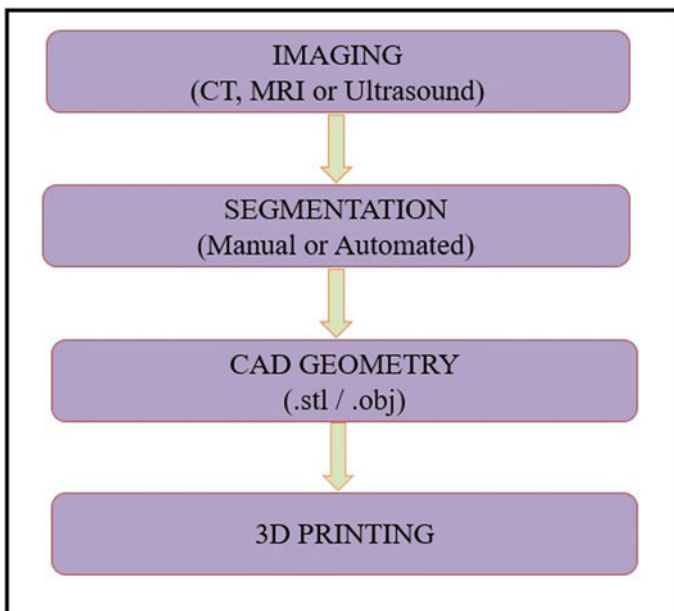
Fig. 5 From medical image to a 3D model

2.1 Stereolithography (SLA)

Stereolithography belongs to the class of additive manufacturing (AM), which is characterized by layer-by-layer fabrication. SLA is a widely used technique because of the advantages offered by it: freedom of the scale at which structures can be made, ranging from sub-micron level to decimeter-sized objects. In biomedical field, it has facilitated the manufacturing of patient-specific models [20]. SLA belongs to the class *vat photopolymerization* of AM. The light reactive resin is exposed to light of certain wavelength, as seen in Fig. 6, and it leads to the solidification of the resin by undergoing polymerization process. The resins used for SLA comprise prepolymers and monomers such as acrylates, vinyl ethers, and epoxy resins. Over a period of 40 years, stereolithography underwent four generations of technological innovations and led to improved resolution and throughput [13]. SLA is one of the most precise 3D printing modalities and can accommodate minimum feature sizes between 50 and 250 μm.
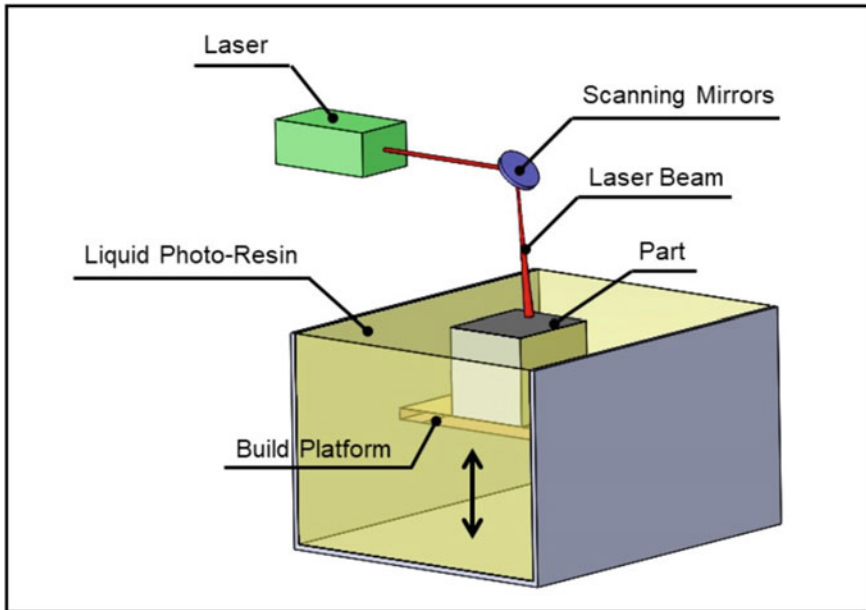
Fig. 6 Schematic of stereolithography (SLA) [31]. Reproduced with permission

2.2 Fused Deposition Modeling (FDM)

FDM is the second widely used technique in AM after SLA and has gained popularity because of its short cycle time, high-dimensional accuracy, and ease to integrate with CAD software package [2]. FDM was introduced commercially back in 1990s by Stratasys Inc., USA [22]. The principle of FDM process, as shown in Fig. 7, consists of the material which is melted into liquid state in a liquefier head and then via tracing across the cross-section, deposition is done via a nozzle. Acrylonitrile butadiene styrene (ABS) and polycarbonate are some of the materials used for FDM.
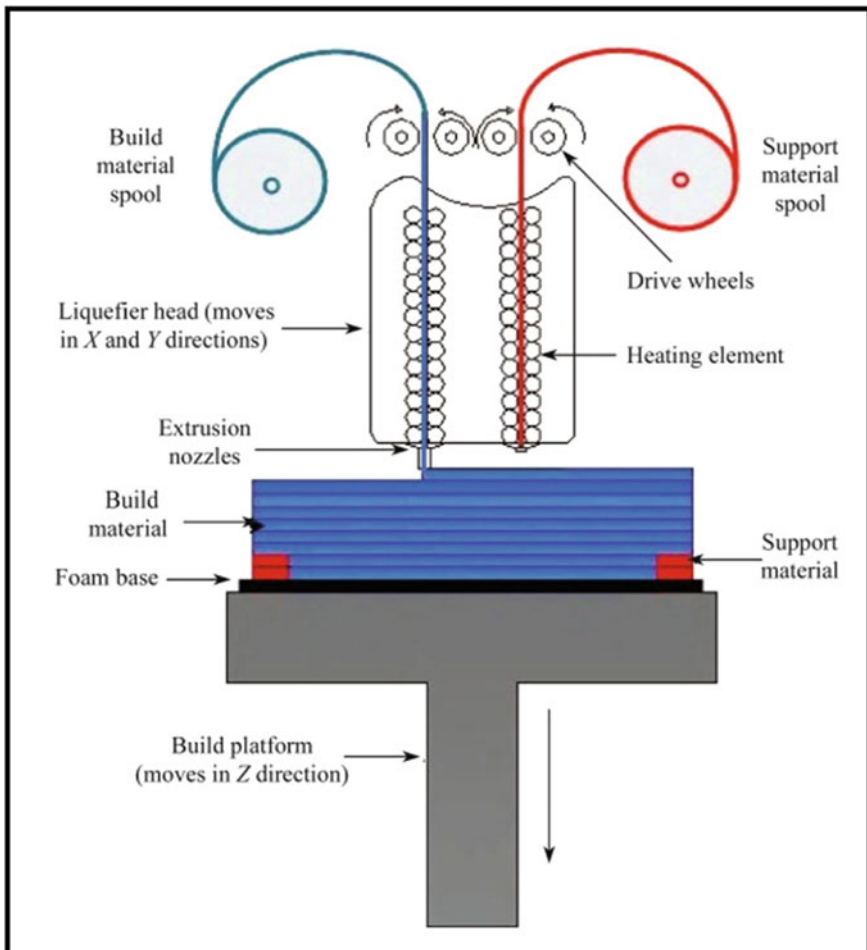

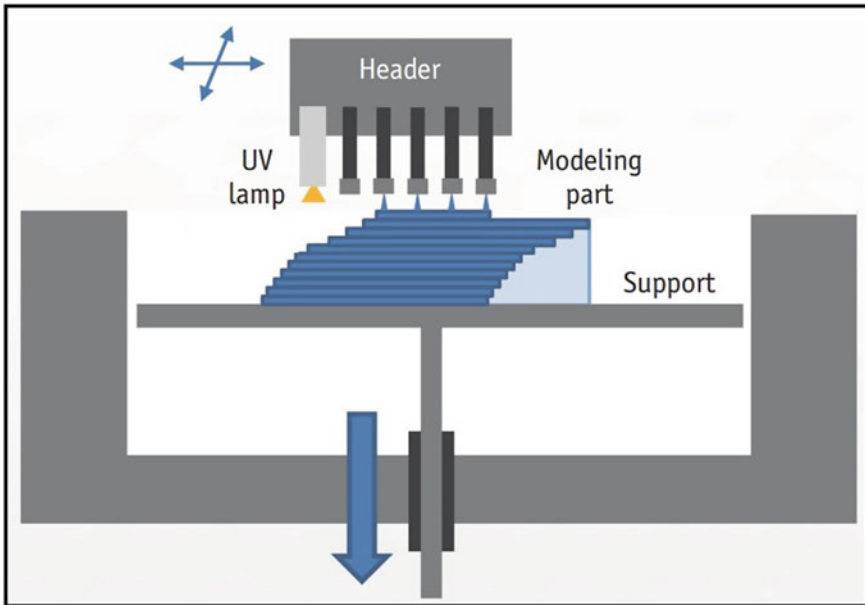**Fig. 7** Principle of FDM process [22]. Reproduced with permission

**Fig. 8** Principle of PolyJet method [17]. Under creative commons license

2.3 PolyJet

PolyJet printing is a powerful 3D printing technique capable of producing smooth and accurate parts. It is based on drop-by-drop deposition which is contrary to the continuous deposition in FDM. Photopolymer layers are jetted into ultra-thin layers, onto a build platform, as seen in Fig. 8, and each layer is treated by UV light until the model is completed [17]. A variety of materials including rubber-like materials can be used for PolyJet printing.

2.4 ColorJet

ColorJet printing also belongs to the class of additive manufacturing consisting of two major components: core material and binder. The powdered core material is spread in thin layers with the help of a roller on the build platform, as seen in Fig. 9. As each layer is spread, it is followed by solidification of the core layer because of the jetting of the color binders from print heads. The lowering of the build platform facilitates the spreading and printing of layers and fabrication of three-dimensional colored model.
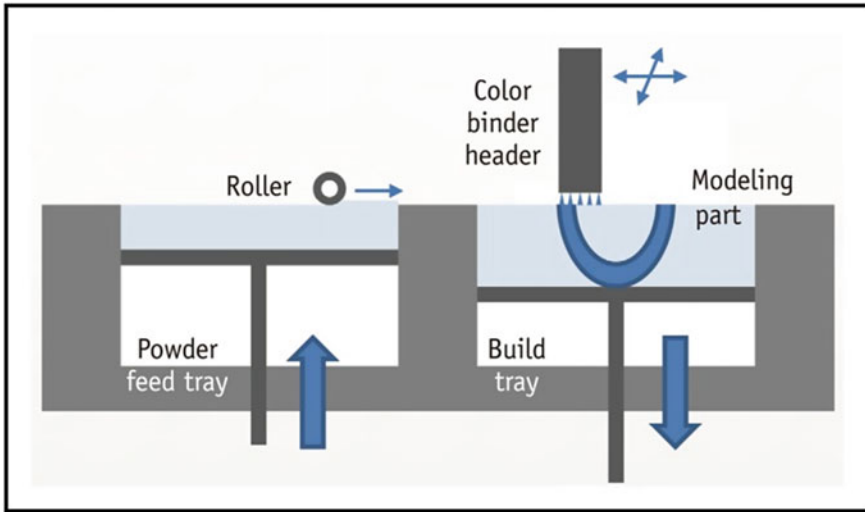
Fig. 9 Principle of ColorJet printer [17]. Under creative commons license
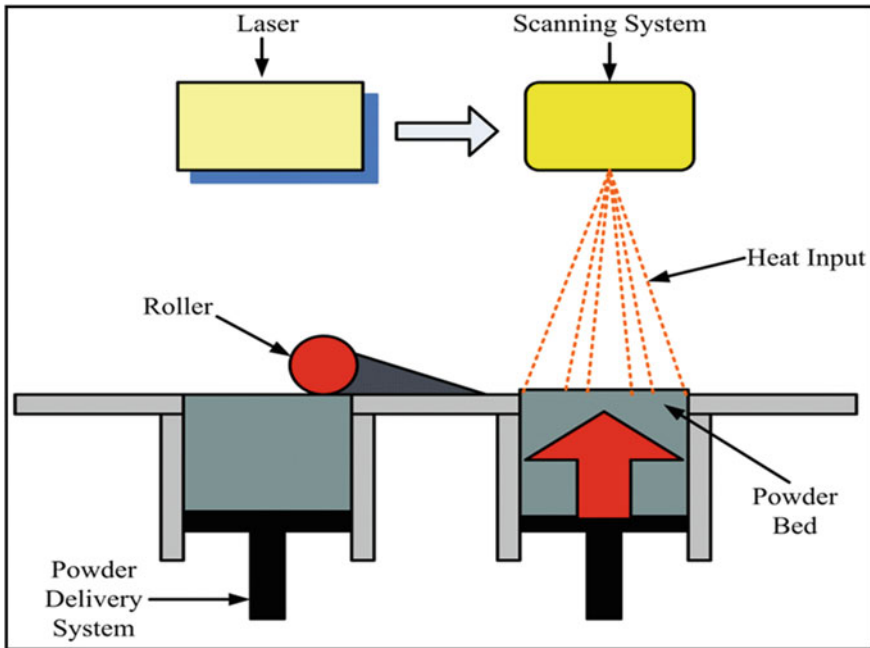
2.5 Laser Sinter

Laser sinter technique uses polymeric powder-based materials which are fused under the presence of high-power laser to fabricate the 3D structure, as depicted in Fig. 10. Each cross section of the model is traced by the laser onto a bed of powder. Similar to the techniques discussed above, the movement of the build platform facilitates the layer-by-layer construction of the model. One of the major advantages of the laser sinter technique is that it doesn't require any separate supporting structures and hence no support removal.

Of the above-discussed technologies, SLA is capable of printing thinnest models and can accommodate models with wall thickness as low as 200 µm. FDM and PolyJet printing allow a minimum wall thickness of 1 mm.

2.6 Materials

A wide range of materials including metals, polymers, ceramics, and composites are used for 3D printing depending on the application. 3D models can be printed by either rigid, semi-rigid, composite, or flexible materials.

The most commonly used materials for fused deposition modeling are polyether ether ketone, polylactic acid, acrylonitrile butadiene styrene, and polyethylene [15, 35]. For PolyJet printing, TangoPlus, VeroClear, and MED610 Resins are the commonly used materials [6, 9]. Literature suggests that urethane and epoxy resins have been frequently used for 3D printing via stereolithography [9].

Fig. 10 Principle of laser sinter process [24]. Reproduced with permission

Apart from the use of synthetic materials in 3D printing, the use of biomaterials was introduced in 1990s and it is termed as *bioprinting.* It was introduced via laser-based method, and can be defined as a 3D fabrication technology which is used to dispense biomaterials loaded with cells for construction of 3D functional tissues or organs [19, 41]. 3D bioprinting has been of great use in the medical research by serving numerous requirements such as drug delivery, regenerative medicine, and functional organ replacement. The three major modalities of bioprinting are laser-assisted bioprinting, inkjet bioprinting, and extrusion-based bioprinting [25, 28]. The main component in the process of bioprinting is the *bioink,* through which artificial tissues and organs are printed. Bioinks consist of biomaterials and living cells in a cellular-matrix environment. A variety of materials such as polymers, elastomers, hydrogels, and ceramics are used for producing bioinks [41]. To overcome the possibility of immune reactions against synthetic materials in bioinks, natural polymers such as gelatin and silk fibroin are also used for synthesizing bioinks [37].

3 Medical Applications of 3D Printing

Over the last two decades, 3D printing has been widely used for biomedical applications spanning across various areas of medicine and tissue engineering [34].

The applications of 3D printing span across various industries, such as aerospace, automotive, food, healthcare, and many more. For pharmaceutical purposes, 3D printing is used for manufacturing of dosage forms such as capsules, tablets, and orodispersible films. Multiple purposes are served such as designing lightweight parts for efficient energy consumption, designing of effective automotive designs, and 3D printing of various tissues and organs.

With advancements in technology, it has been revealed that generic therapies for patient treatment pose some limitations. It further led to the development of patient-specific or precision medicine where the approach is individual-specific rather than targeting a broad population. The use of 3D printing techniques in a patient-specific manner comprises of design of patient-specific in-vitro models and implants [29]. Apart from manufacturing of implants and in-vitro models, 3D printing has also been used for manufacturing of antimicrobial wound dressings and these were found to be more affordable than conventional flat dressings [14]. 3D printing has also facilitated the fabrication of organs and has gained popularity in the maxillofacial applications. It has been used for the fabrication of soft tissue prostheses for ears, for construction of eye models, and intermediate splint models for jaw reconstruction [34]. Surgical planning is one of the emerging areas where the use of 3D printing is observed and has been used in liver and kidney surgeries.

3.1 Cardiovascular 3D Printing: A Brief Review

The use of 3D printing in cardiovascular medicine has emerged recently and has been used successfully for surgical pre-planning, teaching, and developing phantoms [23]. 3D printed models complement the classical methods of anatomical teaching and help in differentiating between normal and abnormal anatomy [10]. 3D printing via the use of bioinks has helped the medical fraternity greatly by enabling the printing of 3D models of blood vessels and heart tissues. It offers some advantages such as visualization, tactile perception, and volumetric assessment of the complex cardiovascular pathology. Spanning across a time period of more than a decade, 3D printing has been used for numerous purposes such as hemodynamic studies in the arterial models, studying the effect of degree of stenosis, and conducting benchtop FFR experiments. Fractional Flow Reserve (FFR) is an important parameter used for commenting upon the severity of stenosis in the arteries. Mathematically, FFR is defined as the ratio of the pressure distal to stenosis to that of the mean aortic pressure and invasive FFR has been the gold standard for severity of the arterial stenosis.

Cardiovascular diseases are the leading cause of death globally and heart transplantation is the only treatment for end-stage heart failure. With limited number of heart donors, a viable alternative solution is highly required for the end-stage heart failures. This need is quenched by the amalgamation of biomaterials and 3D printing in the arena of cardiovascular tissue engineering but the generation of patient-specific vascularized tissues still remains a challenge [26]. Literature analysis has revealed that in the domain of cardiovascular medicine, 3D printing has also been used for

complex pediatric and congenital heart diseases [11]. Structural heart diseases basically comprise non-coronary cardiovascular conditions and 3D printing plays a vital role in the diagnosis and management of these. Valve dysfunction is one of the reasons for heart failure. Valve replacement surgeries have been existing as a curative measure and mechanical and biological prosthetic valves have been used for this. Both the variations offer some limitations such as the risk of thrombogenicity, immune reaction, and short life span. To overcome the shortcomings of mechanical and prosthetic valves, the use of 3Dprinted valves has also been reported. 3D printed valves offer the advantage of generation of mechanically heterogeneous structures and accurate replication of the complex architecture of the valves [10]. 3D printing of aneurysms has also been reported. Hence, it can be said that cardiovascular 3D printing helps in identification of the structures at risk and this knowledge can be used by the surgeons prior to any interventions. 3D printing has also facilitated the decision-making process in the treatment procedure for cardiac tumors as they provide an insight regarding relationship of the tumor with the surroundings. Cardiac patches can be defined as thick and vascularized piece of tissue which is developed in laboratory conditions and match the immunological, cellular, biochemical, and anatomical properties of the patient [26]. Cardiac patches have also been developed via 3D printing techniques which facilitate the replacement of damaged and aging cardiac tissues. Table 1 summarizes the applications of 3D printing in the field of cardiovascular medicine.

Though cardiovascular 3D printing offers a range of advantages, it also poses some limitations such as high cost, which is a major disadvantage. 3D printing facilitates the replication of complex anatomical structures but the in vivo physiological environment can't be mimicked in these 3D models [43]. The first and the vital step for creation of 3D models is identification of the correct anatomical regions of interest in the medical images which is further followed by the segmentation step. Hence, it becomes essential to precisely identify the regions of interest. Printing of models via bioinks demands the correct choice of the material which possesses appropriate stiffness and cell microenvironment [10].

4   Flow Visualization Studies in 3D Printed Models

The literature suggests that 3D printed models have been used for carrying out flow visualization studies. These studies are facilitated by the non-invasive optical technique, *Particle Image Velocimetry (PIV)* using which the velocity field of the entire region is recorded. A typical PIV setup as shown in Fig. 11 consists of high speed camera, double pulsed laser, and optical arrangement for obtaining a laser sheet. The two types of sensors which are present in the high-speed cameras are: Charged coupled device (CCD) and complementary metal oxide sensor (CMOS).

Optical accessibility of the flow field is a must for PIV experiments and hence transparent models are used. Polycarbonate and acrylic-based materials for printing transparent 3D models. The flow is seeded with neutrally buoyant seeding particles

Table 1 Applications of cardiovascular 3D printing

3D printing technology	Discussion
Fused deposition modeling	Anthropomorphic phantoms of coronary arteries were created for optimizing CCTA protocols [23]
Stereolithography	Hemodynamic studies in 3D printed coronary arteries were carried out for varying diseases of stenosis. In-vitro studies were used to validate the computational studies for single phase models. Flow visualization and the effect of printing resolution was studied [4, 5]
PolyJet	Fractional flow reserve (FFR) measurement was done in 3D printed models. It was further compared with non-invasive and invasive FFR [38]
PolyJet	3D printed coronary arteries were used for simulating the placement of coronary stents. These can be further useful in developing optimal CCTA protocols [39]
Stereolithography	3D printed coronary artery models were used to visualize the spatial distribution of stenoses [44]
ColorJet (Produces fully colored models and the technique consists of deposition of a binding adhesive into layers of powdered materials)	3D printing was used for visualization of anatomy and surgical planning for patients with congenital heart disease [1]
Stereolithography	3D models of heart were used for surgical planning in percutaneous mitral annuloplasty [7]
PolyJet	Thoracic aorta was printed and hemodynamic studies were carried out, in combination with MRI data [3]
Laser Sinter (Lasers are used to sinter powder materials layer-by-layer to create a solid structure)	3D heart models were printed from medical images. These can be used for teaching and surgical planning purpose [12]
Inkjet (Consists of deposition of liquid materials or solid suspension, layer-by-layer. Each layer is cured after deposition.)	3D printing was used for creating models of paediatric heart which was used for medical device development [25]

also known as tracer particles which don't disturb the flow. The particles are illuminated by the laser and their motion is recorded by the camera. The velocity of these tracer particle helps in calculating the velocity field of the flow, as a whole. The velocity calculation from the displacement vectors is facilitated by post-processing software programs based on interrogation techniques. Flow visualization studies in 3D printed models also serve as a validation method for the computational hemodynamic analysis.
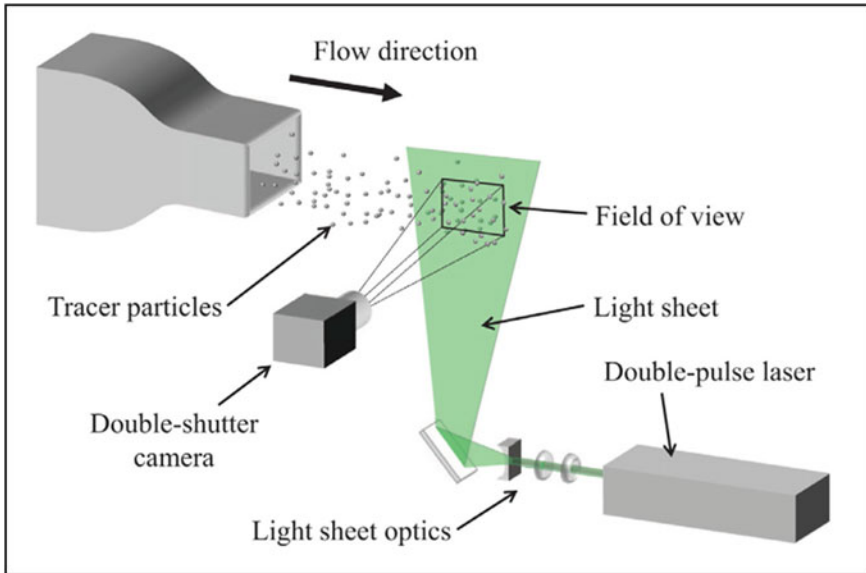
Fig. 11 Principle of PIV [33]. Under creative commons license

5 Conclusion and Future Perspectives

Recently, the use of medical 3D printing is emerging in the field of cardiovascular medicine. It can be seen that 3D printing serves multiple purposes such as teaching tools, used for surgical planning, and for in-vitro flow loop construction. There are numerous prevalent techniques for 3D printing, namely *stereolithography, fused deposition modeling, PolyJet,* which are used according to the geometrical requirements. In recent years, 3D printed models of coronary arteries have been used for flow visualization, hemodynamic studies, and surgical pre-planning.

3D printing of coronary arteries from patient-specific images provides a varied range of models which can be used as anatomical teaching tools. As the physiological state of the artery varies from patient-to-patient, these models represent different states and can help in demonstrating how a diseased artery looks different from a healthy artery. Flow visualization studies in the constructed in-vitro flow loops provide an idea about how the geometry of the artery affects the hemodynamics. These studies can be used for surgical planning purposes. Experimental studies in 3D printed arterial models serve as a validation tool for the computational analysis. With the increasing use of bioinks, development of 3D printed models in the form of vessels, cardiac patches, and valves has also gained some pace.

The advancements in technology have introduced the use of 4D bioprinting in addition to the existing domain of 3D bioprinting. It is known that 3D bioprinted materials don't change with time or in response to the external environmental stimuli but 4D bioprinting overcomes the limitation of the static nature of 3D bioprinting.

Hence, 4D bioprinting considers time as the fourth dimension and the bioprinted materials grow or change with time in response to the change with environmental conditions. 4D bioprinting is based on the use of stimuli-responsive materials and memory-shape polymers for creating structures that modify in the presence of stimulus [27]. The external stimuli can be provided in the form of variation in temperature, pH, light, electric, or magnetic field. Moldable materials can be integrated into the initially 3D bioprinted structures which modify in due course of time for obtaining a structure with desired specifications [16]. 4D bioprinted materials can be used for constructing sophisticated, high resolution, intricate structures mimicking the natural tissues, which can't be constructed via existing static 3D bioprinting techniques. Though in the cardiovascular domain, the use of 4D bioprinting is still in its initial stages and with advancements it can be utilized to develop clinically viable cardiac constructs which can be used for the management crucial conditions such as myocardial infarction [10, 16].

References

1. Anwar S, Singh GK, Varughese J, Nguyen H, Billadello JJ, Sheybani EF, Woodard PK, Manning P, Eghtesady P (2017) 3D printing in complex congenital heart disease. JACC: Cardiovasc Imaging 10(8):953–956
2. Boparai KS, Singh R, Singh H (2016) Development of rapid tooling using fused deposition modelling: a review. Rapid Prototyp J 22(2):281–299
3. Canstein C, Cachot P, Faust A, Stalder AF, Bock J, Frydrychowicz A, Kuffer J, Henning J, Markl M (2008) 3D MR Flow analysis in realistic rapid-prototyping model systems of the thoracic aorta: comparison with in vivo data and computational fluid dynamics in identical vessel geometries. Magn Reson Med 59:535–546
4. Carvalho V, Rodrigues N, Ribeiro R, Costa PF, Teixeira JC, Lima RA, Teixeira S (2021) Hemodynamic study in 3D printed stenotic coronary artery models: experimental validation and transient simulation. Comput Methods Biomech Biomed Eng 24(6):623–636
5. Carvalho V, Rodrigues N, Ribeiro R, Costa PF, Lima RA, Teixeira S (2020) 3D printed biomodels for flow visualization in stenotic vessels: an experimental and numerical study. Micromachines 11(6):549
6. Castiaux AD, Pinger CW, Hayter EA, Bunn ME, Martin RS, Spence DM (2019) PolyJet 3D printed enclosed microfluidic channels without photocurable supports. Anal Chem 91(10):6910–6917
7. Dankowski R, Baszko A, Sutherland M, Firek L, Kalmucki P, Wroblewska K, Szyszka A, Groothuis A, Siminiak T (2014) 3D heart model printing for preparation of percutaneous structural interventions: description of the technology and case report. Kardiol Pol 72(6):546–551
8. Davies MJ, Woolf N (1993) Atherosclerosis: what is it and why does it occur? Br Hear J 69(1 Suppl):S3–S11
9. Garcia J, Yang Z, Mongrain R, Leask RL, Lachapelle K (2017) 3D printing biomaterials and their use in medical education: a review of current technology and trends for the future. BMJ Simul Technol Enhanc Learn 4(1):27–40
10. Gardin C, Ferroni L, Latremouille C, Chachques JC, Mitrecic D, Zavan B (2020) Recent applications of three-dimensional printing in cardiovascular medicine. Cells 9:742
11. Giannopoulos AA, Mitsouras D, Yoo SJ, Liu PP, Chatzizisis YS, Rybicki FJ (2016) Applications of 3D printing in cardiovascular diseases. Nat Rev Cardiol 13(12):701–718

12. Greil GF, Wolf I, Kuettner A, Fenchel M, Miller S, Martirosian P, Schick F, Oppitz M, Meinzer HP, Sieverding L (2007) Stereolithographic reproduction of complex cardiac morphology based on high spatial resolution imaging. Clin Res Cardiol 96(3):176–185

13. Huang J, Qin Q, Wang J (2020) A review of stereolithography: processes and systems. Processes 8(9):1138

14. Jamroz W, Szafraneic J, Kurek M, Jachowicz R (2018) 3D printing pharmaceutical and medical applications–recent achievements and challenges. Pharm Res 35(9):176

15. Layani M, Wang X, Magdassi S (2018) Novel materials for 3D printing by photopolymerization. Adv Mater 30:1706344

16. Kato B, Wisser G, Agrawal DK, Wood T, Thanksm FG (2021) 3D bioprinting of cardiac tissues: current challenges and perspectives. J Mater Sci Mater Med 32:54

17. Kim GB, Lee S, Kim H, Yang DH, Kim YH, Kyung YS, Kim CS, Choi SH, Kim BJ, Ha H, Kwon SU, Kim N (2016) Three-dimensional printing: basic principles and applications in medicine and radiology. Korean J Radiol 17(2):182–197

18. Kindi HN, Yacoub MH (2019) Transection and Relocation of anomalous left coronary artery after aborted sudden cardiac death. Ann Thorac Surg 108(1):e25–e28

19. Mandrycky C, Wang Z, Kim K, Kim DH (2016) 3D bioprinting for engineering complex tissues. Biotechnol Adv 34:422–434

20. Melchels FPW, Feijen J, Grijpma DW (2010) A review on stereolithography and its applications in biomedical engineering. Biomaterials 31(24):6121–6130

21. Mensah GA, Roth GA, Fuster V (2019) The global burden of cardiovascular diseases and risk factors, 2020 and beyond. J Am Coll Cardiol 74(20):2529–2532

22. Mohamed OA, Masood SH, Bhowmik JL (2015) Optimization of fused deposition modelling process parameters: a review of current research and future prospects. Adv Manuf 3:42–53

23. Morup SD, Stowe J, Precht H, Gervig MH, Foley C (2021) Design of 3D printed coronary artery model for CT optimization. Radiography. https://doi.org/10.1016/j.radi.2021.09.001

24. Nandy J, Sarangi H, Sahoo S (2019) A review on direct metal laser sintering: process features and microstructure modeling. Lasers Manuf Mater Process 6:280–316

25. Noecker AM, Chen JF, Zhou Q, White RD, Kopkack MW, Arruda MJ, Duncan MW (2006) Development of patient-specific three-dimensional paediatric cardiac models. Am Soc Artif Intern Organs 52(3):349–353

26. Noor N, Shapira A, Edri R, Gal I, Wertheim L, Dvir T (2019) 3D printing of personalized thick and perfusable cardiac patches and hearts. Adv Sci 6:1900344

27. Ong CS, Nam L, Ong K, Krishnan A, Huang CY, Fukunishi T, Hibino N (2018) 3D and 4D bioprinting of myocardium: current approaches, challenges and future prospects. Biomed Res Int 2018:6497242

28. Ozkerim PS, Inci I, Zhang YS, Khademhosseini A, Dokmeci MR (2018) Bioinks for 3D bioprinting: an overview. Biomater Sci 6:915–946

29. Prendergast ME, Burdick JA (2020) Recent advancements in enabling technologies in 3D printing for precision medicine. Adv Mater 32:1902516

30. Ramanthan T, Skinner H (2005) Coronary blood flow. Contin Educ Anaesth, CritAl Care Pain 5(2):65–66

31. Razavykia A, Brusa E, Delprete C, Yavari R (2020) An overview of additive manufacturing technologies–a review to technical synthesis in numerical study of selective laser melting. Materials 13(17):3895

32. Rengier F, Mehndiratta A, Kobligk HV, Zechmann CM, Unterhinninghofen R, Kauczor HU, Giesel FL (2010) 3D printing based on imaging data: review of medical applications. Int J Comput Assist Radiol Surg 5(4):335–341

33. Scharnowski S, Kahler CJ (2020) Particle image velocimetry: classical operating rule from today's perspective. Opt Lasers Eng 135:106185

34. Shafiee A, Atala A (2016) Printing technologies for medical applications. Trends Mol Med 22(3):254–265

35. Shahrubudin N, Lee TC, Ramlan R (2019) An overview on 3D printing technology: technological, materials and applications. Procedia Manuf 35:1286–1296

36. Shanmugavelayudam SK, Rubenstein DA, Yin W (2010) Effect of geometrical assumptions on numerical modelling of coronary blood flow under normal and disease conditions. J Biomech Eng 132(6)
37. Singh YP, Bandyopadhyay A, Mandal BB (2019) 3D Bioprinting using cross-linker-free silk-gelatin bioink for cartilage tissue engineering. Appl Mater Interfaces 11:33684–33696
38. Sommer KN, Shepard LM, Mitsouras D, Iyer V, Angel E, Wilson MF, Rybicki FJ, Kumamuru KK, Sharma UC, Reddy A, Fujimoto S, Ionita CN (2020) Patient-specific 3D printed coronary models based on coronary computed tomography angiography volumes to investigate flow conditions in coronary artery disease. Biomed Phys Eng Express 6(4):045007
39. Sun Z, Jansen S (2019) Personalized 3D printed coronary models in coronary stenting. Quant Imaging Med Surg 9(8):1356–1367
40. Taki A, Kermani A, Ranjbarnavazi SM, Pourmodheji A (2017) Overview of different medical imaging techniques for the identification of coronary atherosclerotic plaques. Comput Vis Intravasc Imaging Comput-Assist Stenting (Chapter 4) 79–106
41. Vanaei S, Parizi MS, Vanaei S, Salemizadehparizi F, Vanaei HR (2021) An overview on materials and techniques in 3D bioprinting towards biomedical application. Eng Regen 2:1–18
42. Vukicevic M, Mosadegh B, Min JK, Little SH (2017) Cardiac 3D printing and its future directions. JACC: Cardiovasc Imaging 10(2):171–184
43. Wang H, Song H, Yang Y, Cao Q, Hu Y, Chen J, Guo J, Wang Y, Jia D, Cao S, Zhou Q (2020) Three-dimensional printing for cardiovascular diseases: from anatomical modeling to dynamic functionality. Biomed Eng Online 19:76
44. Yang Y, Liu X, Xia Y, Wu W, Xiong H, Zhang H, Xu L, Wong KKL, Ouyang H, Huang W (2017) Impact of spatial characteristics in the left stenotic coronary artery on the hemodynamics and visualization of 3D replica models. Sci Rep 7:1542

Combined Influence of Material Properties of Bone and Implant on Bone Growth Over Macro-Textured Implant Surface

Rajdeep Ghosh , **Souptick Chanda** , **and Debabrata Chakraborty**

Keywords Implant · Surface topology · Macro-textures · Finite element analysis · Tissue-differentiation algorithm · Bone growth

1 Introduction

One of the important parameters of the reliability of orthopedic implants depends on the type of adherence of the implant with the host bone. One type of implant fixation relies on a polymeric composition known as bone cement or PMMA (poly methyl methacrylate) filled between the bone and the implant and is used primarily for elderly patients with reduced bone quality [1]. However, the use of cemented implants itself has a wide range of disadvantages such as exothermic polymeric reaction, brittleness, and lesser reliability [2]. On the contrary, fixation with the bone in uncemented or cementless implants depends primarily on sufficient vascularization

R. Ghosh (✉) · D. Chakraborty
Department of Mechanical Engineering, Indian Institute of Technology Guwahati, Guwahati 781 039, Assam, India
e-mail: rajdeep.mech@iitg.ac.in

D. Chakraborty
e-mail: chakra@iitg.ac.in

S. Chanda
Department of Biosciences and Bioengineering, Indian Institute of Technology Guwahati, Guwahati 781 039, Assam, India

Mehta Family School of Data Science and Artificial Intelligence, Indian Institute of Technology Guwahati, Guwahati 781 039, Assam, India

S. Chanda
e-mail: csouptick@iitg.ac.in

243

followed by bone growth between the bone and the implant. Growth of bone and other connective tissues at the bone-implant interface thus provides a mechanical interlocking and enhances implant stability [1]. Such implants are a common choice for clinicians around the world, especially when working with younger patients because of their capacity for biologic adherence [3]. Despite the phenomenal success of uncemented prostheses globally and strict surgical precautions, there has been a significant increase in the absolute number of failed joints, necessitating revision surgery. Despite the fact that the causes of such failures are multifaceted, the majority of them can be linked to biomechanical causes [4].

One of the most common reasons of aseptic loosening of cementless implants is a lack of biological attachment. MSCs or mesenchymal stem cells are non-hematopoietic pluripotent cells that undergo cell differentiation acted upon by mechanical signals. These differentiated MSCs on attaining maturity form bone, cartilage, and fibrous tissue around the implant surface and thus responsible for biological attachment at the bone-implant interface region [5].

Realistic design adjustments in implant morphology can reduce implant fixation failure to a considerable extent [1, 6–9]. Micro and nano roughness on implant surfaces at the length scale of a mesenchymal stem cell (MSC) were formerly thought to aid osseointegration and bone formation. On the other hand, macro-textured surfaces were thought to be used solely to promote mechanical interlocking between the bone and the implant. However, a recent in vivo study [8] looked at the effect of an implant's surface macro-texture on triggering secondary stability at the bone-implant interface. This study [8] reported that a novel pillared structure (macro-scale surface) spaced uniformly over the substrate of the implant surface promotes better bone growth than traditional micro-porous coatings. In addition, the authors of the present study had also reported earlier into the effect of topological dimensions on bone development [4, 6] through in silico studies [4, 6].

Geometric design parameters on such textured surfaces can be tailored to encourage adequate bone formation around a cementless prosthesis [7, 9]. The non-primitive nature of most surface features on implant surfaces has demonstrated to exhibit complex non-linear relationships with levels of ossification with a variety of major design parameters [7, 10].

Bone, being a living tissue, exhibits site-specific material property variation which was not incorporated in earlier studies [4, 6, 7] of bone growth around textured implant surfaces. However, there are hardly any literature that study the combined influence of varying bone and implant material property on bone growth around macro-textured implant surfaces. The primary goal of this study is to analyze the influence of bone and commercially used implant material properties on bone growth over macro-textured implant surfaces within the ambit of numerical limitations.

2   Materials and Method

Based on distinguishable textures on CORAIL [4, 6] and SP-CL [4] femoral stems, two unique 3D macro-textured implant models were constructed. The CORAIL eqv. model has consistently spaced rectangular ribs that partially replicate the CORAIL [4, 6] hip stem's proximal anterior–posterior surfaces. The proximal section of the SP-CL [4] hip stem is represented by the SP-CL eqv. model, which has evenly spaced hemispherical grooves of equal radius.

The major dimensions of the 3D models were taken from a radiological image [11] using ImageJ v1.53a to preserve clinical approval (National Institutes of Health and Laboratory for Optical and Computational Instrumentation, University of Wisconsin, USA). The average width of an intramedullary hip prosthesis within a femoral cavity, the maximum distance that can be left between the implant and the bone for ossification, and the simplicity of fabrication using current manufacturing techniques were taken into consideration by the authors when selecting the parameter range.

Bone section, granulation tissue (major region of bone development), and the implant section make up the usual volumes of bone-implant interface models (Fig. 1).
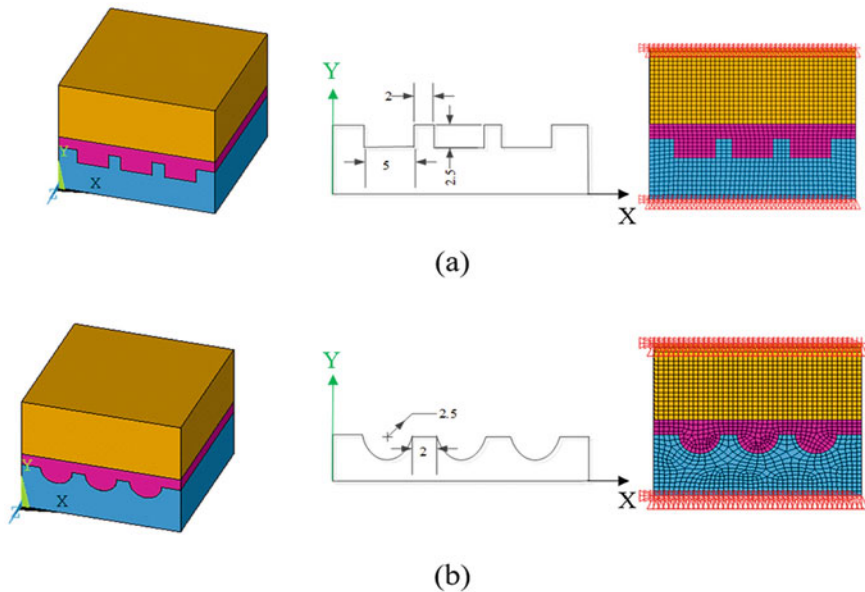
Fig. 1 Solid and FE models of **a** CORAIL eqv.; **b** SP-CL eqv. bone-implant interfaces (Color Map: **Blue** denotes implant section, **Purple** denotes granulation tissue, **Yellow** denotes host bone section)

2.1 Material Attributes, Loading, and Boundary Conditions in FE Modeling

Solid models were developed and discretized in ANSYS V14.5 (ANSYS Inc., Canonsburg, PA, USA). Meshing of each of the FE models was performed with eight-noded hexahedral ANSYS elements (SOLID185). A mesh evaluation was carried out for each of the FE models to find the best grid sizes and get results with a respectable level of accuracy. The host bone, implant, and granulation tissue were all considered linearly elastic, homogenous, and isotropic. The Young's moduli of cancellous bone were considered 5.3 GPa for the first instance and 7.8 GPa in the second instance and that of Titanium-alloy (Ti–6Al–4 V) implant was 113 GPa and Cobalt-alloy (Co–Cr) implant was 210 GPa. The modulus of granulation tissue was considered 1 MPa initially. The Poisson's ratio for bone and implant was set to 0.3, whereas the granulation tissue Poisson's ratio was set to 0.167. All of the model's interfaces were considered perfectly bonded.

The upper surface of the bone was restricted in all directions, whilst the bottom implant surface was displaced normally by 5 μm and a tangentially (bone-implant micromotion) by 20 μm during every iterative time step.

2.2 Tissue Differentiation Based on Mechanoregulatory Principles

A mechanoregulatory algorithm (Table 1) was used to simulate evolutionary progressive bone formation. It is hypothesized that, MSCs at the bone-granulation tissue interface diffuse and migrate uniformly toward the implant-tissue interface over a period necessary for the migration process [4, 6]. The movement of pluripotent stem cells over the region of the bone-implant interface was simulated by the mathematical model of thermal diffusion as utilized in previous work (Fig. 2) [4, 6].

$$\psi \nabla^2 \Omega = \frac{d\Omega}{dt} \tag{1}$$

where Ψ is the diffusion coefficient (0.1 mm^3/day), and Ω denotes the concentration of stem cells per finite element at the granulation tissue section. The magnitude of Ψ was chosen resembling to complete stem cell migration across the granulation tissue within 16 weeks [6].

Initially, red, inflamed granulation tissue—made up of adequate blood vessels to provide nutrients to the formed cells—was used to fill the macroscopic space between the implant and the bone. Local mechanical cues (hydrostatic stress and deviatoric strain) control the development of MSCs into diverse osteogenic cellular phenotypes [6]. These cellular morphologies result in the formation of fibrous tissue, cartilage, and developing bone. The equivalent material properties at each finite element of the

Table 1 Tissue phenotype, its constituent materials, and associated mechanical signals controlling tissue differentiation [4, 6]

Tissue phenotypes	Young's modulus (in MPa)	Poisson's ratio	Deviatoric strain (in %)	Hydrostatic stress (in MPa)
Granulation tissue	1	0.167	–	–
Fibrous tissue	2	0.167	– >5 <−5	>0.15 >−0.15 >−0.15
Cartilage	10	0.167	>15 <−15	<−0.15 <−0.15
Immature bone	1000	0.3	−15 to +15	<−0.15
Mature bone	6000	0.3	−5 to +5	−0.15 to +0.15
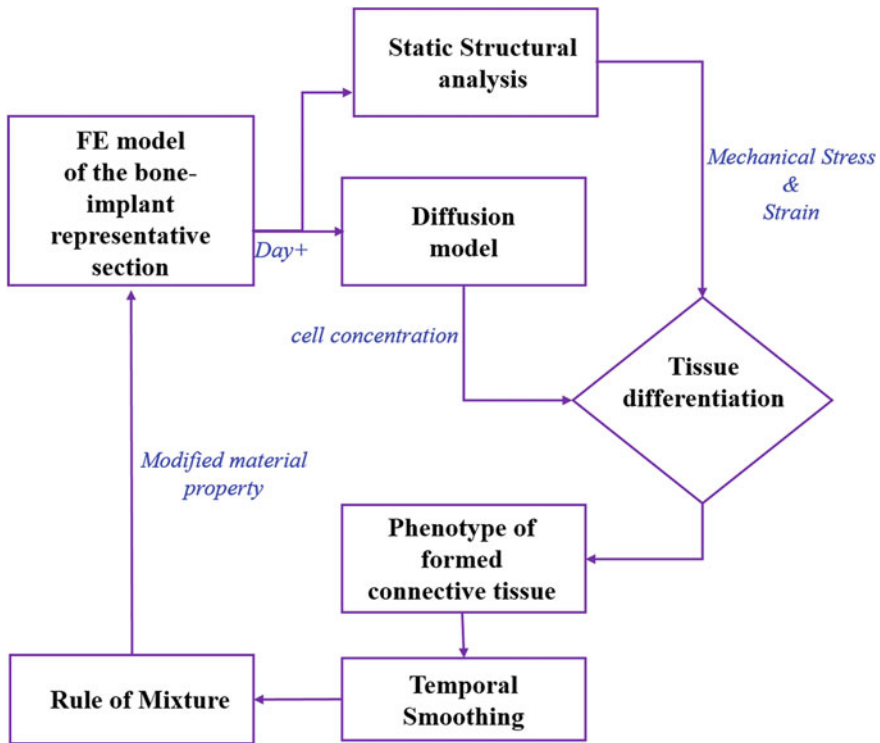
Fig. 2 Schematic framework to evaluate bone growth around macroscopic bone-implant interface

interface were calculated using a rule of mixture, as shown in Eq. 2.

$$Y_{n+1} = \left(\frac{\Omega_{\max} - \Omega_{tissue}}{\Omega_{\max}} \right)\Bigg|_n Y_{granulation} + \left(\frac{\Omega_{tissue}}{\Omega_{\max}} \right)\Bigg|_n Y_{tissue} \tag{2}$$

where $Y_{granulation}$ and Y_{tissue} are the material stiffness of the granulation tissue layer and the newly developed tissue patches, respectively; Ω_{max} and Ω_{tissue} are the highest and the actual cell concentration in each element. The material properties of the model were updated using a temporal smoothing approach [6], as given in Eq. 3.

$$Y_{n+1,smoothed} = \frac{1}{10} \sum_{i=n}^{n-9} Y_i \qquad (3)$$

One iterative cycle refers to one post-operative day in the numerical scheme. The complete healing simulation was planned to last 120 iterations, or roughly 16 weeks after surgery. The mechanoregulatory tissue-differentiation model was implemented using a custom MATLAB script (Matlab 2017a, The MathWorks Inc., Natick, MA, USA). A masterbatch script (DOS) was utilized in each iteration to successively launch the ANSYS for structural FE study and the MATLAB to run numerical calculations of tissue differentiation algorithm. On a Windows 10 Pro platform with an Intel® CoreTM i7-4510U 2-core CPU and 8 GB RAM, the simulation was executed in batch mode.

3   Results and Discussion

3.1   Influence of Implant Material on Bone Growth Around Macro-Textured Surfaces

Results from the study (Table 2) show that the percentage of bone growth with titanium alloy for CORAIL eqv. implant was 8.70% which is ~4% reduction in bone formation as compared to that with cobalt-chromium alloy (9.02%) considering bone material property to be 5.3 GPa. Similarly, considering host bone material to be of 7.8 GPa, the same macro-textured surface has shown a negligible reduction (9.35–9.32%) in bone growth by ~0.3%. Similar finding was observed when tested with SP-CL eqv. macro-textured surface. With bone material to be of 5.3 GPa, the titanium implant resulted in a bone growth of 10.23%, unlike cobalt-chromium implant (10.71%). This shows an increase of bone growth by ~4.7% when tested with cobalt-chromium alloy as compared to titanium implant. In addition, for bone material property considered to be 7.8 GPa, there has been an increase (9.80–10.35%) in bone formation (~5.6%) when cobalt alloy was used as compared to that observed when titanium alloy was used. However, there is not much wide variation in spatial distribution (Fig. 3.) of bone growth when evaluated considering different implant material. Nevertheless, the distribution of fibrous tissues was found to be relatively lesser near the peripheral regions of macro-textured ribs/grooves. These results suggest that there is little influence whatsoever observed on bone growth over macro-textured implant surfaces when compared with different implant materials.

Table 2 Influence of Implant type, Implant material, and Bone material property on bone growth

Implant type	Implant material	Bone material property (in GPa)	Bone growth (%)
CORAIL eqv	Ti–6Al–4 V	5.3	8.70
		7.8	9.32
	Co–Cr	5.3	9.02
		7.8	9.35
SP-CL eqv	Ti–6Al–4 V	5.3	10.23
		7.8	9.80
	Co–Cr	5.3	10.71
		7.8	10.35

(a) (b) (c) (d)

(e) (f) (g) (h)
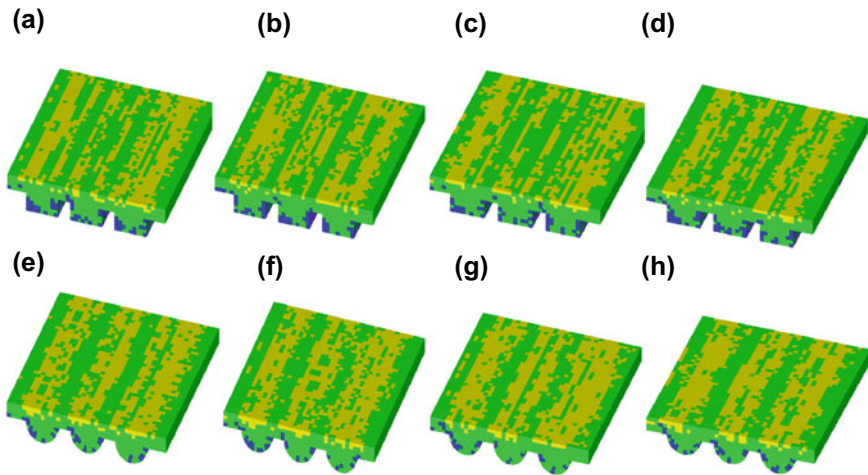
Fig. 3 Spatial distribution of different tissue phenotype at the macroscopic bone-implant interface **a** Ti-alloy with 5.3 GPa (CORAIL eqv.); **b** Ti-alloy with 7.8 GPa (CORAIL eqv.); **c** Co-Cr alloy with 5.3 GPa (CORAIL eqv.); **d** Co-Cr alloy with 7.8 GPa (CORAIL eqv.); **e** Ti-alloy with 5.3 GPa (SP-CL eqv.); **f** Ti-alloy with 7.8 GPa (SP-CL eqv.); **g** Co-Cr alloy with 5.3 GPa (SP-CL eqv.); **h** Co-Cr alloy with 7.8 GPa (SP-CL eqv.) (Color Map: **Blue** denotes fibrous tissue, **Green** denotes cartilage formation, **Yellow** denotes bone formation)

3.2 Influence of Bone Material on Growth of Bone Around Macrotextured Surfaces

It is quite interesting to observe from Table 2 that, bone material indeed has a significant influence on bone growth. However, the relationship between the bone material property and amount of bone formation was found to be dependent on surface design morphology. Results from the study found that, the amount of bone growth

was found to be enhanced from 8.70% to 9.32% for CORAIL eqv. Titanium-based surface texture while increase in bone strength from 5.3 GPa to 7.8 GPa. Similar observation (9.02–9.35%) was found for the similar surface morphology but with cobalt chromium implant material. On the other hand, when tested with SP-CL eqv. designs, bone formation was found to be less with stiffer bone material while considering both the implant material separately. Such a complex non-linear relationship encourages the use of machine learning (ML) techniques to identify and predict the amount of bone growth considering the bone quality (in terms of material strength) as well as different implant material properties and surface design features [10].

3.3 Clinical Usefulness

Clinical usefulness of the present study lies in the formation of distance osteogenesis (Fig. 3.) which shows the secondary stability of the implant [4, 6, 12]. As seen in a few other in silico investigations [4, 6, 13, 14], the calcification of woven bone somewhere toward the boundary of the bone region and further gradual advancement toward the polished implant surface were seen. However, fibrous tissue over the implant surface might prolong bone bridging as well as endochondral ossification over the whole domain The FEA results show that, in comparison to those at the host bone boundary, inter-groove/rib regions were subjected to higher magnitudes of hydrostatic stress but lower deviatoric strain. Intermittent deviatoric strain promotes endochondral ossification and cartilage degeneration [15]. On the contrary, higher hydrostatic pressure towards the stress-concentration regions of groove/rib edges retards the formation of bone growth thus promoting fibrous matrix towards the implant site [15]. However, change in surface texture designs as well as reduced micromotion are encouraged to reduce such fibrous encapsulation at the implant site which otherwise may promote aseptic loosening of the implant.

3.4 Limitations of the Study

The current computational scheme simulates a simplified version of the real post-operative bone growth environment, that is additionally influenced by bone remodeling as well as other factors like physiological loading conditions, site-specific bone anisotropy, bone-implant gap, bone porosity, biochemical as well as patient-based factors. Additionally, the inherently fuzzy nature of the bone-implant interface is not included in the bonded interfacial state examined in this study. When contrasting the bonded and frictional interfacial environments, however, there hasn't been a discernible difference in trends in growth of tissue and average stiffness of the interface layer [4]. Aside from the study's numerical shortcomings, the findings can assist

commercial implant manufacturers and doctors in selecting trade-off implant materials for surgical operations based on bone quality through a ML platform developed on an online platform.

4 Conclusion

The present study focusses on the combined influence of material properties of cancellous bone and metallic implant on bone growth over macrotextured implant surfaces. Results reveal that under similar bone material property, percentage of bone growth with titanium alloy implant was relatively reduced (for CORAIL eqv. implant section (~4% when bone Young's modulus was 5.3 GPa; ~0.3% when bone Young's modulus was 7.8 GPa); for SP-CL eqv. implant section (~4.7% when bone Young's modulus was 5.3 GPa; ~5.6% when bone Young's modulus was 7.8 GPa)) as compared to that with cobalt-chromium alloy. Although cobalt-chromium alloy has been found to be a better implant material than titanium, there is relatively little variation in bone growth for both models, while having a wide variation in implant elastic modulus and cancellous bone quality. Furthermore, a non-linear relationship between implant material properties, bone quality, and implant shape was also observed from the present study. The results of this study can be used to do additional statistical analysis to forecast osseointegration on a full-scale bone-implant model under musculoskeletal loading conditions considering bone remodeling, site-specific anisotropy of the bone, bone-implant interface gap, etc. In addition, in vitro analysis [16, 17] is always warranted to get a better insight into the findings of the present study considering other important bone growth conditions such as growth factors. A topology optimization research could be carried out further to pick proper macrotexture dimensions and forms along with implant material, considering the implant's initial setup and quality of bone. Furthermore, machine learning (ML)-based algorithms may be used to evaluate osseointegration levels on a variety of implants, macrotextures, and physiological loading situations.

Supplementary File

S.1 Type of Finite Element Used

SOLID185 is used for 3D modeling of solid models (Fig. S.1). It constitutes of eight nodes, each of which has 3 degrees of freedom at each node: translation in the nodal X, Y, and Z axes. SOLID185 comes in two different type's viz. homogeneous and layered structural solids. For modeling of homogeneous isotropic materials assumed in the sectional studies of bone-implant-interface geometries, homogeneous structural solid element has been used primarily.

S.2 Numerical formulation to calculate hydrostatic stress and deviatoric strain

Hydrostatic stress ($\sigma_{average}$) can be calculated as:

$$\sigma_{average} = \frac{\sigma_1 + \sigma_2 + \sigma_3}{3}$$

where (σ_1, σ_2, σ_3) are 3 principal stresses. Whereas, deviatoric strain ($\varepsilon_{deviatoric}$) can be computed as:
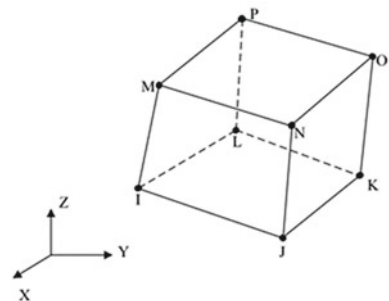
$$\varepsilon_{deviatoric} = \frac{1}{1+\nu} \sqrt{\frac{(\varepsilon_1 - \varepsilon_2)^2 + (\varepsilon_2 - \varepsilon_3)^2 + (\varepsilon_3 - \varepsilon_1)^2}{2}}$$

where (ε_1, ε_2, ε_3) are 3 principal strains and ν is the effective Poisson's ratio.

S.3 Material attributes used in FE modeling

Table S.1 shows the material attributes used in FE modeling.

Fig. S.1 Homogeneous structural solid 8-noded hexahedral finite element (FE) geometry. *Source* ANSYS element reference manual

Table S.1 Implant and bone materials and their material properties

Implant Type	Implant material	Young's modulus (in GPa)	Bone material property (in GPa)	Bone and implant poisson's ratio
CORAIL eqv	Ti–6Al–4 V	113	5.3	0.3
			7.8	
	Co–Cr	210	5.3	
			7.8	
SP-CL eqv	Ti–6Al–4 V	113	5.3	
			7.8	
	Co–Cr	210	5.3	
			7.8	

References

1. Yang L, Kong J, Qiu Z, Shang T, Chen S, Zhao R, Raucci MG, Yang X, Wu Z (2020) Mineralized collagen-modified PMMA cement enhances bone integration and reduces fibrous encapsulation in the treatment of lumbar degenerative disc disease. Regen Biomater 7(2):181–193
2. Tai CL, Lai PL, Lin WD, Tsai TT, Lee YC, Liu MY, Chen LH (2016) Modification of mechanical properties, polymerization temperature, and handling time of polymethylmethacrylate cement for enhancing applicability in vertebroplasty. Biomed Res Int 2016:7901562
3. Puthumanapully PK (2010) Simulation of tissue differentiation in uncemented hip implants based on a mechanoregulatory hypothesis. Dissertation, University of Southampton
4. Ghosh R, Chanda S, Chakraborty D (2020) The influence of macro-textural designs over implant surface on bone on-growth: a computational mechanobiology based study. Comput Biol Med 124:103937
5. Ghosh R, Chanda S, Chakraborty D (2022) Application of finite element analysis to tissue differentiation and bone remodelling approaches and their use in design optimization of orthopaedic implants: a review. Int J Numer Method Biomed Eng e3637
6. Ghosh R, Chanda S, Chakraborty D (2021) Influence of sequential opening/closing of interface gaps and texture density on bone growth over macro-textured implant surfaces using FE based mechanoregulatory algorithm. Comput Methods Biomech Biomed Eng 1–15
7. Ghosh R, Chanda S, Chakraborty D (2021) Qualitative predictions of bone growth over optimally designed macro-textured implant surfaces obtained using NN-GA based machine learning framework. Med Eng Phys 95:64–75
8. Causey GC, Picha GJ, Price J, Pelletier MH, Wang T, Walsh WR (2021) In-Vivo response to a novel pillared surface morphology for osseointegration in an ovine model. J Mech Behav Biomed Mater 119:104462
9. Ghosh R, Chanda S, Chakraborty D (2021) sensitivity of osseointegration to the variation in geometric control factors of the macro-textures on the implant surface. In: Proceedings of the Orthopaedic Research Society (ORS) annual meeting 2021. San Francisco, USA
10. Ghosh R, Chanda S, Chakraborty D (2022) Neural Network (NN) based qualitative assessment of bone growth over textured implant surfaces. In: Popat KC, Kanagaraj S, Sreekanth PSR, Kumar VMR (eds) Advances in mechanical engineering and material science. ICAMEMS 2022. LNME. Springer, Singapore, pp 155–169
11. Zimmer Biomet, UK, Product brochure, https://www.zimmer.co.uk/medical-professionals/products/hip/cls-spotorno.html. Last accessed 08 June 2020
12. Kuzyk PR, Schemitsch EH (2011) The basic science of peri-implant bone healing. Indian J Orthop 45(2)

13. Liu X, Niebur GL (2008) Bone ingrowth into a porous coated implant predicted by a mechano-regulatory tissue differentiation algorithm. Biomech Model Mechanobiol 7(4):335–344
14. Sennerby L, Thomsen P, Ericson LE (1993) Early tissue response to titanium implants inserted in rabbit cortical bone. J Mater Sci: Mater Med 4(3):240–250
15. Carter DR, Orr TE, Fyhrie DP, Schurman DJ (1987) Influences of mechanical stress on prenatal and postnatal skeletal development. Clin Orthop Relat Res 219:237–250
16. Behera RR, Das A, Hasan A, Pamu D, Pandey LM, Sankar MR (2020) Effect of TiO_2 addition on adhesion and biological behavior of BCP-TiO_2 composite films deposited by magnetron sputtering. Mater Sci Eng C Mater Biol Appl 114:111033
17. Behera RR, Das A, Hasan A, Pamu D, Pandey LM, Sankar MR (2020) Deposition of biphasic calcium phosphate film on laser surface textured Ti–6Al–4V and its effect on different biological properties for orthopedic applications. J Alloys Compd 842:155683

Bioprinting: The Current Development of This Additive Manufacturing and Future Challenges

Angkita Talukdar ⓘ**, Barsha Rani Gogoi** ⓘ**, Vaishali Bathari** ⓘ**, Lipika Phukan** ⓘ**, Gaurav Kumar Bhargav, Pallab Kalita** ⓘ**, Rubina Chowdhury** ⓘ**, and Rofiqul Islam** ⓘ

1 Introduction

In India, five lakh individuals may die each year while awaiting organ transplants, and only approximately 4% of the necessary transplant surgeries are carried out nationwide each year. Due to a dearth of organ donors, roughly 17 individuals per day pass away and almost two lakh people nationwide suffer from liver illnesses [1]. However, there aren't enough organ donors to fill these demands and thereby to overcome these issues a new emerging technology called "bioprinting" can hold a great promise. Bioprinting has a great potential to solve the increasing organ shortage crisis.

Bioprinting, a branch of regenerative medicine, and a subcategory of additive manufacturing (AM) which includes designing and fabrication of 3D printed organs for individual patients using their cells is a solution for organ shortages, i.e., currently under development. It is an emerging technique that uses bioink (a printable material that contains living cells) which deposits layers of cells on top of each other to fabricate prospective tissue structures using their cells, which are less likely to be rejected by the body. Extrusion bioprinting, laser-assisted bioprinting, inkjet bioprinting, and

A. Talukdar (✉) · B. R. Gogoi · V. Bathari · L. Phukan · G. K. Bhargav · P. Kalita · R. Islam (✉)
School of Pharmaceutical Sciences, University of Science and Technology Meghalaya, Ri-Bhoi, Meghalaya, India
e-mail: rofiqul52940@gmail.com

R. Chowdhury
Department of Pharmaceutical Sciences, Dibrugarh University, Dibrugarh, Assam, India

255

other methods have all been developed for producing bioprinted structures. Advances have also been achieved in printing tissues, including vascularized heart, bone, cartilage, skin, and liver. Each of these methods has unique advantages, disadvantages, and restrictions; nevertheless, no one bioprinting approach enables the creation of all scales.

Complex tissue engineering scaffolds may now be built using AM technology, which is becoming more and more acknowledged as a potential option. This technique includes the deposition of biological substances on a surface using (CAD/CAM) computer-aided design or computer-aided manufacturing. The chief principle in AM is that structures can be created by adding material layer by layer [2]. Extracellular matrix properties required for cell attachment and shear thinning properties required for the fabrication of multi-layered constructs through additive printing are not compatible with each other, making bioprinting more challenging. Bioprinting has been successful in some areas, such as the bladder, where it can manage the size, shape, internal porosity, and interconnectivity of tissue engineering. Moreover, it shows great potential in tissue engineering for the fabrication of scaffolds, tissues, and organs.

3D bioprinting techniques involve various controversial ethical issues, source, transplantation, animal welfare, and economic and safety questions. Scientists are leaning toward simulating human organs in the lab using stem cell-based techniques as a result of the growing ethical concerns around the research on animals. This has sparked a surge in applications for organs on chips and additive fabrication of structures made from natural hydrogels with live-cell infusions. It is difficult to create 3D printed volumetric structures that are compatible with human cells because they require a soft and watery environment (at least $10 \times 10 \times 10 \, \text{mm}^3$). More accurately than 2D, 3D volumetric structures can simulate the actual living cell environment for biomedical applications involving in vitro cell growth. The extracellular matrix and nano-fibrillated cellulose (NFC) share structural similarities, making them an excellent substrate for 3D cell culture.

Bioprinting has found several advantages in the rate control of cell distribution, scalability, high-resolution cell deposition, and cost-effectiveness. Bioprinting-related research has grown sustainably over the last few years and has various applications in the healthcare sector, drug discovery and testing, regenerative medicine, and high throughput screening. In pharmaceutical research, bioprinting can be used for testing drug efficacy, toxicity, and chemotherapy to reduce the high cost and time of drug discovery. It is also important to note that bioprinting is not limited to organ printing. Even though bioprinting is advancing at a commendable rate there is still a multitude of challenges that need to be overcome. All-inclusive, 3D bioprinting is a rapidly evolving field of research with numerous challenges but tremendous potential for modern medicine and healthcare.

2 Bioink and Its Development

Bio fabrication technologies hold great focus on the production of in vitro models for biological products and for the origination of implantable tissue construct, that imitate the intricacy of localized tissues and organs. Bio fabrication surrounds an extensive assortment of manufacturing processes that includes bioprinting, bioinks, other biomaterials, and biological factors printed into 3D constructs. During bioprinting processes, bioink is essential [2].

The term "Bioink" was first introduced for the requirements of organ printing in the year 2003. This referred to purely cellular components containing various biomaterials, present in hydrogel form which includes cells carrying hydrogels, which were processed using these methods to create 3D printed structures. The design and practices of bioinks have developed greatly over the past ten years with various materials, including natural and synthetic hydrogels to meet the requirements of bioprinting. These bioinks can be stabilized during or immediately after the bioprinting process to generate the final shape, structures, and architectures of the designed tissue construct [3].

An ideal bioinks should possess proper physicochemical properties such as rheological, mechanical, chemical, and biological properties that include: the generation of tissue constructs with acceptable mechanical strength while confining the tissue-matching mechanics, enhancement of encapsulation of desired cell types, sustaining the capability of cells amid and after the process, providing the required cellular environment to assist desired cell action, designing materials that can be used for the advancement of bio fabrication methods at desired resolutions.

The two major application that is taken for the growth of bioinks in bioprinting, as well as bio fabrications, includes:

(i) Evolution of new printing techniques that uphold the previously used biomaterials and bioinks.
(ii) The design of newly evolved bioinks that can be handled using the currently used bioprinting process.

Both of these must accept the final cell environment and whether these are sufficient for the deliberated applications [4, 5].

As of the first approach, various advanced bioprinting techniques enabled the controlled extrusion of hydrogels that has a low viscosity. Low-viscosity hydrogels including methacrylate hyaluronic acid (HA) and Gel MA bioinks can easily balance filaments employing a transparent nozzle that permit cross-linking during extrusion. Another approach for preparing such biomaterials into printable bioinks is the addition of a polymer to stabilize the bioink during the process of extrusion. For example, alginate has been mostly used due to these motives as it can be swiftly cross-linked in the presence of calcium as can be easily washed out [6, 7].

3 Bioprinting Techniques

With the growing concerns over organ demand worldwide, scientists have approached mimicking living tissues or organs by constructing complex 3D functional structures or artificial organs.

The 3D volumetric structures are more precise and relevant than 2D structures. Bioprinting calls for the printing of bioinks such as hydrogels or cell-laden inks in processes like tissue engineering. Bioprinting can be characterized into groups: (1) inkjet bioprinting, (2) extrusion-based bioprinting, (3) lithography-based bioprinting, and (4) laser-based bioprinting. However, this bioprinting technique has certain limitations and challenges as laser-based 3D bioprinting is expensive and sluggish that curbs the alternatives of bioinks to be used.

3.1 Inkjet Bioprinting

Inkjet-based bioprinting is a non-contact printing technique in which droplets of biomaterials are fired thousands of times in a few seconds to generate a 3D image (Fig. 1) [8]. Epson, Hewlett-Packard (HP), and Canon invented the idea of inkjet printing in the early 1950s. The continuous firing on inks through tiny nozzles on predesigned points fabricates 3D tissues [9]. This technique is accompanied by a piezoelectric effect associated with motion so that the deposition of cells doesn't occur at the nozzle [8]. High spatial resolution can be attained between 50 and 300 µm; the printing quality gets reduced if there are gathering of cells [10]. The inkjet printing technology has been introduced years ago and used in the making of text and pictures [8].

Earlier 2D and 3D architectures have been constructed for research, training, and testing purposes. Researchers were acquainted with the prospects that this technology will provide because its picolitre-level printing unit is suitable for depositing biological components. Currently, inkjet technology is evolving into a useful tool in allopathic medicine for the distribution of drug development, scaffold building, and cell deposition [8].

3.2 Extrusion-Based Bioprinting

Extrusion-based bioprinting uses nozzles to extrude bioinks, which are used to build three-dimensional scaffolds or constructs (Fig. 2). The bioink includes biologically relevant living things that are physically or chemically linked together. It serves us applications such as tissue scaffolds, regenerative medicine, and drug development. Bioprinted 3D structures are produced using bioinks, which are biomaterial and living cell combinations. One of the most widely used bioink is the hydrogels which are

Fig. 1 Inkjet bioprinting
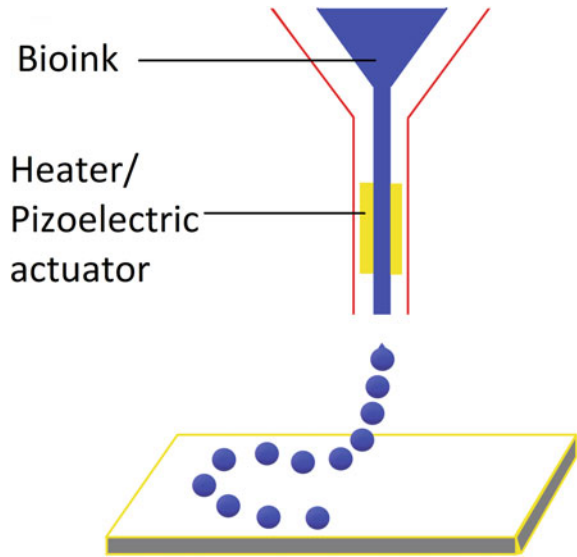
water-based and more adaptable. However, the printing of 3D scaffolds is a challenge as printability influences the quality of printed constructs through their physical, mechanical, biological, and rheological behavior. Printability is the characteristic of bioink to generate scaffolds using the bioprinting technique. The properties that mostly affect the printed constructs are the photophysical properties and printing parameters. With the growing acceptance of extrusion-based bioprinting technology, several new innovative operations are introduced to eliminate the challenges [11].

In extrusion-based printing, hydrogels in the gel state are used as the printing material. High-viscosity bioinks can be printed using extrusion-based bioprinting with high cell density. Extrusion-based bioprinting can be used to forge bioprinted organs to meet the growing demand for transplantation globally which will also serve as a substitute for in vivo testing [8].

3.3 Lithography-Based Bio Printing

Lithography-based bioprinting is a rapidly evolving technology that deals with the development of photo patterning of cell-laden hydrogels to generate complex 3D printed models which involve layer-by-layer patterning of light to photo crosslink particular areas of a bioink that are composed of a low-viscosity cross-linkable hydrogel prototype. Such lithography-based bioprinting includes stereolithography (SLA) (Fig. 3) [12].

A rapid prototyping technique known as SLA is used to make items from 3D CAD data in a couple of hours. SLA, often known as prototyping or 3D printing, is a
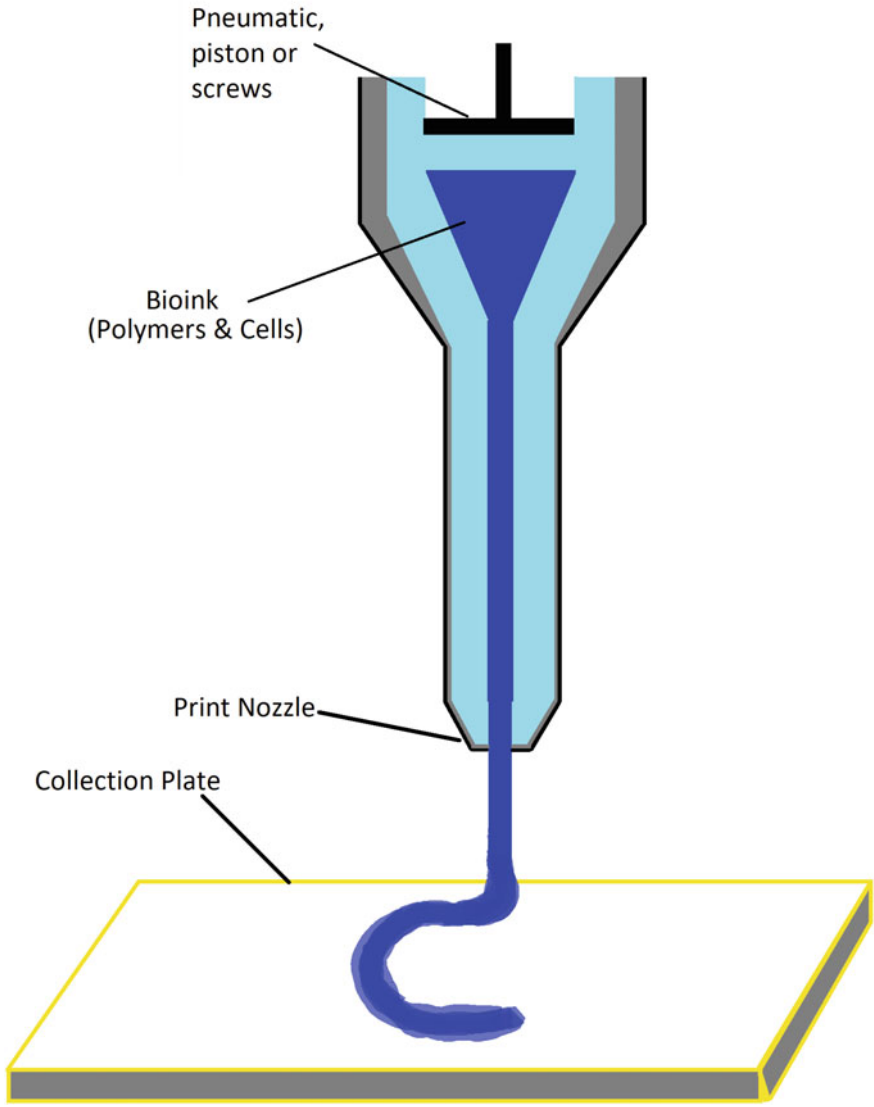
Fig. 2 Extrusion-based bioprinting

highly accurate additive manufacturing process. When UV or laser light is present, this process starts by cross-linking liquid-based polymers in a pattern over a path, forming a layer of hardened material [13]. Additionally, this technology also uses 2-photon polymerization (2PP) and digital light processing (DLP).

Fig. 3 Lithography-based
bioprinting
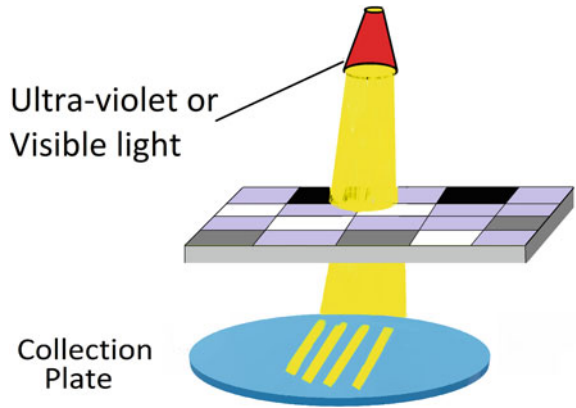
3.4 Laser-Assisted Bioprinting

Laser-assisted bioprinting allows us to approach a well-defined 3D model. This technique uses laser energy to design the cell-laden bioinks. 3D cell systems can be formed by integrating biomaterials and cells and depositing them in stratiform. This technology has 3 major components such as laser source, donor slide, transparent ribbon, and collector slide or substrate (Fig. 4).

The laser falls on the transparent print ribbon. There is a laser absorbing layer through which the laser is absorbed and below which there is the bioink and cell layer. It constrains the bioinks and propels the biomaterials toward the substrate as a result of which a 3D structure is formed. Lasers with different wavelengths from
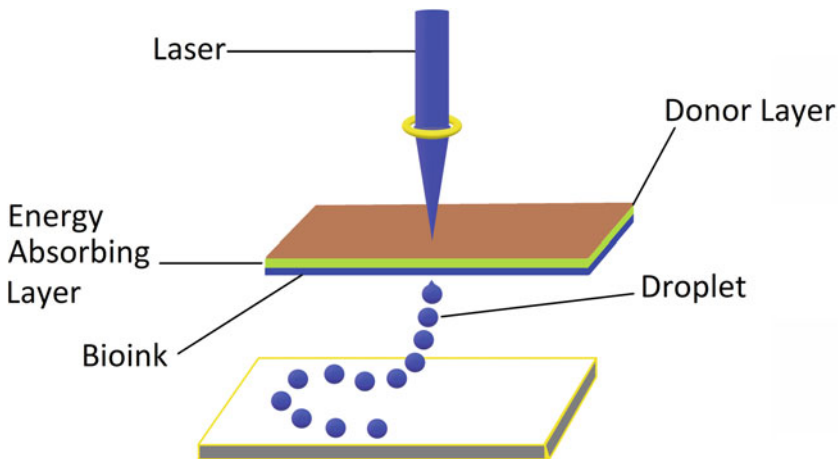
Fig. 4 Laser-assisted bioprinting

193 to 1064 nm are used. The pulse durations are taken in nanoseconds. Ultraviolet lasers are also used [14].

4 Tissue Engineering

The field of regenerative medicine in which tissue substitution occurs is known as tissue engineering [15]. Tissue engineering methods are generated by combining the principles of biology and engineering science. This technique was first developed by Langer and Vacanti in the early 1990s [16]. The tissue engineering technique aims to rehabilitate by repairing tissues or replacing the function of a failing organ that causes due to disease, genetic abnormality, birth defects, or trauma [17]. This methodology depends on four factors:

(1) The right living cells to do the task.
(2) A suitable atmosphere such as a scaffold, for supporting the cells.
(3) The suitable biochemical factors (e.g., growth factors, hormones, morphogenetic factors, collagen, fibers, etc.) make those cells healthier and more productive.
(4) Physical (e.g., cyclic mechanical loading) and mechanical forces reinforce the event of cells.

Tissue engineering uses some biocompatible materials to create those tissue-like structures [18]. The components that are primarily employed in this method are:

(1) Cells: Stem cells (Embryonic stem cells and adult stem cells) are considered the primary component of TE due to their potential to grow (expand) and transform into the specified tissue varieties. But most adult stem cells are highly preferred for TE constructs.
(2) Scaffold: Scaffolds provide mechanical strength to the cells. Metals, ceramics, polymers, etc., are some synthetic natural scaffolds that are widely used for the expansion and development of cells [19].
(3) Signaling molecules: These are also known as biomolecules like growth factors that are already mentioned above. Cells can be taken directly from the patient or, ideally, the target organ.

The three classes of sources of cells used are:

(1) Autologous Transplantation: Cells are harvested from a patient, cultured in vivo, and transplanted back to the same patient.
(2) Allogeneic Transplantation: Cells are harvested from totally different individuals and transplanted into the patient.
(3) Xenotransplantation: Cells are harvested from the organism of various species and transplanted into the patient [20].

The tissue structures are then fabricated by implanting the adult stem cells onto the polymeric scaffold. In a cultural medium that contains the biomolecules, the

scaffolds are inoculated. Since signaling molecules have nutrients and behave like a nutrient medium, the stem cells utilize the nutrients and undergo a proliferation process where the cells grow and divide rapidly. Due to this, the number of stem cells will be increased. As cells extend all around the scaffolds, new viable tissues are produced. Then the tissues can be implanted, transplanted, infused, or transferred into the human recipient along with the infused scaffolds after being absorbed. Some examples of tissues and organs that are applicants for tissue engineering include skin, skeletal muscle tissue (bones, cartilage, and ligaments), cardiac tissue, neural tissue, hepatic tissue, cardiovascular tissue, cornea stroma, kidney, etc. Skin tissue substitution performs a major role in refining the development of skin graft surgery, particularly for complex injuries like burns. Tissue substitution for the urinary system has also been successfully engineered and implanted thereby advancing the remedy approach for UTIs. Artificially created tissues and scaffolds are being examined for their application in the progress of operating bio-artificial appendages. The first success was published in 2015. Tissue engineers have classified tissue engineering into two groups: in situ and in vitro tissue engineering. In situ tissue engineering controls, the body's capability to rejuvenate damaged tissues. It deals with the re-growth of tissues at the site of injury by applying the essential intercellular materials to enhance healing [17]. In contrast, in vitro tissue engineering activates the bio-fabrication of the effective tissues by combing the scaffolds and signaling molecules outside the biological context. The combination of these two-tissue engineering may lead the way to more adequate analysis for tissue and organ repairmen to provide solutions for the present obstacles [21].

5 Bioprinting of Stem Cells

In biomedical research and its application, stem cells serve an important function. Stem cells can be oddly positioned in 3D concerning other cell types or substances using bioprinting. Adipose-derived, neural, and mesenchymal stem cells, which are better defined and more easily cultured, were among the earliest and most successfully applied stem cells for bioprinting [12].

6 Limitations

Even though these customary bioprinting techniques possess different applications and characteristics, few limitations of this general bioprinting process stand based on its features.

(1) In the bioprinting layer-by-layer process of fabricating a new material, every single layer must be fully connected and must have mechanical support since it is imprinted [22].

(2) The bioprinted scaffolds must uphold rapid reciprocation of materials or multi-nozzles with different bioinks [23].
(3) The limit of the vascular network for the growth of tissue exceeds 100–200 μm [18].
(4) The selection of adequate material is a considerable limitation for bioprinting. Integrating multifarious materials is another challenge faced by this modern technology [2].

6.1 Limitations of Different Bioprinting Techniques

6.1.1 Limitations of Inkjet Bioprinting [24–26]

(1) The viscosity of materials should not be greater than 15 mPa/s.
(2) The maximum cell density of bioinks must be 1×10^6 cell/ml. If the limit is crossed,
(3) Then nozzle clogging will happen because of the increased viscosity of bioinks.
(4) Deformation of the cell structure is also a challenge for the printers.

6.1.2 Limitations of Laser-Assisted Bioprinting [12, 27, 28]

(1) The probability of bio solar cell contamination becomes the most critical issue for this printing technique.
(2) For this laser-based bioprinting, the droplet size must be less than 20 μm.
(3) Lower cell viability and the extensibility of the procedure are other limitations.

6.1.3 Limitations of Extrusion Bioprinting [11, 29, 30]

(1) Subordinate resolution is the main limitation.
(2) For a high degree of accuracy, the shear-thinning hybrid bioinks are utilized to decrease the shear stress on the cells to extend cytotoxicity.
(3) One of the crucial limitations of extrusion bioprinting is cellular distortion.
(4) Latent hot end clogging is also included under the current Limitations.

6.1.4 Limitations of Lithography 3D Bioprinting [24, 31, 32]

(1) In this method, only photopolymerizable Hydrogel-based bioinks can be used.
(2) The used bioinks must exhibit low viscosity (~5 Pa s).
(3) The period of post-processing is high.
(4) UV exposure to cells causes cellular disruption and damage to DNA.

The current bioprinting is a very slow and laborious task. The slow process limits the print resolution. Even if the resolution is upgraded to the level that small-diameter

capillaries of less than 3 µm can be restructured, the time needed for the procedure will be tiresomely long and if the printing is not accomplished within the time, the cells will become viable. To resolve these fundamental issues, the engineers are attempting certain strategies. But these strategies should be improved to prevent tissue destruction and to maintain petitioned evolution of tissues.

7 Applications

3D bioprinting is one of the exceptional technologies in today's world. Vaccines, biomaterials, and therapeutics can be produced using this technique. Body implants, medical devices, and surgical guides which respond to each patient's need are manufactured by bioprinting techniques [33]. They are built from replicated cells in laboratories or can be made from one's tissue so that it will have less chance of getting rejected by the body.

This technique allows us to print human tissues, and blood vessels by multiple layering of biomaterials thereby constructing 3D in vitro model [3]. However, engineering complex organs like hearts, liver, and kidneys have not been possible yet as structural integrity is a thing of concern [21].

Tracheomalacia in a newborn is a malformation of tracheal cartilage where the walls are weak and loose which causes breathing problems [34]. A 3D printed device has been modified to treat acute tracheomalacia. Tracheal splints are designed with the help of a laser 3D printer, these are customized splints that allow support and rigidity to expand the trachea [35]. Also, 3D tissue models are designed mainly for research and experimental purposes [36, 37] (Fig. 5).

8 Future Prospects and Conclusion

Bioprinting technology has been an excellent finding for rapid prototyping to develop 3D constructs for therapeutic applications. The primary objective of 3D bioprinting is to construct 3D organs that exactly mimic the native tissue structure and functionalities. This technology plays a pivotal role in the fabrication process to construct scaffolds, cells, biomolecules, tissues and organs with accuracy, proper control, reproducibility, and flexible design for transplants as well as tissue models for drug screening studies. The utilization of 3D bioprinting could conceivably lead the way to personalized patient treatment resulting in better clinical outcomes, which is also aesthetically pleasing.

However, many hurdles associated with complex tissue build-up including multiple cell types in a spatial structure, vascularization resolution enhancement, sophistication and bioink development, reestablishment time, and cost-effectiveness are yet to be addressed.

BIOPRINTING MARKET SHARE BY APPLICATION
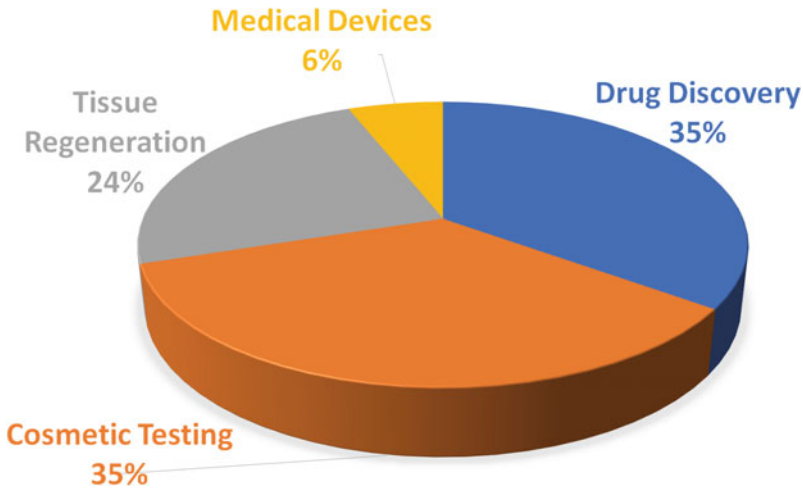
Fig. 5 Bioprinting market share by application

As a consequence, more researches and development are stand in need to overcome these challenges. The emergence of 4D bioprinting can be revolutionary in this sector, where the fourth dimension is time being unified with 3D bioprinting. 4D bioprinting technology can allow the reorganization of materials and cells after printing to enhance effective cell structuring. Even though this technology is still in its very preliminary stage, 4D bioprinting may aid to overcome various challenges in 3D bioprinting [38].

References

1. Five lakh people die waiting for organ transplant in India: Experts-The New Indian Express. https://www.newindianexpress.com/nation/2021/nov/29/five-lakh-people-die-waiting-for-organ-transplant-in-india-experts-2389452.html
2. Ramadan Q, Zourob M (2021) 3D Bioprinting at the frontier of regenerative medicine, pharmaceutical, and food industries. Front Med Technol 2:1–19
3. Gu Z, Fu J, Lin H, He Y (2020) Development of 3D bioprinting: From printing methods to biomedical applications. Asian J Pharm Sci 15:529–557
4. Hölzl K et al (2016) Bioink properties before, during and after 3D bioprinting. Biofabrication 8:032002
5. Ashammakhi N et al (2019) Bioinks and bioprinting technologies to make heterogeneous and biomimetic tissue constructs. Mater Today Bio 1:100008
6. Fatimi A, Okoro OV, Podstawczyk D, Siminska-Stanny J, Shavandi A (2022) Natural hydrogel-based bio-inks for 3D bioprinting in tissue engineering: a review. Gels 8:179
7. Li H, Tan C, Li L (2018) Review of 3D printable hydrogels and constructs. Mater Des 159:20–38
8. Li X et al (2020) Inkjet Bioprinting of Biomaterials. Chem Rev 120:10793–10833

9. Murphy SV, De Coppi P, Atala A (2020) Opportunities and challenges of translational 3D bioprinting. Nat Biomed Eng 4:370–380

10. Xu T, Jin J, Gregory C, Hickman JJ, Boland T (2005) Inkjet printing of viable mammalian cells. Biomaterials 26:93–99

11. Naghieh S, Chen X (2021) Printability–a key issue in extrusion-based bioprinting. J Pharm Anal 11:564–579

12. Sun W et al (2020) The bioprinting roadmap. Biofabrication 12

13. Bishop ES et al (2017) 3-D bioprinting technologies in tissue engineering and regenerative medicine: Current and future trends. Genes Dis 4:185–195

14. Li J, Chen M, Fan X, Zhou H (2016) Recent advances in bioprinting techniques: approaches, applications and future prospects. J Transl Med 14:1–15

15. Tissue Engineering and Regenerative Medicine. https://www.nibib.nih.gov/science-education/science-topics/tissue-engineering-and-regenerative-medicine

16. Langer R, Vacanti JP (1993) Tissue engineering. Science (80-)260:920–926

17. Caddeo S, Boffito M, Sartori S (2017) Tissue engineering approaches in the design of healthy and pathological in vitro tissue models. Front Bioeng Biotechnol 5:1–22

18. Traore MA, George SC (2017) Tissue engineering the vascular tree. Tissue Eng Part B Rev 23:505–514

19. Nikolova MP, Chavali MS (2019) Recent advances in biomaterials for 3D scaffolds: a review. Bioact Mater 4:271–292

20. Lin CS, Lin G, Lue TF (2012) Allogeneic and xenogeneic transplantation of adipose-derived stem cells in immunocompetent recipients without immunosuppressants. Stem Cells Dev 21:2770–2778

21. Chen F-M, Liu X (2016) Advancing biomaterials of human origin for tissue engineering. Prog Polym Sci 53:86–168

22. Vanaei S, Parizi MS, Vanaei S, Salemizadehparizi F, Vanaei HR (2021) An overview on materials and techniques in 3D bioprinting toward biomedical application. Eng Regen 2:1–18

23. Wang Y et al (2022) Tailoring bioinks of extrusion-based bioprinting for cutaneous wound healing. Bioact Mater 17:178–194

24. Kačarević ŽP et al (2018) An introduction to 3D bioprinting: Possibilities, challenges and future aspects. Materials (Basel) 11

25. Wang X et al (2016) 3D bioprinting technologies for hard tissue and organ engineering. Materials (Basel) 9:1–23

26. Ozbolat IT, Yu Y (2015) Bioprinting toward organ fabrication : challenges and future trends bioprinting toward organ fabrication : challenges and future trends. IEEE Trans Biomed Eng 60:691–699

27. Ventura RD (2021) An overview of Laser-assisted Bioprinting (LAB) in tissue engineering applications. Med Lasers 10:76–81

28. Dou C et al (2021) A state-of-the-art review of laser-assisted bioprinting and its future research trends. ChemBioEng Rev 8:517–534

29. Hospodiuk M, Moncal KK, Dey M, Ozbolat IT (2018) 3D printing and biofabrication. 3D Print Biofabrication 255–281. https://doi.org/10.1007/978-3-319-45444-3

30. Malekpour A, Chen X (2022) Printability and cell viability in extrusion-based bioprinting from experimental , computational , and machine learning views

31. Agarwal S et al (2020) Current developments in 3D bioprinting for tissue and organ regeneration–a review. Front Mech Eng 6

32. Jeong HJ, Nam H, Jang J, Lee SJ (2020) 3D bioprinting strategies for the regeneration of functional tubular tissues and organs. Bioengineering 7:1–24

33. Ventola CL (2014) Medical applications for 3D printing: current and projected uses. P T 39:704–711

34. Tracheomalacia: Symptoms, Diagnosis and Treatment. https://www.nationwidechildrens.org/conditions/tracheomalacia

35. Morrison RJ et al (2017) Treatment of severe acquired tracheomalacia with a patient-specific, 3D-printed, permanent tracheal splint. JAMA Otolaryngol Neck Surg 143:523

36. Jensen G, Morrill C, Huang Y (2018) 3D tissue engineering, an emerging technique for pharmaceutical research. Acta Pharm Sin B 8:756–766
37. Bédard P et al (2020) Innovative human three-dimensional tissue-engineered models as an alternative to animal testing. Bioengineering 7:1–40
38. Gao B et al (2016) 4D bioprinting for biomedical applications. Trends Biotechnol 34:746–756

An Insight into the 3D Printing Technology in Pharmaceuticals: A Potential Tool to Developing Personalized Medicines

Taslima Jahan, Himangshu Sarma, Hemanta Kumar Sharma, and Abdul Baquee Ahmed

Keywords 3D printing · Drug delivery system · Personalized medicine

Abbreviations

FDM   Fused Deposition Modeling
FDT   Fast disintegrating tablet
FFF   Fused Filament Fabrication
FLM   Fused Layer Modeling
GIT   Gastrointestinal Tract
HME   Hot-melt extrusion
ODF   Ororodispersible films

Taslima Jahan and Himangshu Sarma have equally contributed to the work.

T. Jahan (✉) · A. B. Ahmed
Department of Pharmaceutics, Girijananda Chowdhury Institute of Pharmaceutical Science-Tezpur, Sonitpur 784501, Assam, India
e-mail: taslima966@gmail.com

H. Sarma
Life Sciences Division, Institute of Advanced Study in Science and Technology, Guwahati 781035, Assam, India

Sophisticated Analytical Instrument Facility (SAIF), Girijananda Chowdhury Institute of Pharmaceutical Science, Guwahati 781017, Assam, India

H. K. Sharma
Department of Pharmaceutical Sciences, Faculty of Science & Engineering, Dibrugarh University, Dibrugarh 784006, Assam, India

SLS   Selective Laser Sintering
SSE   Semisolid Extrusion

1   Introduction

There is a continuing drive for innovative medication design and greater knowledge of ingredients properties, methodologies, and manufacturing technology that promise excellent dosage forms that can reach therapeutic efficiency while being safe. The safety and efficacy of a medicament can be enhanced by controlling the drug release profile, which regulates the pharmacokinetics of the drug [1]. Individual variation is a significant obstacle in treating various diseases due to their physiological and metabolic differences. Because of the undesirable side effects of the drugs, demand for personalized medicine has increased. There is a higher chance of adverse drug reactions in pediatric and geriatric populations as the pharmaceutical companies are primarily focusing on manufacturing dosage forms for the average population [2]. In that condition, therapy is based on a single dosage form having all the medicaments for a specific age group of patients need, thus decreasing adverse drug reactions and enhancing the safety and efficacy of drugs. 3D printing is a novel, innovative prototyping or improver manufacturing technique that makes 3D shapes in a layer-by-layer method straight by computer-aided drug delivery method [3]. Today, 3D printing is one of the fastest-growing technology branches, extending the applications. The term 3D printing is defined by the International Standard Organization (ISO) as the "fabrication of objects through the deposition of a material using a print head, nozzle, or another printer technology."

This is one of the most commonly utilized additive manufacturing processes in which the components are generated from 3D model data by merging materials layer by layer. The application of additive manufacturing is called rapid prototyping (RP). RP is a fundamental device to fit with actual modern bearings in innovative work regions and preferably be characterized as a sunshade term, which includes many assembling in preparing 3D computer-aided design information where there is no tooling required [4, 5]. It offers advantages like reduced prototyping time and costs, the possibility of fabricating small objects, product modifications at a designed level, customized product series, or structures that is not possible to be formed with subtractive techniques [6].

3D printing technique has modified unrivaled flexibility in the dosage form design as well as formulating of complex objects, which became useful in developing customized and programmable dosage forms, an effective approach to overcome drawbacks of conventional pharmaceutical manufacturing methods [7]. Various techniques are available based on the computer-aided design for developing 3D printing methodology to treat many metabolic disorders, such as cancer, etc. These techniques are prototype that focuses on developing various personalized medicines. Various 3D printing techniques currently utilized in pharmaceuticals are fused deposition

modeling (FDM), semisolid extrusion (SSE), binder jet printing, stereolithography (SLA), pressure-assisted microsyringe technology, selective laser sintering (SLS), photopolymerization method, and hot-melt extrusion (HME) utilized to manufacture single and polypill which carries the possible action of all the medicaments required for the therapy into a single unit dosage formulation [8, 9]. This technique uses polycarbonate, which helps draft innovation and programming to deliver 3D objects built by depositing numerous layers onto a substrate. To make the foundation of the object, materials are blasted from a printer head onto an X-ray plane and then the printer strikes along the z-axis. The liquid binder is shot out onto the root of the object to the desired thickness and this process is continued until the product is manufactured layer by layer. After the treatment, the final product is obtained, which discharges the unbound substrate [10].

The 3D printing technique assures the control of thickness, shape, medicament loading, stability, release, dosage form stability, and dose adjustment as per patient requirement. These techniques have been used as novel formulation techniques to produce new solid dosage forms that should satisfy regulatory guidelines, including tests and matching the drug release profile of standard commercial dosage forms [11, 12]. 3D printing is a special unique technology that Charles Hull first portrayed in 1986 and the first 3D printed dosage form approved by the USFDA and brought out to the market by Aprecia Pharmaceuticals in 2016 [13].

2 Methods for Pharmaceutical Dosage Form Development Using 3D Printing Technique

Site-specific delivery of drugs by conventional techniques in the pharmaceutical companies by tablets, injectables, capsules, etc., is challenging. The conventional manufacturing techniques involve multistep processes like milling, mixing, granulation, punching, extrusion, compression, and coating process, which can lead to disparate characters of the final dosages form in terms of medicament loading, stability, release and dosage form stability, etc. Conventional drug development methods are laborious and time-consuming, which do not give the desired results and allow the development of controlled-release systems [2]. So, the 3D printing technique is a novel innovation in a broad range of fields, including pharmaceuticals, biotechnology, medical devices, energy, and many more, which has been developed to fit with fundamental industrial directions of minimizing both time and expenditure of the final product in the manufacturing processes [4]. 3D printing relies on computer-aided designs to develop accurate, cheap, simple, time-saving, structured, personalized drug delivery systems and proposes novel approaches in research and development.

2.1 Material Extrusion

Extrusion is the versatile method and most frequently utilized 3D printing technique to develop pharmaceutical dosage forms rapidly in pharmaceutical manufacturing processes worldwide. In this extrusion process, the ingredients are forced to flow through a robotically actuated nozzle to convert it into the desired shape and size. Fused Deposition Modeling (FDM) or Fused Layer Modelling (FLM), Fused Filament Fabrication (FFF), or Semisolid extrusion is the known process that employs material extrusion mechanism [14]. Fused Layer Modeling was first developed in 1990 and commercialized in late 1991 [15]. The method may be used in a variety of dosage forms, including fast-dissolving devices, implants, multilayered tablets, and zero-order release tablets that use polymers, primarily thermoplastic polymers, as part of the framework. The semisolid extrusion also utilizes a nozzle system, which extrudes a gel on the building plate in a layer-by-layer approach. Like Fused Layer Modeling, the extruded material solidifies after the solvent is evaporated required object is obtained. Upon melting of polymers or gel materials, they can be fed into an FDM 3D printing system [16, 17].

Yu and colleagues created the fast disintegrating tablet (FDT) using a 3D printing technique, in which powder regions were automatically shaped by depositing binder solutions onto specific regions during layer-printing processes, demonstrating excellent result in accordance with pharmaceutical requirements. This results in each tablet disintegrating in 21.8 s and being wet in 51.7 s, which is the precise dosage. Dissolution displays 97.7% drug release in under 2 min, and the tablet's hardness of 54.5 Ncm^{-2} was determined to be satisfactory [18].

Various designs are to be used to manufacture pharmaceutical products like tablets by the FDM 3D printing system. The researcher used extrusion-based 3D printing techniques to formulate a floating drug delivery system with a low-density polymer like hydroxypropyl methylcellulose (HPMC–E15/K4M), Eudragit and microcrystalline cellulose (MCC PH 101) retained the medicament in the stomach via floating and showed sustained release action. The 3D printed gastric-floating tablets were tested in vitro for drug release behavior, consistency of the content, and floating duration time. According to the study, the fluid had sustained medication release for more than eight hours while floating above the stomach. The use of 3D extrusion-based FDM printing to create gastro-retentive dosage forms with standard pharmaceutical additives and a lattice internal structure design was determined to be a feasible method [19]. Khaled and associates developed material extrusion 3D printing for the instant paracetamol release dosage form with high drug loading [20]. In the beginning, the paracetamol paste was formulated utilizing a binder and then filled into a syringe cartridge of the 3D printer and heated on the printing platform to 80 °C for 3 h. The paste is squeezed out layer by layer until the desired dimension of size, shape, and thickness are attained [21]. 3D printing of the FDM method is beneficial in altering the polymorphism of the drug and changing the crystal to an amorphous form during printing. Drugs melted in the polymer matrix in accordance with the characteristics

of the polymer and a faster rate of drug dissolution. Since aripiprazole is not essentially soluble in water, orodispersible films (ODF) were created using 3D printing FDM technology. These films were tested for amorphization and contrasted with casted ones. Aripiprazole in FDM film is an amorphous form, whereas, in casted films is crystalline. It is concluded that 3D printed films of aripiprazole enhanced the dissolution profile. Hence, 3D printing of the FDM method could be an alternative technology to prepare commonly used ODFs [22].

2.2 Inkjet Printing

By substituting the ink with a pharmaceutical formulation containing medicaments and the standard paper with edible sheets known as substrates, which originated from the same method of computer-operated ink-jet printing, this process was modified for use in the pharmaceutical industry. This method also employs powder-based 3D printing, where the sprayed ink is applied on a powder foundation and solidifies into a solid dosage form [23].

The ink-jet printing system consists of two techniques: continuous ink-jet printing and drop-on-demand printing. A continuous ink flow is produced by the liquid ink being forced through an aperture with a diameter of 50 to 80 μm in continuous ink-jet printing, which is managed by an electrostatic field. Multiple heads are used in the drop-on-demand method, which uses either a piezoelectric crystal or a thermal head as a translator. While the piezoelectric head extends to a wide variety of liquids, the thermal head is only effective with volatile liquids [24].

2.3 Stereolithography (SLA) Technique

SLA is a 3D printing manufacturing process in which a formulation is directly converted to solid without liquid utilizing a laser beam. High-energy light is used in 3D printing technology to polymerize liquid resin and create solid parts. The exposed region solidifies as a result of a chemical interaction that is started in the photopolymer by SLA using a digital mirroring tool. This procedure is repeated layer after layer to establish all the component pieces of the item. This method created drug-loaded tablet formulations with modified-release properties, which rely on the polymerization of monomers [25]. SLA technique can make parts with an upper limit size of more or less $50 \times 50 \times 60$ cm ($20'' \times 20'' \times 24''$) and some, for instance, the Mammoth stereolithography machine has a build platform of $210 \times 70 \times 80$ cm. It can develop single parts of more than 2 m in length. Wang and associates manufactured SLA 3D printing of paracetamol and 4-aminosalicylic acid. In this formulation, polyethylene glycol diacrylate was used as monomer and diphenyl (2, 4, 6-trimethyl benzoyl) phosphine oxide was used as photo-initiator and the final product showed significant drug loading as well as extended drug release profiles [26].

2.4   Semisolid Extrusion (SSE) 3D Printing

SSE printing utilizes a syringe-like tool head to deposit semisolid material, which converts to chewable print lets. Using SSE 3D printing, the chewable tablet can be printed in different shapes, sizes, flavors, and combinations with various drugs and developed for pediatric and geriatric patients. In contrast to the widely available dosage form, Khaled and colleagues created guaifenesin bilayer tablets (polypills) using semisolid extrusion and several kinds of polymer. The bilayer tablet has two layers, one for instant release and the other for delayed release. HPMC and poly (acrylic acid) are the polymers employed, together with carbopolR 974P NF as the hydrophilic matrix for sustained release of medicament and sodium starch glycolate as a disintegrant for the immediate release layer. Three different medicaments have been delivered using this method via two different release mechanisms. The printed formulation demonstrated the Korsmeyer-Peppas kinetic drug release model, which showed fickian diffusion through the hydrated HPMC gel layer [27].

Immediate-release tablets were designed using 3D printing by Okwuosa and colleagues as a potent tool for on-demand dosage form individualization. They discussed a method for producing patient-specific tablets at comparatively lower temperatures while utilizing a polymer that has been given pharmacological approval and is known to improve solubility. This work suggests that SSE 3D printing might be expanded to a wide range of temperatures on demand for the production of immediate-drug release dosage forms [28] (Table 1).

3   Future Aspects of 3D Printing in Personalized Medicine

Possibilities for 3D printing in the pharmaceutical industry include the capacity to customize dose formulations for specific patients. This can be accomplished by creating appropriate dosage forms, modifying dosages, combining them, or altering the dosage forms' release profiles to suit the needs of the patients better.

3.1   Dose Personalization

It is necessary to provide dosage form flexibility to the patient; 3D printing may be an option. Pediatric patients, whose therapeutic dose fluctuates based on age and body weight, are a significant demographic group needing dose flexibility. The various dosage forms listed above may be effectively changed by utilizing 3D printers to provide patients with the optimum dose possible. This is simple to do with ODFs by varying the amount of liquid active pharmaceutical ingredients dispensed on the film. ODFs may undergo form and size modifications to personalize therapies (29). Similar to other dosage forms, such as pills or patches, the dose strength can be

Table 1 Different 3D printed dosage forms with corresponding printing technologies

Formulations	Medicament used	3D printed technology	References
Implants (polypill)	Isoniazid, rifampicin	Extrusion	[29]
Tablets	Lisinopril, Rosuvastatin and Amlodipine	FDM	[30]
Oral films	Salbutamol sulfate	Thermal ink-jet printing	[31]
Microneedle	Dacarbazine, Insulin	Micro-Stereolithography, Stereolithography	[32, 33]
Nanosuspensions	Folic acid	Inkjet-type printing technique	[34]
Capsule	Dronedarone hydrochloride, ascorbic acid	FDM	[35]
Bioresorbable nanocomposites	Rifampicin, biphasic calcium phosphate	Ink-jet printer	[36]
Self-micro emulsifying drug delivery system	Celecoxib	Dropwise additive manufacturing system	[33]
Multilayer tablets (polypill)	Captopril, glipizide	Extrusion	[37]
Controlled release	Rifampicin, Levofloxacin	Powder Bed Fusion	[38]
Modified release tablets	5-aminosalicylic acid (5-ASA, mesalazine)	FDM 3DP	[30]
Immediate release tablets	Dipyridamole or theophylline	FDM	[28]
Solid dispersion	Felodipine	FDM 3DP	[39]
Hydrogels	Ibuprofen	Stereolithography	[40]

changed to suit the needs of the patient. For instance, Pietrzak et al. manipulated the printing scale to formulate 3D print theophylline tablets of HME and FDM [41].

To obtain dosage flexibility, pill splitting has been done in the past using a splitter or by hand. This is ineffectual since the subdivided tablets' numerous characterization metrics frequently do not meet pharmacopoeial requirements. In the study, the comparison of split tablets and 3D printed subdivided tablets by Zheng et al. determined that the 3D printed segmented tablets were more precise, secure, and offered the opportunity for customization [41]. Mini-printlets, which are 3D printed pellets that are smaller than tablets, have been created. Additionally, they might be utilized to blend two various medications [42]. To create personalization, mini-print lets can also be mixed and encapsulated at the appropriate dose [43].

3.2 Modifying Release Profiles

Utilizing 3D printing, dosage forms with different release profiles that may be customized to meet individual needs can be obtained. The forms and geometries of tablets can be changed as one method of doing this. It was found that by creating voids in the immediate-release tablets or reducing their thickness, the drug release rates enhanced and the entire medicament release was often obtained in as little as five minutes [44]. Khaled et al. designed paracetamol tablets in-ring and meshed geometries and compared them to solid tablets and other shapes. The mesh tablets produced an immediate release, but the ring and solid tablets produced a prolonged release [21].

Paracetamol tablets in the form of a cube, disc, sphere, pyramid, and torus were created for a different study. The study found that by adjusting the surface area/volume ratio, the medication release from the print lets could be changed [25]. Using 3D printing, tablets with intricate shapes, such as a honeycomb structure, were created. The honeycomb cell sizes were changed from 200 to 1830 µm for different release profiles. It was determined that varied release profiles might be achieved by manipulating dosage form geometries [45].

Additionally, tablets with intricate release profiles that integrated two distinct release mechanisms were created. This comprised tablets with two portions and pH-based drug release mechanisms called immediate-extended release tablet formulations. Breakaway tablets were created, consisting of three sections: two drug-containing subsections that corroded in 45 min in a setting that mimicked the GIT and an internal fast-eroding part. Additionally, enteric dual pulsatory tablets with two release pulses at 1 and 8 h were developed. Additionally, twin pulsatory tablets with opposing pH-based solubility were created, with one portion eroding in the acid dissolving condition within 30 min and the second piece starting to erode 5 h later at the high pH condition [43].

For 3D-designed patches, a variety of forms were employed in addition to solid tablets. Fish gelatin-based polymer hydrogel patches were designed in the cylinder, torus, and gridline shapes to show varying medication releases [46]. Additionally, enhanced capsular devices were developed to control the release of medication from an immediate-release tablet inside them and were suspended in the stomach juice [47]. Gioumouxouzis and co-workers developed 3D printed osmotic dosage forms in which the medicament release was controlled by changing the shape of the cellulose acetate shell that encased the osmotic core [48]. Another study's findings indicated that the tablet size, the number of coats, and the coated sides of the coated tablets affected the control drug release profile in coated tablets [49]. In addition to differences in coating structure, excipients can also control drug release through 3D printing to design tablets containing paracetamol and 4-aminosalicylic acid. Wang et al. concluded that the amount of cross-linkable polymers affects the drug release. Increased poly(ethylene glycol) diacrylate content in the tablets slowed down dissolution but increased PEG 300 concentration accelerated release [25]. Naftopidil tablets

were prepared by Tagami et al. utilizing a semisolid extrusion type 3D printer using hydrogel as the printer ink [50].

Combination Tablets–Polypills

The idea of "polypills" is one of the essential uses of 3D printing in customized medicine. A polypill is a tablet made up of a variety of medications that can be customized for a person taking many medications. Additionally, the medication release may be customized to meet each person's needs. The senior population can greatly benefit from this idea since it can decrease the number of tablets taken each day while also improving patient compliance and medication adherence. Three medications were effectively included in 3D printed polypills by Khaled et al., who may have created a potential treatment option for people with diabetes with hypertension. These tablet formulations contain sustained-release medicaments of nifedipine and glipizide, as well as an osmotic compartment of captopril [51]. The same research group also designed a polypill with five medicaments that represented a cardiovascular disease treatment protocol. The table contains atenolol, pravastatin, and ramipril in three sustained-release chambers together with hydrochlorothiazide and aspirin in two immediate-release medicaments [37]. A different group developed PVA-based polypills containing the four medications amlodipine, indapamide lisinopril, and rosuvastatin. These polypills were investigated for their multilayer and unimatrix architectures. Drug release was slower with unimatrix tablets compared with separate tablets. The position of the medication within the multilayered polypills had an impact on how quickly the drug was released [52]. Using a SLA 3D printer, Martinez et al. created multilayered polypills containing six medications—caffeine, aspirin, naproxen, chloramphenicol, paracetamol, and prednisolone—in cylindrical and ring-shaped forms. Here, the printer was altered so that it could be stopped, the resin tray removed, and other resin solutions added [53].

The 3D printing technique was later improved to formulate polypill capsules with various medication release patterns. Hot-filling syringes were used in conjunction with FDM to accomplish this. The first utilized d non-dissolving capsule shells with free pass corridors and dissolution rate-limiting pore to achieve both instant and delayed medicament release, while the second utilized a concentrical configuration with two outer compartments for instant medicament release and two inner compartments for delayed release of medicament. Both capsule skeletons had four distinct compartments. The capsule's exterior is made of polyvinyl alcohol and polylactic acid. Customized medicament release profiles were produced by altering the shell's thickness in the concentric configuration or the size of the rate-limiting orifices in the parallel design [54].

4 Challenges of 3D Printing

Despite the enormous advantages it offers the pharmaceutical industry, 3D printing has a number of drawbacks. The majority of them deal with technology, dosage form production, safety, quality assurance, legal considerations, and their use in clinical pharmacy.

4.1 Technology

Each type of 3D printer's technology has its drawbacks. The nozzle-based delivery systems may experience nozzle clogging, while the heat and laser-based systems may have active pharmaceutical ingredient degradation. Drug-pharmaceutical additive compatibility is a vital issue that has to be addressed. Additionally, there is a chance that the end product will have structural and surface flaws, which must be corrected by adjusting various production settings [43].

4.2 Polymer Materials

The availability of adequate materials in suitable grades for 3D printing might be another issue. For instance, acceptable polymers for FDM like PVA, HPC, Eudragit, etc., and resins for SLA like poly(ethylene glycol) and di-methacrylate poly(ethylene glycol)di-acrylate, etc. These polymer materials must be compatible with the medication, biodegradable, biocompatible, and appropriate for 3D printing manufacturing [55]. Additionally, they must not produce any hazardous byproducts when processing.

4.3 Safety Aspects

Safety issues must also be taken into account. Because some materials can cause skin or respiratory irritation when heated, extruded, or fused, there is a chance that harmful airborne particles will be released. To reduce the risk of exposure, sufficient safety precautions must be taken and standard operating procedures must be followed [56].

4.4   Clinical Pharmacy Practice

Using 3D printing in hospitals also brings a number of difficulties. The technical components must first be handled on-site by highly qualified technical operators, which may appear unfeasible. Quality control of the 3D printed dosage forms is another difficulty, and ways for it must be created. These approaches must be workable and non-destructive. Diverse process analytical technologies (PAT) have already been used to check the quality to resolve this. A PAT model using near-infrared spectroscopy and Raman confocal microscopy demonstrated remarkable accuracy in determining the drug content and distribution in oral films and tablets [57].

Financial considerations must also be taken into account because installing 3D printers in hospitals might be expensive. The need for customized medicine in a clinical context must also be considered when determining packaging and labeling regulations. Additionally, because each of the aforementioned printing platforms has benefits and drawbacks, it is difficult to say which kind of printer would be most suited for a medical environment. Therefore, more technological advancements are necessary to create "the ultimate 3D printer" for clinical application, which must be quick, simple to use, affordable, and have good resolution.

4.5   Regulatory Aspects

The absence of a regulatory framework is another significant barrier to adopting this technology to produce pharmaceutical products. The FDA released recommendations in 2017 outlining the legal criteria for producing medical devices [43]. There are now a number of 3D printed medical equipment on the market that have received FDA approval, but just one 3D printed pharmaceutical product (Spritam) has received FDA approval. Unfortunately, no regulatory body has yet published standards for producing dosage forms using 3D printing. Furthermore, it is yet unknown if the regulatory clearance will apply to only the finished dosage form or to a set of specifications that would apply to all parts and phases of product design and production [56].

Currently, the FDA would classify a tablet combining multiple medications as a new drug formulation and mandate rigorous clinical trials to ensure patient safety and efficacy. A "Good Manufacturing Practice" (GMP) facility certification would also be required for any site using a 3D printer for manufacturing and dispensing pharmaceutical items. Therefore, proper regulatory requirements must be implemented to produce and distribute pharmaceutical items.

4.6 Anti-Counterfeiting

Due to a lack of restrictions, the emergence of counterfeit drugs is yet another significant issue brought on by the development of 3D printing. These fake medications frequently fall short of the basic standards for quality. Additionally, they may be quickly and affordably acquired. These drugs should not be consumed since they might injure the user and cause further problems. According to the World Health Organization, 10.5% of lower as well as middle-income countries utilize substandard and counterfeit medicines, which are estimated to cost over $30.5 billion yearly. Therefore, appropriate steps must be taken to stop these fraudulent actions [43].

5 Conclusion

A cutting-edge method called 3D printing has emerged as a helpful and potentially effective tool for creating customized medication in the form of layer by layer. Due to this technology, it is now possible to produce immensely sophisticated and elaborate dosage forms. With the approval of Spritam, the first 3D printing dosage form by the FDA and a landmark created since then, promising research has been progressing in the development of new insight into 3D printing technologies for the benefit of human beings. It expands the number of benefits in the pharmaceutical industry, including rapid manufacture, affordability, and formulation flexibility. To create a 3D printer perfect for a medical environment, it is also necessary to weigh the benefits and drawbacks of different platforms. Compared to traditional drug delivery systems, there are a variety of 3D printing options available to improve the safety and effectiveness of medications. Therefore, personalizing the medications to minimize the risk of toxic effects should be the need behind any technological innovation in pharmaceuticals.

Despite having several advantages for pharmaceutical and healthcare systems, there are still a number of technological and regulatory barriers preventing its widespread use. This is because of the multiple difficulties encountered, particularly the technological, quality control, and regulatory aspects. Furthermore, appropriate regulatory standards governing the application of this technology in a clinical environment must be developed. There will be no reverse back once these issues are resolved and the pharmaceutical industry can fully adopt the technology. The healthcare system might change as a result of customized medication in an intelligent future. Therefore, the 3D printing technology may widely be utilized for treatment owing to better patient compliance in the near future which has shown a promising way for novel drug delivery systems to efficiently achieve better patient compliance, optimum drug release profiles, and better shelf life availability. Researchers and scientists believe this technology has immense potential to inspire the pharma industry. In the near future, 3D printing technologies will be more refined and appropriate for a wide range of dosage forms and even for on-demand personalized medicines at a minimum cost.

References

1. Norman J, Madurawe RD, Moore CMV, Khan MA, Khairuzzaman A (2017) A new chapter in pharmaceutical manufacturing: 3D-printed drug products. Adv Drug Deliv Rev 108:39–50. https://doi.org/10.1016/J.ADDR.2016.03.001
2. Horst DJ (2018) 3D printing of pharmaceutical drug delivery systems. Arch Org Inorg Chem Sci 1:65–69. https://doi.org/10.32474/AOICS.2018.01.000109
3. Konta AA, García-Piña M, Serrano DR (2017) Personalised 3D printed medicines: which techniques and polymers are more successful? Bioeng (Basel, Switzerland) 4:79. https://doi.org/10.3390/BIOENGINEERING4040079
4. Wang X, Tuomi JAA, Paloheimo K-S, Partanen J, Yliperttul M (2013) The integrations of biomaterials and rapid prototyping techniques for intelligent manufacturing of complex organs. In: Pignatello R (ed) Advances in biomaterials science and biomedical applications. InTechopen. https://doi.org/10.5772/53114.
5. Yao R, Xu G, Mao SS, Yang HY, Sang XT, Sun W et al (2016) Three-dimensional printing: review of application in medicine and hepatic surgery. Cancer Biol Med 13:451. https://doi.org/10.20892/J.ISSN.2095-3941.2016.0075
6. Trenfield SJ, Awad A, Madla CM, Hatton GB, Firth J, Goyanes A et al (2019) Shaping the future: recent advances of 3D printing in drug delivery and healthcare. Expert Opin Drug Deliv 16:1081–1094. https://doi.org/10.1080/17425247.2019.1660318
7. Alhnan MA, Okwuosa TC, Sadia M, Wan KW, Ahmed W, Arafat B (2016) Emergence of 3D printed dosage forms: opportunities and challenges. Pharm Res 33:1817–1832. https://doi.org/10.1007/S11095-016-1933-1
8. Gebisa AW, Lemu HG (2017) Design for manufacturing to design for additive manufacturing: analysis of implications for design optimality and product sustainability. Procedia Manuf 13:724–731. https://doi.org/10.1016/J.PROMFG.2017.09.120
9. Belhabib S, Guessasma S (2017) Compression performance of hollow structures: from topology optimisation to design 3D printing. Int J Mech Sci 133:728–739. https://doi.org/10.1016/J.IJMECSCI.2017.09.033
10. Ursan I, Chiu L, Pierce A (2013) Three-dimensional drug printing: a structured review. J Am Pharm Assoc 53:136–144. https://doi.org/10.1331/JAPHA.2013.12217
11. Yu DG, Zhu LM, Branford-White CJ, Yang XL (2008) Three-dimensional printing in pharmaceutics: promises and problems. J Pharm Sci 97:3666–3690. https://doi.org/10.1002/JPS.21284
12. Lee VC (2014) Medical applications for 3D printing: current and projected uses. Pharm Ther 39:711
13. Hull CW (1998) Apparatus for production of three-dimensional objects by stereolithography—Google Patents. US4575330A
14. Madla CM, Trenfield SJ, Goyanes A, Gaisford S, Basit AW (2018) 3D printing technologies, implementation and regulation: An overview. In: Basit AW, Gaisford S (ed) 3D printing in

pharmaceutical, vol 31, 1st edn. Springer, pp 21–40. https://doi.org/10.1007/978-3-319-90755-0_2/COVER

15. Shahrubudin N, Lee TC, Ramlan R (2019) An overview on 3D printing technology: technological, materials, and applications. Procedia Manuf 35:1286–1296. https://doi.org/10.1016/J.PROMFG.2019.06.089

16. Tofail SAM, Koumoulos EP, Bandyopadhyay A, Bose S, O'Donoghue L, Charitidis C (2018) Additive manufacturing: scientific and technological challenges, market uptake and opportunities. Mater Today 21:22–37. https://doi.org/10.1016/J.MATTOD.2017.07.001

17. Chaunier L, Guessasma S, Belhabib S, Della Valle G, Lourdin D, Leroy E (2018) Material extrusion of plant biopolymers: opportunities and challenges for 3D printing. Addit Manuf 21:220–233. https://doi.org/10.1016/J.ADDMA.2018.03.016

18. Yu DG, Branford-White C, Yang YC, Zhu LM, Welbeck EW, Yang XL (2009) A novel fast disintegrating tablet fabricated by three-dimensional printing. Drug Dev Ind Pharm 35:1530–1536. https://doi.org/10.3109/03639040903059359

19. Li Q, Guan X, Cui M, Zhu Z, Chen K, Wen H et al (2018) Preparation and investigation of novel gastro-floating tablets with 3D extrusion-based printing. Int J Pharm 535:325–332. https://doi.org/10.1016/J.IJPHARM.2017.10.037

20. Khaled SA, Alexander MR, Wildman RD, Wallace MJ, Sharpe S, Yoo J et al (2018) 3D extrusion printing of high drug loading immediate release paracetamol tablets. Int J Pharm 538:223–230. https://doi.org/10.1016/J.IJPHARM.2018.01.024

21. Khaled SA, Alexander MR, Irvine DJ, Wildman RD, Wallace MJ, Sharpe S et al (2018) Extrusion 3D printing of paracetamol tablets from a single formulation with tunable release profiles through control of tablet geometry. AAPS PharmSciTech 19:3403–3413. https://doi.org/10.1208/S12249-018-1107-Z/TABLES/7

22. Arafat B, Wojsz M, Isreb A, Forbes RT, Isreb M, Ahmed W et al (2018) Tablet fragmentation without a disintegrant: a novel design approach for accelerating disintegration and drug release from 3D printed cellulosic tablets. Eur J Pharm Sci 118:191–199. https://doi.org/10.1016/J.EJPS.2018.03.019

23. Meléndez PA, Kane KM, Ashvar CS, Albrecht M, Smith PA (2008) Thermal inkjet application in the preparation of oral dosage forms: dispensing of prednisolone solutions and polymorphic characterization by solid-state spectroscopic techniques. J Pharm Sci 97:2619–2636. https://doi.org/10.1002/JPS.21189

24. Goole J, Amighi K (2016) 3D printing in pharmaceutics: a new tool for designing customized drug delivery systems. Int J Pharm 499:376–394. https://doi.org/10.1016/j.ijpharm.2015.12.071

25. Wang J, Goyanes A, Gaisford S, Basit AW (2016) Stereolithographic (SLA) 3D printing of oral modified-release dosage forms. Int J Pharm 503:207–212. https://doi.org/10.1016/J.IJPHARM.2016.03.016

26. Patil VG, Mahaparle S, Amilkanthawar V (2020) 3D printing: opportunities and challenges. J Emerg Technol Innov Res 7:828–836

27. Aprecia Pharmaceuticals Company (2015) SPRITAM (levetiracetam) Tablets

28. Okwuosa TC, Stefaniak D, Arafat B, Isreb A, Wan KW, Alhnan MA (2016) A lower temperature FDM 3D printing for the manufacture of patient-specific immediate release tablets. Pharm Res 33:2704–2712. https://doi.org/10.1007/S11095-016-1995-0

29. Wu W, Zheng Q, Guo X, Sun J, Liu Y (2009) A programmed release multi-drug implant fabricated by three-dimensional printing technology for bone tuberculosis therapy. Biomed Mater 4:065005. https://doi.org/10.1088/1748-6041/4/6/065005

30. Goyanes A, Buanz ABM, Hatton GB, Gaisford S, Basit AW (2015) 3D printing of modified-release aminosalicylate (4-ASA and 5-ASA) tablets. Eur J Pharm Biopharm 89:157–162. https://doi.org/10.1016/J.EJPB.2014.12.003

31. Buanz ABM, Saunders MH, Basit AW, Gaisford S (2011) Preparation of personalized-dose salbutamol sulphate oral films with thermal ink-jet printing. Pharm Res 28:2386–2392. https://doi.org/10.1007/S11095-011-0450-5

32. Pere CPP, Economidou SN, Lall G, Ziraud C, Boateng JS, Alexander BD et al (2018) 3D printed microneedles for insulin skin delivery. Int J Pharm 544:425–432. https://doi.org/10.1016/J.IJPHARM.2018.03.031

33. Lim SH, Ng JY, Kang L (2017) Three-dimensional printing of a microneedle array on personalized curved surfaces for dual-pronged treatment of trigger finger. Biofabrication 9:015010. https://doi.org/10.1088/1758-5090/9/1/015010

34. Pardeike J, Strohmeier DM, Schrödl N, Voura C, Gruber M, Khinast JG et al (2011) Nanosuspensions as advanced printing ink for accurate dosing of poorly soluble drugs in personalized medicines. Int J Pharm 420:93–100. https://doi.org/10.1016/J.IJPHARM.2011.08.033

35. Islam R, Sadhukhan P (2020) An insight of 3D printing technology in pharmaceutical development and application: an updated review. Curr Trends Pharm Res 7:55–80

36. Gu Y, Chen X, Lee JH, Monteiro DA, Wang H, Lee WY (2012) Inkjet printed antibiotic- and calcium-eluting bioresorbable nanocomposite micropatterns for orthopedic implants. Acta Biomater 8:424–431. https://doi.org/10.1016/J.ACTBIO.2011.08.006

37. Khaled SA, Burley JC, Alexander MR, Yang J, Roberts CJ (2015) 3D printing of five-in-one dose combination polypill with defined immediate and sustained release profiles. J Control Release 217:308–314. https://doi.org/10.1016/J.JCONREL.2015.09.028

38. Water JJ, Bohr A, Boetker J, Aho J, Sandler N, Nielsen HM et al (2015) Three-dimensional printing of drug-eluting implants: preparation of an antimicrobial polylactide feedstock material. J Pharm Sci 104:1099–1107. https://doi.org/10.1002/JPS.24305

39. Alhijjaj M, Belton P, Qi S (2016) An investigation into the use of polymer blends to improve the printability of and regulate drug release from pharmaceutical solid dispersions prepared via fused deposition modeling (FDM) 3D printing. Eur J Pharm Biopharm 108:111–125. https://doi.org/10.1016/J.EJPB.2016.08.016

40. Martinez PR, Goyanes A, Basit AW, Gaisford S (2017) Fabrication of drug-loaded hydrogels with stereolithographic 3D printing. Int J Pharm 532:313–317. https://doi.org/10.1016/J.IJPHARM.2017.09.003

41. Pietrzak K, Isreb A, Alhnan MA (2015) A flexible-dose dispenser for immediate and extended release 3D printed tablets. Eur J Pharm Biopharm 96:380–387. https://doi.org/10.1016/J.EJPB.2015.07.027

42. Awad A, Fina F, Trenfield SJ, Patel P, Goyanes A, Gaisford S et al (2019) 3D printed pellets (Miniprintlets): a novel, multi-drug. Control Release Platf Technology Pharm 11:148. https://doi.org/10.3390/PHARMACEUTICS11040148

43. Vaz VM, Kumar L (2021) 3D printing as a promising tool in personalized medicine. AAPS PharmSciTech 22:1–20. https://doi.org/10.1208/S12249-020-01905-8/TABLES/3

44. Gültekin HE, Tort S, Acartürk F (2019) An effective technology for the development of immediate release solid dosage forms containing low-dose drug: fused deposition modeling 3D printing. Pharm Res 36:128. https://doi.org/10.1007/S11095-019-2655-Y

45. Kyobula M, Adedeji A, Alexander MR, Saleh E, Wildman R, Ashcroft I et al (2017) 3D inkjet printing of tablets exploiting bespoke complex geometries for controlled and tuneable drug release. J Control Release 261:207–215. https://doi.org/10.1016/J.JCONREL.2017.06.025

46. Liu J, Tagami T, Ozeki T (2020) Fabrication of 3D-printed fish-gelatin-based polymer hydrogel patches for local delivery of PEGylated liposomal doxorubicin. Mar Drugs 18:325. https://doi.org/10.3390/MD18060325

47. Jeong HM, Weon KY, Shin BS, Shin S (2020) 3D-printed gastroretentive sustained release drug delivery system by applying design of experiment approach. Molecules 25:2330. https://doi.org/10.3390/MOLECULES25102330

48. Gioumouxouzis CI, Tzimtzimis E, Katsamenis OL, Dourou A, Markopoulou C, Bouropoulos N et al (2020) Fabrication of an osmotic 3D printed solid dosage form for controlled release of active pharmaceutical ingredients. Eur J Pharm Sci 143:105176. https://doi.org/10.1016/J.EJPS.2019.105176

49. Tsintavi E, Rekkas DM, Bettini R (2020) Partial tablet coating by 3D printing. Int J Pharm 581:119298. https://doi.org/10.1016/J.IJPHARM.2020.119298

50. Tagami T, Ando M, Nagata N, Goto E, Yoshimura N, Takeuchi T et al (2019) Fabrication of naftopidil-loaded tablets using a semisolid extrusion-type 3D printer and the characteristics of the printed hydrogel and resulting tablets. J Pharm Sci 108:907–913. https://doi.org/10.1016/J.XPHS.2018.08.026

51. Khaled SA, Burley JC, Alexander MR, Yang J, Roberts CJ (2015) 3D printing of tablets containing multiple drugs with defined release profiles. Int J Pharm 494:643–650. https://doi.org/10.1016/J.IJPHARM.2015.07.067

52. Pereira BC, Isreb A, Forbes RT, Dores F, Habashy R, Petit JB et al (2019) 'Temporary Plasticiser': a novel solution to fabricate 3D printed patient-centred cardiovascular 'Polypill' architectures. Eur J Pharm Biopharm 135:94–103. https://doi.org/10.1016/J.EJPB.2018.12.009

53. Robles-Martinez P, Xu X, Trenfield SJ, Awad A, Goyanes A, Telford R et al (2019) 3D printing of a multi-layered polypill containing six drugs using a novel stereolithographic method. Pharmaceutics 11:274. https://doi.org/10.3390/PHARMACEUTICS11060274

54. Pereira BC, Isreb A, Isreb M, Forbes RT, Oga EF, Alhnan MA (2020) Additive manufacturing of a point-of-care "Polypill:" fabrication of concept capsules of complex geometry with bespoke release against cardiovascular disease. Adv Healthc Mater 9:1–12. https://doi.org/10.1002/ADHM.202000236

55. Lamichhane S, Bashyal S, Keum T, Noh G, Seo JE, Bastola R et al (2019) Complex formulations, simple techniques: can 3D printing technology be the Midas touch in pharmaceutical industry? Asian J Pharm Sci 14:479. https://doi.org/10.1016/J.AJPS.2018.11.008

56. Gioumouxouzis CI, Karavasili C, Fatouros DG (2019) Recent advances in pharmaceutical dosage forms and devices using additive manufacturing technologies. Drug Discov Today 24:636–643. https://doi.org/10.1016/J.DRUDIS.2018.11.019

57. Trenfield SJ, Goyanes A, Telford R, Wilsdon D, Rowland M, Gaisford S et al (2018) 3D printed drug products: non-destructive dose verification using a rapid point-and-shoot approach. Int J Pharm 549:283–292. https://doi.org/10.1016/J.IJPHARM.2018.08.002

58. Acosta-Velez GF, Wu BM (2016) 3D pharming: direct printing of personalized pharmaceutical tablets. Polym Sci 2:1–10. https://doi.org/10.4172/2471-9935.100011

Influence of Various Organic Acids Towards the Physical and Qualitative Properties of Wound Dressing Applicable Film

Aritra Das, Ramagopal Uppaluri, and Chandan Das

1 Introduction

Both synthetic and natural polymers have their own limitations which lead toward the exploration of composite materials in the pharmaceutical and packaging industries. Natural polymers are costly and have lesser availability, shelf life, cost, and mechanical stability. Whereas, the recycling and disposal of synthetic polymers are hazardous but they are affordable, easily synthesized, and provide various enhancing properties, especially mechanical stability. PVA-St composites are non-toxic, transparent, biocompatible, easily synthesizable, and have high water affinity/absorbency. Hence, a popular field to research for pharmaceutical applications especially as a scaffold supporting material [1].

Studies referred that blending of St with PVA increases the composites' biodegradable behavior also. This research focuses on the production of polyvinyl alcohol (PVA), starch (St), and glycerol (Gl) composite films using alternative organic acids. Citric acid (CA) has 1 hydroxyl (–OH) and 3 carboxyl (–COOH) groups. Tartaric acid (TA) has 2–OH and 2–COOH groups and is the strongest organic acid. Malic

A. Das · R. Uppaluri (✉) · C. Das (✉)

Department of Chemical Engineering, Indian Institute of Technology Guwahati, Guwahati, India
e-mail: ramgopalu@iitg.ac.in

C. Das
e-mail: cdas@iitg.ac.in

A. Das
e-mail: aritra.das@alumni.iitg.ac.in

acid (MA) has 1–OH and 2–COOH group. All these three organic acids are naturally occurring substances in many fruits and plants [2]. In this study, the functional group of the organic acid used caused changes in the Gl-incorporated PVA-St composite films' physical and qualitative characteristics that were relevant to wound dressings.

Targeting variant additive (CA or Gl) concentrations, [2, 3] considered a fixed choice of PVA-St blend constitution to determine the effect of variant concentrations on the characteristics of PVA composite films. The authors targeted DS, TS, %E, and solubility as key response variables. The authors reasoned, based on their data, that aside from solubility, the many –COOH groups present in CA make it easier to attain superior characteristics than those obtained with the Gl [3]. This is also in agreement with the observation that while CA possesses three –COOH groups and one –OH per monomer, Gl possesses only three –OH groups. Shi et al. [4] concluded that with increasing CA concentration, swelling, and TS characteristics usually decreased and percent E always enhanced to attain higher values based on thorough investigations related to PVA-St-Gl-CA composite film fabrication. This is brought on by the remaining free CA's plasticizing effect. Three –COOH groups are included in the chemical structure of the CA, which allows it to efficiently increase the creation of hydrogen bonds by esterifying with the -OH groups of PVA-St. Due to the CA effect, desired composite film properties like TS, modulus of elasticity, water resistance, and swelling behavior are consequently significantly improved [4]. In good agreement with this hypothesis for the CA, it is expected that hypothesized that other organic acids such as malic (with one –OH and two –COOH groups), tartaric (with two –OH and two –COOH groups), and succinic acids (with two –COOH groups) will have a similar effect to enhance the extent of esterification (grafting) and transesterification (crosslinking) between the polymer chains. These reactions enhance compatibility between hydrophilic polymer chains and thereby induce plasticizing effect into the composite blend. Consequently, the polycarboxylic acids promisingly influence and enhance the mechanical, structural, and barrier properties of the base polymers through the principle of reactive extrusion. Yoon et al. (2006) evaluated the influence of alternate organic acids as additives to the St and PVA blend composite films. The authors focused upon organic acids and other additives such as MA, TA, and Gl. For a fixed choice of PVA-St blend (5% each), the authors varied concentrations of the organic acids in the range of 0–54.28 mmol. It was analyzed that, with increasing additive concentration, both DS (3.1–1.65, 3.1–2, and 3.1–2.2 for Gl, MA, and TA, respectively) and TS (56–2, 56–10, and 56–18 MPa for Gl, MA, and TA, respectively) reduced along with a simultaneous enhancement in solubility (0.19–0.35, 0.19–0.51, and 0.19–0.52 for Gl, MA, and TA) and %E (20–150, 20–300 and 20–400% for Gl, MA, and TA). It is well known that the optimal PVA-St composite films possess higher combinations of TS, %E, DS, and S values. Considering this as the subjective bias, the obtained results of the authors can be analyzed to infer upon a hierarchy for various parameters. Accordingly, films with higher TS have been obtained in the order of TA > MA > Gl. Similarly, higher %E and DS were evaluated for films prepared with organic acids in the order of TA > MA > Gl. Also, higher S was obtained for films prepared with the order of organic acids as TA > MA > Gl [2]. The influence of varying concentrations (0–50%) of CA, MA, TA, and Gl

has been investigated by Yun et al. (2006) for PVA-St blend-based composite films. The authors observed that with increasing additive content, the TS reduced 56–19, 56–13, 56–76, and 56–4 MPa, % E increases 20–220, 20–200, 20–1, and 20–155% and DS reduced 2.8–1.95, 2.8–1.55, 2.8–1.85, and 2.8–0.8 for CA, MA, TA, and Gl respectively. Based on desired PVA composite film characteristics, the hierarchical performance of alternate organic acids is as follows: CA > TA > MA > Gl for higher TS; CA > TA > MA > Gl for higher % E, and CA > TA > MA > Gl for higher DS [5]. Similar investigations were conducted by [6]. The authors considered a variation of CA, and Gl and obtained trends similar (DS: 2.4–1.85 and 2.4–0.8; S: 0.19–0.37 and 0.19–0.55; TS: 20–12 and 20–4.5 MPa; %E: 36–150 and 36–120% for CA and Gl, respectively) to those reported by Yun et al. (2006) [6].

The research works of [2, 3, 5, 6] targeted upon the influence of alternate additive concentrations on the physical properties of the PVA-St blended films. However, the authors did not elaborate upon the optimality of such concentrations. Further, the applicability of such organic additive-based PVA-St blended films toward any particular commercial sector has not been targeted by the authors. Thereby, the effectiveness of various organic acids to effectively plasticize and alter antimicrobial effects and in-vitro biocompatibility has not been explored [2, 3, 5, 6]. However, among all the discussed organic acids, MA and TA are with most desirable characteristics in comparison with CA [2, 5]. In summary, the efficacy of alternate organic acids such as MA and TA, to identify the best organic acid for the fabrication of functional PVA composite films shall be regarded as the prime objective of this work.

2 Material and Methods

2.1 Materials

Merck in Germany supplied the PVA (98% hydrolyzed, average molecular weight 72,000 g/mol). From Merck Limited, Mumbai, we obtained St (ACS), CA (monohydrate (ACS), L(+)-TA (ACS), DL-MA, and anhydrous Gl.

2.2 Methods

2.2.1 Preparation of Organic Acid-Based Gl-Incorporated PVA-St Composite Films

For a set composition of all four precursors, a Gl incorporated PVA-St-organic acid blend must be prepared as part of the fabrication process. The best formulations, as suggested by our earlier research, contain 5 w/w% PVA, 10 w/w% St, 15 wt% CA, and 15 wt% Gl [7]. Distinct organic acids (CA-, MA-, and TA-) were substituted

for the same organic acid (CA) to create different experimental formulations. PVA was dissolved in DI water at 95 °C for one hour, rapidly stirred, and then allowed overnight to remove bubbles from the mixture. The starch gelatinized solution was made the following day using DI water at 90 °C for 45 min. At 80 °C for 30 min, the starch solution was combined with the previously made PVA solution, any one organic acid, and glycerol. After that, a film applicator was used to cast this homogenous blended solution on a glass plate while keeping a casting previous 635 μm in thickness. Additionally, these plates were dried at 50 °C for 12 h in order to create the composite films. The films were carefully removed from the glass plate after 12 h and characterized.

2.2.2 Measurement of Swelling Index and In-Vitro Degradation

The capacity of the composite to absorb the wound exudates has been defined as the swelling index (SI). The release rate from the composite network surface is dependent upon weight loss (WL) or hydrolytic in-vitro degradation which creates/influences the environment (protection against microbes, toxicity toward the cell, etc.) around the wound during wound healing. The measuring methodology of SI and WL involved procedures outlined in our previous work [8] and using the following equations.

$$SI = \frac{W_s}{W_0} \times 100\% \tag{1}$$

$$WL\% = \frac{(W_0 - W_f)}{W_0} \times 100\% \tag{2}$$

where W_0 denotes the initial dry weight of the samples, W_s denotes the weight of the sample after 24 h of soaking in PBS solution and W_f denotes the weight of the sample after 6 h of drying at 37 °C following a 27-day soaking period in the PBS solution.

2.2.3 Measurement of Solubility and Gel Fraction

The solubility and gel fraction (GF) characteristics of the organic acid-based PVA composite film samples were determined using the same methodology which has been indicated in our previous article [8].

$$S = \frac{(W_0 - W_d)}{W_0} \times 100\% \tag{3}$$

$$GF = \frac{W_d}{W_0} \times 100\% \tag{4}$$

where W_0 is the initial arid mass of the composite film sample and W_d denotes the weight of the sample as measured after samples that had been soaked in DI water had dried at 37 °C.

2.2.4 Measurement of Mechanical Properties

A wound dressing material must have sufficient durability under a hydrolytic environment, moderate strength, and good elasticity to allow for easy handling and its ability to fit or flexibility on the wound surface to prevent scar formation during wound healing. Tensile strength (TS) and percentage elongation at break (percent E) for the identical material were calculated using the procedure described in our previous article [9].

2.2.5 Qualitative Measurements

Gl-incorporated organic acid-based PVA-St films were tested in vitro for biocompatibility and antibacterial activity in order to assess the composite's potential as a wound dressing film. The antibacterial efficacy measuring test was performed against Gram-positive *Listeria monocytogenes* and Gram-negative *Escherichia coli.* These bacteria were separately inoculated in 10 mL nutrient broth and subsequently kept in a shaking incubator under continuous stirring (160 rpm) at 37 °C. Using a UV–Vis spectrophotometer to assess the optical density at 600 nm absorbance, the bacterial growth was determined to be at its best at an optical density of 0.6. In a clean environment, the broth was distributed over nutritional agar media on a perti-plate. The circular-cut films were then put over the agar surface and incubated for 12 h at 37 °C. Subsequently, the zone of inhibition was visualized on the agar plate. The relative growth rate (RGR) of the HEK cells was determined by following the procedure outlined in our earlier work [9] and using the following expression in accordance with the GB/T16175-1996 standard:

$$RGR = \frac{\text{Absorbance of the treated cells}}{\text{Absorbance of the control or untreated cells}} \times 100\% \tag{6}$$

3   Results and Discussion

## 3.1   Swelling Index and In-Vitro Degradation of Organic Acid-Based Gl-Incorporated PVA-St Composite Films

Among the three formulations, TA- and MA-based films possessed almost similar SI characteristics (350.6 ± 4.55 and 347.6 ± 4.49%, respectively) in hierarchical comparison CA (338.4 ± 4.95%) based films. This could be possibly due to the higher and more efficient crosslinking ability possessed by –COOH groups with the –OH groups of the PVA/St blend [4]. Apart from CA, the other two organic acids (TA and MA) possessed the lowest number of –COOH groups for participation in the esterification reaction [3]. Hence, produced a higher absorption and lower crosslinking capability. It has been deduced that composite films having a SI of less than 260% can be thought of as extremely absorbent [10]. In this sense, the composite films created using all three organic acids have a SI content of around 260%, making them extremely absorbent and suitable for use in wound dressing applications.

Similarly, up to the 14th day of in-vitro degradation or WL, MA, and TA-based film possessed almost similar WL characteristics (59.38 ± 4.89 and 60.39 ± 3.68%, respectively) which are higher than CA-based film (50.32 ± 2.07%) (For TA and MA-based film, higher WL with p-value ≤0.001 and ≤0.05, respectively). After the 14th day, TA resulted in a further higher WL (76.75 ± 4.7%) compared to MA (61.73 ± 0.69%) also. The organic acid-based composite films' in-vitro degrading properties are in good accord with those described in the literature [12] state that the WL values (27 days data) for PVA-HA (20 and 30%) and hydrogel membranes, respectively, have increased from 28 to 48 percent and 29–58% WL, respectively. Hajian et al. [11] corroborate 50–60% WL for PVA-AV (30 percent) hydrogel film [11, 12]. Overall, CA possessed poor WL characteristics because of its higher crosslinking ability compared with TA and MA with the base polymer (PVA and St) in the composite. Figure 1 illustrates the WL data trends for alternate organic acid-based PVA-St composite films during 27 days of observation.

3.2   Solubility and Gel Fraction Characteristics of Organic Acid-Based Gl-Incorporated PVA-St Composite Films

The solubility characteristics of the Gl-incorporated PVA-St composite films for varied organic acid as additives were 58.81 ± 2.25, 68.39 ± 5, and 66.01 ± 4.47, respectively, for TA, MA, and CA. The corresponding variation in GF trends has been 48.19, 31.6, and 33.99% for TA, MA, and CA-based films respectively. To portray the enhancement or detrimental trends of solubility or GF with respect to the organic acid concentrations, the obtained trends have been inconclusive. This was possibly due to the intermolecular reaction between the polymer (PVA and St)

Fig. 1 Effect of alternate organic acids on the in-vitro degradation characteristics of Gl-incorporated PVA-St composite films
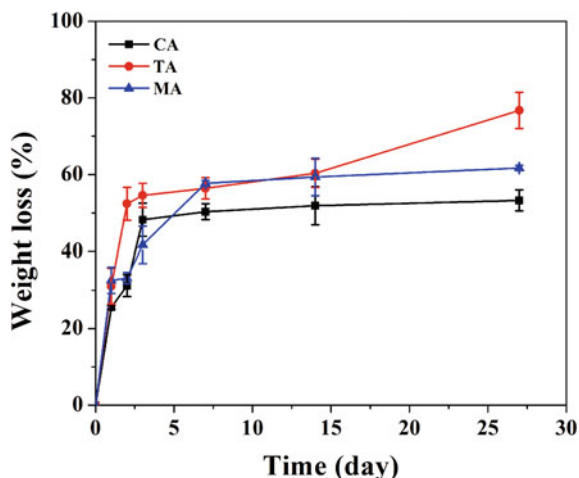
and the additives (Gl and CA/TA/MA organic acid). However, among all organic acids, the CA-based PVA-St composite film exhibited versatile solubility data and required further exploration. Although CA acquired crosslinking ability in comparison with the other two organic acids (TA and MA), CA-based Gl-incorporated PVA-St composite films demonstrated similar solubility characteristics to the MA-based Gl-incorporated PVA-St composite films and which is significantly higher than the TA-based Gl-incorporated PVA-St composite films. In this instance, the TA-based films had the highest GF or had a lower solubility than those made with CA ($p \leq 0.05$ is considered significant) and MA (significance level of $p \leq 0.01$) based films. In this regard, it can be recalled from Sect. 3.1 that for lower organic acid concentration (15 wt%), the extent of the esterification reaction remained almost similar for TA and MA. Hence, the GF characteristics can be anticipated to be of similar trends for TA and MA. However, the trends did not corroborate with the sole hypothesis of crosslinking extent. On the contrary, the pertinent trends indicated the highest, higher, and lower solubility characteristics and vice versa GF characteristics of MA, CA, and TA-based films, respectively. This was possibly due to the effective bonding of TA with St but not the PVA to thereby indicate the lowest solubility of the TA-based PVA-St composite film.

3.3 Mechanical Characteristics of Organic Acid-Based Gl Incorporated PVA-St Composite Films

The TS trends for the alternative films made with different organic acids show similar values for the films made with CA (7.65 MPa) and TA (7.75 MPa), but not MA (1.91 MPa). Basiak et al. [13], Devi et al. [14] reported a said value of TS and %E value to be 3.5 MPa and 12.5%, respectively, and indicated same as adequate

for a composite to be mechanically stable [13, 14]. Hence, The MA-based film possessed significantly weaker mechanical strength in comparison with CA and TA. However, the %E characteristics affirmed lower values for the CA (7.43%) based film formulation in comparison with the TA (16.76%) and MA (18.4%) based films. These trends were similar to those being analyzed for the reported in-vitro degradation characteristics in the former Sect. 3.1. This may happen again because of the higher crosslinking capability of CA following the hypothesis discussed in the previous section. However, the MA-based film was found to possess significantly weaker TS but higher %E in comparison with CA and TA-based film. This may be due to the lowest number of relevant functional groups (total number of –OH groups –COOH groups) available in MA for participation in the esterification reaction [2]. Also, the formulation can be analyzed to possess a higher constitution of the St. Henceforth, the interaction of St and MA could very likely propel the pertinent characteristics. However, the same needs to be assured in the yet to be reported data from investigations addressed in the subsequent sections.

3.4 Qualitative Efficacy of Organic Acid-Based Gl Incorporated PVA-St Composite Films

E. coli and *L. monocytogenes* were used to test the antibacterial effectiveness of alternative films made with different organic acids. Antibiotic, kanamycin (10 μg/mL) was deployed to serve as a positive control. All three organic acid-based PVA-St composite films exhibited antibacterial activity toward *E. coli* and *L. monocytogenes*. However, it was observed that the CA-based PVA-St composite films exhibited higher antimicrobial activity against *L. monocytogenes* in comparison with *E. coli*. Although, the TA and MA-based PVA-St composite films exhibited prominent antibacterial activity for both *E. coli* and *L. monocytogenes*.

After 48 h, HEK cells were used to study the relative cell growth potential of different organic acid-based Gl-incorporated PVA-St composite films, and the results are shown in Fig. 2a, b, respectively. The FBS-supplemented DMEM medium was incubated with the organic acid-based composite films for 24 and 48 h, respectively. This respective diluted treatment was prepared following the details elaborated in our previous work [9]. The RGR of the HEK cells treated with 100 μL treatment has reduced significantly in comparison to the control sample after using 48 h of extracted sample as treatment. Subsequently, the formulation has been observed to achieve higher degradation and antibacterial effectiveness. Hence, the higher leaching capability of TA-based Gl-incorporated PVA-St composite films facilitated higher acidity and toxicity in comparison with CA and MA. For the 24 h extract treatment case, the MA-based Gl-incorporated PVA composite films exhibited the highest amount of RGR compared to the TA and CA-based films for all three treatment dilution cases (5, 10, and 100 μL). However, for the 48 h extract treatment case, a significant reduction in RGR was observed for the MA-based Gl-incorporated PVA-St composite films
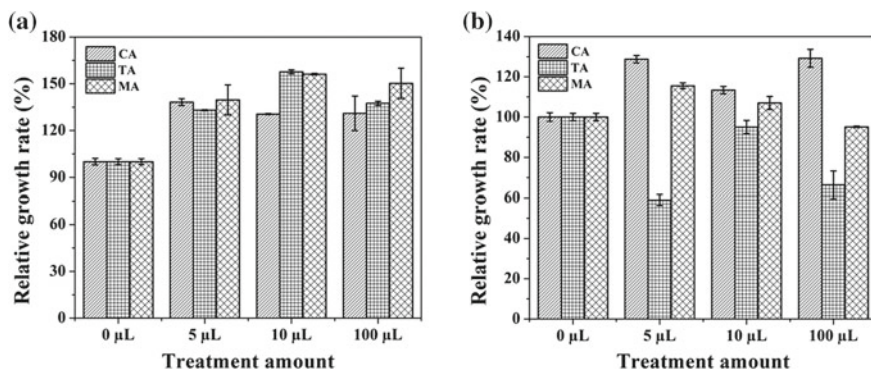
Fig. 2 Effect of alternate organic acids on the relative growth rate characteristics of **a** 24 and **b** 48 h extracted sample of Gl incorporated PVA-St composite films with HEK cells

compared with CA-based Gl-incorporated PVA-St composite films. This is due to the detrimental weight loss rate of the CA-based Gl-incorporated PVA-St composite films which facilitate a steady proliferative effect on cell growth.

4 Conclusion

Several studies refer to CA as an excellent choice for wound dressing or packing applications. This study indicates apart from CA, MA and TA can be explored more for the fabrication of defect-free PVA-St composite films. Especially, MA can be a fascinating choice. Endowed with comparatively weakest crosslinking characteristics and lesser acidity, the MA-based Gl-incorporated PVA-St composite film resulted in higher SI, WL, and %E characteristics. However, even after possessing improved physical properties, TA-based Gl-incorporated PVA-St composite film exhibited toxicity toward HEK cell growth. Hence, TA may not be a suitable choice for influencing and improvising wound dressing compatible PVA composite films.

References

1. Popescu M-C, Dogaru B-I, Goanta M, Timpu D (2018) S Structural and morphological evaluation of CNC reinforced PVA/Starch biodegradable films. Int J Biol Macromol 116:385–393
2. Yoon SD, Chough SH, Park HR (2006) Effects of additives with different functional groups on the physical properties of starch/PVA blend film. J Appl Polym Sci 100(5):3733–3740
3. Yoon SD, Chough SH, Park HR (2006) Properties of starch-based blend films using citric acid as additive II. J Appl Polym Sci 100(3):2554–2560
4. Shi R, Bi J, Zhang Z, Zhu A, Chen D, Zhou X et al (2008) The effect of citric acid on the structural properties and cytotoxicity of the polyvinyl alcohol/starch films when molding at high temperature. Carbohydr Polym 74(4):763–770
5. Yun Y-H, Na Y-H, Yoon S-D (2006) Mechanical properties with the functional group of additives for starch/PVA blend film. J Polym Environ 14(1):71–78
6. Park H-R, Chough S-H, Yun Y-H, Yoon S-D (2005) Properties of starch/PVA blend films containing citric acid as additive. J Polym Environ 13(4):375–382
7. Das A, Uppaluri R, Das C (2020) Compositional synergy of poly-vinyl alcohol, starch, glycerol and citric acid concentrations during wound dressing films fabrication. Int J Biol Macromol 146:70–79
8. Das A, Uppaluri R, Das C (2019) Feasibility of poly-vinyl alcohol/starch/glycerol/citric acid composite films for wound dressing applications. Int J Biol Macromol 131:998–1007
9. Das A, Bhattacharyya S, Uppaluri R, Das C (2020) Optimality of poly-vinyl alcohol/starch/glycerol/citric acid in wound dressing applicable composite films. Int J Biol Macromol 155:260–272
10. Ahmed AS, Mandal UK, Taher M, Susanti D, Jaffri JM (2017) PVA-PEG physically crosslinked hydrogel film as a wound dressing: Experimental design and optimization. Pharm Dev Technol 1–10
11. Hajian M, Mahmoodi M, Imani R (2017) In Vitro assessment of Poly (Vinyl Alcohol) film incorporating aloe vera for potential application as a wound dressing. J Macromol Sci Part B 56(7):435–450
12. Fahmy A, Kamoun EA, El-Eisawy R, El-Fakharany EM, Taha TH, El-Damhougy BK, Abdelhai F (2015) Poly (vinyl alcohol)-hyaluronic acid membranes for wound dressing applications: synthesis and in vitro bio-evaluations. J Braz Chem Soc 26(7):1466–1474
13. Basiak E, Lenart A, Debeaufort F (2018) How glycerol and water contents affect the structural and functional properties of starch-based edible films. Polymers 10(4):412
14. Devi MP, Sekar M, Chamundeswari M, Moorthy A, Krithiga G, Murugan NS, Sastry T (2012) A novel wound dressing material—fibrin–chitosan–sodium alginate composite sheet. Bull Mater Sci 35(7):1157–1163

Design Variations in Double Oblique Device for Osteosynthesis (DODO) of Hip: A Novel Implant for the Northeast Population of India

Soumyadeep Sarkar, Pratik Nag, Bhaskar Borgohain, and Souptick Chanda

Keywords Femoral implant · Intertrochanteric fracture · Extramedullary fixation device · Biomechanics · Von Mises Stress · Maximum axial displacement · Stress shielding · Osteoporotic bone · Finite element analysis

1 Introduction

The geometry of the human body varies from one place to another in the world. It is dependent on many factors, like the average height, the racial history, the health and fitness and average lifespan of the population, the lifestyle and habits of the people of a region over time, the gender of the person, and other such factors. Among the various aspects that vary within the populations, is the length of the femur. This variation in the length of the femur creates a problem when we insert implants that were meant for the Caucasian population into the femurs of a shorter population since most commercial implants used in the present world are made concerning the Caucasian population, and these are not suitable to the other ethnicities, whose

S. Sarkar · P. Nag · S. Chanda (✉)
Department of Biosciences and Bioengineering, Indian Institute of Technology Guwahati, Guwahati, India
e-mail: csouptick@iitg.ac.in

S. Sarkar
e-mail: ssarkar@iitg.ac.in

P. Nag
e-mail: prati176106027@iitg.ac.in

B. Borgohain
Department of Orthopaedics, North Eastern Indira Gandhi Regional Institute of Health and Medical Sciences, Shillong, India

body size and shape vary significantly from the Caucasian population. One such population is the Northeast Indian people, whose femurs are usually shorter than the Caucasian population. The Northeast Indian people are Mongoloids, and thus are shorter in height than the Caucasians. Studies have shown that the height of the femur is calculated to be one-fourth of the average height of the population, which is around 37 cm for the Northeast population [2, 3]. Therefore, modified implants should be used for the Indian morphometry to reduce the number of intraoperative complications such as splintering and fractures, improper distribution of load, aseptic loosening, and long-term surgical failure discomfort. Also, larger metallic implants when implanted on a shorter femur, usually have a high amount of Young's modulus compared to the femur and thus bear a very high physiological load, which leads to a condition called stress shielding. It is due to a high difference in sharing of load among the bone and the implant being used, and the resultant effect of stress shielding is that the bone usually lacks the biomechanical stimuli which is needed for proper maintaining of the bone. Thus, the implants that are modeled using Caucasian patients' bones and their data are larger and have high structural stiffness, and these lead to an increased amount of stress shielding when used on the NE population bone, as their bones are shorter comparatively. As a result, it is necessary to design implants in which the stress shielding is reduced and the loads can be adequately transferred to the bones.

In addition to that, when an implant meant for a larger-sized population is implanted in a smaller-sized population, the mismatch that follows leads to a condition known as micromotion. This further results in thigh pain and aseptic loosening [4, 5]. The problem is that only reducing the size of the implant made for Caucasian patients will not be enough, as there will be other post-surgery problems, like inserting the nail may show a burst in the proximal femur. Thus, it is of utmost importance to design a different femoral implant, unique to the need of the Northeastern population. One such femoral implant was designed by Nag et al. [1]. In this paper, the design of the implant was further modified with certain experiments performed to change the shape and size of the implant and the angle of the distal-most screw of the implant, and compare the results to analyze if the proposed changes can give a more stable implant.

While treating intertrochanteric fractures, two types of fixation devices can be used, which are Intramedullary (IM) and Extramedullary (EM) fixation devices. The implant designed by Nag et al. [1] was an EM fixation device. EM fixation techniques are preferred these days as they keep the anatomy of the bone intact, and support complete bone healing at the fracture site without intervening inside the bone structure [1].

In terms of the size of the implant, a shorter plate ensures less amount of skin incisions and lesser surgical procedures, which means less loss of blood [6]. In previous studies, it has been proposed that the use of a smaller plate has shown more biomechanically stable results and the cosmetic acceptability has been higher compared to larger plates [7]. In another study that uses a similar implant to fix femoral neck fracture, it was observed that the use of a shorter plate has resulted in the implant having a reduced footprint on the bone [8]. Thus, one such model

was proposed in this paper in which the surface area and volume of the base of the implant were reduced significantly to allow a smoother fit into the proximal femur region, without compromising the biomechanical stability of the implant.

The external adaptability is more harmful to extramedullary implants, as patients require more bone union time. An implant with a shorter length helps in placing the screws closer to the point of fracture compared to the longer plates, improves the strain of the bone-implant setup, and increases the potential of bone healing [9]. The use of smaller implants in the proximal femur has also shown a better implant fit [10]. The implant is a metal, foreign to the internal environment of the body and thus, the lesser amount of surface area and volume it occupies, the better it is for the region in which it is being inserted. Having said that, it should not compromise the biomechanical stability, which is the purpose of the implant in the first place. Additionally, concerning the phenomenon of stress shielding, it is observed that the implant with a shorter working area of the plate imparts lower stress on the plate, thus keeping higher stress on the bone, which is necessary for its healing [11].

The objectives of the study were as follows: To design and analyze the parametric variations of an extramedullary fixation device. To study the effect of progressive loading by varying angle of orientation of the distal-most screw in the extramedullary implant. To propose a model with reduced volume and check its biomechanical stability. To compare the biomechanical stability of the implants on healthy and osteoporotic bone.
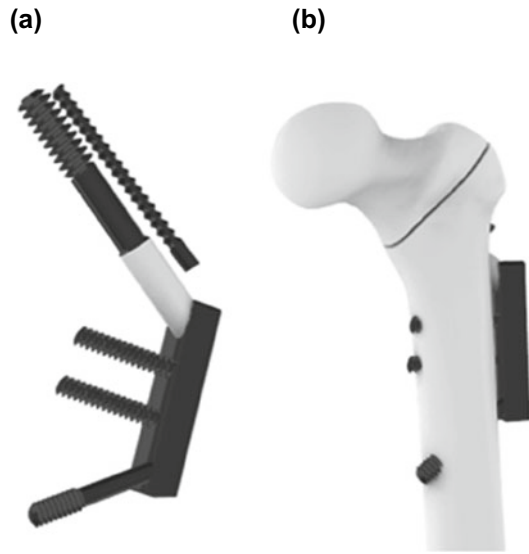
2 Materials and Methods

2.1 Varying the Dimension of the Extramedullary (EM) Fixation Device

1. The FE model of the bone to be fitted to the EM device was created using the manufacturer-supplied CAD model of the left Sawbones femur (Sawbones, Europe AB, Malmo, Sweden, model# 3406) [12]. The CAD model was scaled down to 37 cm. considering the shorter height of the NE population, compared to the Sawbones model used in the paper, for PFLP and DHS models [2, 2]. A two-part fracture was made to simulate a 10 mm gap intertrochanteric fracture [1], as can be seen in Fig. 1.
2. In Rhinoceros v14.0 (Rhinoceros, Robert McNeel & Associates, Seattle, USA), different versions of the EM fixation device were modeled and they were implanted in the CAD left femur, virtually. In each model of the EM device, the dimensions were changed, by taking a different set of length, width, and thickness of the implant. The profile of the changed length, width, and thickness has been noted down in Table 1. The EM device proposed by Nag et al. has 58 mm length, 14 mm width, and 9 mm thickness.

Fig. 1 CAD model of **a** EM device and
b intertrochanteric femoral fracture simulation of the left femur with EM device implanted on it

Model	Length	Width	Thickness
Model variation 1	59	14	9
Model variation 2	57	14	9
Model variation 3	60	14	9
Model variation 4	58	15	9
Model variation 5	58	13	9
Model variation 6	58	14	8
Model variation 7	58	14	10

Table 1 Dimensional variations (mm) of the various models used

The length of the first three modified models has variable length keeping the width and thickness constant, followed by which the next two models have varying widths, keeping the length and thickness constant, and the last two models have a varying thickness keeping the length and width as constant.

3. Four screws were attached virtually in all the variants of the EM devices. One was the cancellous screw or the proximal locking screw, and the other three were the distal dynamic screw or the cortical screw. Under all conditions, all the interfaces were presumed to be bonded. To enhance stability, on top of the cancellous screw, an anti-rotation screw was fixed additionally [1].

4. The 3D models of the various versions of the implant, as shown in Table 1, were fixed on the respective femur, and then they were meshed using Ansys ICEM CFD software (ANSYS Inc., PA, USA) and analyzed using Ansys Mechanical software (ANSYS Inc., PA, USA).

5. In Ansys Mechanical, material properties were assigned to each of the three struc-
   tures involved as per the manufacturer's data [13]. The implant was considered
   to be made of Titanium alloy having Young's modulus of 110,000 MPa. Given
   below is a table of the material properties, as obtained from the manufacturer
   [13].
6. At the femoral head of the bone, a static load of around 1500 N was applied in
   the downward direction as can be seen in Fig. 2, in all the implants. This force
   was applied considering the average weight of the considered population to be
   60 kg. Five nodes were chosen at the head of the implant and 300 N of the load
   was applied to each of them in the -Y direction, which resembles a force being
   applied downward.
7. A zero-displacement condition was selected at distal nodes of the femur.
8. The resultant von Mises stress distribution and maximum axial displacement were
   analyzed from the general post-processing section of the ANSYS Mechanical
   software.

2.2 Varying the Angle of the Distal Screw of the EM Fixation Device

1. The models were varied by changing the angle of the distal screw, which was at
   an angle of 130° in the actual model, being divergent to the base of the implant,
   was varied to 90° or normal to the base of the implant and then further varied to
   50°, making a convergent angle with the base. These can be seen in Fig. 3. These
   three models were chosen, with specifications shown in Table 3.
2. These models were then meshed using ANSYS ICEM CFD software and
   analyzed using Ansys Mechanical software.
3. The loading and displacement conditions were applied, similar to Sect. 2.1 above.
4. The resultant von Mises stress distribution and maximum axial displacement
   were analyzed.

2.3 Progressive Loading Experiment

1. The three 3D CAD models in which the angle of the distal screw was varied, in
   the previous experiment, were taken into consideration as the base models, to
   conduct this experiment. An intact bone 3D CAD model was also considered as
   a reference.
2. The 3D models were fixed on the respective femur, and then they were meshed
   using Ansys ICEM CFD software and analyzed using Ansys Mechanical
   software.
3. A condition was set in ANSYS Mechanical, as can be seen in Fig. 4, in which the
   displacement was set to be zero in the distal-most nodes of the model, as well as

Load 1.5 kN

Zero displacement

in the nodes exactly opposite to the screw. The force of 200 N was then applied
to the femoral head and the resultant displacement of the model was observed.

4. Then, in subsequent analysis, the force was increased, and the resultant displace-
ment was noted till the displacement increased to a value of 5 mm, which was
set as the cut-off value.

5. The force that showed the resultant 5 mm displacement, starting from 200 N
force, was noted down, and the force vs. displacement graph was plotted for the
four models and among the three variations of the distal-most screw angle as
mentioned above, the screw showing 5 mm displacement with the highest force
being applied at the femoral head was accepted as the most stable model.
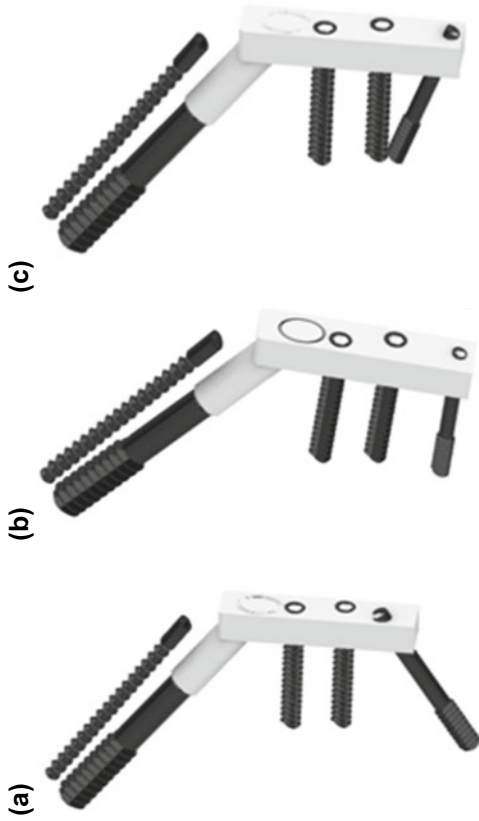
Fig. 3 CAD model of the implants showing **a** divergent **b** right and **c** convergent angle of the distal screw

Fig. 4 FE model of
progressive loading setup

progressive loading

Zero displacement
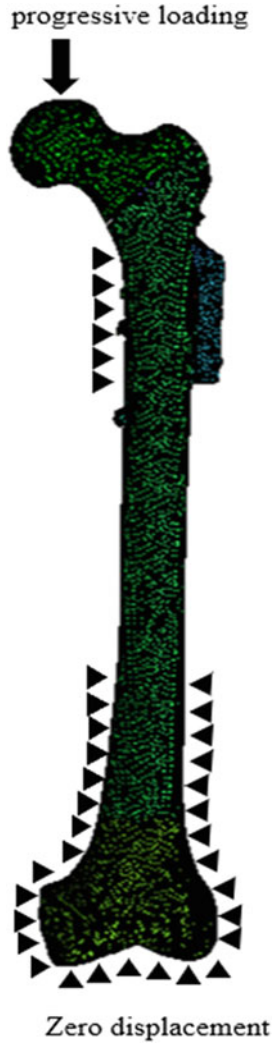
2.4 Biomechanical Comparison Among Healthy and Osteoporotic Bone Data

1. The FE model of the bone to be fitted to the Extramedullary (EM) fixation device used earlier in the study was taken for experimentation. The 3D model was fixed on the respective femur, and then it was meshed, similar to the previous experiments mentioned above
2. While analyzing the model, two different sets of material properties were assigned, one for the healthy bone and another for the osteoporotic bone. In

Table 2 Material properties data

Material	Young's modulus (MPa)	Poisson's ratio
Cortical bone	16,700 (compressive) 10,000 (transverse tensile)	0.3
Cancellous bone	155	0.3
Titanium plate and screw	110,000	0.3

Table 3 The variations of angle of the distal screw for the various models used

Model	The angle of the distal screw (in degrees)
Actual EM device	130
Model variation 1	90
Model variation 2	50

Table 4 Material Properties data of osteoporotic bone

Materials	Young's modulus (MPa)	Poisson's ratio
Cortical	8,308 (compressive) 10,000 (transverse tensile)	0.3
Cancellous	35	0.35
Plate and screw (titanium)	110,000	0.3

the case of the healthy bone, the following material properties were applied, as seen in Table 2.

3. For the osteoporotic bone, the following material property data of the Osteoporotic patients were applied [14].
4. Loading and displacement conditions were applied similar to Sect. 2.1 above.
5. The resultant von Mises stress distribution and maximum axial displacement of both the healthy and osteoporotic bones were analyzed and compared (Table 4).

2.5 Reduction in Implant Base Plate Volume—A Newer Design

1. A 3D CAD model showing a different variation of the shape of the base plate of the EM fixation device was designed in Rhinoceros 6 software, as can be seen in Fig. 5.
2. This CAD model was then implanted virtually into the CAD model of the left femur.
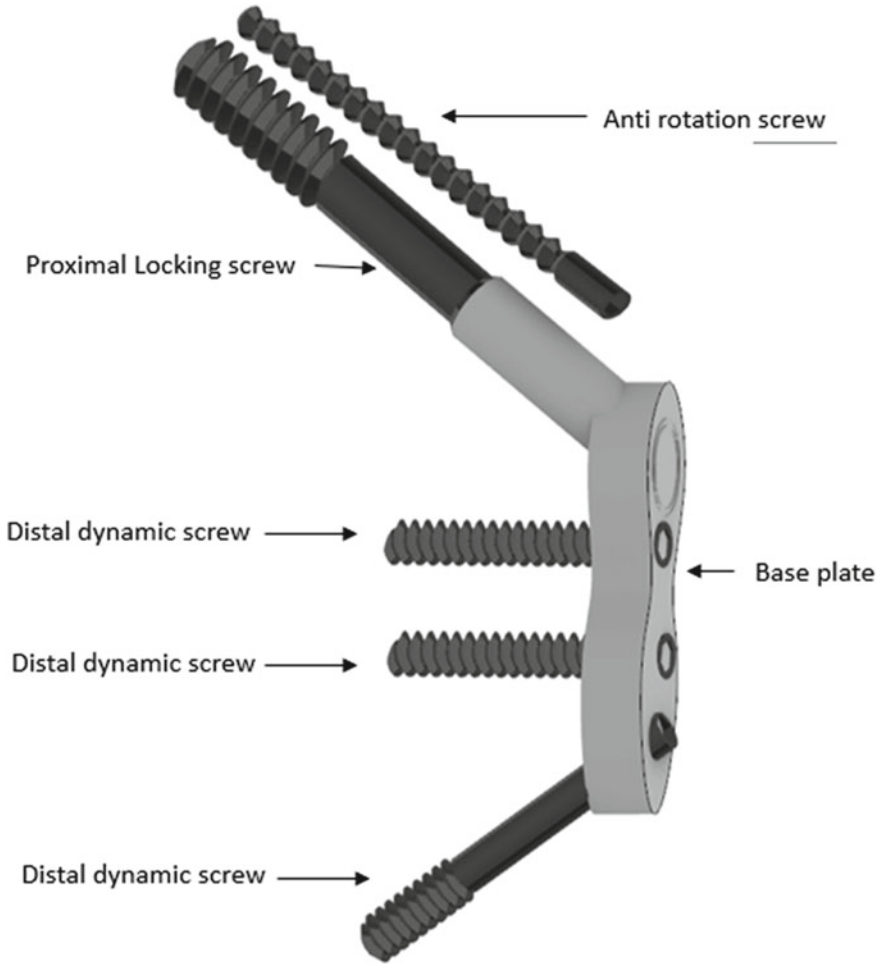
Fig. 5 CAD model of a newer proposed design

3. This model was then meshed using ANSYS ICEM CFD software and analyzed using Ansys Mechanical software, similar to Sect. 2.1.
4. In Ansys Mechanical, material properties of a normal bone were assigned as mentioned in Table 2, and the loading and displacement conditions were set similar to Sect. 2.1.
5. The resultant von Mises stress distribution and maximum axial displacement were analyzed.

3 Result

3.1 Result of the Various Dimensions of the Base Plate of the EM Fixation Device

The von Mises stress distribution contour plots of all the variants along with the intact femur were predicted, as can be seen in Fig. 6. It was observed that the laterally fixed plates shielded the cortex from the lateral tensile stress arising from bending. This was seen for all the implanted models. In an unfractured bone, the distribution of the load was seen to be uniform, but in contradiction to that, in the femoral constructs, the distribution of load was seen to be mediolateral. This means that, in the proximal part of the femur, the flow of load was from the bone to the implant, while in the distal part of the femur, the flow pattern was reversed, i.e., from the implant to the bone.

For the intact femur, the average von Mises stress was found to be 6.8 MPa. The average von Mises stress of the femur fitted with the variations of the implants and their dimensions are shown in the Table 5.

The maximum axial displacement of the femur fixed with the devices was predicted (Table 6).

From the above data, the changes in deformation and the stress shielding were calculated (Table 7) using the intact bone as a reference. The maximum axial displacement of the intact bone was 2.696 mm, and the average von Mises stress was around 6.9 MPa.

3.2 Result of the Various Angles of the Distal Screw

The von Mises stress distribution contour plots of the angular variants and the intact femur were predicted, as can be seen in Fig. 7. It was observed that all the three femoral constructs showed a similar distribution of stress. In the intact femur, the distribution of stress was uniform. Compared to that, in the femoral constructs, there was a flow of load from the femur to the EM fixation device in the proximal region, and from the EM fixation device to the femur in the distal region of the femur. The average von Mises stress and maximum axial displacement were calculated and compared further.

The average von Mises stress values and the maximum axial displacement of the femoral constructs can be seen in Table 8.

From the data in Table 8, the stress shielding and changes in deformation of the three models were calculated and can be seen in Table 9.
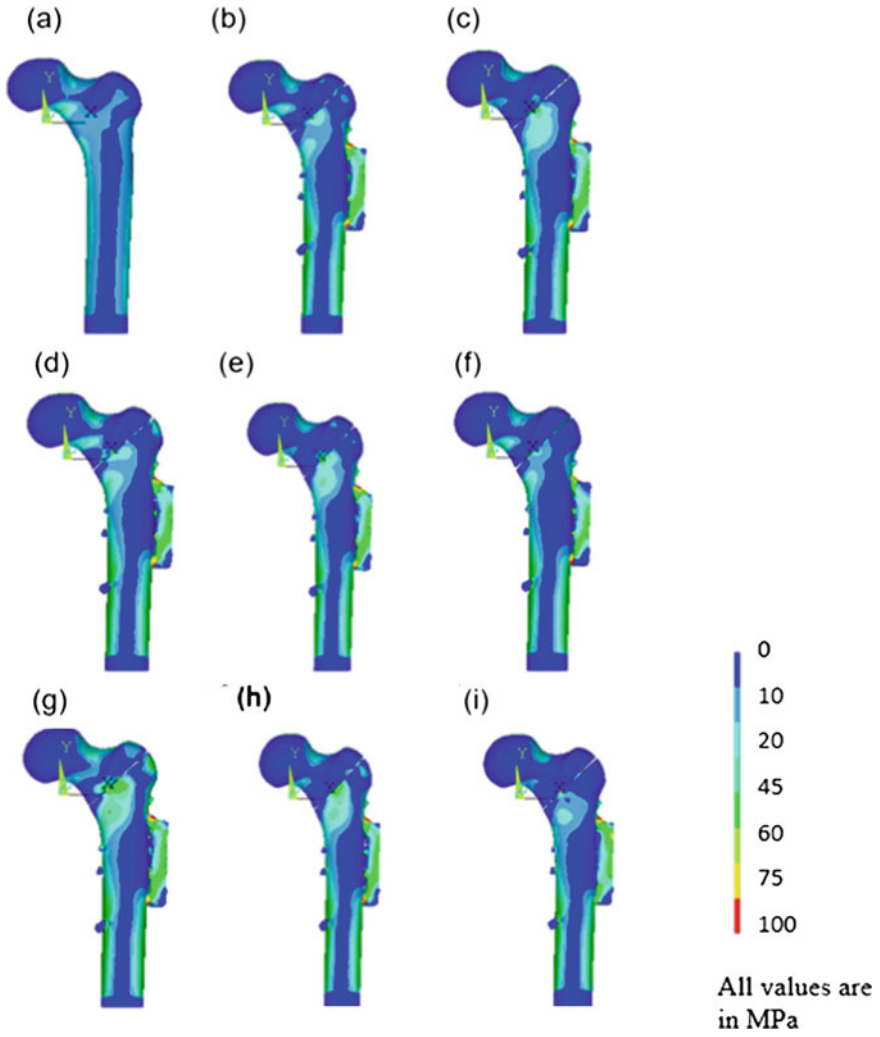
Fig. 6 von Mises stress distribution of the **a** intact bone, **b** actual EM fixation device implanted on the fractured bone and **c–i** the seven variations of the EM fixation device implanted on the fractured bone

3.3 Result of the Progressive Loading Experiment

The Force versus Displacement graph of the three femoral constructs along with the intact bone is shown in Fig. 8. The intact bone withstands a force of 14,950 kN to show 5 mm of maximum axial displacement under progressive loading. Among the femoral constructs, the model B, which had right angled distal screw in Fig. 3 was predicted to be the most stable femoral construct among the three variations as

Table 5 Average von Mises stress associated with different models

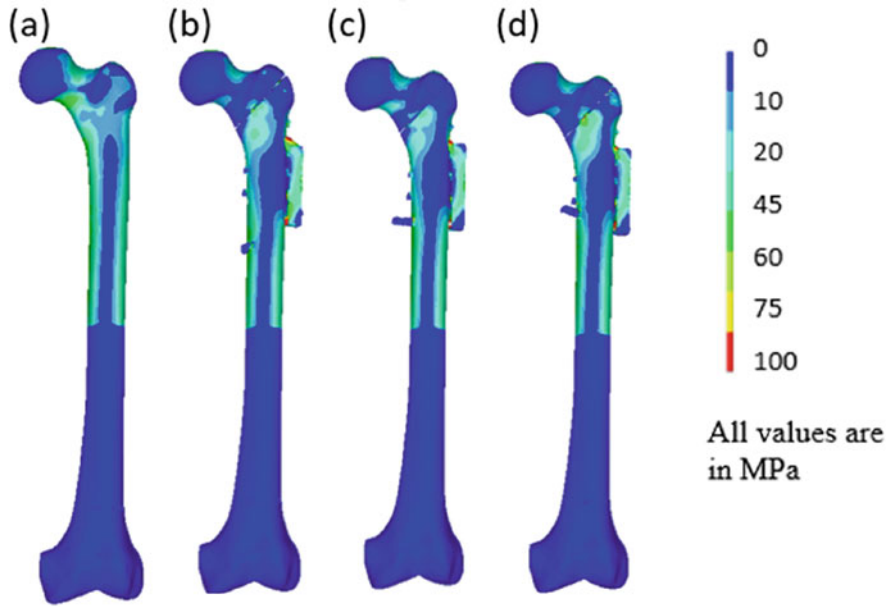| Model	Average von Mises stress (in MPa)
Actual EM device	5.90
Model variation 1 (v1)	5.93
Model variation 2 (v2)	5.92
Model variation 3 (v3)	6.21
Model variation 4 (v4)	5.74
Model variation 5 (v5)	6.26
Model variation 6 (v6)	6.07
Model variation 7 (v7)	5.81

Table 6 Maximum axial displacement associated with different models

Model	Maximum axial displacement (in mm)
Actual EM device	2.53
Model variation 1 (v1)	2.43
Model variation 2 (v2)	2.46
Model variation 3 (v3)	2.56
Model variation 4 (v4)	2.21
Model variation 5 (v5)	2.68
Model variation 6 (v6)	2.51
Model variation 7 (v7)	2.64

Table 7 Change in deformation and stress shielding % associated with different model variations

Variations	Change in deformation (%)	Change in average von Mises stress (Stress shielding %)
Actual model	4.9	13.2
V1	8.5	12.7
V2	7.7	12.8
V3	3.71	7.4
V4	16.9	15.4
V5	0.6	7.9
V6	5.5	10.6
V7	0.9	14.5

it withstands a force of approximately 6500 kN to show 5 mm of maximum axial displacement among the three models. The model C, which had convergent angled distal screw of 50° in Fig. 3, was predicted to be the least stable femoral construct among the three variations as it showed 5 mm maximum axial displacement on

Fig. 7 von Mises stress distribution of the **a** intact bone, **b–d** the three variations of the EM fixation device

Table 8 Average von Mises stress and displacement associated with different models

Model	Average von Mises stress (In MPa)	Maximum axial displacement (In mm)
Intact bone	7.23	2.70
The divergent angle of the distal-most screw	7.29	2.69
The straight angle of the distal-most screw	7.07	2.62
The convergent angle of the distal-most screw	7.43	2.78

Table 9 Stress shielding and change in deformation associated with different models

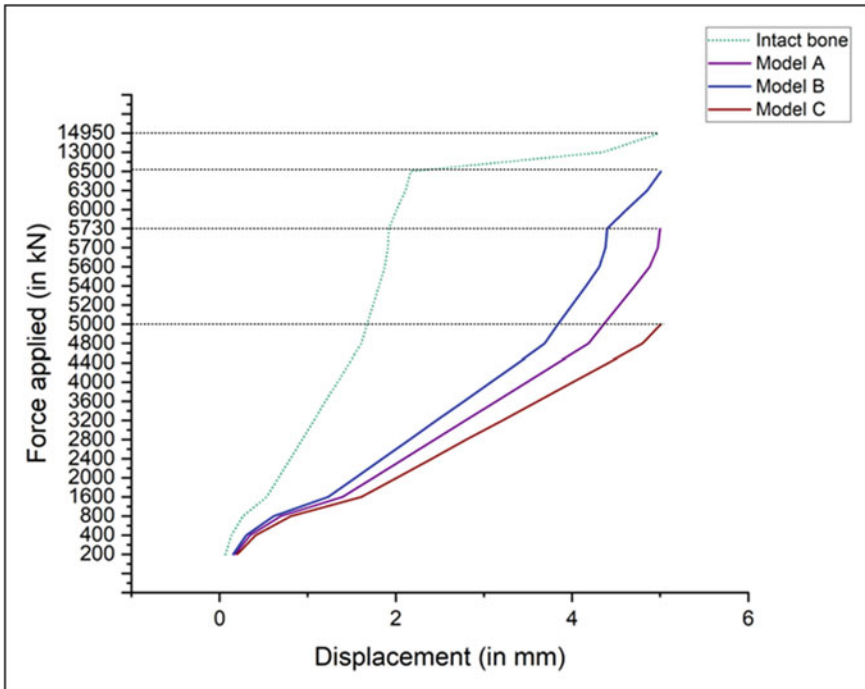| Model	Stress shielding (%)	Change in deformation (%)
The divergent angle of the distal-most screw	1.2	0.24
The straight angle of the distal-most screw	1.9	1.4
The convergent angle of the distal-most screw	3.3	3.36

Fig. 8 Force versus Displacement Graph of the femoral constructs with intact bone

applying 5000 kN force. Model A, which had convergent angled distal screw of 130^0 in Fig. 3 was predicted to have a stability in between the other two femoral constructs in the progressive loading experiment.

3.4 Biomechanical Comparison of the Healthy and Osteoporotic Bone

In Fig. 9, in the von Mises stress distribution contour plots of healthy and osteoporotic patients, it can be seen that the stress is slightly higher in the proximal region of the osteoporotic patients' femoral construct. The average von Mises stress of the femoral construct of an osteoporotic bone was calculated to be 8.67 MPa, compared to 7.29 MPa of the healthy bone. In contrast, the maximum axial displacement of the osteoporotic bone was seen as 4.87 mm, compared to that of 2.69 mm of the normal bone.

Fig. 9 von Mises stress distribution of the **a** healthy bone femoral construct and **b** osteoporotic bone femoral construct
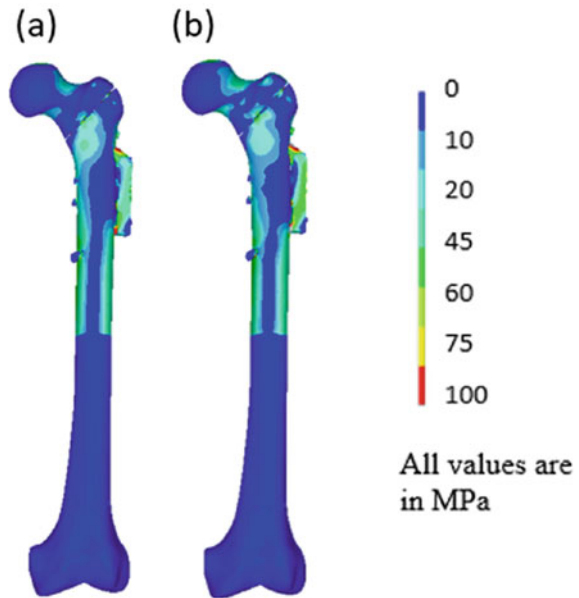
3.5 Biomechanical Comparison of the New Model with the Reference Model

The average stress values of the femoral construct in which the base of the implant model has been modified to reduce surface area and volume have shown a value of around 7.43 MPa, compared to the 7.29 MPa shown by the actual reference model from which the shape of the base was modified, while the maximum axial displacement was shown to be around 2.83 mm, compared to the 2.69 mm of the reference model.

4 Discussion

Intertrochanteric fractures are usually fixated with the help of devices such as IM or EM-type devices. The current project tried to optimize the design of a novel EM device to stabilize an intertrochanteric fracture that takes into account the regional morphometry of the NE population of India. In silico models of the variations of the EM device were designed and the patterns of displacements and stress were analyzed. The desirable conditions for the optimum implant were set as follows:

1. Low stress shielding percentage.

2. The minimum change in deformation as compared to the intact bone.

In the first experiment (Sect. 2.1), in the fourth variation model, the increase in width caused 15.4% stress shielding and changed the deflection by 16.9%. In the seventh variation, an increase in thickness was not playing a crucial role as far as changing the deflection but caused high-stress shielding. An increase in width and thickness is causing more stress shielding as compared to an increase in length. A decrease in length is also causing high-stress shielding. An increase in width caused high-stress shielding and changed deflection highly. An increase in thickness caused high-stress shielding but doesn't play a crucial role in changing the deflection. Decreasing the thickness of the implant is increasing the deflection and is not able to decrease stress shielding much, and it should be avoided as well in the future. An increase in the further amount of length imparts the least change in deflection and also does not cause much stress shielding. A decrease in width is showing the least amount of deformation and the second-best result of stress shielding.

Next, in Sect. 2.2, based on previous studies [15] in which the angle of the screw was changed to check the biomechanical stability of the model, the three variants of the model were analyzed, in which the angle of the distal-most screw was taken to be 1. 130° to the base, i.e., divergent (same as the actual model of DODO), 2. 90° to the base, i.e., at a right angle and 3. 50° to the base, i.e., Convergent (with the tip of the distal-most screw being close to the next screw). Among these models, the divergent model showed the best biomechanical stability as it showed the least stress shielding and least change in deformation under static loading. But, in a study performed similarly to the paper [15] with progressive loading (Sect. 2.3), the second model, in which the distal-most screw is at a right angle showed biomechanical stability. In both the above studies, the convergent model showed the worst stability, thus it is advised to not be used in the future.

While comparing the average von Mises stress and maximum axial displacement of the osteoporotic patients, it was seen that the average stress of the osteoporotic patients was around 18.93% more than normal patients. But the displacement was 81% higher than that of normal patients. The stress and displacement values are significantly higher due to the nature of the osteoporotic bone being biomechanically unstable compared to normal bones.

Lastly, a newer design of the base plate that showed a 29.2% reduction in the volume of the base plate was analyzed and it showed a promising result having a minimal 1.92% variation in the average stress value, while the maximum axial displacement was showing a variation of just 5.2% from the reference model. Thus, this model showed similar biomechanical stability to that of the reference model.

There were limitations in the variants, such as the FE analysis was not conducted on an actual NE femur, which would have been more accurate. In addition to that, the fact that femur length will vary from race to race within the NE population was not considered. Also, the meshing techniques sometimes compromise the efficiency of the designs. The limitations of the designs were that there was stress concentration seen in some locations of the implant. These can be potential places for implant failure. They need to be reduced in the future. Keeping such minor limitations aside,

the optimization study successfully found the biomechanical aspects associated with dimensional variation. The best result out of the variations of the different EM devices was predicted and proposed to be a better alternative.

5   Conclusion

In this work, the primary objective was to explore the design optimization of an EM implant proposed by Nag et al. [1]. The present study found the influence of the increase in length and decrease in thickness to be ideal in terms of less stress shielding and minimum change in deformation. Reducing the implant's width should be avoided while designing future implants as it decreases stress shielding. Further, on analyzing the different angles of the distal-most screw, it was seen that the divergent angles of the screw at 130° with the base plate and at a right angle with the base plate showed a more stable implanted construct compared to the model having a convergent angle of the screw. In our study related to osteoporotic bone models, it was seen that they showed almost twice the amount of displacement compared to healthy bones, but the displacement was around 4.87 mm, which being less than 0.5 cm is still acceptable, but can be reduced further in the future models. The new model, in which the shape of the base plate was modified to reduce implant material surface area and volume, also showed similar biomechanical results compared to the base model, thus making it an ideal alternative.

References

1. Nag P, Chanda S, Borgohain B (2021) Novel design of minimal incision Double Oblique Device for Osteosynthesis (DODO) of hip: results of an in-silico study based on the femur morphometrics of the Northeast (NE) Indian population. Indian J Orthop 55(2):385–394. https://doi.org/10.007/s43465-021-00408-3
2. Mamidi RS, Kulkarni B, Singh A (2011) Secular trends in height in different states of India in relation to socioeconomic characteristics and dietary intakes. Food Nutr Bull 32(1):23–34. https://doi.org/10.1177/156482651103200103
3. Chansa MA (2019) Cross section study to determine human height using femur length in Zambian population. Acta Sci Microbiol 2(11):57–61
4. Rawal BR, Ribeiro R, Malhotra R, Bhatnagar N (2012) Anthropometric measurements to design best-fit femoral stem for the Indian population. Indian J Orthop 46(1):46. https://doi.org/10.4103/0019-5413.91634
5. Reddy VS, Moorthy GS, Reddy SG, Krishna MS, Gopikrishna K (1999) Do we needed a special design of femoral component of total hip prosthesis for patients? Indian J Orthop 33(4):282
6. DHS/DCS System Surgical Technique DePuy Synthes DSEM/TRM/1114/0221 119475–190726 DSEM 12/19. http://emea.depuysynthes.com/hcp/reprocessing-care-maintenance. Last accessed 02 Feb 2022
7. Zhang F, Chen F (2020) Finite element analysis of dual small plate fixation and single plate fixation for treatment of midshaft clavicle fractures. J Orthop Surg Res 15:148. https://doi.org/10.1186/s13018-020-01666-x

8. West ZG, Xiong W (2022) Comparison of femoral neck system versus dynamic hip system blade for the treatment of femoral neck fracture in young patients: a retrospective study. J Orthop Surg Res. https://doi.org/10.21203/rs.3.rs-922692/v1

9. Riedel MD, Oppizzi G, O'Hara N (2020) Biomechanical comparison of distal femoral fracture fixation: analysis of non-locked, locked, and far-cortical locked constructs. Orthop Res Soc. https://doi.org/10.1002/jor.24756

10. Devakara R, Gurung R, Hofmann-Fliri L, Schwyn R, Schuetz M, Windolf M (2021) Biphasic plating improves the mechanical performance of locked plating for distal femur fractures. J Biomech 115:110192. https://doi.org/10.1016/j.jbiomech.2020.1101920021-9290

11. Giordano V, Santos AD, Belangeroc W, Pires RD (2018) Mind the gap between the fracture line and the length of the working area: a 2-D finite element analysis using an extramedullary fixation model. Soc Bras Ortopaedics 53(1):88–93. https://doi.org/10.1016/j.rboe.2017.11.0092255–4971

12. Nag P, Chanda S (2020) Biomechanical design prognosis of two extramedullary fixation devices for subtrochanteric femur fracture: a finite element study. Med Biol Eng Compu 59:271–285. https://doi.org/10.1007/s11517-020-02306-6

13. Biomechanical products catalog Sawbones: Test materials and composite bones (2020) webpage. https://www.sawbones.com/media/assets/product/documents/biomechanical_catalog2020.pdf. Last accessed 04 Apr 2022

14. Metzner F, Neupetsch C, Fischer JP, Drossel WG (2021) Influence of osteoporosis on the compressive properties of femoral cancellous bone and its dependence on various density parameters. Nature 11:13284 (2021). https://doi.org/10.1038/s41598-021-92685-z

15. Zderic I, Gaston C, Willhuber A (2018) Biomechanical comparison between standard and inclined screw orientation in dynamic hip screw side-plate fixation: the lift-off phenomenon. J Orthop Transl. https://doi.org/10.1016/j.jot.2018.10.005

On-Demand Droplet Formation in Lab-On-A-Chip Platforms

Dhruvkumar H. Wankawala and Pranab K. Mondal

Keywords Droplet formation · Non-Newtonian fluid · T-junction · Microfluidics

1 Introduction

The notion of miniaturization has grown immense popularity among researchers since it first surfaced in the early nineties. Microfluidics is one such aspect of miniaturization, potentially transforming the modern diagnosis, which can be well understood with the example of drug delivery. Particularly, droplet-based microfluidics has evolved as a fundamental tool for research and development owing to their broader applicability in point-of-care diagnostics, biotechnology, food engineering, chemical reaction and synthesis, pharmaceutical industries, micro-fabrication, and mixing [11, 13] to name a few. These applications seek consistent, precise, and predictable dominance over microfluidic operations like droplet formation, mixing, alternation, separation, merging, and splitting at a micrometer scale within a microfluidic platform. As such, the physics of droplet manipulation in the constricted microfluidic device is the core application of the biomedical discipline.

Microfluidic droplet formation for a single emulsion involves introducing one phase known as the "dispersed phase" into another immiscible phase called the "continuous phase." The dispersed phase fluid forms droplets while the continuous phase fluid carries formed droplets in a microfluidic channel. The droplet formation in confined space resolves many single-phase micro domain issues, like mixing multiple

D. H. Wankawala (✉) · P. K. Mondal (✉)
Department of Mechanical Engineering, Indian Institute of Technology Guwahati, Guwahati, Assam, India
e-mail: dhruvkumar@iitg.ac.in

P. K. Mondal
e-mail: pranabm@iitg.ac.in

reagent solutions with dispersed droplets acting as individual microreactors without contamination. Droplet formation can be generally achieved by employing active and passive methods. Active control can be attained when external energy sources such as electric, acoustic, optical, temperature, and magnetic field are applied to the microfluidic device [9, 10]. It is important to note that active methods add more complexity with a constant external energy supply. Compared to active control, passive methods use microfluidic systems, for instance, co-flowing streams, flow-focusing streams, and cross-flow geometries for droplet manipulation [2]. Co-flow and flow-focusing devices are a more general choice for high-rate droplet generation, but the T-shaped microfluidic channel is the most commonly used cross-flow geometry due to ease in manufacturing and functioning. Besides, the T-junction channel bestows interfacial and viscous forces dominance over inertia; thus, the continuous train of microdroplets is formed. Four different flow regimes of droplet formation have been commonly identified in T-junction: squeezing, dripping, jetting, and parallel flow. These regimes hold rich dynamics influenced by various parameters, including flow ratio, viscosity ratio and interfacial tension between immiscible fluids, the contact angle between fluid and channel wall, microchannel geometry, and surface chemistry. The present study examines droplet formation in jetting regime within a confined microfluidic T-junction.

Droplet formation is either due to interfacial instability progression or repression between two immiscible fluids, giving rise to an evaluation of droplet emergence and break up. The jet (dispersed thread) formation results from instability caused by the contest between viscous force, interfacial force, and squeezing pressure. While operating in the jetting regime, it is observed that the jet thread of dispersed phase initially pierces into continuous phase channel, after forming initial droplet, the jet is subjected to move downstream of the channel along with droplet formation. Since jet formation is mainly because of interface instability, droplet detachment end gradually progresses until a stable jet is attained [4].

In the past, flow physics of droplet generation is well investigated for two immiscible Newtonian fluids. However, in real-life biological applications, fluids of interest are non-Newtonian, exhibiting viscosity and elasticity dependency. There are several ways to categorize non-Newtonian fluids according to their flow behavior, like shear thinning, shear thickening, and viscoelastic fluids. If with increment in shear rate, viscosity also increases, then the fluid is known as shear thickening fluid. In contrast, if viscosity decreases with an increment in shear rate, the fluid is called shear thinning fluid. Bingham plastic is another non-Newtonian class that exhibits solid behavior at less shear stress; thus, stress should overcome a significant amount to enable the flow. Lately, the work has been advanced to understand the dynamics of viscoelastic and shear thinning time-dependent non-Newtonian droplet generation. For example, [1] conducted an experimental and numerical parametric study to assess the effect of shear thinning rheological parameters, like the power law flow behavior index and the Carreau number, on the droplet dimensions by varying capillary numbers. Additionally, comprehensive 2D numerical computation [7] has been committed to study the influence of viscosity ratio, contact angle, droplet viscoelasticity, wettability, flow ratio, and interfacial tension between two fluids wherein non-Newtonian

fluid goes along through lateral channel. Although, very few studies have focused on non-Newtonian shear thinning droplet generation upon a microfluidic platform. The study on complex shear thinning behavior would enable us to acknowledge the physiological fluids like saliva and blood.

Few studies have been reported on parameters controlling jet (dispersed thread) formation for Newtonian fluid, promoting or preventing the jet thread [8], like channel dimensions, fluid properties, weber number, and flow ratio. To date, best to our knowledge, there is no experimental study on the jet thread and droplet formation enclosing non-Newtonian rheology. Therefore, in this work, we experimentally demonstrate the evolution of jet length at different concentrations ($c = 0.2 - 0.6\%$) and flow conditions of non-Newtonian carboxymethyl cellulose (CMC) aqueous solution. We qualitatively compare the experimental outcomes with numerical simulation. We further show the effect of flow parameters on the control over droplet size.

2   Experimental Setup

The experimental setup shown in Fig. 1 comprises two syringe pumps, a microfluidic channel, a high-speed camera, and an inverted microscope (Make: Leica). The microfluidic device is fabricated using the method of soft lithography. We set a cross-section of a channel with equal width and height of 100 µm. The channel is put beneath an inverted microscope integrated with a camera to capture droplet formation at the T-junction with a high-resolution window integrating 1920×1080 pixels^2. As shown in Fig. 1, continuous phase fluid and the dispersed phase fluid are injected from inlets 1 and 2 via two syringe pumps into a microfluidic device at flow rates of Q_c and Q_d, respectively. The PVC tubes are used to bridge between the syringe pump and the microfluidic device. Both the syringe pumps are commenced simultaneously to cater sufficient time to achieve steady-state droplet formation. The two immiscible fluids meet at the microfluidic T-junction to produce a train of droplets. We use Ostwald–de Waele power-law model to describe the non-Newtonian shear thinning characteristics of CMC concentrations (de Waele A 1923). As per the Ostwald–de Waele model, shear stress is proportional to shear rate, where apparent viscosity is the coefficient of proportionality,

$$\mu_{app} = m(\dot{\gamma})^{n-1} \qquad (1)$$

where $\dot{\gamma}$, μ_{app}, m, n, represents the shear rate, the apparent viscosity, the flow consistency index, and the flow behavior index, respectively. Here, flow behavior index n < 1 speaks for shear thinning nature while n > 1 represents the shear thickening behavior of non-Newtonian fluids.

Our experimental study incorporates different concentrations of shear thinning carboxymethyl cellulose (CMC) as a dispersed phase fluid. Aqua carboxymethyl cellulose (CMC) is a well-known non-Newtonian fluid that showcases the shear
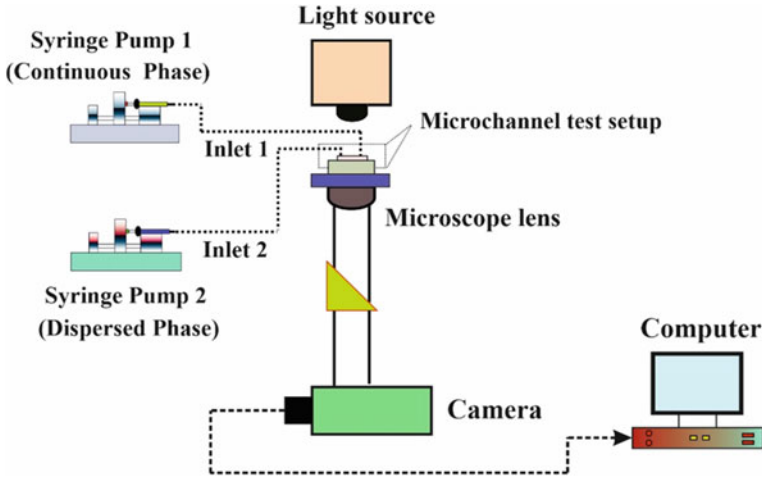
Fig. 1 Illustration of an inverted microscope and microfluidic device used to execute controlled droplet formation. Two immiscible fluids, one mustard oil, and the other CMC aqua solution, are injected from the syringe pumps, which enter via inlets 1 and 2 and link up at a microfluidic junction where a continuous train of mother droplets is formed

thinning nature inside a microfluidic device. The aqua CMC solution is prepared by mixing CMC powder (w/w) in deionized (DI) water, and the mixture is blended well in a magnetic stirrer for uniform mixing. For the present study, we prepared concentrations of aqua CMC solution ranging from $0.2\% - 0.6\%$ to report the rheological impact on the evolution of the dispersed thread length and droplet size. The rheological parameters of CMC concentrations, i.e., flow consistency index (m) and flow behavior index (n), are mentioned in Table 1. Rapeseed mustard oil is selected for continuous phase transported through the main channel with density (ρ_c) and viscosity (μ_c) of 902 kg/m^3 and 0.06 Pa s. We handled flow rate ratio $Q(Q_d/Q_c)$ in the range of 0.1 to 1.5. Here Q_c and Q_d are continuous and dispersed phase flow rates, respectively. Moreover, we employed capillary number $Ca \left(Ca = \frac{\mu_c(Q_c+Q_d)}{w_c^2\sigma}\right)$ in the range of 0.05–0.2. Here, μ_c, w_c and σ speak for the viscosity of continuous phase fluid, the width of the channel, and the interfacial tension, respectively.

Table 1 Rheological properties of fluids used in experiments

CMC concentration (%wt)	Flow consistency index m (Pa s^n)	Flow behavior index n	Interfacial tension σ (N/m)
0.2%	0.065	0.9	5
0.4%	0.130	0.82	4.82
0.6%	0.202	0.75	4.78

3 Numerical Model

The principal aspect of modeling multiphase flow physics is to capture the development of a liquid–liquid or liquid–gas interface. The most admired numerical techniques adopted for time varying interface tracking allying two immiscible fluids are volume of fluid (VOF), lattice Boltzmann model (LBM), phase field approach, and level set method. We adopted a sharp interface-based level set method to simulate droplet formation in microfluidic T-junction owing to its proficiency in providing small interface thickness. Figure 2 showcases the schematic of the computational domain engaged in the present study for controlled droplet formation.

We solve the incompressible Navier–Stokes equation, continuity equation, and the level set equation for the formulation of multiphase flow:

$$\rho \frac{\partial u}{\partial t} + \rho(u.\nabla)u = \nabla.\left[-pI + \mu\left(\nabla u + (\nabla u)^T\right)\right] + F_{st} \tag{2}$$

$$\nabla.u = 0 \tag{3}$$

$$\frac{\partial \phi}{\partial t} + u.\nabla \phi = \psi \nabla.\left(-\phi(1-\phi)\frac{\nabla \phi}{|\nabla \phi|} + \varepsilon \nabla \phi\right) \tag{4}$$

In above Eqs. 2–4, ρ represents the density (kg/m^3), u is flow velocity (m/s), t shows the time (s), and μ showcases dynamic viscosity (Pa s). At the same time, p and F_{st} denote pressure (Pa) and surface tension force (N/m^3), respectively. Moreover, ϵ and ψ are the numerical stabilizing parameters. Here, ϕ represents the level set function. It is essential to mention that level set formulation incorporates the tracking of the evolution of level set function ϕ. Note that ϕ varies from 0 to 1, wherein $\phi = 0$ and $\phi = 1$ indicate the continuous and dispersed phases, respectively.

The following equation expresses the surface tension force (F_{st}):
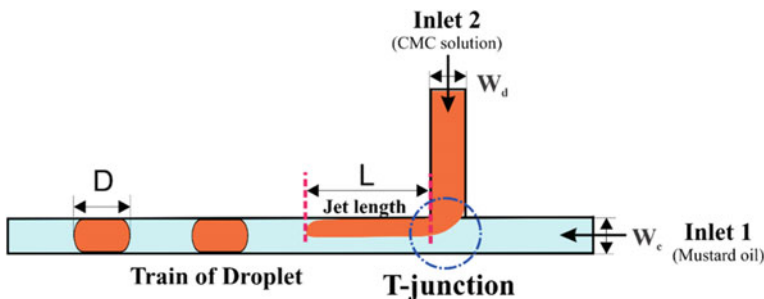
Fig. 2 Schematic of T-shaped microfluidic geometry used in experimental and numerical analysis for generation of droplets. Continuous phase fluid (mustard oil) and dispersed phase fluid (CMC aqua solution) are instigated from inlets 1 and 2, respectively. We took a cross-section of a channel with equal width and height of 100 µm

$$F_{st} = \sigma \kappa n \delta_s \tag{5}$$

where σ, κ, and n represent surface tension, interfacial curvature, and the normal unit vector to a multiphase interface. The curvature of the liquid–liquid interface (κ) is described as:

$$\kappa = -\nabla.n \tag{6}$$

Here n in terms of level set function (ϕ) is showcased as follows:

$$n = \frac{\nabla \phi}{|\nabla \phi|} \tag{7}$$

In addition, density and the viscosity of continuous and dispersed phases are achieved by Eqs. 8 and 9.

$$\rho = \rho_c + (\rho_d - \rho_c)\phi \tag{8}$$

$$\mu = \mu_c + (\mu_d - \mu_c)\phi \tag{9}$$

where ρ and μ denote density and viscosity of fluid while suffix c and d represent continuous and dispersed phase fluids, respectively. We use commercially available finite element-based COMSOL Multiphysics® framework to solve the aforementioned (2)–(9) equations.

4 Results and Discussion

In this section, we study the passive droplet formation in jetting regime within confined microfluidic T-junction. As reported in the literature [6, 12], droplet formation is either due to interfacial instability development or repression between two immiscible phases, giving rise to droplet breakup. As earlier mentioned, based on flow rate and capillary number, droplet formation can be classified into four regimes: squeezing, dripping, jetting, and parallel flow. The squeezing mechanism can be encountered due to pressure gradient, while the surface tension-driven Rayleigh-Plateau instability permits droplet formation in dripping and jetting regimes. In particular, this disturbance or instability may lead to uniform droplet formation after the jet (dispersed thread) becomes stable at a fixed location with a moderate capillary number. Jet thread breakup can be amplified pertaining to an increase in random noise and instability at a much higher capillary number. At this stage, the formed droplet frequency and size tend to be non-uniform compared to the low and moderate capillary number. In the present study, we show the dynamics behind instabilities,

forming droplets with a jet of different lengths for different concentrations of non-Newtonian CMC solution. In addition, we show the effect of flow parameters on jet elongation and control over droplet size.

4.1 Evolution of Jet (Dispersed Thread) Length

To understand the evolution of jet length and the rheological impact of shear thinning fluids on the droplet breakup, we employ the CMC concentration ranging from 0.2% to 0.6%. We alter the continuous and dispersed phase flow rates for individual concentration cases in order to examine the effect of capillary number on the droplet breakup. It is well-known that, during droplet formation, two immiscible continuous and dispersed fluid forms an interface at a T-junction. The dispersed phase's thread (or cap) enters into the main continuous phase channel under the crucial balance of upstream and downstream pressure. The thread gradually begins to thin, and the droplet detaches as the squeezing pressure overcomes the viscous resistance and the interfacial tension. Thus, the droplet detachment from the dispersed thread takes place owning to the inter-balance between squeezing pressure, viscous shear stress, and interfacial tension. As for shear thinning fluids, the role of viscous shear stress becomes more prominent. Needless to mention that, an increase in CMC concentration signifies a decrease in the power law index (n). With a decay in n, viscosity begins to decrease with an increase in shear rate. But, the magnitude of viscosity is greater for lower n as compared to higher n. In other words, with a decrease in n, viscosity of the dispersed phase increases, consequently increasing the viscous resistance of the system. As viscous resistance grows, a dispersed cap opposes a droplet detachment and evolves into a long thread.

As can be observed from Fig. 3a, the dispersed phase CMC solution evolves into a thread, which goes to the main channel and prompts droplet breakup, then moderately progresses downstream of the T-junction until a stable jet is established. The dispersed phase jet thread can be of a length greater than the channel width before the disengagement from the tip. Figure 3b shows the evolution of jet length and droplet formation for 0.2%, 0.4%, and 0.6% CMC concentrations with flow ratio and capillary number of 0.9 and 0.128, respectively. We can observe the similarity between experimental and numerical results in Fig. 3b. We can see that jet length increases with an increase in CMC concentration. Precisely, droplet breakup time and jet thread length are shorter for low CMC concentration (0.2%) than for higher concentrations. This indicates that the viscosity and shear thinning effect may become dominant with increased CMC concentration. It signifies that the viscous force produced by the dispersed phase becomes superior at higher concentrations, which causes the elongated jet to form initial droplets away from the T-junction. Secondly, the shear stress brings about the dispersed phase to elongate when entering through the main channel. In a way, this induced shear may award more instability to a jet thread while moving downstream of the channel. Moreover, the abnormal instability is expected to rise until the jet thread is cut off by interfacial tension between the continuous and

dispersed phases. The balance between the above-stated forces and flow parameters decides the occurrence of jet formation.

In Fig. 4, we show the variation of jet (dispersed thread) length with flow ratio examined for 0.2%, 0.4%, and 0.6% CMC concentration. Herein, the jet length (L) is normalized with the microchannel width (w_c) and is represented by L^*. As shown in Fig. 4, the evolution of jet length can be demarked into three regions: jet-free (*zone I*), transition (*zone II*), and stable regime (*zone III*). It is observed that, in
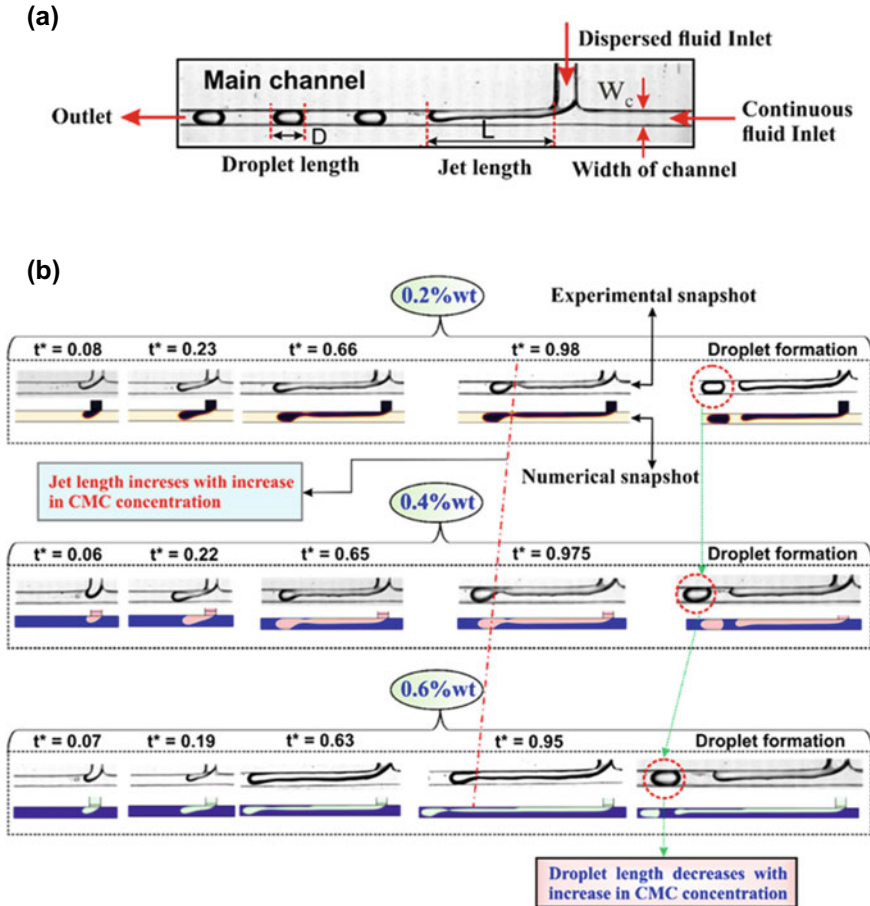
Fig. 3 **a** Experimental image of microfluidic channel framework highlighting the parameters involved in droplet formation. The parameter involved are the width of the channel (w_c), jet length (L), and droplet size (D), **b** Experimental and numerical snapshots of the evolution of jet formation and droplet detachment process in a microfluidic T-junction. Experimental and numerical images showcase the case for $c = 0.2, 0.4,$ and 0.6%, respectively $.t^* = t/T$ represents the dimensionless time of the droplet formation phenomena, wherein t represents the instantaneous time while T signifies the total time required for droplet formation

a jet-free regime, jet length (L^*) remained absent at a low flow rate ratio. With an increase in flow ratio, we observed an increment of jet length in transition and stable regime. The critical flow ratio achieved for jet-free to transition ($CFRI$) and from transition to the stable regime ($CFRII$) is 0.7 and 1.15, respectively. A closer look at Fig. 4 shows that the behavior of jet length follows the same curvature for all CMC concentrations. Moreover, an increase in dispersed phase flow rate (Q_d) engenders an increment in capillary number, which enables an increment in jet length and droplet size. Additionally, the jet produced is of tiny length and detaches near the T-junction in case $Q_c > Q_d$. This is because the shear force imparted by the continuous phase is sufficient to overcome the viscous force nearby the T-junction at low Q_d. In reverse, enhancement in Q_d does not allow droplets to completely fill the continuous phase channel; hence, an elongated filament is formed as a consequence. Further increase in Q_d forms significant jet length and progresses downstream faster, disengaging the larger size droplet. A similar response is reported by Cordero et al. [3] in their study on Newtonian fluids, wherein they determined jet length as a function of dispersed phase flow rate in confined co-axial geometry. They reported that jet length was small and moved very little downstream at lower Q_d but started to grow at higher Q_d showcasing the flow in the jetting regime.
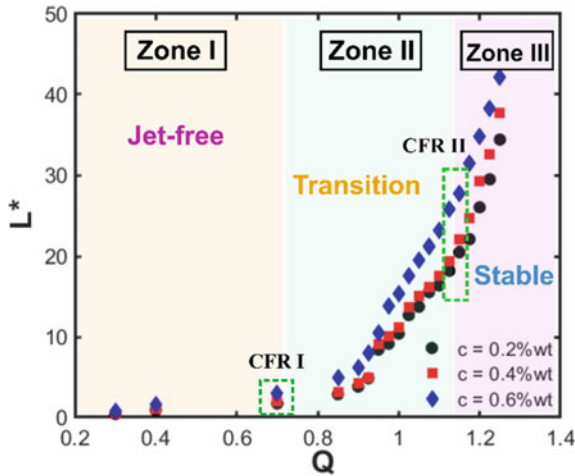

Fig. 4 Experimental evolution of dimensionless jet length (L^*) of dispersed phase as a function of flow ratio (Q). The development of a jet can be classified into three zones: Jet free ($Zone I$), Transition ($Zone II$), and Stable ($Zone III$). The jet length remains absent in zone I. Transformation of zone I into II occurs at a critical flow ratio ($CFRI$) of 0.7, wherein jet thread begins to form and enlarges with an increase in flow ratio. The significant jump in jet length is found in zone III, which occurs on and above the critical flow ratio ($CFRII$) of 1.15. $L^* = L/w_c$, represents the dimensionless jet length wherein L stands for actual jet length while w_c showcase the width of a microchannel. $Q = Q_d/Q_c$ speak for flow ratio

4.2 Effect of Capillary Number and CMC Concentration on Droplet Size

Aside from jet length evolution, variation in CMC concentration and capillary number (Ca) can directly affect the detached droplet size (D). In Fig. 5, we show the effect of dispersed phase flow rate (Q_d) on the droplet size with different CMC concentrations ranging from 0.2% to 0.6%. We mandatorily kept the continuous phase flow rate constant in order to explore the shear thinning nature of the dispersed phase on droplet formation. We employ the flow ratio (Q) from 0.1 to 1.5. It is clearly visible from Fig. 5 that droplet size (D) increases with an increase in capillary number (Ca) (or with an increase in dispersed phase flow rate Q_d) and decreases with an increase in CMC concentration from 0.2% to 0.6% for the same capillary number. Note that, with an increase in dispersed phase flow rate (Q_d), a greater volume of fluid enters the continuous phase channel. Because of this, we observe greater jet thread elongation before droplet detachment. While for a lower value of (Q_d), droplet breaks near the T-junction, and the droplet size is sufficiently less, as shown in Fig. 5. It is important to note that droplets move faster when Q_d increases, which brings a reduction in effective viscosity. As shear thinning rheology is much effective in high CMC concentrations, the effective viscosity declination narrow downs the span of droplet size (D). Apart from these, with an increase in CMC concentration, the apparent viscosity (μ_{app}) considerably increases, providing sufficient viscous drag to a system and producing a smaller droplet for the same capillary number. Thus, we conclude that non-Newtonian CMC droplet size and jet length can be customized by differing capillary number, flow ratios, and shear thinning CMC concentrations.

Fig. 5 Effect of a capillary number on the droplet size (D) for varied CMC concentrations
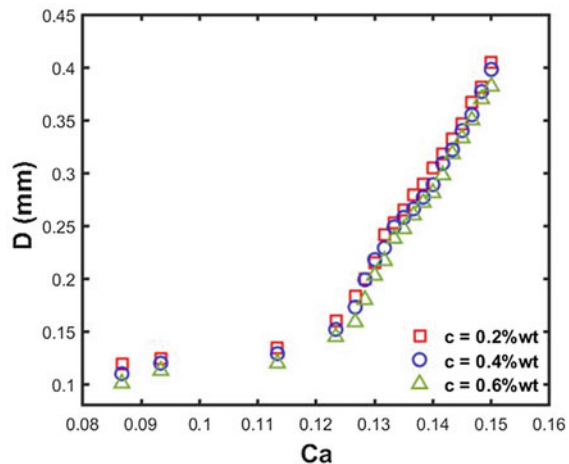
5 Conclusions

In conclusion, we experimentally and numerically investigated non-Newtonian droplet and jet (dispersed thread) formation with continuous phase mustard oil employing varied flow ratio, capillary number, and CMC concentrations on a microfluidic LOC device. We qualitatively compared the experimental observation with the numerical results showcasing the evolution of jet thread formation with change in CMC concentrations from 0.2% to 0.6%. We show that the jet length increases while the droplet size decreases with an increase in CMC concentration for the same flow rate conditions. By varying the flow ratio, we mark off the evolution of jet length into three regimes: jet-free ($zone I$), transition ($zone II$), and stable regime ($zone III$). The jet length was found to be non-existent in the jet-free zone, although shown significant presence in the transition zone with an increase in flow ratio to 0.7 and displayed a sudden jump in jet length in a stable regime for flow ratio on and above a critical value of 1.15. Jet length development follows the same behavior with an increase in CMC concentrations, with the difference that jet length increases for higher concentrations for identical flow conditions. Moreover, we studied the variation of CMC concentrations and capillary number upon droplet size. It is observed that droplet size tends to decrease with an increase in CMC concentration, while for the same CMC concentration, it increases with an increase in flow rate ratio.

References

1. Agarwal VG, Singh R, Bahga SS, Gupta A (2020) Dynamics of droplet formation and flow regime transition in a T-shaped microfluidic device with a shear-thinning continuous phase. Phys Rev Fluids 5(4):044203
2. Baroud CN, Gallaire F, Dangla R (2010) Dynamics of microfluidic droplets. Lab Chip 10(16):2032–2045
3. Cordero ML, Gallaire F, Baroud CN (2011) Quantitative analysis of the dripping and jetting regimes in co-flowing capillary jets. Phys Fluids 23(9):094111
4. De Menech M, Garstecki P, Jousse F, Stone HA (2008) Transition from squeezing to dripping in a microfluidic T-shaped junction. J Fluid Mech 595:141–161
5. de Waele A (1923) Viscometry and plastometry. J Oil Colour Chem Assoc 6
6. Eggers J (1995) Theory of drop formation. Phys Fluids 7(5):941–953
7. Gupta A, Sbragaglia M (2016) Effects of viscoelasticity on droplet dynamics and breakup in microfluidic T-Junctions: a lattice Boltzmann study. Eur Phys J E 39(1):1–16
8. Nie Z, Seo M, Xu S, Lewis PC, Mok M, Kumacheva E, Whitesides GM, Garstecki P, Stone HA (2008) Emulsification in a microfluidic flow-focusing device: effect of the viscosities of the liquids. Microfluid Nanofluid 5(5):585–594
9. Shyam S, Dhapola B, Mondal PK (2022) Magnetofluidic-based controlled droplet breakup: effect of non-uniform force field. J Fluid Mech 944
10. Shyam S, Mondal PK, Mehta B (2021) Magnetofluidic mixing of a ferrofluid droplet under the influence of a time-dependent external field. J Fluid Mech 917
11. Sohrabi S, Moraveji MK (2020) Droplet microfluidics: Fundamentals and its advanced applications. RSC Adv 10(46):27560–27574

12. Stone HA (1994) Dynamics of drop deformation and breakup in viscous fluids. Annu Rev Fluid Mech 26(1):65–102
13. Zhu P, Wang L (2017) Passive and active droplet generation with microfluidics: a review. Lab Chip 17(1):34–75

Biomedical Science and Engineering

Design, Fabrication, and Performance Validation of a Piezoelectric Sensor and Arduino-Based Wearable Device for Knee Joint Health Assessment

Dhirendra Kumar Verma , **Mirsaidin Hussain** , **Poonam kumari** , and **Subramani Kanagaraj**

Keywords Contact microphone · Knee joint disorder · Vibroarthrography · Digital oscilloscope · Signal analysis

1 Introduction

The knee joint is a load bearer and contributes to all dynamic functions of the human body. It involves flexion–extension, rolling-hinge movement, and gliding in the anterior–posterior between femoral and tibial condyle surfaces [1, 2]. Any kind of joint deformity reflects a result of unbalanced bodyweight distribution and mostly an abnormal gait pattern. The most prominent knee joint disorder is knee osteoarthritis (OA) and it is a disease that grows with the increasing age in people and often occurs in females [3]. The femoral condyle and tibial condyle rubbing against one another and the patella gliding causes acoustic signals to be produced. Because the line of action of load passes through the medial side of the joint during a normal gait cycle, this side of the joint is most frequently affected [4, 5]. This age-related, irreversible disorder could lead to circumstances that require a total knee replacement if an early diagnosis is not established. This disease affects the structural tissues, and as it slowly progresses, it develops into a chronic condition. Osteoarthritis (OA),

D. K. Verma (✉) · M. Hussain · P. kumari · S. Kanagaraj
Department of Mechanical Engineering, Indian Institute of Technology Guwahati, North Guwahati, Guwahati 781039, Assam, India
e-mail: vermadk.iitg@gmail.com

S. Kanagaraj
e-mail: kanagaraj@iitg.ac.in

which is predominantly brought on by cartilage breakdown, evolves into an irreversible stage if effective therapy is not quickly provided [6–8]. The diagnosis of this disorder is possible mostly using X-ray and other imaging techniques [9]. Most of the imaging techniques are suitable for diagnosis but have certain limitations in terms of their functional equipment requirements, higher cost, and radiation in a few cases [10]. A further limitation in the image-based diagnosis is that they do not provide any significant information related to osteoarthritis and associated pain in daily life activity [11]. In addition to the existing diagnostic methods, another technique can be used for detecting knee OA which is known as vibroarthrography (VAG). This is used to record knee joint grating sound named as crepitus. It is a kind of sound sensation generated by the knee joint itself due to friction between the cartilage and bone. This stage often comes after joint degeneration with increasing age [12]. Blodgett [13] and Walters [14] are the pioneer researchers in the field of vibroarthrography who gave the concept of knee joint sound recording and its processing for disease detection. Over the hundred years, this technology becomes more reliable with continuous improvements in signal refinement as well as sensor developments. The cited literature in this study [15–17] contains information on the evolution of vibroarthrography as a diagnostic tool and its related fields. The use of accelerometers and wearable device fabrication with miniaturized sensors has been accelerated and opened a broad scope of OA detection [18]. Another development has occurred in the direction of multichannel VAG signal recording in which a series of sensors are placed together on the skin surface and grating sound is caught from different knee locations. This multichannel approach is informative regarding spatial dependencies and analysis of bone underlying conditions [19, 20]. There are mostly two types of sensors used in the previous studies: accelerometers and microphones. The microphone initially measures the change in pressure. In the case of the knee joint, the microphone measures the effect of change in air volume in terms of acoustical energy inside the joint tissue due to the joint articulation [21]. Accelerometers have their different advantages like being lightweight, less sensitive to noise, and providing the direct output of the measured input in (m/s^2) [22]. Therefore, the use of piezoelectric material-based accelerometer sensors is widely used for VAG signal recording. The use of an accelerometer in VAG recording initially requires a hard even surface because there is a dampening effect that comes into the picture due to the soft tissues of the knee joint. The patellar contact, condyle surfaces, and tibial condyle surface jointly provide a location of hard even surface for the sensor placement to compensate for the damping effect of produced joint sound due to the presence of soft tissues and ligaments [23]. Noise is always present to affect the performance of the accelerometer or microphone during VAG signal recording. However, it is quite intensive against the motion artifacts in the case of accelerometers in comparison to the microphone [24]. The initial step is to record a VAG signal and then its postprocessing using various digital signal processing methods available. The primary objective is to differentiate between healthy and pathological subjects by analyzing these signals. Few other studies are also reported for the severity of disorder identifications and identification of injury location in the joint using VAG [25]. There will be multiple effects on the VAG signal processing due to various factors like the
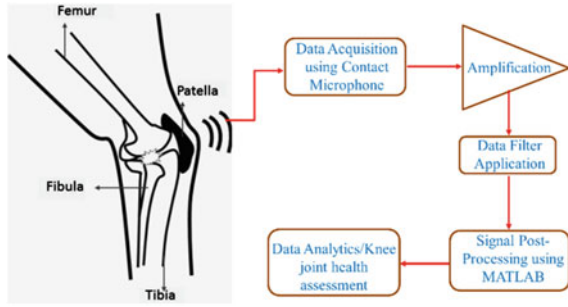
number of placement sensors used in the sound recording, the type of the sensor used, and the decided scientific target. Several studies are reported in the direction where authors aimed for subject classification into groups and on the other side few are reported in the direction of cartilage thickness evaluation, and methodology used in VAG signals analysis [26, 27]. In the current work, a contact microphone (CM-01B) based wearable device is fabricated for the knee joint VAG signal analysis. The primary objective is to develop a circuit from the elementary stage and convert it into the final device by fabricating a printed circuit board. The amplifier is also designed for the signal amplification and data in the form of voltage output w.r.t. time is recorded in the SD card module attached to the device. The device performance is initially validated at different predefined input frequencies and later it is tested on the human knee joint for VAG signal recording. The complete procedure from signal acquisition to feature extraction is shown in Fig. 1.

2 Materials and Methods

2.1 Device Fabrication

In this work, a compact wearable device consisting of a piezoelectric sensor and an Arduino Nano has been fabricated. The piezoelectric sensor has been used in the form of a microphone that senses sound vibrations through contact with solid objects. The piezoelectric microphones transduce only acoustic emission that generates from the sound wave striking a surface and it is not sensitive to air vibrations. An Arduino Nano is a compact, small microcontroller. The two different versions of Nano are ATmega 328 and ATmega168. In an Arduino Nano, there are 22 input/output pins in total, among which 14 pins are digital, and 8 are analog pins. Among the 14 digital pins, 6 are Pulse Width Modulation (PWM). The variation of the operating voltage is between 5 and 12 V. The electronic components have been combined for the primary circuit development and to detect the grating sound obtained from the knee joint, the signal has been amplified. The final circuit has been converted into a printed circuit
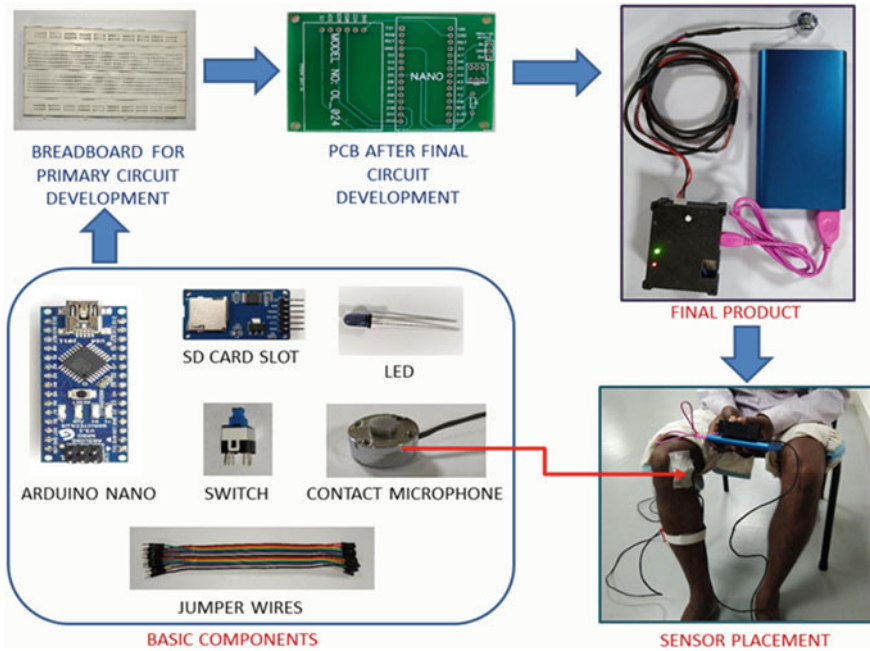
Fig. 2 Schematic of basic components to a final wearable device and sensor placement

board (PCB) and the casing of the product has been designed in SolidWorks followed by 3D printing. The final device with all its components has been shown in Fig. 2.

2.2 Participants

In this study, twenty-two human subjects (fifteen males (29.33 ± 11.91 years, 67.45 ± 10.01 kg, 170.73 ± 8.24 cm) and seven females (29.29 ± 3.64 years, 63.71 ± 9.52 kg, 155.34 ± 6.10 cm)) are recruited for participation. For all the subjects, inclusion and exclusion criteria have been carefully followed. The inclusion criteria initially cover the willingness of the participant to become a study subject and to wear the acoustic emission setup for data collection. Each subject must be able to understand the research protocol for signing the ethical consent and must be able to perform the joint exercises with manual dexterity. The exclusion criteria were also strictly followed for data collection and according to the criteria, the subjects should not have any leg pain, a current musculoskeletal injury, or cognitive deficits. Also, ethical consent has been taken from all the subjects before performing the experiment. The approval for conducting the experiments has been taken from the Institute Human Ethical Committee (IHEC), IIT Guwahati.

2.3　Data Collection Protocol

In knee health assessment, to catch the grating sound using vibroarthrography, it is important to place the sensor in the correct position such that accurate output could be obtained. Thus, the piezoelectric microphone sensor is placed below and outside of the patella in the knee joint, as the anatomical distance of the joint becomes minimum at this position [28]. After placing the sensor in the specified position, each subject sits on a chair in a relaxed position. To collect joint sound in the knee joint with the help of the fabricated device, the subjects are trained to perform the sit-stand-sit (S-T-S) motion which is an active weight-bearing exercise. Each subject is asked to perform five S-T-S cycles in one trial. A cycle starts with the initial sitting position followed by standing and then again sitting. While a subject starts standing, the subject must undergo ascending acceleration and ascending deacceleration phase. Similarly, while going from standing to sitting position, the subject undergoes descending acceleration and descending deacceleration phase. Thus, these four phases complete a cycle. Each cycle is completed within a range of 4.5–6 s by synchronizing the motion of the subjects with the metronome. To distinguish the variation of voltage signal output with respect to different phases in a cycle, a self-developed Inertial measurement unit (IMU)-based digital goniometer has also been used.

3　Results and Discussion

3.1　Device Performance Validation

As shown in Fig. 3 the fabricated wearable device has been tested through a digital oscilloscope. For this goal, an online tone generator has been used using a laptop and a speaker on which the contact microphone is attached. The sensor surface was exactly stuck to the diaphragm of the speaker and tested on different generated sinusoidal sound waves of different frequencies. The aim of this experiment was to validate the input frequency from the tone generator with the output of the contact microphone and the result was verified on the screen of a digital oscilloscope. Here the objective was to verify the performance of the device through the arbitrarily generated sound waves at different frequencies. An instantaneous click of the signal was recorded from the oscilloscope and simultaneously the sensor output was stored in the SD card attached to the device.

　Figure 4 shows the output of the fabricated device at 200 Hz sinewave generated from an online tone generator. The data sampling duration is 2.8 s and the instantaneous signal was recorded on the oscilloscope simultaneously the generated voltage of approximately 3 V was also recorded in the device. The first observation was seen on the oscilloscope as the output frequency was obtained to be 199.8 Hz. Further, the recorded data in the device was post-processed in MATLAB (R2021a) and it was observed in the fast Fourier transform analysis the output frequency is 201.93 Hz
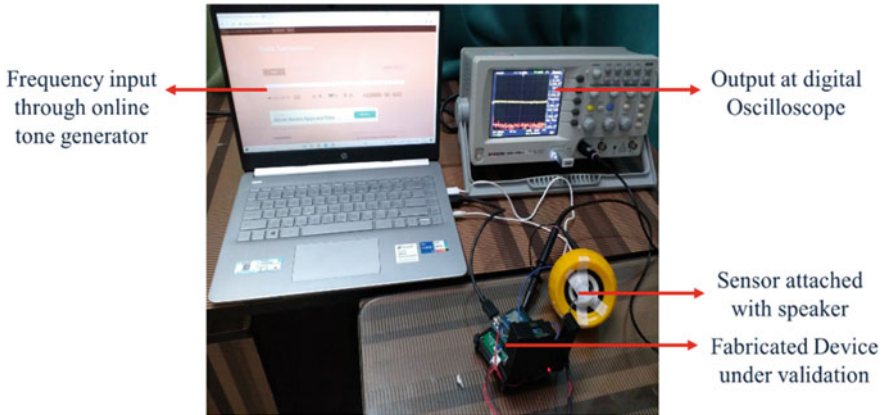
Fig. 3 Device validation through digital oscilloscope

at a decibel value of 74.95 dB. This observation indicates the approximately same frequency output validation from two different methods at the same time in the experiment. This experiment was repeatedly performed for the other frequency inputs also and similar results output was obtained.

3.2 Device Output from the Knee Joint

Figure 5 shows the results from a subject who performed a sit-stand-sit motion for five continuous cycles for the duration of 28 s approximately. The position of the contact microphone and the IMU sensors is also clearly shown in Figs. 2 and 5. Here the three different outputs are shown in the one figure with the same time frame. Knee joint angle and its angular velocity were also measured using a digital goniometer in the same time duration for five cycles. The sensor output was measured in terms of millivolts and recorded at its maximum value up to 8 mV. In Fig. 5, it can be seen that the velocity and angle output is clearly distinguished by the output of sensor voltage and motion phases in five cycles individually. The output velocity can distinguish the four motion phases in each cycle. Comparing the variation of the output voltage with respect to the different motion phases, it has been observed that the value of output voltage becomes higher while the subject starts moving from the sitting position to the standing position from a chair.
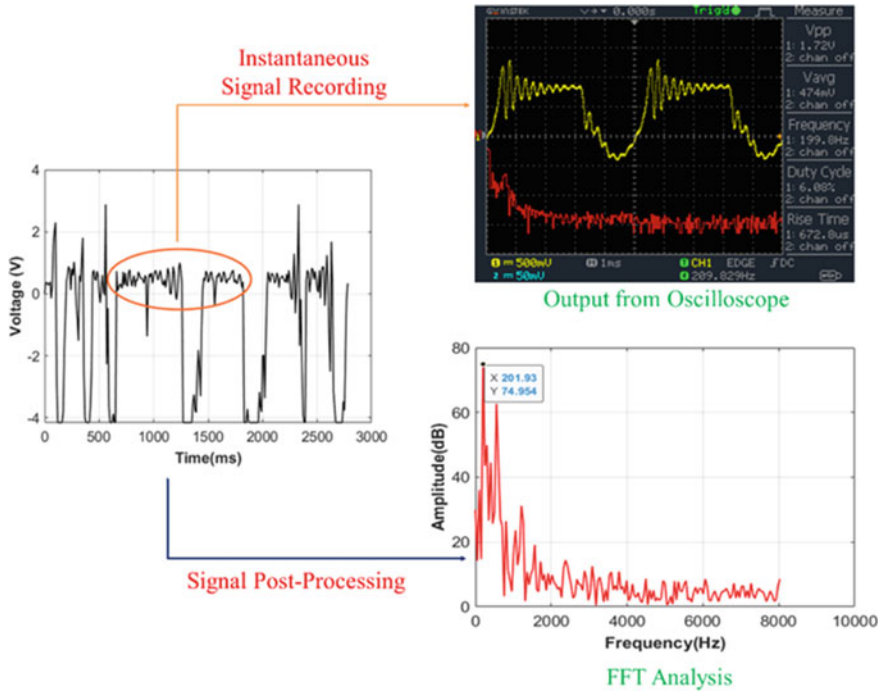
Fig. 4 Sensor output validation at 200 Hz sinusoidal sound wave

3.3 Frequency Spectrum Analysis

The output signal voltage obtained during the weight-bearing S-T-S exercise has been post-processed to find the fast Fourier transform (FFT) and the corresponding Short-time Fourier transform (STFT). From the FFT analysis, the peak frequency components have been obtained during the movement of the healthy subject from sitting position to standing position as shown in Fig. 6a. It is also justified by the higher value of voltage output of the vibroarthrography signal during the same duration as shown in Fig. 5. Figure 6b shows the STFT of the output signal voltage which provides the time-localized frequency information where the frequency component of a signal varies over time. The STFT divides a longer time signal into small segments and then calculates the FFT of individual segments as represented on the spectrogram. The range of peak amplitude of all the healthy subjects has been obtained within 40–45 dB. Moreover, the peak frequency of all the subjects has been obtained to be less than 100 Hz. The obtained results have been validated from the earlier published research [29, 30].
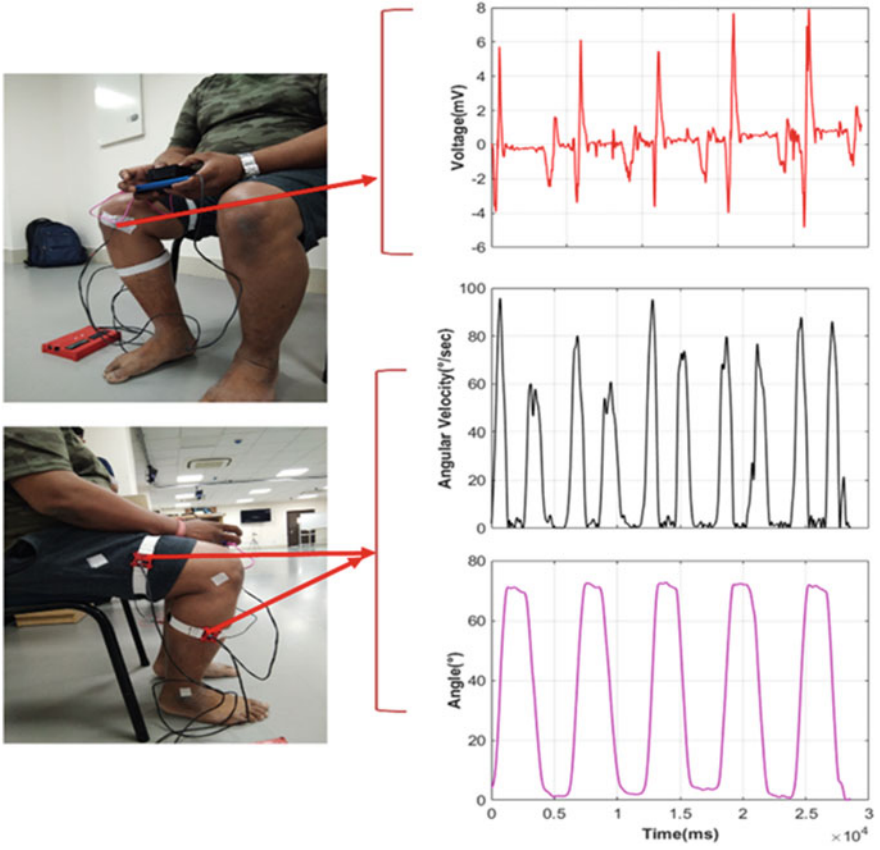
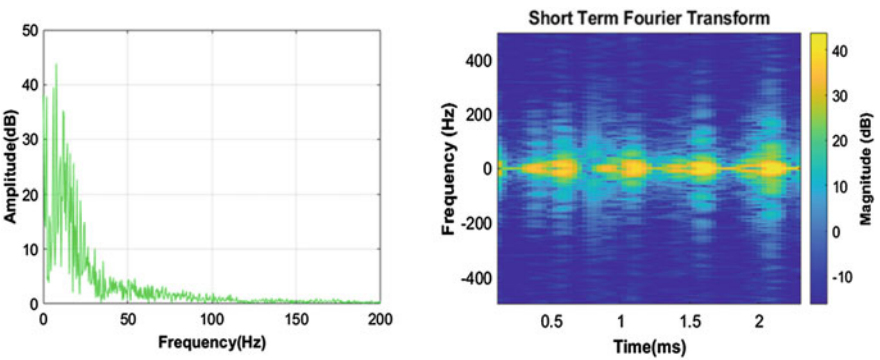**Fig. 5** Joint angle-based vibrarthrography from the knee joint

Fig. 6 **a** FFT analysis for a healthy knee subject; **b** STFT spectrogram from a healthy subject

4 Conclusion

This study demonstrated the utility of a VAG signal analysis to perform a knee joint health assessment. The use of a contact microphone is a preliminary development in this work for the joint sound recording. It can be revealed that wearable device fabrication is decisively possible using Arduino microcontrollers of different versions. However, other advanced developments are also possible using a higher data processing rate microcontroller like Raspberry Pi of their different versions. Future developments in the use of broadband sensors, sophisticated and high-frequency microphones, and Bluetooth or wireless technology-enabled joint health monitoring systems will be evaluated against the successful validation of the frequency output. Vibroarthrography-based knee joint health monitoring is an effective approach for taking home healthcare system in which an individual can self-assess the joint health and preventive care and treatment modalities can be adopted or can be suggested by the physicians.

References

1. Lafortune MA, Cavanagh PR, Sommer III HJ, Kalenak A (1992) Three-dimensional kinematics of the human knee during walking. J Biomech 25(4):347–357 (1992). https://doi.org/10.1016/0021-9290(92)90254-X
2. Bull AMJ, Amis AA (1998) Knee joint motion: description and measurement. Proc Inst Mech Eng, Part H: J Eng Med 212(5):357–372. 10.1243%2F0954411981534132
3. Heidari B (2011) Knee osteoarthritis prevalence, risk factors, pathogenesis, and features: Part I. Caspian J Intern Med 2(2):205
4. Van den Borne MPJ, Raijmakers NJH, Vanlauwe J, Victor J, De Jong SN, Bellemans J, Saris DBF (2007) International Cartilage Repair Society (ICRS) and Oswestry macroscopic cartilage evaluation scores validated for use in Autologous Chondrocyte Implantation (ACI) and microfracture. Osteoarthritis Cartilage 15(12):1397–1402. https://doi.org/10.1016/j.joca.2007.05.005
5. Karpiński R, Machrowska A, Maciejewski M (2019) Application of acoustic signal processing methods in detecting differences between open and closed kinematic chain movement for the knee joint. Appl Comput Sci 15(1)

6. Ahn JH, Kang DM, Choi KJ (2017) Risk factors for radiographic progression of osteoarthritis after partial meniscectomy of discoid lateral meniscus tear. Orthop Traumatol Surg Res 103(8):1183–1188. https://doi.org/10.1016/j.otsr.2017.09.013

7. Jones MH, Spindler KP (2017) Risk factors for radiographic joint space narrowing and patient reported outcomes of post-traumatic osteoarthritis after ACL reconstruction: data from the MOON cohort. J Orthop Res 35(7):1366–1374. https://doi.org/10.1002/jor.23557

8. Cibere J, Sayre EC, Guermazi A, Nicolaou S, Kopec JA, Esdaile JM, Thorne A, Singer J, Wong H (2011) Natural history of cartilage damage and osteoarthritis progression on magnetic resonance imaging in a population-based cohort with knee pain. Osteoarthritis Cartilage 19(6):683–688. https://doi.org/10.1016/j.joca.2011.02.008

9. Peat G, Thomas E, Duncan R, Wood L, Hay E, Croft P (2006) Clinical classification criteria for knee osteoarthritis: performance in the general population and primary care. Ann Rheum Dis 65(10):1363–1367. https://doi.org/10.1136/ard.2006.051482

10. Wu Y, Krishnan S, Rangayyan RM (2010) Computer-aided diagnosis of knee-joint disorders via vibroarthrographic signal analysis: a review. Crit Rev™ Biomed Eng 38(2). https://doi.org/10.1615/CritRevBiomedEng.v38.i2.60

11. Andersen RE, Arendt-Nielsen L, Madeleine PM (2016) A review of engineering aspects of vibroarthrography of the knee joint. Crit Rev Phys Rehabil Med 28:13–32. https://doi.org/10.1615/CritRevPhysRehabilMed.2016017185

12. Wu Y (2015) Knee joint vibroarthrographic signal processing and analysis. Springer, New York. https://doi.org/10.1007/978-3-662-44284-5

13. Blodgett WE (1902) Auscultation of the knee joint. Boston Med Surg J 146(3):63–66. https://doi.org/10.1056/NEJM190201161460304

14. Walters CF (1929) The value of joint auscultation. Lancet 213:920–921. https://doi.org/10.1016/S0140-6736(00)79189-6

15. Reddy NP, Rothschild BM, Mandal M, Gupta V, Suryanarayanan S (1995) Noninvasive acceleration measurements to characterize knee arthritis and chondromalacia. Ann Biomed Eng 23(1):78–84. https://doi.org/10.1007/bf02368303

16. Rangayyan RM, Krishnan S, Bell GD, Frank CB, Ladly KO (1997) Parametric representation and screening of knee joint vibroarthrographic signals. IEEE Trans Biomed Eng 44(11):1068–1074. https://doi.org/10.1109/10.641334

17. Tanaka N, Hoshiyama M (2012) Vibroarthrography in patients with knee arthropathy. J Back Musculoskelet Rehabil 25(2):117–122. https://doi.org/10.3233/bmr-2012-0319

18. Kernohan WG, Mollan RAB (1991) Non-invasive diagnosis and prophylaxis in orthopaedics. Proc Inst Mech Eng, Part H: J Eng Med 205(3):73–187. 10.1243%2FPIME_PROC_1991_205_288_02

19. Heller BW, Clarke AJ, Good TR, Healey TJ, Nair S, Pratt EJ, Reeves ML, van der Meulen JM, Barker AT (2013) Automated setup of functional electrical stimulation for drop foot using a novel 64 channel prototype stimulator and electrode array: results from a gait-lab based study. Med Eng Phys 35(1):74–81. https://doi.org/10.1016/j.medengphy.2012.03.012

20. Shen Y, Rangayyan RM, Bell GD, Frank CB, Zhang YT, Ladly KO (1995) Localization of knee joint cartilage pathology by multichannel vibroarthrography. Med Eng Phys 17(8):583–594. https://doi.org/10.1016/1350-4533(95)00013-D

21. Kaniusas E (2012) Fundamentals of biosignals. In: Biomedical signals and sensors. Springer, Berlin, pp 1–26

22. McCoy GF, McCrea JD, Beverland DE, Kernohan WG, Mollan RA (1987) Vibration arthrography as a diagnostic aid in diseases of the knee. A preliminary report. J Bone Jt Surg Br 69(2):288–293. https://doi.org/10.1302/0301-620X.69B2.3818762

23. Nokes L, Fairclough JA, Mintowt-Czyz WJ, Mackie I, Williams J (1984) Vibration analysis of human tibia: the effect of soft tissue on the output from skin-mounted accelerometers. J Biomed Eng 6(3):223–226. https://doi.org/10.1016/0141-5425(84)90107-9

24. Posatskiy AO, Chau T (2012) The effects of motion artifact on mechanomyography: a comparative study of microphones and accelerometers. J Electromyogr Kinesiol 22(2):320–324. https://doi.org/10.1016/j.jelekin.2011.09.004

25. Maussavi ZM, Rangayyan RM, Bell GD, Frank CB, Ladly KO (1996) Screening of vibroarthrographic signals via adaptive segmentation and linear prediction modeling. IEEE Trans Biomed Eng 43(1):15. https://doi.org/10.1109/10.477697
26. Bassiouni HM, El-Deeb M, Kenawy N, Abdul-Azim E, Khairy M (2011) Phonoarthrography, musculoskeletal ultrasonography, and biochemical biomarkers for the evaluation of knee cartilage in osteoarthritis. Mod Rheumatol 21(5):500–508. https://doi.org/10.3109/s10165-011-0441-8
27. Neely LA, Kernohan WG, Barr DA, Mee CHB, Mollan RAB (1991) Optical measurements of physiological patellofemoral crepitus. Clin Phys Physiol Meas 12(3):219. https://doi.org/10.1088/0143-0815/12/3/002
28. Radzicki V, Matsuura K (2015) Passive acoustic sensing for the assessment of knee conditions. Int Found Telemetering. http://hdl.handle.net/10150/596462
29. Ye Y, Wan Z, Liu B, Xu H, Wang Q, Ding T (2022) Monitoring deterioration of knee osteoarthritis using vibration arthrography in daily activities. Comput Methods Programs Biomed 213:06519. https://doi.org/10.1016/j.cmpb.2021.106519
30. Tarnita D, Marghitu D (2017) Nonlinear dynamics of normal and osteoarthritic human knee. Proc RomIan Acad, Ser A 18(4):353–360

A Brief Review of Image Classification Techniques for Alzheimer's Disease Detection

Mallika Chouhan and Meenakshi Pareek

1 Introduction

Alzheimer's disease (AD) is an epitome of neurodegenerative disorder that impacts the overall cognitive function of the elderly. As a result, people tend to lose their memory much faster and quite often. Alzheimer's disease can affect the brain at multiple stages. Based on the brain condition, the patient can belong to one of the stages, including cognitively normal (CN), mild cognitive impairment (MCI), normal control (NC), and healthy control (HC). Early AD detection is critical to enhancing people's lives and establishing effective care. The detection techniques tend to identify the stages and classify the severity of the disease, which are further categorized based on classification accuracy. Achieving higher accuracy and precision in differentiating healthy aging from early signs of AD is challenging [1].

Many techniques have been proposed to facilitate the early detection of AD. Primarily, the effectiveness of a proposed technique is evaluated on the available datasets. The primary datasets involved in procuring the data images for the purpose of experimentation are Alzheimer's disease neuroimaging initiative (ADNI) [2], open access series of imaging studies (OASIS) [3], and minimal interval resonance imaging in Alzheimer's disease (MIRIAD) [4]. These datasets provide magnetic resonance

M. Chouhan (✉)
Department of Automation, Banasthali Vidyapith, Jaipur, India
e-mail: btbtn20065_mallika@banasthli.in

M. Pareek
Department of Computer Science, Banasthali Vidyapith, Jaipur, India
e-mail: pmeenakshi@banasthali.in

imaging (MRI) and positron emission tomography (PET) scan images. ADNI has been used in the majority of the works for dataset collection, which provides both types of scans. MIRIAD provides only MRI scans as part of the dataset, and OASIS-1, which is a sub-part of the OASIS dataset, has been used to provide MRI scans of young and middle-aged along with nondemented and demented older generations.

For AD detection, many techniques have been proposed in the literature [6–11]. These works have mainly used the MRI modality for the database images. The methods described by Priya et al. [6], and Kumar et al. [7] discuss the comparative methods of determining the severity of the disease. Wang et al. [8] introduced the network-based methods to achieve the classification of AD and HC. The models proposed by Zhang et al. [9] and Jin et al. [10] quantify their results regarding structural similarity index measure (SSIM), peak signal-to-noise ratio (PSNR), mean absolute error (MAE), and mean Squared Error (MSE) index values.

Deep learning (DL) based methods are found to be effective for image-related applications. Some examples are object detection, medical image analysis, crop yield analysis in agriculture, and traffic prediction. Many researchers have used DL for AD detection. Kang et al. [12] use the deep-learning-based reconstruction approach on F-18 florbetaben (FBB) positron emission tomography (PET) scans close to the CNN-based technique for detection and classification. Many researchers have proposed the newly devised techniques, which are based on convolutional neural network (CNN) [14–22].

The CNN-based techniques have mainly used PET and various MRI modalities for the database images. Khagi and Kwon [14], and Feng et al. [15] have proposed their own frameworks which perform classification among various stages. Islam et al. [16], Hosseini-Asl et al. [17], and Kruthika et al. [18] have used the 3D-CNN technique on PET, structural MRI (sMRI), and MRI modalities. Amini et al. [19] compare various techniques with CNN, showing that CNN produces results with maximum accuracy. Farooq et al. [20] have tested the CN-based framework's accuracy for different architectures, and GoogleNet gave the highest accuracy. AbdulAzeem et al. [21] have generated results based on binary and multi-classification of AD and CN. Savaş [22] does not mention any specific detection technique but has compared different architectures based on accuracy, loss, and standard deviation.

Researchers have compared various aspects of AD detection techniques [23–32]. Weller et al. [23] have reviewed imaging techniques as well as invasive clinical methods for AD detection based on the diagnostic accuracy. They have not considered the recent developments in deep learning (DL) techniques. Some surveys focus on a specific technique. For example, Acer et al. [24] review the literature on manual methods of volumetric change quantification of MRIs. Recently, deep learning techniques have gained traction in performing AD detection through imaging techniques.

The reviews presented in [25–32] focus on the DL-based AD detection techniques. Ahmed et al. [25] reviewed machine learning (ML) techniques for AD detection and classified them as conventional machine learning approaches and deep learning approaches. Tanveer et al. [26] have surveyed three ML techniques, namely support vector machine, artificial neural network, and Gautam and Sharma [27]

reviewed the DL techniques used in detecting eight different neuropsychiatric and neurological diseases including Alzheimer's disease. Al-Shoukry et al. [28] have presented a brief review on DL techniques and datasets used for AD detection. Various researchers compared works considering various DL-based methods, and found that CNN performs superior to the other methods [29–32].

In this chapter, we primarily classify the proposed AD detection techniques under the heads of non-CNN-based and CNN-based techniques. We provide a brief review of the major AD detection techniques covering non-CNN-based as well as CNN-based detection techniques. Under the non-CNN-based techniques, the comparison is made on the basis of structural similarity index measure and peak signal-to-noise ratio index values. CNN-based works have been compared on the basis of respective accuracies achieved. Next, we present the organization of the chapter.

1.1 Organization of the Chapter

The research work carried out by various authors has been classified in non-CNN and CNN-based approaches. Discussion and comparison of the non-CNN-based techniques have been presented in Sect. 2. Section 3 presents a brief introduction of the types of artificial neural networks (ANNs). CNN-based AD detection techniques have been discussed in Sect. 4. Multiple methods and techniques have been summarized. Finally, the conclusions are drawn in Sect. 5.

2 Alzheimer's Disease Detection Using Non-convolutional Neural Network-Based Techniques

Advanced neuroimaging techniques are used for AD detection. Different imaging modalities for AD detection include MRI, functional MRI (fMRI), Structural MRI (sMRI), PET, fluoro-deoxy-D-glucose (FDG) PET, single photon emission computed tomography (SPECT), CT scan, and X-ray. The purpose is to achieve a non-invasive and reliable AD diagnosis. Not one modality is sufficient for AD detection as each modality has its benefits and limitations. Johnson et al. [5] have presented a systematic comparison of each modality, its advantages, and limitations. Furthermore, physical quantity, such as brain volume, is estimated from these images to detect AD. The noise present in the image makes this estimation task challenging. In this section, we present works using these neuroimages for predicting AD.

Priya et al. [6] and Kumar et al. [7] have followed the relative classification practice for AD detection. Volume estimation of segmented brain tissue has been done in [6] along with the calculation of total volume of brain tissue. The proposed method falls under the automatic brain volume estimation technique. It is less time-consuming and less laborious as compared to existing manual brain volume estimation techniques.

Also, in their proposal, contrast to other automatic methods, the preprocessing of images is done uniformly and no fine-tuning was needed. Kumar et al. [7] have applied a hybrid approach of segmentation using k-mean clustering and graph-cut approach followed by the classification using game theory.

Wang et al. [8] put forward a visual geometry group (VGG)-inspired network and 18-way data augmentation (DA). Results were obtained in terms of F1 score, Fowlkes–Mallows index, Matthews correlation coefficient, and area under the curve. The proposed Alzheimer's disease VGG-inspired attention network (ADVIAN) gave better results when compared with 11 existing techniques, and an 18-way DA is utilized to prevent overfitting of the training set. A pixel counting-based method (PCBM) was proposed on three different datasets in [8]. The classification resulted in PCBM calculating more volume than statistical parametric mapping (SPM). The deep-CNN is used as a classification technique instrumental in classifying the disease for making proper diagnostic decisions.

Zhang et al. [9] and Jin et al. [10] classified the results concerning PSNR, SSIM, MAE, and MSE index values. A 3D end-to-end generative adversarial network (BPGAN) has been proposed by the synthesis of brain PET from MRI scans in [9]. The results obtained resulted in high PSNR and SSIM index and low MAE values. Compared to stand-alone MRI, the combined MRI with synthetic PET scans improved accuracy by 1%. A framework called generative adversarial networks constrained multiple loss autoencoder (GANCMLAE) is discussed in [10] for individual brain atrophy detection.

Ramana and Nandhagopal [11], aimed at the segmentation of AD region from MRI, have proposed the efficient fuzzy C means adaptive thresholding (EFCMAT) algorithm. The exact region of interest is segmented, and results indicate the proposed method has an accuracy of 98% compared to the existing method having 82% accuracy. Table 1 summarizes these non-CNN-based techniques based on data set type, modality, technique used, result obtained, accuracy, and classification.

3   Overview of Artificial Neural Network Techniques

Artificial neural networks are the broad category of machine learning which encompasses various types of deep learning algorithms. Mainly ANNs are composed of hidden layers in between input and output layers. ANNs are further classified based on the number of hidden layers, the connection between layers, and how the information is processed.

Deep learning is an algorithm that learns multiple levels of abstraction. DL's ability to learn a large amount of data makes it very useful for various applications, especially for audio and video processing. Next, we discuss some significant types of ANNs in DL.

Table 1 Various techniques used for the classification of AD based on non-CNN techniques

Refs.	Data set type	Modality	Technique	Result/Accuracy	Classification
[6]	MIRIAD, ADNI, Real-time images	MRI	Pixel counting-based method	Volume of PCBM more than SPM	AD versus CN
[7]	OASIS	MRI	k-mean clustering, graph-cut, game theory	More than 98%	AD versus MCI versus CN
[8]	OASIS-1	MRI	VGG-inspired network	97.76 ± 1.13	AD versus HC
[9]	ADNI	MRI	3D end-to-end network BPGAN	High PSNR (26.92/ 25.08); Low MAE (0.0318/0.0396); High SSIM (0.7294/ 0.6646)	AD versus MCI versus CN
[10]	ADNI	MRI	GANCMLAE model	Best performance on SSIM (0.934 ± 0.006); PSNR (31.04 ± 0.09); MSE (0.0014 ± 0.0001)	AD versus MCI
[11]	ADNI	MRI	Efficient fuzzy C means adaptive thresholding	98%	Not stated

3.1 Deep Neural Network

A Deep Neural Network (DNN) is a multi-input–output layer network, a subpart of the ANN. Different neural networks exist which can model complex non-linear relationships. Their standard components include neurons, synapses, weights, biases, and functions.

DNNs are feedforward neural networks (FFNNs) in which data flows from the input layer toward the output layer without forming a loop between the layers. It contains at least one hidden layer sandwiched between the input and output layers. DNN uses fully connected layers, i.e., all the neurons between the layers are connected. A typical DNN architecture is shown in Fig. 1. DNN is mainly used for regression and classification of unstructured data.

Major drawbacks of DNNs include a large number of parameters, large memory requirements, and a lack of local information processing.
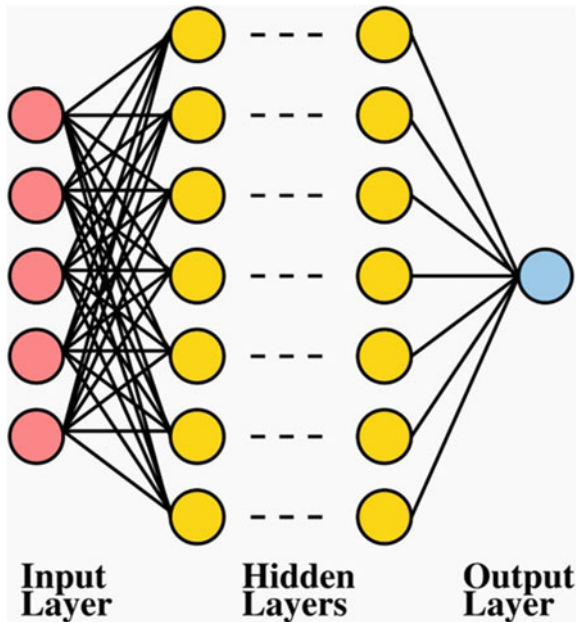
Fig. 1 Deep neural network architecture

3.2 Recurrent Neural Network

A Recurrent Neural Network (RNN) is another class of ANN. It models temporal information. In RNN, nodes are connected as directed graphs, and loops between layers are present (Fig. 2). This allows for the information to flow back. RNN processes the information based on the current input and the past information. It is mainly used in handwriting, speech, and video recognition.

In RNNs, the value of the gradient diminishes or explodes exponentially, and information diminishes over the long term. These drawbacks put a restriction on the number of hidden layers used.

3.3 Convolutional Neural Network

A convolutional neural network, also a class of ANN, addresses the issues with RNN. CNN is utilized for 2D data classification and recognition. It consists of a hidden layer connecting input and output layers, including multiple convolutional, pooling, fully connected, and normalization layers (Fig. 3). Feedforward and backpropagation methods allow correct neuron error computation, adjustment, and data fitting. The computer is fed with labeled content, consistently correlating visual patterns with
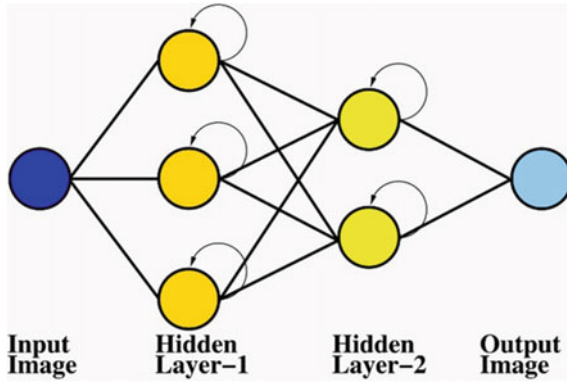
Fig. 2 Recurrent neural network architecture

Fig. 3 Convolutional neural network architecture

particular labels, thus performing tasks by analyzing training examples. During the neural net training, parameters are randomly assigned and continually adjusted until consistency is obtained.

CNNs are found to be very effective in analyzing visuals. Many researchers have explored CNN-based techniques in the detection of AD. In the next section, we discuss these works in detail.

4 Convolutional Neural Network-Based Alzheimer's Disease Detection Techniques

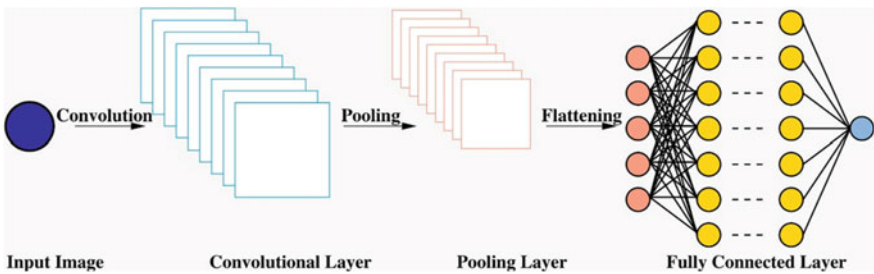Neuroimaging techniques produce high-volume and complex images. For example, MRI generates high-volume 3D images of the brain. Manually analyzing these images poses challenges in terms of effort and accuracy. For more precise diagnosis, computational resources available today can be used effectively to get quantitative results. These results can further be used by the expert, in addition to the patient's personal history, to provide a final diagnosis. This will improve the diagnosis accuracy and precision as well as reduce the diagnosis time. Early detection of AD will help the patient get early treatment and address safety issues, e.g., driving alone, wandering, etc.

Deep learning has recently gained popularity among researchers in AD detection. Among various DL techniques, CNN has shown a significant improvement in early AD detection. In this section, we mainly focus on the works related to the CNN-based techniques used in AD detection.

Kang et al. [12] discussed a deep-learning-based image reconstruction approach using quick data acquisition for F-18 florbetaben (FBB) positron emission tomography (PET) images. To model the real-world images, computer-generated synthetic images have been used. The SSIM index for the synthetic images improved from 0.8818 to 0.9939; thus, short-scanning protocols for clinical applications are possible. Sathiyamoorthi et al. [13] consider noise present in the MRI images obtained and applies 2D adaptive bilateral filter image restoration technique. They used deep CNN for classification of AD and compared the performance with K-nearest neighbor (KNN) algorithm. DCNN was found to perform far better than KNN-based classification with more than 98% accuracy.

Khagi and Kwon [14], and Feng et al. [15] have proposed their own frameworks; 3D CNN has been explored by adding the depth characteristic to 2D CNN in [14]. Results show high dependence of the deep learning process on training materials. Despite the fact that the trained CNN does not represent a complex human brain structurally, it is sufficient enough to classify the MRIs, based on the partitioned features in the convolutional layers. A framework has been designed in [15] using 3D CNN and fully stacked bidirectional long short-term memory (FSBi-LSTM). The method averages 94.82, 86.36, and 65.35% for differentiating AD from NC, progressive mild cognitive impairment (pMCI) from NC, and stable mild cognitive impairment (sMCI) from NC.

Islam et al. [16], Hosseini-Asl et al. [17], and Kruthika et al. [18] have used 3D CNN in their models. In [16], brain PET scans have been used to develop 3D deep CNN using visualization techniques. Results were mapped using heatmap generation and analyzing distributed and concentrated mapping results. Visualization was more focused in comparison to the classification of the results. 3D deeply supervised adaptive CNN for AD classification and prediction is used in [17]. Results indicate that the technique surpasses other state-of-art methods. Computer-aided diagnosis techniques with Content-Based Image Retrieval (CBIR) have been used in [18] along with 3D-Capsule Networks (CapsNets), and 3D CNN architecture.

Amini et al. [19] contrast various machine learning methods and CNN architectures. KNN, decision tree (DT), support vector machine (SVM), linear discrimination analysis (LDA), and random forest (RF) have been considered for comparison.

Farooq et al. [20] have put forward a four-way deep-learning pipeline into AD, MCI, late MCI (LMCI), and NC. The proposal analyzes the similarity between the human visual cortex and CNN. Classification accuracy was reported to be increased by 4%. The sensitivity obtained for all three classes was 97.9% and even higher for LMCI. Table 2 mentions the detailed performance of the proposed framework for each model. AbdulAzeem et al. [21] proposed a five-layer framework for CNN-based AD classification. The framework first achieves acquisition and annotation, then after preprocessing and augmentation, cross-validation, CNN model, and AD classification is done. Binary- and multi-classification accuracies are mentioned in Table 2. The abbreviations used in the chapter are summarized in Table 3 for ease of reading.

Using CNN architecture, the performances of 29 pre-trained models were collated by Savaş [22]. Each model was evaluated for accuracy, and for each class measured specificity, the precision, and sensitivity rates. The highest accuracy of 92.98% was provided by the EfficientNetB0 model. The highest precision value of 89.78% was obtained by EfficientNetB3 model, highest sensitivity of 97.28% was achieved by EfficientNetB3, and highest specificity of 94.42% was brought out by EfficientNetB2 model.

The AD detection technique classification, listing non-CNN and CNN-based techniques, has been presented in Fig. 4.

Table 2 Various techniques used for classification of AD based on CNN techniques

| Ref	Data set type	Modality	Technique	Result/Accuracy	Classification
[12]	ADNI	FBB PET	Deep learning-based reconstruction approach	SSIM index for the synthetic images increased from 0.8818 to 0.9939	Not stated
[13]	ADNI	MRI	2D adaptive bilateral filter algorithm, adaptive histogram adjustment algorithm, Deep CNN	More than 98%	Not stated
[14]	ADNI	MRI PET	divNet	More than 90%	AD versus CN versus MCI
[15]	ADNI	MRI PET	FSBi-LSTM	LSTM can effectively alleviate the gradient vanishing problem	AD versus NC, pMCI versus MC, and sMCI vsNC
[16]	ADNI	PET	3D CNN	Focus on the temporal lobe area, including the hippocampus for CN/ AD classification	CN vs AD
[17]	ADNI	sMRI	3D-DSA-CNN	Model predicts the AD more accurately than other state-of-the-art predictors	AD
[18]	ADNI	MRI	3D CNN, CapsNets	98.42%, 94.06% (for AD vs. NC)	AD, MCI, NC
[19]	ADNI	fMRI	KNN, SVM, DT, LDA, RF, CNN	77.5, 85.8, 91.7, 79.5, 85.1, and 96.7%, respectively	AD
[20]	ADNI	MRI	CN based framework	GoogleNet—98.88%; ResNet-18—98.01%; ResNet-152–98.14%; Accuracy—4%	AD, LMCI, MCI, CN
[21]	ADNI	MRI	CNN	Classification Binary–99.6, 99.8, and 97.8%; Multi—97.5%	AD versus CN
[22]	ADNI	MRI	Not stated	Highest Accuracy: 92.98% (EfficientNetB0); Lowest Loss: 0.0145 (ResNet50); Std deviation: 0–0.02	AD versus MCI versus CN
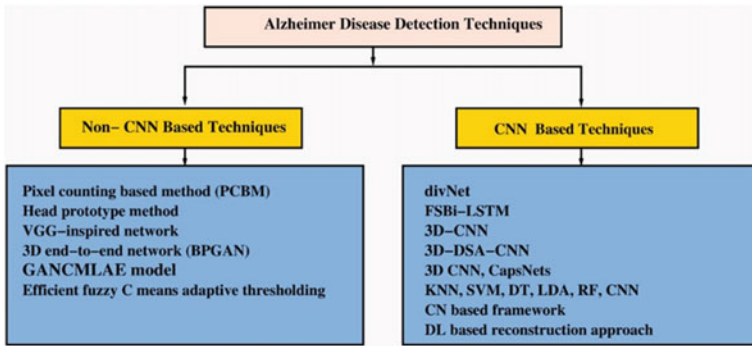
Fig. 4 Alzheimer's disease detection techniques

5 Conclusions

Making quantitative assessment and classification of AD is a challenging task. Various computational models are being developed to tackle this issue involving non-CNN and CNN-based techniques. We briefly reviewed some of the popular methods in this area and compared them to provide a clear picture of this research area. The published research works use different features to predict AD, use different datasets, different modalities, different methodologies to extract features, and their classification techniques are also different. Furthermore, the proposed methods are applied to different cohorts. Hence, most of the published works can only be compared qualitatively. In this chapter, we have given a detailed account of the works on the basis of modality, dataset used, technique applied, detection accuracy, obtained results, and classification for non-CNN-based methods and CNN-based methods (Table 3).

It is observed that CNN-based techniques are more effective in the early detection of AD. The major bottleneck for CNN-based work is the availability of sufficient samples to train the CNN. In future, the researchers may evaluate the effectiveness of combining non-CNN-based and CNN-based techniques. These computational efforts will further enable the risk detection of early dementia, provide early treatment, and reduce self-harm risk and mortality among the elderly.

Table 3 List of abbreviations

AD	Alzheimer's disease
ADNI	Alzheimer's disease neuroimaging initiative
ADVIAN	Alzheimer's disease VGG-inspired attention network
ANN	Artificial neural network
CBIR	Content-based image retrieval
CN	Cognitively normal
CNN	Convolutional neural network
CT	Computed tomography
DA	Data augmentation
DL	Deep learning
DNN	Deep neural network
DT	Decision tree
EFCMAT	Efficient fuzzy C means adaptive thresholding
FBB	F-18 florbetaben
FDG	Fluoro-deoxy-D-glucose
FFNN	Feedforward neural network
fMRI	Functional MRI
FSBi-LSTM	Fully stacked bidirectional long short-term memory
GANCMLAE	Generative adversarial networks constrained multiple loss auto encoder
HC	Healthy control
KNN	K-nearest neighbor
LDA	Linear discrimination analysis
LMCI	Late mild cognitive impairment
MAE	Mean absolute error
MCI	Mild cognitive impairment
MIRIAD	Minimal interval resonance imaging in Alzheimer's disease
ML	Machine learning
MRI	Magnetic resonance imaging
MSE	Mean squared error
NC	Normal control
OASIS	Open access series of imaging studies
PCBM	Pixel counting-based method
PET	Positron emission tomography
pMCI	Progressive mild cognitive impairment
PSNR	Peak signal-to-noise ratio
RF	Random forest
RNN	Recurrent neural network

(continued)

Table 3 (continued)

sMCI	Stable mild cognitive impairment
sMRI	Structural MRI
SPECT	Single photon emission computed tomography
SPM	Statistical parametric mapping
SSIM	Structural similarity index measure
SVM	Support vector machine
VGG	Visual geometry group

References

1. Nestor P, Scheltens P, Hodges J (2004) Advances in the early detection of Alzheimer's disease. Nat Med 10:S34–S41. https://doi.org/10.1038/nrn1433
2. Alzheimer's Disease Neuroimaging Initiative: ADNI https://adni.loni.usc.edu. Last accessed 7 Aug 2022.
3. OASIS Brains—Open Access Series of Imaging Studies. https://www.oasisbrains.org. Last accessed 7 Aug 2022
4. Minimal Interval Resonance Imaging in Alzheimer's Disease: MIRIAD. http://miriad.drc.ion.ucl.ac.uk/. Last accessed 7 Aug 2022
5. Johnson KA, Fox NC, Sperling RA, Klunk WE (2012) Brain imaging in Alzheimer disease. Cold Spring Harb Perspect Med 2(4):a006213. https://doi.org/10.1101/cshperspect.a006213
6. Priya T, Kalavathi P, Prasath VBS, Rajangam S (2021) Brain tissue volume estimation to detect Alzheimer's disease in magnetic resonance images. Soft Comput 25:10007–10017. https://doi.org/10.1007/s00500-021-05621-8
7. Kumar PR, Arunprasath T, Rajasekaran MP, Vishnuvarthanan G (2018) Computer-aided automated discrimination of Alzheimer's disease and its clinical progression in magnetic resonance images using hybrid clustering and game theorybased classification strategies. Comput Electr Eng 72:283–295. https://doi.org/10.1016/j.compeleceng.2018.09.019
8. Wang S, Zhou Q, Yang M, Zhang Y-D (2021) ADVIAN: Alzheimer's disease VGG-inspired attention network based on convolutional block attention module and multiple way data augmentation. Front Aging Neurosci 13:687456. https://doi.org/10.3389/fnagi.2021.687456
9. Zhang J, He X, Qing L, Gao F, Wang B (2022) BPGAN: Brain PET synthesis from MRI using generative adversarial network for multi-modal Alzheimer's disease diagnosis. Comput Methods Programs Biomed 217:106676. https://doi.org/10.1016/j.cmpb.2022.106676
10. Jin S, Sheng C, Shi R, Zhang Q, Zhang S, Zhang L, Ding C, Wang L, Wang L, Han Y, Jiang J (2022) GANCMLAE: individual atrophy detection for AD and MCI. SSRN Electron J. https://doi.org/10.2139/ssrn.4017382
11. Ramana T, Nandhagopal S (2021) Alzheimer disease detection and classification on Magnetic Resonance Imaging (MRI) brain images using Improved Expectation Maximization (IEM) and Convolutional Neural Network (CNN). Turk J Comput Math Educ 12(11):5998–6006
12. Kang SK, Choi H, Lee JS (2021) Translating amyloid PET of different radiotracers by a deep generative model for interchangeability. Neuroimage 232:117890. https://doi.org/10.1016/j.neuroimage.2021.117890
13. Sathiyamoorthi V, Ilavarasi AK, Murugeswari K, Ahmed ST, Aruna Devi B, Kalipindi M (2021) A deep convolutional neural network based computer aided diagnosis system for the prediction of Alzheimer's disease in MRI images. Measurement 171:108838. https://doi.org/10.1016/j.measurement.2020.108838
14. Khagi B, Kwon G (2020) R, 3D CNN design for the classification of Alzheimer's disease using brain MRI and PET. IEEE Access 8:217830–217847. https://doi.org/10.1109/ACCESS.2020.3040486

15. Feng C et al (2019) Deep learning framework for Alzheimer's disease diagnosis via 3D-CNN and FSBi-LSTM. IEEE Access 7:63605–63618. https://doi.org/10.1109/ACCESS.2019.291 3847

16. Islam J, Zhang Y (2019) Understanding 3D CNN Behavior for Alzheimer's disease diagnosis from brain PET scan. https://doi.org/10.48550/arXiv.1912.04563

17. Hosseini-Asl E, Ghazal M, Mahmoud A, Aslantas A, Shalaby AM, Casanova MF, Barnes GN, Gimel'farb G, Keynton R, El-Baz A (2018) Alzheimer's disease diagnostics by a 3D deeply supervised adaptable convolutional network. Front Biosci (Landmark Ed) 23(3):584–596. https://doi.org/10.2741/4606. PMID: 28930562

18. Kruthika KR, Rajeswari, Maheshappa HD (2019) CBIR system using capsule networks and 3D CNN for Alzheimer's disease diagnosis. Inform Med Unlocked 16:100227. https://doi.org/10.1016/j.imu.2019.100227

19. Amini M, Pedram M M, Moradi A R, and Ouchani M (2021) Diagnosis of Alzheimer's disease severity with fMRI images using robust multitask feature extraction method and Convolutional Neural Network (CNN). Comput Math Methods Med. https://doi.org/10.1155/2021/5514839

20. Farooq A, Anwar S, Awais M and Rehman S (2017) A deep CNN based multi-class classification of Alzheimer's disease using MRI. IEEE Int Conf Imag-Ing Syst Tech (IST) 1–6. https://doi.org/10.1109/IST.2017.8261460

21. AbdulAzeem Y, Bahgat WM, Badawy M (2021) A CNN based framework for classification of Alzheimer's disease. Neural Comput Appl 33:10415–10428. https://doi.org/10.1007/s00521-021-05799-w

22. Savaş S (2022) Detecting the stages of Alzheimer's disease with pre-trained deep learning architectures. Arab J Sci Eng 47:2201–2218. https://doi.org/10.1007/s13369-021-06131-3

23. Weller J, Budson A (2018) Current understanding of Alzheimer's disease diagnosis and treatment. F1000Res 7:1161. https://doi.org/10.12688/f1000research.14506.1

24. Acer N, Turgut AT, Turgut M, and Özsunar Y (2011) Quantification of volumetric changes of brain in neurodegenerative diseases using magnetic resonance imaging and stereology. INTECH Open Access Publisher

25. Ahmed MR, Zhang Y, Feng Z, Lo B, Inan OT, Liao H (2019) Neuroimaging and machine learning for dementia diagnosis: recent advancements and future prospects. IEEE Rev Biomed Eng 12:19–33. https://doi.org/10.1109/RBME.2018.2886237

26. Tanveer M, Richhariya B, Khan R, Rashid A, Khanna P, Prasad M, Lin C (2020) Machine learning techniques for the diagnosis of alzheimer's disease: a review. ACM Trans Multimed Comput Commun Appl (TOMM) 16(1s):1–35. https://doi.org/10.1145/3344998

27. Gautam R, Sharma M (2020) Prevalence and diagnosis of neurological disorders using different deep learning techniques: a meta-analysis. J Med Syst 44(2):49. https://doi.org/10.1007/s10916-019-1519-7

28. Al-Shoukry S, Rassem TH, Makbol NM (2020) Alzheimer's diseases detection by using deep learning algorithms: a mini-review. IEEE Access 8:77131–77141. https://doi.org/10.1109/ACCESS.2020.2989396

29. Noor MBT, Zenia NZ, Kaiser MS et al (2020) Application of deep learning in detecting neurological disorders from magnetic resonance images: a survey on the detection of Alzheimer's disease, Parkinson's disease and schizophrenia. Brain Inf 7(11). https://doi.org/10.1186/s40708-020-00112-2

30. Ebrahimighahnavieh A, Luo S, Chiong R (2020) Deep learning to detect Alzheimer's disease from neuroimaging: A systematic literature review. Comput Methods Programs Biomed 187:105242. https://doi.org/10.1016/j.cmpb.2019.105242

31. Fathi S, Ahmadi M, Dehnad A (2022) Early diagnosis of Alzheimer's disease based on deep learning: a systematic review. Comput Biol Med 146:105634. https://doi.org/10.1016/j.compbiomed.2022.105634

32. Gao S, Lima D (2022) A review of the application of deep learning in the detection of Alzheimer's disease. Int J Cogn Comput Eng 3:1–8. https://doi.org/10.1016/j.ijcce.2021.12.002

DR-FL: A Novel Diabetic Retinopathy Grading with Federated Learning Using Fundus Images

N Jagan Mohan, R. Murugan ⓘ**, and Tripti Goel** ⓘ

1 Introduction

Early disease detection improves the accuracy of disease diagnosis in the field of medical image analysis. Diabetes is caused by a lack of insulin, which causes blood glucose levels to increase. It affects 425 million people worldwide [1].

Diabetic Retinopathy (DR) is a diabetes condition that causes the retinal blood vessels (BV) to enlarge and spill liquids and plasma into retinal areas [2]. If DR progresses to an advanced stage, it might result in visual loss. DR causes 2.6% of vision loss worldwide [1]. People with diabetes who have been sick with the condition for a long time are more likely to get DR. Frequent retina examination is necessary for diabetic people to identify and manage DR early enough to avoid vision loss [3]. The presence of various sorts of lesions on a retina image is used to identify DR, such as microaneurysms (MA) [4], soft and hard exudates (EX) [5], hemorrhages (HEM), and abnormal BV [6] growth in optic disc (OD) [7]. Figure 1 shows the fundus images with the corresponding retinal lesions.

The initial symptom of DR is MA, which emerges as little red spherical spots on the eyeball due to a weakening in the BVs sidewalls. There are sharp borders, and the dimension is less than 125 μm. HEMs are larger patches on the retina with an irregular border of more than 125 μm in diameter. Plasma leaking causes hard EX, which looks like bright yellow patches on the retinal surface. They are situated in the retina's outermost layer and feature sharp corners. Soft EXs are white patches on the eyeball generated by nerve fiber enlargement that appears oval or circular.

Based on these abnormal retinal features, the DR is broadly categorized as non-proliferative DR (NPDR) and proliferative DR (PDR) [3]. The NPDR is further

N. Jagan Mohan · R. Murugan (✉) · T. Goel
Bio-Medical Imaging Laboratory (BIOMIL), Department of Electronics and Communication Engineering, National Institute of Technology Silchar, Silchar 788010, Assam, India
e-mail: murugan.rmn@ece.nits.ac.in

**Fig. 1** Typical fundus image with retinal lesions [8]
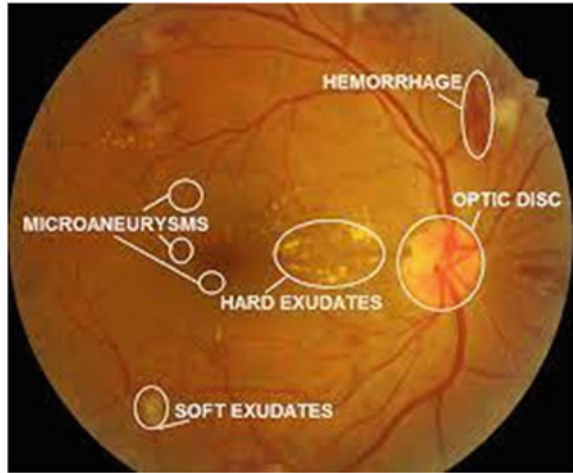
classified as mild, moderate, and severe. The stages of DR are briefly summarized in Table 1. Figure 2 shows a sample of DR images with grading.

Automated solutions for DR identification are less expensive and time-consuming than traditional diagnosis [9]. Manual assessment is more likely to misinterpret and takes more time than automatic procedures. This paper examines contemporary deep learning (DL) based DR automated approaches for detecting and classifying DR. Also, this work proposes a new approach called federated learning (FL), an advanced DL technique for DR classification.

Table 1 DR severity levels

Lesions	DR severity
No lesions found	No DR (Healthy fundus)
Mild NPDR	The presence of MA only
Moderate NPDR	More than Mild with HEM
Severe NPDR	More than 20 HEM, venous bleeding
PDR	Neo vascularization
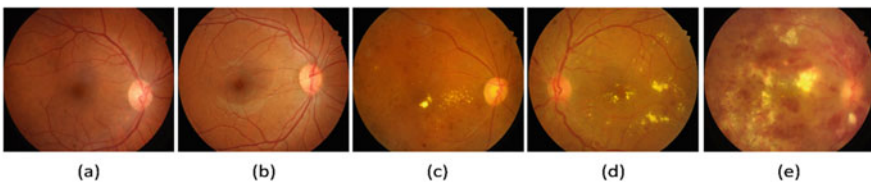
Fig. 2 Typical fundus images with **a** No DR signs **b** Mild **c** Moderate **d** Severe **e** PDR [3]

The novelty of this work includes.

- We propose a novel deep architecture for the central server model that categorizes the DR stages better.
- The proposed model works better for low-resolution fundus images since the server model extracts global features and helps in effective DR classification.

The rest of the paper is organized as follows:

Section 2 explains the DL techniques proposed by the researchers for DR detection or grading. The proposed approach with detailed explanations is presented in Sect. 3. The DR database details and results obtained with the proposed framework are presented in Sect. 4. Section 5 concludes the paper with future works.

2 Literature Review

DL is a subset of ML algorithms. DL uses hierarchy layering of non-linear processes to learn unsupervised characteristics and categorization patterns. DL models help in computer-assisted medical diagnostic [10, 11]. The categorization, segmentation, recognition, extraction, and normalization of images are examples of DL applications in medical imaging. This section briefly explains the works done for the DR grading using DL techniques using fundus images.

Xu et al. [12] proposed a CNN-based DR binary classification model. A total of 1000 fundus images from the Kaggle Database were used and are resized to 224 $\times$ 224 $\times$ 3. The database is increased using the data augmentation techniques such as scaling and rotation. This approach used several CNN layers to classify the DR and reported an accuracy of 94.5%. Quellec et al. [13] suggested a referable DR classification model using a pre-trained AlexNet. In this technique, the database is divided into two categories, namely referable DR (DR stage 2 or more) and non-referable (Healthy or mild). This technique was evaluated on three databases, e-Ophtha, Kaggle, and DIARETDB1. In this work, the fundus images were resized to 448 $\times$ 448 $\times$ 3. This work reported an Area Under Curve (AUC) of 0.954.

IDX-DR device combined with CNN is proposed in [14] for DR classification using 1748 fundus images belonging to the MESSIDOR-2 database. The database was increased using augmentation techniques in this work and reported a Specificity of 87%, Sensitivity of 96.8%. However, this model classifies only healthy and referable DR. A five-stage DR classification model was proposed in [15] using the Kaggle database. In this work, the preprocessing steps included were resizing the fundus images to 512 $\times$ 512 $\times$ 3 and color normalization. The authors reported an Accuracy of 75% and a specificity of 95% with their custom CNN model. However, this model is tested only on a single database. The performance of the pre-trained networks such as Alexnet, InceptionV3, and VGG16 was studied in [16]. They have used only 166 fundus images from the Kaggle database, which were resized to 227 $\times$ 227 $\times$ 3, 299 $\times$ 299 $\times$ 3, and 224 $\times$ 224 $\times$ 3, respectively, to train the pre-trained models. The accuracy reported in this work for DR classification is 37.43, 63.23,

and 50.03%, respectively, for AlexNet, InceptionV3, and VGG16. However, this approach used only one database with a limited number of fundus images, making the model learn insufficient features in DR classification.

Wan et al. [17] examined the performance of the pre-trained models in DR classification. The pre-trained networks used in this work include VGG-16, Alexnet, Googlenet, and Resnet. This work used the Kaggle DR dataset, which comprises 35,126 fundus images, to train the models to recognize DR phases. The final FC layer and hyperparameters were fine-tuned to excellently improve the model's performance. The fundus images were enhanced, clipped, and normalized during the preprocessing phase. VGG-16 had better performance than other models, with an accuracy of 95.68%, an AUC of 0.9786, and a specificity of 97.43%. However, using many datasets improves the reliability and generalizability.

A modified KAZE technique is proposed in [9] for early DR detection with a reliable and quick localization of the EX in fundus images retrieving the feature points using extreme learning machine auto-encoders. The primary phases of the suggested technique were preprocessing, OD localization, dimensionality reduction, and EX localization. This technique was tested on MESSIDOR, DIARETDB0, 1, e-Ophtha, and a locally acquired retinal database. This technique achieved 96.5% sensitivity, 96.4% specificity, and 97% accuracy. Mohan et al. [3] proposed a unique four-step feature selection approach for DR classification using deep ensemble features. The entropy images raise the effectiveness of the fundus attributes in the first stage. The deep ensemble model, a combination of Vgg19, InceptionV3, and Resnet101, retrieved the feature space in the second stage. Then, efficient features were selected using a novel feature selection technique, neglecting the unuseful features. The computational complexity was reduced by picking relevant characteristics using majority voting approaches. This technique was tested on IDRiD, Kaggle, and MESSIDOR-2 and reported an accuracy of 97.78%.

In the literature, most of the works reported by the researchers were tested on a few databases. Most of the works are limited to the specific database only. Therefore, testing the models on various databases is required to generalize the model. One of the biggest challenges in medical imaging is to collect a real-time database. There are several restrictions to collecting real-time fundus images from diabetic patients. Few of them include data privacy and security. The Health Insurance Portability and Accountability Act of 1996, which established requirements for medical professionals to retain, control, and utilize such data, gives patients legal protection to their data and patient data. When private details are destroyed, it is not easy to link data to a specific individual. On the other hand, privacy burglars can swiftly use association methods to identify personal information. Therefore, there is a requirement for automated DR grading techniques with fundus data privacy and protection of patient data. Therefore, we have proposed a novel DR grading technique based on FL, which provides fundus data privacy and security as the client's data is not shared with the central model.

The contributions to this work include.

- We adopted a Federated averaging (FA) algorithm to classify DR.

- We have designed a central server model using deep layers, which provides better DR classification results.
- The server model is designed so that even if the fundus image resolution is low, the model categorizes the DR better.
- The proposed model is trained and tested on the APTOS (Asia Pacific Tele-Ophthalmology Society) and Kaggle DR database.
- We have presented the results obtained with the individual clients trained on the central server and the proposed model.

3 Methods and Materials

The proposed model for DR grading using the FA technique is shown in Fig. 3. A detailed explanation of the proposed approach is made in this section. This section details the database used in the current approach, followed by explaining the proposed model with a novel central server architecture.

3.1 Database

The proposed model is trained and tested using the APTOS [18] and Kaggle DR [19] databases. The APTOS database consists of 3662 training images and 1928 testing images that help DR severity grading. Each database consists of five stages of DR fundus images, including healthy/standard fundus images. The standard retinal fundus images that do not have DR fall into the first type of DR. Each of the latter three categories reflects more significant retinal impairment than the previous one. The fifth category, proliferative DR, includes new BV's in the retina or pre-retinal HEM samples. The Kaggle database consists of 88,702 fundus images of various DR grades. We have used 1500 images in the current work, with each grade consisting

Fig. 3 Generalized model for FA
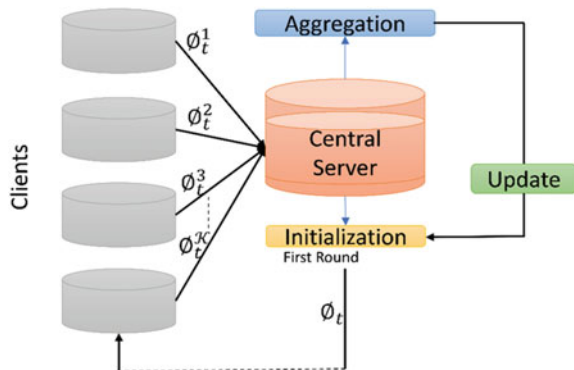
of 300 images. We have used 1200 images to train and 300 images to test the model, dividing the database into an 80:20 ratio.

3.2 Methodology

We have considered a synchronized updating mechanism sent in rounds in this work. We have considered a fixed number of clients represented $\mathscr{K}$ that all have their local database. A random number of clients C_r is chosen at the start of every round. The central server delivers or updates the present model parameters to each client for each round. The experiment trials reveal that integrating more clients above a specific limit results in declining results and require massive computational resources. Therefore, we only picked a subset of our clients for effective DR grading. After that, each chosen client does local computations based on the global state and its database before updating the server. The server then changes (updates) its global level before repeating the operation.

The objective of the DR grading model is to find the optimal value for Eq. (1).

$$\min_{\emptyset \in R^d} f(\emptyset) \text{ where } f(\emptyset) = \frac{1}{n} \sum_{i=1}^{n} f_i(\emptyset) \tag{1}$$

In ML techniques, we consider the loss of the expectation on (P_i, Q_i) as $f_i(\emptyset) = loss(P_i, Q_i, \emptyset)$ with $\emptyset$ parameters. Here, the fundus database is partitioned over the number of clients $\mathcal{K}$, with $A_{\mathcal{K}}$ being the collection of fundus image indices on client K, with $n_{\mathcal{K}} = |A_{\mathcal{K}}|$. Therefore, Eq. (1) can be rewritten as Eq. (2).

$$f(\emptyset) = \sum_{\mathcal{K}=1}^{\mathcal{K}} \frac{n_{\mathcal{K}}}{n} F_{\mathcal{K}}(\emptyset) \text{ where } F_{\mathcal{K}}(\emptyset) = \frac{1}{n_{\mathcal{K}}} \sum_{i \in A_{\mathcal{K}}} f_i(\emptyset) \tag{2}$$

We have distributed the training images uniformly across all the clients in this work. In practice, many developments may be interpreted as modifying the stability of the approach (henceforth loss function) with various stochastic gradient descent (SGD) to make it more accessible to optimization via basic gradient-based approaches [20]. The gradient is calculated for a single batch selected randomly (client) per one communication round in FL. This enables the computation to be effective; however, it requires more rounds to train the model to achieve good results.

As the number of clients increases in FL, the computational resource requirement increases. Therefore, in the present work, we have selected the optimal batch size with SGD. We adopted the FA technique in classifying the DR using a novel central server model in the proposed work. In this technique, the central server averages updated weights $\emptyset_{t+1} \leftarrow \emptyset_t - \rho \sum_{\mathcal{K}=1}^{\mathcal{K}} \frac{n_{\mathcal{K}}}{n} g_{\mathcal{K}}$, since $\sum_{\mathcal{K}=1}^{\mathcal{K}} \frac{n_{\mathcal{K}}}{n} g_{\mathcal{K}} = \nabla f(\emptyset_t)$, and $g_{\mathcal{K}} = \nabla F_{\mathcal{K}}(\emptyset_t)$ Where ρ is a constant learning rate (LR) with $C_r = 1$. For every

client $\mathcal{K}$, the equivalent updates are given to the central server $\emptyset_{t+1} \leftarrow \emptyset_t - \rho g_{\mathcal{K}}$ and then $\emptyset_{t+1} \leftarrow \sum_{\mathcal{K}=1}^{\mathcal{K}} \frac{n_{\mathcal{K}}}{n} \emptyset_{t+1}^{\mathcal{K}}$. In FA, the clients train on the central server using the local data iterating the local update $\emptyset^{\mathcal{K}} \leftarrow \emptyset^{\mathcal{K}} - \rho \nabla F_{\mathcal{K}}(\emptyset^{\mathcal{K}})$ several times before averaging. The computational cost of the proposed model is reduced using the number of communication rounds of 100 and a local batch size of 16 for client updates.

3.3 Central Server Model

This section explains the design of the novel central server model that helps grade the DR. Figure 4 shows the architecture of the server model.

We have used CNN-based server model for DR classification. The central server model consists of two paths, namely short and main paths, that help better DR classification. The fundus images are resized to 256×256 before feeding the server model. The server model consists of five convolutional (Conv) layers, four max-pooling layers, two fully connected (FC) layers, and a softmax and classification layers. The efficient fundus features are required for grading the DR. Therefore, the two paths in the server model provide efficient features that better describe the tiny details of the fundus image, such as MA. The short path provides better retinal lesions such as HEM and EX features. Based on the availability of the computational resources, most of the researchers resize the fundus images to a lower dimension. As

Fig. 4 The central server model
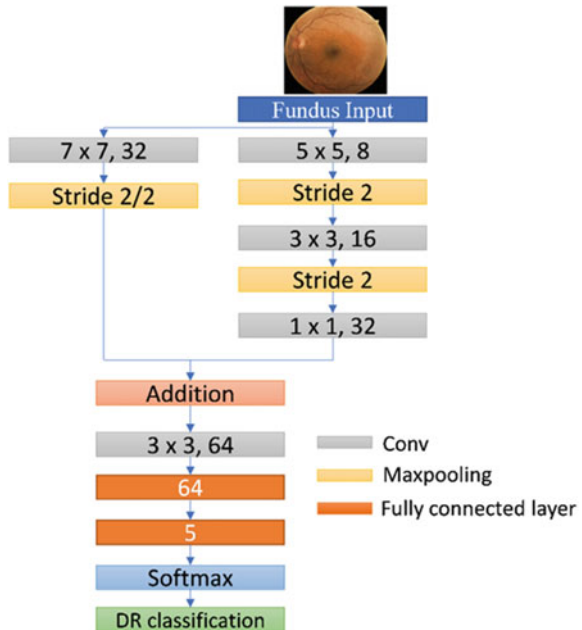
the resolution of the fundus image reduces, there are chances of degrading the quality of the retinal lesions. Also, the low-resolution images make the model susceptible to global noise. Therefore, to solve this issue, motivated by [21], we have designed a short path with 7×7 Conv layer 32 filters to improve the features gained from the early layers for better representations of global structures.

4 Results

The results obtained with the proposed work are discussed in this section with the performance metrics.

4.1 Performance Metrics

One of the most investigated fields globally in medical image processing is classification issues. Almost all medical and industrial contexts have use cases. We need a measure that evaluates discrete categories in some way since classification algorithms provide discrete output. Performance metrics such as Accuracy (Acc) [22], Specificity (Sp), F1-score [23], and Precision (P) [3] assess a model's performance and provide feedback on how excellent or terrible the classification is; however, they do so differently. Therefore, in the current work, we have measured the performance of the proposed approach using performance metrics that reveal the model's suitability for DR detection.

4.2 Experimental Results

This section presents the experimental results obtained for DR classification with individual clients trained on the server model and the average of the updated clients on the server. In this work, we have distributed 1500 fundus data to three clients that receive 500 images in the IID (Independent Identical Distribution). 1200 fundus images train the central server and are tested with 300 fundus images using 100 communication rounds. The performance of the proposed model is tested with individual clients trained on the central server and the average of the central server trained with client data with updated weights. The results obtained with individual clients trained on central with fixed learning of 0.001 are depicted in Table 2. From Table 2, it is observed that client1 achieved a low Acc of 89.71%, and client2 achieved a high Acc of 93.36%. The performance of the individual clients trained on the server model is shown in Fig. 5 in terms of the receiver operating characteristics curve.

We present an extended performance analysis of the proposed method with variable LR. The results obtained with the server model using FA with different LRs

Table 2 Performance of the individual clients trained on the central server

Client	Acc	Sp	P	F1 score
1	89.71	97.418	89.8	0.89
2	93.36	98.4189	93.6	0.939
3	91.39	98.1	91.4	0.916

Fig. 5 The performance of the individual clients in terms of ROC
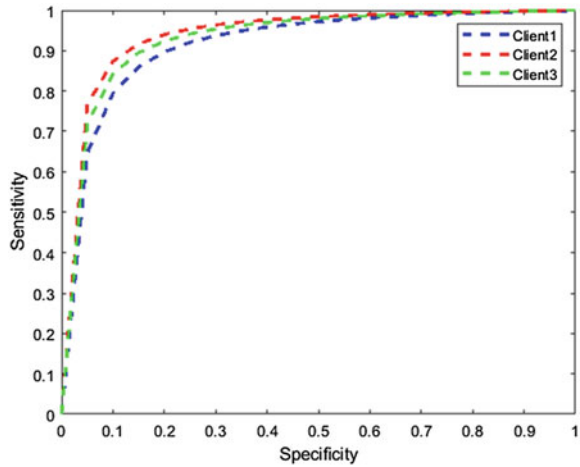
are depicted in Table 3. As depicted in Table 3, the results obtained with LR = 0.001 provide better results than 0.1 and 0.01 with the 100 communication rounds. Figure 6 shows the performance of the proposed model with different LR using the ROC curve. The central model is trained with three clients in 100 communication rounds with a batch size of 32.

Table 3 The performance of the proposed model in DR classification with variable learning rate

LR	Acc	Sp	P	F1 score
0.1	86.33	96.5738	86.6	0.869
0.01	92	97.999	92.2	0.925
0.001	93.8	98.4183	93.8	0.929

Fig. 6 Performance of the
proposed model with
different LR using ROC
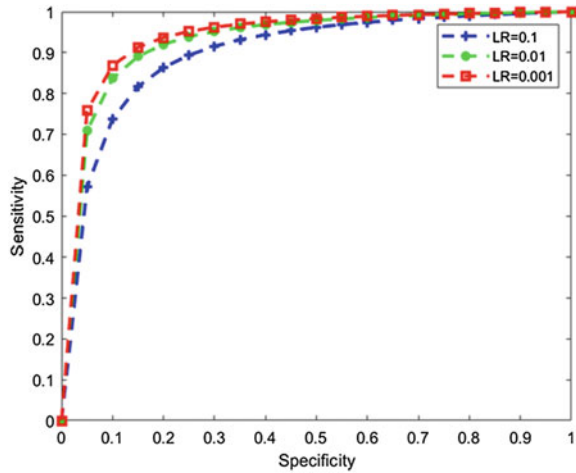
5 Conclusion

Diabetes causes diabetic retinopathy, which results in irreversible vision loss due to excessive blood sugar levels. Manually treating diabetic patients is time-consume and requires experts. Fundus image analysis helps to grade diabetic retinopathy. However, patients and the hospital don't share sensitive data. Therefore, we need an automated diabetic retinopathy grading that provides privacy and security to the fundus data. In this work, we have proposed a DR-FL model that provides better diabetic retinopathy grading results with fewer communication rounds using the federating learning, providing privacy to the fundus data. In DR-FL, we have used a novel convolutional neural network as a central server that grades diabetic retinopathy effectively. We have considered three clients that train the server model with 1200 images. The performance of the individual clients trained on the server model and the DR-FL model are discussed in the paper. The federated learning approach helps train the server model without sharing the actual data providing the data security. Training correct models on dispersed devices, and federated learning is the ideal security paradigm.

References

1. Alyoubi WL, Shalash WM, Abulkhair MF (2020) Diabetic retinopathy detection through deep learning techniques: a review. Inform Med Unlocked 20:100377

2. Mohan NJ, Murugan R, Goel T, Roy P (2021) Exudate localization in retinal fundus images using modified speeded up robust features algorithm. In: 2020 IEEE-EMBS conference on biomedical engineering and sciences (IECBES), pp 367–371

3. Jagan Mohan N, Murugan R, Goel T, Mirjalili S, Roy P (2021) A novel four-step feature selection technique for diabetic retinopathy grading. Phys Eng Sci Med 44(4):1351–1366

4. Jagan Mohan N, Murugan R, Goel T, Roy P (2020) An improved accuracy rate in microaneurysms detection in retinal fundus images using non-local mean filter. In: International conference on machine learning, image processing, network security and data sciences, pp 183–193

5. Mohan NJ, Murugan R, Goel T, Roy P (2021) Exudate detection with improved U-net using fundus images. In: 2021 International conference on computational performance evaluation (ComPE), pp 560–564

6. Mohan NJ, Murugan R, Goel T (2022) Machine learning algorithms for hypertensive retinopathy detection through retinal fundus images. In: Computer vision and recognition systems: research innovations and trends, p 39

7. Mohan NJ, Murugan R, Goel T, Roy P (2020) Optic disc segmentation in fundus images using operator splitting approach. In: 2020 advanced communication technologies and signal processing (ACTS), pp 1–5

8. Borsos B, Nagy L, Iclănzan D, Szilágyi L (2019) Automatic detection of hard and soft exudates from retinal fundus images. Acta Univ Sapientiae, Inform 11(1):65–79. https://doi.org/10.2478/ausi-2019-0005

9. Mohan NJ, Murugan R, Goel T, Roy P (2022) Fast and robust exudate detection in retinal fundus images using extreme learning machine autoencoders and modified KAZE features. J Digit Imaging 1–18

10. Goel T, Murugan R, Mirjalili S, Chakrabartty DK (2021) OptCoNet: an optimized convolutional neural network for an automatic diagnosis of COVID-19. Appl Intell 51(3):1351–1366

11. Jagan Mohan N, Murugan R, Goel T (2022) Deep learning for diabetic retinopathy detection: challenges and opportunities, pp 213–232. https://doi.org/10.1007/978-981-19-2416-3_12

12. Xu K, Feng D, Mi H (2017) Deep convolutional neural network-based early automated detection of diabetic retinopathy using fundus image. Molecules 22(12):2054

13. Quellec G, Charrière K, Boudi Y, Cochener B, Lamard M (2017) Deep image mining for diabetic retinopathy screening. Med Image Anal 39:178–193

14. Abràmoff MD et al (2016) Improved automated detection of diabetic retinopathy on a publicly available dataset through integration of deep learning. Invest Ophthalmol Vis Sci 57(13):5200–5206

15. Pratt H, Coenen F, Broadbent DM, Harding SP, Zheng Y (2016) Convolutional neural networks for diabetic retinopathy. Procedia Comput Sci 90:200–205

16. Wang X, Lu Y, Wang Y, Chen W-B (2018) Diabetic retinopathy stage classification using convolutional neural networks. In: 2018 IEEE international conference on Information Reuse and Integration (IRI), pp 465–471

17. Wan S, Liang Y, Zhang Y (2018) Deep convolutional neural networks for diabetic retinopathy detection by image classification. Comput Electr Eng 72:274–282

18. APTOS 2019 Blindness Detection. https://www.kaggle.com/c/aptos2019-blindness-detection

19. Kaggle Diabetic Retinopathy Detection. https://www.kaggle.com/c/diabetic-retinopathy-detection

20. Heaton J (2018) Ian goodfellow, yoshua bengio, and aaron courville: Deep learning. Springer, Berlin

21. Wang Y, Zhang H, Chae KJ, Choi Y, Jin GY, Ko S-B (2020) Novel convolutional neural network architecture for improved pulmonary nodule classification on computed tomography. Multidimension Syst Signal Process 31(3):1163–1183. https://doi.org/10.1007/s11045-020-00703-6

22. Anupam A, Mohan NJ, Sahoo S, Chakraborty S (2021) Preliminary diagnosis of COVID-19 based on cough sounds using machine learning algorithms. In: 2021 5th International Conference on Intelligent Computing and Control Systems (ICICCS), pp 1391–1397

23. Jagan Mohan N, Kiran PDN (2022) GIL-CNN: a novel multi-path features for COVID-19 detection using CT-scan images. IETE J Res. https://doi.org/10.1080/03772063.2022.2098194

Efficacy of Various Feedback Gains by the Active Dynamics Vibration Absorber for Tremor Suppression Due to Parkinson's Disease

S. Mohanty and S. K. Dwivedy

Keywords Dynamic vibration absorber · Tremor · HBM · Actuator · Feedback

1 Introduction

Tremors are involuntary movements of one or more body parts that are commonly seen in Parkinson's disease (PD) patients. Tremors impact around 25 individuals per 1 lakh people in India, and more than 4% of adults over the age of 40, or 24.91 million people worldwide, suffer from tremors [1, 2]. The tremors in the patient target mainly the forearm, wrist, hand, and in some cases neck and other body parts [1–4]. Tremors in Parkinson's disease patients are caused by a neurological or neural problem that is difficult to treat successfully with medical therapies such as medicines and surgery [1–5]. Though tremors are not life threatening, they significantly decrease the patient's ability to do daily activities such as eating, writing, etc. Therefore, numerous mechanical-based attachments have been developed that are worn on the vibrating/tremoring body parts as a bracelet, ring, or smartwatch to minimize the persistent oscillatory motions [3–8]. Tremors affecting the PD patient's hand are mainly essential tremors which are very common compared to their other forms. Gebai et. al. [3, 4] studied extensively the dynamics of the vibration or tremor suppression of a human hand by using passive DVA. Masoumi et. al. [5] fabricated a passive DVA with a 120 g weight in the form of a wearable device to suppress

S. Mohanty (✉) · S. K. Dwivedy
Department of Mechanical Engineering, Indian Institute of Technology Guwahati, Assam 781039, India
e-mail: siba.mech@gmail.com

S. K. Dwivedy
e-mail: dwivedy@iitg.ac.in

the tremors in the human hand due to PD. Rahnavard et al. [6] obtained the optimal parameters such as stiffness, damping, and distance of attachment of the passive DVA to suppress the tremors in the hand. They used H2 optimization techniques to obtain the optimal parameters of the absorber. Hashemi et al. [7] also worked on the optimization and showed both theoretically and experimentally that an 80% reduction of tremors can be achieved by the passive DVA. López-Blanco et al. [8] used a gyroscope-based smartwatch to reduce tremors in the forearm. Buki et al. [9] designed and fabricated a passive DVA in the form of a bracelet and showed through simulations and patient trials in reducing 85% of tremors in the human forearm at the resonance. Most of the studies carried out in the above literature used a linear approach and passive techniques. Due to this vibration suppression is also limited and suited for a specific range of frequencies. But implementation of an active approach with nonlinearities in the DVA can significantly increase the attenuation and can increase the bandwidth of suppression of tremors. Mohanty and Dwivedy [10–19] and Mohanty et al. [20] investigated vibration attenuation of mechanical and civil systems under various excitations by using an active vibration absorber (AVA). They studied both linear and nonlinear aspects and showed the improved performance of the active approach over the passive approach. From the aforementioned research, it can be observed that tremor suppression of the human forearm considering an active approach by various feedback gains, nonlinear spring stiffness and attenuation of tremors for a broad range are not explored in the previously published works. Hence in the present work study has been undertaken to fill these gaps in the literature. In the next section, the system model is described.

2 System Model for Forearm Tremor Suppression by NADVA

Figure 1 shows the nonlinear ADVA (NADVA) attached to the nonlinear primary system. In this figure, the human forearm is modelled as the single degree of freedom (SDOF) nonlinear primary system having a mass (M), stiffness (K and K_{13}), and a damper (C). The nonlinear primary system (forearm) is considered to be base excited with displacement x_0. This base excitation is assumed as in motor-neuron disease like Parkinson's, many times the tremor to the forearm comes from the elbow and the muscles. Along with the base excitation, the nonlinear primary system is subjected to external harmonic excitation of $F_1 \cos(\Omega t)$ which may arise due to other disturbances such as active feedback gains, attached bracelet/absorber and tremors, etc. Here the secondary system/bracelet consists of a mass (m), stiffness (k and k_{23}), damper (c), PZT stack actuator, and a spring (k_3) in series connection with the PZT stack actuator. The stiffness of the PZT stack actuator is denoted as k_P^E. It may be noted that the active feedback gain (f_c) by the PZT stack actuator and spring k_3 is produced by the combination of displacement, velocity, and acceleration feedback from the primary system. The displacement of the nonlinear primary system and the absorber are

Fig. 1 System model of the nonlinear active dynamic vibration absorber
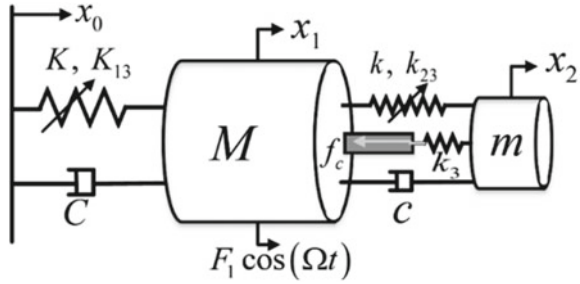
denoted as, x_1 and x_2, respectively. The coupled nonlinear governing equations of motion of the system by using Newton's second law are given below.

$$M\ddot{x}_1 = K(x_0 - x_1) + C(\dot{x}_0 - \dot{x}_1) + k(x_2 - x_1) + c(\dot{x}_2 - \dot{x}_1) - \\ K_{13}(x_0 - x_1)^3 + k_{23}(x_2 - x_1)^3 + F_1 \cos(\Omega t) - f_c \tag{1}$$

$$m\ddot{x}_2 = c(\dot{x}_1 - \dot{x}_2) + k(x_1 - x_2) + k_{23}(x_1 - x_2)^3 + f_c \tag{2}$$

It may be noted that the exclusion of the terms f_c, K_{13}, k_{23}, and $F_1 \cos(\Omega t)$, from Eqs. 1 and 2 will reduce to that of Buki et al. [9]. The governing Eqs. 1 and 2 are rewritten as follows.

$$\ddot{x}_1 = \omega_p^2(x_0 - x_1) + 2\zeta_1\omega_p(\dot{x}_0 - \dot{x}_1) + \mu\omega_a^2(x_2 - x_1) + 2\mu\zeta_2\omega_a(\dot{x}_2 - \dot{x}_1) \\ + \alpha(x_0 - x_1)^3 + \mu\beta(x_2 - x_1)^3 + F \cos \Omega t - F_{act} \tag{3}$$

$$\ddot{x}_2 = 2\zeta_2\omega_a(\dot{x}_1 - \dot{x}_2) + \omega_a^2(x_1 - x_2) + \beta(x_1 - x_2)^3 + F_{act}/\mu \tag{4}$$

where

$$\omega_a = \sqrt{\frac{k}{m}}, \ \mu = \frac{m}{M}, \ \zeta_1 = \frac{C}{2\sqrt{KM}}, \ \zeta_2 = \frac{c}{2\sqrt{km}}, \ \alpha = \frac{K_{13}}{M}, \ \beta = \frac{k_{23}}{m}, \ F = \frac{F_1}{M},$$

$$F_{act} = \frac{f_c}{M}, \ F_{act} = \omega_r(x_1 - x_2) + F_{ac}\ddot{x}_1 + F_v\dot{x}_1 + F_d x_1, \ \omega_r = \frac{k_r}{M}, \ k_r = \frac{k_P^E k_3}{(k_P^E + k_3)}$$

Equations 3 and 4 are solved using the harmonic balance method (HBM) and discussed in the next section.

3   Solution by HBM

In this section, the approximate solution of Eqs. 3 and 4 are obtained using HBM by the following supposition. Here the amplitudes (a_1 and a_2) and phases (φ_1 and φ_2) are assumed

$$x_1 = a_1(t) \cos(\Omega t - \varphi_1(t)) \tag{5}$$

$$x_2 - x_1 = a_2(t) \cos(\Omega t - \varphi_2(t)) \tag{6}$$

to be varying slowly with time t such that the higher-order terms ($\ddot{a}_1$, $\ddot{\varphi}_1$, $\ddot{a}_2$, $\ddot{\varphi}_2$, $\dot{a}_1\dot{\varphi}_1$, $\dot{a}_2\dot{\varphi}_2$, $\dot{\varphi}_1^2$ and $\dot{\varphi}_2^2$) can be neglected. The base excitation x_0 is considered equal to $X_0 \cos \Omega t$. The assumed solutions given in Eqs. 5 and 6 are substituted into Eqs. 3 and 4, and the coefficient of $\sin \Omega t$ and $\cos \Omega t$ are collected, which are given below in a matrix form.

$$\begin{bmatrix} a_1 & a_2 & a_3 & a_4 \\ a_5 & a_6 & a_7 & a_8 \\ a_9 & a_{10} & a_{11} & a_{12} \\ a_{13} & a_{14} & a_{15} & a_{16} \end{bmatrix} \begin{Bmatrix} \dot{a}_1 \\ \dot{\theta}_1 \\ \dot{a}_2 \\ \dot{\theta}_2 \end{Bmatrix} = - \begin{Bmatrix} b_1 \\ b_2 \\ b_3 \\ b_4 \end{Bmatrix} \tag{7}$$

where

$$a_1 = -2\Omega \cos \varphi_1 + 2\zeta_1\omega_p \sin \varphi_1 - 2F_{ac}\Omega \cos \varphi_1 + F_v \sin \varphi_1,$$
$$a_2 = 2\Omega A \sin \varphi_1 + 2\zeta_1\omega_p A \cos \varphi_1 + 2F_{ac}A\Omega \sin \varphi_1 + F_v A \cos \varphi_1,$$
$$a_3 = -2\mu\zeta_2\omega_a \sin \varphi_2, \ a_4 = -2\mu\zeta_2\omega_a B \cos \varphi_2,$$
$$a_5 = 2\Omega \sin \varphi_1 + 2\zeta_1\omega_p \cos \varphi_1 + 2F_{ac}\Omega \sin \varphi_1 + F_v \cos \varphi_1,$$
$$a_6 = 2A\Omega \cos \varphi_1 - 2\zeta_1\omega_p A \sin \varphi_1 + 2F_{ac}A\Omega \cos \varphi_1 - F_v A \sin \varphi_1,$$

$$a_7 = -2\mu\zeta_2\omega_a \cos \varphi_2, \ a_8 = 2\mu\zeta_2\omega_a B \sin \varphi_2,$$
$$a_9 = -2\Omega \cos \varphi_1 + (2F_{ac}\Omega \cos \varphi_1 - F_v \sin \varphi_1)\big/ \mu,$$
$$a_{10} = 2\Omega A \sin \varphi_1 - (2F_{ac}A\Omega \sin \varphi_1 + F_v A \cos \varphi_1)\big/ \mu,$$
$$a_{11} = -2\Omega \cos \varphi_2 + 2\zeta_2\omega_a \sin \varphi_2, \ a_{12} = 2\Omega B \sin \varphi_2 + 2\zeta_2\omega_a B \cos \varphi_2,$$
$$a_{13} = 2\Omega \sin \varphi_1 - (2F_{ac}\Omega \sin \varphi_1 + F_v \cos \varphi_1)\big/ \mu,$$
$$a_{14} = 2\Omega A \cos \varphi_1 - (2F_{ac}A\Omega \cos \varphi_1 - F_v A \sin \varphi_1)\big/ \mu,$$
$$a_{15} = 2\Omega \sin \varphi_2 + 2\zeta_2\omega_a B \cos \varphi_2, \ a_{16} = 2\Omega B \cos \varphi_2 - 2\zeta_2\omega_a B \sin \varphi_2,$$

$$b_1 = \left(\omega_p^2 - \Omega^2\right) A \sin\varphi_1 - 2\zeta_1\omega_p A\Omega \cos\varphi_1 - \mu\omega_a^2 B \sin\varphi_2 + 2\mu\zeta_2\omega_a B\Omega \cos\varphi_2$$

$$+2\zeta_1\omega_P\Omega X_0 + 0.75\alpha A^3 \sin\varphi_1 + 0.75\alpha A X_0^2 \sin\varphi_1 - 0.75\mu\beta B^3 \sin\varphi_2$$

$$-\omega_r B \sin\varphi_2 - F_{ac} A\Omega^2 \sin\varphi_1 - F_v A\Omega \cos\varphi_1 + F_d A \sin\varphi_1,$$

$$b_2 = \left(\omega_p^2 - \Omega^2\right) A \cos\varphi_1 + 2\zeta_1\omega_p A\Omega \sin\varphi_1 - \mu\omega_a^2 B \cos\varphi_2 - 2\mu\zeta_2\omega_a B\Omega \sin\varphi_2$$

$$-\omega_p^2 X_0 - F + 0.75\alpha A^3 \cos\varphi_1 - 0.75\alpha X_0^3 + 1.5\alpha X_0 A^2$$

$$+0.75\alpha X_0 A^2 (\cos\varphi_1 + \sin\varphi_1) + 2.25\alpha A X_0^2 \cos\varphi_1 - 0.75\mu\beta B^3 \cos\varphi_2$$

$$-\omega_r B \cos\varphi_2 - F_{ac} A\Omega^2 \cos\varphi_1 + F_v A\Omega \sin\varphi_1 - F_d A \cos\varphi_1,$$

$$b_3 = -A\Omega^2 \sin\varphi_1 - B\Omega^2 \sin\varphi_2 - 2\zeta_2\omega_a B\Omega \cos\varphi_2 + \omega_a^2 B \sin\varphi_2$$

$$+0.75\beta B^3 \sin\varphi_2 + \left(\omega_r B \sin\varphi_2 + F_{ac} A\Omega^2 \sin\varphi_1 + F_v A\Omega \cos\varphi_1 - F_d A \sin\varphi_1\right)\big/\mu,$$

$$b_4 = -A\Omega^2 \cos\varphi_1 - B\Omega^2 \cos\varphi_2 + 2\zeta_2\omega_a B\Omega \sin\varphi_2 + \omega_a^2 B \cos\varphi_2$$

$$+0.75\beta B^3 \cos\varphi_2 + \left(\omega_r B \cos\varphi_2 + F_{ac} A\Omega^2 \cos\varphi_1 - F_v A\Omega \sin\varphi_1 - F_d A \cos\varphi_1\right)\big/\mu$$
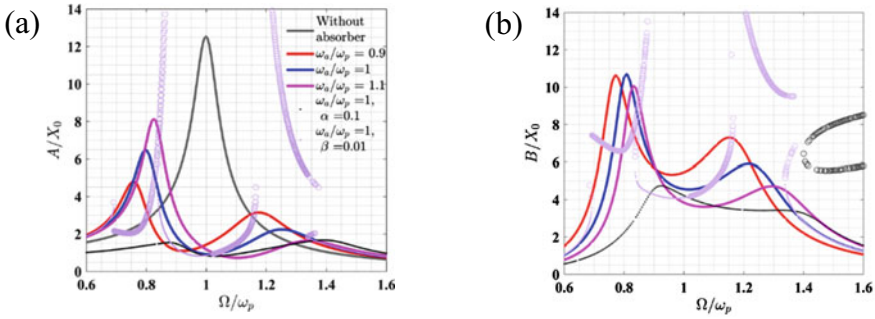
The steady state response of the system is studied from Eq. 7, by considering $\dot{a}_1 = \dot{\theta}_1 = \dot{a}_2 = \dot{\theta}_2 = 0$. The stability of the system is ensured by evaluating the Jacobian matrix of Eq. 7. In the next section, the system responses are studied by considering physical system parameters from the work of Buki et al. [9].

4　Result and Discussions

In this section, the primary mass (forearm) and secondary system responses are investigated by various feedbacks, nonlinear spring stiffness, the amplitude of force excitation and multi-harmonic force and base excitations. The forearm responses are studied through the frequency responses, time responses, phase portraits, and Poincare sections by obtaining the solution of Eq. 7 using Newton's method. The physical system parameters of the forearm and the attached secondary system or bracelet such as mass, linear spring stiffness, and damper are taken from the work of Buki et al. [9]. The active PZT stack actuator parameters are considered from the authors' work [11]. In the next sub-section, frequency responses are studied for the linear and nonlinear systems with and without feedback gains by considering various physical system parameters.

4.1　Frequency Responses with Passive Linear and Nonlinear Secondary System

The frequency response curves of the forearm and the bracelet are shown in Fig. 2 with and without the use of cubic nonlinear stiffness coefficient α and β in the bracelet

Fig. 2 Linear [9] and nonlinear system frequency responses **a** forearm **b** bracelet for $\mu = 0.2$, $\zeta_1 = 0.04$ and $\zeta_2 = 0.1$ amplitude more than that with the linear stiffness. In the next section, the effect of active forces on the frequency response of the system is studied.

which is taken equal to 0.1 and 0.01, respectively. Here the feedback gain (F_{act}) is considered equal to zero. The stable responses are shown by lines and dots while unstable responses are shown by circles. From Fig. 2a it can be observed that the result of the present work which is obtained using HBM is matching exactly with the work of Buki et al. [9] considering linear stiffness. In this figure for $\alpha = 0.1$, the response amplitude of the forearm (primary system) is comparatively less than that with linear stiffness for a wider range of operating frequencies. However, for $\beta = 0.01$, unstable responses have been observed. The bracelet (absorber) responses have been shown in Fig. 2b considering linear and nonlinear stiffness, where similar observations as that of Fig. 2a are noticed. It is inferred from Fig. 2 that the consideration of the nonlinear stiffness coefficient in the primary system reduces the response.

4.2 Effects of Various Feedback Gains on the Frequency Responses

In this section, the frequency responses of the primary system with unit base excitation shown in Fig. 3 are studied with various feedback gains, and considering nonlinear stiffness in the system. Figure 3a shows the frequency responses of the primary system with the AVA by various feedback gains such as displacement (F_d), velocity (F_v), accelerations (F_{ac}), and combination of these feedbacks (F_d, F_v and F_{ac}) considering $\omega_a / \omega_p = 1$. In Fig. 3, the value of F_d, F_v, and F_{ac} gains are considered equals to $-0.9, 0.1$, and -0.9, respectively which are obtained with several trials and error computations. From Fig. 3a it can be observed with F_{ac} and combination feedbacks (F_d, F_v and F_{ac}) gains the response amplitude (A) of the primary system decreases for a broader range of Ω / ω_p values than with other combinations. From this figure, one can notice that with F_{ac} gain the A / X_0 value is less than that with PVA for Ω / ω_p >0.77, while with combination feedback gains A / X_0 value is less than that with PVA for Ω / ω_p >0.7. The F_d gain by the AVA (bracelet) performs

better than PVA for $0.735 < \Omega/\omega_p < 1.63$. However, with F_v gain, the response amplitude of the primary is reduced for a narrow band of Ω/ω_p values, i.e., in the range of 1.07 to 1.37 and 0.53 to 0.82. Also, from this figure, one can notice that the response amplitude of the primary system with F_v gain shows two peaks similar to the PVA. It may be noted that the F_v gain by the AVA increases the damping in the secondary system, which corresponds to the two peaks in the system. Also, by choosing the optimal F_v gain one can obtain Den Hartog's equal peak in the frequency response curve shown in Fig. 3a. The F_{ac} gain by the AVA reduces 52 and 96% of the response amplitude of the primary system at the first and second peaks, respectively than the PVA. However, with F_d, F_{ac} and combination feedback gains the first peak response amplitude of the primary system is more than the PVA. The first peak in the frequency response by F_d, F_{ac} and combination feedback gains occur at a slightly lower frequency than the first peak of frequency response with PVA. From Fig. 3a, it can be inferred that with F_{ac} and combination of feedback gains the primary system response can be reduced for a broader range of operating frequencies, especially at the close proximities of the resonating frequency of operation. In Fig. 3b the frequency response of the primary system is shown with F_{ac} gain and cubic nonlinear stiffness in the system. Considering $\alpha = 0.1$ and $\beta = 0$, it is observed that the high peak response amplitude of the primary system with F_{ac} gain reduces than the corresponding linear system (Fig. 3a). The nonlinear primary system response amplitude with $\alpha = 0.1$ and $\beta = 0$ and F_{ac} gain remains very less than the linear primary system with PVA and AVA with F_{ac} gain (Fig. 6.3a) for $0 < \Omega/\omega_p < 0.77$. It is noticed that with F_{ac} gain and considering $\alpha = 0.1$ and $\beta = 0$ (Fig. 3b), there is a minimum 48% and a maximum 68% reduction in the response amplitude of the primary system than the linear primary system with PVA (Fig. 3a) for $0 < \Omega/\omega_p < 0.8$. However, it is observed that with the consideration of $\alpha = 0.1$ and $\beta = 0$, the unstable solutions are appearing at the higher operating frequencies range. Considering nonlinear stiffness only in the AVA i.e. $\alpha = 0$ and $\beta = 0.01$ (Fig. 3b), one can notice that the response amplitude of the primary system shows unstable responses for $0.57 < \Omega/\omega_p < 0.79$. However, outside for $\Omega/\omega_p > 0.79$, the response amplitude of the primary system with F_{ac} gain is less than PVA. Similar, response amplitude is also observed considering $\alpha = 0.1$ and $\beta = 0.01$, with F_{ac} gain but here for $\Omega/\omega_p < 0.79$ the response amplitude of primary system is less than considering $\alpha = 0$ and $\beta = 0.01$. The unstable solutions appeared considering $\alpha = 0.1$ and $\beta = 0.01$ is in the range of $0.79 < \Omega/\omega_p < 0.88$. In Fig. 3c, d, similar analyses as in Fig. 3b is carried out, but here F_v gain in the feedback is considered. From these figures, one can observe two peaks in the frequency response curves considering α and β coefficients in the stiffness of the primary system and the absorber. The response amplitude of the primary system shows a comparatively better response with nonlinear stiffness present in the primary system (Fig. 3c, $\alpha = 0.1$ and $\beta = 0$ and $\alpha = 0.1$ and $\beta = 0.01$) than considering only nonlinear stiffness in the absorber (Fig. 3d). From Fig. 3 one can observe the efficacy of the F_{ac} and combination feedback gains in reducing the response amplitude of the primary system for a broad range of operating frequencies than with PVA or other combinations of feedbacks. The PVA shows lesser responses in the lower operating frequencies region. Hence

one can use the AVA with zero gain for the lower operating frequency region (Ω / ω_p < 0.77) and for the higher operating frequency region (Ω / ω_p > 0.77), one can use F_{ac} gain by the AVA to broadly suppress the vibration of the primary system. The consideration of cubic nonlinear stiffness in the system shows unstable responses for a particular region of operating frequencies. So, one can avoid operating the AVA in these regions for the nonlinear system. Figure 4, illustrates the unit base excited primary system response amplitude with the F_{ac} gain by the AVA, taking into account physical system parameters of the forearm from the work of Buki et al. [9] viz., ω_p = 28.65 rad/s, ω_a = 36.75 rad/s, ζ_1 = 0.079 and ζ_2 = 0.0263, and μ = 0.2248. Figure 6.4a shows the frequency response amplitude of the primary system with PVA, F_{ac} gain by the AVA and F_{ac} gain with optimal AVA parameters. From this figure, it can be observed that with PVA (bracelet) the two peaks are at 3.83 and 6.95 Hz with response amplitudes of 7.165 and 1.99, respectively. It may be noted that in Fig. 4 in addition to the base excitation [9], a harmonic excitation $F \cos \Omega t$, where F = 0.1 N, is also considered, for the active case (AVA with F_{ac} gain), which may arise due to many other disturbances or feedback gains. The F_{ac} gain by the AVA reduces the response amplitude by 72.5% in the first peak (3.83 Hz) and 92.6% in the second peak (6.95 Hz) than the PVA. The response amplitude of the primary system shows a comparatively lesser amplitude with F_{ac} gain by the AVA for Ω > 3.5 Hz than the PVA. However, with F_{ac} gain the first peak occurs at 3.36 Hz with a response amplitude equal to 7.5. Thus, one can use the AVA with zero feedback gain for $0 < \Omega < 3.5$ Hz and outside this range, F_{ac} gain in the feedback by the AVA can be used to suppress the forearm (primary system) tremor for a broad range of operating frequencies. It is also shown in Fig. 4a that with the optimal parameters for the frequency (ω_a (opt) = 27 rad/s) and damping ratio (ζ_2 (opt) = 0.25) in the AVA there is a significant reduction in the response amplitude of the primary system for a broad range of operating frequencies. With the optimal AVA and F_{ac} gain the maximum peaks in the response amplitude is 2.86 at 2.95 Hz, which is 60% less than the maximum peak by the PVA. The response amplitude of the primary system with optimal AVA and F_{ac} gain is slightly more than PVA for a narrow band of operating frequency Ω in the range of 5.5–6.12 Hz and 1.9–3.15 Hz.

One can obtain the mass ratio, mass of the primary system, stiffness of the primary system, and the absorber from the data provided in the work of Buki et al. [9] as m = 0.28 kg, M = 1.2456 kg, μ = 0.2248, K = 1.0224 kN/m, k = 208.68 N/m (for $\omega_a(opt)$) and k = 378.1575 N/m (for ω_a). Considering α and β equal to 10% and 1% of the corresponding linear stiffness the response amplitude of the primary system is shown in Fig. 4b, c. In Fig. 4b, c the response amplitude of the primary system with PVA is shown. From Fig. 4b it can be observed that considering α = 10% of K and β = 1% of k, , the response amplitude of the primary system with PVA is less than that of the linear passive system (Fig. 4a) for Ω < 4.78 Hz. However, with the nonlinear stiffness, the responses of the primary system show unstable solutions for Ω in the range of 4.78–5.36 Hz and 6.5–7.66 Hz. Considering only β = 1% of k and α = 0, high first peaks in the response amplitude of the primary system are observed, which is similar to the linear system with PVA shown in Fig. 4a. In Fig. 4d the frequency response of the primary system with F_{ac} gain by the AVA
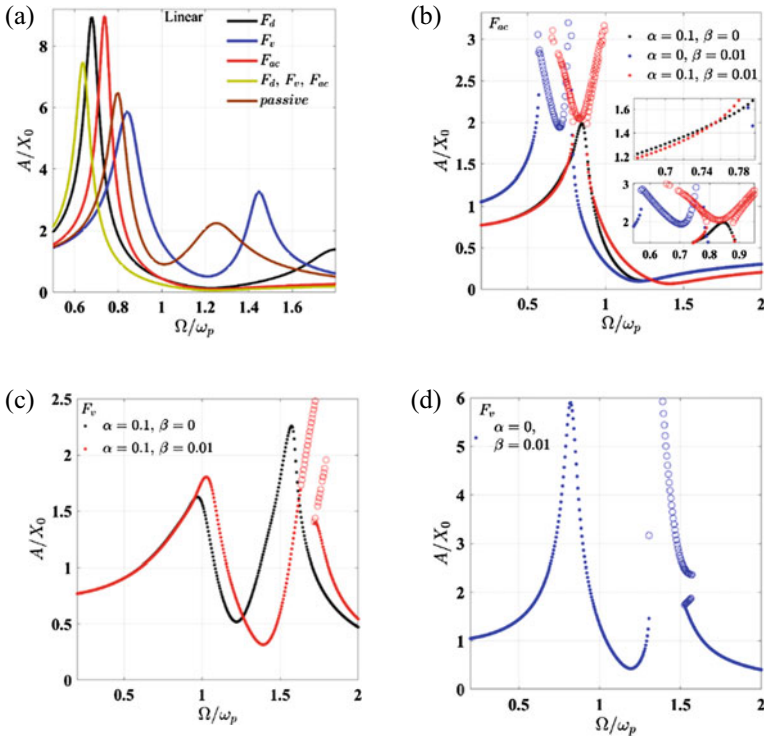
Fig. 3 Frequency response of the primary (forearm) system with various feedback gains by the AVA (bracelet) with linear and nonlinear stiffness for $\mu = 0.2$, $\zeta_1 = 0.04$ and $\zeta_2 = 0.1$

(active bracelet) is shown considering nonlinear stiffness in the system. From this figure, one can observe a significant reduction (44–98%) in the response amplitude of the primary system with the F_{ac} gain by the active bracelet, considering nonlinear stiffness only in the absorber ($\alpha = 0$ and $\beta = 1\%$ of k), for Ω in the range of 3.2–4.2 Hz. The maximum peak of the primary system with a nonlinear passive bracelet is 8.5354 at 3.799 Hz (Fig. 4c), whereas with an active bracelet the response amplitude is 0.259 at the same frequency (Fig. 4d), which is 97% reduction. However, with F_{ac} gain by the active bracelet unstable responses are in the range of 2.41 Hz < Ω < 3.22 Hz. Also, with the passive bracelet, the unstable responses are observed for 6.55 Hz < Ω < 7.24 Hz, whereas with F_{ac} gain by the active bracelet the primary system responses are stable and minimum in these regions of Ω. The efficacy of the F_{ac} gain by the active bracelet is also observed showing stable responses for $\alpha =$ 10% of K and $\beta = 1\%$ of k and $\alpha = 10\%$ of K and $\beta = 0$, near the second peak of the frequency response plot. From Fig. 4 it can be inferred that the F_{ac} gain by the active bracelet significantly suppresses the tremor suppression of the forearm of the patient both for the linear and nonlinear system. The nonlinear stiffness in the system produces unstable responses as shown in Fig. 4b–d, so, one has to avoid these regions
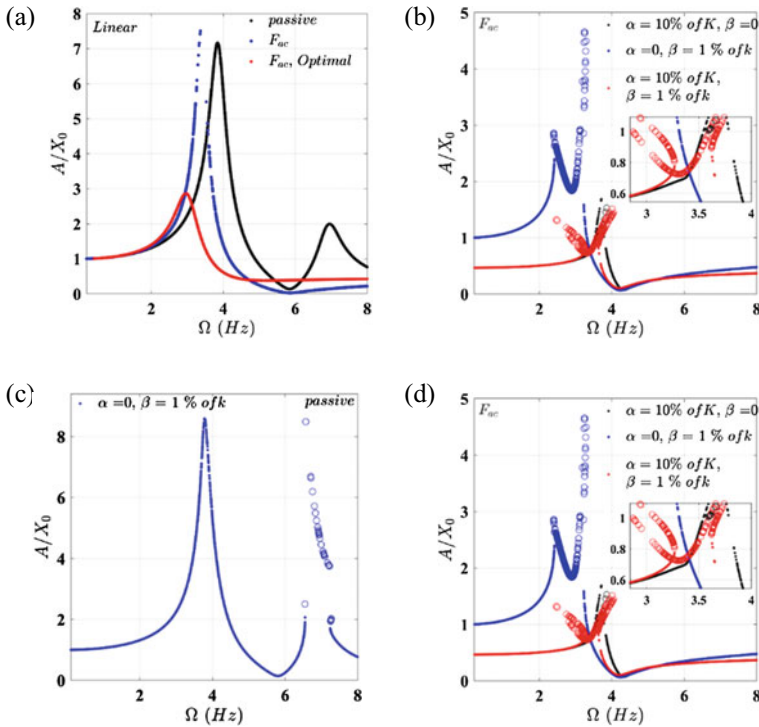
Fig. 4 Frequency response of the primary (forearm) system with F_{ac} gains by the AVA (active bracelet) considering physical system parameters of the forearm [9]. **a** linear system **b** nonlinear primary system with PVA **c** nonlinear PVA **d** nonlinear AVA

of operating frequencies to have less response amplitude in the forearm. In the next sub-section time responses, phase portraits and Poincare sections of the forearm with the passive and active bracelet are studied considering various external excitations acting on the forearm.

4.3 Responses of the System by Acceleration Feedback

In this section, the time responses, phase portraits, and Poincare sections of the unit base excited primary system (forearm) is shown in Fig. 5 considering passive and active bracelet with F_{ac} gain and nonlinear stiffness in the active bracelet. For the passive bracelet (PVA) only base excitation is considered while for the active bracelet (AVA) both unit base and harmonic excitations ($F = 0.1$ N) are considered. It may be noted that the time domain responses, phase portraits, and Poincare sections are obtained by solving Eqs. 3 and 4 using the fourth order Runge Kutta method. In Fig. 5, the effects of linear and only cubic nonlinear stiffness in the secondary system are
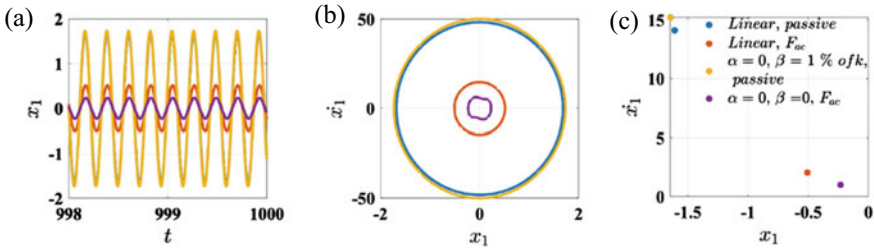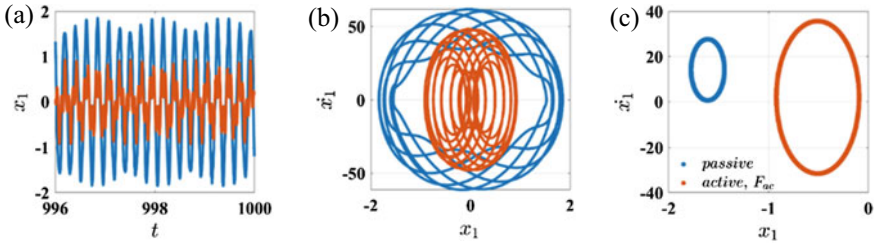
Fig. 5 **a** Time responses, **b** phase portraits, and **c** Poincare sections with passive and active bracelets at $\Omega = \omega_p$

studied at the resonance, i.e., when $\Omega = \omega_p$. Figure 5a–c shows with the linear passive bracelet the response of the primary system is periodic and its value is 1.682. From Figs. 5a–c and 4a one can observe good agreement between.

the HBM and the numerical method responses for the linear system with the PVA. It may be noted that in Fig. 4a the response amplitude of the linear primary system for the linear passive case is 1.683 at 4.5597 Hz ($\Omega = \omega_p$). The F_{ac} gain by the active bracelet reduces the response of the primary system from 1.682 to 0.514, which is a 69.4% reduction. The time response obtained with F_{ac} gain for the primary system at $\Omega = \omega_p$ with the linear bracelet is also in good agreement with the HBM results shown in Fig. 4a, where the response amplitude is 0.512 at 4.5597 Hz. Considering nonlinear stiffness only in the absorber ($\alpha = 0$ and $\beta = 1\%$ of k (378.1575 N/m)) with the passive and active bracelet the responses are also closely matched with the corresponding Fig. 4c, d. From Fig. 5b, c, one can observe periodic responses for the linear and nonlinear passive or active bracelet.

4.4 Responses of the Primary System for Multi-base Excitations

In this sub-section, the performance of the F_{ac} gain by the active bracelet is studied in Fig. 6, considering multi-frequency base excitations in the form $X_0 \cos(\Omega t) + X_0 \cos(2\sqrt{2}\Omega t)$. The corresponding time responses, phase portraits, and Poincare sections are shown in Fig. 6. It may be noted as in the previous figures (Figs. 4 and 5) for the active case in addition to the above base excitations, a harmonic excitation $F \cos \Omega t$ where $F = 0.1$ N, is also considered. From Fig. 6, one can observe around a 50% reduction in the response by the F_{ac} gain with the active bracelet. From the phase portraits (Fig. 6b) and Poincare sections (Fig. 6c), one can observe quasi-periodic responses.

Fig. 6 **a** Time responses, **b** phase portraits and **c** Poincare sections with the passive and active bracelet at $\Omega = \omega_p$ for multi-base excitations

4.5 Responses of the Primary System for Multi-excitations

In this section, the efficacy of the F_{ac} feedback gain is studied in vibration suppression of the primary system when it is subjected to multi-base and harmonic excitations. Figures 7 show the responses when the primary/forearm undergoes multi-base excitations of the form $X_0 \cos(\Omega t) = \sum_{n=0}^{7} X_0 \cos(2^n \Omega t)$. For the active case along with these base excitations an additional harmonic excitation of the form $F \cos(\Omega t) = \sum_{n=0}^{7} F \cos(2^n \Omega t)$, where $F = 0.1$ N is considered. Figure 7a–c shows the responses of the primary (forearm) system with the passive and active bracelets. From this figure, one can observe a slight improvement in suppressing the responses by the active bracelet in comparison to the passive. From the phase portraits (Fig. 7b) and Poincare sections (Fig. 7c), one can observe periodic responses. The performance of the active acceleration feedback gain F_{ac} by the bracelet is also studied considering the optimal frequency ($\omega_a(opt)$) and optimal frequency and damping ratio by the active bracelet as shown in Fig. 7c–f. From Fig. 7c–f, one can observe a substantial decrease in the response of the primary system by the F_{ac} gain with the optimal parameters in comparison to the passive bracelet (Fig. 7a–c). For multiple excitations with a higher amplitude of excitations, one can increase the gain used by the active bracelet to effectively.

suppress the responses of the primary system considering both linear and nonlinear stiffness in the system. Furthermore, from the results shown in Sect. 2.2 one can observe the efficacy of F_{ac} gain in tremor suppression for various excitations and nonlinear stiffness in the system. In the next section, conclusions of the present work are given.
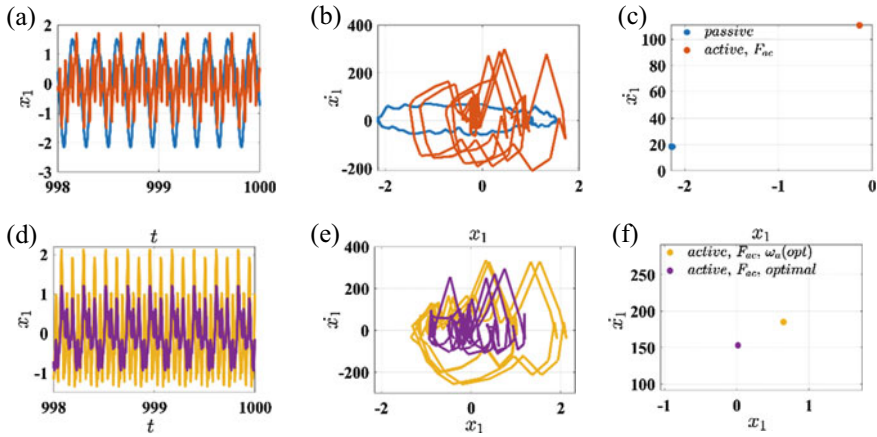
Fig. 7 Time responses (**a**, **d**), phase portraits (**b**, **e**) and Poincare sections (**c**, **f**) of the primary system under multiple excitations at $\Omega = \omega_p$

5 Conclusions

In this work the efficacy of various feedback gains used in the active bracelet, i.e., the ADVA is investigated to absorb the tremors/vibration of the human forearm due to PD. The human forearm is modeled as a base-excited SDOF (single degree-of freedom) spring-mass-damper primary system which is subjected multi-harmonic external excitations. The multi-harmonic external excitations are only considered for the active bracelet which may arise due to the feedback gains or other disturbances. The active feedback gain by the ADVA is produced by the combination of a PZT stack actuator and a spring-in-series connection by which one can tune the frequency of the ADVA effectively to the human forearm's natural frequency. The nonlinear governing equations of motion of the system considering displacement, velocity and acceleration feedback of the forearm by the ADVA are obtained and solved by the modified harmonic balance method (HBM) to generate the reduced equations. These reduced equations are then solved by Newton's method and compared with the numerical method and with the published literature, showing good agreement. From the various parametric analyses using different nonlinear stiffness coefficients, different combinations of feedback gains and external excitations the following conclusions are made from the investigations.

- The acceleration feedback gain (F_{ac}) by the linear ADVA, i.e., active bracelet reduces 52% of response amplitude of the forearm (primary system) in the first peak and the second peak is decreased by 96% than with PVA or passive bracelet.
- Also, considering parameters of the human forearm from the work of Buki et al. [9], with F_{ac} gain in the active bracelet the response amplitude reduces by 72.5% in the first peak (3.83 Hz) and 92.6% in the second peak (6.95 Hz) than the PVA or passive bracelet.

- It is shown that the F_{ac} gain by the AVA (active bracelet) significantly suppresses the tremor suppression of the forearm both for the linear and nonlinear system for $\Omega > 3.5$ Hz than the PVA. For the lower frequency region, one can provide zero control gain and use the active bracelet passively to effectively suppress the tremors for a wide range of operating frequencies.
- The nonlinear stiffness in the system produces unstable responses, so one has to avoid these regions of operating frequencies.
- From the various feedback gains (F_d, F_v and F_{ac}) it is observed that the F_{ac} and combination feedback gains perform better in attenuating tremors of the forearm than other feedbacks (F_d or F_v).
- The effectiveness of the acceleration feedback gain is also observed at the resonating frequencies in suppressing vibration than the PVA when the forearm is undergone multi-base and multi-harmonic excitations.

References

1. Song P, Zhang Y, Zha M, Yang Q, Ye X, Yi Q, Rudan I (2021) The global prevalence of essential tremor, with emphasis on age and sex: a meta-analysis. J Glob Health 11:04028
2. Kamble N, Pal PK (2018) Tremor syndromes: a review. Neurol India 66(7):36–47
3. Gebai S, Hammoud M, Khachfe H (2018) Parametric study of an enhanced passive absorber used for tremor suppression. Struct Control Hlth 25(7):e2177
4. Gebai S, Hammoud M, Hallal A, Al Shaer A (2018) Structural control and biomechanical tremor suppression: comparison between different types of passive absorber. J Vib Control 24(12):2576–2590
5. Masoumi M, Kmanzi S, Wang H, Mohammadi H (2021) Design and fabrication of a novel passive hand tremor attenuator. J Med Eng Technol 45(8):597–605
6. Rahnavard M, Hashemi M, Farahmand F, Dizaji AF (2014) Designing a hand rest tremor dynamic vibration absorber using H_2 optimization method. J Mech Sci Technol 28(5):1609–1614
7. Hashemi SM, Golnaraghi MF, Patla AE (2004) Tuned vibration absorber for suppression of rest tremor in Parkinson's disease. Med Bio Eng Comput 42(1):61–70
8. López-Blanco R, Velasco MA, Méndez-Guerrero A, Romero JP, del Castillo MD, Serrano JI, Rocon E, Benito-León J (2019) Smartwatch for the analysis of rest tremor in patients with Parkinson's disease. J Neurol Sci 401:37–42
9. Buki E, Katz R, Zacksenhouse M, Schlesinger I (2018) Vib-bracelet: a passive absorber for attenuating forearm tremor. Med Bio Eng Comput 56(5):923–930
10. Mohanty S, Dwivedy SK (2021) Linear and nonlinear analysis of traditional and nontraditional piezoelectric vibration absorber with time-delay feedback for simultaneous resonance conditions. Mech Syst Signal Process 161:107980
11. Mohanty S, Dwivedy SK (2019) Nonlinear dynamics of piezoelectric-based active nonlinear vibration absorber using time delay acceleration feedback. Nonlinear Dyn 98(2):1465–1490
12. Mohanty S, Dwivedy SK (2019) Active nonlinear vibration absorber for a nonlinear system with a time delay acceleration feedback under the internal resonance, subharmonic, superharmonic and principal parametric resonance conditions simultaneously. J Aerospace Syst Eng 13(5):9–15
13. Mohanty S, Dwivedy SK (2016) Linear and nonlinear analysis of piezoelectric based vibration absorber with acceleration feedback. Procedia Eng 144:584–591

14. Mohanty S, Dwivedy SK (2017) Dynamic analysis of active vibration absorber by time delay acceleration feedback using higher order method of multiple scales. In: ASME gas turbine India conference, vol 58516, pp. V002T05A033-43
15. Mohanty S, Dwivedy SK (2019) Active vibration absorber for a nonlinear system with time-delay acceleration feedback for superharmonic and subharmonic resonance conditions. In: Machines, mechanism and robotics. Springer, Singapore, pp 681–690
16. Mohanty S, Dwivedy SK (2020) Nonlinear active vibration absorber using HBM. In: Advances in rotor dynamics, control and structural health monitoring. Springer, Singapore, pp 571–578
17. Mohanty S, Dwivedy SK (2020) Active nonlinear vibration absorber for a harmonically excited beam system. In: Nonlinear dynamic, control. Springer, Cham, pp 3–11
18. Mohanty S, Dwivedy SK (2022) Nonlinear analysis of active vibration absorber as a wearable rest tremor suppression in Parkinson's disease. In: Recent advances in computational and experimental mechanics. Springer, Singapore, pp 661–669
19. Mohanty S, Dwivedy SK (2020) Active vibration absorber for super-harmonic resonance condition. J Phys Conf Ser 1706:012102
20. Mohanty S, Sikder S, Dwivedy SK (2020) Nonlinear analysis of rotational inertial double-tuned mass damper by harmonic balance method. In: Advances in mechanical engineering. Springer, Singapore, pp 1183–1190

Finite Element Analysis of the Acetabular Cup in Total Hip Arthroplasty

Mirsaidin Hussain and **Subramani Kanagaraj**

Keywords Hip joint implant · Finite element analysis · Acetabular cup · UHMWPE

1 Introduction

One of the most crucial joints in the body is the hip joint that connects the femurs to the pelvis [1]. The spherical femoral head fits perfectly into the cup-shaped cavity called the acetabulum. The joint is stable as it is encircled by firm ligaments. The hip joint bears the weight of the upper part of our body. Hip joint replacement might be viewed as one of the greatest advancements among all other orthopedic surgeries in the last decades. A hip implant is an artificial joint implanted surgically. This is basically a replacement of the natural one to perform the same function [2]. The surgical operation carried out to place this artificial implant is called total hip arthroplasty (THA). THA is performed to have rehabilitation motions and to reduce the pain caused due to wear and tear of the joint. In THA, the femur head is first sectioned during a hip replacement procedure. The soft bone marrow is taken out of the sectioned head to make a cavity through the femur shaft. A head and a stem-shaped artificial implant are glued into the femoral cavity. The implant's spherical head is inserted into the acetabular socket of the hip bone. There are some issues, which decide the success of total hip replacement. The important issues are: to choose suitable bio-compatible materials, for fixation, use correct operating techniques, and satisfactory design of

M. Hussain (✉) · S. Kanagaraj
Department of Mechanical Engineering, Indian Institute of Technology Guwahati, Assam, India
e-mail: mirsaidin@gmail.com

S. Kanagaraj
e-mail: kanagaraj@iitg.ac.in

the implant. However, the hip implant needs further development due to its limited service life because of the formation of wear debris in the cup. Due to the limitation of service life, the implant is still not satisfactory for young patients.

The implant fixation can is of two types, e.g., cemented fixation and cementless fixation. In cemented fixation, a polymer is used to cement the acetabular cup and femur to the skeleton. The polymer compound is called acrylic cement or bone cement made of polymethylmethacrylate (PMMA). The space between the implant and the bone is filled with the help of bone cement. PMMA hardens within 10 minutes. After the operation, the patients can put their weight on the implant. However, it has been found that cracks on the bone cement occur due to cyclic and repetitive mechanical stresses which lead to cement fragments. From this fragmenting cement, debris generates and it may lead to osteolysis.

In cementless fixation, reaming is done in the bone. In the space made by this reaming, the component of the total hip implant is pushed directly. The implant is held with the help of elastic force in the bone tissue. There is a chance that sliding of the implant may occur against the marrow cavity. Thus, to avoid sliding, the surface of the component to be pushed in the bone is made rough and hence a stable fixation can be achieved. In this case, as there is no bone cement used thus, the debris formed due to bone cement fragmentation in the case of cemented fixation can be avoided. However, cementless fixation does not allow the patient to exert heavy weight on the implant for few weeks.
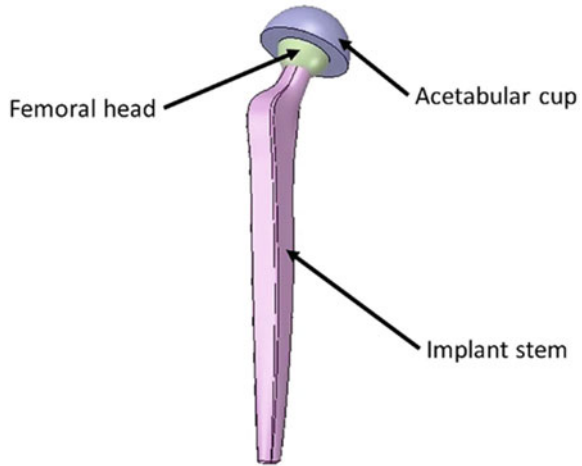
A hip joint implant has three different parts:

  I. Acetabular cup
 II. Femoral head
III. Implant stem.

A hip joint implant with its different parts, designed in AutoCAD 2019 has been shown in Fig. 1.

The size of the implant may vary from person to person. For the size of the acetabular cup, the first step was to optimize its diameter to get the best possible fit with the minimum error. The second step was to find the proper shape of the stem of the implant. The possible cross-section of the stem of the implant is a circle, rectangle, oval, square, etc. Along with the shape of the components, it is also required to have a minimum cross-sectional area. After a lot of research, Chethan et al. [3] noticed that for the stem part, the implant having rectangular cross-sections results in a lower value of von-Mises stress as well as lower total deformation compared to that of having other cross-sections. To enhance these implants' qualities, a variety of materials have been employed [4]. When selecting a material for the implant, the basic requirements are to produce less wear and to be biocompatible [5]. Usually, an acetabular cup can be made of ceramics, polymers, or metals, whereas the stem is made up of metals, and the femoral head can be either ceramic or metal. Using these materials, several combinations can be realized. The first choice about choosing the material for the hip replacement was polymer materials because of their low friction. Highly stable polymer like ultra-high molecular weight polyethylene (UHMWPE) has been

investigated because of its high wear resistance and excellent mechanical properties. Efforts were made to enhance the qualities of UHMWPE for better mechanical properties and to limit the wear particle concentration. Many materials were used for the implant such as polymers, glass, ceramics, composites, metal alloys, etc., for a combination of biocompatibility, stiffness, fatigue resistance, and toughness, to withstand both static and dynamic loads and also chemical and mechanical wear resistance [6]. The main aim to develop these biomaterials is to avoid repeated surgery and improve patient's quality of life [6].

The main reason for failure in a hip joint replacement is the formation of wear debris. A lot of efforts have been done to find the reason for wear. Buford et al. [7] explained the factors for wear debris formation that include, surface roughness and hardness, contact stress, type of material, etc. In one of the works, after revision surgery, the samples were retrieved as found in the literature [8]. From those samples, it was found that the generation of wear debris was in excessive amounts as a result of localized heat build-up, and the generated wear debris was deposited in the area of the joint which leads to osteolysis. Moreover, the increase in stress also resulted in cracking and generating wear debris in the acetabular cups. These cracks can also result in catastrophic failures [8]. However, a patient may have different types of loading as well as motion conditions, e.g., normal walking, going upstairs, chair down/chair up which is difficult to replicate in most of the hip simulators. Because of that, practically different wear patterns are observed in the acetabular cup compared to that of standard loading conditions [9, 10]. Therefore, to demonstrate significant stress in the acetabular cup, under various implant positions and loading conditions, finite element analyses are advantageous [11–13]. Thus, the present work aims to analyze the fatigue life as well as stress distribution in the implant for different boundary and loading conditions using the finite element method. The purpose of the current work is also to validate the stress distribution using experimental data on acetabular cup wear under ISO 14242-3 loading conditions.

(a)   **(b)**
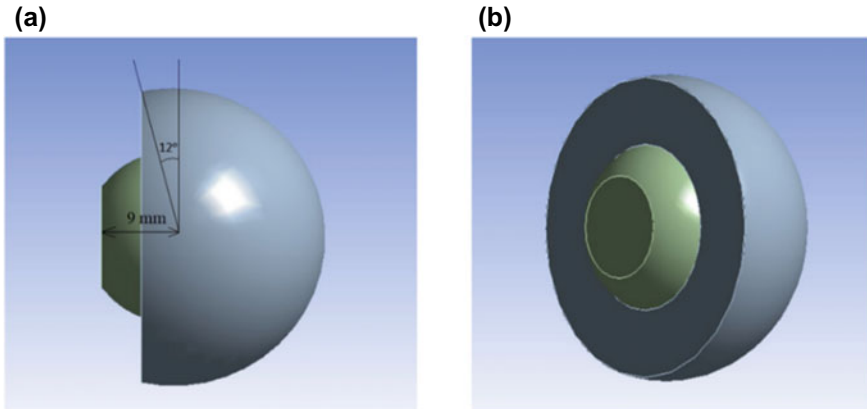
Fig. 2 **a** Side view and **b** perspective view of the CAD model

2 Design Methodology

2.1 Designing the CAD Model

The stress generates on the cup is due to the reaction force on the stem of the implant that passes through the head. Thus, to analyze the cup part, it is sufficient to work with the head and the cup portion where the load is applied on the head. Therefore, in this work, only the acetabular cup and the femoral head have been modeled in ANSYS 14.5. There is a radial clearance of 0.1 mm in between the acetabular cup and the head. The diameter of the femoral head is 21.80 mm, and the concentric acetabular cup has an inner diameter of 22 mm and thickness of 8 mm. The range of the diameter of the femoral head is usually found to be 22 mm to 36 mm [14]. The spherical head part has been cut from the implant stem at a distance of 9 mm from the center of the head to minimize the effort for analyzing purposes. The acetabular cup has been cut by a plane which makes 12º at the center as shown in Fig. 2a such that the head cannot come out of the cup during the dynamic loading condition. The perspective view of the model has been shown in Fig. 2b.

2.2 Choosing the Materials

To enhance these implants' qualities, a variety of materials have been employed. While selecting a material for the implant, the basic requirements are to produce less wear and to be biocompatible. The common characteristics possessed by the materials are:

- The materials are resistant to wear, corrosion, and degradation.

Table 1 Mechanical characteristics of the materials used [15]

Materials	Young's modulus (GPa)	Density (gm/cm^3)	Poisson's ratio	Endurance limit (MPa)
UHMWPE	0.625	0.941	0.41	12.21
SS 316L	200	7.9	0.30	500

- The materials are biocompatible, which means that they can operate inside the body without harming it.
- The materials are having desirable mechanical properties so that they are suitable to replace. For example, as per as requirement, the chosen materials are strong enough to take weight-bearing loads.

Among the polymers, UHMWPE exhibits great potential for low friction, low water absorption, and superior wear resistance. Thus, the material of the femoral acetabular cup has been taken as UHMWPE. Devices for fracture-fixation use alloys of stainless steel from the 316 series. Stainless steel is a strong candidate for material because of its resistance to oxidation as well as its ease in machining, hardening, and shaping. Thus, the material of the femoral head has been taken as stainless steel (SS) 316L. The mechanical properties of these materials are listed in Table 1.

2.3 Meshing and Applying Boundary Conditions

In the model, the components have been meshed with 3D 10-noded and 8-noded tetragonal elements. The names of the elements are SOLID 187 and SURF 154. To define the contact surfaces, TARGE170 and CONTA174 elements have been used. The sliding and contact between three-dimensional target surfaces is represented by CONTA174. For the contact element CONTA 174, TARGE 170 has been used to represent three-dimensional target surfaces. In this study, four different mesh sizes were used in Finite element analysis for the convergence analysis as shown in Table 2. The result obtained by considering element size as 1 mm with 165,764 nodes and the total number of elements 103,696 has been shown in the results and discussion section. The meshed model has been shown in Fig. 3a.

Table 2 Type of element, number of elements, number of nodes for different element size

Type of element	Size of element	Number of elements	Number of nodes
3D 10 noded and 8 noded tetragonal	4	8978	15,069
	3	13,260	22,143
	2	23,234	38,453
	1	103,696	165,764

(a)   **(b)**
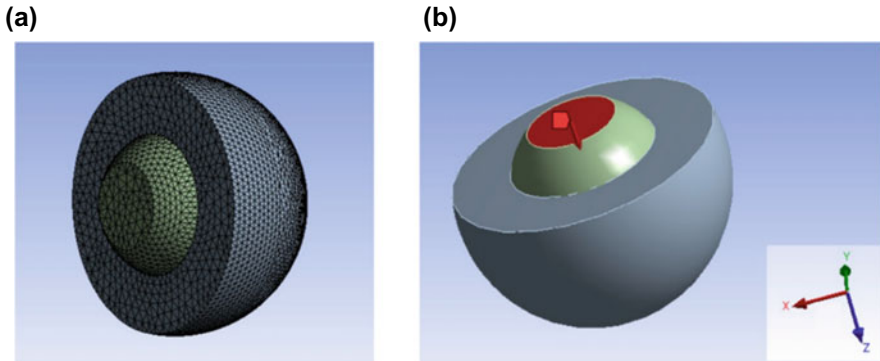
Fig. 3 CAD model with **a** mesh and **b** loading condition

For the analysis of the model, the dynamic load has been applied to the head. Three different types of motion have been given to the model such as:

  I. Extension and Flexion angle
 II. Abduction and Adduction angle
III. Rotation angle.

Load and boundary conditions were applied according to five different cases:

   I. ISO 14242–1
  II. ISO 14242–3
III. Normal walking
IV. Going upstairs
 V. Chair down/chair up.

The maximum load attained corresponds with dynamic loading condition ISO 14242–1 is 3 kN. The assumed body mass of the patient is determined to be 131 kg in order to make the maximum load in the cases of normal walking, going upstairs, and chair down/chair up condition equivalent to the maximum load in ISO 14242–1, i.e., 3 kN. Thus, the patient's weight was normalized to 131 kg for the loading conditions of normal walking, climbing stairs, and sitting in/standing up in a chair [16, 17]. A friction coefficient of 0.05 [18] was defined between the femoral head and the acetabular cup. The model with load has been shown in Fig. 3b. The dynamic load and flexion–extension (FE) have been applied to the head whereas abduction adduction and rotation have been given to the cup.

3 Results and Discussion

The results of the finite element analysis have been reported in Table 3. The equivalent elastic strain and equivalent (von- Mises) stress developed in the acetabular cup have been compared in each of the five cases: ISO 14242-1, ISO 14242-3, normal walking, going upstairs, chair down/chair up. After doing the strain and stress analysis, fatigue analysis has been carried out. From the fatigue analysis, the graph between the number of cycles (along Y-axis) vs loading intensity (along X-axis) which is basically like the inverse S-N curve has been found for each boundary condition. In those graphs, each of the points shows the number of cycles carried out by the component to reach up to its endurance limit for its corresponding loading intensity. Thus, the number of cycles corresponding to the one loading intensity will be the fatigue life, which is basically showing the number of cycles the component will perform to reach its endurance limit for the given loading condition.

From Fig. 4a, The stress distribution developed can be identified for the case of ISO 14242-1. From this figure, it has been found that at the center of the acetabular cup, the stress generation is very less. This is because there is no contact between the head and the cup during the motion. As we move away from the center, the magnitude of stress developed increases because of sliding contact in between the head and cup. In Fig. 4b, the stress distribution developed has been shown for the case of ISO 14242-3. In this case, also the same kind of stress distribution has been observed as that of the case of ISO 14242-1 with a different magnitude.

A similar pattern of the stress distribution has been observed in the case of normal walking conditions as shown in Fig. 4c. In the case of ISO 14242-1 and ISO 14242-3, the stress distribution was uniform about the center. However, in the case of normal walking, stress developed is not uniform about the center, rather its concentration is more at the position of minimum flexion angle due to more sliding between the head and the cup in that area. Here, the maximum stress developed is in between that of the cases of ISO 14242-1 and ISO 14242-3. Figure 4d shows the stress distribution for the case of going upstairs condition. In this case from the stress distribution, it can be noticed that more area near the center of the acetabular cup is there having lesser stress compared to that of the area in the case of ISO 14242-1 and ISO 14242-3 and normal walking. This is because the alignment of the head to the cup in case of going

Table 3 Result of dynamic analysis of hip Implant

| Loading and boundary conditions based on	Maximum equivalent (von-Mises) stress (MPa)	Maximum equivalent elastic strain (mm/mm)	Fatigue life no. of cycles (Million)
ISO 14242–1	3.8928	0.0023694	13.4
ISO 14242–3	3.5430	0.0022447	15.3
Normal walking	3.8543	0.0023191	14.8
Going upstairs	4.8314	0.0028381	9.4
Chair down/chair up	3.1644	0.0021096	16.4
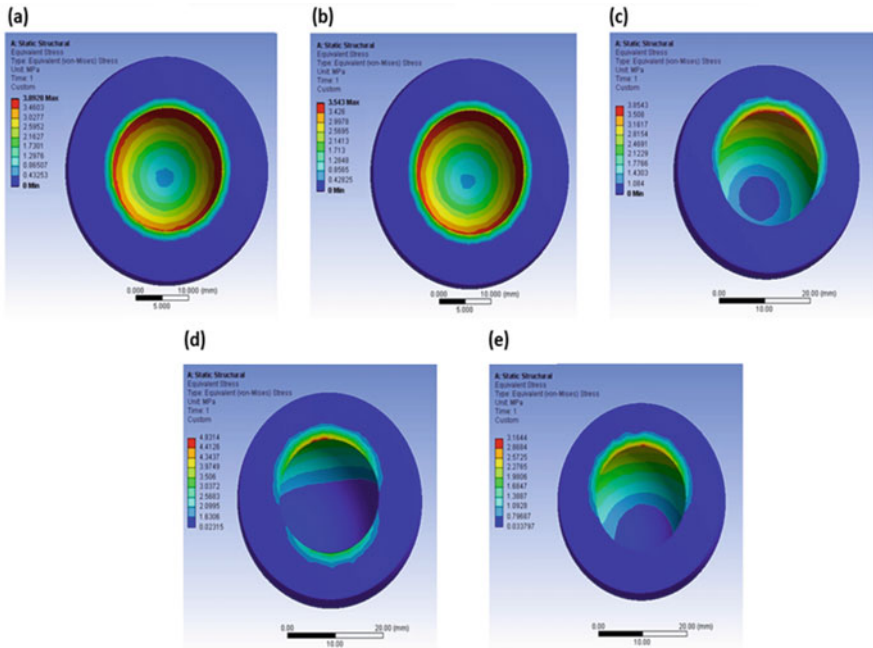
Fig. 4 Von-Mises stress (MPa) developed for the case of **a** ISO 14242–1 **b** ISO 14242–3 **c** normal walking **d** going upstairs, and **e** chair down/chair up condition

upstairs is such that there is more sliding between the acetabular cup and the head away from the center of the cup. However, away from the center, the stress developed increases, and the maximum stress developed in this case is found to be the highest compared to that in the other conditions. The magnitude of stress is least in the case of the chair down/ chair up condition compared to that of the other cases due to the lesser magnitude of applied load on the cup in this case as shown in Fig. 4e.

The results of the strain values found in the finite element analysis for the loading condition ISO 14242-1 have been compared with the results of the experimental and computational analysis that has been done in earlier research [19]. From this comparison, it can be noticed that the maximum value of strain, as well as the time at which the maximum and minimum strain values are obtained for a cycle, are quite comparable. Figure 5a shows the strain found for the loading condition ISO 14242-1

(a)

(b)
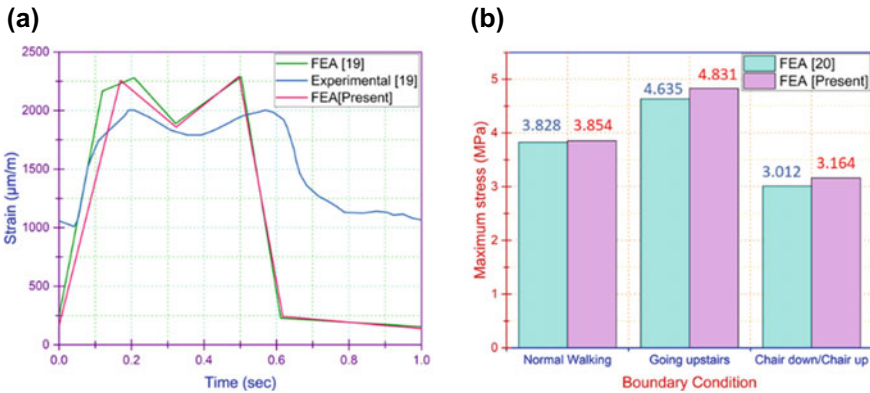
Fig. 5 **a** Strain validation for ISO 14242–1, and **b** maximum stress validation for the case of normal walking, going upstairs, and chair down/ chair up condition

in the present work, and the earlier research work [19]. The difference in lowest strain values can be logically explained by the fact that the material formulation employed in ANSYS 14.5 ignores the polyethylene's viscoelastic relaxation, ignoring the material's time-dependent behavior. The maximum magnitude of stresses for a cycle found in this work for the case of normal walking, going upstairs, and chair down/chair up is also quite comparable with the earlier research [20]. The comparison has been shown in Fig. 5b.

Furthermore, experiments have been conducted in an orbital bearing machine, a hip simulator based on the loading condition of ISO 14242-3. Under microscopic observation, the two different zones have been identified in the acetabular cup after 5 million cycles. Zone 1 exhibits severe adhesive wear called as ploughing wear phenomenon as shown in Fig. 6. Abrasive wear occurs when hard particles or hard surfaces pass over a soft surface which causes loss of material. In this zone, the wear occurs due to rolling and sliding against each other. Zone 2 has been found to be almost unaffected. Similarly, in the finite element analysis, from the stress, and strain distribution it has been observed that in zone 1, the maximum stress, as well as strain, occurs and in zone 2, the stress, and strain has been found to be minimum.
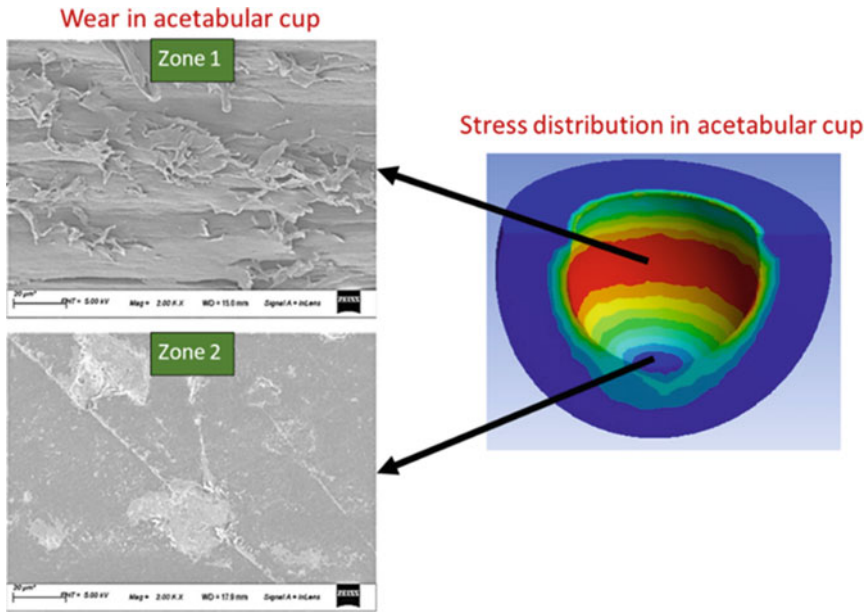
Fig. 6 Comparison of wear and stress distribution in acetabular cup

4 Conclusion

The current work inferences that the results obtained from the finite element analysis are quite comparable with the earlier research. From the analysis, the location of the highest stressed region in the acetabular cup has been identified. It has been observed that for all boundary conditions, the stress generation at the center of the acetabular cup is very less. This is because there is no contact between the cup and the head during the motion. In this work, the validation of the stress distribution using experimental evidence of acetabular cup wear under ISO 14242–3 loading conditions has also been carried out. The work might then be expanded upon by comparing the stress distribution with wear in the acetabular cup for the other loading conditions and focusing on the improvement in the area that is most stressed to avoid conducting the experiments repeatedly. Moreover, the present study shows that fatigue life in the case of going upstairs is lowest and fatigue life in the case of chair down/chair up is highest.

5 Scope for Future Work

Future work could be to conduct experiments for estimating the wear and fatigue life of the acetabular cup and for simulating the gait movement. Further, more recent materials might be investigated as potential implant materials, and analysis could be performed for various activities.

References

1. Mattei L, Di Puccio F, Piccigallo B, Ciulli E (2011) Lubrication and wear modelling of artificial hip joints: a review. Tribol Int 44(5):532–549
2. Pezzotti G, Yamamoto K (2014) Artificial hip joints: The biomaterials challenge. J Mech Behav Biomed Mater 31:3–20
3. Chethan KN, Zuber M, Shenoy S, Kini CR (2019) Static structural analysis of different stem designs used in total hip arthroplasty using finite element method. Heliyon 5(6):01767
4. Goswami C, Patnaik A, Bhat IK, Singh T (2021) Mechanical physical and wear properties of some oxide ceramics for hip joint application: a short review. Mater Today: Proc 44:4913–4918
5. Merola M, Affatato S (2019) Materials for hip prostheses: a review of wear and loading considerations. Materials 12(3):495
6. Aherwar A, Singh AK, Patnaik A (2016) Current and future biocompatibility aspects of biomaterials for hip prosthesis. AIMS Bioeng 3(1):23–43
7. Buford A, Goswami T (2004) Review of wear mechanisms in hip implants: Paper I-General. Mater Des 25(5):385–393
8. Burger NDL, De Vaal PL, Meyer JP (2007) Failure analysis on retrieved ultra high molecular weight polyethylene (UHMWPE) acetabular cups. Eng Fail Anal 14(7):1329–1345
9. Waewsawangwong W, Goodman SB (2007) Unexpected failure of highly cross-linked polyethylene acetabular liner. J Arthroplasty 27(2):323-e1
10. Bradford L, Baker DA, Graham J, Chawan A, Ries MD, Pruitt LA (2004) Wear and surface cracking in early retrieved highly cross-linked polyethylene acetabular liners. JBJS 86(6):1271–1282
11. Hua X, Wroblewski BM, Jin Z, Wang L (2012) The effect of cup inclination and wear on the contact mechanics and cement fixation for ultra high molecular weight polyethylene total hip replacements. Med Eng Phys 34(3):318–325
12. Matsoukas G, Kim IY (2009) Design optimization of a total hip prosthesis for wear reduction. J Biomech Eng 131(5):051003
13. Wang L, Isaac G, Wilcox R, Jones A, Thompson J (2019) Finite element analysis of polyethylene wear in total hip replacement: a literature review. Proc Inst Mech Eng [H] 233(11):1067–1088
14. Girard J (2015) Femoral head diameter considerations for primary total hip arthroplasty. Orthop Traumatol Surg Res 101(1):S25–S29
15. Sabatini AL, Goswami T (2008) Hip implants VII: Finite element analysis and optimization of cross-sections. Mater Des 29(7):1438–1446

16. Fabry C, Herrmann S, Kaehler M, Klinkenberg ED, Woernle C, Bader R (2013) Generation of physiological parameter sets for hip joint motions and loads during daily life activities for application in wear simulators of the artificial hip joint. Med Eng Phys 35(1):131–139
17. Bergmann G, Graichen F, Rohlmann A, Bender A, Heinlein B, Duda GN, Heller MO, Morlock MM (2010) Realistic loads for testing hip implants. Bio-Med Mater Eng 20(2):65–75
18. Xiong D, Ge S (2001) Friction and wear properties of UHMWPE/Al2O$_3$ ceramic under different lubricating conditions. Wear 250(1–12):242–245
19. Zietz C, Fabry C, Baum F, Bader R, Kluess D (2015) The divergence of wear propagation and stress at steep acetabular cup positions using ceramic heads and sequentially cross-linked polyethylene liners. J Arthroplasty 30(8):1458–1463
20. Tong J, Zant NP, Wang JY, Heaton-Adegbile P, Hussell JG (2008) Fatigue in cemented acetabular replacements. Int J Fatigue 30(8):1366–1375

Dual-Band Compact Antenna Development in WiMAX and Wi-Fi Bands for Healthcare Service Wireless Connectivity

Dheeraj Pandey and Surajit Kundu

Keywords Healthcare system · Dual-band antenna · Wi-Fi · WiMAX

1 Introduction

With the increasing population, increasing diseases and busy lifestyle, healthcare society received a prominent attention in recent years all over the world [1]. According to a survey, around 26.16% population of India belongs to the age group of 0–14 years and 67.57%, above 65 years [2] for whom requirement of healthcare facility is much more required and access of hospitals is difficult. According to A. Kasthuri, the Indian healthcare system faces several challenges among them major challenges are: lack of awareness in most of the peoples, lack of access of healthcare facilities or food quality of healthcare facility, less amount of manpower in healthcare system as compared to the total population, affordability of healthcare facilities (due to domination of private healthcare system) and accountability. Thus, it became difficult to provide real-time and on-time healthcare facilities, round the clock to all the persons at a lower cost [3]. Due to implementation delay and ineffectualness of government schemes in rural areas, rural healthcare system is much worse than the urban. Even though approximately 65% Indian population lived in rural areas, only 25% healthcare facilities and resources are available for that population [4]. In India for 10189 persons only one government-facilitated doctor is available

D. Pandey (✉)
Department of Electronics and Communication Engineering, NIT Sikkim, Ravanglak, India
e-mail: phec210008@nitsikkim.ac.in

S. Kundu
Department of Electronics and Communication Engineering, NIT Jamshedpur, Jamshedpur, India
e-mail: surajitkundu.ece@nitjsr.ac.in

and majority of those doctors (around 80%) are working in urban hospitals, in such scenario mobile health system can be very much effective [5]. With the value of $40 billion Indian healthcare industry is a growing industry but out that more than 80% industry is accounted by private sectors that are sometimes out of reach from middle- and lower-class people. By 2030 India will become the most populous country with more than 200 million having the age group of above 60 years which can be another responsibility in healthcare system [6]. United Nations report says that out of 189 countries India's position is 131st in healthcare growth and world health organization report also shows that life expectancy is very less compared to many countries like Japan, China, Australia, United States, United Kingdom, etc. Even though infant mortality, life expectancy, and maternal mortality show a significant growth, it is not up to a significant level. Blockchain technology with the use of Internet of Things (IoT) can be useful for Indian healthcare system in future that can also provide transparency, traceability non-repudiation, etc., to the persons [7]. In the country like India use of e-health system also shows several challenges like patient's data security and privacy, awareness toward e-health, illiteracy, lack of internet connection in remote areas, lack of fund and infrastructure, execution of different languages in software used, with that it also has some opportunities for the educated professionals by delivering such knowledge and services in different remote location at low cost [8]. As the current infrastructure of Indian healthcare system is neither effective nor efficient for the rate of population and diseases are increasing, IoT-based system that will be able to connect the entire Indian healthcare system is very much needed in the current scenario. By making the devices affordable for common peoples to work in remote locations such IoT-based devices are very much useful, and even in most of the developed and developing countries are using the same for different purposes in their daily life [9]. Day by day different diseases that may be the cause of major death in absence of instant medical guidance, like heart related, pulmonary diseases, brain strokes, etc., are increasing. Even in the last few decades pandemics like corona, SARS, plague, camp fever, smallpox, Asian flu, etc., are affecting the mass population and badly affecting the body and may cause instant death [10]. Providing healthcare facilities wirelessly and transmitting the user's data like heart rate, pulse rate, oxygen level, glucose level, etc., to the nearby hospital or to the relative, can be beneficial at the time of emergency for providing the instant relief that can save the human life [11]. In the situations like corona pandemic, when it became more difficult to access the hospitals due to a greater number of patients and a smaller number of facilities, such e-health services can be boon for patients who require daily monitoring and suggestions from medical experts without coming in contact with the infected person [12]. Figure 1 shows the wireless connectivity of a person to local, central hospitals and relatives through the existing 5G (WiMAX), WBAN, and Wi-Fi band in which a person can transmit and receive data like heart rate, pulse rate, oxygen level, temperature, glucose level, etc., at the time of emergency. Different wearable devices are already in the market to provide real-time heart rate, pulse rate, oxygen level, glucose level, body temperature and respiration, etc., so providing device data to the nearest health agencies can be very useful even for remote location area persons [13].
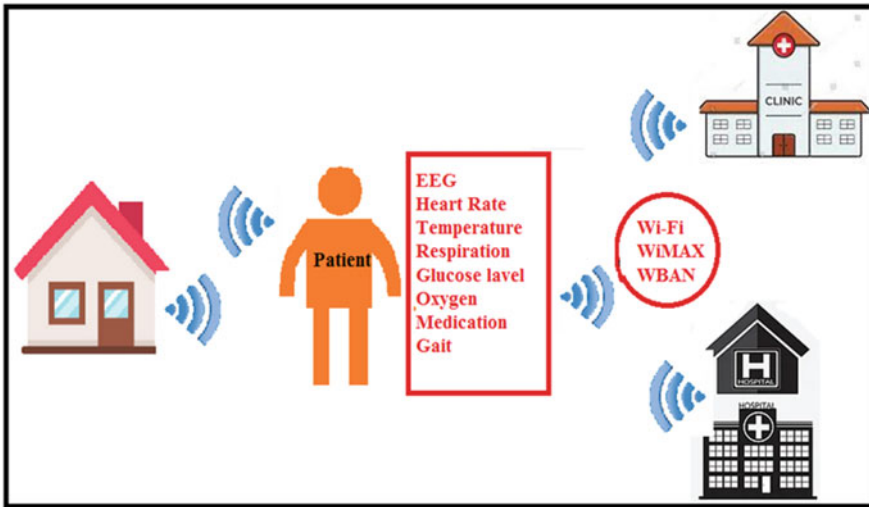
Fig. 1 Healthcare monitoring through wireless connectivity

For transmitting and receiving the real time data with high throughput and high security a proper communication system is required. Different types of antenna to transmit and receive the signal in healthcare services have been introduced in the past. And to keep the overall cost of such devices as low as possible without affecting the device characteristics an effective low-cost antenna system is very much required [14]. Wearable antenna for working in wireless body area network (WBAN) band is popular worldwide nowadays with different geometry of patch antenna and different techniques of antenna characteristics enhancement. A planar inverted F antenna (PIFA) along with meta-surface comprising the 2×3 array to enhance the antenna gain and bandwidth of antenna, for the applications of 5-GHz WBAN has been introduced in [15], but the antenna resonates only at single frequency band. A folded ring dual band wearable rectangular ring-shaped antenna on a combination of flexible and rigid substrate was introduced in [16] to work in WBAN and wireless local area network (WLAN) bands further 3×3 array of square unit cell to create AMC on the back side of antenna enhances the antenna gain and reduce back radiation. To get the multiple bands, different techniques have been used, like U-shaped slots on magneto-electric dipole antenna for dual band, WLAN and WBAN application was proposed in [17]. Another technique using artificial magnetic conductor to improve the radiation characteristics, for WiMAX and WBAN bands was introduced in [18] that gives better SAR (specific absorption rate). A review of multiband antennas based on different types, characteristics enhancement techniques, and different applications was presented in [19]. In [20] circular patch surrounded by mushroom units, central fed for dual-band operation having monopole radiation pattern was proposed. For enhancing the gain, antenna with 1×4 array was introduced in [21] for 5G Sub 6 GHz applications. A small balloon alike coplanar waveguide fed antenna of size

25 mm × 15 mm × 0.8 mm was proposed in [22] to cover the 4.5 GHz to 11 GHz bandwidth. A comparatively bulky rectangular shaped microstrip antenna of size 50 × 50 × 1.6 mm^3 was proposed in [23] that worked in the 2.4 GHz ISM band. A very compact logo shaped antenna of size 17.5 × 17.5 × 1.6 mm^3 only was presented in [24] to cover dual bandwidths from 1.76 to 2.2 GHz and from 2.36 to 3.94 GHz that can be used to cover the various modern and futuristic wireless communication applications. A small U-alike monopole antenna of size 36 × 22 × 0.8 mm^3 was proposed in [25] to cover the 3–12.4 GHz band. Metamaterials can be used for miniaturization as well as characteristics enhancement purposes like, to enhance the efficiency of small wearable antenna a metamaterial-based printed dipole antenna was presented in [26], with the use of split ring resonator and strips, antennas directivity and gain enhances by some amount and antenna can be used for IoT and BAN applications. Designing a wearable and implantable antenna for monitoring the person in real time and 24 × 7 and transmitting and receiving the data is very difficult task, because in contact with the human body antenna characteristics may change and high specific absorption rate of the device may cause problem to the human tissue. A monopole antenna having the fractal geometry with low specific absorption rate to work at GSM-1800 and ISM-2.45 GHz bands, a wearable antenna was presented in [27]. Jean fabric is used to design the antenna, and to reduce the attenuation, and overcome the effect of detuning 3 × 3 electronic band gap structure is used on the back side of the antenna by which antenna becomes a good candidate for wearable purposes. As smartwatch is a widely used type of device nowadays that can monitor heart rate, pulse rate, oxygen level, etc., so transmitting the smart-watch data in case increasing or decreasing the heart rate, pulse rate, oxygen level, or in any other emergency cases, can save the human life. High impedance surface antenna for smartwatch applications having lower specific absorption rate and high directivity, was proposed in [28] having the dimensions of 38 × 38 × 3 mm^3 to work in the frequency range of 2.40–2.48 GHz. With the use of high impedance surface, antenna starts radiating outward and effect of human body was also less. While designing the wearable antenna use of material, dielectric substrate (flexible substrate is preferred), miniaturization techniques, fabrication accuracy, and low specific absorption rate should be kept in mind, because such devices require high accuracy and characteristics may change by human body contact and may affect the human tissue. Other than healthcare, wearable device has many applications like in the field of entertainment and military for sports, battlefield, identification, etc. The conductive material of such antennas should be water-proof, preferred flexible, rigid conductive, high conductivity, and low cost and substrate material should have lower permittivity, lesser loss tangent, and low cost. For the fabrication, 3D inkjet and infrared laser should be used for high accuracy [29]. Implantable devices are another very useful device for monitoring the human body by inserting the device inside the body, but designing of such devices is also a great issue, because its design should be biocompatible and providing the power to such devices for operation is also a big task. A maintenance free technique called radio frequency identification to provide wireless connection between human body and other devices using implanted and wearable antenna in low power and low cost is very useful [30]. Other different

shapes and sizes of antennas are been presented in many research papers for health-care purposes like polygon shaped radiator with circular slots and rectangular slits on the jeans substrate (having the dielectric constant of 1.7) by which antenna becomes very flexible for wearable purposes and it can operate in GSM-900 and GSM-1800 bands was presented in [31]. For keeping a high data rate, small dimensions and less interference millimeter wave antennas are showing great interest nowadays for body area networking purposes. A circular disc-shaped radiator connected electromagnet-ically to feed line on the Duroid 5870 substrate (having dielectric constant of 2.33 and loss tangent of 0.0036) was presented in [32] to work in Ism band of 61 GHz.

Based on the literature survey of Indian healthcare infrastructure and requirement of low-cost e-healthcare system to provide healthcare facility to maximum number of households, this paper proposes a simple CPW fed, triple tringle shaped, triple slot antenna. Section 2 describes the antenna design process and different optimized parameters with its values. Section 3 provides the result analysis of the proposed antenna based on the reflection coefficient (S_{11}), gain, radiation efficiency, and co- and cross-pol radiation pattern. At the end, Sect. 4 gives the conclusion of the designed antenna based on the results obtained and application in the field of healthcare.

2 Proposed Antenna Design

Only to fulfill the antenna requirement in healthcare system, to transmit and receive the data from one place to another in a very efficient way, a low-cost antenna on the FR4 epoxy substrate with the dielectric constant of 4.4, loss tangent of 0.02, and thickness of 0.8 mm is developed. Figure 2a depicts the schematic diagram of the proposed antenna accompanied with the parameters used to define the proposed antenna dimensions. The antenna design starts with the single tringle shaped patch with rectangular shaped ground and CPW feeding, at which antenna resonates above 10 GHz. Further two other tringles are integrated on the patch side, which increases metallic area but reduces the return loss of the antenna.

Without altering the dimensions of ground plane, one by one, three rectangular slots of different dimensions are introduced on the patch side using the optimiza-tion. Multiple overlapped resonances can be introduced by inserting the slots on patch and ground plane [17]. In the proposed antenna by inserting the slots, antenna starts resonating at lower frequency band and reflection coefficient improves signif-icantly because slots increase the overall current flow path and capacitive effects are also introduced by the ground and feed line. Further optimization is done in ground size as well as in feed width to get the desired bands. All the parametric optimiza-tions of designed antenna are evaluated by simulating the antenna geometry in CST microwave simulator. Final simulated and optimized values of different parameters are presented in Table 1. Finally, the antenna is fabricated on the low-cost FR4 epoxy substrate having 0.8 mm thickness, Fig. 2b shows the hardware view of the fabricated antenna.
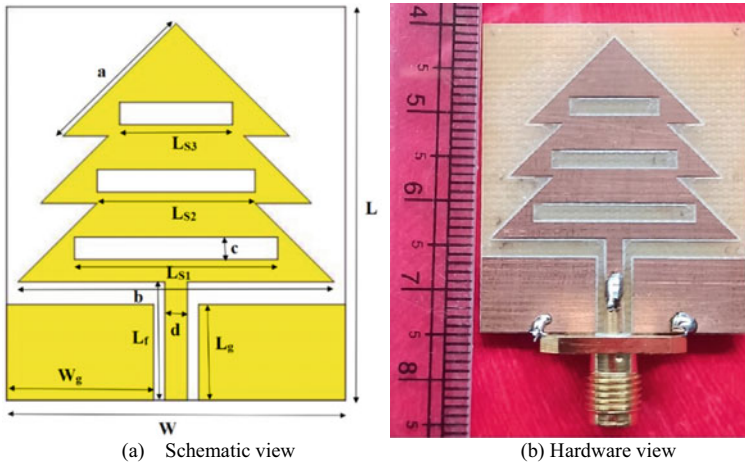
(a) Schematic view   (b) Hardware view

Fig. 2 Schematic and Hardware prototype of the proposed antenna

Table 1 Dimensions of designed antenna

Parameters	Value (mm)	Parameters	Value (mm)
a	14.14	L_g	8.5
b	28	L_{S1}	18
c	2	L_{S2}	14
d	2	L_{S3}	10
L	35	W	30
L_f	10.5	W_g	13

3 Results and Discussions

For the simulation and optimization purpose of the proposed antenna CST microwave studio is used. In Fig 3a. reflection coefficient (S_{11}) of the simulated and measured antenna is plotted, which shows the simulated impedance bandwidth (S_{11} below $-$10 dB) is 810 MHz (3.12–3.93 GHz) and 410 MHz (5.46–5.87 GHz) and measured impedance bandwidth is 790 MHz (3.15–3.85 GHz) and 470 MHz (5.50–5.97 GHz) that gives a close matching between both fabricated and simulated results. Fig 3b shows the variation in gain and radiation efficiency with reference to frequency at resonating bands. It is perceived that maximum antenna gain is 3.5 dBi at 5.5 GHz with the gain variation between 2 and 3.5 dBi and maximum efficiency of 97% at 3.6 GHz with the efficiency variation between 80 and 97% in entire frequency range. Hence the proposed antenna can be suitable for WiMAX (3.3–3.7 GHz) and Wi-Fi (5.5–5.7 GHz) applications. Very good simulated radiation efficiency value is realized at lower band of operation; however, the gain value is comparatively lower as the antenna is monopole in nature and presented a bidirectional/omnidirectional

radiation pattern in the E/H-plane (depicted in Fig. 4). The low directive nature of the antenna makes it well fitted for receiving applications since it has a coverage of almost 360°. Gain augmentation strategies such as use of antenna array, metallic reflector, and partially reflective surfaces can be considered as future course of work.

Co-polarization and cross-polarization radiation patterns at both the resonating bands of 3.6 GHz and 5.67 GHz in both E and H-plane are presented in Fig 4, which represents the omnidirectional radiation pattern. The figure also shows that the difference between cross-polarization and co-polarization is more than 15 dB in both E and H plane, which ensures sufficient isolation among the different polarization.
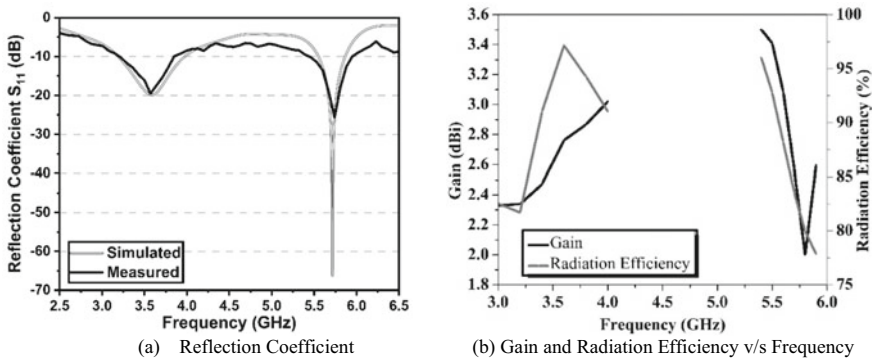

(a)   Reflection Coefficient

(b) Gain and Radiation Efficiency v/s Frequency

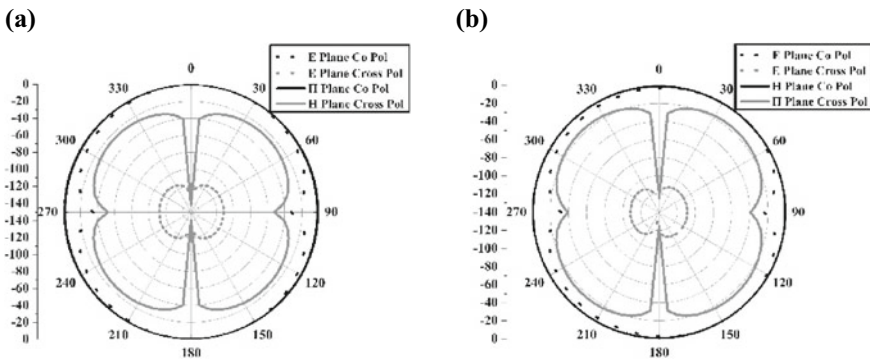**Fig. 3** Characteristic analysis of Proposed Antenna

Fig. 4 Co-Pol and Cross-Pol radiation patterns at **a** 3.6 GHz and **b** 5.67 GHz

4   Conclusion

Healthcare system in India highly requires an uninterrupted, high speed, wirelessly connected system all over the country to provide medical facilities at real time and on time, even at remote and urban locations. A simple planar antenna with two resonant modes to provide uninterrupted wireless connectivity in healthcare system is proposed having very low cost due to its design in low-cost FR4 epoxy substrate. The compact antenna size is $35 \times 30 \times 0.8$ mm^3 only, where rectangular slots of different dimensions are embedded on patch to shift the resonating frequency at the desired bands. The antenna offers 3.12–3.93 GHz (WiMAX) and 5.46–5.87 GHz (Wi-Fi) bands with gain variation between 2 and 3.5 dBi and radiation efficiency variation between 80 and 97% and nearly omnidirectional radiation pattern for both the bands. Optimization in the ground plane as well as slot dimensions is done to accomplish the required bands. Performance of the designed antenna is evaluated by simulating in CST simulator and experimentally measuring the hardware prototype which ensures its applicability for IEEE 802.16 WiMAX and IEEE 802.11n Wi-Fi (ISM) bands simultaneous connectivity in the healthcare services.

References

1. Ahmed I, Karvonen H, Kumpuniemi T, Katz M (2020) Wireless communications for the hospital of the future: requirements, challenges and solutions. Int J Wirel Inf Netw 27(1):4–17
2. https://www.statista.com/statistics/271315/age-distribution-in-india/. Last accessed 10 May 2022
3. Kasthuri A (2018) Challenges to healthcare in India-The five A's. Indian J Community Med: Off Publ Indian Assoc Prev Soc Med 43(3):141
4. Jaysawal D (2015) Rural health system in India: a review. Int J Soc Work Hum Serv Pract 29–37
5. Madanian S, Parry DT, Airehrour D, Cherrington M (2019) mHealth and big data integration: promises for healthcare system in India. BJM Health Care Inf 26(1)
6. Nair SR (2015) Relevance of health economics to the Indian healthcare system: a perspective. Perspect Clin Res 6(4):225
7. Shukla RG, Agrawal A, Shekhar V (2021) Leveraging blockchain technology for indian healthcare system: an assessment using value-focused thinking approach. J High Technol Managem Res 32(2):100415
8. Sharma P, Shivaram TR, Sharma A (2016) A methodical review of e-health system developed for Indian Healthcare sector. Indian J Sci Technol 9944:1–6
9. Zahra SR, Chishti MA (2020) A collaborative edge cloud internet of things-based framework for securing the Indian healthcare system. Int J SensS Wirel Commun Control 10(4):440–457
10. Lin Z, Ye F, Qin W, Cao X, Wang Y, Hu R, Yan R, Qin Y, Yi T, Hong Z (2016) A low-power, wireless, real-time, wearable healthcare system. In: 2016 IEEE MTT-S international wireless symposium (IWS). IEEE, pp 1–4
11. Mokhtar AM (2017) The future hospital: a business architecture view. Malays J Med Sci: MJMS 24(5):1
12. Monaghesh E, Hajizadeh A (2020) The role of telehealth during COVID-19 outbreak: a systematic review based on current evidence. BMC Public Health 20(1):1–9

13. Landers S, Madigan E, Leff B, Rosati RJ, McCann BA, Hornbake R, MacMillan R, Jones K, Bowles K, Dowding D, Lee T (2016) The future of home health care: a strategic framework for optimizing value. Home Health Care Manag Pract 28(4):262–278

14. Sharif A, Ouyang J, Yan Y, Raza A, Imran MA, Abbasi QH (2019) Low-cost inkjet-printed RFID tag antenna design for remote healthcare applications. IEEE J Electromagn, RF MicrowS Med Biol 3(4):261–268

15. Gao GP, Yang C, Hu B, Zhang RF, Wang SF (2018) A wearable PIFA with an all-textile metasurface for 5 GHz WBAN applications. IEEE Antennas Wirel Propag Lett 18(2):288–292

16. Joshi R, Hussin EFNM, Soh PJ, Jamlos MF, Lago H, Al-Hadi AA, Podilchak SK (2020) Dual-band, dual-sense textile antenna with AMC backing for localization using GPS and WBAN/WLAN. IEEE Access 8:89468–89478

17. Le TT, Yun T (2021) Y, Wearable dual-band high-gain low-SAR antenna for off-body communication. IEEE Antennas Wirel Propag Lett 20(7):1175–1179

18. Yan S, Soh PJ, Vandenbosch GA (2015) Wearable dual-band magneto-electric dipole antenna for WBAN/WLAN applications. IEEE Trans Antennas Propag 63(9):4165–4169

19. Kumar S, Dixit AS, Malekar RR, Raut HD, Shevada LK (2020) Fifth generation antennas: a comprehensive review of design and performance enhancement techniques. IEEE Access 8:163568–163593

20. Dai XW, Zhou T, Cui GF (2015) Dual-band microstrip circular patch antenna with monopolar radiation pattern. IEEE Antennas Wirel Propag Lett 15:1004–1007

21. Li Y, Zhao Z, Tang Z, Yin Y (2019) Differentially fed, dual-band dual-polarized filtering antenna with high selectivity for 5G sub-6 GHz base station applications. IEEE Trans Antennas Propag 68(4):3231–3236

22. Kundu S, Jana SK (2017) A compact planar CPW fed monopole antenna for Ultra-Wideband applications. In: 2017 14th IEEE India council international conference (INDICON). IEEE, pp 1–4

23. Pachigolla SY, Dab V, Chatterjee A, Kundu S (2018) A compact rectangular microstrip patch antenna for 2.4 GHZ ISM band applications. In 2018 IEEE Indian conference on antennas and propogation (InCAP). IEEE, pp 1–3

24. Kumar V, Kumar P, Kundu S (2021) A novel NIT Sikkim's logo shaped compact multiband slot antenna. In: 2021 IEEE Indian conference on antennas and propagation (InCAP). IEEE, pp 179–182

25. Kundu S, Kundu S (2021) A compact U-shaped antenna with bandwidth enhancement for ultra-wideband communication. In: 2021 2nd international conference on range technology (ICORT), pp 1–4

26. Sabban A (2020) Small new wearable metamaterial antennas for IoT, medical and 5G applications. In: 2020 14th European conference on antenna and propagation (EuCAP). IEEE, pp 1–5

27. Velan S, Sundarsingh EF, Kanagasabai M, Sarma AK, Raviteja C, Sivasamy R, Pakkathillam JK (2014) Dual band EBG integrated monopole antenna deploying fractal geometry for wearable applications. IEEE Antennas Wirel Propag Lett 14:249–252

28. Chen YS, Ku TY (2015) A low profile wearable antenna using a miniature high impedance surface for smartwatch applications. IEEE Antennas Wirel Propag Lett 15:1144–1147

29. Ali SM, Sovuthy C, Imran MA, Socheatra S, Abbasi QH, Abidin ZZ (2020) Recent advantages of wearable antenna in material, fabrication methods, design, and their applications: state of the art. Micromachines 11(10):888

30. Moradi E, Koski K, Bjorninen T, Sydanheimo L, Rabaey JM, Carmena JM, Rahmat SY, Ukkonen L (2014) Miniature implantable and wearable on body antennas: Towards the new era of wireless body centric system. IEEE Antennas Propag Mag 56(1):271–291

31. Sundarsingh EF, Velan S, Kanagasabai M, Sarma AK, Raviteja C, Alsath MGN (2014) Polygon shaped slotted dual band antenna for wearable applications. IEEE Antennas Wirel Propag Lett 13:611–614

32. Puskely J, Pokorny M, Lacik J, Raida Z (2014) Wearabel disc like antenna for body centric communication at 61 GHz. IEEE Antennas Wirel Propag Lett 14:1490–1493

Hyperelastic Analysis of Adventitial Layer Using Isotropic Gent Model

Sai Kumar Siliveri, Ashok Orepalli, and Nelson Muthu

1 Introduction

In the past few decades, extensive research has been carried out on biomechanics based on continuum theories to understand human health, disease, injury, and treatments [16]. The disciplines of engineering mechanics, biology, and physiology are all brought together through this process. The study of how the fundamentals of mechanics may be utilised in the conception, design, development, and analysis of medical equipment and systems in the fields of biology and medicine is known as biomechanics. As a direct consequence of this, it is now feasible to produce medical apparatus and instruments, as well as artificial replacements and implants, as well as gadgets that are part of assistive technology for people who have impairments. As the field of biomechanics advanced, so did our understanding of how the human body works, including both healthy and diseased states, the mechanics of neuromuscular control, blood flow in the microcirculation, airflow in the lung, and the mechanics of development and shape [22]. Several mathematical models were developed with the concepts of mechanics and their postulates to derive the constitutive equations where the interrelation between structure and functional behaviour of biological materials in response to mechanical loading is investigated [8]. To a large extent, the behaviour

---

S. K. Siliveri · A. Orepalli · N. Muthu (✉)
Department of Mechanical Engineering, Indian Institute of Technology Guwahati, Guwahati, Assam, India
e-mail: nelsonm@iitg.ac.in

S. K. Siliveri
e-mail: sai176103019@iitg.ac.in

of many materials cannot be accurately modelled using linear elastic theories. Rubber is the prototypical example of such a material due to its nonlinear elastic, isotropic, incompressible behaviour. Hyperelasticity provides a paradigm for describing the stress–strain behaviour of these materials.

Hyperelastic materials are a particular type of materials that responds elastically when they are subjected to large deformation loadings. They exhibit both nonlinear material behaviour and significant changes in shape. Hyperelastic materials like rubber are widely used in a variety of structural applications spanning from automotive to aerospace. These materials experience large deformations for very small loads and preserve their original configuration without any permanent deformation after unloading. Figure 1 shows their nonlinear stress–strain response, where a linear elastic modulus is no longer adequate. As a result, it is essential to study the behaviour of these highly nonlinear materials. The properties and the behaviour of these materials were represented by the strain energy density function, which cannot be determined directly from the established behaviours like linear elastic cases. Instead, it requires knowledge of the material's behaviour. Thus, knowledge of the energy function is the key challenge where the increased deformation induces an increase in nonlinearity, which leads to complex stress-stretch relations [1].

The techniques to model the hyperelastic materials can be categorised into: (i) phenomenological and (ii) micromechanical models. The phenomenological models are the mathematical expressions for the strain energy functions that depend on the three invariants of the right Cauchy-Green deformation tensor. They are usually developed by fitting the stress–strain response plots derived from uniaxial, biaxial, and pure shear tests. On the other hand, the micromechanical or mechanistic models are the mathematical expressions derived using statistical mechanics theories, considering the physical and geometrical phenomena at the molecular level. The micromechanical models are better than the phenomenological models for analyzing unfilled rubbers [5]. Several factors must be considered while selecting a suitable constitutive model to analyze these materials. They are, (i) available experiments for various

Fig. 1 Comparison of mechanical behaviour between linear elastic and hyperelastic materials

(a) **(b)**

(c) **(d)**
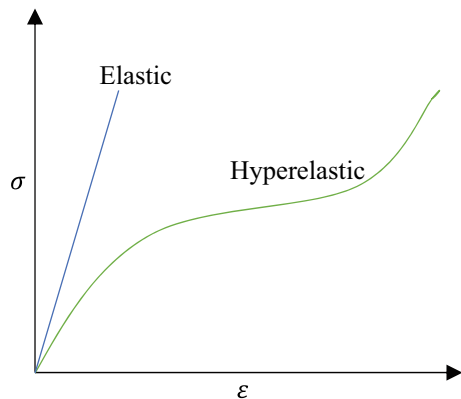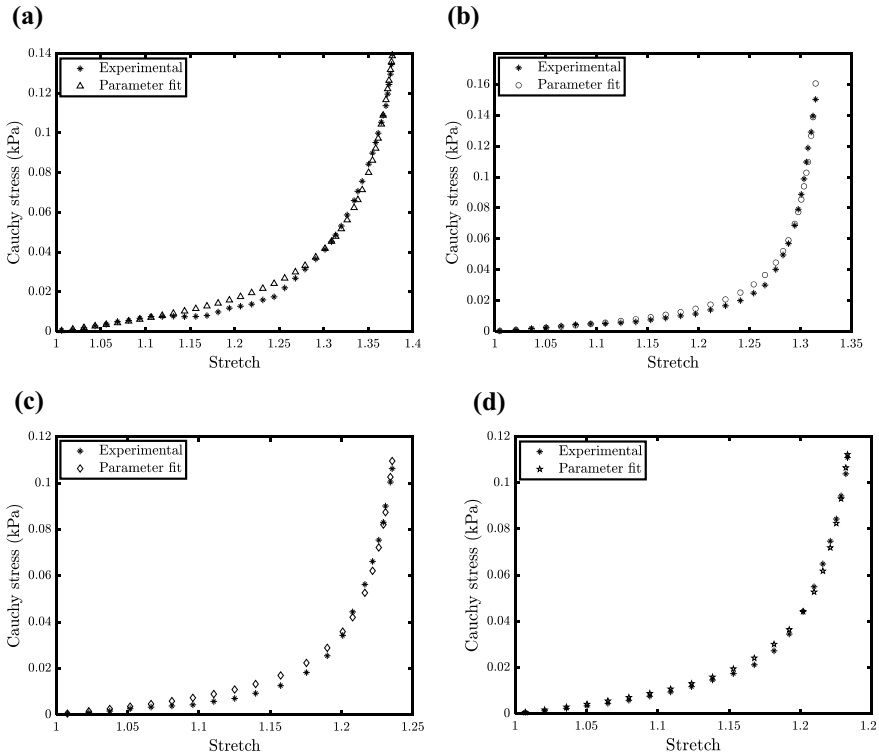
Fig. 2 Least-squares curve fitting for simple tension test of adventitia layer **a** 54 y/o male, **b** 64 y/o male, **c** 73 y/o male, and **d** 77 y/o male

loading like uniaxial, biaxial, and pure shear conditions, (ii) maximum stretch at critical loads, and iii) possibly less number of material coefficients that are physically interpretable.

Soft biological tissues have interested numerous researchers because of their enormous deformations and nonlinear elastic behaviour. Many different cell types, an extracellular matrix, and a lot of water make up soft biological tissue. The tissue's homeostatic drive is activated in response to mechanical stimuli (signals) sensed by a variety of cell types, which are then translated into bioelectrical and biochemical signals [8]. Changes in conformational molecules may elicit responses from certain cells. But macroscopic continuum variables like stress and strain will still be valuable for attributing tissue adaptation to a particular mechanical stimulus [17]. Several mathematical models in the form of strain energy functions representing the hyperelasticity theories have been developed to capture these behaviours in tissues like skin, brain, tendons, ligaments, blood vessels, etc. Many soft tissues have different behaviours where the same strain energy function will not suit all. For example, collagen-rich soft tissues are generally incompressible and have a substantial strain-stiffening response. As a consequence of this, the majority of the currently available

models for these tissues start with a functional form that upholds these particular characteristics while yet being generic enough to be customised for individual systems. On the other hand, the microstructure of brain tissue is not regulated by collagen and elastin fibres, therefore it does not have the strain-stiffening behaviour. The nonlinear stress-stretch response that was predicted using Ogden-type hyperelastic incompressible isotropic models was in good agreement with the actual data for both uniaxial and biaxial loadings when it came to brain and adipose tissues [3, 4, 6, 23]. It was found from the nonlinear least-square fitting that the relative error with the experimental data is comparatively less by using the higher order terms over the lower order. Though the Ogden material model is the most popular among others due to its accuracy in producing the results, it requires more number of material coefficients to approximate the experimental data, making the users look after the other model [20]. So it is essential to understand the family of models and their properties that help choose an appropriate constitutive model to predict the biomaterial's behaviour or to develop a new one.

The study on the mechanical behaviour of the adventitia, the outermost layer of the blood vessels comprised of collagen-rich fibers, has been paid very little attention in research. The main function of the adventitia is to restrain the blood vessel from excessive deformation under tension and recoil [19]. Generally, classical hyperelastic models like Neo-Hookean and Mooney-Rivlin fail to predict this severe stiffening response, and models proposed by Arruda-Boyce and Ogden require more number of material parameters to achieve the exact behaviour of biological tissues acquired through experiments [15, 24], Mihai et al. [21]. References [12, 13] proposed the anisotropic strain energy function where collagen fibres were assumed as perfectly aligned. This model is effective for the media but does not account for the behaviour of the intima and adventitia, which have high fibre dispersion. There are some models to capture the strain-stiffening phenomena, out of which Gent [9] is the simplest of all. The mathematical brevity of the Gent model with just two constitutive coefficients facilitates the analytical closed-form solution for a range of various boundary value problems relevant to soft biological tissues.

In this work, the uniaxial tensile behaviour of the adventitia layer of different ages collected from [14] is used to find the coefficients of the Gent model through the least-squares technique. Furthermore, assuming the adventitia layer as a cube, simple case studies are performed, and the analytically predicted uniaxial stress versus stretch responses are compared with the experimental data. The article is organised as follows. In Sect. 2, the constitutive relations for the hyperelastic material are described. The importance of the right Cauchy-Green tensor, which is expressed in terms of the deformation gradient, is presented. The three invariants of the right Cauchy-Green deformation tensors expressed in principal stretches have become the foundation for the Gent model comprising first and third reduced invariants, presented in Sect. 3. Section 4 outlines a procedure to identify the material parameters of the Gent model from the Cauchy stress vs stretch plots of patients of different ages. The results obtained by the present approach and its comparison with the reference results are discussed in Sect. 5. This is followed by the conclusions in the last section.

2 Constitutive Relation for Hyperelastic Materials

The elastic body, when subjected to various forces (body forces, traction, point loads, etc.) and displacements, changes its geometry from undeformed to deformed state, i.e., from the initial to the current configuration. The material points in the reference configuration, represented by X, are mapped onto the spatial points in the deformed/Eulerian configuration, denoted by x, and expressed as,

$$
\begin{aligned}
x_1 &= x_1(X_1, X_2, X_3) \\
x_2 &= x_2(X_1, X_2, X_3) \\
x_3 &= x_3(X_1, X_2, X_3) \\
&\text{or,} \\
x &= \varphi(X, t)
\end{aligned}
\tag{1}
$$

where φ represents the mapping function. The above equation states that each material point in the initial/Lagrangian configuration has a unique spatial point in the current/Eulerian configuration. Equation (1) can also be written as,

$$
x = X + u(X, t)
\tag{2}
$$

where $u(X, t)$ is the displacement of a material point. The variation of the vector field, i.e., from reference to a deformed configuration via infinitesimal line segments (dX and dx) of a solid body, is measured by the concept of the deformation gradient. The line segment, which is straight in the reference configuration, will also be (nearly) straight in the current geometry. Therefore, the infinitesimal line segments are stretched and rotated by deformation even though the body is subject to large deformations [2]. The line segments dX and dx are associated by

$$
dx = F dX \text{ or, } F = \frac{\partial x}{\partial X}
\tag{3}
$$

Substituting Eq. (2) in Eq. (3), the deformation gradient (F) can be expressed as

$$
F = 1 + \frac{\partial u}{\partial X} = 1 + \nabla_0 u
\tag{4}
$$

here ∇_0 represents the gradient operator in the reference/Lagrangian configuration. In the large deformation theories such as hyperelasticity, the strain energy density plays a prominent role where, unlike the linear elastic materials, constitutive relations derived from the strain energy density functions (SEF) are not always the same while capturing the nonlinear nature of various materials. Due to its similar properties in all directions, the SEFs of isotropic materials are independent of the reference frames. It

follows naturally that the SEFs can be expressed in terms of the right Cauchy-Green deformation tensor's (C) invariants.

$$W = f(I_1, I_2, I_3) \tag{5}$$

The basic representation of strain energy density is provided by

$$W = \sum_{i+j+k=1}^{\infty} A_{ijk}(I_1 - 3)^i (I_2 - 3)^j (I_3 - 1)^k \tag{6}$$

where I_1, I_2 and I_3 are the three invariants of C. They are expressed in terms of principal stretch ratios λ_1, λ_2 and λ_3.

$$F = \begin{bmatrix} \lambda_1 & 0 & 0 \\ 0 & \lambda_2 & 0 \\ 0 & 0 & \lambda_3 \end{bmatrix} \tag{7}$$

$$C = F^T F \tag{8}$$

$$\begin{aligned} I_1 &= tr(C) = \lambda_1^2 + \lambda_2^2 + \lambda_3^2 \\ I_2 &= \frac{1}{2}\left[(trC)^2 - tr(C^2)\right] = \lambda_1^2\lambda_2^2 + \lambda_2^2\lambda_3^2 + \lambda_3^2\lambda_1^2 \\ I_3 &= \det C = \lambda_1^2\lambda_2^2\lambda_3^2 \end{aligned} \tag{9}$$

In general, hyperelastic materials are thought to be incompressible, representing $I_3 = 1$ and leaving W as a function of the first two invariants. Thus, $W(I_1, I_2)$ is the energy that deals only with the change in the shape of the system. Incompressibility (Poisson's ratio ~0.5) is the ideal condition that makes the material models achieve the closed-form solutions, i.e., stress-stretch relations. Nonetheless, in practice, hyperelastic materials such as rubbers, biological tissues, etc., are nearly incompressible, with Poisson's ratios ranging from 0.49 to 0.4999. Thus, the system experiences tiny volume changes for nearly incompressible conditions for significant hydrostatic pressures. The material is relatively rigid in dilatation but soft in distortion, thus, substantial form changes occur under external force. Splitting them apart at the level of strain energy density is essential. As a result, it is required to split these two components at the level of strain energy density [18]. On the other hand, even though the invariants I_1 and I_2 were addressed in relation to the deviatoric portion of Eq. (6), they also change throughout the dilatation. Therefore, the additive decomposition of the strain energy density function is expressed as

$$\widehat{W} = \widehat{W}_{dev}(\overline{I}_1, \overline{I}_2) + \widehat{W}_{vol}(J) \tag{10}$$

where $\overline{I}_1$, $\overline{I}_2$ and J are the reduced invariants which are responsible for the separation of the deviatoric part from the volumetric. They are defined as

$$\overline{I}_1 = I_1 \Big/ I_3^{\frac{1}{3}}, \ldots \overline{I}_2 = I_2 \Big/ I_3^{\frac{2}{3}}, \ldots J = \sqrt{I_3} \tag{11}$$

Many hyperelastic material models exist and are classified into phenomenological, mechanistic, and hybrid types used to model mechanical behaviour. They include (a) Phenomenological models: Ogden, Yeoh, Fung (b) Mechanistic models: Arruda-Boyce, Neo-Hookean (c) Hybrid models: Gent, Van der Waals. The simplest of the hyperelastic material models is the Saint Venant–Kirchhoff model, a nonlinear geometric extension of linear elastic material. Some of the most commonly used hyperelastic models are Neo-Hookean, Mooney-Rivlin, and Ogden.

3 Gent Model

Strain-stiffening is a phenomenon where the deformation locks up for a finite value of the principal stretch, due to which the stress versus stretch curves experience a rapid rise during uniaxial tensile tests [15]. Severe stiffening responses were commonly observed for moderate stretches in soft biological tissues [11]. Commonly used hyperelastic models fail to reflect the same. Many phenomenological models are proposed exclusively to capture the strain-stiffening effect, and Gent is the simplest among them.

Alan Gent [9] proposed a simple strain energy function with only two parameters. Though empirical, it can predict the severe stiffening responses of non-crystallising rubber and various biological tissues. The strain energy function is given as:

$$W = -\frac{\mu}{2} J_m \ln\left(1 - \frac{I_1 - 3}{J_m}\right), \ I_1 < J_m + 3 \tag{12}$$

where μ represents shear modulus and the parameter J_m measures the maximum strain value. J_m typically, ranges from 30 to 100 for rubber-like materials, while the biological tissues have much smaller values (Eg: $\approx$0.4 to 2.3 for arterial wall tissue) [10]. For nearly incompressible materials, the above equation is expressed in the form of deviatoric and volumetric strain energies as [7]:

$$\widehat{W} = -\frac{\mu}{2} J_m \ln\left(1 - \frac{\overline{I}_1 - 3}{J_m}\right) + \frac{K}{2}\left(\frac{1}{2}(J^2 - 1) - \ln J\right) \tag{13}$$

where K represents the bulk modulus that imposes the near incompressibility.

In the field of solid mechanics, stress is one of the most important quantities. As with strain, the components of the stress tensor are context-dependent. Depending

on the frame of reference chosen, stresses may be defined differently. The usual definition of stress is a force acting on a tiny region. In linear analysis, the assumption of infinitesimal deformation eliminated the need to distinguish between deformed and undeformed areas. When deformation is severe, however, it is essential to indicate the area used to quantify stress. Whereas the second Piola-Kirchoff stress (S) is defined with respect to the undeformed configuration, it does not give any physical insight. The Cauchy stress, also known as the actual stress, is the fundamental and most often used stress measure. It is defined by doing an analysis of the forces operating on a very small portion of the surface area of the deformed body. The internal force exerted by the current configuration may be measured with the use of the Cauchy stress tensor. The constitutive relation that derives the S by the differentiation of the SEF with respect to the Green Lagrangian strain (E) is given by

$$S = \frac{\partial \widehat{W}}{\partial E} \tag{14}$$

$$S = -\frac{\mu J_m}{2} \left(\frac{1}{1 - \frac{\overline{I_1}-3}{J_m}} \right) \left(-\frac{1}{J_m} \right) \left(\frac{\partial \overline{I_1}}{\partial E} \right) + \frac{K}{2} \left(J - \frac{1}{J} \right) \left(\frac{\partial J}{\partial E} \right) \tag{15}$$

$$\frac{\partial \overline{I_1}}{\partial E} = 2J^{-\frac{2}{3}} I - \frac{2}{3} \overline{I_1} C^{-1}$$

$$\frac{\partial J}{\partial E} = J C^{-1} \tag{16}$$

Substituting Eqs. (16) in (15) gives

$$S = \frac{\mu J_m}{2} \left(\frac{1}{J_m - (\overline{I_1} - 3)} \right) \left(2J^{-\frac{2}{3}} I - \frac{2}{3} \overline{I_1} C^{-1} \right) + \frac{K}{2} (J^2 - 1) C^{-1} \tag{17}$$

$$\sigma = \frac{1}{J} F S F^T \tag{18}$$

where σ is defined as the Cauchy stress.

4 Parametric Identification

The closed-form expression for stress derived from the SEF requires the stress versus stretch responses to fit the hyperelastic material model. Generally, the significant strain states are combinations of uniaxial tension, uniaxial compression, and pure shear. Along with these simple shear, equi-biaxial tension and volumetric compression are also considered the basic states for the incompressible materials. The uniaxial

tensile test is popular among all. The elastomers used should have dimensions much greater (at least ten times) in the loading direction than the other two to obtain the pure tensile strain state. As discussed in the previous section, the most hyperelastic materials are nearly incompressible. However, the material parameters (μ and J_m) are determined only by assuming it as a perfectly incompressible material. Following the above considerations, a one-dimensional uniaxial case is assumed where a closed-form solution for Cauchy stress as a function of the principal stretch is derived as:

For isotropic and incompressible materials,

$$\lambda_1 = \lambda, \lambda_2 = \lambda_3 = 1 \Big/ \sqrt{\lambda}$$
$$J = \lambda_1 \lambda_2 \lambda_3 = 1 \tag{19}$$
$$\bar{I}_1 = \frac{I_1}{I_3^{\frac{1}{3}}} = \frac{I_1}{J^{\frac{2}{3}}} = I_1$$

Using Eqs. (17) and (19),

$$S = \frac{2\mu}{3} \left(\frac{1}{1 - \frac{\lambda^2 + \frac{2}{\lambda} - 3}{J_m}} \right) \left(1 - \frac{1}{\lambda^3} \right) \tag{20}$$

Therefore, from Eq. (18),

$$\sigma = FSF^T = \frac{2\mu}{3} \left(\frac{1}{1 - \frac{\lambda^2 + \frac{2}{\lambda} - 3}{J_m}} \right) \left(1 - \frac{1}{\lambda^3} \right) \lambda^2 \tag{21}$$

Identifying the material parameters, which entails fitting one or more experimentally determined uniaxial stress-stretch data, can be accomplished with effective use of the analytical solution proposed in Eq. (21). The natural expression to minimise the deviation between calculated and experimental data is given as:

$$\min(A) = \sum_{m=1}^{n} \left(\sigma(\lambda, A) - \sigma_m^{exp} \right)^2 \tag{22}$$

where n is the number of stretch points and A is a set containing the parameters μ, and J_m. The equation mentioned above can be resolved using an optimisation technique or regression analysis, depending on the behaviour of the material.

5 Result and Discussions

The analytical results produced using the Gent model are only possible if the two constitutive parameters in the strain energy function are available. So firstly, these two coefficients are identified by fitting the closed-form expression of Eq. (21) with the uniaxial tensile stress-stretch responses from [14]. The experimental data collected are of the adventitia layer for various ages of male persons, each with a different primary disease provided in [14]. In this work, the material parameters, shown in Table 1 are determined using the least square technique, i.e., lsqfit in the MATLAB environment.

It can be observed from Table 1, the shear modulus does not follow any increase or decrease pattern with age. This may be due to each person's diseases and many other biological reasons. However, the limiting strain shows a decreasing trend with age. In order to study the strain stiffening phenomenon, which is the primary objective, and predict the mechanical behaviour of the material, numerous cases spanning different ages are considered.

Further, to validate the identified parameters at higher dimensions and to model the behaviour of the adventitia, an incompressible unit cube that is the representative volume element (RVE) of the adventitia layer, shown in Fig. 3, is considered. Simple case studies are performed by stretching the RVE along the x-direction. The stresses are estimated at respective principal stretches using the closed-form expression and the parameters determined above.

Figure 4 shows the model behaviour and its comparison with the experimental response. A quantitative study between the analytical and experimental data has been performed, showing L2 normalisation error of 0.1%, 0.086%, 0.081%, and 0.069% for the ages 54 y/o, 64 y/o, 73 y/o, and 77 y/o male. It can be observed from Fig. 4c, and d, i.e., for 73 y/o and 77 y/o males, the maximum stretch limits to approximately 1.2 or 20% of maximum strain, which generally comes under infinitesimal deformation in the case of metals. Gent model shows its ability to capture both the nonlinear nature and strain stiffening phenomenon even at moderate stretches. The analytical solutions are found in good agreement, qualitatively and quantitatively, with the experimental data for different ages.

Table 1 Constitutive parameters of adventitia layer for different ages

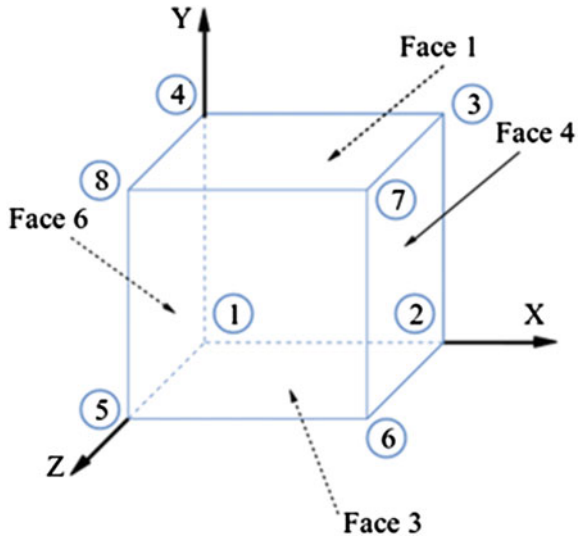| Material parameters	54 y/o male	64 y/o male	73 y/o male	77 y/o male
Shear modulus (μ)	0.0306	0.0231	0.0321	0.0394
Limiting strain (J_m)	0.4208	0.2756	0.1689	0.1709

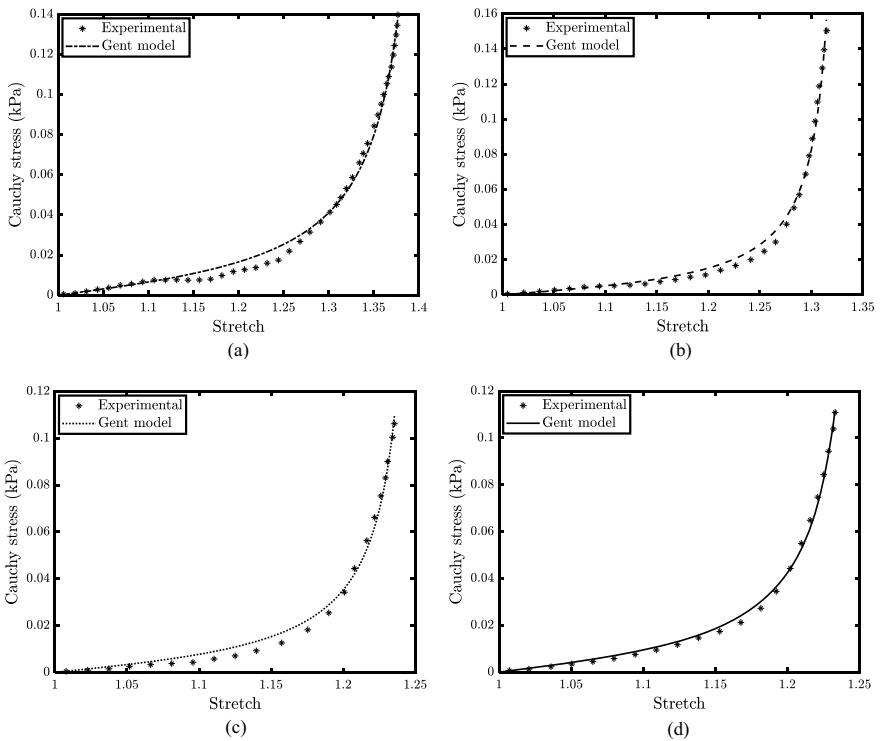**Fig. 3** Incompressible unit cube RVE

Fig. 4 Comparison between analytical and experimental stress-stretch responses for **a** 54 y/o male, **b** 64 y/o male, **c** 73 y/o male, and **d** 77 y/o male

6 Conclusions

In the present work, the uniaxial tensile behaviour of the adventitia layer of different ages was used to determine the parameters of the Gent model through the nonlinear least-squares technique. A cubic representative volume element (RVE) of the adventitia layer was considered, and simple uniaxial case studies were presented. The analytically predicted uniaxial stress versus stretch responses was in good agreement with the experimental data for four different aged male persons. It was observed that the mechanoresponsive behaviour—the strain stiffening effect increases, thereby decreasing the elastic compliance for a relatively aged person. Based on this data, customised vascular implants whose properties are similar to the adventitial layer can be developed for diseased patients.

References

1. Beda T (2007) Modeling hyperelastic behavior of rubber: a novel invariant-based and a review of constitutive models. J Polym Sci, Part B: Polym Phys 45(13):1713–1732. https://doi.org/10.1002/POLB.20928
2. Bower AF (2009) Applied mechanics of solids. Appl Mech Solids 1–795. https://doi.org/10.1201/9781439802489/APPLIED-MECHANICS-SOLIDS-ALLAN-BOWER
3. Budday S, Sommer G, Birkl C, Langkammer C, Haybaeck J, Kohnert J, Bauer M, Paulsen F, Steinmann P, Kuhl E, Holzapfel GA (2017) Mechanical characterization of human brain tissue. Acta Biomater 48:319–340. https://doi.org/10.1016/J.ACTBIO.2016.10.036
4. Comley K, Fleck N (2012) The compressive response of porcine adipose tissue from low to high strain rate. Int J Impact Eng 46:1–10. https://doi.org/10.1016/J.IJIMPENG.2011.12.009
5. Dal H, Kemal A, Badienia Y (2021) On the performance of isotropic hyperelastic constitutive models for rubber-like materials: a state of the art review. Appl Mech Rev 73(2). https://doi.org/10.1115/1.4050978/1108153
6. Destrade M, Gilchrist MD, Murphy JG, Rashid B, Saccomandi G (2015) Extreme softness of brain matter in simple shear. Int J Nonlinear Mech 75:54–58. https://doi.org/10.1016/J.IJNONLINMEC.2015.02.014
7. Dill EH (2006) Continuum mechanics : elasticity, plasticity, viscoelasticity. https://doi.org/10.1201/9781420009828
8. Gasser TC, Ogden RW, Holzapfel GA (2005) Hyperelastic modelling of arterial layers with distributed collagen fibre orientations. J R Soc Interface 3(6):15–35. https://doi.org/10.1098/RSIF.2005.0073
9. Gent AN (1996) A new constitutive relation for rubber. Rubber Chem Technol 69(1):59–61. https://doi.org/10.5254/1.3538357
10. Goriely A, Destrade M, Ben Amar M (2006) Instabilities in elastomers and in soft tissues. Q J Mech Appl Math 59(4):615–630. https://doi.org/10.1093/QJMAM/HBL017
11. Holzapfel GA (2005) Similarities between soft biological tissues and rubberlike materials. In: Constitutive models for rubber IV—proceedings of the 4th European conference for constitutive models for rubber, ECCMR, pp 607–617. https://doi.org/10.1201/9781315140216-105/SIMILARITIES-SOFT-BIOLOGICAL-TISSUES-RUBBERLIKE-MATERIALS-HOLZAPFEL

12. Holzapfel GA, Gasser TC (2001) A viscoelastic model for fiber-reinforced composites at finite strains: continuum basis, computational aspects and applications. Comput Methods Appl Mech Eng 190(34):4379–4403. https://doi.org/10.1016/S0045-7825(00)00323-6

13. Holzapfel GA, Gasser TC, Ogden RW (2000) A new constitutive framework for arterial wall mechanics and a comparative study of material models. J Elast Phys Sci Solids 61(1):1–48. https://doi.org/10.1023/A:1010835316564

14. Holzapfel GA, Sommer G, Gasser CT, Regitnig P (2005) Determination of layer-specific mechanical properties of human coronary arteries with nonatherosclerotic intimal thickening and related constitutive modeling. Am J Physiol-Hear Circ Physiol 289(5 58–5):2048–2058. https://doi.org/10.1152/AJPHEART.00934.2004/ASSET/IMAGES/LARGE/ZH40110562720007.JPEG

15. Horgan CO (2015) The remarkable Gent constitutive model for hyperelastic materials. Int J Nonlinear Mech 68:9–16. https://doi.org/10.1016/J.IJNONLINMEC.2014.05.010

16. Humphrey JD (2003).Review paper: continuum biomechanics of soft biological tissues. Proc R Soc London Ser A: Math, Phys Eng Sci 459:3–46. https://doi.org/10.1098/RSPA.2002.1060

17. Kilpatrick D, Woodruff GW, Sakaguchi Y, Bassiouny HS, Glagov S (2001) Stress, strain, and mechanotransduction in cells. J Biomech Eng 123(6):638–641. https://doi.org/10.1115/1.1406131

18. Kim NH (2015) Introduction to nonlinear finite element analysis. In: Introduction to nonlinear finite element analysis, pp 1–430. https://doi.org/10.1007/978-1-4419-1746-1

19. Maleszewski JJ, Lai CK, Veinot JP (2016) Anatomic considerations and examination of cardiovascular specimens (Excluding Devices). Cardiovasc Pathol: Fourth Ed 1–56. https://doi.org/10.1016/B978-0-12-420219-1.00001-X

20. Mihai LA, Budday S, Holzapfel GA, Kuhl E, Goriely A (2017) A family of hyperelastic models for human brain tissue. J Mech Phys Solids 106:60–79. https://doi.org/10.1016/J.JMPS.2017.05.015

21. Mihai LA, Chin L, Janmey PA, Goriely A (2015) A comparison of hyperelastic constitutive models applicable to brain and fat tissues. https://doi.org/10.1098/rsif.2015.0486

22. Özkaya N, Leger D, Goldsheyder D, Nordin M (2012) Fundamentals of biomechanics. https://link.springer.com/content/pdf/bfm%253A978-1-4757-3067-8%252F1.pdf

23. Rashid B, Destrade M, Gilchrist MD (2014) Mechanical characterization of brain tissue in tension at dynamic strain rates. J Mech Behav Biomed Mater 33(1):43–54. https://doi.org/10.1016/J.JMBBM.2012.07.015

24. Wex C, Arndt S, Stoll A, Bruns C, Kupriyanova Y (2015) Isotropic incompressible hyperelastic models for modelling the mechanical behaviour of biological tissues: a review. Biomed Tech 60(6):577–592. https://doi.org/10.1515/BMT-2014-0146/XML